A.I.Ch.E. JOURNAL

CONTENTS

A.I.Ch.E. JOURNAL

MARCH, 1959 ● VOL. 5, NO. 1

*The Culture Vulture**

A recent article in *The Times Educational Supplement* discussed an experiment at Liverpool which indicated that, on the whole, a group of arts graduates from Liverpool University tended to know more about personalities in the arts and sciences than science graduates from the same university.

In this experiment the best individual performance was given by a chemist. It is a temptation to suggest that this confirms our own belief that chemists need to have very good mental filing systems. Being in possession of a good mental filing system such a person is then able to store up a vast assembly of facts which may have no particular relevance to his specialisation.

If we pick a group of people with roughly comparable mental filing systems and ask them a number of factual questions the answers given by individuals will depend upon the material stored in the filing system. This material will, in turn, have entered the system either from outside influences such as educational organisations, or will have been absorbed during the personal reading or experiences of the individual. Therefore, if one person is able to answer questions on subjects taken from many fields of knowledge with greater accuracy than another person it might be permissible to suggest that the first man has a wider educational background.

This idea of a wider educational background seems to be associated with the subject of culture values. Many people take it for granted that a nodding acquaintance with Molière is more respectable than a detailed knowledge of our most practical inheritance from Mendeleev.

If we may be stubborn for a moment, or obtuse, what conclusions should be drawn from the answers to our own experimental questions? In our test we blend carefully questions on cookery and stamp collecting. We find that one group of people gives better answers on cookery, while the other group gives better answers on stamp collecting, and that the group which gives better answers on stamp collecting manages to obtain better marks overall. What does this suggest about values? In our humble way we should prefer the people who know more about cooking. But a further experiment is immediately suggested. Can they cook?

Now it happens that most graduates in science from British universities undergo practical tests in their subject. For example chemists are required to isolate and identify substances. Do the arts graduates go through a similar practical training? Are they examined in their practical ability? Perhaps three hours would be a fair time to compose a sonnet, given the subject? For a full day of practical examination we suggest the composition of a sestina and a tanka. Already it might seem to the chemist that we are letting our arts graduate off too easily. To the chemical engineer the sights have obviously been set too low.

The chemical engineer has either to take a suitable design paper at university or to pass the Home paper of the I.Chem.E. What is the comparable standard for the arts man? For the English graduate to demonstrate his ability we might suggest questions such as: prepare all the editorial matter for the first copy of a new journal for women, to be called *Mum*; compose a shooting script for a modern version of the "Iliad" in which Marilyn Monroe plays the part of Helen—Ithaca is, of course, in New York State. For a graduate in French an equivalent problem might be: write the complete text of a television play (in French, naturellement) based on an existentialist triangle in Dudley Zoo.

From time to time scholars and others have suggested that one of the great features of the Tudor Elizabethan period was the men who combined intellect and action. Any courtier in those days was expected to be able to throw off a neatly turned verse without hesitation.

For some reason or another it is argued today that scientists tend to be lacking in culture. On the whole it is the scientists who are adding to our culture, yet it is suggested that they should take so-called cultural subjects in their examinations; on them is the blame and the burden.

Might it not be suggested that the great majority of our arts graduates are illiterate? By all means let them advocate cultural subjects for scientists—even science questions for arts men, but is it really creative?

We shall begin to believe that arts men are serious about culture when instead of preserving our heritage they accept the obligation to extend the limits of our culture by practical creation. For too long the high spots of university teaching in the arts subjects have been concerned with criticism, which in turn has led to the sterile contemplation of a vast navel of existing texts and texts about texts. Like Shelley, our vote is for those "whose transmitted effluence cannot die."

Fugacities in High-Pressure Equilibria and in Rate Processes

J. M. PRAUSNITZ

University of California, Berkeley, California

This work considers the importance of vapor-phase nonideal mixing in high-pressure equilibrium and rate-process calculations. New techniques are presented for calculating vapor-phase fugacity coefficients in nonideal mixtures.

The equilibrium properties of gaseous mixtures are represented by a virial equation of state which is adequate for the vast majority of chemical engineering problems. Techniques based on an extension of the corresponding-states theory are given for estimating the various coefficients appearing in the equation of state; these estimates appear to be reliable for a large variety of nonpolar or weakly polar systems. Techniques based on the theory of intermolecular forces are also presented for polar systems and for a limited class of mixtures containing hydrogen-bonding components. The proposed methods of calculation are illustrated by a large variety of problems occurring in common chemical engineering calculations, and it is shown that failure to correct for vapor-phase nonideal mixing can, in some cases, lead to very large errors.

The fugacity of a component in a vapor-phase mixture is needed in numerous chemical engineering computations $(2, 4)$. In simple cases the fugacity is equal to the partial pressure, but generally it is necessary to apply corrections for the nonideality of mixing as well as for the nonideality of the pure vapor. These two corrections are conveniently expressed in terms of one fugacity coefficient ϕ. In many common problems it is correct to assume that ϕ will not differ appreciably from unity unless the total pressure is at least moderately large; in some special cases, however, large deviations from ideality may occur even at a total pressure much less than 1 atm. This paper presents new techniques for calculating vapor-phase activity coefficients and through a variety of applications shows their relevance to typical chemical engineering problems.

RELATIONSHIP BETWEEN FUGACITIES AND VOLUMETRIC PROPERTIES IN MIXTURES

The fugacity coefficient of a component is defined (27) as the ratio of that component's fugacity in the mixture to its partial pressure. It is given precisely by

$$\ln \phi_i \equiv \ln \frac{\bar{f}_i}{y_i P}$$
$$= \frac{1}{RT} \int_0^p \left(\bar{V}_i - \frac{RT}{P} \right) dP \qquad (1)$$

An alternate expression for the fugacity of a component in a mixture is given in terms of an activity coefficient (15), which measures the deviation from the Lewis fugacity rule. This activity coefficient is defined by

$$\ln \gamma_i \equiv \ln \frac{\bar{f}_i}{y_i f_i^0}$$
$$= \frac{1}{RT} \int_0^p (\bar{V}_i - V_i^0) \, dP \qquad (2)$$

The relation between γ_i and ϕ_i is simply

$$\phi_i = \gamma_i \phi_i^0 \qquad (3)$$

The two coefficients ϕ and γ each have definite advantages and disadvantages. The latter is more useful when the component under consideration is a gas rather than a vapor; in that case γ usually does not differ greatly from unity and in fact obeys the limiting relation

$$\lim_{y_i \to 1} \gamma_i \to 1 \qquad (4)$$

Another way of expressing the advantage of γ is to say that the Lewis fugacity rule $(\gamma = 1)$ is always a very good approximation for a component present in excess. A corresponding statement for ϕ can unfortunately not be made. A relation for ϕ analogous to Equation (4) is valid only at very low pressures.

However if the component under consideration is a vapor, it is advantageous to use the coefficient ϕ. For a vapor the fugacity in the pure state f^0 has physical significance only at pressures up to the vapor pressure of that component since the pure vapor cannot exist at higher pressures. The coefficient γ therefore, as indicated by Equation (2), has physical significance only under restricted conditions and is not convenient for condensable components.

EQUATIONS OF STATE FOR GAS MIXTURES

Numerous equations of state have been proposed for pure gases (8). As almost all are empirical or at best semiempirical in nature, it has not been possible to make an accurate assessment of the physical meaning which is associated with the various constants. It is this deficiency of equations of state for pure gases which has made it difficult to extend them to gas mixtures. Various empirical rules have been suggested for predicting the constants of a mixture from the constants of the pure components (8), but while some of these give good results in specific cases, they are generally not reliable. All mixing rules which relate the constants of a mixture to those of the pure components must in some way reflect the nature of the intermolecular forces acting between unlike molecules. These forces are sufficiently complex to render any particular mixing rule valid for only a restricted class of mixtures. Although the mixing rules that are recommended by Benedict give good results for mixtures of paraffinic and olefinic hydrocarbons (1), they are unsatisfactory for hydrocarbon mixtures containing aromatic components and have been shown to fail badly for a mixture of carbon dioxide and propane (5).

The material presented in this work indicates that for the vast majority of chemical engineering problems the virial equation is the most suitable equation of state for fugacity calculations in mixtures. At very high densities the virial equation is not useful, since a large number of virial coefficients are required, but at pressures and temperatures commonly encountered in chemical engineering work the virial equation is both adequate and convenient. This equation can be written in either a pressure- or a volume-explicit form. While the latter has some computational advantages, it is the pressure-explicit form which is more suitable for this work, since it requires a smaller number of terms and its

coefficients have theoretical significance. It is given by

$$z = \frac{P}{RT} = 1 + B\rho$$

$$+ C\rho^2 + D\rho^3 + \cdots \quad (5)$$

B, C, and D are respectively the second, third, and fourth virial coefficients, which are functions of temperature and composition but not of density or pressure. When terminated after the third virial coefficient Equation (5) is valid up to almost the critical density and frequently beyond it, and if the series is terminated after the second virial coefficient, it is reliable up to about one half of the critical density.

Calculation of fugacity coefficients as indicated by the integral in Equation (1) requires a volume-explicit equation of state. Since Equation (5) is pressure-explicit, it is necessary to make a change of the independent variable, and it can be shown (28) that ϕ_i is related to the volumetric properties by

$$\ln \phi_i = \frac{1}{RT} \int_V^\infty \left[\left(\frac{\partial P}{\partial n_i} \right)_{T,V,n_j} - \frac{RT}{V} \right] dV - \ln z \quad (6)$$

VIRIAL COEFFICIENTS

Equation (5) can be derived by the methods of statistical thermodynamics (11) wherein the physical significance of the virial coefficients is related to the intermolecular forces. The temperature dependence of the virial coefficients can be found by calculations based on a suitable potential-energy function, but for most chemical engineering purposes it is much more convenient to use generalized plots or empirical equations within the framework of the theory of corresponding states. The concentration dependence of the virial coefficients however follows directly from their physical significance, and it is because of this feature that the virial equation is so valuable in calculating fugacities in gas-phase mixtures. Since each virial coefficient reflects the forces corresponding to the interaction of a particular number of molecules, it has been shown (12, 20) that the nth virial coefficient is a polynomial of nth degree in the mole fraction. Thus the second virial coefficient of a mixture (B_m) is a quadratic function of the mole fraction; the third virial coefficient of a mixture (C_m) is a cubic function, etc.

$$B_m = \sum_i^n \sum_j^n y_i y_j B_{ij} \quad (7)$$

$$C_m = \sum_i^n \sum_j^n \sum_k^n y_i y_j y_k C_{ijk} \quad (8)$$

Whereas the virial coefficients B_m and C_m are functions of both temperature

and composition, the various coefficients on the right side of Equations (7) and (8) are functions only of the temperature.

Much information (13) is available on the second virial coefficients of numerous gases, and a limited amount (24) is now known about the third virial coefficient; almost nothing is known about the fourth and higher virial coefficients. For all practical purposes therefore the series in Equation (5) must be cut off after the third term.

Equations (7) and (8), respectively, give the composition dependence of the second and third virial coefficients. When these equations are substituted into Equation (5) and the result is further substituted into Equation (6), the final result is

$$\ln \phi_i = 2\rho \sum_i^n y_i B_{ii}$$

$$+ \frac{3}{2} \rho^2 \sum_i^n \sum_k^n y_i y_k C_{iik} - \ln z \quad (9)$$

Equation (9) is an exact expression for the fugacity coefficient subject only to the restriction that the density be sufficiently small to permit neglect of terms involving the fourth and higher virial coefficients. For numerous chemical engineering problems (except those at very high densities) Equation (9) is the most suitable now available. Some applications of this equation are given later.

ESTIMATION OF VIRIAL COEFFICIENTS

Reliable volumetric studies have been reported for only a limited number of mixtures. However a considerable body of results is available for pure gases, and with the help of existing theory of intermolecular forces it is possible in many cases to make good estimates of virial coefficients for mixtures. Most experimental and theoretical work (13) has been concerned with the second virial coefficient, and at present much more is known about the second virial coefficient than about the third. Fortunately however Equation (9) is such that the fugacity coefficient is much more sensitive to the various B terms than to the C terms, and in many practical cases it is permissible to neglect the third virial coefficient entirely. Work on polar and hydrogen-bonded gases is much less plentiful than on nonpolar gases, and work on mixtures of polar gases is almost nonexistent. The initial discussion therefore excludes polar molecules. However even in systems containing polar gases fairly good estimates of virial coefficients can sometimes be made, and mixtures including one or more polar components will be considered later.

A comprehensive study of the volumetric properties of pure gases has been reported by Pitzer and associates (24, 25) who

found that the thermodynamic properties of nonpolar or weakly polar substances could be correlated within the framework of an extended theory of corresponding states by introducing an additional parameter called the *acentric factor*. However since Pitzer's work was concerned only with pure gases, his correlations can be used only for pure-gas coefficients. For the prediction of the so-called "cross coefficients", that is for those having different subscripts such as B_{ij} or C_{ijk} or C_{iik}, Pitzer's correlation by itself is insufficient.

Methods of estimating the second virial cross coefficients of simple gas mixtures have been proposed by Guggenheim and McGlashan (14), and very recently Prausnitz and Gunn (26) have shown how these methods can be modified to handle complex mixtures of a variety of nonpolar or slightly polar components. The principle of these methods lies in an extension of the theorem of corresponding states to mixtures. This extension consists of the definition of parameters which characterize the interactions responsible for the cross coefficients and which, with a suitable rearrangement of Pitzer's results for pure components, are sufficient to estimate the cross coefficients. These ideas can best be summarized by the equation below.

Second Virial Coefficients

For a pure component i the second virial coefficient B_{ii} is given by

$$\frac{B_{ii}}{V_{cii}} = \theta_B \left(\frac{T}{T_{cii}}, \omega_{ii} \right) \quad (10)$$

For a mixture the cross coefficient B_{ij} is given by

$$\frac{B_{ij}}{V_{cij}} = \theta_B \left(\frac{T}{T_{cij}}, \omega_{ij} \right) \quad (11)$$

The generalized function is tabulated in Table 1.* Estimation of B_{ij} therefore requires specification of the parameters V_{cij}, T_{cij}, and ω_{ij}.

An examination of reliable volumetric data (26) indicated that best results could be obtained by adopting a linear average for the characteristic volume and for the characteristic acentric factor; that is

$$V_{cij} = \frac{1}{2}(V_{ci} + V_{cj}) \quad (12)$$

$$\omega_{ij} = \frac{1}{2}(\omega_i + \omega_j) \quad (13)$$

The characteristic temperature T_{cij} could not be correlated in a completely general way. Instead a correction term ΔT_{cij}, characteristic of the $i - j$ interaction, was included:

*The tabulated values are based on the correlating equation of Pitzer and Curl (25). Whereas these authors used the critical temperature and pressure to obtain the reduced virial coefficients, the tabulated values shown here are reduced with the critical volume.
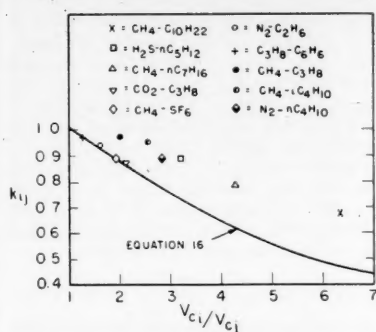
Fig. 1. Correction to the characteristic temperature

Fig. 2. Reduced third virial coefficients.

$$T_{cij} = (T_{ci} T_{cj})^{\frac{1}{2}} - \Delta T_{cij} \qquad (14)$$

For nonpolar components ΔT_{cij} is always positive and increases with the ratio V_{cii}/V_{cjj} (where component i is chosen such that $V_{cii}/V_{cjj} \geq 1$). If the ratio of critical volumes is not very much different from unity, the correction is usually negligible; only for molecules of quite different size does ΔT_{cij} become important. The correlation given by Prausnitz and Gunn makes it possible to estimate ΔT_{cij} for a large number of systems.

Another way to write Equation (14) is

$$T_{cij} = k_{ij}(T_{ci} T_{cj})^{\frac{1}{2}} \qquad (15)$$

with $k_{ij} \leq 1$, since $\Delta T_{cij} \geq 0$.

Equation (15) is an inequality indicating that the geometric mean is a maximum value; this expression follows from the London theory of dispersion forces (16). The geometric-mean rule for the critical temperatures is valid if the size of molecule i is approximately the same as that of molecule j; for molecules of different size however the geometric mean is too large. After making some simplifying assumptions one can show from the London formula that

$$k_{ij} = \left(\frac{4\beta}{(1+\beta)^2}\right)\left(\frac{2\zeta^{\frac{1}{2}}}{1+\zeta}\right) \qquad (16)$$

where

$$\beta = V_{ci}/V_{cj} \qquad (17)$$

$$\zeta = U_i/U_j \qquad (18)$$

In Equation (16) k_{ij} is always equal to or less than unity for all physically significant values of β and ζ.

It is gratifying that the analysis of experimental data as summarized by the empirically found relationship $k_{ij} \leq 1$ is in good qualitative agreement with theory; the quantitative agreement however is not very good, becoming progressively worse as β increases. Figure 1 shows a comparison between a few observed results and those calculated

from Equation (16) with ζ equal to unity, and it is evident that the theoretical expression overcorrects for molecules of very different size. This is not surprising since the London expressions are valid only for spherical monatomic molecules, and while they serve as good approximations for small polyatomic molecules, they cannot be expected to hold for such large molecules as heptane or decane. Since no convenient theory for dispersion forces of polyatomic molecules has as yet been presented, it is necessary to make empirical modifications for systems having polyatomic components of high molecular weight. In many cases it is possible to make very good estimates of the small corrections required by interpolating the results given previously (26). Where such interpolations cannot be reasonably made, it appears quite satisfactory for many nonpolar systems to use the approximate empirical relations:

for the characteristic volume

for
$$\frac{V_{ci}}{V_{cj}} > 3.0,$$
$$V_{cij} = \frac{1}{2}(0.9V_{ci} + V_{cj}) \qquad (19)$$

and for the characteristic temperature

for
$$\frac{V_{ci}}{V_{cj}} \leq 2.0$$

k_{ij} as given by Equation (16)

for
$$3.0 > \frac{V_{ci}}{V_{cj}} > 2.0 \quad k_{ij} \approx 0.90$$

and for
$$\qquad (20)$$

$$\frac{V_{ci}}{V_{cj}} > 3.0, \qquad k_{ij} \approx 0.85$$

Third Virial Coefficients

Very precise volumetric data are required for computing third virial coefficients. Such data are scarce, but, where available, third virial coefficients can be correlated by Pitzer's extended theory of corresponding states. The extension to mixtures can also be carried out in a manner analogous to that used for the second virial coefficient. Thus

$$\frac{C_{ijk}}{V_{cijk}^2} = \theta_c\left(\frac{T}{T_{cijk}}, \omega_{ijk}\right) \qquad (21)$$

Approximate values of the function θ_c are given in Figure 2. The plots are based on Pitzer's generalized compressibility tables and on volumetric data for

TABLE 1. COMPUTED VALUES OF THE GENERALIZED FUNCTION $-\theta_B$

T_r/ω	0.0	0.1	0.2	0.3	0.4	0.5
0.50	4.008	5.412	6.897	8.473	10.144	11.923
0.55	3.388	4.237	5.135	6.088	7.099	8.175
0.60	2.908	3.497	4.121	4.783	5.484	6.231
0.65	2.526	2.945	3.388	3.858	4.356	4.887
0.70	2.216	2.526	2.855	3.203	3.572	3.966
0.75	1.960	2.194	2.441	2.704	2.982	3.278
0.80	1.746	1.925	2.114	2.315	2.528	2.754
0.85	1.564	1.701	1.845	1.999	2.162	2.335
0.90	1.408	1.512	1.623	1.740	1.864	1.996
0.95	1.273	1.352	1.436	1.524	1.618	1.718
1.00	1.155	1.213	1.274	1.339	1.408	1.481
1.05	1.051	1.093	1.138	1.185	1.235	1.289
1.10	0.959	0.985	1.014	1.043	1.075	1.109
1.15	0.877	0.893	0.909	0.926	0.945	0.965
1.20	0.803	0.808	0.813	0.818	0.823	0.829
1.25	0.736	0.733	0.730	0.727	0.724	0.720
1.30	0.676	0.665	0.653	0.640	0.627	0.613
1.40	0.571	0.548	0.524	0.498	0.471	0.442
1.50	0.483	0.451	0.418	0.382	0.345	0.304
1.60	0.408	0.370	0.329	0.286	0.240	0.192
1.70	0.344	0.301	0.256	0.208	0.157	0.102
1.80	0.288	0.241	0.190	0.137	0.080	0.020
1.90	0.238	0.187	0.133	0.076	0.016	−0.048
2.0	0.195	0.142	0.086	0.026	−0.037	−0.104
2.5	0.036	−0.023	−0.086	−0.153	−0.223	−0.298
3.0	−0.064	−0.125	−0.189	−0.258	−0.330	−0.407
3.5	−0.133	−0.194	−0.258	−0.327	−0.399	−0.475
4.0	−0.183	−0.243	−0.307	−0.374	−0.445	−0.522

argon, nitrogen, methane, *n*-butane, and *n*-heptane. These values for the third virial coefficient are less accurate than those for the second virial coefficients given in Table 1.

The theory of dispersion forces is insufficiently advanced, and experimental data on mixtures are not sufficiently precise to suggest definite mixing rules relating the characteristic parameters for the cross coefficients ($i \neq j \neq k$) to those of the pure components ($i = j = k$). However it is possible to extend to the third virial coefficient the mixing rules used for the second virial coefficient, and it has been shown by Rowlinson on theoretical grounds (29) that such extension is a very reasonable approximation. Thus
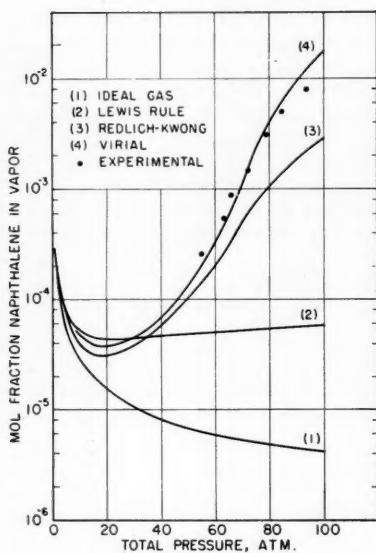
$$V_{cijk} = \tfrac{1}{3}(V_{ci} + V_{cj} + V_{ck}) \quad (22)$$

$$\omega_{ijk} = \tfrac{1}{3}(\omega_i + \omega_j + \omega_k) \quad (23)$$

$$T_{cijk} = (T_{ci}T_{cj}T_{ck})^{\tfrac{1}{3}} \quad (24)$$

Empirical modifications of these mixing rules analogous to those given by Equations (16), (19) and (20) cannot as yet be made.

While the various C terms in Equation (9) cannot be estimated accurately, it should not be concluded that the accuracy of ϕ is seriously impaired. In many cases the density is sufficiently low to permit neglect of the third virial coefficient, and in any case in which Equation (9) may legitimately be used

the second virial coefficient always plays a much more important role than the third. In a typical case where the third virial coefficient may not be neglected, an error of perhaps 20 or 30% in the various C terms may introduce an error of only 2 or 3% in the logarithm of ϕ.

APPLICATIONS IN NONPOLAR SYSTEMS

Phase Equilibria

One major use of fugacities is in the thermodynamic theory of phase equilibrium; if a vapor phase is in equilibrium with a condensed phase, then for any component i

$$\bar{f}_i^c = \bar{f}_i^V \quad (25)$$

where the bar indicates that the component i is in a solution. Equation (25) is of little use until the fugacities can be related to the mole fractions; this relationship is established by the activity coefficients. Thus Equation (25) is rewritten

$$\gamma_i^c x_i f_i^c = \phi_i y_i P \quad (25a)$$

Example 1

Consider the solubility of solid naphthalene in compressed ethylene gas at 35°C. Figure 3 shows various computed results as well as the experimental data of Diepen and Scheffer (6). The curves were computed by using Equation (25a) with the appropriate simplification that $\gamma_i^c x_i = 1$ (i refers to naphthalene), which follows from the fact that the solubility of ethylene in the

solid naphthalene is negligible. Curve 1 was computed on the assumption of ideal gas, curve 2 assumes the Lewis fugacity rule, and curve 3 uses the Redlich and Kwong equation for the fugacity coefficient ϕ. Curve 4 is the virial equation (9), the coefficients having been evaluated as described earlier. In this particular case the solubility of naphthalene is so small that any terms proportional to y_i (or y_i^2) are negligible, causing further simplification. In this case Equation (9) reduces to

$$\ln \phi_1 = 2\rho B_{12} + \tfrac{3}{2}\rho^2 C_{122} - \ln z \quad (25b)$$

where subscript 1 refers to naphthalene, 2 to ethylene.

Since the concentration of naphthalene in the vapor is very small, the quantities ρ and z have been evaluated from the properties of pure ethylene (7).

Fig. 3. Vapor-phase solubility of naphthalene in ethylene at 35°C.

Fig. 4. Minimum carbon monoxide content in hydrogen purification.

Fig. 5. High-pressure absorption of butane at 400 lb./sq. in. abs. and 20°C.

Figure 3, which is a semilogarithmic plot, shows that assumption of the validity of the Lewis fugacity rule or of ideal-gas behavior can introduce errors by a factor of 100 or 1,000. The Redlich and Kwong equation gives the correct trend but is still in error by a factor of about four, and thus the virial equation alone gives reliable results.[*]

The abnormally high solubility of condensed components in ethylene is due to the fact that in the vicinity of room temperature ethylene is only slightly above its critical temperature, a condition where gas-phase nonideality is a maximum.

[*]The data for this system were not included in the correlation of Prausnitz and Gunn (26). The coefficients B_{12} and C_{122} were estimated by the approximate methods described. They are $B_{12} = -600$ cc./g. mole and $C_{122} = 17,100$ (cc./g. mole)^2.

Example 2

An important application of vapor-phase fugacity coefficients is in the accurate specification of *K* values used in petroleum technology. From Equation (25a)

$$K_i \equiv y_i/x_i = \frac{\gamma_i^e f_i^e}{\phi_i P} \quad (25c)$$

and thus *K* is strongly dependent on ϕ. The effect of vapor-phase nonideality is most pronounced when the volatility of a high-boiling component whose mole fraction in the vapor is small is considered. An example of this effect is shown in Table 2, where *K* values for *n*-decane at 104°F. and 294 lb./sq. in. abs. are given for mixtures of decane with hydrogen, methane, and ethylene. The calculated values were computed by use of Equation (25b) and neglect of the second term, together with Equation (25c) and with the very reasonable assumption that the liquid-phase activity coefficient for decane is unity in all cases. For comparison the data of Nederbragt (23)* are shown as well as the values given by the standard *K* charts for paraffins. The computed values are in good agreement with those observed; in this particular case all the nonideality of mixing is in the vapor phase. (If the *K* values for the light component were to be calculated for these mixtures, all the nonideality of mixing would be in the liquid phase.) Table 2 shows clearly that the *K* value is not only a function of the pressure and temperature but also of the nature of the other components which are present. The generalized values from the standard *K* charts therefore cannot be valid for all cases.

Example 3

For another practical application of vapor-phase fugacity coefficients, consider the production of hydrogen gas. Very pure hydrogen gas is needed in catalytic reactions (such as the synthesis of ammonia), since small amounts of impurities can act as catalyst poisons. The impurity most difficult to remove from hydrogen is carbon monoxide, and an effective purification procedure is to cool the impure hydrogen to very low temperatures and then by compression condense out the solid carbon monoxide. At a given temperature there is an optimum pressure which minimizes the equilibrium carbon monoxide content in the vapor phase. When the mole fraction of impurity in the vapor is plotted against the total pressure, a graph is obtained which re-

sembles that shown for naphthalene in Figure 3; the plot first falls and then rises, going through a minimum which gives the coordinates of the optimum conditions. Equation (9) was used to calculate the minimum impurity content for the hydrogen–carbon monoxide system at several temperatures. Terms involving the third virial coefficient were neglected, and it was assumed that the solubility of hydrogen in solid carbon monoxide is negligible.* The results are shown in Figure 4 together with the experimental values reported by Dokoupil et al. (10). If the vapor phase in this problem were considered ideal, the mole fraction of carbon dioxide would be approximately inversely proportional to the pressure. Higher compression should therefore reduce the impurity concentration. Equation (10) however clearly shows that compression beyond the optimum pressure would actually increase rather than decrease the mole fraction of carbon monoxide in the vapor phase.

Chemical Equilibria and Kinetics

The equilibrium yield of a chemical reaction can be computed from the equilibrium constant for the reaction and from relationships between the fugacities of the components in the equilibrium mixture and their mole fractions. In the vapor phase these relationships are established by the fugacity coefficients. Thus for example for a reaction of the type

$$A + B \rightarrow AB \quad (26)$$

$$K_a = K_{\bar{f}} = \frac{K_\phi K_y}{P}$$

where

$$K_\phi = \frac{\phi_{AB}}{\phi_A \phi_B}$$

and
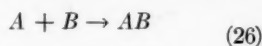
$$K_y = \frac{y_{AB}}{y_A y_B}$$

provided that the standard state for all components is unit fugacity.

The equilibrium constant is computed from free energies of formation and is independent of the pressure. To compute the equilibrium yield it is necessary to estimate the fugacity coefficients of all the species in the solution; such a computation is necessarily of the trial-and-error type, since the equilibrium composition must be known to estimate the fugacity coefficients. However it is only in those cases where high accuracy is required and where the equilibrium constant is known with at least moderate accuracy that such a computation is worthwhile. In most common gas-phase reactions corrections due to nonideal mixing in the gas phase are of the same order as the uncertainties in the chemical equilibrium constant. Also at high temperatures

it is frequently satisfactory to use the Lewis fugacity rule in this type of calculation as pointed out by Dodge (9). However if the temperature of the vapor mixture is below, at, or slightly above the critical temperature of one of the components, the Lewis fugacity rule is likely to be in severe error, and accurate calculation of the equilibrium composition will require the use of vapor-phase fugacity coefficients. Chemical equilibrium calculations at high pressure are discussed more fully by Comings (4).

At present chemical kinetic data in the gas phase are insufficiently precise to make an empirical test for whether or not fugacity coefficients are required in the kinetic rate expression; however theoretical considerations based on the activated complex theory suggest that fugacities should be used in expressing high-pressure reaction rates. As our understanding of chemical kinetics increases and as more precise kinetic data become available, it will probably become necessary to include fugacity coefficients in an exact formulation of chemical rate laws at advanced pressures.

Mass Transfer

The theory of mass transfer between phases requires information on the concentrations prevailing at the interface. The customary procedure is to assume that the interface is at equilibrium, and it is as a result of this assumption that fugacity coefficients enter into equations expressing the rate of interphase mass transfer. Fugacity coefficients therefore find application in such unit operations as high-pressure absorption as illustrated in the following.

Example 4

Consider the contacting of a natural gas with an absorbing oil at 68°F. and 400 lb./sq. in. abs. The initial composition of the gas is 20 mole % hydrogen, 75% methane, and 5% butane; the butane is to be absorbed, and its solubility in the oil is given by a Henry's law constant $H = 3.1$ atm. The equation for the rate of absorption N is

$$N_4 = k_s a p(y_4 - y_4^*) \quad (27)$$

where subscript 4 refers to butane.

If equilibrium exists at the interface, the mole fraction of butane at the interface is given by

$$y_4^* = \frac{H x_4}{\phi_4 P} \quad (28)$$

The fugacity coefficient can be computed from Equation (9). In this case virial coefficients beyond the second are not needed, and the expression for ϕ_4 is

$$\ln \phi_4 z = 2\rho[y_0 B_{04} + y_1 B_{14} + y_4 B_{44}] \quad (29)$$

where subscript 0 refers to hydrogen and 1 to methane.

---

*The data for these systems were not included in the correlation of Prausnitz and Gunn (26). The B_{12} coefficients were estimated by the approximate methods described.

*At the low temperatures considered here the actual rather than the pseudocritical parameters for hydrogen were used to compute B_{12}. No correction was made for V_{c12} and T_{c12}.

To obtain rapidly a value for z and ρ a modification of Kay's rule (8) was used with fictitious critical parameters for hydrogen. The cross coefficients were estimated by the methods described earlier yielding $\phi_4 = 0.71$. The mole fraction of butane in equilibrium with the liquid is shown as a function of liquid composition in Figure 5. For comparison, results are also shown for two other methods of calculation, ideal-gas behavior and ideal-vapor-phase mixing (Lewis fugacity rule). For the latter case the fugacity coefficient for pure butane was estimated from extrapolated curves on generalized plots (17). Figure 5 points out that in this case the assumption of ideal gas behavior actually gives results as good as or even slightly better than those obtained by assuming the Lewis fugacity rule. This is a result of compensating errors which frequently occur for a condensable component

were analyzed. The theory of intermolecular forces of polar molecules (22) suggests that an approximate extension of Pitzer's treatment is to write the reduced, second virial coefficient (30)

$$\frac{B_{ii}}{V_{c_i}} = \theta_B\left(\frac{T}{T_{c_i}}, \omega_i^{\,h}\right)$$
$$+ \theta_B{}^1\left(\frac{T}{T_{c_i}}, \frac{\mu_i^4}{V_{c_i}^2}\right) \qquad (30)$$

The empirical function θ_B is given in Table 1; the empirical function $\theta_B{}^1$ is shown in Figure 6. The plots in Figure 6 were obtained from data for ammonia, methyl chloride, acetone, and acetonitrile. This correlation is necessarily quite approximate and should be used only

Figure 7 together with experimental results reported by Michels (21). This system is another example of a case where, because of compensating nonidealities, calculations based on ideal-gas behavior give better results than those based on the Lewis fugacity rule.

Virial coefficients for mixtures of weakly polar, nonassociating components can be estimated the same way as for nonpolar components. For such components Table 1 is applicable. For mixtures of highly polar, nonassociating components, however, Equation (30) should be used. For calculating B_{ii} Equation (30) becomes

$$\frac{B_{ii}}{V_{c_{ij}}} = \theta_B\left(\frac{T}{T_{c_{ij}}}, \omega_{ij}^{\,h}\right)$$
$$+ \theta_B{}^1\left(\frac{T}{T_{c_{ij}}}, \frac{\mu_i^{\,2}\mu_j^{\,2}}{V_{c_{ij}}^{\,2}}\right) \qquad (31)$$

Fig. 6. Excess second virial coefficient for highly polar gases (V_c is in cc/g-mole, μ in Debyes).

Fig. 7. K values for methanol in hydrogen at 75°C.

Fig. 8. Phase equilibria for acetic-acid–propionic acid at 20°C.

present in small concentrations in a gas which is remote from its critical conditions. In the example given here the deviation from nonideality for pure butane vapor tends to reduce ϕ, while the nonideality of mixing tends to raise ϕ (positive deviations from Raoult's law in the gaseous solution). Therefore the total effect of the two nonidealities is somewhat less than that obtained when either one is taken separately.

POLAR MOLECULES

Reliable data on virial coefficients for polar molecules are scarce. The correlation of Pitzer and Curl for the second virial coefficients gives good results for weakly polar gases, but it is not valid for strongly polar gases, especially at reduced temperatures well below unity where the effect of polarity is most important. To augment the generalized second virial coefficients given in Table 1 data for a few polar but nonassociating molecules

in the absence of other data. It is not valid for associating molecules like water or methyl alcohol.

The second virial coefficient of a mixture containing one polar and one nonpolar component presents no difficulties. The polar molecule induces a dipole in the nonpolar (22), but the contribution of this induced polarity to the intermolecular forces is small compared to the much more important dispersion forces. The cross coefficient B_{12} for such a mixture can therefore be estimated by the same methods used for nonpolar mixtures, provided that the acentric factor of the polar component is replaced by that of its homomorph.

Example 5

Consider phase equilibrium in the system methanol-hydrogen at 75°C. The K value for methanol is given by Equation (25c), and the assumption of Henry's law for the solubility of hydrogen in methanol leads to $\gamma^c = 1.0$.

The fugacity coefficient is computed from Equation (25b) by neglecting the second term. At 75°C., T_{c12} is such that B_{12} is practically zero. The properties of pure hydrogen were used to estimate z. Computed K values for several pressures are shown in

Unfortunately no data are available for testing this equation. In the absence of any experimental data it is probably best to use the arithmetic mean for $\omega_{ij}^{\,h}$ and $V_{c_{ij}}$ and the geometric mean for $T_{c_{ij}}$.

Prediction of the virial coefficients of mixtures of polar gases is particularly difficult because of hydrogen bonding resulting in association and solvation. Equations (30) and (31) are not valid for mixtures where hydrogen bonding is important either amongst molecules of the pure component (for example, water) or between molecules of different components (for example, chloroform-acetone).

If hydrogen bonding is significant, a different approach may sometimes be used to correct for vapor-phase imperfections (18). This approach considers all deviations from ideal behavior in the vapor phase to be due to the formation of dimers (or higher polymers). Thus for example the vapor of a hydrogen-bonding substance A is considered to be an ideal gas consisting of species A and A_2. The relative amount of each species is given by an equilibrium constant K_H; thus at moderate pressures

$$2A \rightleftarrows A_2 \quad \text{and} \quad K_H = \frac{p_{A_2}}{p_A^{\,2}}$$

The equilibrium constant is a function of temperature and must be determined experimentally. This technique is best illustrated by a numerical example as shown below.

Example 6

Consider the vapor-liquid equilibria of mixtures of acetic acid and propionic acid at 20°C. At this temperature the total pressure is in the neighborhood of 15 mm. Hg, and it would appear that at such a low pressure vapor-phase imperfections would be entirely negligible. However the dimerization of these acids in the vapor phase is so strong that large deviations from ideal behavior result. For each acid a dimerization equilibrium constant is defined:

$$K_{H_a} = \frac{p_{a_2}}{p_a^2} \quad \text{and} \quad K_{H_b} = \frac{p_{b_2}}{p_b^2}$$

where a refers to acetic acid and b to propionic acid.

In addition there is the solvation equilibrium

$$K_{H_{ab}} = \frac{p_{ab}}{p_a p_b}$$

K_{H_a} and K_{H_b} have been measured (19), and a reasonable assumption for $K_{H_{ab}}$ is to set it equal to $(K_{H_a}K_{H_b})^{\frac{1}{2}}$. In this procedure the nonideal binary vapor phase is now considered to be equivalent to an ideal five-component mixture consisting of two monomers and three dimers. When this treatment of the vapor phase (3) is combined with the assumption that Raoult's law holds for the liquid phase, a $y - x$ diagram can be constructed as shown in Figure 8, which also shows the curve computed without vapor-phase corrections as well as the experimental data of Christian (3). The results suggest the rather surprising conclusion that in this system, in spite of the very low total pressure, the deviations from ideality are predominantly in the vapor rather than in the liquid phase.

This approach to vapor-phase nonideality is necessarily limited to the few systems where the polymerization constants have been measured and where, because of chemical similarity, a geometric mean may be a good approximation for the cross dimerization constant.

ACKNOWLEDGMENT

NOTATION

B	=	second virial coefficient
C	=	third virial coefficient
D	=	fourth virial coefficient
$\bar{f}_i$	=	fugacity of component i in gaseous solution
f_i^0	=	fugacity of pure component i as a gas or vapor
f_i^a	=	fugacity of pure condensed component i
$k_a a$	=	mass transfer coefficient
k_{ii}	=	a characteristic parameter defined by Equation (16)
K	=	vaporization equilibrium constant $= y/x$
K_a	=	chemical equilibrium constant
K_H	=	dimerization constant
N	=	rate of mass transfer
p	=	partial pressure
P	=	total pressure
R	=	gas constant
T	=	absolute temperature
U	=	ionization potential
v	=	molar volume
V	=	volume
$\bar{V}_i$	=	partial molar volume of component i
V_i^0	=	volume of pure component i as a gas or vapor
x_i	=	mole fraction of component i in the condensed phase
y_i	=	mole fraction of component i in the gas phase
y_i^*	=	mole fraction of component i in the gas phase at the gas-liquid interface
z	=	compressibility factor, property of mixture

Greek Letters

γ	=	gas-phase activity coefficient [See Equation (2)]
γ^c	=	condensed phase activity coefficient
ϕ	=	vapor-phase fugacity coefficient [See Equation (1)]
ϕ^0	=	vapor-phase fugacity coefficient for the pure component
ν	=	fugacity to pressure ratio for pure gas or vapors
ρ	=	molar density
θ_B	=	generalized function for the second virial coefficient
θ_c	=	generalized function for the third virial coefficient
ω	=	acentric factor
ω^h	=	acentric factor of homomorph; see Bondi, A., *A.I.C.H.E. Journal*, 3, 4, 473 (1957).
β	=	ratio of critical volumes
ζ	=	ratio of ionization potentials
μ	=	dipole moment

Subscripts

c	=	critical (or characteristic)
$i, j, k \cdots$	=	components
m	=	mixture
r	=	reduced
$1, 2 \cdots$	=	components

Superscripts

v	=	vapor phase
c	=	condensed phase

LITERATURE CITED

1. Benedict, Manson, G. B. Webb, and L. C. Rubin, *J. Chem. Phys.*, **10**, 747 (1942).
2. Brown, G. G., and associates, "Unit Operations," John Wiley, New York (1950).
3. Christian, S. D., *J. Phys. Chem.*, **61**, 1441 (1957).
4. Comings, E. W., "High Pressure Technology," chap. 10, McGraw-Hill, New York (1956).
5. Cullen, E. J., and K. A. Kobe, *A.I.Ch.E. Journal*, **1**, 452 (1955).
6. Diepen, G. A. M., and F. E. C. Scheffer, *J. Am. Chem. Soc.*, **70**, 4085 (1948).
7. Din, Fazul, ed., "Thermodynamic Functions of Gases," Vol. II, Butterworth Scientific Publications, London (1956).
8. Dodge, B. F., "Chemical Engineering Thermodynamics," Chap. 5, McGraw-Hill, New York (1944).
9. *Ibid.*, chap. 11.
10. Dokoupil, Z., *et al.*, *Appl. Sci. Research*, **A5**, 182 (1955).
11. Fowler, R. H., and E. A. Guggenheim, "Statistical Thermodynamics," Cambridge (1939).
12. Fuchs, Klaus, *Proc. Roy. Soc. (London)*, **A179**, 408 (1941).
13. Guggenheim, E. A., *Revs. Pure and Appl. Chem. (Australia)*, **3**, 1 (1953).
14. Guggenheim, E. A., and M. L. McGlashan, *Proc. Roy. Soc. (London)*, **A206**, 448 (1951).
15. Hildebrand, J. H., and R. L. Scott, "Solubility of Non-Electrolytes," 3rd ed., Chap. 14, Reinhold, New York (1950).
16. Hirschfelder, J. O., C. F. Curtiss, R. B. Bird, "Molecular Theory of Gases and Liquids," John Wiley, New York (1954).
17. Hougen, O. A., and K. M. Watson, "Chemical Process Principles," Vol. II, p. 622, John Wiley, New York (1947).
18. Lambert, J. D., *et al.*, *Proc. Roy. Soc. (London)*, **A196**, 113 (1949).
19. MacDougall, F. H., *J. Am. Chem. Soc.*, **58**, 2585 (1936); **63**, 3420 (1941).
20. Mayer, J. E., *J. Phys. Chem.*, **43**, 71 (1939).
21. Michels, Antonius, *et al.*, *Appl. Sci. Research*, **A4**, 105 (1954).
22. Moelwyn-Hughes, E. A., "Physical Chemistry," chap. 7, Pergamon Press, London (1957).
23. Nederbragt, G. W., *Appl. Sci. Research*, **A1**, 237 (1948).
24. Pitzer, K. S., *et al.*, *J. Am. Chem. Soc.*, **77**, 3427 (1955).
25. Pitzer, K. S., and R. F. Curl, Jr., *J. Am. Chem. Soc.*, **79**, 1269 (1957).
26. Prausnitz, J. M., and R. D. Gunn, *A.I.Ch.E. Journal*, **4**, 430 (1958).
27. Redlich, Otto, and J. N. S. Kwong, *Chem. Revs.*, **44**, 233 (1949).
28. Rossini, F. D., ed., "Thermodynamics and Physics of Matter," Part C, Chap. 3, Princeton Univ. Press, Princeton, New Jersey (1955).
29. Rowlinson, J. S., *et al.*, *Trans. Faraday Soc.*, **50**, 1 (1954).
30. Stockmayer, W. H., *J. Chem. Phys.* **9**, 864 (1941).

Equilibria in the Hydration of Ethylene at Elevated Pressures and Temperatures

C. S. COPE and B. F. DODGE

Yale University, New Haven, Connecticut

Values of equilibrium composition for the hydration of ethylene to form ethanol have been calculated for a series of elevated pressures and temperatures by using equilibrium data available from previous low-pressure studies. To obtain satisfactory agreement between these values and those measured experimentally, it is essential (1) to take into account the formation of ethyl ether and (2) to use available vapor-liquid equilibrium data for the binary ethanol-water system at elevated temperatures, instead of the standard "mixture rules" often employed.

Thermochemical data and low-pressure equilibrium data for both the ethylene hydration and ether formation reactions are critically reviewed. Experimentally measured values for the equilibrium concentrations of ethanol and ether in the liquid phase at 221°C. and 273 atm., with dilute sulfuric acid used as catalyst in a lined rocking-bomb reactor, are presented.

This paper compares equilibrium compositions measured experimentally for the hydration of ethylene at elevated pressures and temperatures with those predicted from available thermodynamic data and presents a critical review of these data.

The hydration of ethylene to form ethanol, as well as the reverse reaction, has been the subject of numerous past investigations. Most of the equilibrium studies for the ethylene-water-ethanol system were carried out at relatively low pressures such that a vapor phase only was present. The investigation by Gilliland, Gunness, and Bowles (16) is the only published work pertaining specifically to equilibrium states for the hydration of ethylene at conditions under which both liquid and vapor phases were simultaneously present. A similar study of the hydration of propylene is reported by Majewski and Marek (30).

Dodge (13) has presented a comparison of predicted and measured equilibrium compositions for both the liquid and vapor phases for a specific set of conditions used by Gilliland, Gunness, and Bowles. At the time that the predicted values were calculated it was necessary to make a considerable number of simplifying assumptions. Later pertinent vapor-liquid equilibrium data at elevated temperatures for the binary ethanol-water system were obtained by Griswold, Haney, and Klein (17), and also recently in this laboratory by Barr-David (6). During the present work inconsistencies were found in the results given by Gilliland, Gunness, and Bowles, and it therefore appeared advisable both to recalculate the predicted values of composition and to remeasure equilibrium compositions experimentally.

PREDICTION OF EQUILIBRIUM COMPOSITIONS FROM THERMODYNAMIC DATA

In order to calculate values of equilibrium composition for a two-phase system it is essential to know what the fugacities of the various participating substances are and how the fugacities vary as functions of the composition of each phase. In this specific case values of K_f, the equilibrium constant defined in terms of fugacities, are known from equilibrium studies at low pressures and at various temperatures. This equilibrium constant is independent of pressure and composition. By determining (or assuming) how the fugacities of the various substances are affected by pressure and by the composition of each phase, it is possible to calculate the equilibrium compositions of the two phases for given conditions of pressure and temperature.

The difficulty lies in the fact that rigorous calculation of the fugacities of components of solutions requires partial volume data for one of the phases coupled with phase-equilibrium data, both of which are seldom available. As a consequence one is forced to make various assumptions which cannot usually be tested, and the accuracy of the calculated result is in doubt. It seemed desirable, nevertheless, to attempt a calculation of the equilibrium composition, since if it agreed reasonably well with the experimental data, the confidence in both would be strengthened. Another, and perhaps more important, purpose of the calculation was to show the great difference between equilibrium in the system ethylene-water-ethanol and that in the system ethylene-water-ethanol-ether. Many investigators have ignored the formation of ether, but the present calculations, confirmed by experimental data, show that this leads to very large errors.

The method of calculating the fugacities of these four substances was as follows. Fugacities of ethanol and water in binary vapor solutions at the vapor pressure were calculated from the equilibrium data of Griswold, Haney, and Klein (17)* by using the method proposed by Joffe (25). The appropriate generalized charts of Hougen and Watson (21) were used to obtain compressibility factors, enthalpy differences, and fugacity coefficients for the mixture (f_m/p). The limitations of such charts are apparent when applied to mixtures of substances as polar as ethanol and water, but under the circumstances no entirely reliable approach seems available.

The values of fugacity thus obtained must be corrected to the total pressure at which the hydration reaction is to be carried out by using the standard relation for the change of fugacity with pressure. Such calculations can generally be made more conveniently via calculations on the liquid phase rather than on the vapor phase, especially here, since the concentrations of ethylene and ethyl ether in the liquid phase can reasonably be assumed to be negligible. However, since volumetric data for the liquid solutions are unavailable, the following two assumptions are made: (1) for water, the partial molal volume is assumed equal to the true molal volume at the same temperature, and the change in volume with pressure is neglected; and (2) for ethanol, for which the assumptions to be made are less reliable, one starts with data (35) from which the partial molal volume in dilute aqueous solutions at 25°C. may be obtained and assumes that the fractional increase in the partial molal volume with temperature is the same as that shown by pure *water* over the same temperature range. This assumption very probably underestimates the value of the true increase of the partial molal volume and therefore may increase somewhat the final calculated values for ethanol concentration in the liquid phase. However the error

C. S. Cope is with E. I. du Pont de Nemours and Company, Inc., Wilmington, Delaware.

*The results recently obtained for this system by Barr-David (6) were not available at the time the calculations given here were carried out. The agreement between the two sets of data is sufficiently close that no significant differences in the final results are obtained when one set or the other is used.

TABLE 1. CALCULATED VALUES OF EQUILIBRIUM COMPOSITION FOR THE HYDRATION
OF ETHYLENE

Pressure, atm.	Ethanol concentration in liquid phase		Concentrations in vapor phase Mole %			
	Weight %	Mole %	Ethanol	Water	Ethylene	Ether

A. Formation of Ethyl Ether Assumed

Temperature = 200°C.

100	10.2	4.3	11.1	23.6	18.7	46.6
200	12.8	5.5	14.2	19.5	13.2	54.1
300	14.1	6.1	16.6	19.2	10.8	53.4

Temperature = 250°C.

100	8.0	3.3	10.5	49.5	24.9	15.1
200	12.3	5.2	14.6	36.7	21.8	26.9
300	14.6	6.4	15.8	35.2	19.3	29.7

B. Formation of Ethyl Ether Neglected

Temperature = 200°C.

100	42.0	22.	27.0	20.2	52.8	
200	62.1	39.	38.1	15.1	46.8	
300	67.5	45.	45.5	13.9	40.6	

Temperature = 250°C.

100	12.4	5.3	15.1	48.2	36.7	
200	26.0	12.1	25.0	34.7	40.3	
300	36.0	18.0	29.0	33.3	37.7	

is probably not large, especially in view of the fact that these corrections being calculated are fairly small in magnitude. The use of the molal volume of pure *ethanol* as a means of estimating the partial molal volume in dilute solution would result in an overestimate of the true correction to the fugacity, especially at temperatures above the critical temperature of ethanol (243°C.), in all probability.

The fugacities and mole fractions of all four substances in the vapor phase are assumed to be related by the ideal-solution law (Lewis and Randall rule). At temperatures below the critical temperature of ethanol this requires extrapolation into a region where ethanol cannot actually exist as a gas, but the chart of Hougen and Watson shows lines to guide the extrapolation. The same is true in the case of water. It is unfortunate that recourse to the Lewis and Randall rule must be made in all four instances, but there appears to be no alternative more satisfactory than the use of this or of some similar rule. The severe limitations of the Lewis and Randall rule at elevated pressures have long been recognized.

The calculation of the equilibrium concentrations proceeds by the following steps. (1) For the temperature in question select the appropriate value of K_f (as given in a later section) for each of the two simultaneous reactions:

$$C_2H_4 + H_2O = C_2H_5OH \qquad (1)$$

$$2C_2H_5OH = C_2H_5OC_2H_5 + H_2O \qquad (2)$$
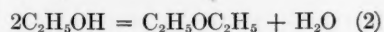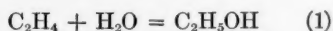
The standard state chosen for each substance is the gas at a fugacity of 1 atm. (2) Assume an ethanol concentration in the liquid phase. (This fixes the composition, since water is the only other component.) (3) Obtain the fugacities of ethanol and water at the desired temperature and total pressure from log graphs of fugacity vs. liquid-phase composition, based on the calculations previously described. (4) Obtain the vapor-phase concentrations of ethanol and water from their respective fugacities via the Lewis and Randall rule. (5) Assume an ethylene concentration in the vapor phase and calculate its fugacity. (6) Obtain the concentration of ethyl ether from the relation $\sum y_i = 1$, and from this calculate the fugacity. The calculated fugacities must satisfy the two equilibrium constants, and trial values of ethanol concentration in the liquid phase and ethylene concentration in the vapor phase are taken until they are satisfied.

The results of the calculations are given in Table 1A. If the formation of ethyl ether according to reaction (2) is not taken into account, the results are as given in Table 1B. A comparison of these two sets of figures shows that formation of ether causes significant reductions in the concentrations of ethanol and ethylene at equilibrium but has little influence on the concentration of water in the vapor phase.

When the formation of ether is taken into account, the following observations are significant.

1. The change in the concentration of ethanol in the liquid phase as a function of temperature is small, and the concentration may even rise with increasing temperature at higher pressures. This behavior may seem surprising in view of
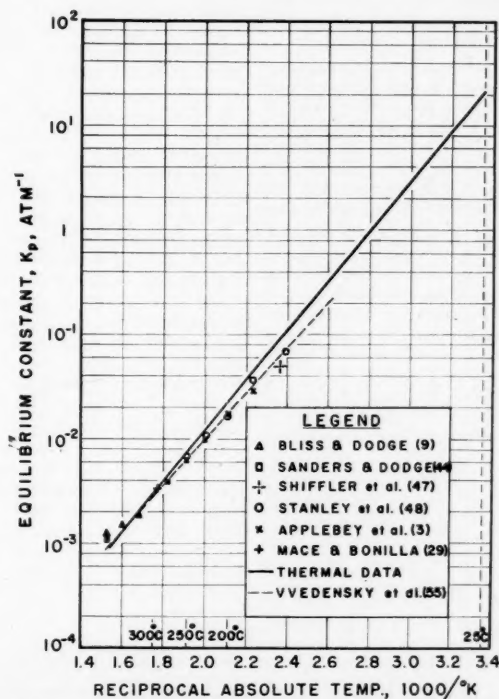
Fig. 1. Logarithm of equilibrium constant vs. reciprocal absolute temperature
$$C_2H_4(g) + H_2O(g) = C_2H_5OH(g).$$

the quite highly exothermic nature of reaction (1) but is caused by the endothermic nature (with respect to ethanol formation) of reaction (2) and the manner in which phase-equilibrium relationships change with temperature.

2. At constant temperature an increase in pressure raises the concentration of ethanol in the liquid phase; the rate of increase with pressure in general falls off with increasing pressure.

3. The concentration of ether drops fairly rapidly with rising temperature.

4. It is interesting that the $K = y/x$ value (column 4/column 3, Table 1A) for ethanol does not change greatly with temperature or with pressure, whereas it drops rather rapidly with rise in temperature (and hence in pressure) for dilute solutions of ethanol of fixed liquid-phase composition in the binary ethanol-water system.

In the preceding discussion it was necessary to know values of the equilibrium constants for reactions (1) and (2) as functions of temperature. Generally these values may be obtained by direct studies of equilibrium composition, usually made at low pressures, or they may be predicted from auxiliary data by means of thermodynamics. In the following section both methods of approach are considered by use of data already available in the literature.

RESULTS OF PREVIOUS DIRECT LOW-PRESSURE MEASUREMENTS OF EQUILIBRIUM CONSTANTS; CALCULATION OF EQUILIBRIUM CONSTANTS FROM THERMAL DATA

Ethylene Hydration Reaction

The results of a number of investigators who determined equilibrium compositions directly for the vapor-phase hydration of ethylene by using a variety of catalysts are given in Figure 1, which is a semilogarithmic graph of the equilibrium constant K_p (based on partial pressures) against the reciprocal of absolute temperature. For most of these investigations K_p can be assumed equal to K_f, since the pressure was sufficiently low. The results of Sanders and Dodge (44) and of Mace and Bonilla (29)* have also been included for the sake of completeness, even though both these studies were made at pressures of about 70 atm. The solid line on the graph represents values of equilibrium constant calculated from thermal data by using standard procedures. Thermal data are summarized in Table 2.

A recent article by Barrow (7) has done a great deal to resolve the discrepancies which previously existed between experimental thermal data for ethanol and the values calculated by means of statistical mechanics. The primary cause of these discrepancies was the underestimation of the important effects of hydrogen bonding on the thermal properties of ethanol. A

---

*Mace and Bonilla converted their value of K_p measured at high pressure to a K_f value by assuming ideal-solution behavior and using a generalized activity-coefficient chart.

---

successful quantitative treatment of hydrogen-bonding phenomena, first achieved by Weltner and Pitzer (56) for methanol, has been extended to ethanol by Barrow and to water by McCullough et al. (31).

This new approach gives a correction of 60 cal./mole† for converting the value obtained by Rossini (39) for the heat of formation of ethanol to the ideal-gas state at 1 atm. The value of 5 cal./mole given by Aston (4) is typical of previous estimates of the magnitude of this correction.

The experimental equilibrium results in Figure 1 are perhaps, but may not necessarily be, in agreement with those calculated purely from thermal data when allowance for the uncertainty of each is made. Should the data not be in agreement, no specific cause of any discrepancy is apparent at this time. For practical applications the data are satisfactory at all temperatures. Probably the best representation of the purely experimental results is that proposed a number of years ago by Vvedensky and Feldman (55), as indicated by the dashed line in Figure 1; the values of equilibrium constant used for the calculations described in the previous section are based on this relationship.

Ether Formation Reaction

No thermal data for ethyl ether are listed in reference 43, but data are given in other standard listings (23, 35). Closer inspection reveals that the heats of combustion (or heats of formation) given were derived from the data of either Thomsen (52) or Stohmann (49) or perhaps from an average of the two. Both of these series of measurements were made long before the advent of precise modern thermochemical techniques, and so the data must be evaluated very carefully and subjected to several corrections to bring them to the same bases and standard conditions as are now used in thermochemical work. Space limitations prevent elaboration of the various individual corrections made. (For details see reference 12.) The value finally obtained for the heat of formation of ether is judged to be accurate to within ±1.0 kcal./mole.

The absolute entropy of ethyl ether was obtained by Parks and Huffman (33a) in a study of the specific heat over the range of temperature from about 90° to 300°K. By means of a method which they had devised from studies on a number of compounds down to about 20°K. they extrapolated the curve of specific heat vs. temperature for ether from 90°K. to absolute zero and were then able to calculate the absolute entropy at 25°C. by standard methods. The standard entropy change for reaction (2) as obtained from thermal data is questionable, as it appears to be primarily responsible for the lack of agreement of the more reliable experimental values of equilibrium constant for this reaction with those predicted by thermal methods. Since the entropy data for ethanol and water appear to be reliable, the major source of error must lie in the value for the absolute

---

†The existence of a numerical error in the value of 250 cal./mole calculated by Barrow for this correction by means of an equation of state has been confirmed by him in a private communication. Also, the correction to the reported heat of combustion at 25°C. should strictly be calculated at 32.5°C., the temperature of ethanol vapor just before combustion in the experiments of Rossini.

TABLE 2. THERMAL DATA FOR ETHYLENE, WATER, ETHANOL, AND ETHER

Ideal Gas State at 1 Atm. and 298.2°K. (25°C.)

Substance	Heat of formation, kcal./mole	Absolute entropy, cal./(mole) (°K.)
Ethylene	$+12.366^a$	52.45^b
Water	-57.798^b	45.106^b
Ethanol	-56.18^c	67.58^d
Ethyl ether	-58.62^e	81.85^f
Water (liq)	-68.3174^b	
Carbon dioxide (g)	-94.0518^b	

Specific Heat Equations^g Ideal Gas State

$$C_p^0 = \alpha + \beta T + \gamma T^2, \text{ cal./(mole)(°K.)}$$

Substance	α	$\beta \times 10^3$	$\gamma \times 10^6$	Temperature range, °K.
Ethylene^h	1.52	33.6	-12.75	300–700
Water^b	7.85	-0.217	2.656	300–700
Ethanol^i	4.3	40.25	-7.5	300–600
Ethyl ether^i	6.8	80.5	-25.0	300–600

^{a}Derived from a value of 32.59 kcal./mole for the standard heat of hydrogenation of ethylene, based mainly of the precise heat-of-reaction measurements of (27), as corrected by Rossini (40) and supported by equilibrium data summarized in (51). This value is lower by 0.14 kcal./mole than that given in (43), which is a weighted average of the data of (27) and (41). The necessary auxiliary value for the standard heat of formation of ethane is taken from (43). The correction to the ideal-gas state given by Aston (4) has been applied.
^{b}(43).
^{c}(39) and (7), corrected (see text).
^{d}(7).
^{e}(49) and (52), corrected to 25°C. and to modern values of the calorie (38) and of the molecular weight of ether; weighings corrected to vacuum. The data in (49) for liquid ether were rejected as being too low. The relatively large negative corrections generally made by Kharasch (26) to the results of Thomsen (52) were not felt to be applicable in this specific case.
^{f}(33) corrected to the ideal-gas state at 1 atm. by using data from (45) and the modified Berthelot equation (4).
^{g}Fitted to tabulated or graphed data given in the specific references cited.
^{h}(42).
^{i}(15).

---

entropy of ether, although possible errors in the equilibrium data, in the specific heat of ether vapor, and in the heat of combustion of ether could account for a portion of the discrepancy. Since the low-temperature specific-heat measurements of Parks and Huffman for various organic compounds are generally regarded as being reliable, the main source of possible error in their value for the absolute entropy lies in the extrapolation of the specific-heat data from 90°K. to absolute zero. The general reliability of the extrapolation method has already been questioned by Pitzer (36). A thorough study of equilibrium in reaction (2), together with studies of the heat of combustion of ether at 25°C. and of the heat capacity from near 0° to about 600°K., would be most desirable.

When one attempts to calculate values of equilibrium constant for reaction (2) from thermal data, the situation is somewhat different from that already used for reaction (1), since in the present instance the values

for both the heat of reaction and (especially) for the entropy change of reaction at 25°C. are open to question. Studies giving direct experimental determinations of equilibrium composition have been numerous, but unfortunately many of the results conflict, as shown in Figure 2, which is a semilogarithmic graph of equilibrium constant against the reciprocal of absolute temperature. Care must be taken in judging which sets of data are likely to be the most reliable. The chief causes of error in some studies appear to have been interference by competing reactions, inaccuracy of measurement of temperature, and/or failure to reach true equilibrium (usually by deactivation of catalyst).

The most reliable determinations appear to have been those of Semerano (46), Newitt and Semerano (32), Clark, Graham, and Winter (11) (all at about 250°C.), and a hitherto unpublished one of Atherton (5) at 135°C. A recent study by Valentin (53) over a fairly considerable range of temperature appears to be far out of line with other results and would indicate that reaction (2) is strongly endothermic, which is highly improbable according to the thermal data of Table 2. The error in Valentin's work may be ascribed to deactivation of the catalyst, and it is thought runs involving synthesis of ethanol from ethylene and water would have shown at once that equilibrium conditions were not being reached merely by decomposition of ethanol.

From the value of 20 for the equilibrium constant as furnished by Atherton at 135°C. and an average best value of 8.0 selected from the results mentioned previously for the neighborhood of 250°C., together with the specific heat relationships given in Table 2, it is possible to calculate values of both the standard enthalpy and entropy changes of reaction at 25°C. The values so obtained are −4,220 cal./mole of ether and −4.63 cal./°K./mole of ether, respectively; the curve marked I in Figure 2 is based on these values. The values obtained purely from the thermal data given in Table 2 are −4,060 and −8.20 and give the curve marked II in Figure 2. The agreement of the two values for the enthalpy change of reaction is very good and lies well within the possible errors involved; there appears to be little reason to doubt that reaction (2) is exothermic. The values for the entropy change of reaction are not in agreement; as indicated previously, this is ascribed primarily to a possible discrepancy in the available value for the absolute entropy of ether, which appears to be too low. The values of equilibrium constant used for the calculations described in the first section are based on the relationship given by curve I.

DISCUSSION OF PREVIOUS EQUILIBRIUM STUDIES AT ELEVATED PRESSURES

The experimental data presented in the aforementioned paper of Gilliland, Gunness, and Bowles were taken from the dissertation of Gunness (18). From the results for the composition of the vapor phase it was possible to calculate changes of standard free energy of reaction by using the Lewis and Randall rule and generalized activity-coefficient charts. When these values were plotted against absolute temperature, they described a straight line in good agreement with previous low-pressure equilibrium measurements. The authors have repeated the calculations of changes of standard free energy and believe that significant errors were made in the original calculations at both the lowest and highest of the four temperatures involved; the corrected values of free-energy change vary erratically with temperature. It is difficult to determine how much the divergence of the corrected values from the results of other workers at low pressure can be ascribed to inaccuracies in the compositional data or to the limitations of the assumptions made in calculating the standard free-energy changes from data obtained at these high-pressure conditions. However the relatively erratic behavior of the $K = y/x$ values for the various species in the system as functions of temperature and pressure suggests that the data are not wholly accurate.

In view of the authors' experimental observations, due account of ether formation was not taken in the experiments performed by Gunness, who reported a considerable concentration of ether in the vapor phase at 218°C. but zero concentration at both lower and higher temperatures. In the paper by Gilliland, Gunness, and Bowles the statement is made that at temperatures below 220°C. ether formation was very noticeable, but no indication of the presence of ether is given in the tabulation presented for the composition of the vapor phase at the lowest temperature, 176°C. The following probably represents the two main reasons why ether formation was not adequately considered: slow rate of formation of ether at 176°C. and inadequate means of separation of the highly volatile ether in the analytical train. Fortunately however the formation of ether should not have caused the measured concentrations of ethanol in the liquid phase to be much different from those which actually existed. Nevertheless some uncertainty does exist as to whether a state of over-all equilibrium was closely approached in all cases.

The importance of formation of ethers in olefin hydration reactions is clearly shown in the experimental results of Majewski and Marek (30) and also in the unpublished work of Winer (57) and of Holden and Stackpole (20) on the hydration of propylene at elevated pressures and temperatures. Ethyl ether was found to be present by Antonio (2) in a study of the continuous hydration of ethylene at elevated pressures and temperatures with sulfuric and phosphoric acids as catalysts and also by Reynoso (37), Van Alphen (54), and Erlenmeyer and Tscheppe (14) in simple sealed-tube experiments, sulfuric acid being used as catalyst in each case. For nearly all conditions employed by Antonio the mole fraction of ethylene converted to ether was greater than that converted to ethanol.

The general difficulty of preventing entirely the formation of ether in the acid-catalyzed hydration of ethylene would be predicted on the basis of kinetic studies* of other olefin hydration reactions and of etherification reactions of alcohols. Thus it is probable that a common species, specifically the conjugate acid of ethanol,

$C_2H_5OH_2^+$, is involved in both the hydration of ethylene and the etherification of ethanol. The pi-electron complex $C_2H_5^+$, which is a precursor to the foregoing intermediate (or transition) state in the hydration of ethylene, is probably also important in the sequence of steps leading to the polymerization of ethylene.

EXPERIMENTAL

The hydration of ethylene was studied at a constant absolute pressure of 273 atm. by using first dilute phosphoric acid as catalyst at a temperature of 296°C. and later dilute sulfuric acid as catalyst at 221° and 248°C. The hydration was carried out in a rocking-bomb reactor by a modified batch technique. A tantalum liner was used in the bomb for the runs with sulfuric acid; copper liners were used for the runs with phosphoric acid, since the tantalum liner was not available when these runs were made. Both liners were of the removable type. Pressure in the reactor was maintained within ± 7 atm. of the desired value by admitting ethylene to the bomb from a high-pressure storage tank whenever necessary. A precise Bourdon-tube gauge, with a scale having a range from 0 to 6,000 lb./sq. in. and divided into 20 lb./sq. in. intervals, was used to measure the pressure.

A calibrated chromel-alumel thermocouple located in a bayonet which extended well into the interior of the reactor was used to measure the temperature of the bomb to within ± 3°C.

Concentrations of ethanol and ether in liquid-phase samples taken during the runs were measured, and the concentration of acid in each sample was also determined. Attempts to analyze vapor-phase samples quantitatively were unsuccessful, primarily because no satisfactory method of separating ethylene and ether could be found which would be both accurate and reasonably rapid for samples as obtained in these experiments.

ANALYTICAL

Prior to the development of quantitative analytical procedures a careful qualitative analysis was carried out to determine what substances were present in reacted mixtures of ethylene, water, and catalyst. The only substances present in significant concentration were ethylene, water, ethanol, ethyl ether, acetaldehyde, polymers of ethylene, and acid (catalyst). In particular, C_4 derivatives, which conceivably could have arisen by dimerization of ethylene and subsequent reaction of the dimer, were found to be absent. In the runs made in copper liners small concentrations of copper ion were present in the liquid samples. The tantalum liner appeared to be inert under the conditions used. When phosphoric acid was used as catalyst, the presence of organic

---

*See, for example, a number of papers by R. W. Taft, Jr., and coworkers during the past several years in *J. Am. Chem. Soc.* and reference 10.

phosphate esters could not be detected; in the runs with sulfuric acid as catalyst the absence of organic sulfate esters was not certain, but if such substances were present, their concentrations must have been small. Small concentrations of sulfur dioxide were formed in the runs made at 221°C., but considerable decomposition of the acid occurred at 248°C.

For the quantitative determination of the combined amounts of ethanol and ether in aqueous solutions, the method proposed by Szeberényi (50) was used with slight modifications. In this method both substances are oxidized to acetic acid with an excess of a concentrated solution of potassium dichromate in sulfuric acid, and the excess dichromate is titrated iodimetrically. It was discovered that dilution of the reagent with an appropriate amount of distilled water would give a reagent capable of oxidizing ethanol quantitatively to acetic acid while leaving the ether essentially unattacked. By making analyses with both concentrations of reagent it was possible to determine concentrations of ether by difference. Generally the rather broad range of applicability of chromic acid reagents for the determination of organic substances in dilute aqueous solution was impressive. The analytical procedures were calibrated by using dilute aqueous solutions of ethanol of known concentration available commercially and also by using the saturated

water-rich layer of the two-phase ether-water system. Precise data for the solubility of ether in water as a function of temperature in the neighborhood of 25°C. are available from a number of investigators; in this study the data of Hill (19) were selected as being the most reliable. The ether-water mixture was maintained in a water bath at 25.2 ± 0.1°C. prior to use.

The concentrations of phosphoric and sulfuric acid in samples from the hydration runs were measured by titration with a standard solution of sodium hydroxide. Phosphoric acid was titrated to the second equivalence point by using slight modifications of the method proposed by Kolthoff (28); sulfuric acid was titrated to a pale rose color of phenolphthalein indicator.

Concentrations of acetaldehyde in the liquid phase were determined by precipitation of the aldehyde with 2,4-dinitrophenylhydrazine reagent, according to the gravimetric method of Iddles and Jackson (22). In all cases the concentration of acetaldehyde was negligible.

The quantity of ethylene polymer formed during a run was determined by fractional distillation of the liquid mixture recovered from the reactor after it had cooled to room temperature at the end of the run. For the runs made at 221°C. the amount of polymer recovered was negligible.

Analytical reagent-grade chemicals were used throughout the work.

RESULTS AND DISCUSSION

Equilibrium was not attained in any of the runs with phosphoric acid as catalyst. The failure to reach equilibrium is attributed both to the slow rates of approach to an equilibrium state for reactions (1) and (2), even at the relatively high temperature of 296°C., and to disturbing effects caused by polymerization of ethylene. As criteria of equilibrium both the attainment of a constant pressure in the reactor and the attainment of the same (final) liquid-phase concentration of ethanol (and also of ether) in separate runs made with different concentrations of ethylene, water, ethanol, and/or ether in the original charge were selected.*

Equilibrium appeared to be quite closely approached however in runs of about 18 hr. made at 221°C. and 273 atm. absolute pressure with sulfuric acid as catalyst. The equilibrium concentration of ethanol in the liquid phase was judged to be 111 ± 5 g./liter of withdrawn sample; the equilibrium concentration of ether, known with less precision, was estimated to be 20 ± 7 g./liter. The acid concentrations of near-equilibrium liquid-phase samples varied from 1.4 to 2.1 molar in different runs, primarily because of variations in the ratio of acid to water in the mixtures charged to the reactor.

Expressed in terms of mole percentage the measured equilibrium concentration of ethanol is 4.6. By interpolation in Table 1A the calculated value of concentration for the same conditions is 6.0 mole %. These two values are in quite good agreement, especially in view of the following considerations.

1. As indicated previously, the calculated value of concentration is expected to be somewhat high because of the assumption made concerning the behavior of the partial molal volume of ethanol as a function of temperature. Unfortunately it is difficult to estimate the limits of uncertainty of the calculated compositions because of the several assumptions made in obtaining them.

2. If the formation of ether were neglected, as appears to have been almost universally the case in the past, the calculated value of equilibrium concentration would be considerably greater than 6.0, thereby giving a marked divergence between the calculated and experimental results. For example the concentration obtained by interpolation in Table 1B is roughly 30 mole %, nearly an order of magnitude higher than the measured value.

3. In addition to the necessity of taking into account the formation of ether, the use of available vapor-liquid equilibrium
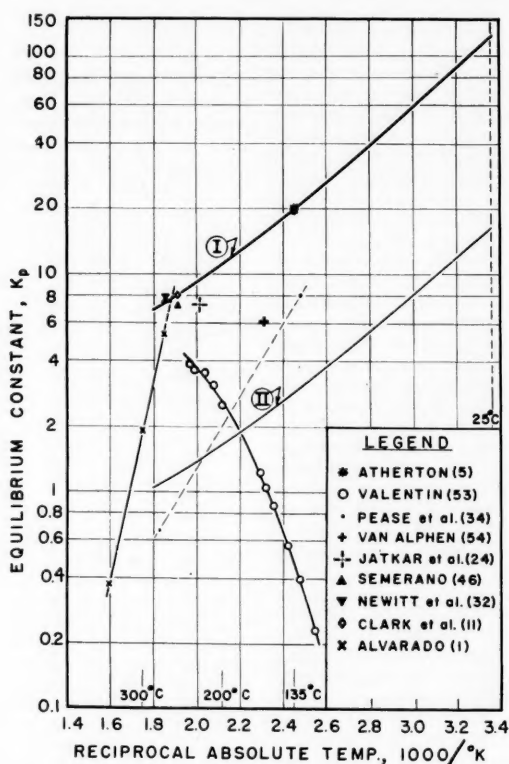
Fig. 2. Logarithm of equilibrium constant vs. reciprocal absolute temperature

$$2\,C_2H_5OH(g) = C_2H_5OC_2H_5(g) + H_2O(g).$$
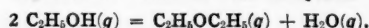
Curve I: based on selected experimental and specific-heat data.
Curve II: based entirely on thermal data.

LEGEND

* ATHERTON (5)
O VALENTIN (53)
• PEASE et al. (34)
+ VAN ALPHEN (54)
⊥ JATKAR et al. (24)
▲ SEMERANO (46)
▼ NEWITT et al. (32)
◆ CLARK et al. (11)
X ALVARADO (1)

*In such a case as that involved here, in which two simultaneous equilibria occur, the traditional concept of approaching equilibrium from both sides must necessarily be expanded to a more "generalized" form.

data for the binary ethanol-water system at elevated temperatures appears to be essential to obtain values of about the correct magnitude for equilibrium concentrations of ethanol in the liquid phase for the hydration of ethylene. When the phase-equilibrium relationships for ethanol are predicted solely on the basis of vapor-pressure data and of fugacity data obtained from generalized charts, together with the assumption of ideal-solution or ideal-gas behavior or of the applicability of other equivalent "mixture rules," the predicted equilibrium concentration of ethanol is almost invariably too high. Space limitations prevent the presentation of detailed examples to substantiate this conclusion, which is based on considerable experience with various methods of calculating equilibrium compositions for this system. Unfortunately vapor-liquid equilibrium data at elevated pressures and temperatures are in general not available for most binary systems, and so the number of high-pressure, high-temperature reactions for which this general method of approach can presently be used is very limited. Most of the necessary basic data are available (6, 47, 48) to permit application of the method to the hydration of propylene at elevated pressures and temperatures, for comparison with the experimental results of Majewski and Marek (30). However equilibrium constants for the dehydration of isopropanol to isopropyl ether at various temperatures can at present be derived only from thermal data which are quite uncertain. For isopropyl ether the available value (33b) of the absolute entropy is questionable, and the heat of formation can only be estimated from data on other compounds, since no direct measurements of the heat of combustion appear to have been reported.

4. Further support for the method of calculation presented here is obtained when the calculated values of equilibrium composition are compared with the experimental results of Gunness for the liquid phase. Although it is important to keep in mind that both of these sets of values are subject to some uncertainties, the agreement between them is close enough to indicate that the calculated values are at least of the correct magnitude; they are probably correct within a factor of about two. Thus for the wide ranges of temperature and pressure used by Gunness the observed range of ethanol concentrations was 1.4 to 8.4 mole %; the range of the calculated values for the same conditions is about 3.0 to 6.0 mole %. The observed change in concentration with pressure at constant temperature (254°C.) is somewhat greater than the calculated one but is in the same direction. The trend of concentration as a function of temperature is predicted less well; the calculated results indicate a slow decrease of concentration

with rising temperature at a constant pressure of 200 atm., whereas a maximum was found experimentally over the same temperature range at about this pressure.

The experimental value of equilibrium composition reported here is lower by perhaps 40 % than the value which would be predicted on the basis of Gunness's data. Although there is some uncertainty in extrapolating Gunness's results to the conditions of these experiments, most of this difference is best explained by the fact that these runs were of considerably longer duration than those of Gunness. This may have permitted a closer approach to true equilibrium with respect to both the ethylene hydration and (especially) the ether formation reactions, with a consequent reduction in the final measured ethanol concentration. It is significant in this regard that nearly all Gunness's runs were made with an initial ethanol concentration greater than the final equilibrium value and that in no run was any ether charged to the reactor.

In the determination of the calculated values of equilibrium composition the presence of catalyst in the liquid phase has been neglected. The experimental value of equilibrium composition has not been converted to a catalyst-free basis, however, since the assumption that the catalyst behaves merely as an inert diluent seems questionable.

The relatively small solubility of ether in liquid-phase samples was found, as would be expected, to depend strongly on the ethanol concentration and rose as the ethanol concentration increased. Presumably the same was true for ethylene, but its (small) solubility was not measured. It is unfortunate that most rules used for thermodynamic calculation, including Lewis and Randall's rule, make no allowance for these specific solubility effects, which are often pronounced at high pressures. The apparently small solubilities of ether and ethylene provide some justification for assuming the concentrations of these substances negligible in the previous equilibrium calculations.

The formation of sulfur-containing decomposition products caused the authors to terminate the run made at 248°C. rather quickly. Perhaps the use of a lower concentration of catalyst would have prevented substantial decomposition. Nevertheless the trend of early analyses did not exclude the possibility that the equilibrium concentration of ethanol may be higher at this temperature than it is at 221°C., at a pressure of 273 atm. If so, this behavior would be in agreement with the results of Gunness at temperatures of 218° and 254°C. and a pressure of 197 atm. but would differ from that observed by Majewski and Marek for the hydration of propylene. Unfortunately it was necessary to terminate the experimental

program shortly after this run had been made.

On the basis of some rough measurements of vapor-phase composition, as well as from the results of other investigators, it is thought that the calculated concentrations of ether in equilibrium mixtures are in general probably higher than the true values and that the predicted proportions of the other substances, especially ethylene, are correspondingly low. Whether this comes about through errors in the values of equilibrium constant selected for the ether formation reaction and/or from assumptions made in the calculations which may not be valid for high-pressure conditions cannot be determined. In spite of the formation of substantial concentrations of ether in these experiments, it is reasonably certain that only a single liquid phase was present under reaction conditions.

Mention should be made of calculated values of equilibrium composition published not long ago by Bennett (8), who applied the method of Joffe on a trial-and-error basis to the ternary gaseous system ethylene-ethanol-water and combined this with the vapor-liquid equilibrium data of Griswold, Haney, and Klein to predict liquid-phase compositions of ethanol for the hydration of ethylene. Although the details of the calculations are not given, the numerical result obtained by Bennett for ethanol concentration is much too high, even in view of the fact that formation of ether has been neglected. At relatively high values of pseudoreduced pressure, such as are involved here, the method of Joffe may properly be applied only in the region in which the pseudoreduced temperature is equal to or greater than 1. In this specific calculation a set of vapor-phase concentrations which would permit this requirement and the existing equilibrium and compositional restrictions to be satisfied simultaneously could not be found.

SUMMARY

Values of equilibrium constant calculated for the hydration of ethylene to form ethanol over a range of temperature appear to be in good agreement with those determined experimentally by other investigators in studies made at low pressures and elevated temperatures. For the dehydration of ethanol to ethyl ether there is wide variation in the experimental values of equilibrium constant measured by different investigators, and the thermal data also are subject to greater uncertainty. However by the selection of what appear to be the most reliable experimental equilibrium results it is possible to obtain satisfactory agreement with the standard heat of reaction obtained from thermal data. For the standard entropy change of reaction

the agreement is poor, primarily because of a probable error in the value available for the entropy of ethyl ether.

In an extension of the low-pressure equilibrium results to the prediction of equilibrium compositions for the hydration of ethylene at elevated pressures, it is necessary to allow for the formation of ethyl ether and to make use of available vapor-liquid equilibrium data for the binary system ethanol-water at elevated temperatures. Failure to take these two factors into account generally results in an overestimation of the equilibrium concentration of ethanol; when both are properly allowed for, the agreement between the calculated and measured concentrations in the liquid phase appears to be good. Previous studies of this system have neglected to take the formation of ether into account.

NOTATION

α, β, γ = empirical constants in equation expressing molar specific heat as a function of absolute temperature

C_p = molar specific heat of a gas, cal./(mole)(°K.)

f_m = fugacity of a gas mixture, defined by the equation $\ln f_m = (1/RT) \int_0^p V_m \, dp$ (T constant), where V_m is the molal volume of the mixture

K_f = equilibrium constant of a chemical reaction based on the fugacities of the participating substances

K_p = equilibrium constant of a chemical reaction based on the partial pressures of the participating substances

P = (total) pressure, atm.

R = gas constant, consistent units

T = absolute temperature, °K. = °C. + 273.2

y = mole fraction in vapor phase, dimensionless

Subscripts

m = mixture (solution)

i = individual component of a mixture

Superscript

0 = standard state (ideal gas at a pressure of 1 atm.)

LITERATURE CITED

1. Alvarado, A. M., J. Am. Chem. Soc., 50, 790 (1928).
2. Antonio, A. L., Sc.D. thesis, Mass. Inst. Technol., Cambridge (1939).
3. Applebey, M. P., J. V. S. Glass, and G. F. Horsley, J. Soc. Chem. Ind. (London), 56, 279 T (1937).
4. Aston, J. G., Ind. Eng. Chem. 34, 514 (1942).
5. Atherton, P. G., B. App. Sci. thesis, Univ. of Queensland, Brisbane, Australia (1952).
6. Barr-David, F. H., D. Eng. dissertation, Yale Univ., New Haven, Conn. (1956).
7. Barrow, G. M., J. Chem. Phys., 20, 1739 (1952).
8. Bennett, C. O., Chimie & industrie, 70, 656 (1953).
9. Bliss, R. H., and B. F. Dodge, Ind. Eng. Chem., 29, 19 (1937).
10. Bonhöffer, K. F., and O. Reitz, Z. physik. Chem., A179, 135 (1937).
11. Clark, R. H., W. E. Graham, and A. G. Winter, J. Am. Chem. Soc., 47, 2748 (1925).
12. Cope, C. S., Ph.D. dissertation, Yale Univ., New Haven, Conn. (1956).
13. Dodge, B. F., "Chemical Engineering Thermodynamics," Chap. XI, McGraw-Hill, New York (1944).
14. Erlenmeyer, E., Ann. Chem. Justus Liebigs, 162, 373 (1872); —— and Tscheppe, Z., Chem., 11, 342 (1868).
15. Eucken, A., and E. U. Franck, Z. Elektrochem., 52, 195 (1948).
16. Gilliland, E. R., R. C. Gunness, and V. O. Bowles, Ind. Eng. Chem., 28, 370 (1936).
17. Griswold, John, J. D. Haney, and V. A. Klein, ibid., 35, 701 (1943).
18. Gunness, R. C., S.M. thesis, Mass. Inst. Technol., Cambridge (1934).
19. Hill, A. E., J. Am. Chem. Soc., 45, 1143 (1923).
20. Holden, J. H., and T. B. Stackpole, S.B. thesis, Mass. Inst. Technol., Cambridge (1934).
21. Hougen, O. A., and K. M. Watson, "Chemical Process Principles," Part Two, pp. 489, 495, 622, John Wiley, New York (1947).
22. Iddles, H. A., and C. E. Jackson, Ind. Eng. Chem. Anal. Ed., 6, 454 (1934).
23. "International Critical Tables," Vol. V, McGraw-Hill, New York (1929).
24. Jatkar, S. K. K., and H. E. Watson, J. Indian Inst. Sci., 9A, 71 (1926); J. Soc. Chem. Ind. (London), 45, 168T (1926).
25. Joffe, Joseph, Ind. Eng. Chem., 40, 1738 (1948).
26. Kharasch, M. S., J. Research Natl. Bur. Standards 2, 359 (1929).
27. Kistiakowsky, G. B., H. Romeyn, Jr., J. R. Ruhoff, H. A. Smith, and W. E.

Vaughan, J. Am. Chem. Soc., 57, 65 (1935).
28. Kolthoff, I. M., Chem. Weekblad, 12, 644 (1915); 13, 284 (1916).
29. Mace, C. V., and C. F. Bonilla, Chem. Eng. Progr., 50, 385 (1954).
30. Majewski, F. M., and L. F. Marek, Ind. Eng. Chem., 30, 203 (1938).
31. McCullough, J. P., R. E. Pennington, and Guy Waddington, J. Am. Chem. Soc., 74, 4439 (1952).
32. Newitt, D. M., and G. Semerano, Proc. Roy. Soc. (London), A157, 348 (1936).
33a. Parks, G. S., and H. M. Huffman, J. Am. Chem. Soc., 48, 2788 (1926); 51, 1969 (1929).
33b. ——, and Mark Barmore, ibid., 55, 2733 (1933).
34. Pease, R. N., and C-C. Yung, ibid., 46, 390, 2397 (1924).
35. Perry, J. H., ed., "Chemical Engineers' Handbook," 3rd ed., McGraw-Hill, New York (1950)
36. Pitzer, K. S., J. Chem. Phys., 8, 711 (1940).
37. Reynoso, Alvaro, Ann. chim. et phys. (3), 48, 385 (1856); see also Ann. Chem. Justus Liebigs, 101, 100 (1857).
38. Rossini, F. D., "Chemical Thermodynamics," John Wiley, New York (1950).
39. ——, J. Research Natl. Bur. Standards, 8, 119 (1932); 13, 189 (1934).
40. ——, ibid., 17, 629 (1936).
41. ——, and J. W. Knowlton, ibid., 19, 249 (1937).
42. Rossini, F. D., et al., U. S. Natl. Bur. Standards Circ. 461, U. S. Government Printing Office, Washington, D. C. (1947).
43. ——, ibid., No. 500 (1952).
44. Sanders, F. J., and B. F. Dodge, Ind. Eng. Chem., 26, 208 (1934).
45. Schnaible, H. W., and J. M. Smith, Chem. Eng. Progr. Symposium Ser. 7, 49, 159 (1953).
46. Semerano, G., Gazz. chim. ital., 66, 162 (1936).
47. Shiffler, W. H., M. M. Holm, and L. F. Brooke, Ind. Eng. Chem., 31, 1099 (1939).
48. Stanley, H. M., J. E. Youell, and J. B. Dymock, J. Soc. Chem. Ind. (London), 53, 205 (1934).
49. Stohmann, F., J. prakt. Chem. (2), 33, 241 (1886); 35, 136 (1887).
50. Szeberényi, P., Z. anal. Chem., 54, 409 (1915).
51. Teller, Eduard, and Bryan Topley, J. Chem. Soc., 137, 876 (1935).
52. Thomsen, J., "Thermochemische Untersuchungen," Vol. IV (Organische Verbindungen), J. A. Barth, Leipzig (1886); see also Z. physik. Chem., 52, 343 (1905).
53. Valentin, F. H. H., J. Chem. Soc., 152, 498 (1950).
54. Van Alphen, J., Rec. trav. chim., 49, 754 (1930).
55. Vvedensky, A. A., and L. F. Feldman, J. Gen. Chem. (U.S.S.R.), 15, 37 (1945).
56. Weltner, William, Jr., and K. S. Pitzer, J. Am. Chem. Soc., 73, 2606 (1951).
57. Winer, Max, S.B. thesis, Mass. Inst. Technol., Cambridge (1934).

Thermodynamic Properties of Acetylene

JAMES H. WEBER

University of Nebraska, Lincoln, Nebraska

The derived thermodynamic properties of acetylene have been determined over a temperature range of 32 to 500°F. and up to pressures of 2,000 lb./sq. in. abs. The data were calculated from vapor pressure, volumetric, and heat-capacity data by the use of rigorous thermodynamic relationships. The calculated data were found to be internally consistent. The enthalpy values are believed to be accurate within ±1.0 B.t.u./lb. and the entropy values to ±0.001 B.t.u./(lb.)(°R.).

In view of the increasing use of acetylene as a raw material in various chemical industries, a study was initiated to determine its derived thermodynamic properties. Sufficient thermal, volumetric, and vapor pressure-temperature data are available in the literature to permit the determination of these properties over the temperature range of 32° to 500°F. and up to pressures of 2,000 lb./sq. in. abs.

The determination of the volumetric data for acetylene has been the subject of a number of investigations. Sameshima (9) investigated the volumetric behavior over the temperature range of 32° to 77°F. and up to a pressure of 176 lb./sq. in. abs.; Rimarski and Konshak (8) up to 303 lb./sq. in. abs. at 32°F.; Kiyama, Ikegami, and Inous (6) over the temperature range of 18° to 482°F. and the pressure range of 294 to 1,760 lb./sq. in. abs.; and Hölemann and Hasselmann (5) over the temperature range of 32° to 122°F. and up to pressures of 353 lb./sq. in. abs.; the last investigators correlated their data by the equation

$$PV = RT - aP - bP^2 \qquad (1)$$

where

$$a = 4.89 \times 10^{-1} - 1.08 \times 10^{-3}T$$

$$b = 6.99 \times 10^{-3} - 2.1 \times 10^{-5}T$$

and the pressure is expressed in atmospheres, the temperature in degrees Kelvin, and R in consistent units.

Teranishi (11) rechecked the data of Kiyama et al. (6) and reported volumetric data for acetylene over the temperature

range of 32° to 482°F. and from a pressure of 147 to 1,907 lb./sq. in. abs. The volumetric behavior of the saturated liquid and vapor phases as well as vapor pressure-temperature data are reported in Lange's handbook (7).

The most recent heat-capacity data for acetylene are those reported in (1). These data were calculated from the spectroscopic data of Wagman, Kilpatrick, Pitzer, and Rossini (12). Teranishi (11) calculated heat-capacity data by the

TABLE 1. THERMODYNAMIC PROPERTIES OF SATURATED ACETYLENE

Temperature, °F.	Pressure, lb./sq. in. abs.	Fugacity pressure f/p	Volume, cu. ft./lb.		Enthalpy, B.t.u./lb.			Entropy, B.t.u./(lb.)(°R.)		
			Liquid	Vapor	Liquid	Vaporization	Vapor	Liquid	Vaporization	Vapor
32	386.6	0.771	0.03457	0.357	−63.9	164.2	100.3	1.153	0.334	1.487
40	433.5	0.763	0.03558	0.316	−59.2	158.9	99.7	1.154	0.318	1.472
60	570.1	0.737	0.03844	0.226	−38.2	135.0	96.8	1.187	0.260	1.447
80	739.0	0.704	0.04399	0.152	−5.6	97.4	91.8	1.256	0.180	1.436
97.4	905.0	—	0.0695	0.0695	0	0	—	—	0	
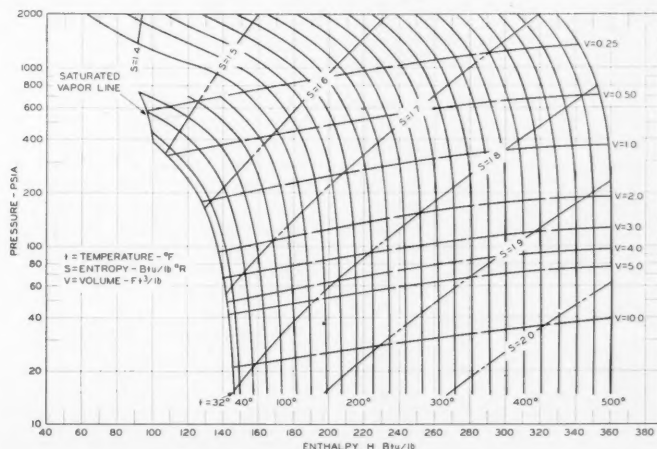
Fig. 1. Pressure-enthalpy diagram for acetylene.

TABLE 2—THERMODYNAMIC PROPERTIES OF SUPERHEATED ACETYLENE

Temperature °F.	Volume cu. ft./lb.	Enthalpy B.t.u./lb.	Entropy B.t.u./(lb.)(°R.)	Fugacity pressure f/p
14.696 lb./sq. in. abs. (−119.0°F.)*				
32	13.60	147.1	1.807	0.991
60	14.47	157.8	1.828	0.994
100	15.62	174.0	1.858	0.996
140	16.77	190.8	1.887	0.998
180	17.91	208.1	1.915	0.999
220	19.04	226.0	1.943	0.999
260	20.16	244.4	1.969	1.000
300	21.29	262.8	1.994	1.000
340	22.41	281.9	2.019	1.000
380	25.53	301.3	2.043	1.000
420	24.65	321.1	2.065	1.000
460	25.76	341.1	2.088	1.000
500	26.92	361.0	2.110	1.000
50 lb./sq. in. abs. (−76.9°F.)				
32	3.914	142.6	1.707	0.971
60	4.183	154.2	1.729	0.978
100	4.548	171.3	1.761	0.987
140	4.905	188.8	1.792	0.993
180	5.250	206.7	1.820	0.997
220	5.585	224.9	1.848	0.998
260	5.923	243.4	1.874	0.998
300	6.253	262.3	1.900	0.999
340	6.583	281.5	1.925	0.999
380	6.913	301.0	1.949	0.999
420	7.240	320.8	1.972	0.999
460	7.574	340.9	1.994	0.999
500	7.904	360.9	2.016	0.999
100 lb./sq. in. abs. (−45.8°F.)				
32	1.894	137.2	1.645	0.942
60	2.043	150.3	1.671	0.957
100	2.240	168.8	1.704	0.973
140	2.434	187.2	1.736	0.986
180	2.615	205.3	1.766	0.993
220	2.785	224.3	1.794	0.995
260	2.953	243.2	1.821	0.997
300	3.119	262.1	1.847	0.997
340	3.286	281.5	1.872	0.998
380	3.452	301.0	1.896	0.998
420	3.617	320.7	1.919	0.998
460	3.783	340.9	1.941	0.999
500	3.945	360.8	1.963	0.999
150 lb./sq. in. abs. (−25.2°F.)				
32	1.216	130.3	1.604	0.913
60	1.324	145.7	1.633	0.935
100	1.465	165.7	1.669	0.959
140	1.605	185.0	1.703	0.978
180	1.732	204.0	1.733	0.989
220	1.847	223.6	1.762	0.992
260	1.961	242.6	1.789	0.994
300	2.073	261.8	1.815	0.995
340	2.185	281.3	1.840	0.996
380	2.296	300.9	1.864	0.997
420	2.407	320.7	1.887	0.997
460	2.517	340.9	1.910	0.998
500	2.629	360.8	1.931	0.998
200 lb./sq. in. abs. (−9.4°F.)				
32	0.870	125.6	1.573	0.883
60	0.959	141.8	1.605	0.912
100	1.074	163.4	1.644	0.943
140	1.185	183.8	1.679	0.969

*Saturation temperatures are given in parentheses.

TABLE 2*—(Continued)

Temperature °F.	Volume cu. ft./lb.	Enthalpy B.t.u./lb.	Entropy B.t.u./(lb.)(°R.)	Fugacity pressure f/p
180	1.285	203.4	1.711	0.984
220	1.375	222.7	1.740	0.988
260	1.462	242.0	1.768	0.991
300	1.546	261.3	1.794	0.993
340	1.632	280.8	1.820	0.994
380	1.716	300.5	1.842	0.995
420	1.800	320.5	1.867	0.996
460	1.883	340.7	1.890	0.996
500	1.968	360.8	1.911	0.997
500 lb./sq. in. abs. (50.1°F.)				
(At satn.)	0.268	98.3	1.457	0.751
60	0.288	107.2	1.478	0.774
100	0.359	140.2	1.540	0.837
140	0.416	167.2	1.587	0.894
180	0.464	190.9	1.625	0.930
220	0.507	213.0	1.659	0.946
260	0.546	234.1	1.689	0.957
300	0.585	254.7	1.717	0.964
340	0.623	275.0	1.743	0.970
380	0.659	295.3	1.768	0.974
420	0.694	315.6	1.792	0.978
460	0.730	336.0	1.814	0.981
500	0.766	356.8	1.837	0.983
1,000 lb./sq. in. abs.				
140	0.141	129.2	1.485	0.694
180	0.183	165.1	1.543	0.781
220	0.212	193.6	1.587	0.829
260	0.239	218.6	1.622	0.873
300	0.263	241.8	1.653	0.892
340	0.285	263.8	1.682	0.908
380	0.305	285.2	1.708	0.920
420	0.324	306.4	1.733	0.930
460	0.343	327.6	1.756	0.938
500	0.362	348.9	1.779	0.944
1,500 lb./sq. in. abs.				
140	0.0529	83.8	1.392	0.588
180	0.0912	133.7	1.473	0.689
220	0.120	170.3	1.528	0.749
260	0.143	200.2	1.571	0.794
300	0.163	226.6	1.607	0.827
340	0.179	250.8	1.638	0.852
380	0.194	273.7	1.666	0.870
420	0.208	295.8	1.691	0.886
460	0.222	317.7	1.716	0.898
500	0.236	339.8	1.739	0.909
2,000 lb./sq. in. abs.				
140	0.0433	62.0	1.349	0.485
180	0.0557	105.9	1.420	0.591
220	0.0760	146.4	1.481	0.666
260	0.0962	181.1	1.530	0.725
300	0.112	210.6	1.570	0.770
340	0.126	236.8	1.604	0.803
380	0.138	261.2	1.633	0.827
420	0.150	284.6	1.660	0.848
460	0.162	307.4	1.686	0.865
500	0.173	330.0	1.710	0.880

*Table 2 is somewhat abbreviated here.

equation

$$C_P = C_p^0 - \int_{P_o}^{P} T\left(\frac{\partial^2 V}{\partial T^2}\right)_P dP \quad (2)$$

He used the values of the heat capacity in the ideal-gas state and unit fugacity as calculated by Spencer (10), who had used the experimental results of Wagman et al. (12) in his calculations.

The critical constants $t_c = 97.4°F.$, $P_c = 905$ lb./sq. in. abs., and $V_c = 0.0695$ ft./lb. reported in (2) were used in this work. Additional constants used were the molecular weight of acetylene, 26.036; gas-law constant, R, 10.7335 (lb./sq. in.)(cu. ft.)/(lb.-mole)(°R.); ice point, 491.69°R. One pound of acetylene was used as the basis of calculation, and the enthalpy and entropy values of acetylene in the ideal-gas state, unit fugacity, and 0°R. were set equal to zero. This is the reference state used in (3, 4).

Residual volumes were calculated from the volumetric data of Sameshima (9), Hölemann and Hasselmann (5), and Teranishi (11) and for the saturated vapor. A plot of α vs. pressure with temperature parameters was made and the data were smoothed. The data of Sameshima, and Hölemann, and Hasselmann were compared at 32° and 77°F. up to pressures of 176 lb./sq. in. abs. Agreement between the two sets of data was good, usually within 0.5%.

A number of comparisons between the data of Hölemann and Hasselmann (5) and of Teranishi (11) were made. In some instances the agreement between the two sets of data was not so good as might have been expected. For example, over the temperature range of 32° to 122°F. and at a pressure of 147 lb./sq. in. abs. the reported molal volumes differed from 0.05 to 2.11%, with the values reported by Teranishi being consistently the larger of the two at the six temperatures investigated. At the same temperatures but at 247 lb./sq. in. abs. the reported molal volumes differed from −3.20 to +1.99%, with the values of Hölemann and Hasselmann being the greater at the lower temperatures and the lesser at the higher temperatures. To calculate these percentages, the differences in the reported molal volumes were multiplied by one hundred and the products then divided by the molal volumes reported by Teranishi.

The data of Teranishi however appeared to be consistent with the data for the saturated vapor. Hence at conditions of high pressure the data of Teranishi were used to calculate the thermodynamic properties, while under conditions of low or moderate pressures, up to about 176 lb./sq. in. abs., the data of Hölemann and Hasselmann (5) were used.

At temperatures above 122°F. the temperature parameters on the α vs. pressure plot were extrapolated from 147 to 0 lb./sq. in. abs., as the required volumetric data have not been determined. In most cases these extrapolations were approximately straight lines. This assumption was made after studying the

temperature parameter below 122°F. over the same pressure range.

Through the use of the α vs. pressure plot previously mentioned the fugacity to pressure ratios were determined. The basic relationship used was

$$\ln \frac{f}{P} = -\frac{1}{RT} \int_0^P \alpha \, dP \qquad (3)$$

The value of the integral was determined graphically.

Latent heats of vaporization were calculated by the Clapeyron equation

$$\frac{dP}{dT} = \frac{\Delta H_v}{T \Delta V} \qquad (4)$$

since the equation is thermodynamically rigorous, and the necessary vapor-pressure, temperature, and volumetric data were available.

The enthalpy values of the superheated vapor were calculated as differences between the values for the real gas and the ideal gas at the same temperature. The relationship used was

$$_M(H_p - H^0)_T$$
$$= -\int_{P^o}^P \left[\alpha - T\left(\frac{\partial \alpha}{\partial T}\right)_p \right] dP \qquad (5)$$

The expression could be evaluated analytically at low pressures, where the volumetric data of Hölemann and Hasselmann (5) could be represented by Equation (1). The expression for the residual volume at constant temperature developed from this equation of state is

$$\alpha = a + bP \qquad (6)$$

Once $(H_p - H^\circ)_T$ was calculated, the enthalpy could be determined after the value of the enthalpy in the ideal-gas state had been obtained from (3).

At elevated pressures where the volumetric data of Teranishi (11) were used, the enthalpy could be calculated from the expression

$$dH = \int_{T_1}^{T_2} C_p \, dT \qquad (7)$$

because Teranishi had previously determined the effect of pressure on the heat capacity of the superheated vapor by Equation (2). The value of the integral was determined graphically.

Entropy differences between the real gas and the ideal gas at the same temperature in the superheated vapor region were determined by the expression

$$_M(S_p - S^0)_T = -\int_{P^o}^P \frac{R}{P} \, dP$$
$$+ \int_{P^o}^P \left(\frac{\partial \alpha}{\partial T}\right) dp \qquad (8)$$

The entropy difference $(S_p - S^\circ)_T$ could be evaluated entirely analytically under conditions of low pressure, where the data of Hölemann and Hasselmann

were used. Once the entropy differences were calculated, the entropy could be determined with the aid of entropy values of the ideal gas obtained from (4).

At elevated pressures the heat-capacity data calculated by Teranishi (11) were employed, and entropy values were calculated by the expression

$$dS = \int_{T_1}^{T_2} \frac{C}{T} p \, dT \qquad (9)$$

The integral was evaluated graphically.

The enthalpy values for the saturated vapor were determined by plotting H vs. T and extrapolating the isobars to the saturation temperature. The entropy data for the saturated vapor were determined by plotting S vs. T and again extrapolating the isobars to the saturation temperature.

Enthalpy and entropy data for the saturated liquid phase were obtained by subtracting the enthalpy or entropy of vaporization from their respective values in the saturated vapor phase. Finally all the data were plotted and smoothed on large scale H vs. S, S vs. T, and H vs. S plots. The smoothed data are reported in tabular form in Tables 1 and 2* and the data for the saturated and superheated vapors are shown graphically in the form of a log P vs. H plot (Figure 1).

The final results were checked for internal consistency through the relationship

$$dH = T \, dS + V \, dP \qquad (10)$$

which is a statement of the first and second laws of thermodynamics. Setting the value of the entropy at a constant reduces the equation to

$$dH = V \, dP \qquad (11)$$

If the right-hand side of Equation (11) is multiplied by P/P and integrated, the result is

$$H_2 - H_1 = \frac{144}{778.3} \int_{P_1}^{P_2} PV \, d \ln P \qquad (12)$$

The right-hand side of the equation can be evaluated graphically and compared with the enthalpy differences obtained from the calculated data. A number of consistency checks of this type were made and showed that the results presented are internally consistent. Data however are not available to check the accuracy of the final results, but the enthalpy values are probably accurate to ±1.0 B.t.u./lb. and the entropy values accurate to 0.001 B.t.u./(lb.)(°F.).

In summation f/P ratios, enthalpy, and entropy data, determined by rigorous thermodynamic methods, are presented

for acetylene over the temperature range of 32° to 500°F. and up to pressures of 2,000 lb./sq. in. abs. The results are internally consistent.

NOTATION

C_p	=	heat capacity at constant pressure, B.t.u./(lb.)(°R.)
H	=	enthalpy, B.t.u./lb.
P	=	pressure, lb./sq. in. abs., unless otherwise specified
S	=	entropy, B.t.u./(lb.)(°R.)
T	=	absolute temperature, °R., unless specified as °K.
V	=	specific volume, cu. ft./lb.
a and b	=	empirical constants of Equation (1)
f	=	fugacity, same units as pressure
t	=	temperature, °F.
α	=	residual volume, cu. ft./lb.-mole, $RT/P - V_M$

Subscripts

c	=	critical property
M	=	molal quantity
v	=	vaporization

Superscripts

0	=	property in the ideal-gas state at unit fugacity

LITERATURE CITED

1. "Am. Petroleum Inst. Research Proj. 44, Table 25v-E, Carnegie Inst. Technol., Pittsburgh, (1953).
2. Ibid., Table 20i.
3. Ibid., Table 2u-E.
4. Ibid., Table 20-t.
5. Hölemann, P., and R. Hasselmann, Forschungsb. Des Wirtschafts und Verkehrsmnisteriums, No. 78, (1954).
6. Kiyama, Ryo, Tatsuya Ikegami, and Kazuo Inoue., Rev. Phys. Chem. Japan, 21, 58 (1951).
7. Lange, N. A., ed., "Handbook of Chemistry," 8th ed., Handbook Publishers, Inc., Sandusky, Ohio (1952).
8. Rimarski, W., and M. Konshak, Autogene Metallbearbeit., 26, 129 (1933).
9. Sameshima, Jitsusaburo, Bull. Chem. Soc., Japan, 1, 41 (1926).
10. Spencer, H. M., Ind. Eng. Chem., 40, 2152 (1948).
11. Teranishi, Hiroshi, Rev. Phys. Chem., Japan, 25, 25 (1955).
12. Wagman, D. D., J. E. Kilpatrick, K. S. Pitzer, and F. D. Rossini, J. Research Natl. Bur. Standards, 35, Research Rept. 1682, 467 (1948).

*Tabular material has been deposited as document 5824 with the American Documentation Institute, Photoduplication Service, Library of Congress, Washington 25, D. C., and may be obtained for $1.25 for photoprints or $1.25 for 35-mm. microfilm.

Nonequilibrium Thermodynamics: A Survey

K. G. DENBIGH

The University of Edinburgh and Heriot-Watt College, Edinburgh, Scotland

This paper presents a review of the field of thermodynamics of irreversible processes. The three essential steps in the use of this form of thermodynamics are the calculation of the entropy production, the setting up of the linear phenomenological equations, and the use of the Onsager reciprocal relation. The most important applications are to the transport processes, especially to the coupling phenomena which occur when two or more such processes take place in the same system.

To a classical thermodynamicist, such as Clausius or Willard Gibbs, the existence many years later of a flourishing branch of thermodynamics which purports to deal with nonequilibrium states might have seemed very unlikely. To be sure the first law applies equally to equilibrium and nonequilibrium but is very limited in its scope. The most interesting parts of classical thermodynamics were based on the use of the second law as much as on the first. As such its results were applicable only to equilibrium, for it is only for reversible processes that the second law gives equations as distinct from inequalities. For all irreversible change the relation $dS > 0$ can be used only for the derivation of other inequalities, and these are comparatively unimportant. (For example, viscosities, conductivities, etc., cannot be negative.)

Thus at the time of Gibbs, and indeed up to 1931, what was called thermodynamics was essentially an equilibrium thermodynamics. However there had been one conspicuous exception: the derivation by William Thomson, Lord Kelvin (11), of the equation relating the Peltier heat to the electromotive force in a thermoelectric circuit, a system which is certainly not at equilibrium because of the temperature gradients. In this derivation Thomson was well aware that he was using a new hypothesis which could not be justified on the basis of the first and second laws; what it amounts to is the statement that an infinitesimal displacement from a steady state creates no entropy. To the thermodynamics of Clausius and Gibbs this would have appeared quite inadmissible unless the words *steady state* were replaced by the more restricted *condition of equilibrium*.

Nevertheless the equation obtained as a result of Thomson's intuitive genius was substantially confirmed by experiment, and the same hypothesis was subsequently used by Eastman (9) and Wagner (20) as a basis for the theory of thermal diffusion and thermocells*.

However the real breakthrough into a fully fledged nonequilibrium thermodynamics came in 1931 as a result of Onsager's famous papers (14, 12). The essential feature was the use of a third physical principle, microscopic reversibility, in addition to the first and second laws. By using all three together, Onsager was able to establish entirely new relations, applicable to any system in which there are two or more irreversible processes between which there is some mechanism of coupling. Many of these relations have been verified experimentally. Their great merit—and among them are included the thermoelectric equations—is that they are based on three well-established principles and not, as in Thomson's derivation, on two such principles together with a new hypothesis.

The starting point of Onsager's work was his observation that the chemist makes implicit use of the principle of microscopic reversibility whenever he asserts the detailed balancing of reactions in a system at equilibrium in which several reactions are coupled.† One should consider a substance which can exist in three tautomeric forms, A, B, and C, between which there is interconversion. A state of equilibrium could be maintained if there were a steady flow, at the molecular level, round the cycle:

$$A \underset{\searrow}{\overset{\nearrow}{}} \begin{array}{c} B \\ \downarrow \\ C \end{array}$$

The chemist rather believes that each of the three reactions, at equilibrium, takes place with equal frequency in the forward and backward directions. This is expressed symbolically:

$$A \rightleftarrows \begin{array}{c} B \\ \\ C \end{array}$$
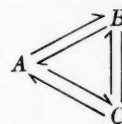
In the case of coupled reactions, such as those above, this assertion of detailed balancing is not deducible from classical thermodynamics but is a special case of the principle of microscopic reversibility which has its origin in quantum mechanics. It has been expressed by Tolman (19) as follows: ". . . under equilibrium conditions any molecular process and the reverse of that process will be taking place on the average at the same rate . . . ."

This principle places a restriction on physical as well as chemical processes when there is coupling or interaction

---

*See reference (6) for a more extended discussion of Thomson's hypothesis in relation to Onsager's theory.

†Admittedly the detailed balancing at equilibrium of reactions which are not coupled is provided for by the second law. However when there is coupling, relationships such as $K = k_1/k_2$ cannot be deduced from this law; the principle of microscopic reversibility must be used instead.

between them. But for its operation, equilibrium could be maintained by a cyclic process.

It will be noticed that frequent mention has been made of *equilibrium*, for example in Tolman's enunciation of the principle. It may be asked, how does it help in the development of a nonequilibrium thermodynamics? An extra assumption is needed, namely that the linear equations connecting forces and flows (as described in the next section) apply also to the natural fluctuations about the equilibrium state. These fluctuations are regarded as transient flows of heat, matter, etc., and the symmetric relationship between them, brought to light by microscopic reversibility, is regarded as being equally applicable to the large-scale flows which are the irreversible processes. This will be discussed in more detail later.

LINEAR EQUATIONS

To a usually satisfactory degree of approximation the rates of the transport processes are known to be proportional to the gradients of suitable potential functions. For example the flow of heat or electricity or the diffusion of a chemical substance is known to be proportional to the gradients of temperature, electric potential, and concentration* respectively, as expressed in Fourier's, Ohm's, and Fick's laws. Thus if J is the flow and X is the generalized force,

$$J = LX$$

When a type of system is considered in which two such processes take place simultaneously, their rates are J_1 and J_2 and the conjugate forces X_1 and X_2 respectively. Rather than to suppose that J_1 is uniquely and linearly determined by X_1 and J_2 by X_2, a more general assumption is that each flow is a linear function of both forces. Thus

$$\left.\begin{aligned} J_1 &= L_{11}X_1 + L_{12}X_2 \\ J_2 &= L_{21}X_1 + L_{22}X_2 \end{aligned}\right\} \quad (1)$$

Such an assumption is necessary to give expression to the reality of the interaction if it exists in the particular system. The thermoelectric effect, for example, is due to the coupling between a flow of current and a flow of heat. When electrons flow through a wire, they carry with them not only their charge but also their kinetic energy. Their motion as current I thus creates a contribution to the over-all heat flow q. If $\Delta\phi$ and ΔT are differences of electric potential and of temperature, then in accordance with Equations (1) one writes

$$I = \text{const. } \Delta\phi + \text{const. } \Delta T$$

*In the case of diffusion the chemical potential should preferably be used in place of concentration in the expression of Fick's law.

$$q = \text{const. } \Delta\phi + \text{const. } \Delta T$$

The first and fourth constants are related to the electric and thermal conductivities respectively. The second constant represents the effect of the temperature difference on the current, and the third shows the effect of the electromotive force on the flow of heat. The function of the Onsager theory in this particular example is to show the relationship which exists between these two coupling coefficients and thereby to derive the same equation relating the Peltier heat to $d\phi/dT$ as had been previously obtained by Thomson by use of his *ad hoc* hypothesis.

ENTROPY PRODUCTION

So far the forces, X, have not been closely defined and there is certainly a good deal of latitude in their choice. One should consider for example a region in a body where there is a local temperature T and a temperature difference dT over a distance dx. According to Fourier's law the component of heat flow in this direction is proportional to dT. However the thermal force could equally well be taken as dT itself, or as $d(1/T)$, etc. These changes merely alter the meaning of the scalar coefficient L and its relationship to the thermal conductivity, as conventionally defined. (Thus in the instance quoted the value of L is changed by a factor $-1/T^2$.)

A more restricted choice of the forces may be made on the basis of the entropy production in the system. In any irreversible process entropy is "created," and to an extent which depends on the magnitude of the flows J_i and the forces X_i. For example in a simple process of heat conduction the entropy creation (or energy dissipation) is proportional to the product $q\Delta T$, where q is the amount of heat which has been transmitted and ΔT is the temperature difference over which this amount of energy has been degraded.

The rate of entropy creation due to a number of processes taking place at rates J_1, J_2, etc., is dS/dt. It will be shown by use of an example that the entropy creation can be expressed as a sum of products. Thus

$$\frac{dS}{dt} = J_1X_1 + J_2X_2 + \cdots \quad (2)$$

where the quantities X_1, X_2, etc., are proportional to the same forces which are used in the expression of Fourier's law, Ohm's law, etc.; that is to say, the forces which have been introduced into the linear equations (1) can always be chosen in such a way that they also satisfy Equation (2). When this has been done, the essential content of Onsager's theory is to show that the coupling coefficients L_{12} and L_{21} are equal:

$$L_{12} = L_{21} \quad (3)$$

In more general terms the procedure in applying the thermodynamics of irreversible processes is as follows:

1. Determines the form of the quantities X_i which satisfy the relation

$$\frac{dS}{dt} = \sum J_iX_i \quad (4)$$

2. Assume that the flows J_i can be expressed with sufficient accuracy in the particular system as linear functions of the X_i:

$$J_i = \sum_{k=1}^{n} L_{ik}X_k \ (i = 1, 2, \cdots n) \quad (5)$$

3. Use Onsager's reciprocal relation

$$L_{ik} = L_{ki} \quad (6)$$

to eliminate some of the coefficients from (5) and thus obtain physical relations which can be tested by experiment. (It may be noted that the trivial case $L_{ik} = L_{ki} = 0$ corresponds to the absence of coupling.)

The basic theory will be discussed later.

EXAMPLE OF THE THERMOMOLECULAR PRESSURE DIFFERENCE

The application of *nonequilibrium thermodynamics* could be illustrated by reference to a variety of phenomena in which there is coupling. Two of the simplest of these are the thermoelectric effect and the thermomechanical pressure difference. The latter is probably of greater interest and will be chosen for illustration.

Thermomolecular pressure difference is a generic term which includes at least three effects, quite distinct from each other at the molecular level but the same in regard to their macroscopic description. These are as follows: (1) The Knudsen effect in a gas; a stationary pressure difference develops between two vessels communicating with each other through holes small compared with the mean free path, as the result of a temperature difference. (2) Thermoosmosis; here again there is a stationary pressure difference as the result of a temperature difference, but the two vessels are separated from each other by a membrane in which the fluid (which may be a liquid) is slightly soluble. Pores are not involved. (3) The fountain effect in liquid helium 2; the liquid flows spontaneously through a capillary connecting two vessels at different temperatures and builds up a stationary difference of hydrostatic head.

In each of these systems the flow of energy between the two vessels is coupled to the flow of matter. For apart from the normal conduction of heat through the substance of the barrier (that is, the membrane, capillary, etc.) there is also a transport of energy which is carried by the molecules of the fluid. It will be shown that a stationary pressure dif-

ference will arise, as the result of the temperature difference, whenever the mean energy of the molecules passing across the barrier is not equal to the enthalpy of the bulk fluid on either side.

On the basis of these preliminaries, the problem is formally treated by use of the theory as described in the previous section. The two vessels, 1 and 2, communicating with each other through a small hole, capillary, or membrane, will each be taken to be of constant volume. The fluid in vessel 1 is at a uniform temperature T and pressure P, and the fluid in vessel 2 at a uniform temperature $T + dT$ and a pressure $P + dP$. The two vessels together form an isolated system (but they may be thought of as having been brought to their particular temperatures by recent contact with two heat reservoirs). The problem is to determine whether or not dP is zero when any flow of the fluid comes to an end; more particularly the problem is to obtain an expression for dP/dT.

It is an implicit assumption of the nonequilibrium thermodynamics that the Gibbs equation

$$dU = T\, dS - P\, dV + \sum \mu_i\, dn_i \quad (7)$$

may be used, even though there is an absence of equilibrium. This will be discussed at a later stage. Bearing in mind the constancy of volumes and the fact that there is a single component fluid, one may write the Gibbs equation for the two vessels as

$$dU_1 = T\, dS_1 + \mu\, dn_1 \quad (8)$$

$$dU_2 = (T + dT)\, dS_2 \\ + (\mu + d\mu)\, dn_2 \quad (9)$$

The entropy created in the process is

$$dS = dS_1 + dS_2 \quad (10)$$

Using Equations (8) and (9), and noting that $dn_2 = -dn_1$ and $dU_2 = -dU_1$ (since one is concerned with an isolated system) one obtains

$$dS = -dU_2 \cdot \frac{dT}{T^2} - dn_2 \cdot d(\mu/T) \quad (11)$$

It will be noted that these equations allow for the passage of heat between the two vessels, due to normal heat conduction across the barrier, as well as for the energy associated with the transport of matter.

If the process takes place in a time dt, one obtains for the rate of entropy creation

$$\frac{dS}{dT} = -\frac{dU_2}{dt} \cdot \frac{dT}{T^2} - \frac{dn_2}{dt} \cdot d\left(\frac{\mu}{T}\right) \quad (12)$$

Since $dU_2 = -dU_1$, the quantity dU_2/dt is the rate J_u of passage of energy from vessel 1 to vessel 2. Similarly dn_2/dt is

the rate J_m of flow of matter. The last equation may therefore be written

$$\frac{dS}{dt} = -J_u \frac{dT}{T^2} - J_m\, d\left(\frac{\mu}{T}\right) \\ = J_u\, d\left(\frac{1}{T}\right) - J_m\, d\left(\frac{\mu}{T}\right) \quad (13)$$

The forces X_u and X_m to be associated with the flow of energy and matter are therefore $d(1/T)$ and $-d(\mu/T)$ respectively.

One assumes the linear relations

$$J_m = -L_{11}\, d\left(\frac{\mu}{T}\right) - L_{12}\, \frac{dT}{T^2} \quad (14)$$

$$J_u = -L_{21}\, d\left(\frac{\mu}{T}\right) - L_{22}\, \frac{dT}{T^2} \quad (15)$$

Because of Onsager's relation, equation (3), the first of these equations may be written

$$J_m = -L_{11}\left\{ d\left(\frac{\mu}{T}\right) + \frac{L_{21}}{L_{11}}\frac{dT}{T^2} \right\} \quad (16)$$

By dividing (15) by (14) for the special case $dT = 0$ one obtains

$$\frac{L_{21}}{L_{11}} = \left(\frac{J_u}{J_m}\right)_{dT=0} \equiv Q \quad (17)$$

The ratio L_{21}/L_{11} is therefore the energy flow per unit matter flow under isothermal conditions where there will be no heat conduction. The quantity Q as defined by Equation (17) will be called the *energy of transport*. Thus from (16) and (17)

$$J_m = -L_{11}\left\{ d\left(\frac{\mu}{T}\right) + Q\frac{dT}{T^2} \right\} \quad (18)$$

and at the stationary state where all transfer of matter has come to an end

$$d\left(\frac{\mu}{T}\right) = -Q\frac{dT}{T^2} \quad (19)$$

From the classical thermodynamics of a single component system*

$$d\left(\frac{\mu}{T}\right) = \frac{\partial(\mu/T)}{\partial T}\, dT + \frac{\partial(\mu/T)}{\partial P}\, dP \\ = \frac{-h}{T^2}\, dT + \frac{v\, dP}{T} \quad (20)$$

Combining (19) and (20) one finally obtains

$$\frac{dP}{dT} = -\frac{(Q - h)}{vT} \quad (21)$$

The thermomechanical pressure difference is thus proportional to the difference between the energy of transport and the enthalpy of the fluid in bulk. Before the significance of this equation is commented upon, an alternative treatment of the problem will be discussed.

_____
*See for example page 101 of reference 4.

ALTERNATIVE CHOICE OF THE FLOWS AND FORCES

As remarked previously, for the purpose of applying Onsager's relation the conjugate flows and forces must always be chosen to satisfy Equation (4). However this still leaves a good deal of latitude. For example, by combining Equations (13) and (20) one obtains

$$\frac{dS}{dt} = -J_u\frac{dT}{T^2} - J_m\left(\frac{-h}{T^2}dT + \frac{v\, dP}{T}\right) \\ = -(J_u - J_m h)\frac{dT}{T^2} - J_m\frac{v\, dP}{T} \quad (22)$$

The flow J_q is defined by

$$J_q \equiv J_u - J_m h \quad (23)$$

and its physical significance will be discussed below. Then (23) may be written

$$\frac{dS}{dT} = -J_q\frac{dT}{T^2} - J_m\frac{v\, dP}{T} \quad (24)$$

which represents a different choice of the conjugate flows and forces as compared with Equation (13). In particular, the force conjugate to the flow of matter is now proportional to the pressure difference. This is perhaps a more intuitive choice than the quantity $d(\mu/T)$ of Equation (13).

Since there is nothing in the Onsager theory to make one choice of flows and forces preferable to any other, provided they satisfy Equation (4), a new set of linear equations can be written in the form

$$J_m = -L_{11}'\frac{v\, dP}{T} - L_{12}'\frac{dT}{T^2} \quad (25)$$

$$J_q = -L_{21}'\frac{v\, dP}{T} - L_{22}'\frac{dT}{T^2} \quad (26)$$

together with $L_{12}' = L_{21}'$. Hence

$$J_m = -L_{11}'\left(\frac{v\, dP}{T} + \frac{L_{21}'}{L_{11}'}\frac{dT}{T^2}\right) \quad (27)$$

Dividing (26) by (25) for $dT = 0$ one obtains

$$\frac{L_{21}'}{L_{11}'} \equiv \left(\frac{J_q}{J_m}\right)_{dT=0} \equiv Q^* \quad (28)$$

where Q^* is called the *heat of transfer*. Combining (27) and (28) one obtains

$$J_m = -L_{11}'\left(\frac{v\, dP}{T} + Q^*\frac{dT}{T^2}\right) \quad (29)$$

Therefore at the stationary state, $J_m = 0$,

$$\frac{dP}{dT} = \frac{-Q^*}{vT} \quad (30)$$

This equation is the same as (21), since Q^* is equal to $Q - h$. Thus from the definitions (28), (23), and (17)

$$Q^* = \left(\frac{J_q}{J_m}\right)_{dT=0} = \left(\frac{J_u}{J_m}\right)_{dT=0} - h \quad (31)$$

$$= Q - h$$

It will now be shown that Q^* has a direct physical significance and is measurable, at least in principle.

The discussion in the previous section, leading to Equations (11) and (13), was based for convenience on an isolated system, recently separated from suitable heat reservoirs at temperatures T and $T + dT$. The energy of transport was defined by Equation (17):

$$Q \equiv \left(\frac{J_u}{J_m}\right)_{dT=0} = \left(\frac{dU_1}{dn_1}\right)_{dT=0}$$

Therefore $Q dn_1$ is the change of energy of vessel 1 when dn_1 moles pass through the barrier, under conditions of equal temperatures. This energy change may be expected to cause a change in the intensive variables in vessel 1 unless steps are taken to prevent this. To maintain constancy of the temperature and the pressure it will be necessary to restore contact with the heat reservoir, taking in heat dq, and also to use a piston and cylinder to adjust the pressure, with a work effect dw. At the end of this process—the loss of dn moles and the restoration of the original temperature and pressure—the energy change of vessel 1 is $-Q dn + dq - dw$. This is equal to $-udn$, since the temperature and pressure are constant over the process. Similarly $dw = -Pv dn$. Hence

$$-u\,dn = -Q\,dn + dq + Pv\,dn \quad (32)$$

or

$$dq = (Q - h)\,dn = Q^*\,dn \quad (33)$$

The heat of transport is therefore equal to the heat which must be supplied from a heat reservoir to maintain conditions of constant temperature and pressure in vessel 1, when 1 mole of the fluid passes from 1 to 2 when their temperatures are equal ($dT = 0$). The corresponding quantity J_q, defined in Equation (23), is the rate of heat flow from the reservoir. In fact the whole of this analysis, instead of being based on an isolated system, could equally well have been based on a system in which the two vessels were continuously in contact with the reservoirs (10). This would have resulted in Equation (24) as the immediate result, and Equation (13) could then have been obtained by the same transformation in reverse.

PHYSICAL SIGNIFICANCE OF THE EQUATIONS

Equation (21) and (30) were first obtained by use of the reciprocal relation (6) by Deryagin and Sidorenkov (8) but previously by Eastman (9) by adopting Thomson's hypothesis.

The simplest application of these equations is to the Knudsen effusion effect for which the energy and heat of transport are calculable from kinetic theory. By integration of Maxwell's equation it is readily shown that the mean kinetic energy of the molecules passing through a small hole is $2 RT$/mole, whereas their mean kinetic energy in the bulk of the gas in $\frac{3}{2} RT$/mole (18). This difference arises from the fact that relatively more fast-moving molecules pass through in unit time than slow-moving ones. Thus the energy of transport is given by

$$Q = 2RT + E \quad (34)$$

The enthalpy h of the gas is

$$h = \frac{3}{2} RT + E + Pv$$
$$= \frac{5}{2} RT + E \quad (35)$$

Hence the heat of transport is

$$Q^* = Q - h$$
$$= -RT/2 = -Pv/2 \quad (36)$$

Substituting in (30) and integrating over a finite difference of temperatures between the two vessels, one obtains

$$\frac{P_2}{P_1} = \sqrt{\frac{T_2}{T_1}} \quad (37)$$

This equation, which is also directly deducible from kinetic theory, has been amply confirmed by experiment by Knudsen and others. The heat effect corresponding to Q^* had also been detected experimentally by Dufour as early as 1872 and confirmed by Knudsen (18).

Thermoosmosis, which is the second example of the thermomolecular pressure difference, is quite different in its molecular mechanism. Here the two vessels are separated by a membrane in which the fluid is slightly soluble. To pass from one vessel to the other the fluid must undergo a process of solution at the one membrane surface and a process of evolution at the other. Within the membrane there is a concentration of dissolved fluid, this concentration varying across the thickness owing to a thermal diffusion process.

The effect has been investigated theoretically and experimentally by Denbigh and Raumann (7), Bearman and Koenig (1), and Crowe (2). Whereas in the Knudsen effect the higher pressure always develops on the warmer side, this is by no means necessarily the case in thermoosmosis which depends on a specific interaction between the fluid and the membrane. Hydrogen for example builds up the higher pressure on the cold side of a rubber membrane and has a heat of transport of 100 cal./mole, as determined by use of Equation (30). Carbon dioxide tends to pass through the same membrane in the reverse direction and has a heat of transport of $-1,800$ cal./mole.

In these experiments it was not possible to determine the value of Q^* other than by use of Equation (30) itself, and in this respect the theory has not been completely verified. However it will be seen that Equation (29) reduces to

$$J_m = \frac{-L_{11}'v\,dP}{T} \quad (38)$$

in the absence of a temperature difference. The coefficient L_{11}' is thus related to the permeability of the membrane as measured under ordinary isothermal conditions. It was a satisfactory feature of the experiments that the approach to the stationary state under the nonisothermal conditions of the thermoosmosis system, could be used to obtain values of the membrane permeability, by use of Equation (29), in good agreement with values determined isothermally. This gives support to the assumptions underlying this equation, that is the supposition that the flow through the membrane depends linearly on the temperature difference dT as well as on the pressure difference dP.

The third example of the thermomolecular pressure difference is the fountain effect in liquid helium 2. The phenomenon seems to be due to a quantum effect which give rise to a large value of Q^* in the particular system. The experimental results of Mayer and Mellink and of Kapitza are stated to be in good agreement with Equation (30).

REVIEW OF THE THEORY

The discussion of the thermomolecular pressure difference was introduced to give some idea of nonequilibrium thermodynamics in action. Some other fields of application will be described more briefly later. At the present stage it is convenient to go back to the theory as outlined under Linear Equations and Entropy Production.

Two important assumptions have been used so far. The first of these is that the rates of the processes can be expressed in the form of Equation (5), that is as linear functions of certain thermodynamic forces which must be chosen so as to satisfy Equation (4). The experimental evidence shows that this is indeed the case with transport processes, their rates being proportional to gradients of temperature, electric potential, etc. Chemical reactions however are an exception. For a reaction $A \rightleftarrows B$ the rate of entropy production is proportional to the product of the reaction rate and the difference $\mu_A - \mu_B$ of chemical potentials. The latter is therefore the appropriate force, but it is not a quantity to which the reaction rate is linearly related, except when the reaction is close to equilibrium (5). For this reason alone the application of nonequilibrium thermodynamics to

chemical reactions is somewhat limited.

The second important assumption is that the Gibbs equation $dU = TdS - PdV + \sum \mu_i dn_i$ can be used, despite the absence of equilibrium. In more general terms, what is assumed is that the entropy of a system, during an irreversible process, is completely determined by the energy, volume, and composition and does not depend on the gradients within the system.

By use of the kinetic theory of gases, or statistical mechanics, it can be shown that the extent to which this assumption holds depends on the smallness of the deviation from the equilibrium Maxwellian distribution of velocities, etc., during the course of the irreversible process. This has been done by Meixner (13) and Prigogine (16), who came to the conclusion that the Gibbs equation is applicable to a satisfactory degree of approximation in the typical field of the application of nonequilibrium thermodynamics, that is the transport processes. It would break down if for example the change in temperature over the distance of a mean free path was comparable in magnitude to the temperature itself, but this is not likely to be the case, except under extreme conditions.

There is however another important assumption which occurs in the deduction of the reciprocal relation $L_{ik} = L_{ki}$. A detailed derivation of this equation is much beyond the scope of the present paper, but a brief outline follows.

The proof of the relation is based not on the macroscopic deviations from equilibrium, such as one is concerned with when there are irreversible processes, but with the fluctuations which take place within a molecular system at equilibrium. Even at equilibrium of course the entropy does not always remain at its absolute maximum value, but oscillates irregularly over a minute range, corresponding to the fluctuating deviations from the smoothness of the energy and matter distribution within the system.

The principle of microscopic reversibility places a certain limitation on these fluctuations. For the sake of a concrete illustration one considers once again the distribution of matter and energy between two vessels, as described. However as an "aged system" is being discussed, there is a state of equilibrium. The quantities dU_2 and dn_2 in Equation (11) therefore now refer to fluctuations of energy and matter about the equilibrium state rather than to infinitesimal parts of finite changes. One supposes that at a given instant $dn_2 = -dn_1 = 10^{-22}$ moles (owing to a fluctuation of matter between the two vessels) and that τ seconds later $dU_2 = -dU_1 = 10^{-12}$ ergs (owing to a fluctuation of energy between the vessels). According to the principle of microscopic reversibility, this compound event is just as likely to occur on the average as the

converse situation in which a disparity 10^{-12} ergs in the energy is followed by τ sec. later by a disparity 10^{-22} moles in the amount of matter.

In more general terms, α and β are the amounts by which two variables deviate from their equilibrium values owing to the fluctuations. $\alpha(t)$ is the value of α at time t and $\beta(t + \tau)$ the value of β, τ sec. later. The mean value of the product $\alpha(t)\beta(t + \tau)$ is taken over a long duration (but the β value is always taken at τ sec. after the α value). According to microscopic reversibility the same mean value for the product $\alpha(t + \tau)\beta(t)$ will be obtained, in which it is now the α variable which is to be taken τ sec. later. Thus

$$\overline{\alpha(t)\beta(t + \tau)} = \overline{\alpha(t + \tau)\beta(t)} \qquad (39)$$

Substracting $\overline{\alpha(t)\beta(t)}$ from both sides of (39) and dividing by τ one obtains

$$\overline{\alpha(t)\left\{\frac{\beta(t + \tau) - \beta(t)}{\tau}\right\}}$$
$$= \overline{\beta(t)\left\{\frac{\alpha(t + \tau) - \alpha(t)}{\tau}\right\}} \qquad (40)$$

The quantities in brackets are the changes in the variables β and α respectively divided by the time τ. It will be assumed—and this is the important assumption that has to be made—that the rate of changes of these fluctuating variables follows the ordinary linear macroscopic laws. That is to say, one assumes

$$\left\{\frac{\alpha(t + \tau) - \alpha(t)}{\tau}\right\}$$
$$= L_{11}X_\alpha + L_{12}X_\beta \qquad (41)$$

and

$$\left\{\frac{\beta(t + \tau) - \beta(t)}{\tau}\right\}$$
$$= L_{21}X_\alpha + L_{22}X_\beta \qquad (42)$$

where X_α and X_β are suitably defined forces. The time derivatives of the fluctuations are thus regarded as transient flows of energy and matter, obeying relations such as (14) and (15)*.

Substituting (41) and (42) in (40) one obtains

$$\overline{\alpha(L_{21}X_\alpha + L_{22}X_\beta)}$$
$$= \overline{\beta(L_{11}X_\alpha + L_{12}X_\beta)} \qquad (43)$$

ΔS is the entropy deviation from its maximum owing to the fluctuations. According to Einstein's fluctuation theory the probability that the one variable lies in the range α to $\alpha + d\alpha$ and the other variable lies in the range β to $\beta + d\beta$ is proportional to

$$e^{\Delta S/k} \, d\alpha \, d\beta$$

*For further discussion see de Groot (3).

By use of this distribution function it is possible to work out mean values such those occurring in Equation (43). For example

$$\overline{\alpha X_\alpha} = \frac{\displaystyle\iint \alpha X_\alpha e^{\Delta S/k} \, d\alpha \, d\beta}{\displaystyle\iint e^{\Delta S/k} \, d\alpha \, d\beta} \qquad (44)$$

(where the denominator normalizes the probabilities to unity)

Provided that the forces X_α and X_β which are suitable for use in (41) and (42) will also satisfy

$$\begin{aligned}\left(\frac{\partial \Delta S}{\partial \alpha}\right)_\beta &= X_\alpha; \\ \left(\frac{\partial \Delta S}{\partial \beta}\right)_\alpha &= X_\beta\end{aligned} \qquad (45)$$

the mean values, as given by integrals such as (44), can be evaluated*. The result is

$$\overline{\alpha X_\alpha} = \overline{\beta X_\beta} = -k \qquad (46)$$

$$\overline{\alpha X_\beta} = \overline{\beta X_\alpha} = 0 \qquad (47)$$

Substituting these mean values in (43) one obtains

$$L_{12} = L_{21}$$

and similarly $L_{ik} = L_{ki}$ in the general case where there are more than two fluctuating variables.

Thus an important feature of the theory is the supposition that the linear equations apply equally to the fluctuations and to the macroscopic deviations from equilibrium which are observable in the form of the irreversible processes. The linear equations stretch outward from the equilibrium state, and the property $L_{ik} = L_{ki}$, which is provable for the fluctuations, must apply also to the irreversible processes themselves, provided that these processes actually obey linear equations, for example that the coefficients L_{ik} are independent of the magnitude of the gradients.

FIELD OF APPLICATION OF THE THEORY

Nonequilibrium thermodynamics does not have any very substantial applications to chemical reactions. Indeed the condition of microscopic reversibility has already been applied by the chemist, in an implicit form, whenever he uses the idea of detailed balancing to obtain a relationship between the velocity constants. Also, as previously mentioned, the rate of a reaction is not linearly related to the appropriate thermodynamic force, except when reaction is close to equilibrium. Even if this were

*See for example Prigogine (17), page 49.

not the case, the field of application would still be very limited, because reaction rate is a scalar quantity and cannot be coupled with the vector transport processes (Curie's symmetry principle). Nevertheless Prigogine (17) has made a number of interesting and tentative applications to biological systems in which there may be two or more reactions coupled among themselves.

The most important field of application is undoubtedly the transport processes, whose interaction at the molecular level leads to very interesting phenomena. Of course the new thermodynamics is unable to predict the magnitude of the coupling, but whenever it is nonzero the coupling coefficients $L_{ik}(i \neq k)$ are also nonzero, and in this situation the application of the reciprocal relation leads to physical relations which can be verified by experiment.

Examples already mentioned are the thermoelectric effect and the thermomolecular pressure difference. The coupling in the former case is due to the fact that the passage of electrons is simultaneously both an electric current and a flow of thermal energy; similarly, in the latter case a flow of matter carries with it an associated heat of transport under certain special conditions.

In multicomponent systems in which there is a temperature gradient the phenomenon of thermal diffusion can occur. Here again there is a fruitful field of application, and it can be shown that the separation achievable in thermal diffusion depends on the difference in the heats of transport of the individual components. The measurement of these quantities, and the attempt to interpret them in molecular terms, is an attractive line of enquiry in the theory of liquids.

Strictly speaking the chemical engineer should apply nonequilibrium thermodynamics whenever he is concerned with simultaneous heat and mass transfer. However the coupling is rather small, and the traditional methods, which assume these processes to be independent, are not likely to be much in error. The coupling is important only when one sets up a special type of apparatus which brings it into prominence, for example the thermogravitational system (Clusius-Dickel) which is used to magnify the separation achievable by thermal diffusion.

Simultaneous flows of energy and electricity and of energy and matter have been discussed so far. Coupling can also take place between the flows of electricity and of matter, in an isothermal system. This occurs for example when there is a diffusion of an electrolyte and a simultaneous flow of current, as in the concentration cell with transport. Here the coupling is due quite simply to the fact that the ions are charged; unequal diffusion of the ions implies a flow of current and vice versa. For this reason

the rate of diffusion depends not only on the gradient of chemical potential or concentration but also on the gradient of electric potential. By application of the Onsager relation the well-known equation giving the diffusion potential in terms of the transport numbers of the ions can be readily derived. This had been obtained much earlier by Nernst, using a method similar to Thomson's.

Closely similar are the relationships which can be established between the various electrokinetic effects, for example the relation between the streaming potential and electroosmosis or between the electroosmotic pressure and the streaming current. There is also the possibility of the coupling of individual diffusion processes in a multicomponent system, as occurs (although only to a small extent) in solutions of electrolytes. Still another interesting application is heat conduction in anisotropic materials; also a number of interesting effects take place when an externally applied magnetic field interferes with the flow of heat and electricity. For further details of these phenomena and also for a much fuller account of the general theory, the reader is referred to monographs 3, 6, and 17.

While the field of application of nonequilibrium thermodynamics may thus appear to be rather extensive, it should also be emphasized that it is strictly limited. The useful applications are to systems in which there are two or more processes between which there exists some mechanism of coupling. (And even in these systems the coupling is not often of a large order of magnitude.) What is not sufficiently realized is that the new branch of thermodynamics has nothing useful to say about irreversibility in general. Thus it offers no information whatever on such problems as the speed of chemical reaction, the rate of mass transfer, or the magnitude of fluid friction. And even in a system in which these processes take place simultaneously they are not of a kind between which coupling takes place. With these remarks in mind the chemical engineer will not be inclined to overexaggerate the practical uses of the new branch of thermodynamics but instead may hold it of value for its own intrinsic interest.

NOTATION

E = any additional energy associated with internal degrees of freedom of molecule (vibration, rotation)
h = molar enthalpy of fluid (at T, P)
I = current
k = Boltzman's constant
J_i = a generalized flow
J_m = flow of matter
J_u = flow of energy
L = scalar coefficient of nature of conductance or diffusion coefficient

L_{12} = coupling coefficient
L_{21} = coupling coefficient
L_{ik} = coefficient relating J_i to X_k
n_i = number of moles of species i
P = pressure
Q = energy of transport
Q^* = heat of transport
R = gas constant
S = entropy
t = time
T = absolute temperature
u = internal energy per mole
U = internal energy
v = molar volume of fluid (at T, P)
V = volume
X_i = force conjugate to the flow J_i

Greek Letters

α, β = values of fluctuating variables
μ_i = chemical potential of species i

LITERATURE CITED

1. Bearman, R. J., and F. O. Koenig, *J. Am. Chem. Soc.*, **78**, 691 (1956).
2. Crowe, C. M., *Trans. Faraday Soc.*, **53**, 692 (1957).
3. de Groot, S. R., "Thermodynamics of Irreversible Processes," North Holland Publ. Company (1951).
4. Denbigh, K. G., "The Principles of Chemical Equilibrium," Cambridge Univ. Press (1955).
5. ———, *Trans. Faraday Soc.*, **48**, 389 (1952).
6. ———, "The Thermodynamics of the Steady State," Methuen, London (1951).
7. ———, and Gertrud Raumann, *Proc. Roy. Soc. (London)*, **A210**, 377, 518, (1951).
8. Deryagin, B. V., and G. Sidorenkov, *Compt. rend. U. R. S. S.*, **32**, 622 (1941).
9. Eastman, E. D., *J. Am. Chem. Soc.*, **48**, 1482 (1926); **49**, 794 (1927); **50**, 283 (1928).
10. Keenan, J. H., *Appl. Mechanics Revs.*, **49** (1955).
11. Kelvin, Lord, "Math. and Phys. Papers," vol. I, pp. 232 et seq.
12. Machlup, S., and Lars Onsager, *Phys. Rev.*, **91**, 1505, 1512 (1953).
13. Meixner, J., *Ann. Physik.*, **39**, 333 (1941).
14. Onslager, Lars, *Phys. Rev.*, **37**, 405 (1931); **38**, 2265 (1931).
15. Prigogine, I., *Physica*, **15**, 272 (1949).
16. ———, *J. Phys. & Colloid Chem.*, **55**, 765 (1951).
17. ———, "Thermodynamics of Irreversible Processes," Charles C. Thomas, Illinois (1955).
18. Taylor, H. S., and Samuel Glasstone, "Treatise on Physical Chemistry," 3 ed., vol. II, pp. 138–9, Van Nostrand, New York (1951).
19. Tolman, R. C., "The Principles of Statistical Mechanics," Oxford Univ. Press (1938).
20. Wagner, C., *Ann. Physik*, **3**, 629 (1929); **6**, 370 (1930).

Simplified Calculation of Chemical Equilibria in Hydrocarbon Systems Containing Isomers

BUFORD D. SMITH

Humble Oil and Refining Company, Baytown, Texas

An improved method is presented for handling isomer groups in the calculation of chemical equilibria in complex hydrocarbon mixtures. The new method reduces the number of simultaneous equations involved and makes practical the rigorous calculation of any hydrocarbon system for which free-energy data are available, no matter how complex.

The constant search for new raw materials for the petrochemical industry has led to the development of elaborate separation processes to recover specific compounds from petroleum fractions. Quite often the particular compound desired is present in such small amounts in the crude that it is impossible to meet the demand by recovery of the virgin material alone. In these cases isomers or homologues of the desired compound may be recovered and converted by some catalytic process to the specific compound desired. In a study of the catalytic conversion processes it is worthwhile to calculate the equilibrium composition of the reaction mixtures. This paper describes a method for simplifying the equilibrium calculations when the system contains isomer groups.

Brinkley (*1, 2*) and Kandiner and Brinkley (*3*) have described a basic method of calculating chemical equilibria in complex mixtures which simplifies the arithmetic considerably. This simplification and the improved method of handling isomer groups which is described in this paper permit the calculation of hitherto neglected systems with only a minimum expenditure of technical manpower.

THERMODYNAMIC EQUATIONS REQUIRED

The chemical equilibrium constant, K_a, for a chemical reaction represented by the following stoichiometric equation

$$bB + cC = mM + nN$$
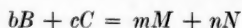
is defined by

$$K_a = K_f = \frac{(n_M)^m (n_N)^n}{(n_B)^b (n_C)^c}$$

$$\cdot \frac{(f/p)_M{}^m (f/p)_N{}^n}{(f/p)_B{}^b (f/p)_C{}^c} \left(\frac{p}{n}\right)^{m+n-b-c} \quad (1)$$

Buford D. Smith is at Purdue University, Lafayette, Indiana.

for real gases in ideal solutions and by

$$K_a = \frac{(\gamma_M)^m (\gamma_N)^n}{(\gamma_B)^b (\gamma_C)^c} \frac{(x_M)^m (x_N)^n}{(x_B)^b (x_C)^c}$$

for nonideal liquid solutions. The standard states are unit fugacity for gases, and for liquids and solids the pure component at the temperature and pressure of the reaction.

The calculation of K_a is accomplished through the use of free-energy data (*4*) and the equation

$$\Delta F^\circ = RT \ln K_a$$

where

$$\Delta F^\circ = \sum (\Delta F_f{}^\circ)_{products}$$
$$- \sum (\Delta F_f{}^\circ)_{reactants}$$

CHOICE OF INITIAL AND FINAL STATES

The equilibrium composition calculated depends upon the initial and final states (not standard states) specified for the reacting system. The temperature and pressure for both states are of course the temperature and pressure chosen for the reaction. The specification of the initial state is completed by specifying the amounts of each of the chemical elements present in the feed. A change in the feed composition which changes the relative amounts of the elements present will result in a changed equilibrium composition.

Similarly the specification of the final state is completed by specifying which chemical species are to be present in the equilibrium mixture. The equilibrium composition calculated depends upon the chemical constituents which the calculator assumes to be present at equilibrium. Choosing fewer or more constituents results in different equilibrium compositions. In some cases the calculator may purposely omit some of the constituents known to be present; for example, in any reaction system where hydrocracking results in the

formation of carbon and light hydrocarbons, the true equilibrium mixture would contain only traces of compounds heavier than methane. This fact can be illustrated by choosing carbon and hydrogen as the independent components and then writing Equation (1) for methane, ethane, and benzene. (Ideal gases and a reaction temperature of 800°K. were assumed.)

$$n_{CH_4} = 1.41 \, (p/n)(n_{H_2})^2$$

$$n_{C_2H_6} = 4.49 \times 10^{-5} \, (p/n)^2 (n_{H_2})^3$$

$$n_{C_6H_6} = 3.68 \times 10^{-15} \, (p/n)^2 (n_{H_2})^3$$

The values for K_f were obtained from reference *4*.

Omission of carbon and the lightest hydrocarbons from the equilibrium system permits the calculation of more useful results. In any case the calculator should realize that the equilibrium composition calculated depends upon the final state assumed.

CHOICE OF INDEPENDENT COMPONENTS

The fact that thermodynamic equilibrium is independent of the reaction paths assumed permits one to assume that the reaction mixture is formed from a certain number of independent components. All the other constituents assumed present are then derived from these independent components. The feed constituents may or may not be chosen as independent components. Kandiner and Brinkley (*3*) describe an analytical method for determining how many independent components are required and list several rules for their selection. For simple hydrocarbon systems containing only carbon and hydrogen the number required is two. The number chosen cannot exceed the number of elements present but must be sufficient to permit the writing of chemical equations in which each of the derived constituents is formed individually from one or more of the independent components. Each chemical equation must contain no more than one derived constituent. Also the independent components must be related by at least one of the chemical equations, and for ease of calculation they should predominate

TABLE 1. CALCULATION OF THE EQUILIBRIUM CONSTANT K_a FOR EACH OF THE DERIVED CONSTITUENTS

Constituent	Chemical equation	$\Delta F°$	K_a*
1, 2 DMB	1, 3 DMB = 1, 2 DMB	1.004	0.4305
1, 4 DMB	1, 3 DMB = 1, 4 DMB	0.961	0.4470
1, 2, 3 TMB	1, 2, 4 TMB = 1, 2, 3 TMB	2.573	0.1159
1, 3, 5 TMB	1, 2, 4 TMB = 1, 3, 5 TMB	1.158	0.3780
1, 2, 3, 4 TMB	2[1, 2, 4 TMB] − 1, 3 DMB = 1, 2, 3, 4 TMB	2.854	0.0913
1, 2, 3, 5 TMB	2[1, 2, 4 TMB] − 1, 3 DMB = 1, 2, 3, 5 TMB	1.417	0.3045
1, 2, 4, 5 TMB	2[1, 2, 4 TMB] − 1, 3 DMB = 1, 2, 4, 5 TMB	1.893	0.2045
Benzene	3[1, 3 DMB] − 2[1, 2, 4 TMB] = benzene	2.572	0.1159
Toluene	2[1, 3 DMB] − 1, 2, 4 TMB = toluene	0.382	0.7262
Penta MB	3[1, 2, 4 TMB] − 2[1, 3 DMB] = penta MB	3.893	0.03817
Hexa MB	4[1, 2, 4 TMB] − 3[1, 3 DMB] = hexa MB	10.636	0.000134

$*K_a = 1.0$ for an independent component.

hydro-
ixture
ounds
an be
and
onents
) for
(Ideal
re of

$_{H_2})^3$

$_{H_2})^3$

from

ghtest
ystem
useful
ulator
brium
upon

S

quilib-
action
ssume
from
com-
uents
from
e feed
hosen
diner
ytical
many
quired
ction.
con-
the
mber
r of
icient
qua-
rived
from
mpo-
must
rived
com-
t one
ease
inate

1959

in the equilibrium mixture. If pure carbon is assumed to be present, it must be chosen as an independent component, since because of the choice of standard state its concentration will not appear in any of the equilibria equations.

USE OF K VALUES TO SIMPLIFY ISOMER CALCULATIONS

Rossine [5] has described the importance of K values in calculating the equilibria between isomers. This principle can be expanded to simplify the calculation of equilibrium in complex systems containing one or more isomer groups.

If one considers an isomer group containing constituents R, S, $T \cdots$ formed from independent components B and C, the stoichiometric coefficients for B and C will be the same in all the chemical equations

$$bB + cC = R$$
$$bB + cC = S, \quad \text{etc.}$$

Assuming ideal gases for the sake of simplicity and solving for the moles of each isomer, one can write Equation (1) for each isomer as

$$\left. \begin{array}{l} n_R = K_R \left(\frac{n}{p}\right)^{1-b-c} (n_B)^b (n_C)^c \\ n_S = K_S \left(\frac{n}{p}\right)^{1-b-c} (n_B)^b (n_C)^c, \text{ etc.} \end{array} \right\} \quad (2)$$

Then

$$n_S = \left(\frac{K_S}{K_R}\right) n_R, \quad n_T = \left(\frac{K_T}{K_R}\right) n_R, \quad \text{etc.}$$

Letting n_I be the total moles of isomers present and x_R the mole fraction of R in the isomer group, one can show that

$$x_R = \frac{n_R}{n_I}$$

$$= \frac{K_R}{K_R + K_S + K_T + \cdots} = \frac{K_R}{\sum K\text{'s}}$$

When one generalizes,

$$x_i = \frac{K_i}{\sum K\text{'s}} \quad (3)$$

Equation (3) illustrates the fact that for ideal gases the ratio of one isomer to its fellow isomers is independent of what other constituents are present at equilibrium and depends on temperature only. If one is interested in the isomer group alone, the log K_f values tabulated in reference 4 are very convenient.

Inspection of Equation (2) shows that

$$n_I = (K_R + K_S + K_T + \cdots)$$
$$\cdot \left(\frac{n}{p}\right)^{1-b-c} (n_B)^b (n_C)^c \quad (4)$$

This means that in calculating the equilibrium for the entire system the equilibria equations for the various isomers in the group can be reduced to one equation representing the entire group. The K value in this equation is the summation of the K's of the various isomers. Once n_I is obtained Equation (3) can be used to calculate the breakdown within the group. This method significantly reduces the number of equations required, particularly if any of the higher isomer groups are included in the equilibrium system.

EXAMPLE

The chemical equilibrium existing at 600°K. in a system containing benzene and all the methylbenzenes and originating from a feed of trimethylbenzenes will be calculated as an illustration. Experimental results have indicated that 1, 3 dimethylbenzene and 1, 2, 4 trimethylbenzene will be predominant in the equilibrium mixture, and they will be used as the independent components. Table 1 lists the chemical equations written for each derived constituent and the corresponding free energies of reaction and equilibrium constants. The free-energy data were obtained from reference 4 and from a paper by Hastings and Nicholson [6].

The next step is to write the expressions defining K_a for each chemical equation. This is done by substituting in Equation (1). Ideal gases can be assumed, and since the $(m + n - b - c)$ term is zero for each chemical equation, Equation (1) reduces to

$$n_i = K_i n_1{}^{v_{i,1}} n_2{}^{v_{i,2}}$$

The exponents $v_{i,1}$ and $v_{i,2}$ may be positive or negative in sign.

Two other equations are necessary before the calculations can be started. These are material-balance equations on the independent components. If q_1 and q_2 represent the amounts of the independent components present initially, then the amounts present at equilibrium must be

$$n_1 = q_1 - \sum_{i=3}^{i=13} v_{i,1} n_i$$

$$n_2 = q_2 - \sum_{i=3}^{i=13} v_{i,2} n_i$$

TABLE 2. MATERIAL-BALANCE AND EQUILIBRIA EQUATIONS

Constituent or isomer group	i	$v_{i,1}$	$v_{i,2}$	Material-balance and equilibria equations
1, 3 DMB	1	—	—	$n_1 = 0.0 - \sum_{i=3}^{i=13} v_{i,1} n_i$
1, 2, 4 TMB	2	—	—	$n_2 = 1.0 - \sum_{i=3}^{i=13} v_{i,2} n_i$
DMB's	1, 3, and 4	1	0	$n_{DMB} = 1.877\, n_1$
Tri MB's	2, 5, and 6	0	1	$n_{Tri\ MB} = 1.494\, n_2$
Tetra MB's	7, 8, and 9	−1	2	$n_{Tetra\ MB} = 0.6003\, \frac{(n_2)^2}{n_1}$
Benzene	10	3	−2	$n_{Benzene} = 0.1159\, \frac{(n_1)^3}{(n_2)^2}$
Toluene	11	2	−1	$n_{Toluene} = 0.7262\, \frac{(n_1)^2}{n_2}$
Penta MB	12	−2	3	$n_{PMB} = 0.03817\, \frac{(n_2)^3}{(n_1)^2}$
Hexa MB	13	−3	4	$n_{HMB} = 0.000134\, \frac{(n_2)^4}{(n_1)^3}$

The q_1 and q_2 are obtained by transforming the original feed into equivalent amounts of the independent components containing the same number of moles of all the elements as the original feed. In this example, since the feed is all trimethylbenzene, the q for 1, 3 dimethylbenzene must be zero and the q for 1, 2, 4 trimethylbenzene must be 1.0 if 1 mole of original feed is taken as the calculation basis.

Table 2 lists the material-balance equations for the independent components and the equilibria equations for each of the derived constituents. The stoichiometric coefficients are listed also for convenience in making the material balances on the independent components. It must be noted that when an isomer group contains an independent component, the n for the isomer group cannot be used in the material-balance equations without first subtracting the n assumed for the independent component.

The number of equations which must now be solved simultaneously has been reduced from thirteen to nine by representing each isomer group by a single equation. Solution of these equations involves assuming values of n_1 and n_2, calculating the n's for all the derived constituents by means of the equilibria equations, and then checking on the assumed values of n_1 and n_2 by utilizing the material-balance equations. Since two unknowns, n_1 and n_2, must be assumed each time, it is impractical to guess the values to be used for the next trial. Kandiner and Brinkley (3) describe three methods which sometimes aid in selecting the values of n_1 and n_2 for the successive trials. However a direct graphical approach is usually the surest and often the quickest way of obtaining a solution. Select a value of n_2 and run through the solution of the equations three times with this assumed n_2 and three evenly spaced values of n_1. Then select another value of n_2 and repeat the calculations with this n_2 and the same three values of n_1. Calculate Δn_1 and Δn_2 by subtracting the assumed from the calculated values. Plot the Δn_1's and Δn_2's vs. n_1 with parameters of constant n_2. The Δn_1 and Δn_2 curves will intersect at zero when the correct values of n_1 and n_2 are assumed. Interpolation or extrapolation on a line drawn through the two intersections obtained will indicate the correct n_1 and n_2 to assume for the final trial.

Figure 1 illustrates the solution of the nine equations. It was known that the concentration of 1, 2, 4 trimethylbenzene would be in the 20 to 30% range, and values for n_2 of 0.26 and 0.23 were therefore selected for the six preliminary trials. Likewise the concentration of 1, 3 dimethylbenzene was expected to be 10 to 15%, and values for n_1 of 0.11, 0.13, and 0.15 were used. Interpolation on the straight line drawn between the two intersections indicates the correct values for n_1 and n_2 to be 0.131 and 0.251, respectively, and these were the values used in the final trial, trial 7. The numerical calculations for trial 7 are shown in Table 3 to illustrate the labor required for each trial and the degree of convergence obtained in this example.

The calculation time required for this example was approximately 4 hr., when a desk calculator was used. This time was about evenly divided between the calcula-
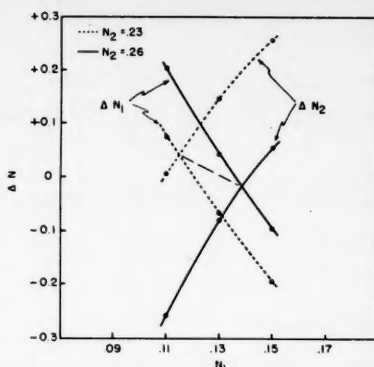
Fig. 1. Estimation of the final answer from the six preliminary trials.

TABLE 3. SOLUTION OF THE EQUILIBRIA AND MATERIAL-BALANCE EQUATIONS

Trial	7
Assumed n_1	0.1310
Assumed n_2	0.2510
Calculated n's	
DMB's	0.2459
Tri MB's	0.3750
Tetra MB's	0.2887
Benzene	0.0041
Toluene	0.0497
Penta MB	0.0352
Hexa MB	0.0002
1, 3 DMB balance	
q_1	0
$-(1.0)(n_{DMB}) + n_1$	-0.1149
$+(1.0)(n_{Tetra MB})$	0.2887
$-(3.0)(n_{Benzene})$	-0.0123
$-(2.0)(n_{Toluene})$	-0.0994
$+(2.0)(n_{PMB})$	0.0704
$+(3.0)(n_{HMB})$	0.0006
Calculated n_1	0.1331
Δn_1 = calculated-assumed	0.0021
1, 2, 4 TMB balance	
q_2	1.0
$-(1.0)(n_{Tri MB}) + n_2$	-0.1240
$-(2.0)(n_{Tetra MB})$	-0.5774
$+(2.0)(n_{Benzene})$	0.0082
$+(1.0)(n_{Toluene})$	0.0497
$-(3.0)(n_{PMB})$	-0.1056
$-(4.0)(n_{HMB})$	-0.0008
calculated n_2	0.2501
Δn_2 = calculated-assumed	-0.0009

tion of the K's from free-energy data and the solution of the nine simultaneous equations.

Another way of making the material-balance calculation or of checking the calculations made in Table 3 is to calculate the methyl-group-to-benzene-ring ratio. This ratio must be the same in the equilibrium mixture as in the original feed. In this example, since a trimethylbenzene feed was used, the ratio must be 3.0.

CONCLUSIONS

Calculation methods have been developed to the point where the rigorous calculation of chemical equilibrium is practicable for any system for which free-energy data are available. The number of equations which must be solved can be reduced considerably in systems containing isomer groups by representing each isomer group by a single equation. For example, a reformate containing all saturated paraffins, five- and six-ring naphthenes, and aromatics. with saturated side chains boiling below 350°F. can be represented by twenty-five equilibria equations and two material-balance equations. The time required for solution would be approximately three times that required for the example problem. The number of components represented by the twenty-five equilibria equations is one hundred and thirty-six. If pentanes and lighter are eliminated from the equilibrium mixture in order to study the relations between the heavier paraffins, naphthenes, and aromatics, the number of equilibria equations is reduced to twenty.

NOTATION

a	=	activity, $f/f°$
f	=	fugacity, $f°$ denotes fugacity in the standard state
$\Delta F_f°$	=	free energy of formation in the standard state
$\Delta F°$	=	free energy of reaction in the standard state
K_a or K_f	=	chemical equilibrium constant in terms of activities or fugacities
n	=	moles
Δn	=	calculated n minus the assumed n for the independent components
p	=	total pressure, atm.
q_1 and q_2	=	moles of independent components 1 and 2 equivalent to the original feed in terms of the amount of each element contained
$v_{i,1}$ and $v_{i,2}$	=	stoichiometric coefficients for independent components 1 and 2 in the chemical equation for derived constituent i
x	=	mole fraction
x_1	=	mole fraction of ith isomer in isomer group only
(f/p)	=	fugacity coefficient
γ	=	activity coefficient = a/x

LITERATURE CITED

1. Brinkley, S. R., Jr., J. Chem. Phys., **14**, 9, 563 (1946).
2. Ibid., **15**, 2, 107 (1947).
3. Kandiner, H. J., and S. R. Brinkley, Jr., Ind. Eng. Chem., **42**, 850 (1950).
4. Am. Petroleum Inst. Project **44** (1953).
5. Rossini, F. D., "Chemical Thermodynamics," John Wiley and Sons, New York (1950).
6. Hastings, S. H., and D. E. Nicholson, J. Chem. Phys., **61**, 6, 730 (1957).

Compressibility of *n*-Hexane

RICHARD G. GRISKEY and LAWRENCE N. CANJAR

Carnegie Institute of Technology, Pittsburgh, Pennsylvania

Although a considerable amount of work has been done on the compressibility of *n*-hexane, it has been impossible until now to compare or evaluate the work of the various investigators. There has also been a serious lack of information in the region above the critical temperature. It is the purpose of this work to make an extensive study of temperatures of 240° to 300°C. and of pressures up to 225 atm. in order to provide the lacking information and to overlap with the work of other investigators so that a proper evaluation of their work may be made.

Thomas and Young (*10*) studied the volumetric properties of *n*-hexane in the superheated vapor region from 240° to 280.45°C. up to a pressure of 37.19 atm. using the capillary-glass method. The highest density investigated was 1.4193 g.-mole/liter. Higher density data was obtained by Kelso and Felsing (*6*); however their lowest measured density was 2.5 g.-mole/liter, leaving a considerable gap between their results and the earlier work of Thomas and Young (*10*) and making a comparison impossible. Furthermore Kelso and Felsing measured only two isotherms, 250° and 275°C., in the region above the critical temperature, with the result that the temperature coefficient of isometrics could not be determined for the purpose of fitting an equation or state. Stewart, Sage, and Lacey (*9*) more recently turned their attention to the volumetric behavior of *n*-hexane in the liquid phase. Comparison between their work and that of Kelso and Felsing (*6*) can be made only at temperatures below 238°C. This comparison indicates that in general Kelso and Felsing measured smaller densities in the high-pressure region and that the discrepancy increases with increasing temperature. Eduljec, Newitt, and Weale (*4*) also measured liquid volumes of *n*-hexane in the region 0° to 60°C. This investigation bridges the gap in the measurements of the earlier investigators. The densities measured in this work ranged from 1.3 to 5.8 g.-moles/liter for isotherms of 240°, 252°, 264°, 276°, 288°, and 300°C.

The apparatus used in this investigation is a modification of the design of Keyes (*7*) and Beattie (*1*). Except for certain changes, which have been described by Li and Canjar (*8*), a detailed description of the equipment was published by Cherney, Marchman, and York (*3*). A sample of *n*-hexane with a purity of 99.99 ± 0.01 mole % was made available for this investigation by the American Petroleum Research Project 44 at the Carnegie Institute of Technology from the series of samples of hydrocarbons purified by the American Petroleum Institute Research Project 6.

To determine whether appreciable decomposition had taken place at higher temperatures, the pressure at a density of 4.869 g.-moles/liter and a temperature of 276°C. was remeasured after all the data had been obtained and the sample exposed to temperatures of 300°C. The pressure measured originally was 117.789 atm., compared with a pressure of 117.839 atm. measured at the end of the 300°C. run, an indication of negligible decomposition.

A summary of experimental data is presented in Table 1. The over-all uncertainty of the measurements is estimated to vary from 0.12% at low pressures to 0.21% for the high-pressure measurements. Figure 1, a plot of the superheated vapor isotherms of Thomas and Young (*10*) and the low-density data of the present investigation, shows that the data of the present work exhibit somewhat higher pressures than the data of Thomas and Young at the same temperature and density. This same discrepancy was noted earlier in the work on isopentane (*5*). Figure 2 compares the 252° and 276°C. isotherms of the present work with the 250° and 275°C. isotherms of Kelso and Felsing. At the medium densities the data seem to be in fair agreement; however at the higher densities the data of Kelso and Felsing show higher pressures than those of the present work, which is
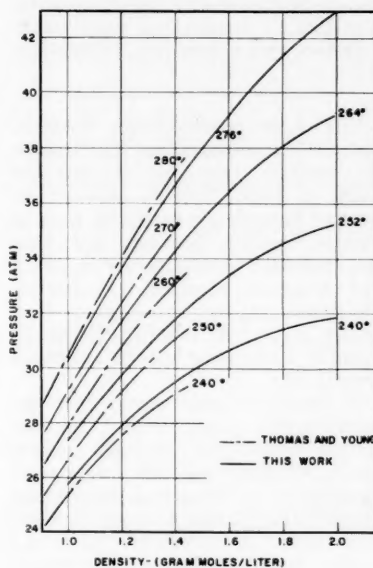
Fig. 1.
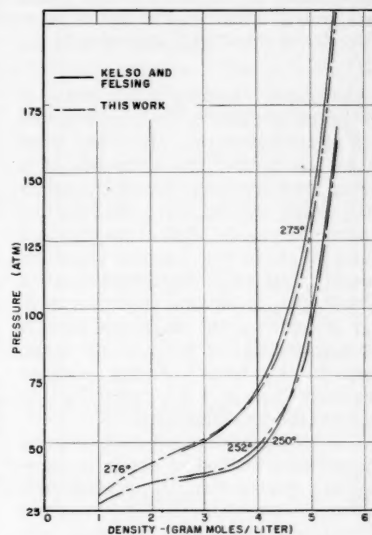
Fig. 2.

TABLE 1. P-V-T DATA FOR *n*-HEXANE

	P, atm.					
d, g.-mole/liter	240°C.	252°C.	264°C.	276°C.	288°C.	300°C.
1.0	25.689	27.275	28.739	30.256	31.747	33.222
1.5	30.110	32.583	35.264	37.812	40.326	42.840
2.0	31.842	35.245	39.337	42.943	46.644	50.329
2.5	32.461	37.644	42.468	47.381	52.399	56.955
3.0	32.925	39.192	45.959	51.988	58.788	65.321
3.5	34.009	41.821	49.988	58.249	67.138	75.852
4.0	37.606	48.312	58.765	68.912	82.247	91.994
4.5	47.575	65.012	76.914	89.730	105.148	119.449
5.0	74.575	94.623	114.597	131.356	147.064	172.273
5.5	135.695	161.980	186.657	210.277	228.277	

just the opposite of the situation when the work of Thomas and Young is considered.

The discrepancies among the various investigators are outside the limits of estimated experimental uncertainty. Critical analysis and selection of the most reliable data are in the province of another laboratory, where the system is now under study (2).

LITERATURE CITED

1. Beattie, J. A., *Proc. Am. Acad. Arts and Sci.*, **69**, 589 (1934).
2. Canjar, L. N., *Ind. Eng. Chem., Chem. Ind. Data Series*, **3**, No. 2, 185 (1958).
3. Cherney, B. J., Henry Marchman, and Robert York, *Ind. Eng. Chem.*, **41**, 2653 (1949).
4. Eduljec, N. E., D. M. Newitt, and K. E. Weale, *J. Chem. Soc.*, 3086 (1951).
5. Isaac, Reginald, K. L., and L. M. Canjar, *Ind. Eng. Chem.*, **46**, 199 (1954).
6. Kelso, E. A., and W. A. Felsing, *J. Am. Chem. Soc.*, **62**, 3132 (1940).
7. Keyes, F. G., *Proc. Am. Acad. Arts and Sci.*, **68**, 505 (1933).
8. Li, Kun, and L. N. Canjar, *Chem. Eng. Progr. Symposium Ser.* 7, **49**, 147 (1953).
9. Stewart, D. E., B. H. Sage, and W. N. Lacey, *Ind. Eng. Chem.*, **46**, 2529 (1954).
10. Thomas, G. L., and S. Young, *J. Chem. Soc.*, **67**, 1071 (1895).

Control-System Design for a Chemical Process by the Root-Locus Method

WALTER R. ELLINGSEN and NORMAN H. CEAGLSKE

University of Minnesota, Minneapolis, Minnesota

This paper illustrates the application of the root-locus method in the design of a control system for a theoretical stirred-tank reactor. The merits of control by measuring reactor concentration or temperature were considered at both an unstable and stable steady state reactor condition. The modes of control studied were proportional, proportional-integral, and proportional-integral-rate.

The primary concern in the design of all control systems is the time response of a given system to a prescribed input or set of inputs. The dynamics of a system is analyzed experimentally and/or analytically by one or a combination of several methods. Most of the standard methods utilize the Laplace transform since it transforms a differential equation in time into an algebraic equation in S, and in addition the transform permits the consideration of analysis and design problems in terms of the complex frequency $S = \sigma + i\omega$, rather than in terms of the time functions.

The frequency-response analysis is the conventional method of obtaining time-response information. It provides such information as system stability, frequency of damped oscillation, damping, and steady state error. The method is simple to apply, and the frequency response of a component or system may be obtained mathematically or by laboratory measurement. The inherent reasons for the simplicity of this method, however, result in limiting its usefulness. At the outset of a design the complex frequency S is replaced only by $i\omega$, and thus the analysis is narrowed to the $i\omega$ axis of the S plane. Since the real part of S, (σ), is not considered, the opportunity of maintaining control over both frequency and transient responses is discarded.

The more recent design methods, such as the root-locus (1) and Guilleman's (1) methods, take into account the entire S plane. This is achieved by working through the poles and zeros of various transfer functions and thus simultaneously controlling the frequency and transient responses. A detailed description of the root-locus method (which is used in this paper) may be found in most recent texts on automatic control (1).

It should be pointed out that the control-system design is not for any specific stirred-tank chemical reactor but is concerned with the fundamental variables of a theoretical stirred-tank reactor. The calculated results have not been verified experimentally.

The basic continuous stirred-tank reactor process used in this paper was originally described by Aris and Amundson (2).

GENERAL CONTROL PROBELM

Description of Control-System Process

The process to be controlled is the continuous stirred-tank chemical reactor shown in Figure 1. The influent consists of a reactant A and an inert carrier. The reaction occurring in the reactor is

$$2A \rightarrow \text{products}$$
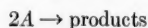
The reaction is assumed to be exothermic, irreversible, and second order. The material balance around the reactor may be written

$$\frac{V dA}{dt} = Q(A_0 - A) - kVA^2 \quad (1)$$

Equation (1) states that the rate of accumulation of A in the reactor is equal to the difference between the amount of A entering minus the amount of A leaving and the amount that has disappeared owing to the reaction.

The energy balance is

$$Vc\rho \frac{dT}{dt} = Qc\rho(T_0 - T) - ha(T - T_c) + kVA^2(-\Delta H) \quad (2)$$

Thus the accumulation of heat in the reactor is equal to the difference in the total heat removed (by warming the influent and by the cooling coil) and the heat generated by the reaction.

The average coolant temperature and the inlet coolant temperature are related by

$$T_c = \frac{(\alpha/Q_c)T + T_{ec}}{(\alpha/Q_c) + 1} \quad (3)$$

where α is defined as

$$\alpha = \frac{ha}{2c_c\rho_c} \quad (4)$$

Equation (5) is then obtained by substituting Equations (3) and (4) into Equation (2):

$$Vc\rho \frac{dT}{dt} = Qc\rho(T_0 - T) - \frac{Q_c ha}{\alpha + Q_c} \cdot (T - T_{ec}) - kVA^2(\Delta H) \quad (5)$$
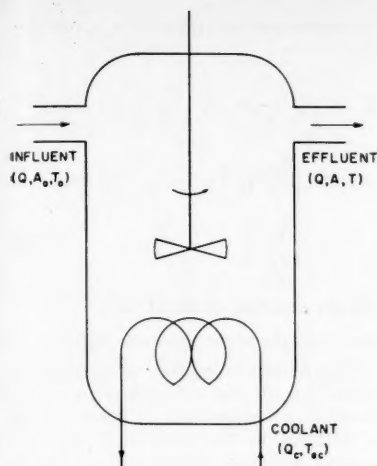
Fig. 1. Continuous stirred-tank reactor.

Also the reaction velocity coefficient may be represented by

$$k = k_1 e^{-\epsilon/RT} \qquad (6)$$

It has been shown (3) that if these equations are solved in terms of A or T with steady state conditions being assumed (that is, dT/dt and dA/dt equal zero), then there may exist one to three solutions depending upon the values of the equation parameters. For the case of three solutions there will be three sets of steady state values of T and A. The high and low values

state however a temperature increase will cause the rate of heat generation to be greater than the rate removed, and the reactor will thus adjust to a higher temperature. The reverse is true if the reactor temperature is slightly decreased from the unstable steady state temperature.

Therefore to obtain an over-all satisfactory control of the reactor special attention must be centered on obtaining proper control at an unstable steady state. In the following sections both the unstable and stable steady state conditions will be considered, and each will be separately analyzed with concentration and temperature as the directly controlled variables.

Derivation of Process Equation

The solution of the basic Equations (1), (5), and (6) in terms of an explicit variable A or T would be difficult if not impossible. A simplification of Equations (1) and (5) may be effected by linearizing the nonlinear terms. This may be accomplished by expanding each nonlinear term in a Taylor's series and retaining only the linear terms. The Taylor's series for a function of two variables may be written as

$$f(x, y) = f(x_0 y_0) + \left(\frac{\partial f}{\partial x}\right)_{x_0, y_0} (x - x_0)$$

$$+ \left(\frac{\partial f}{\partial y}\right)_{x_0, y_0} (y - y_0) + \cdots$$

The expansion is about a steady state value, and these constants will be denoted by a subscript, s.

With Equation (6) substituted into (1) and (5) these equations then become

$$\frac{dA}{dt} = -\left(\frac{Q_s}{V} + 2k_s A_s\right)A - \left(\frac{k_s A_s^2 \epsilon}{RT_s^2}\right)T$$
$$+ \left(\frac{Q_s}{V}\right)A_0 + k_s A_s^2 + \frac{k_s A_s^2 \epsilon}{RT_s} \quad (7)$$

$$\frac{dT}{dt} = -\left(\frac{2\Delta H k_s A_s}{c\rho}\right)A$$
$$- \left(Q_s + \frac{\Delta H k_s A_s^2 \epsilon}{c\rho RT_s^2} + \frac{Q_{cs} ha}{Vc\rho(\alpha + Q_{cs})}\right)T$$
$$+ \left(\frac{Q}{V}\right)T_0 + \left(\frac{Q_{cs} ha}{Vc\rho(\alpha + Q_{cs})}\right)T_{ec}$$
$$- \left(\frac{\alpha ha(T_s - T_{ecs})}{Vc\rho(\alpha + Q_{cs})^2}\right)Q_c + \frac{\Delta H k_s A_s^2 \epsilon}{c\rho RT_s}$$
$$+ \left(\frac{\alpha ha(T_s - T_{ecs})}{Vc\rho(\alpha + Q_{cs})^2}\right)Q_{cs} \quad (8)$$

Values of the constants in Equations (7) and (8) are chosen specifically to produce either a stable or unstable steady state reactor. The constants are reasonable values but are not for any real system.

Upon substitution of the values, solution of the equations for A or T, and transformation, Equations (9), (10), (11), and (12) result.

For the unstable steady state

$$A = \frac{0.005(S - 0.0159)A_0 - 3.39 \times 10^{-7}T_0 - 1.13 \times 10^{-7}T_{ec} + 1.97 \times 10^{-5}Q_c + (0.704S^2 - 9.75 \times 10^{-3}S + 2.88 \times 10^{-4})(1/S)}{(S - 0.0113)(S + 0.00457)}$$

$$\qquad (9)$$

$$T = \frac{7.0 \times 10^{-3}A_0 + (0.005T_0 + 0.00167T_{ec} + 0.290Q_c)(S + 9.20 \times 10^{-3})}{(S - 0.0113)(S + 0.00457)} + \text{constant} \qquad (10)$$

For the stable steady state

$$A = \frac{0.005(S - 0.0410)A_0 - 7.16 \times 10^{-7}T_0 - 2.39 \times 10^{-7}T_{ec} + 7.83 \times 10^{-5}Q_c + (0.0589S^2 + 0.00228S + 0.000160)(1/S)}{(S + 0.116)(S + 0.00740)} \qquad (11)$$

$$T = \frac{0.266A_0 + (0.005S + 8.23 \times 10^{-4})T_0 + (0.00167S + 2.75 \times 10^{-4})T_{ec} - (0.547S + 0.090)Q_c}{(S + 0.116)(S + 0.00740)} + \text{constant} \qquad (12)$$

of T are stable steady states, and the intermediate value represents an unstable steady state. The physical behavior of these steady state locations may be explained as follows. If the reactor is being operated at either the upper or lower steady state and a perturbation in reactor temperature occurs, the reactor will tend to adjust itself back to the original steady state value. If the temperature increases slightly, the rate of heat removed by the cooling coil is greater than that generated by the reaction and the reactor cools to the original steady state. At the unstable steady

Since the variables in Equations (1) and (5) are A, A_0, T, T_0, T_{ec}, and Q_c, the following terms must be linearized:

$$kA^2; \quad \frac{Q_c haT}{\alpha + Q_c}; \quad \frac{Q_c haT_{ec}}{\alpha + Q_c}$$

The linearization of kA^2, for example, is

$$kA^2 = k_1 e^{-\epsilon/RT} A^2$$
$$= k_s A_s^2 + 2k_s A_s(A - A_s)$$
$$+ k_s A_s^2 \frac{\epsilon}{RT_s^2}(T - T_s)$$

The constant input terms in Equations (10) and (12) (last terms), represent the steady state values of A and T. This may be shown by the application of the initial-value theorem, which gives the value of the function at time = 0. Therefore these terms may be neglected and the steady state value then added to the ordinate of all transient response curves.

In the following sections it will be shown that the control of this process essentially consists of maintaining the system at some predetermined steady state value by regulating it against

variations due to changes in A_0, T_0, and T_{ec}. (Disturbances in Q_c are assumed negligible.)

No time lags that would be introduced into the control loop by the actual operation of the control equipment (values, sensing elements, etc.) will be considered in this analysis.

Block Diagram

The variables A_0, T_0, T_{ec}, and Q_c in Equations (9) and (11) may be considered as signals which are operated on by their transfer functions and contribute accordingly to the value of A. The same is true for Equations (10) and (12) where T is the measured variable. The control of the reactor at some specified value of A or T may be accomplished by a single feedback loop regulation of one or more of the variables A_0, T_0, T_{ec}, and Q_c.

The block diagram for the case in which the controller regulates the flow of water through the cooling coil is shown in Figure 2. The desired concentration A or temperature T in the reactor is indicated by θ_i; the measured variable A or T is denoted by θ_0. If a signal is entered into the system by a change in one or a combination of the variables A_0, T_{ec}, T_0, or Q_c, each signal is operated on by the transfer function of the block and contributes to the value of the output variable. This signal is fed back to the comparitor (usually part of the controller) where it is compared with the desired variable θ_i. The difference in signals (error signal) then goes to the controller which acts to correct the error by readjusting the flow in the cooling coil. In actual operation θ_i is held constant for long periods of time, so that the response specification for control over changes in θ_i may be within a very liberal range. The dotted lines represent signals within the reactor that cannot be measured; that is it is not possible in the physical system to isolate any concentration or temperature measurement as being due to A_0, T_{ec}, T_0, or Q_c. It is convenient however to consider the signals as isolated; as will be shown later, this assumption offers no significant limitation in the control system design. The single-loop feedback type of control system (Figure 2) will be used throughout this paper. It is by no means the only or possibly even the best system to use in controlling this process; it is practical, however, since it is simple and widely used in industry today. It should therefore be analyzed first as a possible suitable control system. Other systems might include a minor feedback loop to the node at Q_c, feed forward control of A_0 (4), and combinations of these with concentration and/or temperature being the measured variables. An equation representing the block diagram in Figure 2 may be derived as follows. From Figure 2 it is seen that

$$\theta_0 = \theta_i - E \qquad (13)$$

and

$$E = \frac{\theta_0}{G} \qquad (14)$$

where

$$\theta_0 = GE + L_{T_0}T_0 + L_{T_{ec}}T_{ec} + L_{A_0}A_0 + N(1)$$

and

$$G = G_{EQ_c}G_{Q_c}.$$
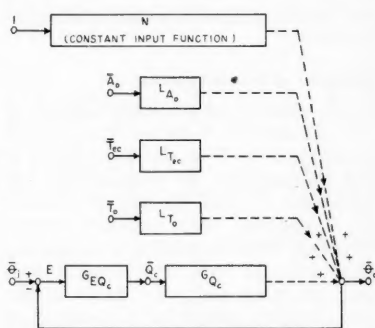
Fig. 2. Block diagram for control of reactor coolant.
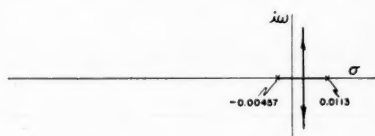
Fig. 3. Root loci for Equation (22).

Fig. 4. Root loci for Equation (24) with $z_1 = 0.003$.

Fig. 5. Root loci for Equation (26) with $z_1 = 0.003$ and $z_2 = 0.02$.

Fig. 6. Root loci for Equation (26) with $z_1 = 0.005$ and $z_2 = 0.020$.

Therefore the block diagram is represented by

$$\theta_0 = \frac{G}{1+G}\,\theta_i + \frac{L_{T_0}}{1+G}\,T_0 + \frac{L_{T_{ec}}}{1+G}\,T_{ec} + \frac{L_{A_0}}{1+G}\,A_0 + \frac{N(1)}{1+G} \qquad (15)$$

DESIGN IN TERMS OF ROOT LOCI

Basic Principles of the Root-Locus Method

The root-locus method is a graphical technique for the determination of the roots of a polynomial. It has a special application in the analysis of feedback control systems, however, since unique functional relationships exist in these systems.

The basic elements of the root-locus method may be illustrated by consideration of the system in Figure 2. If for the sake of simplicity one assumes that there are no disturbances in the system, Equation (15) (the closed-loop system function) may be written as

$$\frac{\theta_0}{\theta_i} = \frac{G}{1+G} \qquad (16)$$

Since G is usually a ratio of rational algebraic functions, it may be represented by two polynomials in S:

$$G = \frac{p(S)}{q(S)} \qquad (17)$$

Substitution of Equation (17) in (16) gives

$$\frac{\theta_0}{\theta_i} = \frac{\frac{p(S)}{q(S)}}{1+\frac{p(S)}{q(S)}} = \frac{p(S)}{p(S)+q(S)} \qquad (18)$$

Thus since the zeros of $p(S)$ and $q(S)$ are known, the root-locus method is a graphical technique for determining the zeros of $p(S) + q(S)$ from the zeros of $p(S)$ and $q(S)$ individually.

Also since G contains the variable gain factor, the root loci then are the roots of the equation $G = p(S)/q(S) = -1$, as a function of the gain. Further discussion of this material and rules for construction of the root loci may be found in standard texts (1, 5).

Unstable Steady State

Concentration as the Measured Variable

The process for this condition is represented by Equation (9). As mentioned previously, control will be maintained through the regulation of flow in the cooling coil. This will be true for all systems studied in this paper.

The block diagram for $\theta_i = A_i$ and $\theta_0 = A_0$ is then represented by rewriting Equation (21) (closed-loop equation) to give

$$A = \frac{G}{1+G} A_i + \frac{L_{T_0}}{1+G} T_0$$
$$+ \frac{L_{T_{ec}}}{1+G} T_{ec} + \frac{L_{A_0}}{1+G} A_0$$
$$+ \frac{N(1)}{1+G} \qquad (19)$$

where

$$G = G_{EQ_c} G_{Q_c} = \frac{A}{E} \qquad (19a)$$
$$= G_{EQ_c} \frac{1.97 \times 10^{-5}}{(S-0.0113)(S+0.00457)}$$

$$L_{T_0} = \frac{A}{T_0}$$
$$= \frac{-3.39 \times 10^{-7}}{(S-0.0113)(S+0.00457)} \qquad (19b)$$

$$L_{T_{ec}} = \frac{A}{T_{ec}}$$
$$= \frac{-1.13 \times 10^{-7}}{(S-0.0113)(S+0.00457)} \qquad (19c)$$

$$L_{A_0} = \frac{A}{A_0}$$
$$= \frac{0.005(S-0.0159)}{(S-0.0113)(S+0.00457)} \qquad (19d)$$

$$N = \frac{A}{1} \qquad (19e)$$
$$= \frac{0.704S^2 - 9.75 \times 10^{-3} S + 2.88 \times 10^{-4}}{S(S-0.0113)(S+0.00457)}$$

The characteristic equation for which the root loci are to be calculated is the polynomial $1 + G = 0$, or $G = -1$. This will be solved for various controller functions, G_{EQ}, as a function of the control gain.

The root loci of $G = -1$ are the S-plane points at which

$$\angle G = \tan^{-1} 0/-1$$
$$= 180° + n360° \qquad (20)$$

This equation is the basis for all rules and techniques for construction of the root loci.

Proportional Control

The controller equation for proportional control is given by

$$G_{EQ_c} = K \qquad (21)$$

The open-loop equation is then

$$G = G_{EQ_c} G_{Q_c}$$
$$= \frac{K 1.97 \times 10^{-5}}{(S-0.0113)(S+0.00457)} \qquad (22)$$

The root-locus plot for Equation (22) is shown in Figure 3. It is obvious from the location of the loci that the roots
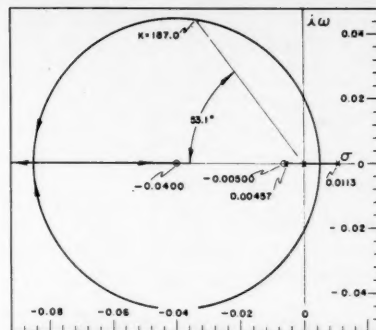
Fig. 7. Root loci for Equation (26) with $z_1 = 0.005$ and $z_2 = 0.040$.
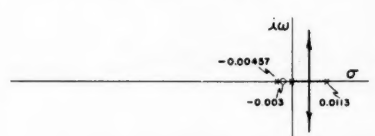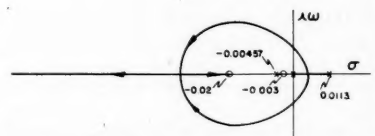

Fig. 8. Root loci for Equation (26) with $z_1 = z_2 = 0.003$.

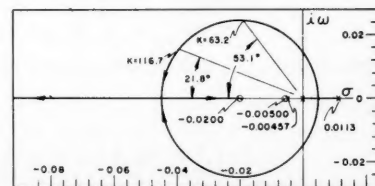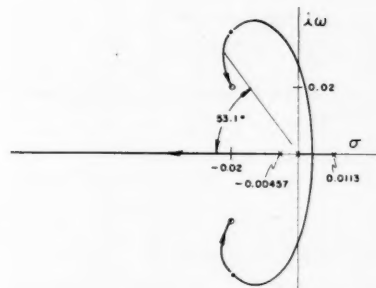Fig. 9. Root loci for Equation (26) with $z_1 = 0.02 + i0.02$ and $z_2 = 0.02 - i0.02$.
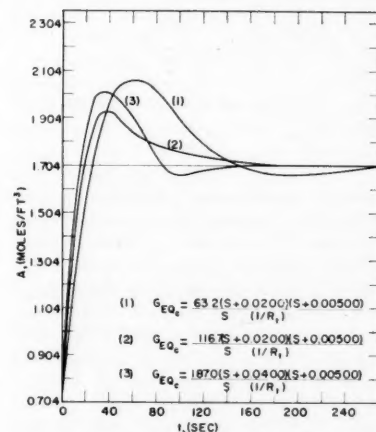
Fig. 10. Transient response of concentration A to a unit step input in A_i; reactor at an unstable steady state.

are positive, and the system will therefore be unstable for all values of K.

Proportional-Integral Control

The equation for the controller is

$$G_{EQ_c} = \frac{K}{S}\left(S + \frac{1}{I_t}\right)$$
$$= \frac{K}{S}(S + z_1) \qquad (23)$$

The open-loop equation may then be written as

$$G = \frac{K 1.97 \times 10^{-5}(S+z_1)}{S(S-0.0113)(S+0.00457)} \qquad (24)$$

The root loci for G in Equation (24) (with $z = 0.003$) are shown in Figure 4. Two of the roots are positive for all values of K, and thus this system will always be unstable.

Proportional-Integral-Rate Control

The equation for the controller is given by

$$G_{EQ_c} = \frac{KR_t}{S}\left(S^2 + \frac{S}{R_t} + \frac{1}{I_t R_t}\right)$$
$$= \frac{KR_t}{S}(S + z_1)(S + z_2) \qquad (25)$$

The open-loop equation is therefore

$$G = \frac{KR_t 1.97 \times 10^{-5}(S+z_1)(S+z_2)}{S(S-0.0113)(S+0.00457)} \qquad (26)$$

For $z_1 = 0.003$ and $z_2 = 0.02$ the root loci are sketched in Figure 5 (without any regard for accuracy). In this case it is evident that the system will be stable for all values of K for which the loci are on the negative side of the $i\omega$ axis. Thus it is seen that the addition of the rate action is necessary to attain system stability. Other root-locus diagrams may be constructed for the proportional-integral-rate action by moving the zeros of G to different locations in the S plane. Some of these loci curves are shown in Figures 6 to 9. The loci of Figures 6 and 7 are accurate; those of Figure 8 are not accurate, and those of Figure 9 are accurate only at the points indicated on the loci curve. System stability may be attained with each of these loci configurations.

Response Specifications

The problem now arises as to which of the infinite number of possible root-locus diagrams should be used as the basis for the control system design. First of all, since no specific response specifications are known, only the relative effect of the change in a zero location can be analyzed. This does not limit the usefulness of the design, however, since optimum specifications for various systems are known. Thus the control system design is concerned with approaching the optimum specifications.

Complete control over the effects of disturbances is ordinarily achieved through a transient response analysis, since simple correlations between the frequency and time domain are usually not available. Design by shaping the frequency-response
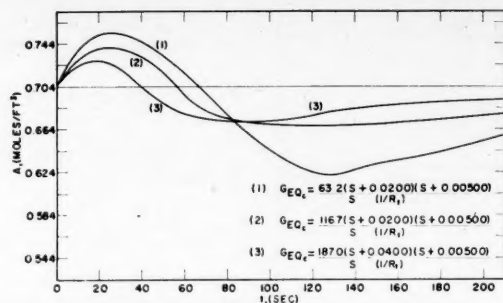
Fig. 11. Transient response of concentration A to a unit step input in A_0, reactor at an unstable steady state.
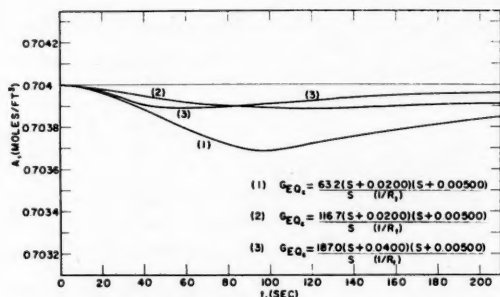
Fig. 12. Transient response of concentration A to a unit step input in T_0, reactor at an unstable steady state.
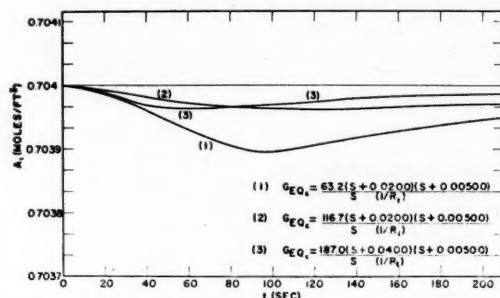
Fig. 13. Transient response of concentration A to a unit step input in T_{ec}, reactor at an unstable steady state.

curve is more applicable in control-point changes. The time-domain specifications commonly include the following three characteristics of the response of the system to a unit-step function of input: (1) the ultimate state or steady state value, (2) the settling time (or longest significant time constant), and (3) the maximum overshoot. The first quantity measures the steady state error, which is the difference between the steady state value and a constant input signal; the second measures the speed at which the system settles down after a control-point change or a disturbance, and the third measures the relative stability. The frequency-response specifications vary according to whether control is to be mainly over a disturbance or a control-point change. In either case a compromise must be made, since satisfying the specifications for a disturbance usually results in producing a less favorable response for a control-point change. The reverse is likewise true.

The optimum system for control of a disturbance is one in which the ratio of the output signal to each disturbance input signal is equal to zero. This ideal situation can be realized if the controller gain is infinite. Therefore in systems in which both reference input changes and disturbances occur the design attempts to realize a high gain while at the same time ensuring suitable relative stability and/or freedom from noise interference. An attempt at this compromise in gain usually involves the proper choice of the controller function.

Interpretation of the Root Loci

The relative merits of the various root-locus diagrams may now be analyzed with regard to satisfying the general

response specifications. For the control of a continuous stirred-tank reactor it is evident that the main problem is in minimizing the effect of disturbances. The effect of reference input changes will also be analyzed, since the physical operation of a stirred-tank reactor would at times entail a change in the control point (during a start-up, etc.).

When one again refers to the root-locus diagrams (Figures 3 to 9), it is obvious that any further consideration of Figures 3 and 4 is unnecessary, since the system will be unstable for all values of K. Figures 5 to 9 on the other hand should be analyzed further to determine which would give the most desirable system response. The same scale was used in constructing these plots in order to facilitate a visual comparison of the vector magnitudes. Figures 5, 6, and 7 are of the same general type, all exhibiting possibilities of obtaining a suitable transient and frequency response. In each of these plots the gain may be increased to cause an increase in stability. The settling time is determined by the closed-loop pole nearest the $i\omega$ axis if the pole has a significant residue magnitude. For disturbances this pole is seen to be approximately -0.005. The root-locus plot in Figure 8 likewise indicates that increasing K will increase the relative stability; however the over-all stability is less, owing to the large amplitude of the cyclic part of the time response. Also the settling time for this design will be longer since the complex poles are closer to the $i\omega$ axis (with a significant residue in the complex pole) than the closest significant pole in the previous loci plots. If the loci in Figure 9 were used as the basis for design, the range over which K may be moved to adjust the response characteristics is limited by the zero locations. Hence a system with high damping could not be achieved.

The root-locus diagrams just discussed were intended to represent a rough distribution of the infinite number of possible configurations. From the preliminary analysis of these loci plots it is now reasonable to assume that the most suitable control-system design should be based on a root-locus plot similar to those shown in Figures 5, 6, and 7.

Transient Response

The transient response was obtained by introducing a unit-step function into Equation (19) and then performing the inverse transformation of this equation. Figures 10 to 13 are the results obtained for root-loci values corresponding to a ζ of 0.6 ($K = 63.2$) and 0.929 ($K = 116.7$) in Figure 6, and for a ζ of 0.6 ($K = 187.0$) in Figure 7.

From a comparison of the transient response curves the following conclusions are apparent:

1. An increase in K from 63.2 to 116.7,

as described by response curves 1 and 2 in Figures 10 to 13, causes a decrease in the settling time for both a change in reference input (A_i) and for all the disturbance inputs (T_0, T_{ec}, and A_0). An additional increase in K would further minimize the disturbance inputs. This desirable effect would however become offset with continued increases in K, since the controller would have become sensitive to extraneous (noise) signals.

2. The maximum overshoot decreases with an increase in K. This is observed for a reference-input change as well as for all disturbance inputs and may be interpreted as an increase in relative stability.

3. In all cases the principal effect of moving the zero from -0.0200 to -0.0400 (response-curve 3) is to decrease the settling time. For the disturbance-response curves the result is due to a decrease in magnitude of the residue in the dominant pole. This effect for a change in A_i is due to an increase in damping of the dominant complex poles.

4. The overshoot of curve 3 is larger than curve 2 for a step change in A_i, which means that curve 3 represents a less stable response than curve 2. The relative stability of these two response curves in the case of disturbance inputs (Figures 11, 12, and 13) is approximately the same.

Realistic Inputs

The unit-step input just discussed is obviously not of a realistic magnitude. If a step input of a different magnitude were introduced into the variables, the only effect would be to change the scale of the ordinate (A). Therefore any point on the unit-step input response curve can be interpreted as the percentage change in A (from A_s) at the corresponding lapsed time.

In order that the relative effect of each disturbance might be easily seen, the ordinate of curve 1 in Figures 11, 12, and 13 was changed by introducing the following inputs into Equation (19):

Variable	Input
A_0	0.03 lb.-mole/cu. ft.
T_0	10.0°R.
T_{ec}	5.0°R.

These input values are more realistic, and it has been shown (4) that disturbances of this order of magnitude are sufficiently small so that their effects may be described by the linearized equation. A plot of the transient response for each disturbance is shown in Figure 14. From a comparison of these curves it is reasonable to generalize that under actual conditions of reactor operation disturbances in A_0 and T_0 would be the most difficult to control. If some or all of the disturbances should occur simultaneously, the effect may be easily seen by a visual summation of the curves.
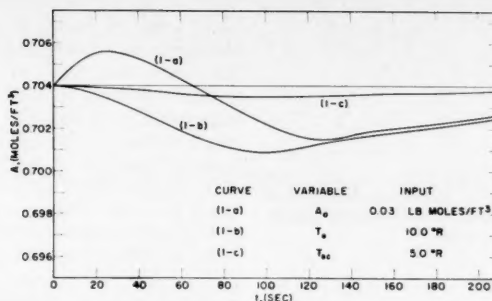
Fig. 14. Transient response of concentration A to various step input disturbances, reactor at an unstable steady state.
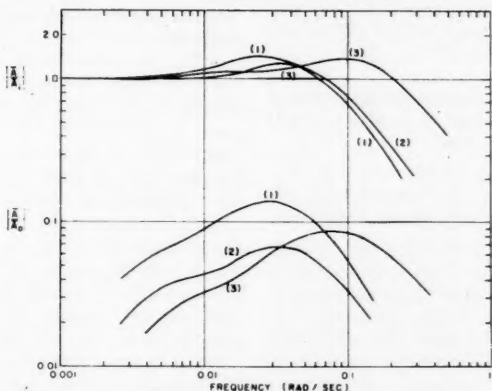
Fig. 15. Closed-loop gain characteristic of concentration, reaction at an unstable steady state.

Frequency Response

The closed-loop gain characteristics of $|\mathbf{A}/\mathbf{A}_i|$ and $|\mathbf{A}/\mathbf{A}_0|$ are shown in Figure 15. The numbers on the curves refer to the associated transient-response curves in Figures 10 and 11. The interpretation of the shapes of the curves for the frequency response of $\mathbf{A}/\mathbf{A}_i$, in terms of the expected transient response characteristics, is seen to correspond to the results shown in Figure 10. The frequency-response curves of $\mathbf{A}/\mathbf{A}_0$ however show only a correlation and do not have a simple transient-response interpretation.

OTHER REACTOR CONDITIONS

Stable Steady State

Concentration as The Measured Variable

The problem of controlling the reactor at a stable steady state should be relatively easy, since this kind of stability is autoregulatory. Under these conditions however the problem still amounts to a control of disturbances in A_0, T_0, and T_{ec} (disturbances in Q_c considered negligible). It has been shown (3) that a disturbance from a stable steady state, although self-correcting, theoretically takes an infinite amount of time to come back to the steady state, the speed decreasing as the steady state is

approached. With no control it can be shown that the settling time is described by

$$Me^{-0.00740t}$$

Thus the aid of a control system is necessary to reduce this long settling time.

The root-locus curve for proportional control is shown in Figure 16. It is evident from the location of the loci that the system will be stable for all values of K. Additional root-locus diagrams were constructed for the other modes of control, and a transient- and frequency-response analysis was made for the case of proportional-integral control. From the over-all analysis it was apparent that this process condition was decidedly easier to control than the unstable steady state condition.
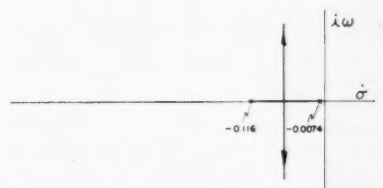
Fig. 16. Root loci for proportional control of concentration, reactor at a stable steady state.
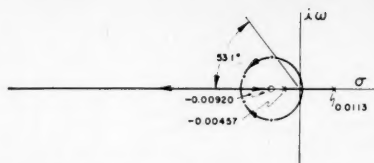
Fig. 17. Root loci for proportional control of temperature, reactor at an unstable steady state.
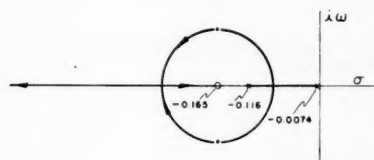
Fig. 18. Root loci for proportional control of temperature, reactor at a stable steady state.

Temperature as the Measured Variable

The unstable and stable steady state process conditions are now represented by Equations (10) and (12), respectively.

Root-locus plots were constructed for the three modes of control, of which only the plots for proportional control are shown (Figures 17 and 18). From a comparison of these two diagrams with those for concentration as the measured variable (Figures 3 and 16), it is seen that stable control of reactor temperature is easily attained at the unstable steady state; as previously explained, stable control is not possible when concentration is the measured variable (Figure 3). At the stable steady state for control of temperature (or concentration), the system will be stable for all values of K.

Introducing the other modes of control was seen to provide additional flexibility in shaping the root-locus curves, thus making possible more desirable control.

SUMMARY

The control system for a theoretical, continuous stirred-tank reactor was designed by the use of the root-locus method. The root-locus method is a well established procedure in the servomechanism field (5). Application of this method to process-control systems has been shown to be a valuable aid. The process was approximated by a linear system which has been shown (4) to be a good approximation for small disturbances about the steady state. The design was carried out for stable and unstable steady state reactor conditions. Also each condition was examined in terms of both concentration and temperature as the controlled variables.

The methods of control considered were the proportional, the proportional-integral, and the proportional-integral-rate. Numerous controller settings were exam-

ined, some of which were analyzed in detail be calculating the transient and frequency responses of the systems.

The root-locus method proved to be exceptionally useful in providing a rapid means of obtaining a picture of system behavior. A preliminary study of a large variety of systems could be made in a very short time from sketches of the approximate root loci.

To control the system at an unstable steady state, with concentration as the measured variable, proportional-integral-rate was necessary. At the stable steady state any one of the three modes of control could be used; however proportional-integral-rate action was the most desirable.

With temperature as the measured variable both the unstable and stable steady states could be controlled with any one of the modes of control the proportional-integral-rate seeming equally adequate in both cases and better than proportional control.

If it is assumed that the proportional-integral-rate action would be used as the most suitable mode of control in all four systems, it is seen that the relative difficulty of control at the unstable steady state, as compared with the control at the stable steady state, is not as pronounced as might first be expected. The reason for this is that the auto-regulatory nature of the stable steady state is not fast acting, and the system needs some help from a controller to reduce the settling time.

The control of the influent concentration was of the same order of difficulty as the control of influent temperature, while both were considerably more difficult to control than a disturbance in the inlet coolant temperature.

NOTATION

A	=	concentration of A in reactor
A_i	=	desired concentration of A
A_0	=	inlet concentration of A
E	=	$\theta_i - \theta_0$, error signal
G	=	forward or open-loop transfer function
I_t	=	integral time
K	=	variable gain factor
k	=	reaction velocity coefficient
M	=	residue in pole at -0.00740
n	=	any positive or negative integer
Q	=	flow rate of reactant mixture through reactor, cu. ft./sec.
Q_c	=	coolant flow rate
R_t	=	rate (or derivative) time
S	=	Laplace transform variable
t	=	time, sec.
T	=	temperature of reactor
$\mathbf{T}$	=	measured variable
T_c	=	average temperature of coolant
T_{ec}	=	inlet coolant temperature
T_i	=	desired temperature of reactor
T_0	=	temperature of inlet reactant mixture
$\mathbf{V}$	=	volume, cu. ft.

Greek Letters

α	=	$ha/2c_c\rho_c$
θ_i	=	input signal
θ_0	=	output signal
ζ	=	damping coefficient

bold face or bar = transformed variable

Constants

a	=	area of cooling coil, 500 sq. ft.
A_s	=	concentration in reactor at steady state, 0.704 lb.-mole/cu. ft.
A_s'	=	concentration in reactor at steady state, 0.0589 lb.-mole/cu. ft.
A_{0s}	=	concentration in inlet mixture at steady state, 1.00 lb.-mole/cu. ft.
c	=	mean heat capacity of reactant mixture, 1.0 B.t.u./(lb.)(°R.)
c_c	=	mean heat capacity of coolant, 1.0 B.t.u./(lb.)(°R.)
ϵ	=	Activation energy, 44,700 B.t.u./lb.-mole
h	=	heat transfer coefficient, 100 B.t.u./(hr.)(sq. ft.)(°R.)
ΔH	=	heat of reaction, 20,000 B.t.u./lb.-mole
k_1	=	reaction velocity constant, 2.7×10^{11} cu. ft./(lb.-mole)(sec.)
k_s	=	reaction velocity coefficient, 2.98×10^{-3} cu. ft./(lb.-mole)(sec.)
k_s'	=	reaction velocity coefficient, 1.354 cu. ft./(lb.-mole)(sec.)
Q_{cs}	=	steady state coolant flow rate, 0.289 cu. ft./sec.
Q_s	=	steady state reactant flow rate, 0.5 cu. ft./sec.
R	=	gas constant, 1.987 B.t.u./(lb.-mole)(°R.)
ρ	=	density of reactant mixture, 60.01 lb./cu. ft.
ρ_c	=	density of coolant, 62.4 lb./cu. ft.
T_{ecs}	=	steady state temperature of inlet coolant, 520°R.
T_{0s}	=	steady state temperature of inlet reactant mixture, 661.6°R.
T_s	=	steady state temperature of reactor, 700°R.
T_s'	=	steady state temperature of reactor, 859.5°R.
V	=	volume of reactor, 100 cu. ft.

LITERATURE CITED

1. Truxal, J. G., "Automatic Feedback Control System Synthesis," McGraw-Hill, New York, (1955).
2. Aris, Rutherford, and N. R. Amundson, Chem. Eng. Progr., 53, 227 (1957).
3. Bilous, Olegh, and N. R. Amundson, A.I.Ch.E. Journal, 1, 4 (1955).
4. Tierney, J. W., C. J. Homan, D. J. Nemanic, and N. R. Amundson, Control Eng., 166 (September, 1957).
5. Murphy, G. J., "Basic Automatic Control Theory," D. Van Nostrand, Princeton, N. J. (1957).
6. Ceaglske, N. H., "Automatic Process Control for Chemical Engineers," John Wiley, New York (1956).
7. Ceaglske, N. H., lecture notes (1957).

The Study of Flow and Reaction Rates in Turbulent Flames

R. P. BARBOR, J. D. LARKIN, H. E. VON ROSENBERG, and C. W. SHIPMAN University of Delaware, Newark, Delaware

It is proposed that measurements of reaction rate as a function of position within turbulent flames be the basis of an approach to the problem of turbulent-flame propagation. As a test of the method, measurements of static pressure, impact pressure, and chemical composition were made at several positions within the burning zones of two simulated ramjet combustion chambers. From these measurements a complete mapping of compositions, velocity components, densities, and static pressures could be carried out. By calculation of the appropriate derivatives of the latter quantities, the differential form of the equation of continuity for the species desired could be solved for net reaction rate as a function of position, turbulent diffusion being neglected. By a similar technique the equation of momentum was used to obtain eddy viscosities. The latter results were used to estimate the effect of turbulent diffusion by assuming a turbulent Schmidt number of unity.

It is concluded that the method of attack used is a reasonable approach to the problem of turbulent flame propagation, having a special advantage in that it can be used to discover relationships between the rate of reaction and the patterns of the mean flow.

The development of the high-output combustion chamber for jet power plants has aroused considerable interest in turbulent flame propagation in consequence of the joint requirements of high heat-release rate, (British thermal units per hour per cubic foot), and small frontal area for such engines. These requirements mean efficient use of combustion-chamber volume at high feed velocities; the unavoidable result is turbulent flow.

The laminar flame and the well-stirred reactor (8, 14) are two cases of flame propagation sufficiently well understood for quantitative treatment by the engineer. As long as the region of interest is not far removed from these extremes, adequate treatments for engineering use can be developed by modification of the quantitative descriptions of the extremes (7, 9, 11, 20, 29, 32, 36, 38, 39).

Theoretical discussion of turbulent flame propagation has to a large extent been based on relationships between the character of the flame front and the turbulence parameters of the unburned mixture (3, 10, 11, 19, 24, 26, 37, 38). Scurlock (24, 25, 33) has pointed out however that velocity gradients caused by combustion of part of the feed can generate turbulence in an initially laminar stream. Such turbulence can affect the combustion of the remainder of the feed, and his data on confined flames (25, 33) indicate that it can have a stronger effect on the flame than turbulence produced by flame holders or turbulence of the feed mixture.

Some measurements of over-all reaction rate of both confined and open turbulent flames have been made (4, 28, 40), and Petrein et al. (18) have reported measurements of combustion efficiency as a function of longitudinal position for confined flames. Calculations of burning velocity and reaction time at several positions within confined flames have been made by Archer (1A), Jacobi (1B), and Schilly (21A) [see also 37] from measurements of composition, impact and static pressures, and flame luminosity. Their results indicate a complex interplay of flame and flow.

The complexities shown by the work cited indicate that a more detailed treatment of the turbulent burning zone than attempted heretofore is required. It was the purpose of the work described herein to attempt determniation of reaction rates as a function of position within the flame by means of sufficiently detailed mapping of the composition and velocity patterns.

For purposes of the present discussion the rate of production of any species, j, will be defined as the net efflux of j from any elemental volume of the system when the efflux is considered in terms of the time-mean variables of the system only. Thus the equation of continuity for species j may be written

$$\rho \vec{u} \cdot \nabla \chi_i - \nabla \cdot \xi \nabla \chi_i = Q_i \qquad (1)$$

where the first term on the left is the mass flux, the second term is the diffusive flux, and all quantities are time-mean values. It has been assumed in writing Equation (1) that the coefficient of turbulent diffusion is independent of direction and that molecular diffusion is negligible. Neglect of molecular diffusion allows one to use mass fraction as the composition variable, eliminating the necessity for treatment of mass linear velocity and mole linear velocity in the same expression; χ_i is the mass fraction of j.

If one assumes for the moment that the eddy diffusivity is a known quantity, the quantities required for calculation of Q_i are the velocity components, the density, and the mass fraction of the component in question as functions of position within the flame. The simplest measurements from which to obtain these data are impact pressure, static pressure, and gas composition. A measurement of the temperature is difficult in a flame, and it was decided to calculate the density from the gas composition by assuming that the system is adiabatic, that molecular transport of energy is negligible, and that turbulent heat conduction cannot be distinguished from its associated transfer of mass. Thus since changes in kinetic energy of the flowing gases were always small, the density could be determined by the composition alone; that is, the energy equation becomes

$$H = \text{constant}$$

Since impact pressure is dependent on the square of the velocity, there is no procedure in the absence of knowledge of the turbulence intensity for deducing the true time-mean velocity from measurements of impact and static pressures. In the interest of expediency it was decided to ignore the difference between the velocity determined from these two measurements and the true time-mean velocity.

R. P. Barbor is with the Sun Oil Company, Marcus Hook, Pennsylvania; J. D. Larkin with Monsanto Chemical Company, Springfield, Massachusetts; H. E. von Rosenberg with Humble Oil and Refining Company, Baytown, Texas; and C. W. Shipman with Worcester Polytechnic Institute, Worcester, Massachusetts.
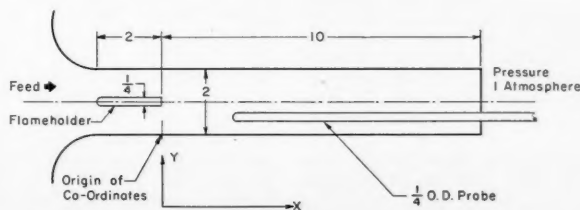
Fig. 1. Atmospheric burner mixture: stoichiometric propane-air, entrance velocity 60 ft./sec.
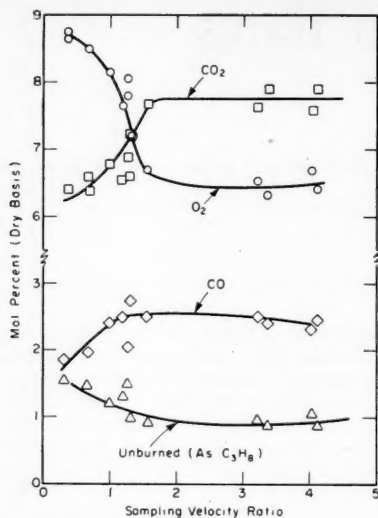
Fig. 2. Effect of sampling rate on sample composition.
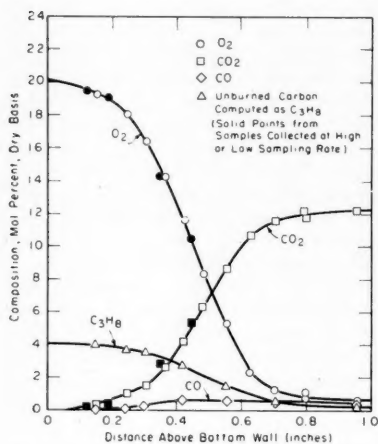
Fig. 3. Gas compositions 8 in. from flame holder. Exhaust pressure 1 atm. Inlet velocity 60 ft./sec., stoichiometric propane-air.

EXPERIMENTAL

It was decided to attempt some measurements of reaction rate in a simulated ramjet combustor. In such burners the flame is first subjected to a flow pattern owing primarily to the flame holder or pilot and in a secondary way to the approach flow; as the combustion proceeds, the flow pattern is altered by velocity gradients generated by the flame itself; finally, as the flame propagates to the confining walls, the geometry of the duct becomes important. It was thought that if the measurements of reaction rate could be made with some success in such a system, the feasibility of this method of attack would be established.

Two experimental arrangements were available at the University of Delaware Combustion Laboratory, both constructed under the supervision of Kurt Wohl. A detailed report of the work on one burner follows, and a summary of the results from the other is given at the end of the discussion. Complete descriptions of both combustors may be found (1, 22, 30).

The atmospheric combustion chamber is shown schematically in Figure 1. The feed stream of homogeneously mixed propane and air was introduced into the 2- by 1½- by 12-in. duct through a plenum chamber and nozzle to ensure a flat entrance velocity profile and an initial turbulence level of less than 0.5% (22, 30). The exit of the chamber was open to the atmosphere. The flame holder was a flat plate, ¼ in. thick, 2 in. long, and 1½ in. wide, aligned with its long (2 in.) dimension parallel to the flow. The leading edge was rounded to form a semicylinder. The origin of the coordinate system used in later discussion is shown in Figure 1.

For the experiments described herein the inlet velocity varied from 59 to 61 ft./sec., and the feed composition varied from 4.01 to 4.06 mole % propane. Measurements of composition, impact pressure, and static pressure were made at approximately 0.05-in. intervals in the direction normal to the bulk flow (y direction or transverse direction) and at distances of 2, 3, 4, 5, 6, 8, and 10 in. from the downstream end of the flame holder (x or longitudinal positions). Measurements were confined to half the chamber, symmetry and two-dimensionality of the mean flow being assumed.

The probe for measuring impact pressure and withdrawing samples was 20 in. long, 0.25 in. O.D., and 0.04 in. I.D. The tip of the probe was hemispherical in shape. When the probe was employed for withdrawing samples, the pressure drop through the probe was used to measure the sampling rate, the probe having been calibrated for this purpose. The probe used for measurement of static pressure was similar, except that the 0.04 in. pressure-tap hole was located 0.72 in. from the tip and oriented so that the normal to the hole was parallel to the 1½ in. dimension of the combustor. Both probes were inserted into the chamber from the downstream end. No attempt was made to correct measurements of probe position for variations in effective stagnation point due to velocity and density gradients because quantitative methods for making the latter correction are not available. Schlieren photographs and visual observations gave no indication that the character of the flame was altered by the presence of the probe at longitudinal distances greater than 2 in.

Analyses of gas samples were made by the Orsat technique, carbon dioxide being obtained by absorption in 28% (by weight) potassium hydroxide, O_2 by absorption in Oxsorbent, carbon monoxide and H_2 by partial oxidation over copper oxide at 295°C., followed by absorption of the carbon dioxide produced in potassium hydroxide; unburned materials remaining were found by catalytic oxidation with 200% excess oxygen followed by absorption of the carbon dioxide produced in potassium hydroxide and absorption of the excess O_2 in Oxsorbent. Since there is always some uncertainty in Orsat analyses for unburned hydrocarbon, coincidence of the carbon: nitrogen ratio of the sample as analyzed with that of the feed mixture was used as a criterion for the correctness of the analysis in an effort to avoid repeated analyses.

Fig. 4. Composition correlation, 1 atm. flame.

Fig. 5. Schlieren photograph, 1 atm. flame.

Fig. 6. (Carbon monoxide)/(carbon dioxide) mole ratio, 1 atm. flame.

60 FT./SEC. ATMOSPHERIC PROPANE-AIR FLAME

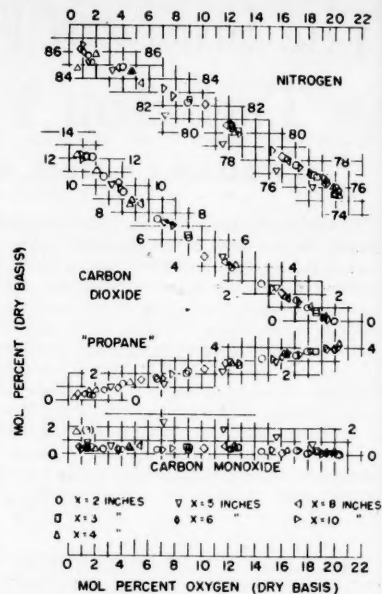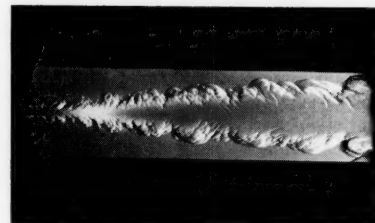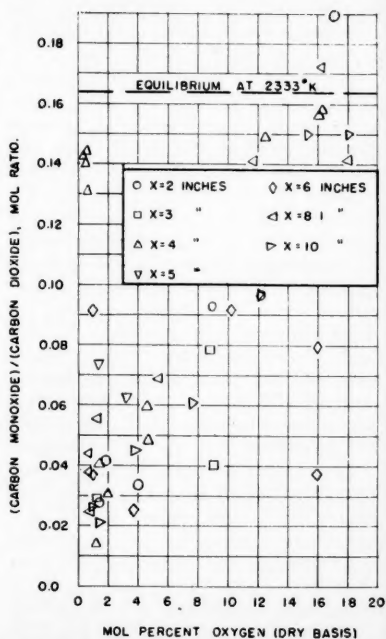Because of nonuniformity in sampling positions and space limitations presentation of all original data is not possible. The following tables show some of the smoothed results. Original data may be found in (1) and (21)

TABLE 1. STATIC PRESSURES (LB./SQ. FT. GAUGE)

y	$x = 1$	$x = 2$	$x = 3$	$x = 4$	$x = 5$	$x = 6$	$x = 8$	$x = 10$
0.1	17.53	16.3	14.74	12.88	11.08	9.2	4.95	0.573
0.2	17.42	16.3	14.7	12.7	11.03	9.08	4.76	0.416
0.3	17.22	16.25	14.62	12.6	10.91	9.08	4.89	0.52
0.4	17.04	16.03	14.47	12.5	10.82	9.08	4.89	0.573
0.5	16.9	15.98	14.36	12.55	10.85	9.1	4.89	0.573
0.6	16.9	15.78	14.31	12.7	10.91	9.14	4.89	0.573
0.7	16.9	15.74	14.36	12.75	10.97	9.14	4.89	0.573
0.8	17.07	15.95	14.47	12.75	10.97	9.14	4.89	0.468
0.9	17.28	16.06	14.47	12.75	10.97	9.14	4.89	0.468
1.0	17.48	16.02	14.47	12.8	10.97	9.14	4.89	0.468

TABLE 2. VELOCITY (ABSOLUTE VALUE OF TOTAL VELOCITY)

y	$x = 1$	$x = 2$	$x = 3$	$x = 4$	$x = 5$	$x = 6$	$x = 8$	$x = 10$
0.1		70	80	89	95	107	123.5	138
0.2		70	80	89	96	108.5	132	163
0.3		70	80	90	100	115	147	175
0.4		70	80	94	112.5	129.5	167	197
0.5		70	82.5	107.5	128	147	187	219
0.6		70	91	122.5	144	165.5	206.5	241.5
0.7		73.5	104.5	137	160	183	226	264
0.8		91	117.5	152	176	201	246	286
0.9		86	131	167	191	219	265	307.5
1.0		84.5	139	174.5	197	228	274	315

TABLE 3. DENSITIES (LB./CU. FT.)

y	$x = 1$	$x = 2$	$x = 3$	$x = 4$	$x = 5$	$x = 6$	$x = 8$	$x = 10$
0		0.0758	0.0757	0 0758	0.0757	0.0753	0.0752	0.075
0.1		0.0758	0.0757	0.0758	0.0757	0.0722	0.0641	0.063
0.2		0.0758	0.0757	0.0758	0.0745	0.0668	0.0485	0.036
0.3		0.0758	0.0757	0.0758	0.0685	0.0507	0.0308	0.0223
0.4		0.0758	0.074	0.071	0.048	0.0317	0.0187	0.0156
0.5		0.0758	0.0658	0.0385	0.024	0.0187	0.0128	0.0113
0.6		0.0743	0.046	0.0207	0.0135	0.0133	0.0103	0.01
0.7		0.0518	0.0213	0.0119	0.0103	0.0102	0.0096	0.0097
0.8		0.0172	0.0113	0.0099	0.0099	0.0096	0.0094	0.0095
0.9		0.010	0.0099	0.0097	0.0097	0.0094	0.0094	0.0094
1.0		0.0097	0.0096	0.0096	0.0095	0.0094	0.0094	0.0094

TABLE 4. WEIGHT FRACTION BURNED

y	$x = 1$	$x = 2$	$x = 3$	$x = 4$	$x = 5$	$x = 6$	$x = 8$	$x = 10$
0							0.005	0.026
0.1						0.001	0.029	0.070
0.2						0.017	0.087	0.171
0.3					0.017	0.07	0.217	0.326
0.4				0.012	0.083	0.208	0.408	0.535
0.5			0.001	0.086	0.265	0.438	0.643	0.738
0.6			0.06	0.317	0.556	0.707	0.834	0.879
0.7		0.021	0.348	0.677	0.825	0.885	0.924	0.935
0.8		0.359	0.795	0.901	0.929	0.943	0.954	0.957
0.9		0.894	0.934	0.947	0.953	0.959	0.963	0.963
1.0		0.936	0.944	0.95	0.955	0.959	0.963	0.963

bauer (16). Simple theory indicates that variations in density cause variations in pressure at the tip of the sampling probe, when the velocity at the probe tip is different from the stream velocity. Generally if the sampling velocity is less than the stream velocity, higher density material will be sampled preferentially, et contra. This simple theory seems to be borne out by the data shown in Figure 2. Theory and experiment (12) indicate that samples withdrawn at the velocity of the stream will contain the correct proportions of high- and low-density material.

It might at first be supposed that the increased fraction of burned gases with increasing sampling velocity is a consequence of increased time required for quenching the gases sampled at higher velocity. Application of the available heat transfer correlations (15) shows that the time required for cooling the sampled gases is independent of sampling velocity.

Thus it was decided to remove samples at stream velocity. This could be accomplished only if the stream velocity were known, and a trial-and-error procedure was necessary. From an assumed stream density and impact and static pressure measurements, a trial value of the stream velocity was calculated, and a sample was withdrawn at that velocity. From an analysis of this sample a new value of density was computed and the procedure repeated until the assumed and calculated densities agreed within 5%. At those points where concentration gradients were steepest, three or four samples were sometimes required. Figure 3 is a typical set of composition profiles.

The method of calculation of density from an analysis of the sample is important. Since it is impossible to determine by catalytic combustion the exact structure of the unburned material in the sample, and since the effect of sampling rate on sample composition indicates that the reaction zone is inhomogeneous, it was assumed for purposes of density calculation that the material oxidized by catalytic combustion was fuel, and the amount was computed as the average equivalent of the carbon dioxide and water produced by the oxidation. The inhomogeneity of the burning zone is a consequence of rapid chemical reaction rates as opposed to mixing rates, and in the extreme this means that the burning zone consists of completely burned gases and feed mixture. The sample was divided into a burned part, assumed to be at its adiabatic flame temperature, and an unburned part, assumed to be at the temperature of the feed mixture. The reciprocal of the mass-average specific volume of the two parts was used as the mean density of the stream.

For a few cases the density was calculated by assuming homogeneity of the stream. This required extrapolation of the available heat-capacity data for propane. The results were not significantly different from those obtained by the method described above.

Figure 4 is a plot of the experimentally determined mole fractions (dry basis) of nitrogen, carbon dioxide, carbon monoxide, and propane against mole fraction (dry basis) of oxygen. For the sake of clarity some overlapping points have been omitted from this plot. It can be seen that compositions at all longitudinal positions

It was discovered at the outset that there is a significant effect of rate of sample withdrawal on the composition of the sample obtained. This is illustrated in Figure 2, where the mole percentages of O_2, carbon dioxide, carbon monoxide, and unburned material (calculated as the average of the propane equivalent to the carbon dioxide and to the water produced by the catalytic oxidation) on a dry basis are plotted against the ratio of sampling velocity to stream velocity. The analytical techniques were in a process of evolution at the time these data were taken, and the precision is poorer than obtained in later work. The carbon monoxide fraction is higher than reported in the final data because the fractional combustion was carried out at 320°C., and probably part of the unburned hydrocarbon was also oxidized. However the influence of sampling rate is unmistakable.

It is believed that the variation in sample composition with sampling rate is a consequence of sampling an unmixed stream of varying density; that is, the reaction zone is not homogeneous. This problem has been examined by Leeper (12) and Muhl-
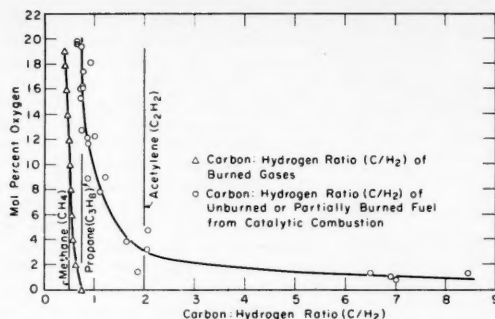
Fig. 7.

Fig. 9. Lines of mean flow, atmospheric burner.

except $x = 5$ in. can be found within experimental error from a knowledge of carbon dioxide or oxygen content alone. The deviation of the data at $x = 5$ in. for carbon monoxide, propane, and nitrogen is consistent with the possible oxidation of some unburned fuel in the fractional combustion step. The correlation indicated by Figure 4 was used to complete the compositions for $x = 5$ in. from measurements of carbon dioxide and oxygen concentrations. A similar procedure was used for the 3 in. longitudinal position, where insufficient complete analyses were available.

The correlation of Figure 4 was used to reduce the amount of work required to estimate the stream velocity, for the correlation allows estimation of the density from a knowledge of the oxygen concentration. Once sufficient data had been obtained to establish the correlation, a good estimate of the stream density could be obtained by analysis for oxygen alone.

Smoothed results are shown in Tables 1 to 4.

RESULTS AND DISCUSSION

Chemical Structure of the Burning Zone

Examination of the composition traverse in Figure 3 shows the expected behavior of a gradual decrease of unburned species and an increase of burned species as the center of the flame is approached. In addition an increase in breadth of the zone of changing composition with increasing downstream distance was found. In all cases unburned material, that is, that part of the sample burned to carbon dioxide and water upon catalytic combustion with oxygen at 500°C., was found at the center of the flame, usually less than 0.5 mole % (dry basis). The presence of such unburned material is apparently a consequence of the inhomogeneity of the burning zone, and unburned material is thrown into the middle of the flame by the random motion of the gases. Figure 5 is a short-exposure schlieren photograph of the flame, and a few striations near the center of the flame support the conclusion that this region is inhomogeneous. If such striations are present 1.5% of the time at any given longitudinal position, the required amount of unburned material would be accounted for.

It is interesting to note that any hydrogen found in the samples was less than the analytical error except at $x = 5$ in. where the data appear to be unreliable. When one considers only the burned part of the samples, if this material is really completely burned, the carbon monoxide : carbon dioxide ratio should be the equilibrium value. Rough calculations of the equilibrium composition for adiabatic reaction (23) indicate that this ratio should be 0.164. The carbon monoxide : carbon dioxide ratios for data of reasonable precision are shown in Figure 6, and it can be seen that the ratios are near or below the equilibrium value, tending to lower values with decreasing oxygen content (increasing fraction burned). This seems to indicate some reaction of carbon monoxide with oxygen as the burned part of the sample is cooled in the probe.

The analyses were carried out in sufficient detail to permit determination or the carbon : net-hydrogen ratio of the unburned material, and by oxygen balance the carbon : hydrogen ratio of the burned part of the sample could be
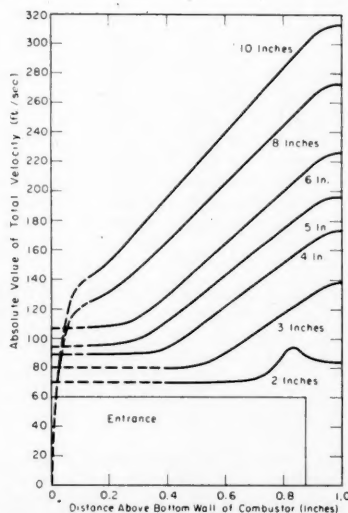
Fig. 8. Velocities calculated from impact pressure, atmospheric burner.
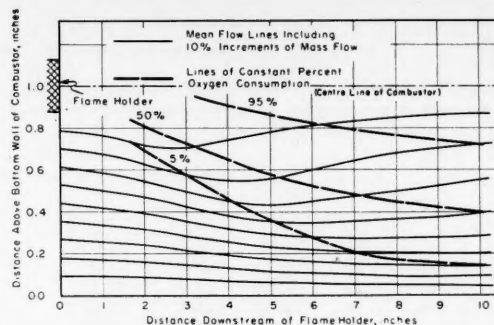
found. Figure 7 shows these carbon : net-hydrogen ratios as a function of the oxygen content of the samples. It appears from this plot that the hydrogen is burned from the hydrocarbon molecule before the carbon and that partial oxidation of the hydrocarbon does take place to some extent. The extremely high carbon : net-hydrogen ratios of the unburned material for low oxygen concentrations are probably the result of poor precision in analysis of small amounts of material. This result bears further study with more reliable analytical techniques.

Calculation of Reaction Rates

The quantities required, in addition to the compositions and densities already discussed, are the velocity components. Velocities were determined from measurements of impact and static pressures, and the resulting profiles are shown in Figure 8 with longitudinal position as the parameter. The peculiarly shaped profile for $x = 2$ in. is probably a consequence of the acceleration produced by the reaction in combination with the low velocity downstream of the flame holder; the other profiles show a consistent increase of velocity and velocity gradient with increasing distance downstream from the flame holder.

Some evaluation of the accuracy of the velocity data must be made. The only physical principle which can be used for such an evaluation is conservation of mass, since the feed rates of fuel and air were metered independently of the measurements within the flame itself. On the assumption that the velocities obtained from the impact measurements are the longitudinal components, evaluation of the data can be made by comparing the integrated-mass flow rates, calculated from the burning-zone data with the metered flow rates. The results are shown in Table 5.

It can readily be seen that on the basis of this comparison the data are reasonably consistent.

As pointed out in connection with the calculation of density from the chemical analyses, it was convenient to divide the
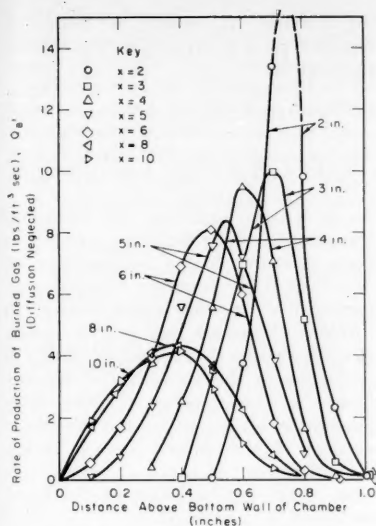
Fig. 10.
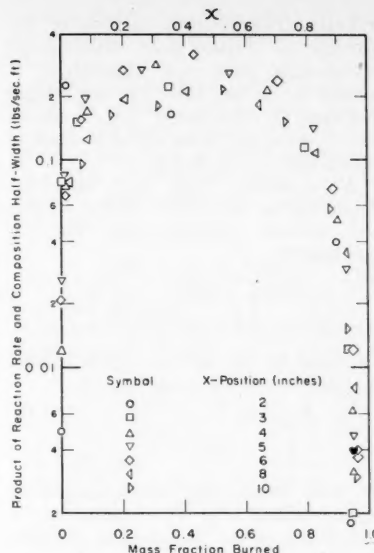
Fig. 11.

TABLE 5—ATMOSPHERIC PROPANE-AIR
BURNER

Longitudinal position, in.	One-half the metered mass flow, lb./sec.	Integrated mass flow for one-half the duct, lb./sec.	Error, %
2	0.0414	0.0428	+3.4
3	0.0426	0.0439	+3.1
4	0.0427	0.0442	+3.5
5	0.0425	0.0424	−0.2
6	0.0425	0.0422	−0.7
8	0.0422	0.0411	−2.6
10	0.0421	0.0425	+1.0

samples into burned and unburned parts. This division permitted determination of the mass fraction burned for each sample. It was decided to calculate the rate of generation of burned gas rather than the rate of generation of any particular molecular species. Although detailed treatment of the gas analyses shows that the unburned material is not all propane (Figure 7), the check of mass flow rates indicates that the error in assuming the unburned material to be propane is not great. The correlation of compositions with oxygen concentration (Figure 4) indicates that mass fraction burned is correlated with oxygen content and that the rate of generation of burned gas is nearly proportional to the rate of oxygen consumption.

The results of calculation of rates of generation with turbulent diffusion neglected (or rate of generation plus diffusion) will be presented first. Rewriting Equation (1) yields

$$\rho \vec{u} \cdot \nabla \chi_B = Q_B + \nabla \cdot \xi \nabla \chi_B = Q_B' \quad (2)$$

The left-hand side can be calculated without knowledge of the turbulent diffusion coefficient. The evaluation of

the density and mass fraction burned from the data has already been discussed.

The calculation of the two velocity components was carried out as follows. First it was assumed that the impact pressure was owing to the longitudinal velocity component alone. Lines of constant $\int_0^y \rho u_x \, dy$ were plotted on y vs. x coordinates, the direction of the lines at any point being the direction of the mean velocity vector. Some of the mean flow lines are shown in Figure 9 together with lines of 5, 50, and 95% oxygen consumption, an indication of the spreading of the reaction zone. The general character of the mean flow pattern is similar to that calculated by Scurlock (25, 33), although the quantitative details are necessarily different. Second, the slopes of the mean flow lines (tan α) were found by the Douglass-Avakian method (27), which involves fitting the quartic equation having the

least squared error to seven equally spaced points and finding the derivative of the resulting equation, at the central point where possible. The velocity components were then computed from the equation

$$u_y = u_x \tan \alpha \quad (3)$$

The impact pressure is insensitive to direction of the probe axis for angles between probe axis and velocity vector of less than 6 deg. The largest angle between the mean flow lines and the axis of the combustor was 5.5 deg., and while this indicates that the impact pressure was a measure of the absolute value of the total velocity, the cosine of 5.5 deg. is 0.9954 and $u_x = |\vec{u}|$ within an accuracy of 0.5% for the worst case. Thus it was not considered necessary to modify the results obtained as previously described.

The partial derivatives $\partial \chi_B/\partial x$ and $\partial \chi_B/\partial y$ were found by the Douglass-Avakian method (27) from tabulations of χ_B at x intervals of 1 in. and y intervals of 0.05 in. The values of χ_B were taken from smooth curves through the data.

Figure 10 shows the calculated values Q_B' as functions of the distance above the bottom wall of the chamber with longitudinal position as a parameter. The increased thickness of the reaction zone with increased distance from the flame holder is not surprising, as this corresponds to the pattern of the luminosity and the schlieren image. It is perhaps more surprising that the maximum value of the volumetric reaction rate decreases with increasing downstream distance. If this is real and not a consequence of failure to account for turbulent diffusion, it might be explained by a rather simple model. One might suppose that the reaction takes place at the periphery of parcels of unburned gas, that the flame surrounding each parcel is laminar, and that the rate of burning is the laminar burning velocity, the effect of variations in flame-front curva-
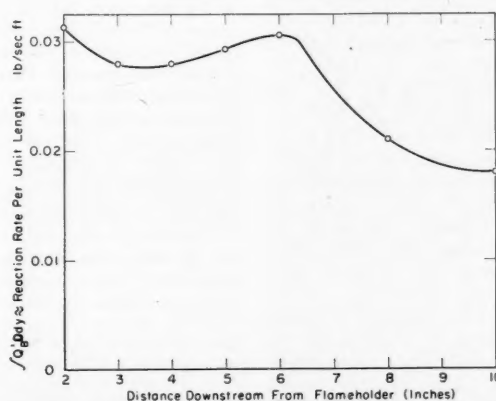

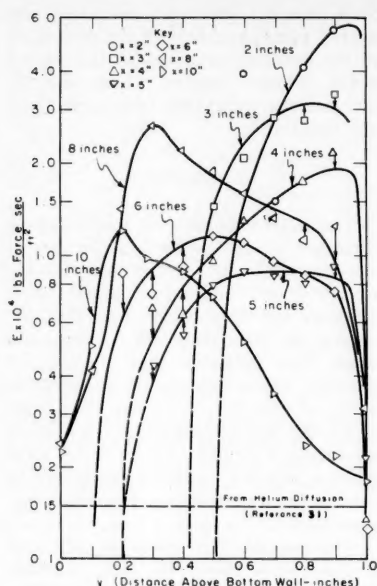**Fig. 12. Reaction rate per unit length (diffusion negligible).**

Fig. 13. Eddy viscosities.

ture being neglected. For a given mean composition (fraction burned) the size of the parcels of unburned gas may be visualized as proportional to the scale of the turbulence. Assuming that the parcels are, on the average, spherical, one may write

$$m = \frac{4}{3}\pi\left(\frac{l}{2}\right)^3 n\rho_u \quad (4)$$

The area of the parcels may be written $\pi l^2 n$, and the reaction rate per unit volume is

$$Q_B = \rho_u S_L \pi l^2 n = \frac{6 S_L m}{l} \quad (5)$$

Thus it might be expected on the basis of this simplified model that the product $Q_B l$ is a function of the mean composition. If one assumes further that the scale of turbulence is proportional to the composition half-width of the reaction zone (the schlieren image shows increasing scale of wrinkles with increased spreading of the flame), the relationship suggested by Equation (5) may be tested by plotting the product of Q_B' and the value $(1 - y)/12$, with y chosen to correspond to the point at which $\chi_B = (1/2)\chi_{BCL}$, against mass fraction burned. Figure 11 is such a plot, semilogarithmic coordinates being used to spread low values of the ordinate. (It should be noted that a similar relationship could be obtained using the wrinkled flame model.) While the correlation is not impressive, it does illustrate a useful result of this method of attack on the problem of turbulent flame propagation. The correlation could probably be improved by taking cognizance of other flow-pattern parameters (for example,

velocity gradient), but in view of the paucity of data more complicated correlations were not attempted. It should be noted that for engineering purposes a correlation which allows prediction of Q_B' is as useful as a set of correlations for Q_B and ξ.

A necessary (but not sufficient) condition on the values of Q_B' is that the over-all reaction rate for the combustor

$$\int_0^{0.833}\left[\int_0^{0.0833} Q_B'\, dy\right] dx$$

be equal to the rate at which burned material leaves the burner

$$\left[\int_0^{0.0833}\rho u_x \chi_B\, dy\right]_{x=0.833}$$

It was found that these quantities agreed within 5%. This comparison is valid because the longitudinal diffusion is small.

The over-all reaction rates per unit length at various longitudinal positions have been compared in Figure 12, and it can be seen that the over-all reaction rate per unit length is relatively constant except for a decrease near the combustor exhaust, where the flame has nearly reached the wall. The data of Petrein et al. (18) show similar behavior.

Next the problem of proper allowance for turbulent diffusion is considered. (In terms of gradients of mean composition neglect of molecular diffusion is justified.) The only published data on turbulent diffusion in flames of this sort known to the authors are those of Westenberg (31). These data consist of measurements of mean displacement of helium injected into the flame as a function of distance downstream from the injection point and velocity of the gas stream in the region of interest. Data were corrected for molecular diffusion. By means of the Einstein equation

$$\overline{d^2} = 2\xi\theta \quad (6)$$

a turbulent diffusion coefficient can be calculated. The values thus obtained are so low that the turbulent-diffusion term is negligible in comparison with Q_B'.

Owing to the fact that Westenberg's data were obtained from a burner of a different configuration and his published measurements confined to the center of the duct (Westenberg reports that measurements at other points gave similar results), it was decided to attempt calculation of the eddy viscosity from the present data and to estimate the eddy diffusivity by assuming a turbulent Schmidt number of unity.

$$\frac{E g_c}{\xi} = 1 \quad (7)$$

There remains the problem of an adequate definition of eddy viscosity

for the case at hand. The definition chosen is given by writing the momentum equation as

$$-\nabla p + 2(\nabla \cdot E \nabla)\vec{u} + \nabla$$
$$\times [E(\nabla \times \vec{u})] = \frac{1}{g_c}[(\rho\vec{u}\cdot\nabla)\vec{u}] \quad (8)$$

As in writing Equation (1), molecular transport has been neglected, and E has been assumed to be independent of direction. This definition assumes proportionality between stress owing to turbulent transport and rate of strain. It will be noted that Equation (8) is not analogous to the equations of Navier-Stokes in two respects: (1) the static pressure is not defined as the arithmetic average of the normal stresses owing to turbulence, and (2) allowance has been made for variation of transport coefficient with position.
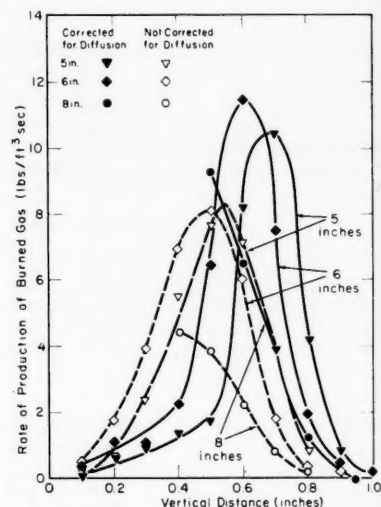
Of the three components of Equation

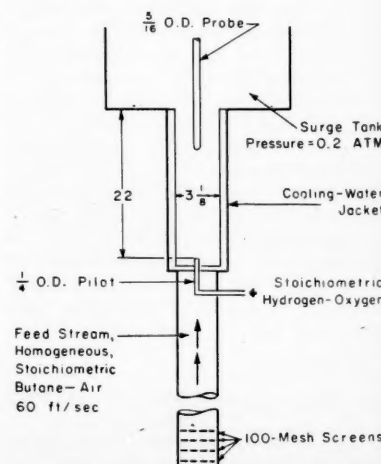**Fig. 14. Effect of turbulent diffusion on calculated reaction rates.**

Fig. 15. Low-pressure burner.

(8) the longitudinal (x) component was chosen for finding eddy viscosities because it could be evaluated more accurately, and the x component of the stress is, in the present case, primarily due to mass transport in the y direction; examination of the composition gradients shows that it is this transport which is most important in calculating the reaction rates.

The longitudinal component of the momentum equation is, in cartesian coordinates,

$$-\frac{\partial p}{\partial x} + E\left[2\frac{\partial^2 u_x}{\partial x^2} + \frac{\partial^2 u_x}{\partial y^2} + \frac{\partial^2 u_y}{\partial x\,\partial y}\right]$$
$$+ 2\left(\frac{\partial E}{\partial x}\right)\left(\frac{\partial u_x}{\partial x}\right)$$
$$+ \frac{\partial E}{\partial y}\left(\frac{\partial u_x}{\partial y} + \frac{\partial u_y}{\partial x}\right)$$
$$= \frac{1}{g_c}\left[\rho u_x \frac{\partial u_x}{\partial x} + \rho u_y \frac{\partial u_x}{\partial y}\right] \quad (9)$$

The longitudinal gradient of the static pressure was obtained by fitting a cubic equation to the data and finding the derivatives of the cubic at the points of interest. Since static-pressure data were available at longitudinal positions 1, 2, 3, 4, 5, 6, 8, and 10 in. downstream from the flame holder, the procedure was found to give reasonable results at all positions reported except at $x = 10$ in. For the evaluation at the 10-in. position it was assumed that the static pressure at distances greater than 10 in. downstream from the flame holder was 1 atm., and the Douglass-Avakian method (27) was used to obtain the derivatives. The velocity derivatives were obtained at 0.05-in. y intervals by the Douglass-Avakian method. Second derivatives were

calculated by the same method from smoothed curves through the first derivatives.

In the calculation of E from Equation (9) it was found that the term $\partial E/\partial x$ had a relatively small influence and could be neglected as a first approximation. This permitted rewriting Equation (9) as a total differential equation in the form

$$\frac{dE}{dy} + \frac{E}{g(y)} = \frac{f(y)}{g(y)} \quad (10)$$

Equation (10) can be integrated directly to give

$$E_2 \exp\left[\int_0^{y_2}\frac{dy}{g(y)}\right] - E_1 \exp\left[\int_0^{y_1}\frac{dy}{g(y)}\right]$$
$$= \int_1^2 \frac{f(y)}{g(y)}\left[\exp\left(\int_0^y \frac{dy}{g(y)}\right)\right]dy \quad (11)$$

This equation was then used to calculate E by graphical integration of the separate terms. It is of course necessary that one value of E be known. By symmetry $E = f(y)$ at the center line, but unfortunately the integrand on the right is indeterminate at that point. For the 8- and 10-in. positions it was found that the values of E were relatively insensitive to various extrapolations of the integral on the right, and the centerline values of E were used. For all other positions it was assumed that $E = 0$ in the region where the velocity was practically independent of y, giving another fixed value.

The results of the calculations are shown in Figure 13, where the calculated points are shown. A value of the eddy viscosity calculated from Westenberg's data (31) by use of Equations (6) and (7) is also shown.

In spite of the apparent confusion of the curves they do follow a reasonable pattern. There are in the system studied three sources of velocity gradients which could result in turbulence and consequently in appreciable values of eddy viscosity.

1. Velocity gradients caused by the flame holder. Turbulence from this source would be expected to spread and to die out with increasing distance from the flame holder. The high values of eddy viscosity near the center of the duct which decrease with increasing values of x are apparently due to this source. The flame holder used for this study probably has a greater influence on the flow than the flame holders in general use, owing to its length, which causes appreciable boundary-layer build up, and to its bluff nose, which probably causes a bow wave.

2. Velocity gradients caused by the combustion process itself. As already pointed out, this is a major source of flame-generated turbulence in confined flames. This source of turbulence accounts for increasing values of eddy viscosity in the region $5 < x < 8; 0.2 < y < 0.6$.

3. Velocity gradients at the wall. As the boundary layer at the wall increases in
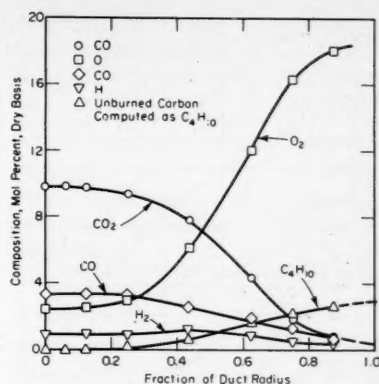
Fig. 17. Gas composition 16 in. from pilot, exhaust pressure 0.2 atm.
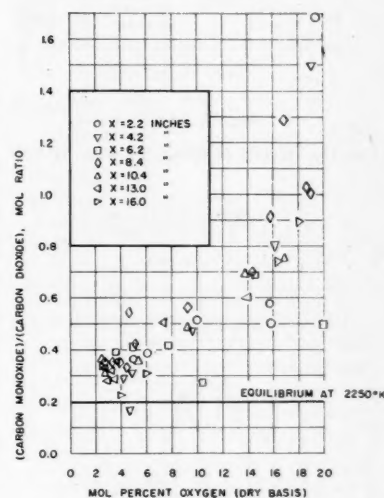
Fig. 18. (Carbon monoxide)/(carbon dioxide) mole ratio, 0.2 atm. flame.

thickness, turbulence from this source would be expected to have an increasing influence. In this case its influence appears in the region $6 < x < 10; 0 < y < 0.2$.

As shown by the dotted horizontal line in Figure 13, the values obtained agree reasonably well with those obtained from Westenberg's data at the center line. Values reported for the 2- and 10-in. positions are inaccurate because these positions are the terminal points of the data and the derivatives are not well defined.

The smooth curves of Figure 13 were used to calculate eddy diffusivities by means of Equation (7). The necessary derivatives again being obtained by the Douglass-Avakian method (27), the results were applied to calculation of reaction rates by means of Equation (1). In the region where the flame itself is thought to be the chief source of turbulence, reasonable values of reaction rate were obtained, and these values together with the corresponding results

Fig. 16. Composition correlation, 0.2 atm. flame.
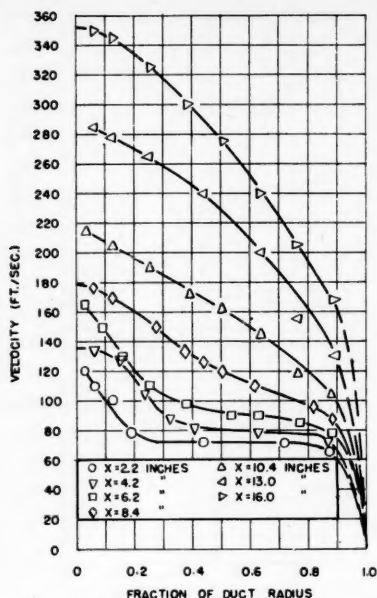
Fig. 19. Velocity profiles—0.2 atm. burner.
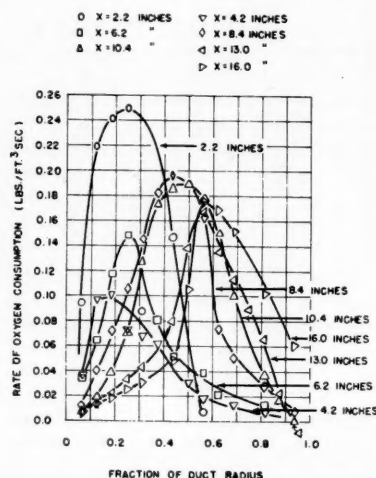
Fig. 20. Rates of oxygen consumption, 0.2 atm. flame.

obtained by neglecting turbulent diffusion are shown in Figure 14. It is obvious that on the basis of these calculations allowance for diffusion is very important, but the results are too meager for generalization. The maximum reaction rate corresponds to a heat release rate of about 50×10^6 B.t.u./(hr.)(cu. ft.).

In the region where the chief source of turbulence is thought to be velocity gradients at the flame holder or the combustion-chamber wall, and where $\nabla^2 \chi_B$ is positive, it was found that with few exceptions application of the curves of Figure 13 with Equations (7) and (1) gave negative values of Q_B. Such a result is of course untenable. The coincidence of negative values and source of

turbulence together with the consistency of negative values seems to eliminate random errors in computation as the source of the difficulty. It seems rather that the fault lies with the value of the turbulent Schmidt number and that a value greater than unity should be used. While studies of turbulent mass and momentum transport (5) have yielded values of the turbulent Schmidt number between 0.63 and 0.74, in most such studies the initial velocity gradient responsible for the turbulence was exactly correlated with the initial composition gradient causing the mass transfer. Furthermore the systems studied were of nearly constant density. While the introduction of a significant density variation alone may affect the turbulent Schmidt number, this is apparently not sufficient to give ridiculous values in that region of the flame where the turbulence is generated by the combustion process and velocity and composition gradients are related. However where gradients of velocity at the wall or flame holder are the predominate source of turbulence, the composition gradient is introduced by the reaction after the generation of turbulence. It may be that most of the reaction takes place in a particular part of the turbulence spectrum. At any rate it is believed that this difference is sufficient to admit the explanation for negative reaction rates in terms of Schmidt numbers greater than unity, but no mechanism can be offered at this time. Numerical values of reaction rates (Q_B'), eddy viscosities and the sample compositions are given in Tables 7, 8, and 9.*

THE 0.2-ATM. SYSTEM

Figure 15 schematically shows the apparatus. The cylindrical combustion chamber was made of Vycor glass. The cold-gas velocity through the pilot tube was 50 ft./sec. Experimental techniques and methods of treating the data were similar to those already described with two exceptions: (1) no provision was made for control of sampling rate and (2) in the analysis of unburned hydrocarbon only the carbon dioxide produced by catalytic combustion was measured.
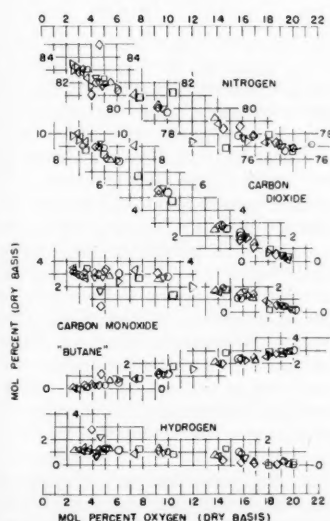
Figure 16 shows the composition correlation, and a typical set of composition profiles is shown in Figure 17. The scattering of the data points in Figure 16 is probably a result of lack of control of sampling rate. It should be pointed out that while variations in sampling rate affect the relative portions of high- and low-density material, the chemical composition of the two parts is not altered.

The amounts of carbon monoxide and

*Tabular material has been deposited as document 5823 with the American Documentation Institute, Photoduplication Service, Library of Congress, Washington 25, D. C., and may be obtained for $1.25 for photoprints or $1.25 for 35-mm microfilm.

hydrogen found in samples from this flame are significant. A comparison of the carbon monoxide : carbon dioxide ratios of the samples with the equilibrium ratio calculated for adiabatic reaction is shown in Figure 18. While the departure from equilibrium is not great, the reasons for it may be important, especially in view of the results found for the atmospheric flame (Figure 6). The presence of carbon monoxide in excess of the equilibrium amount may be due to (1) quenching of partially burned material in the sampling probe, (2) quenching of small elements of flame by the action of turbulence as shown experimentally by Olsen and Gayhart (17), or (3) separation of fuel and oxidant by preferential molecular diffusion of the latter to burning zones within the turbulent flame brush as suggested by Wohl and Shore (38) to account for the excessively high-turbulent burning velocity of rich butane-air mixtures. In the latter case the physical picture of a small part of the flame is similar to the patterns obtaining at the edge of the wake of a bluff-body flame holder, and the existence of preferential diffusion in such cases has been demonstrated by Williams and Shipman (34), Williams, Woo, and Shipman (35), and Zukoski and Marble (41).

Figure 19 shows the velocity profiles. Table 6 shows clearly the effect of lack

TABLE 6. THE 0.2 ATM. BUTANE-AIR FLAME

Distance downstream from pilot, in.	Metered mass flow, lb./sec.	Integrated mass flow, lb./sec.	% Error
2.2	0.04941	0.0566	+14.55
4.2	0.04941	0.0561	+13.55
6.2	0.04941	0.0575	+16.4
8.4	0.04941	0.0574	+16.2
10.4	0.04941	0.0553	+11.95
13.0	0.04941	0.0600	+21.5
16.0	0.04941	0.0614	+24.3

of control of the sampling rate. Qualitative estimates indicated that the sampling velocity was always lower than the stream velocity, and this is supported by the results. Figure 20 shows the rates of oxygen consumption calculated by neglecting diffusion. Obviously these results are at best subject to qualitative interpretation only. The high initial reaction rates are undoubtedly a consequence of the action of the pilot. The subsequent decrease in reaction rates with increasing downstream distance is probably due to dissipation of the pilot stream by turbulence, and the increase in reaction rates at the farthest downstream positions may be attributed to increased velocity gradients and a consequent increase in turbulence intensity. This latter situation was not observed in the atmospheric data because the combustor was too short.

CONCLUSIONS

The analyses of samples from the reaction zone of the atmospheric, propane-air flame show that the composition can be characterized by oxygen concentration only, an indication that the reaction rate can be satisfactorily represented by the rate of oxygen consumption. Results for the low-pressure flame are similar, but the conclusion is less firm because of the effect of lack of control of the sampling rate.

Since the carbon monoxide : carbon dioxide ratios of the samples from the atmospheric flame are less than those corresponding to equilibrium, it appears that there is some reaction in the sampling probe. Since there is an effect of pressure on the composition of the burned gas beyond that expected from equilibrium considerations, it is concluded that there is quenching of flame elements either in the sampling probe or within the turbulent flame itself; preferential diffusion of oxidant from unburned parcels to burning zones within the flame is also considered a possible explanation.

The calculation of reaction rates is hampered by inadequate knowledge of eddy diffusion. While calculations of eddy diffusivity from data in the literature indicate that the effect is negligible, estimates from the present data based on analogy of mass and momentum transfer indicate that turbulent mass transfer is significant. These same estimates, applied to regions where shear at the wall of the combustor or the flame holder is believed to be the chief source of turbulence, gave negative reaction rates. It is concluded therefore that the turbulent Schmidt number is dependent on the relationship between the shear causing turbulence and the introduction of the composition gradient causing mass transfer and possibly on the density patterns.

It was found that the calculated reaction rates are a function of position within the flame as well as of fractional completion of combustion. The data indicate that the reaction rates obtained by neglecting turbulent diffusion are a result of competition between increased turbulence generated by increased velocity gradients and increased scale of turbulence, the former increasing and the latter decreasing apparent reaction rates.

Finally the importance of taking samples from the inhomogeneous reaction zone of a turbulent flame in such a way as to prevent preferential sampling of low- or high-density material cannot be overemphasized. The unsatisfactory results obtained from the 0.2-atm., butane-air flame seem to be directly related to errors of this type.

While neither of the flames studied is in the range of practical, high-output combustor operation, the results show that the method of attack employed is profitable. This is especially so because it affords direct study of relationships between flow patterns, rates of reaction, and general character of combustion products. The work involved in future studies of this kind has been materially reduced by the finding of suitable computational techniques, and the chemical, analytical work may be greatly reduced by use of gas chromatography in conjunction with an oxygen analyzer (dependent on the paramagnetism of oxygen).

From the theoretical viewpoint the method may seem less attractive than those studies involving interaction between a flame and a stream of known turbulence characteristics, but the effect of even unconfined flames on the flow pattern of the feed mixture is too often neglected. It should be pointed out that the same techniques used for the measurement of reaction rates might be used for the study of turbulent mass transfer. The measurement of a coefficient of turbulent diffusion by this method is basically no different from that used in the studies of heat and mass transfer between phases, where systematic measurements have produced results of great utility.

ACKNOWLEDGMENT

NOTATION

D = depth of combustor, normal to xy plane

$\overline{d^2}$ = mean square displacement of injected helium

E = eddy viscosity, (lb.-force)(sec.)/ sq. ft.

$f(y)$ = function of y [cf. Equations (9) and (10)]

$g(y)$ = function of y [cf. Equations (9) and (10)]

g_c = conversion constant, (lb.-mass) (ft.)/(lb.-force)(sec.²)

H = enthalpy.

l = scale of turbulence or size of unburned parcels

m = mass of unburned gas per unit volume

n = number of unburned parcels per unit volume

p = static pressure

Q = rate of generation of subscript component, lb.-mass/(cu. ft.) (sec.)

Q_B' = rate of generation of burned gas plus diffusion rate

S_L = laminar burning velocity

$\vec{u}$ = velocity vector, $|\ \vec{u}\ |$ absolute value of velocity

u_x = longitudinal velocity component

u_y = transverse velocity component

x = longitudinal position

y = transverse position

Greek Letters

α = angle between mean flow line and longitudinal coordinate

θ = time

ξ = coefficient of turbulent diffusion (lb. mass/(sec.)(ft.)

ρ = density

ρ_u = density of unburned gas

χ = mass fraction of subscript component

∇ = vector operator, $(\vec{i}(\partial/\partial x) + \vec{j}(\partial/\partial y) + (\partial/\vec{k}\partial z))$ in Cartesian coordinates

Subscripts

B = burned gas

CL = center-line position

LITERATURE CITED

1. Barbor, R. P., and J. D. Larkin, M.Ch.E. thesis, Univ. Delaware, Newark (1954).
1A. Archer, D. H., Ph.D. thesis, Univ. Delaware, Newark (1953).
1B. Jacobi, W. M., M.Ch.E. thesis, Univ. Delaware, Newark (1953).
2. Berl, W. G., J. L. Rice, and P. Rosen, *Jet Propulsion*, **25**, 341, (1955).
3. Damköhler, Gerhard, *Z. Elektrochem.*, **46**, 601 (1940). English translation: *Natl. Advisory Comm. Aeronaut., Tech. Mem.* 1112 (1947).
4. Fine, B. D., and Paul Wagner, *Natl. Advisory Comm. Aeronaut., Tech. Note* 3277 (June, 1956).
5. Forstall, Walton, Jr., and A. H. Shapiro, *Mass. Inst. Technol. Meteor Rept.* 39 (July, 1949).
6. Fristrom, R. M., and A. A. Westenberg, *Combustion and Flame*, **1**, 217 (1957).
7. Grumer, Joseph, J. M. Singer, J. K. Richmond, and J. R. Oxendine, *Ind. Eng. Chem.*, **49**, 305 (1957).
8. Hottel, H. C., G. C. Williams, and M. L. Baker, "Sixth Symposium (International) on Combustion," p. 398, Reinhold, New York (1957).
9. Hottel, H. C., G. C. Williams, and R. S. Levine, "Fourth Symposium (International) on Combustion," p. 636, Williams and Wilkins, Baltimore (1953).
10. Karlovitz, Bela, "High Speed Aerodynamics and Jet Propulsion," Vol. II, p. 342, Princeton Univ. Press, Princeton, N. J. (1956).
11. Karlovitz, B., D. W. Denniston, Jr., and F. E. Wells, *J. Chem. Phys.*, **19**, 541 (1951).
12. Leeper, C. K., Sc.D. thesis, Mass. Inst. Technol., Cambridge (1954). See also Leeper, C. K., S.M. thesis, Mass. Inst. Technol., Cambridge (1949).
13. Lewis, Bernard, and Guenther von Elbe, "Combustion, Flames, and Explosions of Gases," p. 766, Academic Press, New York (1951).
14. Longwell, J. P., and M. A. Weiss, *Ind. Eng. Chem.*, **47**, 1634 (1955). Longwell, J. P., "Fifth Symposium (International) on Combustion," p. 48, Reinhold, New York (1955).

	% Error
	14.55
	13.55
	16.4
	16.2
	11.95
	21.5
	24.3

15. McAdams, W. H., "Heat Transmission," 3rd ed., p. 238, McGraw-Hill Book Co., New York (1954).
16. Muhlbauer, H. G., M.Ch.E. thesis, Univ. Delaware, Newark (1950).
17. Olsen, H. L., and E. L. Gayhart, *Jet Propulsion*, 25, 276 (1955).
18. Petrein, R. J., J. P. Longwell, and M. A. Weiss, *ibid.*, 26, 81 (1956).
19. Richardson, J. M., "Proceedings of the Gas Dynamics Symposium on Aerothermochemistry," p. 169, Northwestern Univ., Evanston, Illinois (1956).
20. Richmond, J. K., J. M. Singer, E. B. Cook, J. R. Oxendine, Joseph Grumer, and D. S. Burgess, "Sixth Symposium (International) on Combustion," p. 303, Reinhold, New York (1957).
21. Rosenberg, H. E., von, Ph.D. thesis, Univ. Delaware, Newark (1955).
21A. Schilly, R. A., M.Ch.E. thesis, Univ. Delaware, Newark (1953).
22. Ries, H. B., Ph.D. thesis, Univ. Delaware, Newark (1951).
23. Rossini, F. D., K. S. Pitzer, R. L. Arnett, Rita M. Braun, G. C. Pimentel, et al., *Am. Petroleum Indust. Res. Proj. 44*, Carnegie Press, Pittsburgh, Pennsylvania (1953).
24. Scurlock, A. C., and J. H. Grover, "Fourth Symposium (International) on Combustion," p. 645, Williams and Wilkins, Baltimore (1953). See also "Selected Combustion Problems, Fundamentals and Aeronautical Applications," p. 215, Butterworths, London (1954).
25. Scurlock, A. C., *Mass. Inst. Technol. Fuels Research Laboratory, Meteor Rept.* 19 (May, 1948).
26. Shelkin, K. I., *J. Tech. Phys. (USSR)*, 13, 9, 10 (1943). English translation: *Natl. Advisory Comm. Aeronaut., Tech. Mem.* 1110 (1947).
27. Sherwood, T. K., and C. E. Reed, "Applied Mathematics in Chemical Engineering," 1 ed., pp. 287, 266, McGraw-Hill Book Co., New York (1939).
28. Simon, Dorothy M., and Paul Wagner, *Ind. Eng. Chem.*, 48, 129 (1956).
29. Summerfield, Martin, S. H. Reiter, Victor Kebely, and R. W. Mascolo, *Jet Propulsion*, 25, 377 (1955).
30. Weil, C. W., Ph.D. thesis, Univ. Delaware, Newark (1950).
31. Westenberg, A. A., *J. Chem. Phys.*, 22, 814 (1954).
32. Williams, D. T., and L. M. Bollinger, "Third Symposium on Combustion and Flame and Explosion Phenomena," p. 176, Williams and Wilkins, Baltimore (1949).
33. Williams, G. C., H. C. Hottel, and A. C. Scurlock, *ibid.*, p. 21.
34. Williams, G. C., and C. W. Shipman, "Fourth Symposium (International) on Combustion," p. 733, Williams and Wilkins, Baltimore (1953).
35. Williams, G. C., P. T. Woo, and C. W. Shipman, "Sixth Symposium (International) on Combustion," p. 427, Reinhold, New York (1957).
36. Wohl, Kurt, Leon Shore, H. E. von Rosenberg, and C. W. Weil, "Fourth Symposium (International) on Combustion," p. 620, Williams and Wilkins, Baltimore (1953).
37. Wohl, Kurt, "Sixth Symposium (International) on Combustion," p. 333, Reinhold, New York (1957).
38. Wohl, Kurt, and Leon Shore, *Ind. Eng. Chem.*, 47, 828 (1955).
39. Wright, F. H., *Jet Propulsion Laboratory, Cal. Inst. Tech., Progress Rept. 3-21* (1953).
40. Zelinski, J. J., W. T. Baker, L. J. Mathews, III, and E. C. Bagnall, "Proceedings of the Gas Dynamics Symposium on Aerothermochemistry," p. 179, Northwestern Univ., Evanston, Ill. (1956).
41. Zukoski, E. E., and F. E. Marble, "Combustion Researches and Reviews 1955," p. 167, for AGARD, Butterworths, London (1955).

Low-Temperature Vapor-Liquid Equilibria in Ternary and Quaternary Systems Containing Hydrogen, Nitrogen, Methane, and Ethane

HARRY F. COSWAY and DONALD L. KATZ

University of Michigan, Ann Arbor, Michigan

Experimental data are presented for three ternary systems and the quaternary at pressures of 500 and 1,000 lb./sq. in. abs. and at temperatures of −100° and −200°F. These data along with information in the literature were correlated to give charts of equilibrium ratios as a function of temperature, pressure, and composition.

The compositions of equilibrium vapors and liquids were measured for the quaternary system hydrogen-nitrogen-methane-ethane and three of its ternaries at conditions shown in Table 1. The apparatus and procedures employed were essentially the same as those used by Aroyan, Williams, and Benham (1, 12, 2). The phase compositions were determined by mass spectrometer.

The experimental data are given in Tables 2 to 5. The binary-system data from the literature are included in the tables at the conditions of the measurements in this research. The following binary-system data were used in correlating the data for the ternary systems: hydrogen-methane (2); hydrogen-ethane (12), hydrogen-nitrogen (7, 9, 10, 11),

nitrogen-methane (5, 6), and methane-ethane (4). Ternary data for hydrogen-nitrogen-methane (10) and hydrogen-methane-ethane (8) also were used in correlating the phase behavior of these systems.

For the ternary systems the equilibrium ratios were plotted on three types of cross plots: equilibrium ratios vs. pressure, lines of constant temperature, and charts of constant percentage methane, in the liquid phase; equilibrium ratios vs. temperature, lines of constant percentage methane, and charts of constant pressure; and equilibrium ratio vs. percentage of methane in the liquid,

Fig. 1. Equilibrium ratios for constituents in the hydrogen-nitrogen-methane system at 0 mole % methane in the liquid phase as a function of pressure for various temperatures.
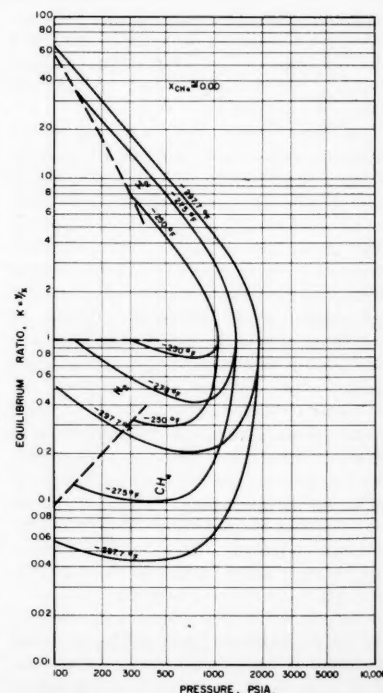
Harry F. Cosway is with the American Cyanamid Company, Stamford, Connecticut.

TABLE 1. EXPERIMENTAL CONDITIONS CHOSEN FOR STUDY

System	Pressures, lb./sq. in. abs.	Temperatures, °F.
Hydrogen-methane-ethane	500 and 1,000	−100 and −200
Hydrogen-nitrogen-methane	500 and 1,000	−200
Nitrogen-methane-ethane	500 and 1,000	−100 and −200
Hydrogen-nitrogen-methane-ethane	1,000	−100
Hydrogen-nitrogen-methane-ethane	500	−200

TABLE 2. EXPERIMENTAL DATA FOR THE HYDROGEN-METHANE-ETHANE SYSTEM INCLUDING BINARY SYSTEM DATA FROM THE LITERATURE

Run or reference	Liquid-phase composition			Vapor-phase composition		
	Mole % H_2	Mole % CH_4	Mole % C_2H_6	Mole % H_2	Mole % CH_4	Mole % C_2H_6
Pressure = 500 lb./sq. in. abs. Temperature = −100°F.						
(12)*	1.87	0.00	98.13	91.66	0.00	8.34
15	1.33	29.42	69.25	46.23	45.86	7.91
14	1.34	32.55	66.11	39.40	52.30	8.30
17	1.20	38.59	60.21	30.62	61.53	7.86
16	1.01	43.25	55.75	23.08	69.13	7.79
(4)*	0.00	66.00	34.00	0.00	93.00	7.00
Pressure = 1,000 lb./sq. in. abs. Temperature = −100°F.						
(12)*	3.90	0.00	96.10	94.76	0.00	5.24
29	3.82	0.00	96.18	94.83	0.00	5.17
10	3.51	4.41	92.08	93.25	3.24	3.51
11	4.00	11.53	84.47	83.72	11.02	5.26
12	3.76	49.57	46.67	45.79	48.62	5.59
Pressure = 500 lb./sq. in. abs. Temperature = −200°F.						
(12)*	1.20	0.00	98.80	99.69	0.00	0.31
24	1.67	52.24	46.09	81.54	18.19	0.272
26	1.75	76.08	22.17	74.12	25.72	0.164
22	3.27	92.03	4.70	69.15	30.80	0.051
(2)*	3.43	96.37	0.00	63.92	36.08	0.00
Pressure = 1,000 lb./sq. in. abs. Temperature = −200°F.						
(12)*	2.25	0.00	97.75	99.74	0.00	0.26
18	2.42	11.15	86.43	97.10	2.66	0.231
19	2.96	35.04	62.00	91.15	8.56	0.290
20	3.13	40.81	56.07	90.09	9.68	0.230
23	4.87	75.71	19.42	82.33	17.54	0.136
21	6.43	87.32	6.25	79.29	20.65	0.061
30	8.32	91.68	0.00	76.01	23.99	0.00
(2)*	7.81	92.19	0.00	76.18	23.82	0.00

*Data from literature.

Fig. 2. Equilibrium ratios for constituents in the hydrogen-nitrogen-methane system at 20 mole % methane in the liquid phase as a function of pressure for various temperatures.

Fig. 3. Equilibrium ratios for constituents in the hydrogen-nitrogen-methane system at 40 mole % methane in the liquid phase as a function of pressure for various temperatures.

lines of constant temperature, and pressure. Figures 1 to 6 give the smoothed results for the hydrogen-nitrogen-methane system, illustrating the first of these methods; Figure 7 is a similar plot for the hydrogen-methane-ethane system at 0.2 mole-fraction methane in the liquid. Figures 8 and 9 illustrate for this system the equilibrium ratio vs. temperature relationships, and the data for the nitrogen-methane-ethane system are given in Figures 10 and 11 as equilibrium ratios vs. composition. The full ternary behavior is not presented, since the nitrogen-ethane binary system data were not available.

A quaternary system is bounded by the four possible ternary systems. In this case the behavior of all the ternary

systems is known at the conditions of the measurements on the quaternary system except that of hydrogen-nitrogen-ethane system. Interpolations among these three ternary systems were made at 500 lb./sq. in. abs. and −200°F. The equilibrium ratios are presented for hydrogen, nitrogen, ethane, and methane in Figures 12, 13, and 14, the experimental quaternary data being included in these figures. Although unintentionally, the methane concentration in the quaternary system was varied only from 0.079 to 0.088 mole fraction in the liquid, and the liquid should have fallen approximately on the 0.085 mole-fraction methane curve.

The need for four variables to describe the quaternary system is illustrated by Figures 12, 13, and 14. If three variables
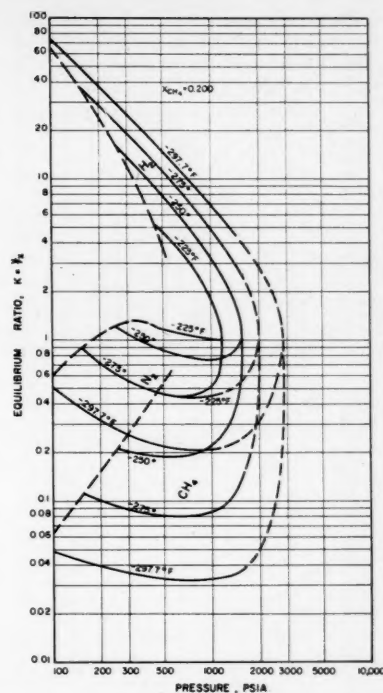
Fig. 4. Equilibrium ratios for constituents in the hydrogen-nitrogen-methane system at 60 mole % methane in the liquid phase as a function of pressure for various temperatures.

Fig. 5. Equilibrium ratios for constituents in the hydrogen-nitrogen-methane system at 80 mole % methane in the liquid phase as a function of pressure for various temperatures.
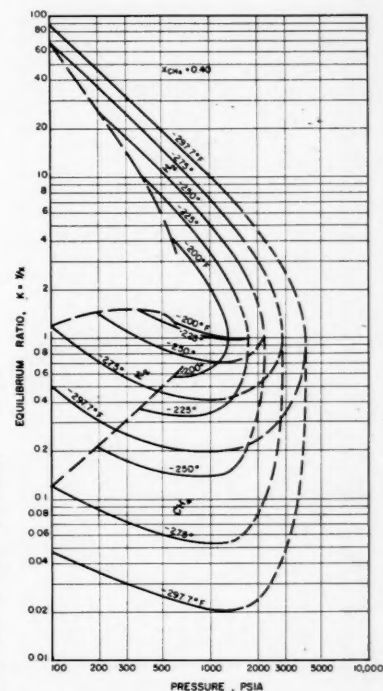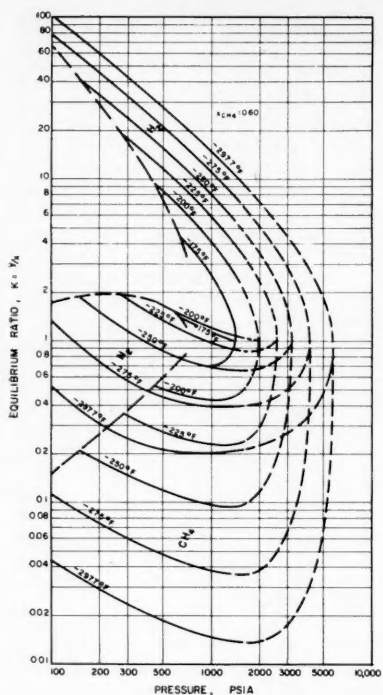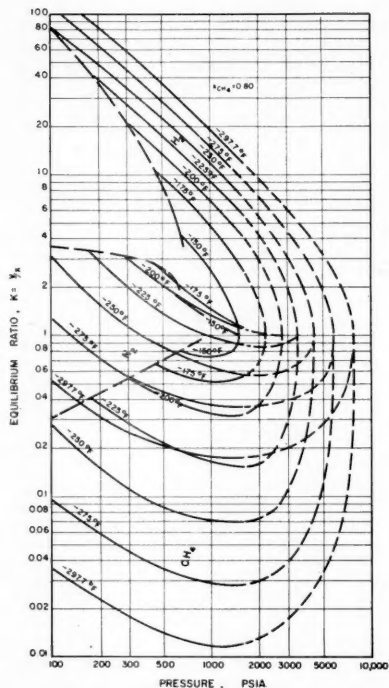
TABLE 3. EXPERIMENTAL DATA FOR THE NITROGEN-METHANE-ETHANE SYSTEM INCLUDING BINARY SYSTEM DATA FROM THE LITERATURE

Run or reference	Liquid-phase composition			Vapor-phase composition		
	Mole % N_2	Mole % CH_4	Mole % C_2H_6	Mole % N_2	Mole % CH_4	Mole % C_2H_6
		Pressure = 500 lb./sq. in. abs.				
		Temperature = −100°F.				
50	9.56	0.00	90.44	89.22	0.00	10.78
51	7.15	19.89	72.96	60.29	29.79	9.92
(4)*	0.00	66.00	34.00	0.00	93.00	7.00
		Pressure = 1,000 lb./sq. in. abs.				
		Temperature = −100°F.				
31	21.29	0.00	78.71	90.55	0.00	9.45
35	20.64	15.64	63.72	74.60	16.42	8.98
38	17.52	56.12	26.36	34.35	56.08	9.57
		Pressure = 500 lb./sq. in. abs.				
		Temperature = −200°F.				
32	18.26	0.00	81.74	99.23	0.00	0.766
33	24.03	25.25	50.72	88.10	11.31	0.593
34	35.06	44.99	19.95	79.75	19.79	0.463
(5)*	49.00	51.00	0.00	73.00	27.00	0.00
(6)*	50.90	49.10	0.00	75.20	24.80	0.00

*Data from literature.

TABLE 4. EXPERIMENTAL DATA FOR THE HYDROGEN-NITROGEN-METHANE SYSTEM INCLUDING BINARY SYSTEM DATA FROM THE LITERATURE

Run or reference	Liquid-phase composition			Vapor-phase composition		
	Mole % H_2	Mole % N_2	Mole % CH_4	Mole % H_2	Mole % N_2	Mole % CH_4
		Pressure = 500 lb./sq. in. abs.				
		Temperature = −100°F.				
(2)*	3.43	0.00	96.57	63.92	0.00	36.08
37	2.86	9.98	87.16	43.37	21.91	34.72
42	1.55	27.39	71.06	16.77	50.80	32.43
45	0.302	41.76	57.94	2.36	67.93	29.71
(5)*	0.00	49.00	51.00	0.00	73.00	27.00
(6)*	0.00	50.90	49.10	0.00	75.20	24.80
		Pressure = 1,000 lb./sq. in. abs.				
		Temperature = −200°F.				
(2)*	7.81	0.00	92.19	76.18	0.00	23.82
30	8.32	0.00	91.68	76.01	0.00	23.99
47	8.26	6.17	85.57	67.35	8.38	24.27
43	8.49	17.91	73.60	50.02	23.77	26.21
46	9.15	37.33	53.52	31.30	42.91	25.79
44	9.32	39.12	51.56	30.05	44.13	25.82
49	9.26	41.37	49.37	27.58	46.37	26.05
48	11.57	53.54	34.89	—	—	—

*Data from literature.

TABLE 5. EXPERIMENTAL DATA FOR THE HYDROGEN-NITROGEN-METHANE-ETHANE SYSTEM

Run		52	53	54	55	56	57	58
Pressure, lb./sq. in. abs.		1000	1000	500	500	500	500	500
Temperature, °F.		−100	−100	−200	−200	−200	−200	−200
Liquid-phase composition, mole %	H_2	0.296	1.46	0.462	0.626	0.698	0.743	0.882
	N_2	18.80	14.10	12.15	9.73	7.95	7.05	6.33
	CH_4	8.52	7.91	8.80	8.73	8.41	8.44	8.48
	C_2H_6	72.39	76.53	78.59	80.91	82.95	83.77	84.31
Vapor-phase composition, mole %	H_2	4.10	20.73	24.54	34.48	44.76	50.44	56.76
	N_2	61.96	62.82	70.87	61.01	50.96	45.32	39.32
	CH_4	8.66	8.14	3.98	3.91	3.74	3.71	3.46
	C_2H_6	25.28	8.31	0.606	0.608	0.549	0.525	0.456
Equilibrium ratios $K = y/x$	H_2	13.9	14.2	53.1	55.1	64.1	67.9	64.4
	N_2	3.30	4.46	5.83	6.27	6.41	6.43	6.21
	CH_4	1.02	1.03	0.452	0.448	0.445	0.440	0.408
	C_2H_6	0.349	0.109	0.00771	0.00751	0.00662	0.00627	0.00541

had been sufficient, these charts at constant temperature and pressure would have been a single curve of equilibrium ratio vs. composition. In this case the full number of variables indicated by the phase rule is required to correlate the phase behavior. Benham, Katz, and Williams (3) found a similar situation for a six-component system involving hydrogen and light hydrocarbons.

Fig. 6. Equilibrium ratios for constituents in the hydrogen-nitrogen-methane system at 0 mole % nitrogen in the liquid phase as a function of pressure for various temperatures.
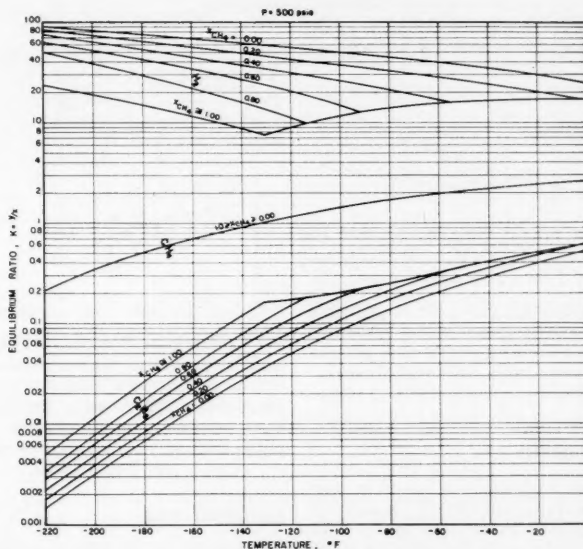
Fig. 8. Equilibrium ratios for constituents in the hydrogen-methane-ethane system at 500 lb./sq. in. abs. as a function of temperature with varying amounts of methane in the liquid phase.

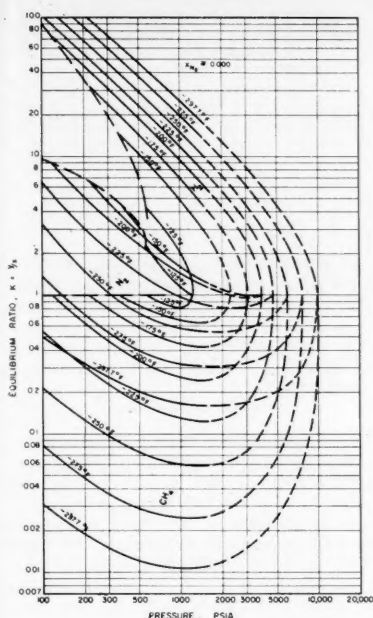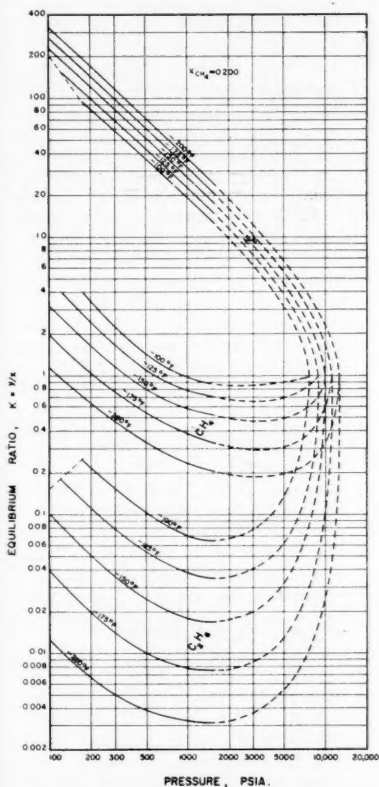Fig. 7. Equilibrium ratios for constituents in the hydrogen-methane-ethane system at 20 mole % methane in the liquid phase as a function of pressure for various temperatures.
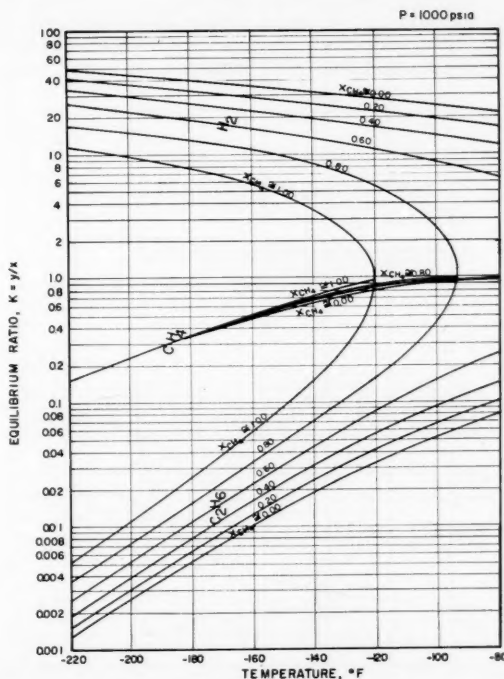
Fig. 9. Equilibrium ratios for constituents in the hydrogen-methane-ethane system at 1,000 lb./sq. in. abs. as a function of temperature with varying amounts of methane in the liquid phase.
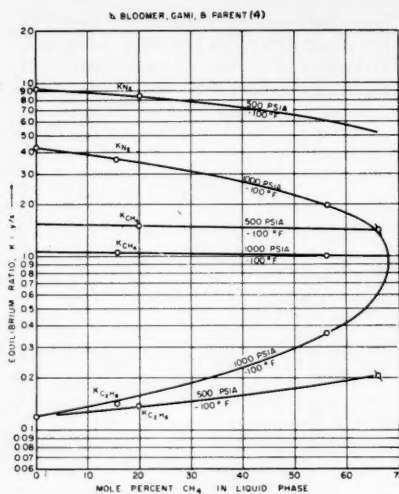
Fig. 10. Equilibrium ratios for constituents in the nitrogen-methane-ethane system at −100°F. as a function of the mole percentage of methane in the liquid phase.

ACKNOWLEDGMENT
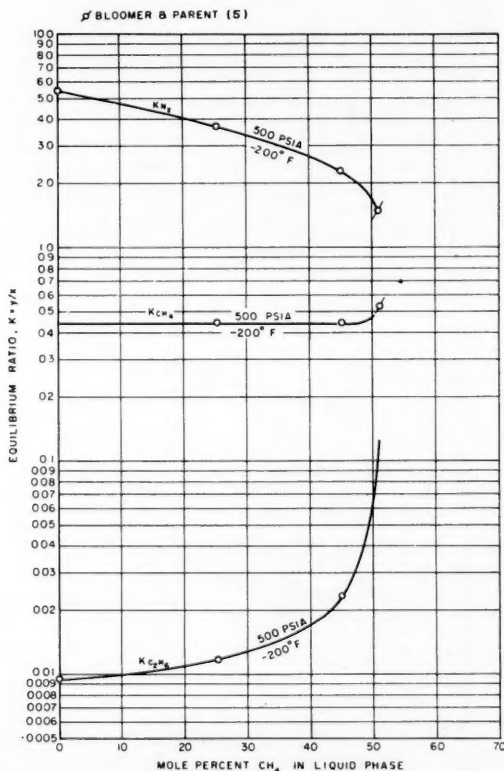
Fig. 11. Equilibrium ratios for constituents in the nitrogen-methane-ethane system at −200°F. as a function of the mole percentage of methane in the liquid phase.
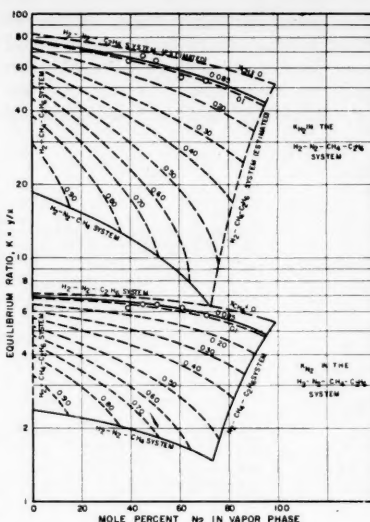
Fig. 12. Equilibrium ratios for hydrogen and nitrogen in the hydrogen-nitrogen-methane-ethane quaternary system at 500 lb./sq. in. abs. and −200°F. as a function of the mole percentage of nitrogen in the vapor phase with varying amounts of methane in the liquid phase.

LITERATURE CITED

1. Aroyan, H. J., and D. L. Katz, *Ind. Eng. Chem.*, **43**, 185 (1951).

2. Benham, A. L., and D. L. Katz, *A.I.Ch.E. Journal*, **3**, 33 (1957).
3. ——, and R. B. Williams, *ibid.*, p. 236.
4. Bloomer, O. T., D. C. Gami, and J. D. Parent, *Inst. Gas. Tech. Res. Bull.* **22**, p. 1 (1953).
5. Bloomer, O. T., and J. D. Parent, *Chem. Eng. Progr. Symposium Ser.* No. 6, **49**, p. 11 (1953).
6. Cines, M. R., J. T. Roach, R. J. Hogan, and C. H. Roland, *ibid.*, p. 1.
7. Gonikberg, M. G., V. G. Fastowsky, and I. G. Gurwitsch, *Acta Physicochim. U.S.S.R.*, **11**, 865 (1939).
8. Levitskaya, E. P., *J. Tech. Phys. (U.S.S.R.)*, **11**, 197 (1941).
9. Ruhemann, M., and N. M. Zinn, *Physik. Z. Sowjetunion*, **12**, 389 (1937).
10. Steckel, F. A., and N. M. Zinn, *J. Chem. Ind. (U.S.S.R.)*, **16**, 24 (1939).
11. Verschoyle, T. T. H., *Trans. Roy. Soc. (London)*, **230A**, 189 (1931).
12. Williams, R. B., and D. L. Katz, *Ind. Eng. Chem.*, **46**, 2512 (1954).

Fig. 13. Equilibrium ratios for ethane in the hydrogen-nitrogen-methane-ethane quaternary system at 500 lb./sq. in. abs. and −200°F. as a function of the mole percentage of nitrogen in the vapor phase with varying amounts of methane in the liquid phase.
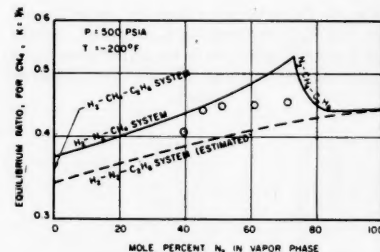
Fig. 14. Equilibrium ratios for methane in the hydrogen-nitrogen-methane-ethane quaternary system at 500 lb./sq. in. abs. and −200°F. as a function of the mole percentage of nitrogen in the vapor phase.

Transitional Velocity Patterns in a Smooth Concentric Annulus

J. E. WALKER and R. R. ROTHFUS

Carnegie Institute of Technology, Pittsburgh, Pennsylvania

Profiles of mean local velocities have been experimentally determined in a smooth, concentric, horizontal annulus having a radius ratio of 0.331. The test fluid was water at room temperature flowing steadily at Reynolds numbers in the viscous, transition, and lower turbulent ranges. The transitional profiles, obtained by means of an impact probe, are summarized and discussed. Limits of the transition zone are established, and variation of the radius of maximum velocity with Reynolds number is confirmed.

Relatively little is known about laminar-turbulent transition in concentric annuli. There is published information about fluid friction in this region but no adequate indication of what velocity patterns are to be expected. The present investigation has been undertaken as a first step in determining the effect of Reynolds number on the transitional velocity profiles. A calibrated impact probe has been used to obtain mean local velocities in water flowing steadily and isothermally through a smooth, horizontal annulus having a radius ratio of 0.331. Data have been obtained at various Reynolds numbers from 250 to 10,000 with most attention centered on the transition zone.

The pressure-drop data supplementing the present velocity measurements have already been reported by Walker, Whan, and Rothfus [7]. The correlated results on pressure drop cover the entire range of radius ratios from zero to unity. The data indicate that the extent of the transition region on the Reynolds-number scale depends to some degree on the radius ratio. For the radius ratio examined herein, namely 0.331, the major transitional changes in the curve of Fanning friction factor against Reynolds number occur at Reynolds numbers between 2,200 and 3,100.
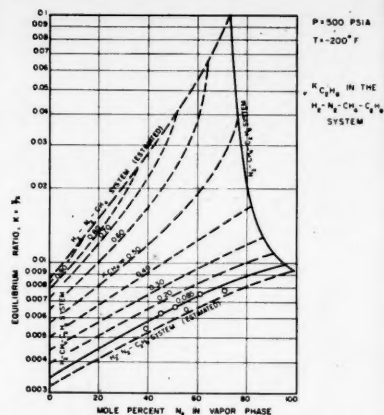
The frictional data have been correlated in terms of the Reynolds number

$$N_{Re_2} = \frac{2(r_2^2 - r_m^2)}{r_2} \frac{V\rho}{\mu} \quad (1)$$

The characteristic length in this case is four times the hydraulic radius of that portion of the stream lying between the outer radius and the radius of maximum local velocity. The bulk average linear velocity is taken over the whole annular section between the outer radius and the inner or core radius. The cited friction factor in turn is the one at the outer wall, defined as

$$f_2 = \frac{2\tau_2 g_c}{\rho V^2} \quad (2)$$

The pressure-drop data show that the relationship between f_2 and N_{Re_2}, in fully turbulent flow, is coincident with the corresponding correlation for smooth tubes. Thus, the method of hydraulic radius can be applied to the portion of the annulus outside the radius of maximum velocity, regardless of the radius ratio. This is the reason for using the Reynolds number defined in Equation (1) when the frictional data are correlated.

The fully turbulent velocity profiles measured in the present experiments are reported in a paper by Rothfus, Walker, and Whan [5]. A means of correlating these data with smooth-tube and parallel-plate profiles is described there. It appears that a successful method has been found for predicting fully turbulent velocity patterns, regardless of the radius ratio of the annulus. In addition the velocity data confirm observations of Rothfus, Monrad, and Senecal [3] and of Knudsen and Katz [1] that the radius of maximum velocity in full turbulence corresponds to that in fully viscous flow. The latter value is easily shown to be related to the annular dimensions through the equation

$$r_m^2 = (r_2^2 - r_1^2)/2 \ln (r_2/r_1) \quad (3)$$

When the radius of maximum velocity is either unknown or of primary interest, it is convenient to correlate data in terms of the Reynolds number obtained by combing Equations (1) and (3).

Some direct measurements of the skin friction on the cores of annuli having radius ratios of 0.507 and 0.337 have been made by Rothfus, Monrad, Sikchi, and Heideger [4]. From such data the friction factor at the inner wall of the annulus can be calculated from the defining equation
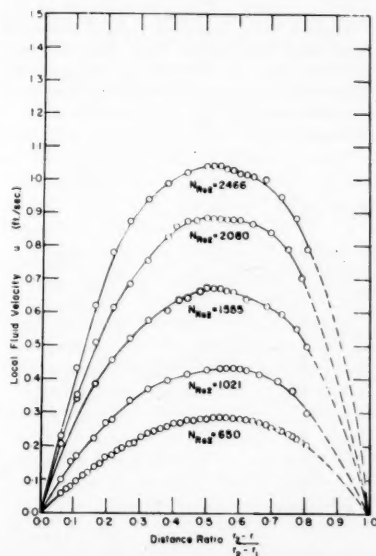

Fig. 1. Transitional velocity profiles for water at 20°C. flowing in a smooth annulus; radius ratio $r_1/r_2 = 0.33$.
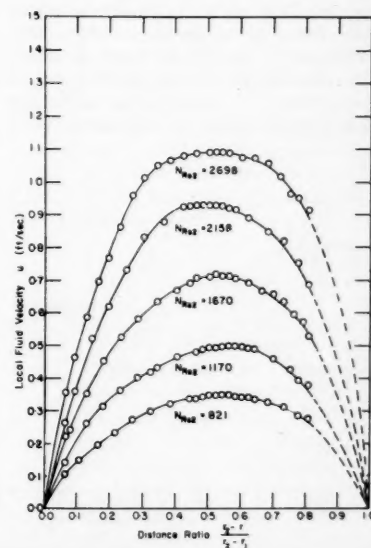

Fig. 2. Transitional velocity profiles for water at 20°C. flowing in a smooth annulus; radius ratio $r_1/r_2 = 0.33$.
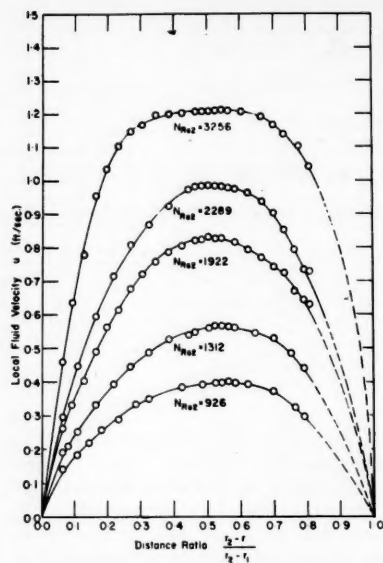
Fig. 3. Transitional velocity profiles for water at 20°C. flowing in a smooth annulus; radius ratio $r_1/r_2 = 0.33$.

$$f_1 = \frac{2\tau_1 g_c}{\rho V^2} \qquad (4)$$

Simple force balances on the fluid inside and outside the radius of maximum velocity show that

$$\frac{\tau_1}{\tau_2} = \frac{f_1}{f_2} = \frac{r_2\,(r_m{}^2 - r_1{}^2)}{r_1\,(r_2{}^2 - r_m{}^2)} \qquad (5)$$

Since the force balances are independent of the flow regime, Equation (5) must involve the actual value of the radius of maximum velocity, whatever it may be. Thus if the flow is fully viscous or fully turbulent, r_m can be calculated by means of Equation (3). In the transition zone however r_m proves to have other values as shown in reference *4*, where the pressure-drop data of reference *3* were used in combination with the skin-friction data of reference *4* to

obtain separate values of f_1 and f_2. Equation (5) was then utilized to determine the influence of Reynolds number on the radius of maximum velocity. The results indicated that a regular and appreciable deviation of r_m from its viscous-flow value occurred in the transition range. It consequently became a concern of the present investigation to verify such behavior through measurement of local fluid velocities.

EXPERIMENTAL EQUIPMENT

The experimental apparatus was basically a simple, open, hydraulic loop equipped with accessories for control of flow rate and temperature. Water at room temperature was circulated at steady rates which were measured by means of a calibrated volumetric tank. The test section for the velocity measurements consisted of 30 ft. of smooth brass conduit having a 0.750-in. I.D. which was fitted with a concentric, smooth, copper core of 0.248 in. diameter. The middle 3 ft. of the outer tube were replaced by a Lucite section having exactly the same inside diameter. The transparent tube, which was held in perfect alignment by a shouldered joint, permitted the position of the velocity probe to be checked visually from time to time. As the test section was horizontal, it was necessary to prevent sagging of the core by applying tension on the core through a screw mechanism.

The impact probe was a straight length of stainless steel hypodermic tubing having an outside diameter of 0.058 in. The probe was capped with 0.008-in. thick stainless steel, silver-soldered in place, and ground flush with the sides of the tubing. The impact opening, 0.020 in. in diameter, was drilled in the side of the probe with its edge approximately 0.003 in. from the capped end. The probe was attached to a feed mechanism which permitted the center of the impact opening to be positioned in the fluid stream with a precision of 0.001 in. Distances were measured from a reference point on a micrometer scale. The reference position was established by temporarily removing the core and permitting the probe to make contact with the opposite side of the outer tube.

The differences between the total pressure on the opening in the probe and the static pressure at the wall of the outer tube were measured by means of vertical U-tube manometers filled with carbon tetrachloride, monochlorobenzene, or monofluorobenzene, depending on the desired amplification of the readings. To maintain proper behavior of the liquid interfaces the manometers were carefully cleaned and a silicone layer was baked on their inner surfaces.

EXPERIMENTAL PROCEDURE

The test section was aligned by means of a transit theodolite, and the core diameter was measured after tension had been applied to eliminate appreciable sag. The impact probe was calibrated by the method of Stanton, Marshall, and Bryant (*6*). No investigation of calming length was made, since the impact probe was situated at a point where there were 725 equivalent diameters of calming length upstream from it and 676 equivalent diameters downstream.

In a typical run the flow rate was established and sufficient time allowed for steady state to be reached. Local velocities were then measured at various points in the fluid cross section. Approximately half an hour elapsed between successive settings of the probe position. The distance between successive positions and the direction of approach to them were varied both regularly and at random.

Enough data were taken to establish the relationship between the radius of maximum velocity and the Reynolds number. Additional measurements of the maximum velocity were then made at these radii. The relationship between the Reynolds number and the ratio of average to maximum velocity could thus be determined without measuring a full velocity profile at each flow rate.

Since the water was recycled by means of pumps, it tended to increase in temperature over long periods of operation. The temperature was held within 0.1°C. of a constant value, however, by the addition of a small amount of cold water to the system at intervals of approximately 1 hr. The water and room temperatures were kept essentially the same to assure isothermal flow in the test section.
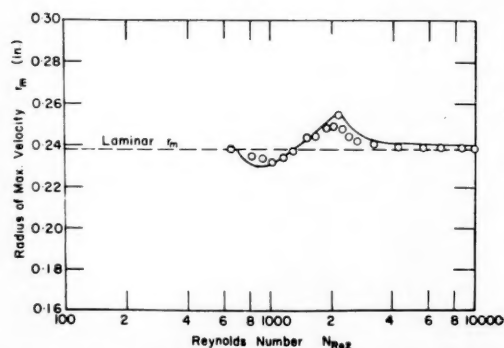

Fig. 4. Effect of Reynolds number on radius of maximum velocity; radius ratio $r_1/r_2 = 0.33$. (Solid line shows prediction based on pressure drop and drag measurements. Circles show experimental velocity data.)
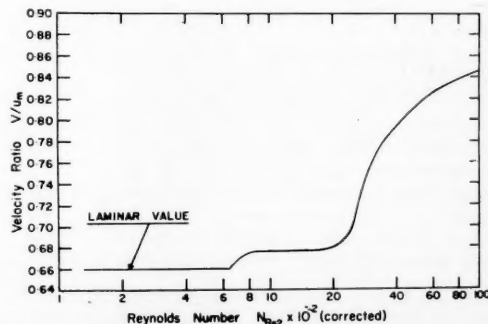

Fig. 5. Effect of Reynolds number on ratio of bulk average to maximum velocity for annulus with $r_1/r_2 = 0.33$.

The velocity profiles obtained in the transition range of flow are shown in Figures 1, 2, and 3. The ordinates are dimensional in feet per second, but the abscissae are dimensionless ratios. The symbols r_1 and r_2 denote the inner and outer radii of the annulus respectively. The distance r is the radius from the center of the whole configuration to the point of measurement in the fluid. The left boundary of each graph is therefore the outer wall of the annulus, and the right boundary is the surface of the core. The Reynolds numbers indicated on the separate curves are as defined in Equation (1) with r_m computed from Equation (3) as a matter of convenience.

Figure 4 summarizes the effect of Reynolds number on the radius of maximum velocity. Again the Reynolds number is the one used in the preceding figures. If the actual value of r_m were included in the Reynolds number, it would appear in both the ordinate and abscissa, a situation which is not desirable in this case. The circles represent the experimental velocity data; the solid line is the result of combining the pressure-drop data obtained in the present work with the core-side, skin-friction data of reference 4. Since the latter authors experimented with an annulus of 0.337 radius ratio, their data can be applied directly to the present case with negligible error.

Figure 5 shows the experimentally determined relationship between the ratio of bulk average to maximum velocity V/u_m and the Reynolds number used in the preceding figures. The value of the bulk-average velocity is the one obtained directly from volumetric flow-rate measurements.

DISCUSSION AND RESULTS

The ordinates of Figures 1, 2, and 3 have been left in dimensional form to separate the curves on the graphs. It appears reasonable to assume however that the velocity ratio u/u_m is solely a function of Reynolds number N_{Re_2} and distance ratio $(r_2 - r)/(r_2 - r_1)$ in annuli having equal radius ratios r_1/r_2. On this basis point velocities can be predicted from the present data for annuli having $r_1/r_2 = 0.33$, even though they are not of the same absolute size as the experimental test section. If the bulk average velocity is known in such an annulus, the Reynolds number can be calculated and the velocity ratio V/u_m read from Figure 5. The maximum velocity can then be calculated immediately. Interpolation to the proper Reynolds number in Figure 1, 2, or 3 yields a unique velocity profile which can be reduced to a series of u/u_m values at the desired points in the fluid stream. The actual maximum velocity is then multiplied by

these ratios to produce the velocity pattern for the case at hand.

Figure 4 shows remarkably good agreement between the experimental values of the radius of maximum velocity and those computed from frictional data. The drag measurements of reference 4 extend downward only to a Reynolds number of 1,500, and so it was necessary to use extrapolated values in the lower transition range. The extrapolation was based on the expectation of reaching fully viscous flow at a Reynolds number of about 700, since dye studies by Prengle and Rothfus (2) had suggested such a limit. As seen in Figure 4, the values of r_m obtained from the velocity profiles start to deviate from the laminar-flow position at a Reynolds number of 650. The friction factors calculated from the pressure-drop data of the present investigation also show a slight positive deviation from the laminar relationship, starting at about the same Reynolds number.

The radius of maximum velocity appears to shift toward the core in the lower transition zone and then to reverse its direction upon further increase in the Reynolds number. The outward progression takes r_m past its viscous-flow value and stops only when the lower critical Reynolds number of 2,200 is attained. This is the Reynolds number at which the friction factor at the outer wall reaches a minimum value and begins its sharp transitional increase. The authors of reference 2 have related this point to the casting off of the first large disturbance eddy. As the frequency of the disturbance eddies increases with further increase in Reynolds number, the radius of maximum velocity reapproaches its laminar value.

The friction factor at the outer wall indicates that the transition zone reaches its upper limit at a Reynolds number of about 3,100. Figure 4 shows that the radius of maximum velocity closely approaches the viscous-flow value given in Equation (3) at Reynolds numbers of 3,100 or more. Thus the deviation of r_m from the laminar value appears to be confined to the Reynolds number range in which frictional data show transitional behavior.

Figure 5 shows a sharp departure of the V/u_m curve from its viscous-flow value at the Reynolds number of 650. Another rapid change in slope occurs at the lower critical Reynolds number of 2,200 similar to the corresponding change at 2,100 Reynolds number in the case of smooth tubes. The Reynolds number is computed with r_m taken at its actual value. If the value of r_m obtained from Equation (3) were used in the Reynolds number, its effect would be to shift the curve of Figure 5 to the left in the lower transition zone and to the right in the upper transition region. Since the maximum shifting amounts to only 9.4% decrease in the Reynolds number at the

critical value of 2,200, the modification is slight in any range.

Smooth tubes and parallel plates can be considered to be limiting cases of annuli, as the radius ratio r_1/r_2 goes to zero and unity respectively. Since neither of these configurations demonstrates any lack of symmetry in the transition range, the observed shifting of the radius of maximum velocity must be a function of the radius ratio of the annulus. The friction factors computed from pressure-drop measurements show that the limits of the transition zone on the Reynolds-number scale are also functions of the radius ratio. The correlation of transitional velocities is therefore likely to be rather strongly dependent on r_1/r_2. Thus it is impractical to attempt a generalized correlation of transitional velocity patterns on the basis of data from one size of annulus. Further work on annuli of other radius ratios is currently in progress.

As an over-all check on the accuracy of the velocity data, the bulk average linear velocity of the stream was calculated by means of integration under the experimental profile. The result was compared with the corresponding flow rate determined directly by volumetric measurement. On the average the integrated velocities were 1.7% higher than the measured ones. The maximum deviation occurred at Reynolds numbers from 2,000 to 2,300 where the integrated velocities exceeded the measured values by about 3.5%. As differences of this magnitude are ordinary in such work, it can be concluded that the present data show no abnormal characteristics in this respect. Most of the error can be presumed to lie in the points nearest the bounding surfaces. Velocity probes calibrated in laminar flow usually read a few per cent too high in the region of a wall when the main flow is turbulent. It is also to be expected that local errors might be magnified to some extent in the transitional range. Since the local flow fluctuates over relatively long time intervals in this regime, the measurement of the time-mean local velocity is made more difficult than in fully laminar or fully turbulent flow.

NOTATION

f_1 = Fanning friction factor at inner surface of annulus, defined by Equation (4), dimensionless

f_2 = Fanning friction factor at outer surface of annulus, defined by Equation (2), dimensionless

g_c = conversion factor in Newton's second law of motion, equal to 32.2 (lb.-mass)(ft.)/(lb.-force) (sec.^{2})

N_{Re_2} = Reynolds number defined by Equation (1), dimensionless

r = radial distance from center of whole annular configuration to point of measurement in fluid, ft.

r_1 = radius of inner surface, or core, of annulus, ft.

r_2 = radius of outer surface of annulus, ft.

r_m = radius of maximum local fluid velocity, ft.

u = mean local fluid velocity, ft./sec.

u_m = maximum value of mean local fluid velocity, ft./sec.

V = bulk average linear fluid velocity, ft./sec.

Greek Letters

μ = viscosity of fluid, lb.-mass/(sec.) (ft.)

ρ = density of fluid, lb.-mass/cu. ft.

τ_1 = skin friction at inner surface of annulus, lb.-force/sq. ft.

τ_2 = skin friction at outer surface of annulus, lb.-force/sq. ft.

LITERATURE CITED

1. Knudsen, J. G., and D. L. Katz, "Proc. Midwestern Conf. Fluid Dynamics, 1st Conf.," No. 2, 175 (1950).

2. Prengle, R. S., and R. R. Rothfus, *Ind. Eng. Chem.*, **47**, 379 (1955).
3. Rothfus, R. R., C. C. Monrad, and V. E. Senecal, *ibid.*, **42**, 2511 (1950).
4. Rothfus, R. R., C. C. Monrad, K. G. Sikchi, and W. J. Heideger, *ibid.*, **47**, 913 (1955).
5. Rothfus, R. R., J. E. Walker, and G. A. Whan, *A.I.Ch.E. Journal*, **4**, 2 (1958).
6. Stanton, T. E., D. Marshall, and C. N. Bryant, *Proc. Roy. Soc. (London)*, **A97**, 413 (1920).
7. Walker, J. E., G. A. Whan, and R. R. Rothfus, *A.I.Ch.E. Journal*, **3**, (1957).

Some Effects of Baffles on a Fluidized System

R. H. OVERCASHIER, D. B. TODD, and R. B. OLNEY

Shell Development Company, Emeryville, California

Some characteristics are reported for the fluidization of an air-microspheroidal catalyst system in a 16-in.-diameter bed equipped with baffles. The back-mixing characteristics and retention-time distributions of gas and solids, allowable gas and solids velocities, entrainment rate, and bed density are studied as functions of baffle design.

It is shown that the use of baffles narrows the retention-time spectrum and permits either concurrent or countercurrent flow while not seriously reducing gas or solids throughput or solids holdup.

For many reactions a fluidized-bed system offers important advantages, such as uniform temperatures under conditions of high heat release, large surface-to-volume ratio of the solids medium, and ease of transfer of the solids from one process vessel to another. The principal disadvantage of the fluid bed is its broad spectrum of gas and solids holding times. It has been shown that the residence-time spectrum of the fluid bed is much closer to that of a single well-mixed stage than to the more desirable infinite stages (piston flow). As reactor volume and the formation of unwanted by-products via consecutive reactions are both minimized by piston flow, this disadvantage can be serious.

The broad residence-time distribution of the conventional fluidized bed is well established. Singer, Todd, and Guinn (5) have shown that for the solids residence times used in commercial catalytic cracking (5 to 40 min.) the catalyst in each vessel could be regarded as perfectly mixed. The gas–retention-time studies of Gilliland, Mason, and Oliver (2, 3) in small columns showed that while the gas phase appeared neither

well mixed nor in piston flow, it was much closer to the former. The present authors' measurements, shown in Figure 1 for a 16-in.–diam. fluid bed, confirm these previous findings. Gilliland, Mason, and Oliver postulated that the gas effluent from the bed results from the combination of two internal streams, one flowing slowly through the interstices of the solid and the other flowing rapidly via large bubbles or cavities containing very little solids. According to this analysis the majority of the gas travels via the rapidly moving bubbles and exchanges incompletely with the interstitial gas (that is, partially by-passes the bed). The resulting system effluent has a retention-time curve approximating the broad spectrum of a well-mixed stage. Similar findings are also reported by Handlos, Kunstman, and Schissler (4) for commercial fluidized beds.

If this analysis is correct, the bubbles play an important role in bed dynamics, providing both the density gradient which mixes the solids and the rapid escape path for part of the gas. They also appear inherent in the fluid bed, since they have been observed in many investigations, and their inevitability has

been shown recently on theoretical grounds by Baron and Mugele (1). Thus the goal of narrowing the residence-time spectrum of the fluid bed appears to rest on minimizing the effect of the bubbles rather than on their elimination.

Many workers in the field of fluidization have suggested compartmenting the bed with horizontal baffles to narrow the residence-time spectrum. These baffles should narrow the spectrum by decreasing the velocity difference between the bubble and interstitial flows and by promoting transfer between them. In addition the baffles should impede the complete mixing of solids and result in staging of the solids flow, either for concurrent or countercurrent flow of solids and gas. Finally, since bubbles would still be present, the individual compartments would still have good heat-transfer characteristics.

The purpose of this investigation is to show the effect of horizontal baffles on the residence-time spectrum of solids and gas and on other characteristics of the fluid bed, such as allowable flow rates, mixture density, and solids entrainment. The experimental apparatus, operating techniques, and calculation

TABLE 1. BAFFLE CONSTRUCTION

Baffle type	Free area %	Openings		Baffle thickness, in.	Baffle spacing, in.	No. of baffles
		Size	Number			
Grid trays	15	¼ in. slots	11	⅛	24	4
	30	¼ in. slots	22	⅛	8, 24	12, 4
	30	1 in. slots	5	⅛, 1	24	4
Tube trays	2.4	1.5 in. tubes	3	6	42	2
	4.6	2.0 in. tubes	3	6	42	2
	9.2	2.0 in. tubes	6	6	42	2
	4.7	1 in. tubes	12	1, 3	27	4
	14.5	1 in. tubes	37	3	27	4

TABLE 2. CATALYST PROPERTIES

Surface area	90 sq. meters/g.
Pore volume	0.23 cc./g.
Skeletal density	2.3 g./cc.
Particle density	1.5 g./cc.
Size distribution*	
D_{10}	51 μ
D_{50}	77 μ
D_{90}	103 μ

*D_{10}, D_{50}, and D_{90} are the particle diameters corresponding to 10, 50, and 90% respectively of the cumulative weight distribution, as determined by Micromerograph analysis.

methods are described in the following sections.

APPARATUS

All the measurements were made in the system diagrammed in Figure 2. The fluid bed was contained in a plastic column, 16 in. in diameter by 10 ft. high. Humidified air was metered through a standard A.S.M.E. long-radius approach nozzle and flowed up through the dense bed. Separation of the air and solids took place initially in the disengaging section above the fluid bed and finally in a two-stage cyclone system.

For concurrent flow, solids were entrained up the column and returned to the bottom of the bed continuously via the standpipe of the primary cyclone and intermittently from the secondary cyclone. The external solids circulation rate was dependent upon the gas velocity and the inventory of solids contained in the system.

For countercurrent flow a large-diameter disengaging space was provided at the top of the column. Solids were withdrawn from the bottom of the bed and transported to the top of the bed through a calibrated dilute-phase riser. The solids circulation rate was controlled by a butterfly valve at the bottom of the column. The entrained solids were returned to the top of the bed directly from the cyclone standpipes. The solids entrainment rate to the cyclones was estimated from the air flow and pressure drop through a calibrated nozzle placed in the column exit line.

Helium and Freon, used as tracers in both steady and unsteady state gas experiments, were analyzed in a thermal conductivity apparatus. The analyzer required about 300 cc. of gas and 3 min. for each determination. Gas samples were withdrawn into brine-trapped bottles via assemblies containing six fritted-glass filters arranged along a column diameter. These assemblies could be installed at 4-in. intervals up the

column. In the back-mixing experiment (steady state) the sample was withdrawn slowly over a long period (~5 min.) to ensure sampling the interstices rather than the rising bubbles. In the by-passing experiments the samples were withdrawn quickly (300 cc. in about 1 sec.) at a point far enough above the dense bed to assure mixing of both the bubble and interstitial gas. Samples taken at varying heights above the dense bed were related by assuming plug flow in the dilute zone after this practice was shown experimentally to be justified.

The types of baffles investigated are depicted in Figure 2 and described in detail in Table 1. All the trays studied were without downcomers; that is, both the gas and solids passed through the same openings. The number of compartments in operation during any one run depended upon the total solids inventory. Occasionally there was no dense phase above the top baffle.

CATALYST PROPERTIES

In all the tests the fluidized solids were equilibrium, microspheroidal, silica-alumina, cracking catalyst which had been regenerated to whiteness. The catalyst had the average properties given in Table 2 with an incipient fluidization velocity of less than 0.01 ft./sec.

INTERPRETIVE MODELS

The change in gas- and solids-residence-time distributions brought about by the use of baffles was investigated by studying the outlet response to step or pulse input functions.

For the gas studies both transient retention time and steady state back-mixing experiments were performed. The retention-time data were compared with theoretical curves calculated for several
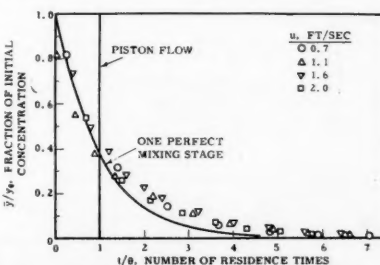
Fig. 1. Gas retention time in a 16-in. diameter unbaffled bed.

models suggested by observation of a fluidized bed. These models are

1. Perfect mixing in each stage
2. Perfect mixing within each stage but with a fraction of the gas by-passing the stage at infinite velocity and subsequently mixing with the unby-passed fraction
3. Perfect mixing in which the by-passed gas fraction travels at some finite velocity
4. Mass transfer occurring between a plug-flow bubble phase and a well-mixed interstitial gas phase, with the gas entering and leaving the system via the bubble phase, which travels at some finite velocity
5. Mass transfer occurring between a well-mixed bubble phase and a well-mixed interstitial phase with gas entering and leaving via the bubbles, which travel at some finite velocity

Since the experimental curves were not precisely fitted by any of the models, the experiments were interpreted primarily on the basis of the width of the residence-time spectrum. For this reason the models are described here superficially and in more detail in the supplement.*

For perfect mixers without by-passing, the time-concentration history of the effluent is given by

$$y_1/y_0 = \exp(-t/\theta) \qquad (1)$$

for a single stage and

$$y_n/y_0 = \exp\left(-\frac{t}{\theta}\right) \sum_{p=0}^{n-1} \frac{1}{p!}\left(\frac{t}{\theta}\right)^p \qquad (2)$$

for n identical stages in series.

For perfect mixers with infinite-velocity by-passing of a fraction $(1 - \epsilon)$ around each stage and with remixing of the fractions $(1 - \epsilon)$ and ϵ between stages

$$\bar{y}_1/y_0 = \epsilon \exp\left(-\epsilon\frac{t}{\theta}\right) \qquad (3)$$

for a single stage, and

$$\bar{y}_n/y_0 = \epsilon \exp\left(-\epsilon\frac{t}{\theta}\right) \sum_{p=0}^{n-1} c_p \frac{\epsilon^p}{p!}\left(\frac{t}{\theta}\right)^p \qquad (4)$$

for n identical stages in series, where

$$c_0 = \frac{1 - (1 - \epsilon)^n}{\epsilon}$$

$$c_{p+1} = -\frac{1}{p+1}\frac{dc_p}{d\epsilon}$$

For finite-velocity by-passing in a single stage

$$\bar{y}_1/y_0 = \epsilon \exp\left[-\frac{f\epsilon}{f - (1 - \epsilon)}\left(\frac{t}{\theta}\right)\right]$$
$$+ (1 - \epsilon) \quad \text{for} \quad t/\theta < 1/f \quad (5a)$$
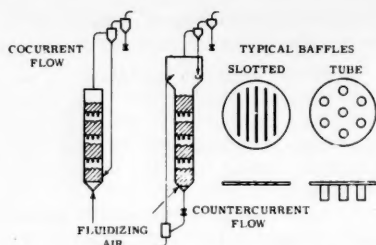
Fig. 2. Experimental apparatus.
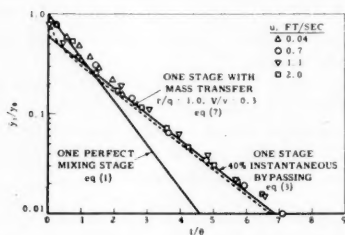
Fig. 3. Gas retention time in the unbaffled column.
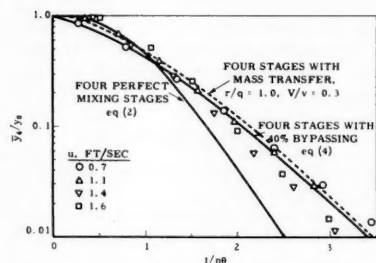
Fig. 4. Gas retention time in a compartmented column. 15% free-area grid trays, 24-in. spacing, 1/4-in. slots.
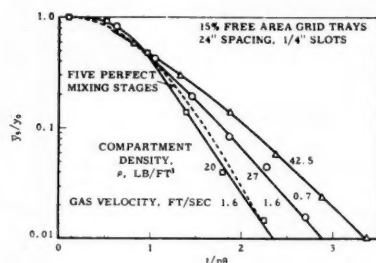
Fig. 5. Effect of compartment density on gas retention time.

$$\bar{y}_1/y_0 = \epsilon \exp\left[-\frac{f\epsilon}{f-(1-\epsilon)}\left(\frac{t}{\theta}\right)\right]$$

$$\text{for} \quad t/\theta > 1/f \quad (5b)$$

where f is the ratio of by-passing velocity to superficial gas velocity.

For mass transfer between plug-flow bubbles and a single well-mixed interstitial gas phase

$$\frac{\bar{y}_b}{y_0} = \frac{1}{\left[1-\frac{r}{2q}-\frac{v}{V}\right]} \exp\left(-rt/V\right)$$

$$+\left\{1-\frac{1}{\left[1-\frac{r}{2q}-\frac{v}{V}\right]}\right\} \exp\left(\alpha t\right)$$

$$\text{for} \quad t < V/q \quad (6a)$$

and

$$\frac{\bar{y}_b}{y_0} = \left[1-\frac{1}{1-\frac{r}{2q}-\frac{v}{V}} \exp\left(\alpha t\right)\right]$$

$$-\left[1-\frac{1}{1-\frac{r}{2q}-\frac{v}{V}}\right] \exp\left(-r/q\right)$$

$$\cdot \exp\left[\alpha\left(t-\frac{V}{q}\right)\right] \text{ for } t > V/q \quad (6b)$$

where α is a zero of the following transcendental equation, in which s is the Laplace transform variable

$$s(s^2+as+b)+c(1$$

$$-\exp\left[-r/q\right]\exp\left[-Vs/q\right])=0$$

and

$$a = \frac{2Vvr+V^2r}{vV^2} = \frac{r(2v+V)}{Vv}$$

$$b = \frac{r^2(V+v)}{vV^2}$$

$$c = \frac{qr^2}{vV^2}$$

For mass transfer between a well-mixed bubble phase and a well-mixed interstitial phase

$$\frac{\bar{y}_b}{y_{b0}} = \frac{\left(\frac{q}{V}+m_1\right)\exp\left(m_2 t\right)-\left(\frac{q}{V}+m_2\right)\exp\left(m_1 t\right)}{m_1-m_2} \quad (7)$$

for a single stage, where

$$m_1 = -\frac{q}{2V}\left[\left\{1+\frac{r}{q}\left(1+\frac{V}{v}\right)\right\}-\sqrt{\left\{1+\frac{r}{q}\left(1+\frac{V}{v}\right)\right\}^2-4\frac{r}{q}\frac{V}{v}}\right]$$

$$m_2 = -\frac{q}{2V}\left[\left\{1+\frac{r}{q}\left(1+\frac{V}{v}\right)\right\}+\sqrt{\left\{1+\frac{r}{q}\left(1+\frac{V}{v}\right)\right\}^2-4\frac{r}{q}\frac{V}{v}}\right]$$

For the multistage case no analytic solution was made. Instead the differential equations (see supplement) were solved numerically where needed: that is, for use in Figure 4.

The model curves were next compared with the experimental retention-time curves. Since the latter contained no pronounced discontinuities for $t/\theta \leqslant 1.0$, the models for finite velocity by-passing and mass transfer into plug-flow bubbles were eliminated from further consideration. As will be shown later, the other models (perfect mixers, perfect mixers with infinite-velocity by-passing and mass transfer into well-mixed bubbles) do fit some of the experiments reasonably well. However it is quite clear that this agreement is never sufficient to show unambiguously the actual contact mechanism. When it became apparent that additional models, more plausible but of greater complexity, would contain parameters impossible to evaluate if only the effluent composition were known, model-making ceased. The experimental results were then examined in terms of the spread of gas-residence times rather than for evidence of the contact mechanism.

In the studies of steady state back-mixing of gas the concentration gradient existing upstream of the tracer injection point was used to calculate an effective diffusion coefficient. When one assumes the tracer introduced from a plane source, a homogeneous bed of solids, circular symmetry, and the absence of radial gradients,

$$D_e = \frac{uL}{\ln y_0/y} \quad (8)$$

Over a baffle itself it is more convenient to use the concentration ratio alone as a measure of the back-mixing reduction because of the discontinuity in the concentration gradient.

It should be noted that the actual back-mixing system is much more complex than is postulated in the derivation (see supplement) of Equation (8). For example, radial gradients are not absent. In addition a plane source is only approximated by introducing the tracer downward along the column axis to impinge against a horizontal disk of a diameter about 1/4 column. Finally the tracer is back-mixing against a bulk gas flow with a velocity that varies radially from much more, to considerably less (indeed negative near the wall), than superficial. Nevertheless the effective diffusion coefficient is a convenient way of describing the back-mixing characteristics of a complex system, that is of stating the diffusivity which would be required in the ideal system postulated.

The model used for description of the solids-mixing patterns in the countercurrent flow-baffled bed considers each compartment perfectly mixed, with

TABLE 3. AVERAGE SOLIDS INTERMIXING RATES

Radioactive tracer test	Tray type	Tray, % free area	Gas velocity, ft./sec.		Average solids flow, lb./(min.)(sq. ft.)						
					Net		Intermixing		Gross	
			U	U_r	G_c	G_r	I_c	I_r	Column	Constriction
I	Tube	4.7	0.4	8.5	0	0	9	190	9	190
II	Tube	4.7	0.4	8.5	17	350	3.5	75	20	425
	Tube	4.7	0.4	8.5	23*	480*			>23	>480
III	Tube	4.7	0.6	12.8	0	0	8.5	180	8.5	180
	Tube	4.7	0.6	12.8	12*	260*			>12	>260
IV	Tube	14.5	0.5	3.4	0	0	16.5	114	16.5	114
V	Tube	14.5	0.5	3.4	29	200	7.8	54	36.8	254
	Tube	14.5	0.5	3.4	83*	570*			>83	>570
VI	Tube	14.5	1.0	6.9	0	0	34.5	238	34.5	238
VII	Tube	14.5	1.0	6.9	29	200	29	202	58	402
VIII	Tube	14.5	1.0	6.9	58	400	26.5	183	84.5	583
	Tube	14.5	1.0	6.9	87*	600*			>87	>600
IX	Tube	14.5	1.5	10.3	0	0	39	272	39	272
	Tube	14.5	1.5	10.3	36*	250*			>36	>250

*Limiting solids downflow rates.

entrainment from the compartment below and to the compartment above and downflow from the compartment above and to the compartment below. The equations describing the transient behavior of a series of n compartments with net flow from one to n being returned to one and with intermixing are

First compartment

$$m_1 \frac{dC_1}{dt} = WC_n + w_2C_2 - (W + w_2)C_1 \quad (9)$$

Intermediate compartments

$$m_i \frac{dC_i}{dt} = (W + w_i)C_{i-1} + (w_{i+1})C_{i+1} - (W + w_i + w_{i+1})C_i \quad (10)$$

End compartment

$$m_n \frac{dC_n}{dt} = (W + w_n)(C_{n-1} - C_n) \quad (11)$$

The individual intermixing rates may be determined by injecting a pulse of tracer into one of the compartments, following the change in tracer concentration with respect to time in all the compartments, and by solving Equations (9) to (11). The solution of these equations was obtained by numerical procedures or with an analogue computer.

GAS RESIDENCE-TIME DISTRIBUTION

In these experiments the bed was first fluidized with air containing about 5% helium. The flow of helium was then cut off, and the composition of the effluent from the fluid bed was determined as a function of time. Typical residence-time curves are shown in Figures 3, 4, and 5. Figure 3 represents the results for the unbaffled bed and Figure 4 for the bed compartmented by 15%-free-area slotted baffles spaced at 2-ft. intervals. The same compartmented bed is shown in Figure 5 with compartment density as

parameter. The experimental data are compared with the calculated curves for three of the models discussed in the previous section: (1) perfect mixers, (2) perfect mixers with instantaneous gas by-passing, and (3) mass transfer between interstitial and bubble phases,
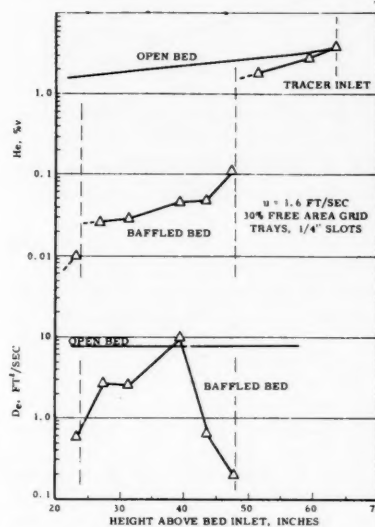
Fig. 6. The effect of baffles on gas backmixing.
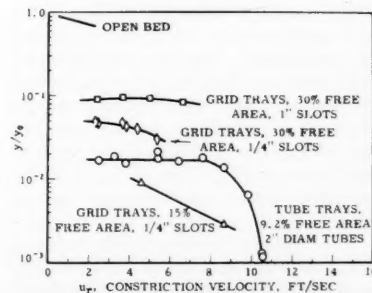
Fig. 7. Gas back-mixing as a function of slot velocity. Concentration ratio over 12 in. interval (including baffle).

each one perfectly mixed. The particular values of the parameters shown in Figures 3 and 4 are those which give about the best fit with the experimental results. In the single-stage case (Figure 3) the effect of by-pass fractions can easily be seen. The curve for 40% by-passing is shown, as is zero by-passing [the curve for Equation (1)]. For the case of by-pass fraction equals 0.7 the curve would decline from $\bar{y}/y_0 = 0.3$ at $t/\theta = 0$ to 0.020 at $t/\theta = 9.0$, an indication of a much slower purging rate than obtained experimentally.

The results in Figures 3 and 4 demonstrate that

1. The residence-time spectrum is considerably narrowed by the use of baffles but usually not to the extent corresponding to perfect mixers.

2. None of the models fit the experimental data with sufficient precision to indicate complete agreement with the postulated contact mechanism.

3. In the unbaffled bed the effect of gas velocity on the spectrum is insignificant in the range 0.05 to 2.0 ft./sec.

Figure 5 shows that compartment density has an effect on the residence-time distribution. The spectrum is narrowed by decreasing the compartment density either by increasing the gas velocity or decreasing the solids upflow rate. The approach to perfectly mixed compartments apparently results from the increase of the ratio of mixing energy to mass of solids within the compartment. It is not unique to the data shown but is supported by other results with the
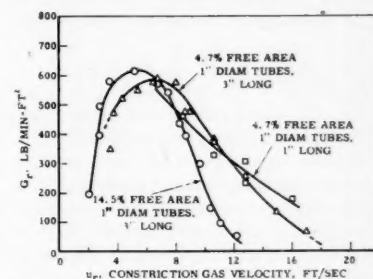
Fig. 8. Limiting solids downflow through tube trays.
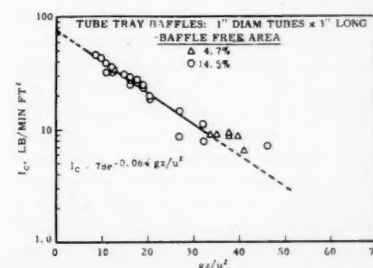
Fig. 9. Correlation of intermixing between compartments—countercurrent flow.

same baffles and higher free-area baffles. One concludes therefore that while the mass transfer and by-passing models do not correspond to the contact mechanism within the fluid bed, the residence-time spectrum can be narrowed by the use of baffles to approach, under some conditions, perfectly mixed stages.

In addition to the results reported here, other experiments were made by using slotted baffles of 30% free area and tube baffles of 2.5 to 10% free area. These results do not alter the foregoing conclusions but indicate that the 15% slotted tray may be near the best design from the standpoint of residence-time distribution and allowable velocities.

In most of the gas residence-time measurements the tracer was displaced from the bed, as determined by integration of the retention-time curve, was usually about 10% greater than that calculated to be present at zero time. This is evident in Figures 1, 3, and 4 in that the experi-

over a 1-ft. interval as a function of gas velocity through the baffle opening. It is evident that the flow of interstitial gas through the baffle becomes nil at restriction velocities of 6 to 10 ft./sec.

SOLIDS RESIDENCE TIME

In most fluid-bed processes there is a net flow of solids through the process vessel. In addition to this net flow, secondary flow patterns arise from the action of the bubbles. In the compartmented bed, solids are entrained by the rising gas into the next higher compartment; solids also flow down by gravity into the next lower compartment. In the authors' system of designation the net flow of solids is the difference between the gross flow in the same direction and a back flow (called *intermixing*) in the opposite direction. In concurrent operation reported here entrainment between the compartments is the gross flow, and

are summarized for 4.7 and 14.5% free-area tube trays in Figure 8. The maximum solids downflow rate occurs at 4 to 7 ft./sec. constriction velocity. Lower velocities apparently result in a loss in catalyst fluidity; higher velocities load the openings with entrained solids, thus lowering the downflow rate.

The solids intermixing rate in countercurrent flow was determined by use of a radioactive tracer. A pulse of 20 g. of equilibrium catalyst, tagged with gold-198, was injected into the middle of the five-compartment bed, and the change of radioactivity concentration with time was followed in all compartments (by sample withdrawal at 15-sec. intervals). Gold-198 is a β and γ emitter with a half-life of 2.7 days. Its use permitted several experiments in a relatively short time without raising the background radioactivity of the catalyst inordinately. Lack of long-term contamination allowed continued use of the inventory catalyst.
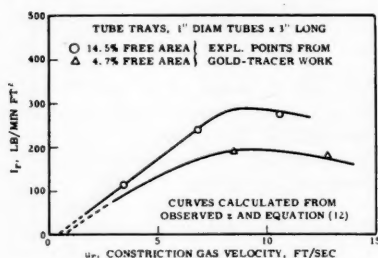
Fig. 10. Solids intermixing, zero net-solids flow.
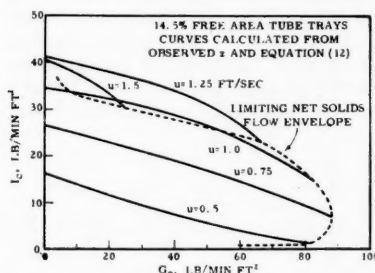
Fig. 11. Effect of solids net flow on intermixing.
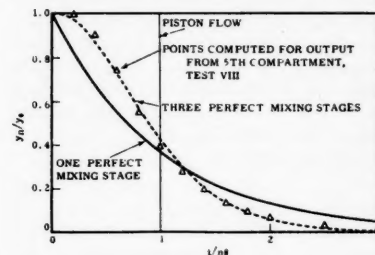
Fig. 12. Distribution of solids residence times, 14.5% free-area tube trays.

mental points usually lie to the right of the calculated curves; the cause of this phenomenon was not determined.

GAS BACK-MIXING

In the steady-state–gas backmixing runs gas samples were withdrawn at a low flow rate for long time periods, and so the samples were more likely to represent the interstitial volume rather than the rapidly moving bubbles. Results of typical runs are shown in Figures 6 and 7. Figure 6 shows that the concentration of helium tracer is relatively uniform throughout the unbaffled bed and within a compartment but that the concentration drops sharply across the baffles. This suggests that the solids mix freely in unbaffled regions but that their flow through the baffle is impeded. The magnitude of the latter effect will be shown in a later section. For the 16-in. unbaffled column typical values of the effective gas-diffusion coefficient are 3 to 6 sq. ft./sec., which corresponds to a Peclet number (uL/D_e) of 1 to 2 when bed length is 6 ft. The coefficients increase with velocity but not proportionally; therefore the Peclet number increases with increasing velocity.

Figure 7 shows the concentration ratio

the entrainment out the top of the column is the net flow; in countercurrent operation the entrainment between compartments is the intermixing flow. For the case of zero net flow the gross and intermixing flows are of course equal.

In much of this study (the work on gas residence time, compartment density, and entrainment at the top of the column) the column operated with a small net upflow resulting from the external entrainment being returned to the base of the column. For this condition the residence-time distribution and intermixing rate of solids were not determined. For countercurrent operation, however, solids net-flow rate, intermixing rates, and residence-time spectra were studied in some detail. Although both grid and tube trays were used in the concurrent studies, the countercurrent experiments were done exclusively in tube-tray baffles, because of the need for low-area baffles demonstrated by the early study and the fabrication advantage of the tube tray in cases of low free area.

The limiting solids net-flow rates in countercurrent operation were determined as a function of gas velocity by slowly increasing the withdrawal rate until a steady level could no longer be maintained in the lower compartments. These results

Samples were counted in a well type of scintillation counter described elsewhere (6).

In the first runs multiple samples were taken from each compartment. When these were found to be identical because of the intense mixing action, subsequent tests were made on the basis of one sample per compartment.

The amount of solids internal recycle was determined by solving the set of simultaneous differential Equations (9) to (11), which describes the transient change of radioacitvity concentration in each of the compartments. The best solutions, obtained on a Goodyear Electronic Data Analyzer analogue computer, indicated a different degree of solids intermixing between stages, with a greater exchange across the upper baffles. It is believed that momentary fluctuations in inventory can readily occur in the upper compartments, since the solids level in the top compartment is not constrained but that these same fluctuations are severely dampened in the lower compartments. Average values for the interchange rates are indicated in Table 3. On the basis of the individual intermixing rates and the observed dilute zone heights existing under each baffle the following correlation was developed:

$$I_c = 78e^{-0.064gz/u^2} \qquad (12)$$

This correlation, shown in Figure 9, is comparable in form to entrainment correlations arising with other types of baffles.

This correlation was then used to estimate the solids intermixing rates from the observed dilute zone heights at other gas- and net-solids–flow conditions. The data and calculated curves are shown in Figures 10 and 11. Figure 10 illustrates the degree of intermixing at no net solids flow; figure 11 shows the calculated effect of net-solids flow rate on intermixing, with superficial gas velocity as parameter. Apparently intermixing increases almost linearly with increasing gas velocity until the higher gas rate limits the solids downflow and consequently the entrainment. The correlation for intermixing presented in Equation (12) is not necessarily valid for other systems, and its usefulness is limited in

of perfect mixers for various conditions of net and intermixing flows. In the construction of this relationship the two cases are examined in terms of the variance in the solids residence-time distribution. The required Laplace transformations are handled in the same manner as this author's treatment of longitudinal mixing in various flow regimes (8). The resulting equation is

$$\frac{N}{n} = \frac{(1 - x)^2}{1 - x^2 - \dfrac{2x}{n}(1 - x^n)} \qquad (13)$$

where

$$x = I/(G + I)$$

In the case of test VIII

$$x = \frac{I}{G + I} = \frac{26.5}{58 + 26.5} = 0.314$$

For $n = 5$ compartments $N/n = 0.6$ from Figure 13, or $N = 3$. This close

density is about equal to that of the bed at incipient fluidization. As the gas velocity increases, the volume ratio of bubble phase to dense phase increases, and so the average bed density decreases. Measurements in the 16-in. column for bed heights of about 6 ft. and gas velocities of 0.01 to 3 ft./sec. show that average bed density obeys the relationship

$$\rho = 53.5 - 4.2u \text{ lb./cu. ft.} \qquad (14)$$

This relation is based on the mass of solids within the bed and the height of the dense bed estimated visually or from pressure profiles.

When baffles are present in a fluid bed, the system is complicated by the appearance of dilute zones under the trays. Figure 14 shows typical pressure profiles and the existence of dilute zones in a compartmented bed. These profiles represent the axial gradient of pressure measurements at the column wall. Since the pressure drop over a length of bed
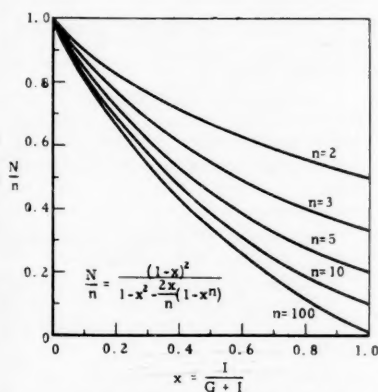
Fig. 13. Relation between number of stages and degree of intermixing.

Fig. 14. Pressure profiles in compartmented bed.

Fig. 15. Effect of baffles on solids entrainment with exit gas.

that the dilute zone height cannot be determined accurately. However use of the Froude number may be helpful as a correlating parameter for extending meager data for some other system.

The distribution function for solids residence times may be calculated from the analogue solutions of the gold-tracer experiments or generated directly on the analogue computer. An example of the staging that can be accomplished despite the solids intermixing is depicted in Figure 12. The points shown are the calculated values of C_n following a step function change in C_1 by using Equations (9) through (11), with individual W_i's from test VIII, and setting $WC_n = 0$ in Equation (9). The curves shown are for one, three, and infinite theoretical stages.

For the general case of the reduction in staging due to intermixing, it is convenient to refer to a plot prepared by van der Laan (7) and reproduced here as Figure 13. This plot shows the relation between n actual compartments with back-mixing and the equivalent number

agreement is indicated in Figure 12 between the calculated data and theoretical curve for three perfect-mixing stages. Thus a knowledge of the degree of solids intermixing permits determination of the number of compartments required to assure a given number of mixing stages. If the net solids downflow rate is low, a baffle design must be selected which will keep intermixing (entrainment) to a minimum.

OTHER STAGED-BED PHENOMENA

In the course of obtaining these data other characteristics of a staged fluid bed were observed. Installation of a baffle causes the formation of a dilute zone, the height of which is determined by the dynamic balance between solids downflow and solids entrainment. The presence of the dilute zone thus lowers the over-all compartment density. A detailed discussion of the effects of baffles on entrainment and compartment density follows.

Fluid-Bed Density

The fluidized bed is composed of a bubble phase of low catalyst density and a dense or interstitial phase, where
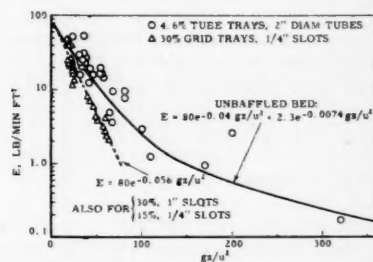
is equal to the weight of catalyst suspended, the slopes of the pressure profile are equivalent to bed density. The average density in the compartmented bed depends on the relative heights of dense and dilute zones and the density of the former. The dense-phase density probably changes with velocity in about the same manner as in the unbaffled column. The height of the dilute zone is fixed by the entrainment equation (12) for the entrainment rate and gas velocity prevailing. Thus this height will be a function of net-solids flow rate only if the net flow is large with respect to the entrainment. In most of the concurrent work the net flow rate was probably much smaller than the entrainment between compartments. Consequently, except in the case of low free-area trays, solids net-flow rate has little effect on compartment density. Equations for the average over-all compartment density as a function of superficial gas velocity at small, concurrent solids flow rates are listed in Table 4. For high, concurrent solids flow rates the densities will be higher than, and for countercurrent flow of solids the densities will be slightly lower than, those indicated by Table 4.

The effect of tray spacing was not studied in detail. From visual observa-

TABLE 4. COMPARTMENT DENSITY, WITH GRID BAFFLES

Baffle				Average compartment density, lb./cu. ft.
Free area, %	Slot width, in.	Baffle spacing, in.	Thickness, in.	$\rho =$
30	1	24	$\frac{1}{8}$	$53.5 - 12u$
30	1	24	1	$53.5 - 13u$
30	$\frac{1}{4}$	24	$\frac{1}{8}$	$53.5 - 16u$
30	$\frac{1}{4}$	8	$\frac{1}{8}$	$53.5 - 23u$
15	$\frac{1}{4}$	24	$\frac{1}{8}$	$53.5 - 18u$

tion it is concluded that the dilute zone existing at any other tray spacing will vary between a constant height and a constant percentage of the tray spacing at the same gas velocity. In Figure 14, which is for concurrent flow, it is apparent that the dilute zone height is greater under the top tray than under the lower trays. With countercurrent flow the opposite was observed; that is, the greatest dilute zone height was under the lowest tray, a situation consistent with the intermixing rates determined in the gold-tracer test. Size classification of solids was detectable only with the 2.4% free-area trays and then only to the extent of a several-micron difference in average size between adjacent compartments.

Solids Entrainment with Exit Gas

Solids entrainment into the 3-in. exit line was measured as a function of disengaging height and superficial gas velocities up to 2 ft./sec. In these measurements the disengaging section was the same diameter (16 in.) as the column, and the solids entrainment rate was estimated from the pressure drop in the calibrated exit-line nozzle. As shown in Figure 15, the rate of entrainment is either reduced or unaffected by the baffles, depending on the local velocities produced. In the unbaffled bed there is a tendency for the gas to flow at a high velocity up the center of the column rather than uniformly over the cross section. The 15 and 30% free-area baffles lower entrainment by distributing the gas flow over the column cross section. With the low free-area (2.5 to 10%) tube trays the gas flow is redistributed but into jets of high entraining power.

This comparison of baffled and unbaffled operation was made at short disengaging heights (2 to 5 ft.), where entrainment is correlated by equations similar to Equation (12). Larger disengaging heights (up to 8 ft.) were tested in the unbaffled column; in this region, as the decline of entrainment with height is less rapid, two exponential terms are required for empirical correlation of the data. At the greater heights (15 to 30 ft.) used in commercial catalytic-cracking units catalyst density has been determined by others using gamma-ray attenuation. These data indicate entrain-

ments an order of magnitude larger than the entrainment predicted by the 16-in. open-bed correlation. The increased entrainment in the commercial units may be due partly to the very high local velocities resulting from gas maldistribution in large beds.

DISCUSSION AND CONCLUSIONS

The data discussed here are typical of the information which one must obtain to assess the potentialities of baffled fluidized beds for specific process applications. Thus one must have information on the residence-time distribution, allowable velocities, entrainment rate, and mixture density as a function of baffle design, in order to estimate the most suitable vessel configuration. Additionally one should know the chemical kinetics and the mass and heat transfer rates between gas and catalyst, if pilot-scale process data are not available.

The results presented herein demonstrate that

1. Because extensive solids and gas mixing occur in unbaffled fluidized beds, the residence-time distributions approximate a well-mixed stage. The spread in residence times may be effectively narrowed by the use of baffles, although not to the extent corresponding to an equivalent number of perfect-mixing stages in series.

2. A zone of low catalyst density appears under the baffles which lowers the over-all density in the compartment and limits the closeness of baffle spacing.

3. Solids downflow through the baffle is a function of gas velocity through the restriction and is a maximum at gas velocities of 5 to 7 ft./sec. for this system.

4. Solids entrainment between compartments and from the top of the bed is exponentially related to the Froude group. Under some conditions entrainment from the top of the bed is reduced by the presence of baffles.

ACKNOWLEDGMENT

The authors wish to acknowledge the contributions of A. E. Handlos, R. W. Kunstman, Mrs. D. K. Lidtke, M. E Stromsmoe, and J. J. Sutfin.

NOTATION

C = tracer concentration of solids, counts/(min.)(lb.)

D_e = effective diffusion coefficient, length²/time

E = entrainment rate, mass velocity, lb./(min.)(sq. ft.)

f = parameter in Equation $(5a, b)$

G = net-solids feed rate, mass velocity, lb./(min.)(sq. ft.)

g = acceleration of gravity, ft./sec.²

I = solids intermixing mass velocity between compartments, lb./(min.)(sq. ft.)

L = distance between sample points (where the radial average concentrations y_0 and y are measured), bed length, ft.

m = mass of solids contained in compartment, lb.

N = number of perfect-mixing stages (no intermixing or by-passing)

n = number of compartments

p = pressure, in. of water

q = volumetric gas feed rate, cu. ft./sec.

r = volumetric transfer rate of gas between bubble and interstitial phase, cu. ft./sec. of flow in (or out) of each well-mixed interstitial phase

t = time

u = superficial gas velocity, ft./sec.

u^2/gz = Froude number based on the superficial gas velocity

V = volume of bubble phase, cu. ft.

v = volume of interstitial gas phase, cu. ft.

W = solids net mass feed rate, lb./min.

w = solids intermixing mass flow rate, lb./min.

x = $I/(G + I)$

y = tracer gas mole fraction

z = solids disengaging distance above dense bed, ft., dilute zone height in a compartment

Greek Letters

ϵ = fraction of gas not by-passing

θ = residence time per stage

ρ = density of gas-solids mixtures, lb./cu. ft.

Subscripts

$1, 2, 3$ = sequence of stages

0 = initial or reference value

b = bubble phase

c = column cross-sectional area

g = gas

n = nth stage

r = constriction (open area of baffle)

Superscripts

$-$ = average value

LITERATURE CITED

1. Baron, Thomas, and R. A. Mugele, unpublished paper.
2. Gilliland, E. R., and E. A. Mason, *Ind. Eng. Chem.*, **44**, 218 (1952).
3. ———, and R. C. Oliver, *ibid.*, **45**, 1177 (1953).
4. Handlos, A. E., R. W. Kunstman, and D. O. Schissler, *ibid.*, **49**, 25 (1957).
5. Singer, Emanuel, D. B. Todd, and V. P. Guinn, *ibid.*, **49**, 11 (1957).
6. Todd, D. B., and W. B. Wilson, *ibid.*, **49**, 20 (1957).
7. Van der Laan, E. T., Koninklijke/Shell Laboratorium, Amsterdam, private communication.
8. ———, *Chem. Eng. Sci.*, **7**, 187 (1958).

Sublimation from Sharp-edged Cylinders in Axisymmetric Flow, Including Influence of Surface Curvature

WILLIAM J. CHRISTIAN and STOTHE P. KEZIOS

Illinois Institute of Technology, Chicago, Illinois

An experimental investigation was performed on the mass transfer by sublimation from the outer surfaces of hollow naphthalene cylinders, 0.75 and 1.00 in. in diam., in parallel air streams at velocities between 20 and 120 ft./sec. Local mass transfer rates on the cylinders were obtained by a profilometric technique consisting of accurate determinations of changes in radii of the subliming surfaces at points along elements of the cylinders.

Local coefficients of mass transfer obtained with laminar boundary layers for Reynolds numbers (based on axial length) between 12,000 and 100,000 were found to be up to 8% greater, because of surface curvature, than corresponding values for flat surfaces. Moreover comparison of the mass-transfer data with a theoretical prediction for laminar skin friction on circular cylinders indicates an effect of surface curvature on the Chilton-Colburn anology between momentum and mass transfer amounting to as much as 6% in the range of air velocity employed. For turbulent boundary layers obtained by artificial triggering of turbulence at the leading edges of the cylinders no effect of surface curvature was found. The results obtained for Reynolds numbers of 40,000 to 1,000,000 are lower than previously published correlations of turbulent heat, mass, and momentum transfer, when compared by the Boelter, Martinelli, and Jonassen form of the analogy.

Theoretical and semiempirical studies dealing with the influence of transverse curvature on axially symmetric laminar and turbulent boundary layers have appeared in the literature (1 through 11) for the specific case of the circular cylinder. These analyses have been based on an idealized model, with walls of zero thickness, which admits flow through its center without disturbance of the external field at the leading edge. Whereas the results of experimental investigations with cylinders oriented axially with the flow have been published (2, 4, 12 through 15), experimental information on transport processes (momentum, heat, and mass) for the particular case of the sharp-edged cylinder in axisymmetric flow apparently does not exist.

In this investigation experimental data were obtained for a transport process at the surface of a cylinder which simulates the ideal model. In this connection experiments based on any of the three transport processes usually employed, namely momentum, heat, and mass transfer, are possible. Since there is flow on the inside as well as the outside of such a model, it would be extremely difficult, if at all possible, to determine the skin friction at the outer surface by direct force measurements. Moreover the alternative method of finding the skin friction by probing the boundary layer along the outer surface is unattractive because of unduly delicate instrumentation and fine techniques. Likewise a heat transfer model would present the usual problems of insulation

William J. Christian is with the Armour Research Foundation, Chicago, Illinois.

TABLE 1—DIMENSIONS OF HOLLOW SUBLIMATION MODELS IN INCHES

Dimension	Model 1	Model 2
Outside diameter*	0.998	0.749
Inside diameter	0.625	0.432
Over-all length	26.0	18.2
Active length	20.0	11.3
Starting length	0.127	0.129

*Tolerance: model 1, +0.010, −0.000 in.; model 2, +0.005, −0.000 in.

and guard heating, particularly near the sharp leading edge.* Therefore a study based on the mass transfer phenomenon presents the least difficult experimental approach and was used in this work. Several years' work in the Illinois Institute of Technology Heat Transfer Laboratory with sublimation of organic solids, particularly naphthalene, has demonstrated the utility of this technique.

APPARATUS AND TECHNIQUES

Models

The hollow sublimation models consist of sharp-edged metal tubes over which layers of naphthalene were cast (Figure 1). Table 1 shows the important dimensions of of the two cylinders employed. The sharp leading edge of each cylinder is formed by a 60-deg. conical inlet at the nose. To provide permanent (nonsubliming) leading edges and to maintain finite naphthalene thicknesses at the forward edges of the

*The leading edge of the hollow cylinder may be likened to the usual conception of the sharp leading edge of a flat plate. In realty the flat plate is a special kind of cylinder for which the radius of curvature is infinitely large.

subliming surfaces, metal sections (hydrodynamic starting sections) about ⅛ in. long were used ahead of the naphthalene on both cylinders. Molds for casting the naphthalene layers on the metal tubes were made from dental plaster by using polished, stainless steel cylinders as master patterns.

A small naphthalene cylinder light enough to weigh on an analytical balance was used to compare the true weight loss by sublimation to the weight loss determined from surface profile measurements. This cylinder is 1 in. in diameter and about 4 in. long with an approximately spherical metal nose.

A hollow cylinder made entirely of metal was used to study pressure distributions for flows over the experimental models. This pressure model simulates the 1 in. sublimation model in all dimensions except its length, which is 12 in. Pressure taps (a total of sixteen) distributed over its exterior consist of $\frac{1}{32}$ in.-diameter holes drilled at right angles to the surface and so located around the cylinder that no tap is immediately downstream of any other.

The models are shown in Figure 2 along with one half of each mold used for casting the naphthalene. From left to right they are: the 1-in. sublimation model, the 1-in. pressure model, the ¾-in. sublimation model, and the hemispherically capped sublimation model.

Flow Facility

The air stream used was produced in an open-circuit, induced-draft wind tunnel shown schematically in Figure 3. Its diameter is 48 in. at the inlet and 12 in. at the throat; the length of the test section is 36 in., and the over-all length of the tunnel is approximately 20 ft. Turbulence-damping screens and the large nozzle-contraction ratio (16 to 1) favor low turbulence in the test region. The velocity of air in the unobstructed test section is constant within 2% in the central 10 in. of the throat over its entire length.

As shown in Figure 3, the tapered socket supporting the models is connected to a short length of pipe which is suspended within the diffuser by six steel wires. Connection is made from this pipe through an orifice flow meter to a vacuum tank for exhausting air through the center of the hollow models. The required vacuum pressures of up to 3 lb./sq. in. were maintained in the tank by a rotary-lobe type of blower.
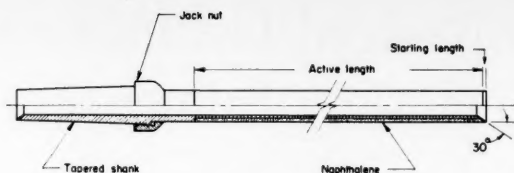
Fig. 1. Details of hollow cylinders.

Surface Profilometer

Material losses and hence sublimation rates for the naphthalene cylinders were obtained from precise measurements of changes in radii at a number of points along the surface. These measurements were made by using a micrometer dial indicator while the cylinders were held between centers of a 42 in.-long lathe bed. The indicator is mounted on the lathe carriage to provide for axial movement along the cylinders; it is graduated in 0.0001 in., and its reading may be estimated within about 0.00002 in. Contact of the indicator with the top surface of the cylinder is made through a $\frac{1}{16}$-in.-diam. tip, the working end of which is rounded to a $\frac{3}{16}$-in. radius. To minimize loss of naphthalene during measurement of the cylinders the apparatus is housed in an enclosure with the atmosphere essentially saturated with naphthalene vapor.[*] Provision is made for external control of the position of the indicator.

Indicator readings were obtained at a number of stations along each cylinder before and after exposure to the air stream. To minimize marring of the naphthalene, the indicator tip was raised from the surface (by using a solenoid) while positions were changed. Clearly the difference in indicator readings at each station is a direct measure of the local mass transfer. Measurement of the axial position of each station with respect to the leading edge of the cylinder was obtained from the number of revolutions made by the lead screw and its pitch.[†]

Values of the change in radius of the naphthalene cylinders were obtained for four circumferential positions at each axial station; these values were within 5% of their arithmetic average, which was used in all cases for determining the local mass transfer at each position along the cylinders.

Temperature Measurement

The vapor pressure–temperature relationship for naphthalene, which follows the Clausius-Clapeyron form, requires an accuracy of 0.1°F. in temperature measurement if the vapor pressure is to be known within 1%. This accuracy was sought in this work.

Direct measurement of the surface temperature of the solid, which would be complicated because of the continuous removal of surface material through sublimation, was not employed in this work. Instead only the temperature of the air
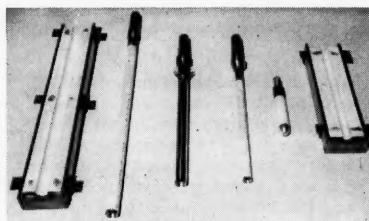

Fig. 2. Experimental models.

stream was measured by using a calibrated copper-constantan thermocouple located 3 in. downstream of the subliming surfaces, $1\frac{1}{2}$ in. above the cylinder axis. Surface temperatures of the cylinders were within the required 0.1°F. of the indicated air temperatures, since aerodynamic heating[*] and surface-temperature depression[†] due to sublimation were negligible in the range of variables employed.

Physical Properties

Air densities were calculated according to the ideal-gas law with the usual value of 0.0808 lb./cu. ft. used for the density at standard conditions (32°F., 1 atm.). Values of the kinematic viscosity were taken from a compilation of air properties published by Jakob (16 and 17).

In the absence of reliable data on the diffusion coefficient for air and naphthalene vapor. Gilliland's semiempirical correlation (18) was employed. Introduction of appropriate constants in Gilliland's equation results in the following relation for air-naphthalene mixtures:

$$\delta = \frac{20.25T^{\frac{3}{2}}}{p} \quad (1)$$

Here δ is in sq. ft./hr., T in °R., and p in atm.

The specific gravity of solid naphthalene seems to be available at only two temperatures (19), 62.6 and 68.0°F. Extrapolation to higher temperatures was carried out on the assumption of a linear temperature dependence, namely

$$\rho_s = 82.42 - 0.1611t \quad (2)$$

Density is given in pounds per cubic foot by Equation (2) with temperature t in degrees Fahrenheit.

The literature on vapor pressure of solid naphthalene has been reviewed by Kezios (20), who also obtained vapor-pressure data for a grade of naphthalene comparable to that used in the present work (Baker's C.P.). His results[*] and those of others (21, 22) which appear to be mutually consistent have been used here to determine a vapor pressure-temperature relationship. The data are shown in Figure 4 along with the straight line fitted by the method of least squares. The correlating equation is

$$\log_{10} p^* = 12.198 - 6{,}881/T \quad (3)$$

In Equation (3) vapor pressure is in pounds per square foot, and temperature in degrees Rankine.

FLOW AND PRESSURE DISTRIBUTION

The ideal sharp-edged cylinder which admits air through its center would have uniform pressure over its outer surface, and all stream surfaces would be circular cylinders if the external and internal flows were balanced. But in practice an exact balance of internal and external flow is difficult to maintain because of minor variations in the flow rates. The consequences of unbalance of the flows may be understood if the potential flow near the inlet of an idealized hollow cylinder is considered qualitatively (23). Figure 5, showing cross-sectional sketches of the stream surfaces for R_u greater and less than unity, depicts the two conditions of unbalance. Clearly the stagnation of the flow occurs on the inside of the cylinder for $R_u < 1$ and on the outside for $R_u > 1$, whereas it would be expected to occur just at the leading edge for the balanced situation, where R_u is unity. For both $R_u \lessgtr 1$, the stagnation stream surface must branch into two separate parts at the stagnation line, and each of these parts must follow the solid boundary, one in the upstream direction the other downstream. Theoretically the branch that moves upstream must turn through 180 deg. at the leading edge to maintain contact with the surface. Since such a sudden turn is not physically possible, the real flow is characterized by a separation at the leading edge with the formation of a burble and the generation of turbulence. Moreover the turbulence will be created on the outer surface for $R_u < 1$ and on the inner surface for $R_u > 1$. It is evident then that a laminar boundary layer can occur on the outside of the cylinder only when $R_u \geq 1$, and if a turbulent boundary layer is to be generated on the outside surface, transition of flow can be promoted by operation with $R_u < 1$.

The present sublimation experiments demonstrated that the models did indeed behave in this manner; accordingly, the nature of the boundary layer was

*In spite of this, small losses during measurement did occur. Loss rates were determined in auxiliary tests and used as a basis for correction of the main sublimation data; the maximum correction encountered was about 2.5%.

†The accuracy of the pitch was found to be 1% or better for all distances from the leading edge greater than 1 in. The screw was calibrated with a dial indicator for distances less than 1 in. from the leading edge to provide 1% accuracy in that region also.

*Though the recovery temperature of the cylinder was as much as 0.8°F. above ambient temperature in some of the experiments, the difference between the recovery (indicated) temperature of the thermocouple and that of the cylinder could not have been more than 0.05°F.

†The surface-temperature depression amounted to slightly more than 0.1°F. at places within about $\frac{3}{8}$ in. of the leading edge of the cylinder. Correction for this small effect seemed unwarranted, since the heat transfer data for this region were uncertain for other reasons, for instance the approximate correction used to account for the effect of the metal starting section.

*Kezios's data for temperatures above about 85°F. are probably somewhat high, as he himself indicated, and were disregarded here.
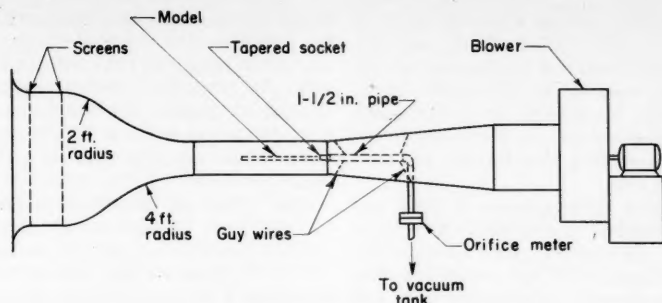
Fig. 3. Schematic of flow circuit.

controlled by proper adjustment of the velocity ratio R_u. Experimentally the value of R_u at which the transition occurs was found to be within the narrow range of 0.99 to 1.01.

To compare the test cylinders with the ideal model from the standpoint of uniformity of the velocity along the surface, pressure distributions over the outer surface were measured for various values of R_u. It was found that the pressure is essentially constant over the cylinder length for turbulent boundary layers, but that large velocity gradients occur near the leading edge (in the region of flow stagnation) for laminar boundary layers. However no influence of these gradients on the sublimation rate could be detected in sublimation experiments in which the velocity gradient was varied by altering R_u.

PRELIMINARY SUBLIMATION EXPERIMENTS

Verification of Profilometric Measurements

The small hemispherically-capped cylinder was used to check the profilometric technique gravimetrically. The total mass transfer rates obtained by the graphical integration of the measured local values were compared with direct weight-loss measurements. In every case the profilometric measurement was found to be within 2.8% of the gravimetric determination.

Effect of Velocity Ratio

Experiments with laminar boundary layers showed that variation of R_u from 1.01 to 1.25 caused no effect on the sublimation rates. The main sublimation experiments were performed in this range of R_u.

Effects of Yaw

The alignment of the models with the air stream was such that the yaw angle never exceeded 0.23 deg. The effect of such a small yaw on the mass transfer was shown to be negligible by direct sublimation experiments in which the angle of yaw was varied by 0.53 deg.

Disturbance Created at $x = x_{st}$

During sublimation a discontinuity at the juncture between the metal starting section and the subliming material was unavoidable. Experiments with laminar boundary layers established limits within which the sublimation rate was unaffected by changes in dimension of the subliming surface near its leading edge; these limits were observed in subsequent experiments.

In the turbulent-boundary-layer experiments a transient condition of the flow resulted from the gradually changing surface discontinuity at $x = x_{st}$ which caused mass transfer rates to vary continuously with time. This had to be taken into account in analyzing the turbulent-flow data.

RESULTS AND DISCUSSION

As it is usually defined, the mass-transfer coefficient is related to the local mass-transfer rate per unit area by the equation

$$\dot{m}'' = k_c \Delta c \qquad (4)$$

Since the relation of the local mass transfer rate to the rate of radius change is

$$\dot{m}'' = \rho_s (\Delta r / \Delta \tau) \qquad (5)$$

local mass transfer coefficients may be calculated from the profilometric data by the equation

$$k_c = (\rho_s / \Delta c)(\Delta r / \Delta \tau) \qquad (6)$$

In this instance the concentration difference of the vapor is virtually equal to the concentration at the surface (equilibrium concentration of the naphthalene for the prevailing temperature), since the free-stream concentration is immeasurably small. Consequently the concentration difference may be simply related to the vapor pressure of naphthalene by the ideal-gas law; that is,

$$\Delta c = c^* = p^* M / RT_s \qquad (7)$$

Correlations presented here are based on local coefficients of mass transfer calculated by using Equations (6) and (7) and on average coefficients obtained from the local values in accordance with

$$\bar{k}_c = (1/x) \int_0^x k_c \, dx \qquad (8)$$

The integral was obtained graphically from the laminar data; an empirical expression of k_c in terms of x was integrated analytically for the turbulent data.

Laminar Boundary Layer

Since the mass transfer coefficients are influenced by the presence of the metal starting section at the leading edge of the cylinder, allowance was made for this effect by analogy to the theoretical result of Bond (24) for the heat transfer through laminar boundary layers on a flat plate with unheated starting sections. According to Bond's analysis, if k_c is the measured mass-transfer coefficient and k_c' is the value of the coefficient that would exist at the same place if the starting section were replaced by subliming material, then the two are related as follows:

$$k_c' = k_c [1 - (x_{st}/x)^{\frac{3}{4}}]^{\frac{1}{3}} \qquad (9)$$
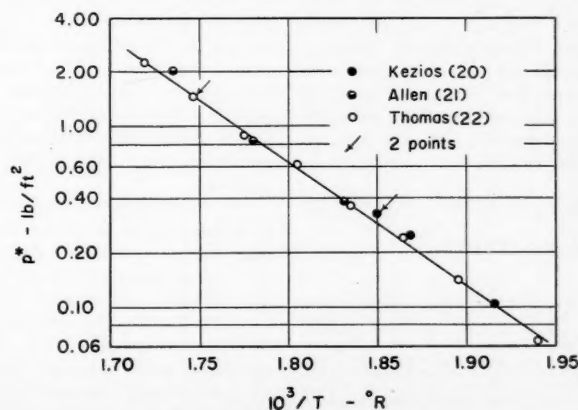

Fig. 4. Vapor pressure of naphthalene.

Any error introduced by this procedure is very small for distances from the leading edge greater than 1 in., where the magnitude of the correction is less than 7%.

Experimental results for the two cylinders with the highest range of air velocities employed (48 to 122 ft./sec.) have been correlated by the usual Sherwood-number*–Reynolds-number relationship†, as shown in Figure 6, since the effect of cylinder curvature is very small in this range of velocities. For the Reynolds number range of 4,000 to 100,000, where laminar boundary layers occurred, the data are represented by

$$N_{Sh}' = 0.454(N_{Re})^{\frac{1}{2}} \qquad (10)$$

$$\bar{N}_{Sh}' = 0.908(N_{Re})^{\frac{1}{2}} \qquad (11)$$

Maximum deviations of the data from Equations (10) and (11) are 8.0 and 3.5%, respectively, and average deviations are 2.5 and 1.6%, respectively.
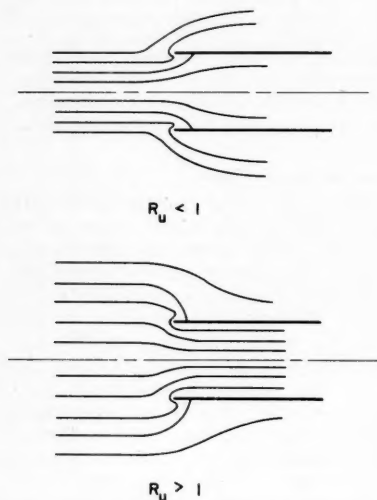

Fig. 5. Potential flow patterns for sharp-edged inlet.

For comparison of the results of Figure 6 with existing information on heat transfer and friction, it is convenient to use the Chilton-Colburn analogy, which is exact for the flat plate with small temperature and concentration differences. Reduced to the standard j-factor arrangement, Equations (10) and (11) take the form

$$j_M' = 0.339(N_{Re})^{-\frac{1}{2}} \qquad (12)$$

$$\bar{j}_M' = 0.678(N_{Re})^{-\frac{1}{2}} \qquad (13)$$

---

*Both Reynolds number N_{Re} and Sherwood number N_{Sh}' are based on total length x, the only characteristic length remaining after the condition $x_{si} = 0$ has been imposed.

†It has been suggested that this group $k_c x/\mathfrak{D}$, formerly referred to as the modified Nusselt number, be called the Colburn number. While there appears to be some justification for each of these designations, the name *Sherwood number* is employed here in conformance with the recently accepted chemical engineering terminology.

The results are thus shown to be 2.1% high compared with the Blasius equation for friction and the Pohlhausen relation for heat transfer. As shown later in the discussion of low-velocity experiments, this difference may be attributed to the effect of surface curvature on the mass transfer rate.

Previous investigations of heat and mass transfer from cylinders in axisymmetric flow have not utilized the sharp-edged model but rather cylinders with some sort of streamlined nose, and the results cannot be expected to agree with the present data. In fact the mass transfer data of Sogin and Jakob (4) for 0.37- and 1.3-in. naphthalene cylinders with inert hemispherical noses and the heat transfer data of Berman (12) for a 0.92-in. cylinder of ice with a rounded nose are generally lower than the present results at a Reynolds number of 10,000 and higher at Reynolds numbers near 100,000. Since these blunt leading edges may be expected to cause separation of the flow near the forward part of the cylinder and early transition of the boundary layer, the behavior of the results of Sogin and Jakob and of Berman can be logically attributed to the influence of the nosepieces. Their results might be expected to be low at small Reynolds numbers because of the predominant influence of the separated boundary layer, whereas the effect of early transition would cause the transfer rates to be unusually high at higher Reynolds numbers.

The heat transfer correlation reported by Jakob and Dow (2) for laminar flow over 1.3-in. cylinders with ellipsoidal and conical nosepieces is 2% lower than the present results and in excellent agreement with the exact solution of Pohlhausen for the flat plate. This agreement seems to be fortuitous however since Jakob and Dow made no allowance for the starting-length effect of their unheated nosepieces. If adjustment is

made for the starting length according to Equation (9), their correlation falls about 6% below the Pohlhausen solution and 8% below the present results. A possible explanation for this discrepancy may be a separation of the boundary layer which extended over part of the heated cylinder.

The effect of transverse curvature on the mass transfer is demonstrated by the results for low air velocities (23 to 33 ft./sec.). The data are shown in Figure 7 in coordinates suggested by the results of previous theoretical treatments. These have invariably led to expressions of the following form:

$$(f/2)/(CN_{Re}^{-\frac{1}{2}}) = \psi_f(\xi) \qquad (14a)$$

$$j_H/(CN_{Re}^{-\frac{1}{2}}) = \psi_H(\xi) \qquad (14b)$$

$$j_M/(CN_{Re}^{-\frac{1}{2}}) = \psi_M(\xi) \qquad (14c)$$

In Equation (14) $\xi + (x/r)^2(N_{Re})^{-1}$ and C must equal 0.332 if the results are to

Fig. 6. Experimental results for mass transfer from sharp-edged cylinders with air velocities between 48 and 122 ft./sec.

agree with Blasius and Pohlhausen. Accordingly the mass transfer data (adjusted to zero starting length) are shown in the form $\psi_M = j_M'/(0.332N_{Re}^{-1/2})$ as a function of the variable ξ, along with curves representing the various theoretical results. The symbols used in Figure 7 are explained by Table 2.

Curve 1 in Figure 7, found originally by Young (1) for friction, was later obtained by Jakob and Dow (2) and applied to heat transfer by using the Reynolds analogy. Jakob and Dow evaluated the momentum integral through the boundary layer on a cylinder by using Pohlhausen's fourth-power polynomial for the velocity distribution and by assuming the boundary-layer thickness to be equal to that on a plane surface. Sogin and Jakob (4) performed a more elaborate analysis of the momentum boundary layer in obtaining curve 2 by using the same boundary-layer velocity profile without any assumption of the boundary-layer thickness; they applied

their results to mass transfer in accordance with the Chilton-Colburn analogy. The high value of C compared to the Blasius equation obtained by Young, by Jakob and Dow, and by Sogin and Jakob is apparently the result of the approximate velocity profile employed. Curve 3 was obtained by Seban and Bond (3), who numerically integrated the complete boundary-layer equations of energy and motion with $N_{Pr} = 0.715$, and it represents the only existing treatment of the effect of curvature on heat transfer which does not rely on some form of the analogy to friction. Seban and Bond also obtained results for friction that were later adjusted slightly by Kelly (5) (shown as curve 4). A solution for the friction on cylinders by Glauert and Lighthill (8), also represented by curve 3, is based on the momentum-integral approach with a logarithmic velocity profile in the boundary layer and results in a constant C which is 13% below the Blasius value. Curve 5 was obtained by Sowerby and Cooke (6), who used a modified Rayleigh analogy with the exact solution for the friction in the unsteady laminar flow over an impulsively started cylinder; the same result was found independently by Cooper and Tulin (7), who integrated linearized forms of the boundary-layer equations.

All of these analyses and the present work have neglected compressibility effects. Mention may be made that a theoretical treatment of the effect of transverse curvature on the skin friction in compressible flow has been given by Probstein and Elliot (9).

The experimental results are presented in Figure 7 by curve 6, which corresponds to the least-square correlation of the functional form suggested by the theoretical expressions, namely

$$\psi_M = 1 + 1.77\xi^{\frac{1}{2}} - 9.62\xi \quad (15)$$

The maximum deviation of the data from Equation (15) is 6.7%, and the average deviation is 1.3%. Equation (15) may be written

$$j_M' = 0.332 N_{Re}^{-1}$$
$$\cdot (1 + 1.77\xi^{\frac{1}{2}} - 9.62\xi) \quad (16)$$

This equation is based on data for N_{Re} between 12,000 and 100,000 and ξ between 0.0001 and 0.005.

On the basis of Equation (16) the discrepancy of 2.1% between Equation (12) and the Blasius and Pohlhausen expressions for flat surfaces may be attributed to surface curvature. Equation (16) indicates an increase of from 0.6 to 3.0% over the flat-plate values for the range of variables represented by Equation (12). The average increase of 1.8% is in good agreement with the actual difference of 2.1%.

Comparison of the present mass transfer results with the best solution
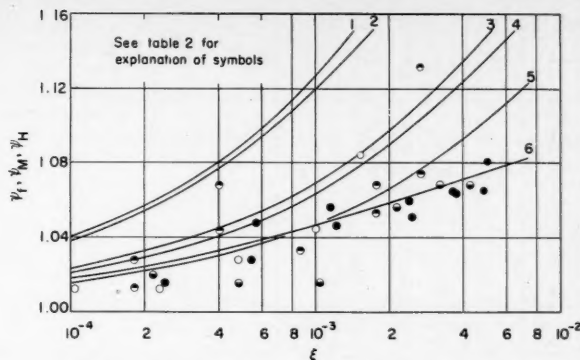
for skin friction, represented by curve 4 in Figure 7, indicates that there is an effect of surface curvature on the analogy between skin friction and mass transfer amounting to about 6% at $\xi = 0.005$. Seban and Bond have already shown theoretically that such an effect occurs for the heat-transfer–friction analogy and have evaluated it for the specific case of $N_{Pr} = 0.715$. (Compare curves 3 and 4.) It is clear from their work that a corresponding effect of surface curvature on the mass-transfer–friction analogy must exist and that the magnitude of the effect is dependent on the Schmidt number (which is analogous to Prandtl number). This dependence is however not discernible solely on the basis of the differential equations of the boundary layer; exact comparison of the present experimental results with theory must await the solution of the system of nonlinear differential equations involved.

Turbulent Boundary Layer

Turbulent-boundary-layer experiments were performed at $R_u = 0.99$ and for $u_0 = 122$ ft./sec. by using both the 3/4- and 1-in. cylinders. Under operation at $R_u = 0.99$ the stagnation line falls on the inside of the nose of the cylinder, and therefore the production of turbulence is immediate at the leading edge.

The influence on the mass transfer of the transient discontinuity created at the end of the starting section had to be considered in the analysis of the data for turbulent boundary layers. While it is practically impossible to define accurately the geometry of such a discontinuity, its influence can be indexed in terms of the magnitude of the erosion Δr_i at a prescribed position just downstream. The position selected was about 1/16 in. behind the starting section. Mass transfer rates along the cylinder were obtained for various values

Fig. 7. Comparison of experiment values of ψ_M with theoretical results for the laminar boundary layer.

TABLE 2. SYMBOLS FOR FIGURE 7

Symbol or curve number	Explanation	Source
○	$u_0 = 32.6$ ft./sec., $D = 0.998$ in.	Present
◑	$u_0 = 32.9$ ft./sec., $D = 0.749$ in.	Present
●	$u_0 = 23.5$ ft./sec., $D = 0.749$ in.	Present
◐	$u_0 = 27.4$ ft./sec., $D = 0.749$ in.	Present
1	$\psi_H = \psi_f = 1 + 4\xi^{1/2}$ $C = 0.343$	$(1, 2)$
2	$\psi_M = \psi_f = \left[\dfrac{0.1762 + 0.153B/r}{6 - B/r}\right]^{1/2} \left[\dfrac{35.0}{6 - B/r}\right]^*$ $\xi = (B/r)^2 \left[\dfrac{0.1762 + 0.153B/r}{6 - B/r}\right]^{1/2}; C = 0.343$	(4)
3	$\psi_H = 1 + 2.30\xi^{1/2} + \cdots ; C = 0.332$	(3)
3	$\psi_f = 1 + 2.31\xi^{1/2} - 2.60\xi + \cdots$ $C = 0.289$	(8)
4	$\psi_f = 1 + 2.10\xi^{1/2} - 1.92\xi + \cdots$ $C = 0.332$	$(3, 5)$
5	$\psi_f = 1 + 1.50\xi^{1/2} - 0.722\xi + 1.09\xi^{3/2} + \cdots$ $C = 0.332$	$(6, 7)$
6	$\psi_M = 1 + 1.77\xi^{1/2} - 9.62\xi$ $C = 0.332$	Least-squares correlation of present results

*The symbol B denotes boundary-layer thickness.

Fig. 8. Extrapolation of local mass transfer coefficients to zero-ridge conditions for induced-turbulence experiments.

TABLE 3. CONSTANT C AND EXPONENT n OF THE EQUATION $\bar{N}_{Sh} = C(N_{Re})^n$ FOR TURBULENT BOUNDARY LAYERS ACCORDING TO VARIOUS INVESTIGATORS

Source	Kind of work	Surface	C	n
(26)	Theo. (heat)	Plane	0.0178	0.876
(28)	Exp. (heat)	Plane	0.0330	0.849
(27)	Theo. (heat)	Plane	0.0245	0.876
(29)	Exp. (heat)	Plane	0.0226	0.876
(2)	Exp. (heat)	Cylinder	0.0196	0.876
(31)	Exp. (heat)	Plane	0.0226	0.876
(32)	Exp. (mass)	Plane	0.0273	0.872
(33)	Exp. (mass)	Plane	0.0624	0.792
(14)	Exp. (heat)	Cylinder	0.0216	0.876
Friction	Exp.	Plane	0.0342	0.837
Present work	Exp. (mass)	Cylinder	0.0109	0.910

of Δr_i from successive experiments with identical operating conditions. Then to obtain mass transfer coefficients uninfluenced by the discontinuity at $x = x_{st}$ the data were e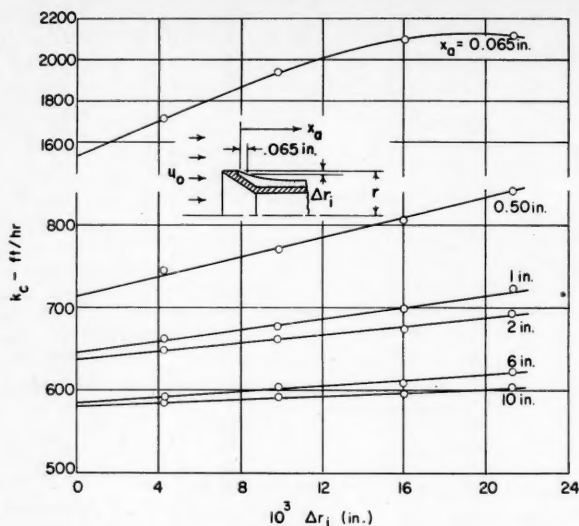xtrapolated to $\Delta r_i = 0$ (corresponding to time zero) when the naphthalene surface was continuous with the metal starting section. These extrapolated values of k_c were used in the correlations. Figure 8 is a typical plot of k_c vs. Δr_i for various axial positions along a cylinder.

The small starting-length effect of the metal nose of the cylinder was taken into account in accordance with an approximate procedure based on the empirical starting-length function defined by Tessin and Jakob (14) for turbulent boundary layers. If differentation of their expression is allowed, the relationship appropriate for adjusting the present data is*

$$k_c' = k_c[1 - x_{st}/x]^{0.09} \qquad (17)$$

As in the case of the laminar boundary layer, the magnitude of the adjustment obtained from Equation (17) is quite small, and the degree of accuracy achieved is sufficient, except near the leading edge.

The experimental results for both cylinders are presented in Figure 9; the range of Reynolds number covered is 10,000 to 1,000,000. Sherwood numbers employed there are based on values of the mass transfer coefficient reduced to zero starting length and to no surface discontinuity at the leading edge. In the Reynolds-number interval of 40,000 to 1,000,000 the data may be represented by a straight line having

$$N_{Sh}' = 0.00989(N_{Re})^{0.910} \qquad (18)$$

*That the exponent of 0.09 in Equation (17) remains unchanged in the differentiation is fortuitous; this occurs only when the exponent in Equation (18) is 0.910.
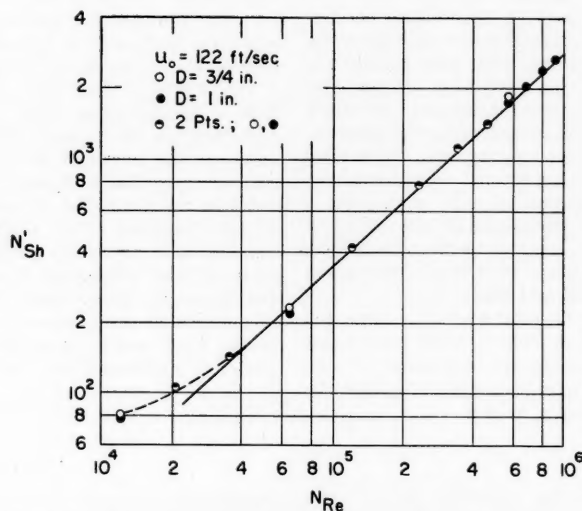
Fig. 9. Experimental results for local mass transfer from sharp-edged cylinders with artificially induced turbulence.

For comparison of the present data with the results of others it is convenient to use mean coefficients of mass transfer. The expression for the mean Sherwood number obtained by integration of Equation (18) is

$$\bar{N}_{Sh}' = 0.0109(N_{Re})^{0.910} \qquad (19)$$

It must be emphasized that Equation (19) is a form of the results which is suitable for comparison and as such is not an exact representation of the actual mean rates of mass transfer that occurred in the experiments, since Equation (18) does not hold over the entire cylinder length but fails in the vicinity of the leading edge, as can be seen from the data below $N_{Re} \cong 40,000$ in Figure 9 (dashed line). The reason

for this behavior is not completely understood, but presumably it results from some sort of transitional flow near the leading edge or from invalidity of Equation (17) in that region.

Table 3 and Figure 10 compare the present results with those from a number of previous investigations. The comparisons have been made on the basis of the Boelter, Martinelli, and Jonassen (25) form of the heat-mass-momentum–transfer analogy, all results being transformed to Schmidt number $N_{Sc} = \nu/\delta = 2.40$. The power-function representations indicated in Table 3 are close approximations to the more complicated expressions obtained by means of the analogy.

Latzko's (26) theoretical work for

turbulent heat transfer along a flat plate is well-known; it is based on the von Kármán seventh-power law for velocity distribution and is carried out for a Prandtl number of unity. Seibert (27) obtained theoretical results for the flat plate with turbulent flow by employing a modification of Prandtl's momentum theory for Prandtl numbers other than unity, according to Jakob and Dow (2). Also, the experimental results of Juerges (28) and of Parmelee and Huebscher (31) were obtained with heated flat plates, none of which had a sharp leading edge. The correlation by Colburn (29) is based on the results of Juerges (28) and those of Elias (30), who used heated plates having sharp-edged, unheated nosepieces. The form presented here is based on the results obtained by Jakob and Dow (2) after correcting Colburn's original equation to zero starting length. Maisel and Sherwood (32) and Albertson (33), on the other hand, gathered data for the evaporation of water from flat plates. The friction results are those based on the well-known expression for skin friction on a flat surface, found by employing the Blasius expression for shear stress and the one-seventh-power velocity profile. Finally the heat transfer results of Jakob and Dow (2) and of Tessin and Jakob (14) were obtained by using cylinders having unheated nosepieces of various shapes and lengths.

The present results fall below all of the others shown in Figure 10, and they are in best agreement with the theoretical work of Latzko, being 14% below Latzko's value at $N_{Re} = 40,000$ but only about 2% lower at $N_{Re} = 1,000,000$. Comparison of results obtained on cylinders only shows that transfer rates for the sharp-edged cylinder are about 13% lower than those of Jakob and Dow and about 25% lower than those of Tessin and Jakob. This is not surprising in view of the disturbing influence of the nosepieces employed in both those investigations.

Though several approaches to the solution of laminar-boundary layers on cylinders in axial flow have been possible,

one of which is apparently capable of producing exact results (3), treatment of the turbulent boundary layer has been limited to essentially one approach, based on assumptions that may not be valid. The procedure consists in evaluating the skin friction by a momentum integral with the one-seventh-power law of von Kármán assumed for the velocity profile of the boundary layer. Jakob and Dow (2) assumed in addition that the boundary-layer thickness on a cylinder is the same as on a plane surface and arrived at

$$\bar{f}/\bar{f}_p = 1 + 0.1125(N_{Re})^{-1/5}(x/r) \quad (20)$$

Landweber (10), Eckert (11), and Sogin and Jakob (4) all performed essentially the same analysis by assuming the flat-plate relation for skin friction in terms of boundary-layer thickness to be valid for the cylinder but with no restriction on the boundary-layer thickness. The results of these analyses is expressed by

$$\bar{f}/\bar{f}_p = \frac{2.41 + 0.723B/r}{(3 + B/r)^{4/5}} \quad (21)$$

$$(x/r)^{5/4}(N_{Re})^{-\frac{1}{4}}$$
$$= 1.137(B/r)^{5/4}(3 + B/r) \quad (22)$$

Eckert's results, obtained for compressible flow, reduce to Equations (21) and (22) for Mach number zero.

The uncertainty of both of these solutions for $\bar{f}/\bar{f}_p$ is suggested by the results for laminar flow presented in Figure 7. It will be noted from comparison of curves 1 and 4 in that figure that the assumption of a fourth-power polynomial for the velocity profile of the boundary layer results in an error of about 10% in ψ_f when $\xi = 0.002$. A similar sensitivity of the solution to the assumed velocity profile may be inferred for the turbulent boundary layer also, and Eckert (11) has argued convincingly that such is the case. Furthermore Chapman and Kester (15) have demonstrated that there is a significant difference between the velocity profile of the turbulent boundary layer on a 1-in. cone cylinder and on a flat plate at $N_{Re} =$

6,000,000 for supersonic flow. They also found an increase in the mean drag coefficient for subsonic flow over the cone cylinder amounting to 4%, as x/r increased from 16 to 46. For the same flow conditions, Equation (20) predicts an increase of 15%, and Equations (21) and (22) predict an increase of 1.5%; this fact suggests that the true solution for $\bar{f}/\bar{f}_p$ is intermediate to the existing theories but closer to Equations (21) and (22).

The present experimental results for turbulent boundary layers are unfortunately not sufficient to evaluate conclusively the effects of surface curvature on the mass transfer, since there seem to be no appropriate flat-plate values with which to compare. However the almost exact correspondence between data for the two cylinders (see Figure 9) suggests that the curvature effect is not large, thus favoring the result obtained by Landweber, by Eckert, and by Sogin and Jakob [Equations (21) and (22)]. At $N_{Re} = 600,000$ Equation (20) indicates a difference of over 10% between the local friction factors for the two cylinders employed here, whereas Equations (21) and (22) predict a difference of less than 1%. [Calculations by Sogin and Jakob (4) using the Boelter, Martinelli, and Jonassen (25) analogy indicate that the effect of curvature on the mass transfer with $N_{Sc} = 2.40$ is not significantly different from the effect of curvature on friction.]

The present results therefore lend some further confirmation to the result of Chapman and Kester (15), that the true effect of surface curvature on the turbulent boundary layer is close to that predicted by Equations (21) and (22). This being the case, mean coefficients of friction and heat or mass transfer should not exceed flat-plate values by more than 5% up to $(x/r)^{5/4}(N_{Re})^{-1/4} = 10$, as stated by Sogin and Jakob (4). Since this condition is not likely to occur* in practical situations, it seems safe to assume that no effect of transverse curvature exists in most instances where turbulent boundary layers occur.

CONCLUSIONS

1. Local mass transfer coefficients for subliming cylindrical surfaces made of naphthalene can be precisely determined by mechanical profilometry.

2. It is possible to eliminate boundary-layer separation and premature transition associated with the use of solid nosepieces on cylinders in axisymmetric flow by employing sharp-edged hollow cylinders with internal suction.

3. By proper adjustment of the internal flow of a sharp-edged hollow cylinder, stable laminar boundary layers can be obtained on the external surface up to

Fig. 10. Comparison of present experimental results with results of other investigators, turbulent boundary layers.

*For air flow at 100 ft./sec. over a 1-in. cylinder the value of $(x/r)^{5/4}(N_{Re})^{-1/4}$ will exceed 10 only when the cylinder is over 5 ft. long.
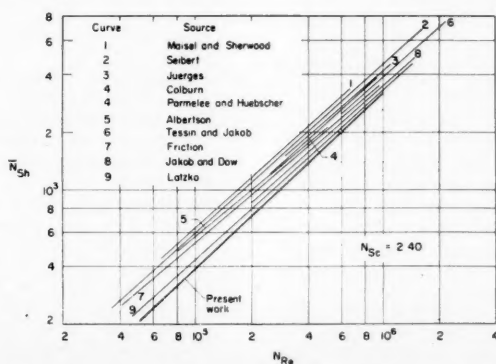
Reynolds numbers of at least 100,000 (based on axial length). Also transition to turbulent boundary layer can be made to occur at the leading edge.

4. From the viewpoint of external flow the hollow cylinders employed closely simulate the idealized model, which has walls of zero thickness and uniform free-stream velocity along its length.

5. Local mass transfer rates through laminar boundary layers on the external surfaces of the test cylinders were found to be somewhat larger than corresponding flat-plate values because of transverse curvature. Also an effect of transverse curvature on the Chilton-Colburn analogy between momentum and mass transfer is indicated.

6. No influence of transverse curvature on the mass transfer through turbulent boundary layers was evident from the limited data obtained.

7. With allowance for the effect of curvature, the experimental results for laminar boundary layer are in excellent agreement with the theoretical predictions of Blasius and Pohlhausen for flat surfaces.

8. Based on the Boelter, Martinelli, and Jonassen analogy, the experimental results for turbulent boundary layers are in good agreement with Latzko's theoretical prediction for heat transfer from flat surfaces.

ACKNOWLEDGMENT

NOTATION

B = boundary-layer thickness, ft.

$c(\Delta c)$ = concentration (concentration difference) of diffusing vapor, lb./cu. ft.

c^* = equilibrium concentration of naphthalene vapor for prevailing temperature, lb./cu. ft.

C = constant

D = diameter, ft.

f = local friction factor

$\bar{f}/\bar{f}_p$ = ratio of mean friction factor on a cylinder to that on a flat surface at equal Reynolds number

g = gravitational constant

$j_M, \bar{j}_M$ = local and average mass-transfer factors, respectively, $(k_c/u_0)(N_{Sc})^{2/3}$, $(\bar{k}_c/u_0)(N_{Sc})^{2/3}$

$k_c, \bar{k}_c$ = local and average mass transfer coefficients for air film, respectively, ft./hr.

$\dot{m}''$ = local mass-transfer rate, lb./sq. ft.

M = molecular weight of naphthalene

N_{Pr} = Prandtl number, ν/α

N_{Re} = Reynolds number, u_0x/ν

N_{Sc} = Schmidt number, ν/δ

$N_{Sh}, \bar{N}_{Sh}$ = local and average Sherwood numbers, respectively, $k_c x/\delta$, $\bar{k}_c x/\delta$

p = pressure, lb./sq. ft.

p^* = vapor pressure of solid naphthalene, lb./sq. ft.

$r(\Delta r)$ = radius (radius change) of cylinder, in., ft.

R = universal gas constant, ft.-lb./(lb.-mole)(°R.)

R_u = ratio of velocity at cylinder inlet to free-stream approach velocity (uniform distribution of internal flow over cylinder inlet assumed)

t, T = temperature. °F. and °R. respectively

u = air velocity, ft./sec., ft./hr.

x = axial distance from leading edge, in., ft.

α = thermal diffusivity, sq. ft./hr.

δ = mechanical diffusivity, sq. ft./hr.

ν = kinematic viscosity, sq. ft./hr.

ξ = $(x/r)^2(N_{Re})^{-1}$

ρ_0 = density, lb./cu. ft.

ρ_0 = air density

$\Delta\tau$ = time increment, hr.

$\psi(\xi)$ = function defined by Equation (14) and represents ratio of transfer from curved surface to transfer from flat plate

Subscripts

a = active (subliming) length

1 = local condition at outer edge of boundary layer

M = mass transfer

f = friction

H = heat transfer

0 = free-stream approach condition

s = surface or solid

st = starting length

Superscripts

$'$ (prime) = adjusted to zero starting length

LITERATURE CITED

1. Young, A. D., *Aeronaut. Research Council (Great Britain) Rept. Mem.* 1874 (1939).
2. Jakob, Max, and W. M. Dow, *Trans. Am. Soc. Mech. Engrs.*, **68**, 123 (1945).
3. Seban, R. A., and R. Bond, *J. Aeronaut. Sci.*, **18**, 671 (1951).
4. Sogin, H. H., and Max Jakob, *Heat Transfer and Fluid Mech. Inst., Preprints*, p. 5, Univ. Southern Calif., Los Angeles, California (1953).
5. Kelly, H. R., *J. Aeronaut. Sci.*, **21**, 634 (1954).
6. Sowerby, L., and J. C. Cooke, *Quart. J. Mech. and Appl. Math.*, **6**, 50 (1953).
7. Cooper, R. D., and M. P. Tulin, *David W. Taylor Model Basin, Rept.* 838 (1953).
8. Glauert, M. B., and M. J. Lighthill, *Proc. Roy. Soc. (London)*, **A230**, 188 (1955).
9. Probstein, R. F., and David Elliot, *J. Aeronaut. Sci.*, **23**, 208, 236 (1956).
10. Landweber, L., *David W. Taylor Model Basin, Rept.* 689 (1949).
11. Eckert, H. U., *J. Aeronaut. Sci.*, **19**, 23 (1952).
12. Berman, Kurt, *Trans. Am. Soc. Mech. Engrs.*, **76**, 397 (1954).
13. Powell, R. W., *Trans. Inst. Chem. Engrs. (London)*, **18**, 26 (1940).
14. Tessin, William, and Max Jakob, *Trans. Am. Soc. Mech. Engrs.*, **75**, 473 (1953).
15. Chapman, D. R., and R. H. Kester, *Natl. Advisory Comm. Aeronaut., Tech. Note* 3097 (1954).
16. Jakob, Max, and G. A. Hawkins, "Elements of Heat Transfer and Insulation," John Wiley, New York (1942).
17. Eucken, Arnold, and Max Jakob, ed., "Der Chemie Ingenieur," vol. I, part 1, pp. 69–73, Akademische Verlagsgesellschaft M.B.H., Leipzig (1933).
18. Gilliland, E. R., *Ind. Eng. Chem.*, **26**, 681 (1934).
19. "International Critical Tables," vol. I, p. 233, McGraw-Hill, New York (1926).
20. Jakob, Max, S. P. Kezios, Alexander Sinila, H. H. Sogin, and Maurice Spielman, *U. S. Air Force, Tech. Rept.* 6120, Part 5, Illinois Inst. Tech., Chicago (1952).
21. Allen, R. W., *J. Chem. Soc. (London)*, **77**, 400 (1900).
22. Thomas, J. H. G., *J. Soc. Chem. Ind. (London)*, **35**, 506 (1916).
23. Fradenburgh, E. A., and D. D. Wyatt, *Natl. Advisory Comm. Aeronaut., Tech. Note* 3004 (1953).
24. Bond, R., *Inst. Eng. Research, Univ. California*, Berkeley (March, 1950).
25. Boelter, L. M. K., R. C. Martinelli, and Finn Jonassen, *Trans. Am. Soc. Mech. Engrs.*, **63**, 447 (1941).
26. Latzko, H., *Z. angew. Math. u. Mech.*, **1**, 268 (1921); transl.: *Natl. Advisory Comm. Aeronaut., Tech. Mem.* 1068 (1944).
27. Seibert, Otto, *Jahrb.* 1938 *deut. Luftfahrforsch.*; transl.: *Natl. Advisory Comm. Aeronaut., Tech. Mem.* 1044 (1943).
28. Juerges, W., *Beih. Gesundh. Ingr.*, Reihe 1, Beih. 19, Munich and Berlin (1924).
29. Colburn, A. P., *Trans. Am. Inst. Chem. Engrs.*, **29**, 174 (1933).
30. Eliás, Franz, *Z. angew. Math. u. Mech.*, **9**, 433 (1929); **10**, 1 (1930); transl.: *Natl. Advisory Comm. Aeronaut., Tech. Mem.* 614 (1931).
31. Parmelee, G. V., and R. G. Huebscher, *Trans. Am. Soc. Heating and Ventilating Engrs.*, **53**, 245 (1947).
32. Maisel, D. S., and T. K. Sherwood, *Chem. Engr. Progr.*, **46**, 131 (1950).
33. Albertson, M. L., *Heat Transfer and Fluid Mech. Inst., Preprints*, 243, Stanford Univ., Stanford, Calif. (1951).

Theoretical Plate Concept in Chromatography: Part II

A. S. SAID

College of Physicians and Surgeons, Columbia University, New York, New York

Part A of this paper is essentially a continuation of a previous paper on the theoretical plate concept in chromatography (4). It deals with some special cases of eluting conditions and zone shapes. A more general equation, which combines both elution and deposition, is derived, and methods for approximating a continuous zone by means of a discontinuous one are discussed.

Part B discusses the effect of the finite size of samples and the dead free volume at the bottom of the column on the shape of elution curves. The effect of representative sample volumes is calculated, and the deviation between the experimental and the true elution curves is illustrated.

A simple expression for the number of theoretical plates utilizing the ratio between the maximum concentrations at the top and bottom of the column is derived and corrected for the effect of the finite size of samples.

PART A

In a previous paper (4) the theoretical plate concept in chromatography was treated on the basis of continuous flow of eluant through the plates of the column. Deposition and elution equations were derived for important cases from the practical point of view. One more case of particular theoretical interest is that in which during the elution process the eluant entering the column contains the solute at a certain constant concentration, and so the process is really a combination of elution and deposition. The derived equation can be considered as a general elution-deposition equation from which both the general elution and the deposition equations can be deduced as two special cases. This general case also has practical applications, especially when enrichment rather than complete separation is required and the eluant or one or more of the components to be separated are valuable, as in the case of the separation of uranium isotopes. In such cases it is sometimes more economical to recycle a portion of the effluent which might contain one or more of the solutes at a certain small and constant concentration. A hypothetical flow sheet is shown in Appendix 1 through 6.*

Three cases of an initial zone shape have been treated previously: case 1, where the zone occupies only one plate (1, 2, 3, 4); case 2, where the zone is deposited evenly on a finite number of plates (2, 4); and case 3, where an actual zone is deposited at the top of the column with the assumption that the total number of plates during deposition is the same as it is during elution (4). The total number of plates in the column depends on many variables, especially the nature of the eluant, temperature, and flow rate. The first two factors can be made the same during the two proc-

esses; yet it is not always convenient to make the two rates of flow during deposition and elution equal. Since the flow rate during deposition is usually less, or can conveniently be made less, than the rate of flow during elution, a column will contain a larger number of theoretical plates during the former than during the latter process. If the ratio between the number of plates during deposition and that during elution is λ, then the initial distribution in reference to the column during elution will be $R_n{}^0 = P_{\lambda n}{}^{\lambda u_0}$, and if one substitutes this value in the general elution equation, it will be very difficult if not impossible to obtain an analytical solution. Therefore the initial concentration on each plate will have to be calculated and substituted in the general elution equation

$$y_n = \sum_{r=1}^{n} y_r{}^0 \phi_{r-1}{}^u$$

Since when u_0 is a large number the calculations will be tedious, the initial distribution is approximated by an even distribution ($\lambda = \infty$) if λ is large enough ($\lambda > 10$), or by the Poisson distribution $R_n{}^0 = P_n{}^{u_0}$, (i.e. $\lambda = 1$) if λ does not differ much from 1, $(1.1 > \lambda > 0.9)$. For other values of λ one can replace $P_{\lambda n}{}^{\lambda u_0}$ by a discontinuous distribution made up of a series of uniform zones averaged over the actual zone such that the total amount of solute in both the actual and discontinuous zones is the same. An analytical expression is possible for such a zone, and the larger the number of steps in the discontinuous zone the better the approximation but the more elaborate the calculations. For $\lambda > 1$ a less elaborate but fairly satisfactory approximation is to replace the initial distribution $P_{\lambda n}{}^{\lambda u_0}$ by a zone made up of two parts: a uniform zone consisting of n_1 plates with solute concentration ratio equal to unity, followed immediately by a zone having the concentration distribution $P_n{}^{u_1}$ such that $n_1 + u_1 = u_0$. This distribution also yields an analytical

expression, and the ratio u_1/n_1 is determined according to a formula derived on the basis of theoretical reasoning.

Derivation of the General Elution-Deposition Equation

The only difference between this case case and the general elution case treated in the previous paper (4) is that here the eluant contains the solute at a certain constant concentration $\bar{y}_0$ before entering the column.

A material balance around plate 1 gives

$$k(y_0 - y_1)\, dx = dy_1$$

Integrating and substituting the boundary condition $y_1 = y_1{}^0$ when $x = 0$ one gets

$$\frac{y_0 - y_1}{y_0 - y_1{}^0} = e^{-kx} = e^{-u}$$

$$\therefore \quad y_1 = y_0(1 - kx) + y_1{}^0 e^{-kx}$$

By means of a differential material balance around plate 2 one can show that

$$y_2 = y_0[1 - e^{-u}(1 + u)] + y_1{}^0 e^{-u}u + y_2{}^0 e^{-u}$$

Continuing to plate n one finds that

$$y_n = y_0 P_n{}^u + \sum_{r=1}^{n} y_r{}^0 e^{-u}\frac{u^{n-r}}{(n-r)!} \quad (1)$$

which is the general elution-deposition equation.

It is evident that by substituting $y_0 = 0$ in this formula one obtains the general elution equation and that by substituting $y_r{}^0 = 0$ the equation reduces to the deposition equation.

Elution of an Initially Discontinuous Zone

Any discontinuous zone can be treated during its elution by applying the general elution equation to it, but only a few cases will lead to simple analytical expressions. Two such cases which are also of practical interest are treated in this paper.

1st Case: a Series of Uniform Zones

$$
\begin{aligned}
y^0 &= y_1{}^0 \cdots & 1 \le n \le n_1 \\
y^0 &= y_{11}{}^0 \cdots & n_1 < n \le n_2 \\
&\vdots \\
y^0 &= y_i{}^0 \cdots & n_{i-1} < n \le n_i
\end{aligned}
$$

By substitution in the general elution equation

$$y_n = \sum_{r=1}^{n} y_r{}^0 e^{-u} \frac{u^{n-r}}{(n-r)!}$$

$$\therefore y_n = \sum_{r=1}^{n_1} y_I{}^0 e^{-u} \frac{u^{n-r}}{(n-r)!}$$

$$+ \sum_{r=n_1+1}^{n_2} y_{II}{}^0 e^{-u} \frac{u^{n-r}}{(n-r)!}$$

$$+ \cdots + \sum_{r=n_{j-1}+1}^{n_j} y_j{}^0 e^{-u} \frac{u^{n-r}}{(n-r)!}$$

$$= y_I{}^0 (P_{n-n_1}{}^u - P_n{}^u)$$

$$+ y_{II}{}^0 (P_{n-n_2}{}^u - P_{n-n_1}{}^u) \qquad (2)$$

$$+ \cdots + y_j{}^0 (P_{n-n_j}{}^u - P_{n-n_{j-1}}{}^u)$$

so that if $y_I{}^0 = y_{II}{}^0 = \ldots = y_j{}^0 = y^0$
Equation (2) reduces to

$$\frac{y_n}{y^0} = P_{n-n_j}{}^u - P_n{}^u$$

2ND CASE: A UNIFORM DISTRIBUTION FOLLOWED BY A POISSON DISTRIBUTION

$$y^0 = y_I{}^0 \qquad \cdots 1 \le n \le n_1$$

$$y^0 = y_{II}{}^0 P_{n-n_1}{}^{u_0} \qquad n_1 < n$$

It can be proved by applying the general elution equation, expanding it, and rearranging it that

$$y_n = y_I{}^0 (P_{n-n_1}{}^u - P_n{}^u)$$

$$+ y_{II}{}^0 (P_{n-n_1}{}^{u+u_0} - P_{n-n_1}{}^u) \qquad (3)$$

if $y_I{}^0 = y_{II}{}^0 = y^0$

$$R_n = \frac{y_n}{y^0} = P_{n-n_1}{}^{u+u_0} - P_n{}^u \qquad (4)$$

This case can arise in practice if a zone is introduced at the top of a column by first equilibrating a small part of the adsorbent with the solvent containing the solute and then adding the mixture as a slurry at the top of the column. In this case $y_I{}^0 = y_{II}{}^0$, and therefore the distribution during elution is calculated from Equation (4); n_1 represents the amount of solute adsorbed on the adsorbent in the slurry, while u_0 represents the amount of solute in the solvent in the slurry.

Approximation of a Continuous by a Discontinuous Zone

An initial zone having a Poisson distribution in reference to the column during deposition (total number of plates = N_d) can be approximated by a discontinuous zone consisting of two parts, the top part having an even distribution and the lower part having a Poisson distribution in reference to the column during elution (total number of plates = N_e). This simplifies the analytical treatment of the elution process, and analytical expressions can be obtained.

Only the case where $N_d > N_e$ will be

considered here. This is also the case which is more common in practice, since the rate of flow during elution is usually greater than that during deposition.

If the distribution of the zone in reference to the column during elution is

$$R_n{}^0 = P_{\lambda n}{}^{\lambda u_0} \qquad (5)$$

and the approximate discontinuous distribution is

$$R_n{}^0 = 1 \qquad \cdots 1 \le n \le n_1$$

$$= P_{n-n_1}{}^{u_1} \qquad n_1 < n$$

Then, since the total amount of solute in the two zones is the same

$$n_1 + u_1 = u_0 \qquad (6)$$

To evaluate both n_1 and u_1 another relation between the two values is required.

After many trials it was found that it is convenient as well as reasonable to choose the ratio n_1/u_1 such that the fraction of solute beyond the point where $R_n{}^0 = \frac{1}{2}$ is the same for both the continuous and the discontinuous distributions. Appendix 2 shows that this condition leads to the simple relation

$$\frac{n_1}{u_1} = \sqrt{\lambda} - 1 \qquad (7)$$

and therefore two equations exist in two unknowns, and both n_1 and u_1 can be determined.

PART B

This part of the paper deals with the difference between experimental and true elution curves. An experimental elution curve does not represent accurately the concentration of solute in the effluent as it emerges from the bottom of the column as a function of u, usually because the sample taken for analysis has a finite volume, and there is always a space at the bottom of the column of a finite volume b in which the effluent is mixed.

Evidently to get a true elution curve each of the two volumes should be infinitesimally small; the larger they get the more the experimental elution curve will deviate from the true one. To be compared with the theoretical curve the experimental curve should therefore be corrected for the error due to these two factors. In this way the true experimental curve will be compared with the true theoretical curve. An alternate approach is to compare the experimental curve with the true theoretical curve after correcting the latter for the mentioned factors. This procedure is usually simpler, since the equation for the theoretical curve is known. In this paper the method of correcting the theoretical curve has been applied to one of the simple, theoretical elution curves, and relatively

simple analytical expressions were deduced.

The most widely used method for the determination of the number of theoretical plates N in a chromatographic column is a graphic method (5) whereby tangents to the elution curve at the points of inflection are drawn and the number of plates for an extremely thin initial zone is calculated from distances between certain points on the elution curve.

A method for the determination of N was derived by this author (4). It is applicable to both thin and thick zones and makes use of the ratio between the maximum concentrations at the bottom and top of the column. It requires the solution of two simultaneous equations or the use of prepared charts. When the initial zone is extremely thin, the calculations can be simplified, and a very simple relation in terms of the maximum concentration ratio deduced. Another simple relation is also deduced for a zone which is moderately thin.

The magnitude of the maximum effluent concentration and also the slope at the point of inflection are affected by the finite size of samples, and deviations from the true values increase with increase in the size of the sample. Values obtained for N by using the previously mentioned formulas can be improved further by applying a simple correction factor which is derived in this paper.

Effect of Finite Size of Sample and Dead Free Volume on the Shape of the Elution Curve

Both the finite size of samples and the dead free volume at the bottom of the column affect the shape of the elution curve, and the larger the sample and the dead free volumes the larger the deviation from the shape of the true curve. The theoretical elution curve represented by the simple relation $R_N = \phi_{N-1}{}^u$ will be considered; and the effect of each of these factors will be treated separately first and then combined.

Effect of Finite Size of Sample on the Shape of the Elution Curve

The size of each sample may be assumed to be s in the same units as u, and the experimental curve may be assumed to be obtained by plotting the concentration of solute in each sample vs. u such that $u = u_- + s/2$, where u_- represents the amount of eluant that left the column before taking the sample. If R_s denotes R_n corrected for the finite size of sample, then

$$R_s = \frac{1}{s} \int_{u-s/2}^{u+s/2} R_N \, du$$

$$= \frac{1}{s} \int_{u-s/2}^{u+s/2} \phi_{N-1}{}^u \, du$$

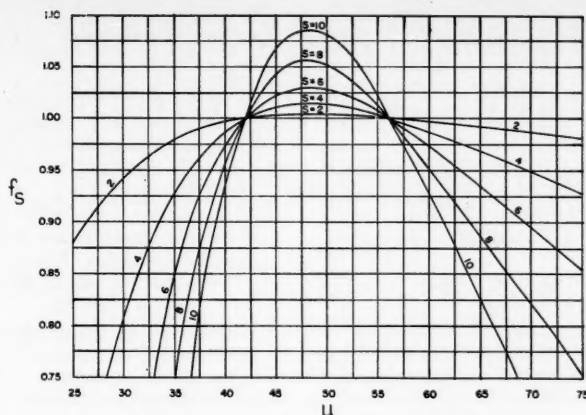$$= \frac{1}{s} [P_N{}^{u+s/2} - P_N{}^{u-s/2}] \qquad (8)$$

Fig. 1. Plot of f_s vs. u for $N = 50$.

By differentiating and equating to zero one can show that the maximum of the corrected curve lies at u_c, where

$$u_c = \frac{s}{2}\left[\frac{e^{s/n-1}+1}{e^{s/n-1}-1}\right] \qquad (9)$$

Since the maximum of the theoretical curve occurs at $u_m = n - 1$, the relation between u_c and u_m becomes

$$u_c = \frac{s}{2}\left[\frac{e^{s/u_m}+1}{e^{s/u_m}-1}\right] \qquad (10)$$

Effect of Dead Free Volume on the Shape of the Elution Curve

The dead free volume is the volume at the bottom of the column in which the effluent is mixed before the samples are taken.

It will be assumed that the weight of effluent in this volume is equal to b, that the effluent is completely mixed in it, and that it is filled with pure eluant at the start of the elution process.

A material balance on the solute in this free volume gives

$$\bar{y}_N\, dw - y_f\, dw = b\, dy_f$$

when one divides both sides by $\bar{y}_0$ and substitutes

$$R_N = \frac{\bar{y}_N}{\bar{y}_0} = \phi_{N-1}{}^u$$

$$\therefore\ \phi_{N-1}{}^u\, dw - \frac{y_f}{\bar{y}_0}\, dw = \frac{b}{\bar{y}_0}\, dy_f$$

When

$$\frac{y_f}{\bar{y}_0} = R_f$$

$$(\phi_{N-1}{}^u - R_f)\, dw = b\, dR_f$$

and since

$$u = w\,\frac{kN}{S}$$

$$\therefore\ (\phi_{N-1}{}^u - R_f)\, du = a\, dR_f \qquad (8)$$

where $a = bkN/S =$ the dead free volume expressed in the same units as u

$$\frac{dR_f}{du} + \frac{1}{a}R_f = \frac{1}{a}\phi_{N-1}{}^u$$

Solving this first-order linear differential equation one gets

$$R_f = e^{-u/a}\left[\int \frac{1}{a}\phi_{N-1}{}^u e^{u/a}\, du + c\right]$$

Integrating and substituting the boundary condition $R_f = 0$ when $u = 0$ one finally gets

$$R_f = \frac{e^{-u/a}}{a\left(1-\frac{1}{a}\right)^N}P_N{}^{(u-u/a)} \qquad (11)$$

Combined Effect of Finite Size of Sample and Dead Free Volume on the Shape of the Elution Curve

$$R_{sf} = \int_{u-s/2}^{u+s/2}\frac{e^{-u/a}}{a\left(1-\frac{1}{a}\right)^N}P_N{}^{u(1-1/a)}\, du$$

Appendix 4 shows that by means of integration by parts,

$$R_{sf} = \left[P_N{}^u - \frac{e^{-u/a}}{\left(1-\frac{1}{a}\right)^N}P_N{}^{u(1-1/a)}\right]_{u-s/a}^{u+s/a} \qquad (12)$$

Of these effects the effect of the finite size of samples is the more important, since in most cases it is unavoidable while the dead free volume can easily be made very small; consequently its effect becomes negligible. In the following discussions the effect of the sample size alone will be considered.

Figure 1 is a plot of f_s vs. u for $N = 50$ and for different values of s. For larger values of N the main features of the curves remain almost the same except that they become more and more symmetrical, and as N becomes very large the curves approach those obtained by sampling the normal distribution.

The sampling function $y(s)$ corresponding to any function $y = f(x)$ is represented by the equation

$$y(s) = \frac{1}{s}\int_{x-s/2}^{x+s/2}f(x)\, dx \qquad (13)$$

and in the case of the normal distribution

$$y(s) = \frac{1}{s\sqrt{2\pi}}\int_{x-s/2}^{x+s/2}e^{-x^2/2}\, dx$$

and

$$f(s) = y/y(s) = se^{-x^2/2}\Big/\int_{x-s/2}^{x+s/2}e^{-x^2/2}\, dx$$

As shown in Appendix (6C) the right hand side is approximately equal to $1 - s^2/24\,(x^2 - 1)$ for reasonably small values of s, say $s < 1$, and

$$f(s) = 1 - \frac{s^2}{24}(x^2 - 1) \qquad (14)$$

For different values of s Equation (14) represents a family of parabolas intersecting at the points $(\pm 1,\ 0)$ which are inflection points on the normal distribution. They also cross the ordinate at their maximum values which are equal to $1 + s^2/24$.

For the Poisson distribution, $f(s)$ can be satisfactorily calculated according to Equation (14) with the transformation $x = (u - N)/\sqrt{u}$ and with the following limitations

$$N \text{ is large, say } N > 50$$

$$x \text{ is small, say } x < 1.5$$

$$s \text{ is small, say } s < 1.$$

Number of Theoretical Plates in a Chromatographic Column

According to the recommended method for the determination of the number of theoretical plates (5)

$$N = 16\left(\frac{\mu}{\theta}\right)^2 \qquad (15)$$

where θ represents the length of the intercept on the abscissa between the tangents to the elution curve at the points of inflection, and μ represents the distance between the origin and the midpoint of the intercept.

In spite of the large uncertainties in drawing tangents Equation (14) has the advantage of being dependent on the effluent concentrations only; yet when the concentration of solute at the top of the column is known, a more representative value for the number of theoretical plates is obtained from the formula

$$N = 2\pi\left(\frac{\alpha}{\gamma}\right)^2 \qquad (16)$$

Equations (15) and (16) both assume an extremely thin initial zone.

Equation (16) has the following advantages over Equation (15): The total volume of effluent need not be recorded; only a small part of the elution curve around the maximum point need be drawn; and it is easier to correct Equation (16) for the effect of the finite size of samples. When the initial zone is moderately thin, better values for N are obtained by using

$$N = 2\pi\left(\frac{\alpha}{\gamma}\right)^2\left[1 + \frac{\alpha^2}{2}\right] \qquad (17)$$

The difference between Equations (16) and (17) is in the term $\alpha^2/2$, neglected in the first equation, which depends upon initial zone thickness and the number of theoretical plates; it increases when γ and N increase. Equations (16) and (17) are derived in Appendix 5.

Formulas (15), (16), and (17) are subject to errors owing to the finite size of samples, and in Appendix 6C it is shown that

$$\epsilon_r(\alpha) \cong h^2/24$$

where

$$h = s/\sqrt{N} = w_s k\sqrt{N}/S$$

To correct for the sampling effect the method of successive approximations is used. One of the aforementioned formulas is chosen, and a preliminary value $N_{(0)}$ is calculated which is used to calculate $\epsilon_r(\alpha)$ giving a better value for α from which a better value $N_{(1)}$ for N is obtained and so on. Since $h^2/24$ is usually a small fraction, one approximation will be enough.

Illustrative Example

To calculate N for the following two cases: 10 mg. of solute were introduced by 2 g. of solvent at the top of a chromatographic column made up of 12 g. of adsorbent. The same solvent (pure) was used as the eluant, and the maximum concentration in the effluent was found to be 2.23 mg. solute/g. solvent. The weight of the sample = 1.50 g., and $k = 0.122$; 11 mg. of solute were introduced at the top of a 15 g. adsorbent column by 1.2 g. solvent and eluted by a different eluant. Maximum concentration in the effluent was 2.1 mg. solute/g. effluent. The weight of the sample = 2.20 g.; k for solvent = 0.037, and k for eluant = 0.093.

Solution

a) $\gamma = 0.122 \times 2/12 = 0.0203$

Maximum concentration in eluant at top of column = $10/2 = 5$ mg. solute/g. eluant

$$\alpha = 2.23/5 = 0.446$$

$$N_{(0)} = 2\pi\left(\frac{0.446}{0.0203}\right)^2$$

$$\cdot\left[1 + \frac{0.446^2}{2}\right] = 3,340$$

$$h = \frac{s}{\sqrt{N}} = w_s k\sqrt{N}/S$$

$$= 1.5 \times \frac{58}{12} \times 0.122 = 0.88$$

$$\epsilon_r(\alpha) = (0.88)^2/24 = 0.032$$

$$N_{(1)} = 2\pi\left(\frac{0.446 \times 1.032}{0.0203}\right)^2$$

$$\cdot\left[1 + \frac{(0.446 \times 1.032)^2}{2}\right] = 3,590$$

It is evident that a second approximation is not necessary, and $N \cong N_{(1)} = 3,590$ theoretical plates

b) $\gamma = \dfrac{0.037 \times 1.2}{15} = 0.00296$

$$\bar{y}_0 = \frac{11}{1.2} \times \frac{0.093}{0.037} = 23.0$$

mg. solute/g. eluant. $\alpha = 2.1/23.0 = 0.0913$ α is small, and $\alpha^2/2$ can be neglected.

$$\therefore N_{(0)} = 2\pi\left(\frac{\alpha}{\gamma}\right)^2$$

$$= 6.28.\left(\frac{0.0913}{0.00296}\right)^2 = 5,950$$

$$h = w_s k\sqrt{N}/S$$

$$= 2.2 \times \frac{77.2}{15} \times 0.093 = 1.053$$

$$\epsilon_r(\alpha) = \frac{h^2}{24} = 0.046$$

$$N_{(1)} = 5,950 \times 1.046^2 = 6,510$$

$$\therefore N \cong N_{(1)} = 6,510$$

theoretical plates.

NOTATION

a	=	bkN/S = dead free volume in the same units as u
b	=	weight of effluent in dead free volume
f_s	=	ratio between ordinate on the true elution curve and corresponding ordinate on the experimental curve
j, r	=	positive integer numbers
k	=	adsorption or exchange coefficient
N	=	total number of theoretical plates in column
N_d	=	total number of theoretical plates during deposition
N_e	=	total number of theoretical plates during elution
$N_{(r)}$	=	value of N after r successive approximations
n	=	plate number from top of column—top plate number $n = 1$ and bottom plate number $n = N$
n_1	=	number of plates occupied by uniform zone at start of the elution process

$P_n{}^u$	=	$\sum_{r=n}^{\infty} \phi_r{}^u$
R_n	=	y_n/y_0
$R_n{}^0$	=	$y_n{}^0/y_1{}^0$ = concentration ratio on plate n before elution
$R_N{}^{um}$	=	maximum value of R_N
R_f	=	R_N corrected for the dead free volume
R_s	=	R_N corrected for the sample size
R_{sf}	=	R_N corrected for both sample size and dead free volume
s	=	weight of sample in same units as $u = w_s kN/S$
S	=	total weight of adsorbent in column
u	=	kx during elution
u_0	=	kx during deposition
u_1	=	$u_0 - n_1$
u_c	=	u_m corrected for size of sample
u_-	=	value of u before taking sample
u_m	=	value of u when peak of zone has reached plate N
w	=	weight of eluant or solvent that has passed through any plate in column
w_s	=	weight of sample
x	=	wN/S
y_n	=	concentration of solute on plate n, g. solute/g. adsorbent, for the elution process
$\bar{y}_n$	=	concentration of solute in eluant in equilibrium with plate n during elution
y_0	=	$\bar{y}_0/k$ = concentration of solute on adsorbent if in equilibrium with solvent containing solute at a concentration $\bar{y}_0$
$\bar{y}_0$	=	concentration of solute in solvent before entering plate 1
y_f	=	concentration of solute in dead free volume
$y_n{}^0$	=	concentration of solute on plate n before elution

Greek Letters

α	=	ratio between the maximum concentrations of solute at bottom and top of column
γ	=	fraction of column loaded with solute at start of elution process
$\phi_n{}^u$	=	$e^{-u}u^n/n!$ = Poisson exponential function
$\epsilon_r(\alpha)$	=	relative error in α
λ	=	N_d/N_e

LITERATURE CITED

1. Glueckauf, E., *Trans. Faraday Soc.*, **51**, 34 (1955).
2. Martin, A. J. P., and R. L. N. Synge, *Biochem. J.*, **35**, 1358 (1941).
3. Mayer, S. W., and K. R. Tompkins, *J. Am. Chem. Soc.*, **69**, 2966 (1947).
4. Said, A. S., *A.I.Ch.E. Journal*, **2**, 477 (1956).
5. Desty, ed., "Vapor Phase Chromatography," p. 13, Academic Press Inc., New York (1957).

Simultaneous Development of Velocity and Temperature Distributions in a Flat Duct with Uniform Wall Heating

ROBERT SIEGEL and E. M. SPARROW

National Aeronautics and Space Administration, Cleveland, Ohio

Laminar forced-convection heat transfer in a parallel-plate channel (flat duct) with uniform heat flux at the walls is analyzed. The velocity and temperature distributions, both uniform at the entrance section, develop simultaneously as the fluid flows through the duct. The heat transfer results, obtained for the Prandtl-number range of 0.01 to 50, include the Nusselt-number variation along the channel and the wall-temperature variation corresponding to the prescribed uniform heat flux.

Forced-convection heat transfer in the thermal entrance region of tubes and ducts has been a subject of analytical study since the pioneering work of Graetz (1883). In most instances consideration has been given to the entrance of the fluid into the heated (or cooled) region of the duct with an already fully developed velocity profile which is unchanging along the duct length. This simplification is not realistic when the fluid enters the heated channel directly from a reservoir or large header. In such a situation the velocity is more nearly uniform across the entrance section, and the velocity and thermal boundary layers develop simultaneously as the fluid moves through the tube.

For laminar flow, which is the condition considered in this paper, the problem of simultaneous development of velocity and thermal boundary layers has been solved for a circular tube and flat duct under the condition of uniform wall temperature (1 to 4). For uniform wall heat flux results are available only for the circular tube (1). The purpose of the present study is to analyze the uniform wall heat-flux situation in a parallel-plate channel (often referred to as a *flat duct*). The heat transfer results to be presented include the Nusselt-number variation along the channel and the wall-temperature variation corresponding to the prescribed uniform heat flux.

ANALYSIS

Physical Model

In Figure 1 fluid is pictured as flowing from left to right through a parallel-plate channel of half width a. Both the temperature and velocity are assumed to be uniform across the entrance section ($x = 0$). A uniform heat flux is maintained at the channel walls. As the fluid progresses down the channel, the respective action of viscosity and heat conduction at the wall causes vorticity and heat to spread from the channel walls into the main stream. The distance (away from the wall) to which these effects propagate into the main

stream can be measured in terms of boundary-layer thicknesses. Depending upon the fluid properties, the velocity and thermal effects diffuse at different rates, and hence the thicknesses of the velocity and thermal boundary layers will generally be different. Figure 2 illustrates schematically how the boundary layers develop in the entrance region of a duct. Figure 2a refers to low-Prandtl-number fluids where $\Delta > \delta$, Figure 2b is for high Prandtl numbers where $\Delta < \delta$.

The temperature of the fluid outside the thermal boundary layer is essentially the same as the entering temperature; however because the fluid near the channel walls is retarded owing to viscosity, the velocity outside the velocity boundary layer must increase along the channel length to preserve the same total mass flow. Within the boundary layers the temperature and velocity vary with both x and y.

Far down the channel, when both the velocity and thermal boundary layers have completely filled the section, it is well established that the local heat transfer coefficient becomes a constant. For this fully developed thermal condition the temperature distribution across the channel can be calculated to be

$$\frac{T - T_{CL}}{\frac{qa}{k}} = \frac{5}{8}\left[1 - \frac{8}{5}\left(\frac{y}{a}\right) + \frac{4}{5}\left(\frac{y}{a}\right)^3 - \frac{1}{5}\left(\frac{y}{a}\right)^4\right] \quad (1a)$$

and the fully developed heat transfer coefficient based on the definition $q = h(T_w - T_b)$ is given by

$$\frac{ha}{k} = \frac{35}{17} \quad (1b)$$

Mathematical Solution

To compute entrance-region heat transfer coefficients one begins with the equation expressing conservation of energy within the fluid. A control surface situated in the thermal boundary layer (Figure 3) will be considered. Eckert (5) has shown that conservation of energy for this element is

$$\rho c_p \frac{d}{dx}\left[\int_0^\Delta u(T - T_e)\, dy\right] = q \quad (2)$$

The left side of Equation (2) represents the convective transport of heat; the right side is the wall heat transfer, which is prescribed to be uniform along the channel for the present problem.

Equation (2) represents a means of solving for the temperature distribution $T(x, y)$, provided that the velocity distribution $u(x, y)$ is known. Fortunately information on the development of the velocity boundary layer in a parallel-plate channel is already available. An approximate solution was first formulated by Schiller (4), who gives the velocity profile as

$$u = U_s\left[2\left(\frac{y}{\delta}\right) - \left(\frac{y}{\delta}\right)^2\right],$$
$$0 \leq y \leq \delta \quad (3a)$$

$$u = U_s \qquad \delta \leq y \leq a \quad (3b)$$

where both U_s and δ vary with x. Once δ and U_s are known, the velocity distribution is completely determined. These functions have been computed (4) and are used in the present investigation.

With the velocity distribution specified, Equation (2) can be used to solve for the temperature distribution in the boundary layer. This solution is readily found by expressing the temperature as a polynomial in y the coefficients of which are unknown functions of x. Then the unknown coefficients are found from Equation (2). A form for the polynomial which immediately suggests itself is that in Equation (1a). This equation is modified to the following form, so that the fluid takes on the temperature T_e at the edge of the thermal boundary layer

$$T - T_e = \frac{5}{8}\frac{q\Delta}{k}\left[1 - \frac{8}{5}\left(\frac{y}{\Delta}\right) + \frac{4}{5}\left(\frac{y}{\Delta}\right)^3 - \frac{1}{5}\left(\frac{y}{\Delta}\right)^4\right],$$
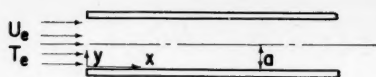$$0 \leq y \leq \Delta \quad (4a)$$

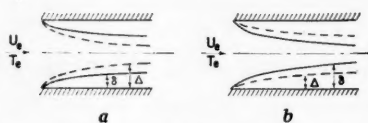Fig. 1. Geometric configuration and coordinate system.

Fig. 2a. Boundary layer growth for low Prandtl numbers.

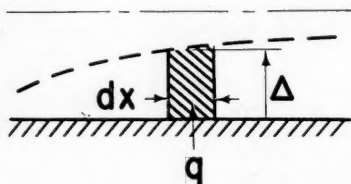Fig. 2b. Boundary layer growth for high Prandtl numbers.
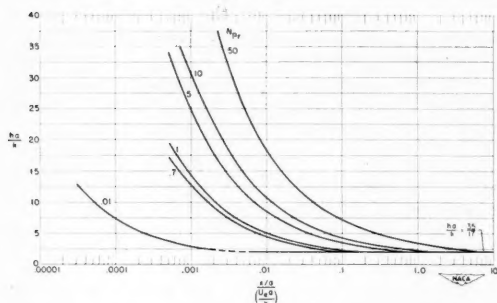

Fig. 3. Control volume for deriving energy equation.

Fig. 4. Nusselt number variation along the duct length.

$$\bar{\Delta}^2\left[\frac{9}{25} - \frac{1}{3}\frac{\delta}{\bar{\Delta}} + \frac{2}{15}\left(\frac{\bar{\delta}}{\bar{\Delta}}\right)^2 - \frac{1}{75}\left(\frac{\bar{\delta}}{\bar{\Delta}}\right)^4\right.$$

$$\left. + \frac{1}{525}\left(\frac{\bar{\delta}}{\bar{\Delta}}\right)^5\right] = \frac{8}{5N_{Pr}}\frac{\bar{x}}{\bar{U}_s},$$

$$\Delta > \delta \qquad (5b)$$

Since $\bar{\delta}$ and $\bar{U}_s$ are known functions of $\bar{x}$, the variation of $\bar{\Delta}$ with $\bar{x}$ can be calculated from these equations for a fluid with any Prandtl number. For high Prandtl numbers Equation (5a) applies, and for low Prandtl numbers Equation (5b) is used. The values of $\bar{\Delta}$ are then used to evaluate the heat transfer results.

wall. This gives

$$T_b - T_e = \frac{q}{\rho a c_p U_e} x \qquad (8)$$

The temperature difference in Equation (6) can then be evaluated in terms of Equations (7) and (8); the following is the result for the Nusselt number:

$$N_{Nu} = \frac{ha}{k} = \frac{1}{\dfrac{5}{8}\left(\dfrac{\Delta}{a}\right) - \dfrac{x/a}{\left(\dfrac{U_e a}{\nu}\right)N_{Pr}}} \qquad (9)$$

By means of the calculated values of Δ/a (which depend on $(x/a)/(U_e a/\nu)$ and N_{Pr}), this dimensionless local heat
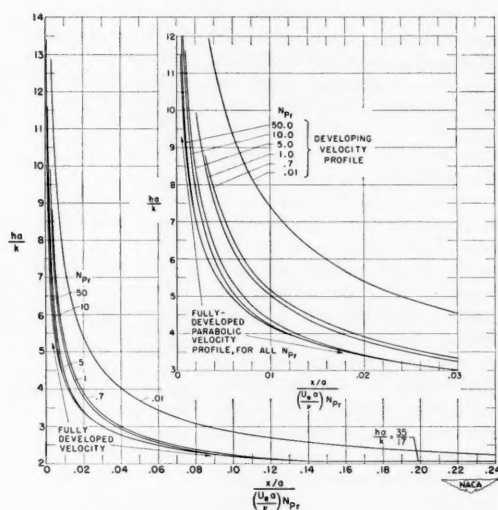
Fig. 5. Effect of developing velocity profile on Nusselt number variation.

$$T = T_e \qquad \Delta \leq y \leq a \qquad (4b)$$

The only unknown appearing in Equation (4a) is the thermal-boundary-layer thickness; once this function has been determined [with the aid of Equation (2)], the temperature distribution is completely specified for every x and y. It is worth noting that when the thermal boundary layer fills the channel, that is $\Delta = a$, Equation (4a) coincides with the fully developed temperature distribution (1a)

To find the variation of Δ with x, Equations (3a), (3b), (4a), and (4b) are introduced into the energy equation (2). After the indicated operations have been carried out, a pair of algebraic equations for computing Δ as a function of x results:

$$\frac{\bar{\Delta}^3}{\bar{\delta}}\left[\frac{14}{75} - \frac{4}{105}\frac{\bar{\Delta}}{\bar{\delta}}\right] = \frac{8}{5N_{Pr}}\frac{\bar{x}}{\bar{U}_s},$$

$$\Delta < \delta \qquad (5a)$$

RESULTS

Heat Transfer Coefficients

The heat transfer results will be presented in terms of a local heat transfer coefficient defined as

$$h = \frac{q}{T_w - T_b} \qquad (6)$$

The local wall temperature may be evaluated from Equation (4a) by setting $y = 0$, with the result

$$T_w - T_e = \frac{5}{8}\frac{q\Delta}{k} \qquad (7)$$

where the thermal boundary layer thickness has been computed as described in the previous section. The local bulk temperature can be written directly from an over-all energy balance by equating the enthalpy increase of the fluid to the total heat transfer at the

transfer result has been computed and plotted on Figure 4. For a given flow situation it is seen that with increasing x the Nusselt numbers approach the fully developed value of 35/17. For fluids with low Prandtl numbers the fully developed heat transfer condition is approached much more rapidly than for fluids with high Prandtl numbers. This is a consequence of the fact that the thermal boundary layer develops more rapidly for low-Prandtl-number fluids. Similar results have been obtained for laminar flow in tubes and ducts having uniform wall temperature.

The influence of the developing velocity profile on heat transfer will now be examined. To accomplish this, a comparison is made with the analysis carried out for a velocity distribution which is fully developed at the duct entrance and unchanging along the duct length (Figure 5). Figure 5 is constructed in two parts to permit better examination

of the entire range of the abscissa. The heat transfer results, corresponding to the fully developed velocity profile, plot as a single curve for all Prandtl numbers when presented with this abscissa variable. It is seen that the lower the Prandtl number the greater the effect of the developing velocity distribution. In all

stant in the present problem, the important unknown in a practical situation would be the wall temperature. On each curve there is a change in slope at the end of the thermal entrance region, because of the simplification in the analysis. In reality the transition from the entrance region to the fully developed

are expected to apply also for annuli where the radius ratio is close to unity.

Fig. 6. Wall temperature variation along the duct length.

Fig. 7. Effect of developing velocity profile on wall temperature variation.

cases the simultaneous velocity development causes an increase in heat transfer relative to the situation of unchanging velocity distribution.

From Figures 4 and 5 one can obtain an estimate of the length of duct required to establish fully developed heat transfer conditions. This gives

$$(x/a)_{ent} = 0.14 \left(\frac{U_e a}{\nu} \right) N_{Pr}$$

$$N_{Pr} \geq 0.7 \qquad (10a)$$

$$(x/a)_{ent} = 0.003 \frac{U_e a}{\nu}$$

$$N_{Pr} = 0.01 \qquad (10b)$$

The approximate nature of the mathematical formulation does not permit precise calculations for thermal entrance length.

Wall-Temperature Variation

An alternate presentation of the results may be made in terms of the wall-temperature variation along the channel (Figures 6 and 7). Since the wall heat transfer rate is a prescribed con-

heat transfer condition would be smooth. In the fully developed region the wall-temperature variation is given by

$$\frac{T_w - T_e}{qa/k} = \frac{17}{35} + \frac{x/a}{\left(\frac{U_e a}{\nu} \right) N_{Pr}} \qquad (11)$$

This relation can be used when x/a exceeds the entrance lengths given by Equations (10a) and (10b).

On Figure 7 the wall-temperature variations are compared with the corresponding results for the case of a fully developed, unchanging velocity profile. It is seen that the simultaneous development of the velocity profile tends to lower the wall temperature in the entry region, with the effect increasing with decreasing Prandtl number. On the abscissa scale of Figure 7 the results for $N_{Pr} = 0.01$ may be clearly read, and on Figure 6 the curve for this Prandtl number is crowded against the ordinate axis and hence does not appear.

CONCLUDING REMARK

While the analysis presented here is for a parallel-plate channel, the results

NOTATION

a = half width of parallel-plate channel
c_p = specific heat at constant pressure
h = local coefficient of heat transfer, $q/(T_w - T_b)$
k = thermal conductivity of fluid
N_{Nu} = local Nusselt number, ha/k
N_{Pr} = Prandtl number, $c_p \mu/k = \nu/\alpha$
q = local heat flux per unit area at channel walls
T = temperature; T_b, bulk fluid temperature; T_e, uniform temperature of entering fluid (equal to fluid temperature external to thermal boundary layer); T_w, wall temperature; T_{CL}, temperature at channel center line
U_e = uniform velocity of entering fluid
U_s = fluid velocity external to velocity boundary layer
$\bar{U}_s$ = dimensionless velocity, U_s/U_e
u = fluid velocity
x = axial coordinate measured from channel entrance
$\bar{x}$ = dimensionless axial coordinate, $(x/a)/(U_e a/\nu)$
y = transverse coordinate measured from channel wall

Greek Letters

α = thermal diffusivity, $k/\rho c_p$
Δ = thermal-boundary-layer thickness
$\bar{\Delta}$ = dimensionless thermal-boundary-layer thickness, Δ/a
δ = velocity-boundary-layer thickness
$\bar{\delta}$ = dimensionless velocity-boundary-layer thickness, δ/a
μ = absolute viscosity
ν = kinematic viscosity
ρ = fluid density

Subscript

ent = thermal entrance length

LITERATURE CITED

1. Kays, W. M., *Trans. Am. Soc. Mech. Engrs.*, 77, 1265 (1955).
2. Toong, Tau-Yi, and Joseph Kaye, *Second U.S. Natl. Cong. of Appl. Mech.*, Univ. Mich., Ann Arbor (June, 1954).
3. Sibahayasi, Minoru and Eitaro Sugino, *Proc. Sixth Japan Natl. Cong. for App. Mech.*, p. 389 (1956).
4. Sparrow, E. M., *Natl. Advisory Comm. Aeronaut.*, Tech. Note 3331 (1955).
5. Eckert, E. R. G., "Introduction to the Transfer of Heat and Mass," p. 87, McGraw-Hill Book Co., Inc., New York (1950).

Liquid-Liquid Extraction Equilibrium Data of Cobalt Nitrate–Nickel Nitrate–Nitric Acid Solutions

E. J. SCHARF and C. J. GEANKOPLIS

The Ohio State University, Columbus, Ohio

Studies of the solvent extraction of cobalt and nickel nitrates from aqueous solution would add to the fundamental knowledge of extraction of metal salts. In experiments performed to determine the extractability of these metals as nitrates from aqueous solutions by organic solvents, normal butanol was found to be the best solvent and gave equilibrium distribution coefficients K for cobalt or nickel nitrate of about 0.3. The presence of nitric acid tended to decrease these at high metal concentrations.

In mixtures of the two metals the K value of either metal was found to depend on the total metal concentration. Low separation factors of about 1.3 were obtained. Very high K values of over 5 were obtained for the equilibrium extraction of the nitric acid in the presence of the metal nitrates by the n-butanol an indication of commercial possibilities.

Solvent extraction of cobalt and nickel salts from aqueous solutions has received considerable attention in recent years, partly owing to the development of many hydrometallurgical or chemical processes which are being used to separate metals in ores. The evaluation of extraction as a potential method of removing metals from aqueous solutions has been very limited by the lack of basic equilibrium data for the distribution of the metal salts between the two imiscible solvent layers.

Detailed studies on the extraction of cobalt and nickel chlorides (3), thiocyanates (5), perchlorates (4), sulfates (7), and acetates (5) are available. In the first three systems the distribution coefficients of the two metals depended on the total concentration of the anion, which was the same as the anion of the nickel and cobalt salts. High separation factors or ratios of distribution coefficients were obtained in the chloride and thiocyanate systems.

The nitrates of cobalt and nickel could easily be formed from the nitric acid leaching of ores. Study of the nitrate system should add to the fund of basic knowledge of the solvent extraction of metal salts. Hence experiments were performed on the nitrate system in this work. Templeton and Daly (10, 11) have obtained some experimental data using n-hexyl alcohol as a solvent.

In the present work the distribution coefficients of cobaltous and nickelous nitrate between water and various imiscible organic solvents were determined. Then n-butyl alcohol was selected as the best solvent, and further studies were carried out with the cobalt and nickel nitrates and various additives such as nitric acid.

EXPERIMENTAL METHODS

Cobalt, alone in the aqueous or organic phase, was determined colorimetrically in

E. J. Scharf is with American Cyanamid Company, Bound Brook, New Jersey.

a sulfuric acid solution by using the method of Gagnon (2). When the organic solvent was present, it was removed by evaporation with nitric acid. For very dilute solutions the method of Yoe (12) was used. When the ferric ion was present, it was removed by extraction with isopropyl ether. Also cupric ion, when present, was removed by precipitation as the sulfide.

In the solvent search phase, when nickel nitrate was alone in either layer, it was analyzed colorimetrically by the method
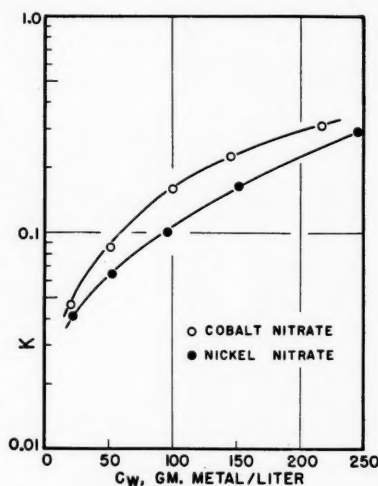
Fig. 1. Distribution coefficients in the ternary systems cobalt or nickel nitrate–water–n-butanol at 25.0°C. (Cobalt or nickel equilibrated separately.)
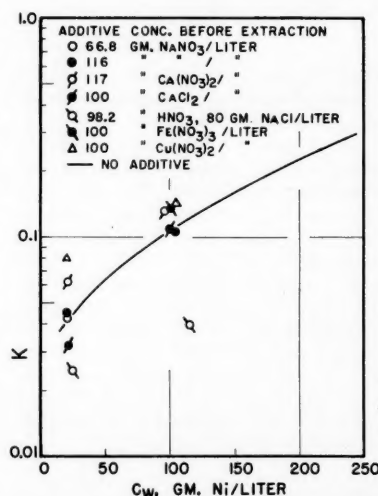
Fig. 2. Effect of additives in the system nickel nitrate–water–n-butanol at 25.0°C.

Table 1. Solvent Search Data at 25.0°C.

(Metals equilibrated separately)

Solvent	Metal	C_w, g./ liter	C_0, g./ liter
Alcohols			
n-Butanol	Ni	21.15	8.76×10^{-1}
n-Butanol	Ni	96.50	9.76
n-Butanol	Co	20.70	9.75×10^{-1}
n-Butanol	Co	99.60	16.00
n-Amyl alcohol	Ni	20.30	3.97×10^{-2}
n-Amyl alcohol	Co	22.00	6.47×10^{-2}
Isoamyl alcohol	Ni	20.75	4.33×10^{-2}
Isoamyl alcohol	Co	22.00	5.76×10^{-2}
n-Hexyl alcohol	Ni	96.00	6.80×10^{-2}
n-Hexyl alcohol	Ni	20.20	1.29×10^{-2}
n-Hexyl alcohol	Co	21.20	2.15×10^{-2}
Cyclohexanol	Co	21.80	2.80×10^{-1}
2-Octanol	Ni	20.85	9.78×10^{-3}
n-Decyl alcohol	Ni	20.78	6.91×10^{-3}
Ketones			
Methyl ethyl ketone	Ni	15.15	1.18×10^{-1}
Methyl isopropyl ketone	Co	22.55	$<1.0 \times 10^{-3}$
3-Pentanone	Ni	19.38	2.60×10^{-3}
4-Methyl, 2-pentanone	Ni	18.85	6.04×10^{-3}
4-Methyl, 2-pentanone	Co	21.30	1.52×10^{-3}
Diisobutyl ketone	Ni	19.70	1.98×10^{-3}
Ethers			
Diethyl ether	Ni	18.18	8.7×10^{-4}
Isopropyl ether	Ni	19.52	8.84×10^{-4}
Isopropyl ether	Co	20.7	$<1.0 \times 10^{-3}$
Ethylene glycol monoethyl ether	Ni	16.35	1.05×10^{-2}
Nitrogen Compounds			
2-Nitropropane	Ni	19.60	6.07×10^{-4}
Others			
Carbon tetrachloride	Ni	19.65	2.59×10^{-4}
Benzene	Ni	19.23	4.66×10^{-4}
Ethyl acetate	Ni	18.97	3.5×10^{-4}

of Snell and Snell (9). When *n*-butanol was the solvent, the method of Gagnon (2) in sulfuric acid solution was adopted for use with nickel. In the presence of iron, nickel was analyzed by the dimethylglyoxime gravimetric method. This was necessary, since even traces of ferric ion interfere in the colorimetric determination of nickel sulfate at 397 mμ. (6).

A colorimetric procedure was developed for the analysis of cobalt and nickel when together in sulfuric acid solution. Beer's law can be written for the peak absorbance of nickel sulfate solution at 397 mμ., another Beer's law equation can be written for the relatively weak absorbance at 518 mμ., separate equations can be written for cobalt sulfate at its peak of 518 and at 397 mμ., and these four equations can then be combined. Then the absorbance of solutions containing both metals was measured at the two peaks of 397 and 518 mμ. and the concentrations calculated from the combined equations. Known mixtures were analyzed and gave an average devia-

tion of 1.8% and a maximum of 2.8% (6).

Nitric acid was determined by using 0.2N sodium hydroxide and an electrotitrimeter. Ferric ion was analyzed by the dichromate method and copper by electrodeposition. The *n*-butyl alcohol and metal salts used were reagent grade.

Equal volumes of initial aqueous-phase solution and pure solvent were used in the equilibrium experiments. The equilibrium extractions were performed in rubbersealed, glass-stoppered flasks agitated by magnetic stirrers and totally immersed in a bath. The densities were determined by weighing the contents from calibrated pipettes. The ternary-phase diagram was determined by titrating known amounts of one phase with another until the solution became cloudy. Experimental details are available elsewhere (6).

DISCUSSION OF SOLVENT SEARCH DATA

To select the best solvents distribution ratios (ratio of concentration in

organic to concentration in aqueous phase) of cobalt nitrate and nickel nitrate alone were obtained between water and a variety of solvents (Table 1) at 25.0°C. The solvents used were restricted to those known to have some ability to extract metal salts.

The ketones gave distribution ratios K of about 0.008 as a maximum, and the ethers gave values less than 0.001 for the cobalt and nickel nitrates. The alcohols were the best solvents with maximum K values of about 0.2, the K value decreasing with increasing solvent molecular weight. N-butyl alcohol was selected for further studies because of its high K value compared with that of other solvents. This solvent was also used in the studies of the sulfate system (7).

N-BUTANOL–COBALT OR NICKEL NITRATE–WATER–ADDITIVE SYSTEM

No Additives

Distribution data from the solvent *n*-butanol when either the cobalt or nickel is alone are given in Table 2. Figure 1 shows that the K for nickel or cobalt increases markedly as the concentration of the metal in the water increases. At about 250 g. metal/liter the K is approximately 0.3. The K of cobalt is slightly greater than that of nickel.

If the distribution coefficient is assumed to follow the equation

$$K' = C_0/(C_w)^n \qquad (1)$$

than a log-log plot of C_0 vs. C_w should be a straight line with slope n. Plots of the cobalt nitrate and nickel nitrate data give straight lines which are almost parallel with an n value of 1.69 for cobalt and 1.82 for nickel. The chloride data (3) give slopes of about 7 for both cobalt and nickel. The values for the nitrates

TABLE 2. DISTRIBUTION OF COBALT NITRATE OR NICKEL NITRATE IN N-BUTANOL-WATER AT 25.0°C.

(Metals equilibrated separately)

| Water phase concentration before extraction | | | Phases at equilibrium | | | | | |
| | | Water phase | | | Alcohol phase | | |
C_w', g./liter Metal	g./liter HNO$_3$	C_w, g./liter Metal	g./liter HNO$_3$	ρ_w, g./ml.	C_0, g./liter Metal	g./liter HNO$_3$	ρ_0, g./ml.
N-Butanol–nickel nitrate–water system							
20	0	21.15	0		0.876	0	
50	0	52.5	0		3.42	0	
100	0	96.5	0		9.76	0	
150	0	152.2	0	1.350	25.25	0	0.888
260.5*	0	244.5	0	1.555	71.50	0	0.996
N-Butanol–nickel nitrate–water–nitric acid system							
150	197.0	182.5	35.21	1.441	7.25	135.2	0.917
150	49.48	161.2	6.87	1.372	17.37	37.70	0.889
150	98.5	175.5	15.22	1.402	12.49	71.20	0.895
100	197.0	130.0	60.75	1.327	5.46	119.2	0.910
100	49.48	114.2	11.90	1.260	8.93	33.45	0.871
100	98.5	119.5	26.72	1.281	7.18	63.3	0.883
50	98.5	61.3	43.25	1.156	3.44	52.30	0.877
50	197.0	66.6	91.5	1.192	3.73	100.8	0.910
50	49.48	55.2	20.39	1.132	3.17	27.05	0.857
20	98.5	24.90	54.5	1.072	1.40	44.2	0.876
20	197.0	27.45	111.1	1.101	2.34	90.8	0.911
20	49.48	23.15	28.55	1.057	0.948	22.01	0.857
N-Butanol–cobalt nitrate–water system							
20	0	20.7	0		0.975	0	
50	0	52.0	0	1.118	4.50	0	0.841
105	0	99.6	0		16.00	0	
150	0	145.5	0	1.352	33.05	0	0.913
236*	0	217.0	0	1.503	68.5	0	1.009
N-Butanol–cobalt nitrate–water–nitric acid system							
150	49.48	151.2	7.52	1.360	21.35	36.3	0.906
150	98.5	167.8	16.05	1.387	16.71	70.0	0.913
150	197.0	188.7	37.60	1.441	10.35	131.6	0.923
100	49.48	107.9	12.05	1.262	10.87	32.7	0.879
100	98.5	113.9	26.68	1.278	9.31	62.95	0.890
100	197.0	122.5	61.0	1.319	6.35	117.5	0.917
50	49.48	54.8	20.45	1.132	3.88	27.00	0.861
50	98.5	58.7	42.80	1.157	3.95	52.20	0.880
50	197.0	65.1	90.80	1.188	4.375	100.0	0.910
20	49.48	23.21	28.05	1.057	0.942	21.75	0.856
20	98.5	23.95	55.5	1.069	1.645	44.1	0.876
20	197.0	26.80	110.1	1.101	2.66	91.0	0.912

*Water phase saturated with metal nitrate before extraction.
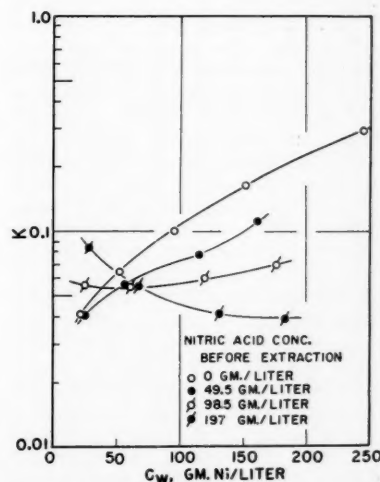
Fig. 3. Effect of nitric acid in the system nickel nitrate–water–nitric acid–*n*-butanol at 25.0°C.

(One run made with nitric acid as an additive)

Water phase before extraction			Phases at equilibrium			Density			K		β,
C_w', g./l.			C_w, g./l.			ρ_w,	ρ_0,				K_{Co}/K_{Ni}
Co	Ni	Co	Ni	Co and Ni	g./ml.	g./ml.	Co		Ni	
20	20	21.4	21.9	43.3	1.069	0.8361	7.77×10^{-2}		6.30×10^{-2}	1.233
50	50	47.3	51.2	98.5	1.027	0.8641	1.51×10^{-1}		1.20×10^{-1}	1.258
100	100	92.0	97.7	189.7	1.445	0.9586	2.73×10^{-1}		2.15×10^{-1}	1.270
100	25	97.3	26.4	123.7	1.293	0.8887	1.84×10^{-1}		1.46×10^{-1}	1.260
25	100	25.2	99.8	125.0	1.293	0.8768	1.84×10^{-1}		1.44×10^{-1}	1.278
50*	50*	56.1	57.2	113.3	1.278	0.8880	7.78×10^{-2}		6.14×10^{-2}	1.266

*98.5 g. HNO₃/liter before extraction.

which are near 2 might possibly be explained by dissociation of the salt in the aqueous phase. However the real significance of these n values is not yet apparent.

Runs made at different temperatures show that the K vaules for cobalt and nickel both decreased by approximately 30% in going from 5.5° to 69.5°C. (1) with little effect on the separation factor of K of cobalt over K of nickel. The data for the sulfates (7) show the reverse trend with the K values approximately doubling in this temperature range.

Additives

Data where additives were put into the n-butanol–metal nitrate–water system are plotted in Figure 2 for nickel (1), and the curve for no additives from Figure 1 is shown for comparison. A plot of the cobalt data gave very similar curves. The data show that the additive cupric nitrate has the largest effect, approximately doubling the K value. A mixture of nitric acid and sodium chloride decreased the K, and other additives such as calcium nitrate, calcium chloride, sodium nitrate, and ferric nitrate had little effect (1).

Since the cobalt and nickel nitrate salts would often occur in nitric acid solution, data were obtained for nitric acid as an additive; this also allows comparison with other studies where the acid counterpart of the anion of the cobalt and nickel salts was used. Figure 3 for nickel shows the effect of initial nitric acid concentration on the K value. Initial rather than equilibrium acid concentrations were used as parameters, since it is extremely difficult to control experimentally the final equilibrium acid concentrations. A similar type of plot for cobalt, which is not shown, gave the same trends as nickel. At low metal concentrations the K value increases with increasing acid concentration, but at higher metal concentrations the trend reverses and K decreases with increasing nitric acid concentration. These effects are quite different from the sulfate system, where the K of both cobalt and nickel sulfate increased a hundredfold in

going from low to high sulfuric acid concentrations. In the chloride system the K and the separation factor also increased greatly with increases in hydrochloric acid concentration.

Distribution Coefficient for Nitric Acid

The distribution coefficient data for nitric acid in the presence of nickel nitrate (Table 2) are plotted in Figure 4. This plot shows a very large increase in K with increasing nickel concentration in the aqueous phase with K values over 5. A similar curve is obtained when only cobalt nitrate is present, an indication of a very high extraction of nitric acid by n-butanol with metals present. This could be the basis for a good extraction process to recover nitric acid from aqueous salt solutions. Methods such as distillation or addition of a second solvent might then be tried to recover the acid from the n-butanol solvent, but further research would be needed. At zero concentration of metal the K value approaches approximately 0.7.

N-BUTANOL–COBALT NITRATE–NICKEL NITRATE–WATER SYSTEM

Distribution Coefficients

In Table 3 the K values are given for the complex system n-butanol–cobalt nitrate–nickel nitrate–water. The absolute concentrations of the cobalt and nickel were varied fivefold, and the ratio of concentration of cobalt to nickel was varied from 4 : 1 to 1 : 4. Only one run was made with nitric acid present.

In Figure 5 the K value of nickel from Table 3 is plotted vs. the total cobalt plus nickel concentration in the water at equilibrium. For comparison curves A and B from Figure 3 are shown for nickel when equilibrated in the absence of the cobalt. A similar type of plot for cobalt, which is not shown, was made, the K of
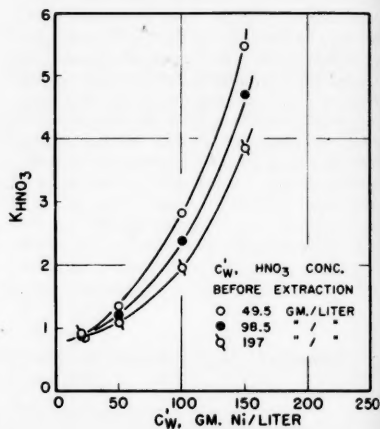

Fig. 4. Distribution coefficient of nitric acid in the system nickel nitrate–water–nitric acid–n-butanol at 25.0°C.
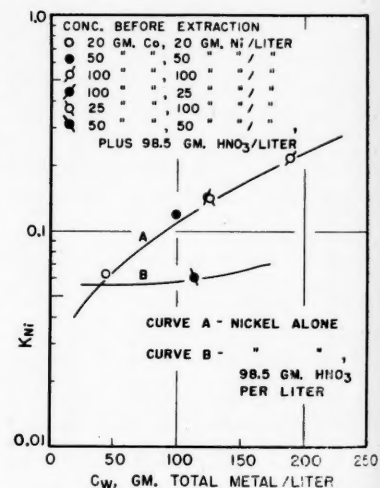

Fig. 5. Distribution coefficient of nickel nitrate in the system nickel nitrate–cobalt nitrate–water–n-butanol at 25.0°C.
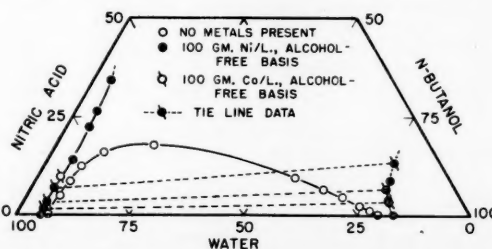

Fig. 6. Phase diagram for the system nitric acid–water–n-butanol at 25.0°C. (Data on a weight-percentage metal-free basis.)

cobalt being plotted vs. the total metal concentration in the water at equilibrium. This gave the same trends as nickel. That the distribution coefficient of cobalt or nickel in a mixture of the two depends only on the total metal concentration is concluded.

Separation Factors

When cobalt and nickel were equilibrated separately with no nitric acid present, and the initial concentration was 100 g. each metal/liter, the calculated separation factor was a maximum at 1.49. When the two metals were equilibrated together, the actual separation factor was 1.27 for the same concentrations. Hence having both metals present decreased the maximum separation factor by about 15%. These separation factors in Table 3 are all low and constant at about 1.26. The separation factor for sulfates increased slightly when the metals were equilibrated together and was between 1.2 to 1.5 depending on the sulfuric acid concentration (7). The separation factor for the chlorides increased very greatly with increases in hydrochloric acid concentration (3).

Phase Diagram

The phase diagram (Figure 6) is shown for the ternary system n-butanol–nitric acid–water on a metal-free basis; it is very similar to the n-butanol–sulfuric acid–water system (8). When the metal salts cobalt or nickel nitrate are present, the solubilities of the alcohol in the aqueous phase and the aqueous phase in the alcohol phase are lowered and change the phase diagram markedly (Figure 6). Densities were determined and reported in Tables 2 and 3 and elsewhere (6).

Inspection of experimental phase solubility and tie line data, reported elsewhere (1) and used to plot Figure 6 show that the ratio of the nitric acid content to the water content in the phases at equilibrium are as follows. In the aqueous phase the ratio varies from 0.03 to 0.08 depending on the concentration of nitric acid. In the organic phase the ratio is about 0.2 to 0.8. Hence at equilibrium the nitric acid to water ratio is considerably higher in the organic than in the aqueous phase, and the acid is extracted preferentially by the organic solvent.

Using the triangular diagram (Figure 6) and Figures 1, 3, 4, or 5 one can predict the compositions and amounts of the two phases resulting from the equilibrium of equal volumes of an aqueous solution and the solvent. Density data can then be used to calculate relative volumes of the resultant equilibrium solutions.

ACKNOWLEDGMENT

NOTATION

C = concentration, g. metal/liter (not g. metal salt/liter)

C_0 = equilibrium concentration of metal or nitric acid in organic phase, g./liter

C_w = equilibrium concentration of metal or nitric acid in aqueous phase, g./liter

C_w' = concentration of metal or nitric acid in aqueous phase before extraction, g./liter

K = distribution coefficient, C_0/C_w

K' = distribution coefficient, $C_0/(C_w)^n$

n = constant

Greek Letters

β = separation factor = $K(\text{cobalt})/K(\text{nickel})$

ρ_0 = density of organic phase at equilibrium, g./ml.

ρ_w = density of aqueous phase at equilibrium, g./ml.

LITERATURE CITED

1. Geankoplis, C. J., and E. J. Scharf, Doc. 5827, A.D.J. Auxiliary Publications Project, Washington, D. C.; $1.25 for photoprints or 35-mm. microfilm.
2. Gagnon, J., Chemist Analyst, No. 1, 43, 15 (1954).
3. Garwin, Leo, and A. N. Hixson, Ind. Eng. Chem., 41, 2298, 2303 (1949).
4. Moore, T. E., R. J. Laren, and P. C. Yates, J. Phys. Chem., 59, 90 (1955).
5. Rigamonti, R., and E. Spaccemela-Marchetti, Chim. e ind. (Milan), 36, 91 (1954).
6. Scharf, E. J., Ph.D. dissertation, Ohio State Univ., Columbus, Ohio (1957).
7. Schlea, C. S., and C. J. Geankoplis, Ind. Eng. Chem., 49, 1056 (1957).
8. Schlea, C. S., Ph.D. dissertation, Ohio State Univ., Columbus, Ohio (1955).
9. Snell, F. D., and C. T. Snell, "Colorimetric Methods of Analysis," 3 ed., Vol. II, p. 346, D. Van Nostrand, New York (1948).
10. Templeton, C. C., and L. K. Daly, J. Am. Chem. Soc., 73, 3989 (1951).
11. ———, J. Phys. Chem., 56, 215 (1952).
12. Yoe, J. H., "Photometric Chemical Analysis," Vol. I, p. 172, John Wiley, New York (1948).

Heat and Mass Transfer from Wall to Fluid in Packed Beds

SAKAE YAGI and NORIAKI WAKAO

University of Tokyo, Tokyo, Japan

Experiments of heat and mass transfer from the tube wall to the fluids flowing through the packed beds were carried out separately. In heat transfer air was used as the fluid, and several kinds of solid particles with low and high thermal conductivities were investigated to determine effective thermal conductivities and wall heat transfer coefficients. In mass transfer the dissolution rate of the coated material on the inner wall of the packed tube to the water stream was measured, and wall mass transfer coefficients were analyzed. It was found that a close similarity exists between the J_H and J_D factor for the wall coefficients in the turbulent-flow region.

The rate of heat transfer in a packed bed is of particular interest in the process design not only of heat exchangers but also of catalytic reactors. The problem of the rate of heat transfer from the tube wall to a fluid flowing through a packed tube has been the subject of considerable study. The first work of heat transfer in a packed bed was made by Colburn (6) in 1931. He correlated the data as the over-all heat transfer coefficients, which are similar to those for an empty tube. Thereafter several investigators (4, 12, 13) reported the correlations for over-all coefficients.

For the calculation of the temperature distributions and explanation of the mechanism of heat transfer in the bed, the concept of the so-called "effective thermal conductivity" was introduced. Smith et. al. (21) determined values of the local effective thermal conductivity in the packed bed and found that the resistance to heat transfer increased greatly near the wall. Hatta and Maeda (15), Coberly and Marshall (5), and later workers (2, 9, 18, 19, 23) found that an additional resistance to heat transfer existed at the wall. They assumed the effective thermal conductivity to be constant within the bed and expressed the additive effect in the wall vicinity as the wall heat transfer coefficient.

This paper reports the results of both heat and mass transfer from the wall of

TABLE 1. SOLID PARTICLES USED FOR HEAT TRANSFER EXPERIMENTS.

G.S.—glass spheres
C.C.—cement clinkers (granular)
L.S.—lead shots (spherical)
S.B.—steel balls (spherical)

Reactor type 1
Diameter of tube: $D_T = 36$ mm., height: $L = 200$ mm.

Reactor type 2
$D_T = 36$ mm., $L = 360$ mm.

Run	Reactor type	Solid material	Particle size* (Tyler mesh range)	Average diameter of particle D_p, mm.	D_p/D_T
(A)	2	G.S.	20–24	0.764	0.0212
(B)	1	G.S.	20–24	0.764	0.0212
(C)	2	G.S.	16–20	0.909	0.0252
(D)	1	G.S.	16–20	0.909	0.0252
(E)	1	G.S.	—	2.60	0.0722
(F)	1	G.S.	—	6.00	0.167
(H)	2	C.C.	12–14	1.28	0.0355
(I)	2	C.C.	9–10	1.81	0.0503
(J)	1	C.C.	8–10	1.97	0.0547
(K)	2	C.C.	7–8	2.57	0.0714
(L)	1	C.C.	4–5	4.31	0.120
(N)	2	L.S.	20–24	0.764	0.0212
(O)	2	L.S.	14–16	1.08	0.0300
(P)	1	L.S.	—	1.50	0.0417
(Q)	1	S.B.	—	3.10	0.0861

*Geometrical mean size was taken as D_p.

AIR IN

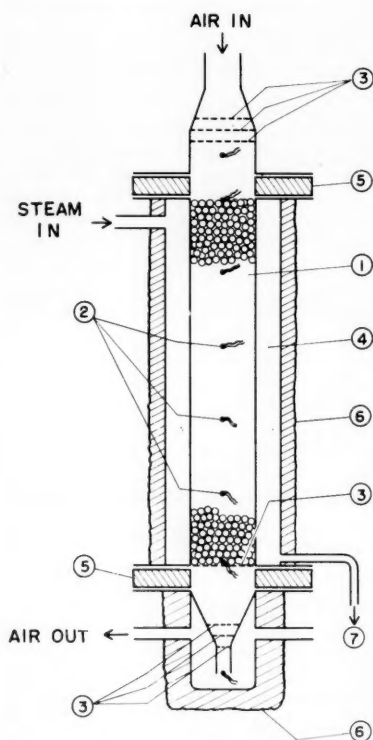STEAM IN →

AIR OUT ←

Fig. 1. Schematic diagram of reactor used for heat transfer experiment. (1) packed bed, (2) thermocouple, (3) screen, (4) steam jacket, (5) bakelite ring plate, (6) asbestos, (7) steam trap.

the packed tube to fluid flowing through the beds investigated separately. At first the effective thermal conductivities and wall heat transfer coefficients were

determined for various kinds of solid particles in the heat transfer experiment. Then the wall mass transfer coefficients were obtained from the mass transfer experiment. The relationship between heat and mass transfer on the coefficient will be discussed.

HEAT TRANSFER EXPERIMENTS

Apparatus and Techniques

The main apparatus was a steam-jacketed, brass tube of 36-mm. I.D. with 1.0-mm. wall thickness. Two identical reactors with tubes of different lengths were used, the length of the shorter tube being 200 mm. and that of the longer one 360 mm. The experimental apparatus of the shorter tube is shown in Figure 1. The tube was packed with solid particles until their top level coincided with the upper steam-jacket flange. Thick Bakelite ring plates and rubber packing sheets were inserted between the flanges at either ends of the steam-jacketed tube to insulate heat from the heating section to the connecting ones. Steam was introduced at the top of the jacket, and the condensate was withdrawn through the trap.

Various temperature measurements were made by means of the copper-constantan thermocouple leads of 0.1-mm. diameter which were connected to a potentiometer. Prior to entering the packed bed the air passed successively through several sheets of screen, which obtained uniform flow and temperature distributions. The temperature of the inlet air was measured by the thermocouples located about 20 to 25 mm. above the entrance of the bed. The range of the inlet air temperature was from 10° to 30°C. The air stream was heated while flowing downward through the bed under the condition of uniform wall temperature. The longitudinal temperature gradients along the center axis of the tube were measured

at every 40-mm. depth from the inlet to the exit of the bed. Mixing of the effluent air was done by passing it through three sheets of screen placed in the throttle of the adapter, which was made of the heat-insulating material to avoid heat loss. Just below the last screen a thermocouple was set to measure the mixed mean temperature of the effluent air; the preliminary runs assured that the correct mean temperature could be obtained this way.

The temperature difference between the saturation steam and outer surface of the tube was calculated by the equation for the film type of condensation (16) and found to be negligible for the purpose. The temperature drop through the wall of the brass tube was also negligible. The temperature of the inner surface of the packed tube was then taken as the temperature of the saturation steam in the jacket, 100°C. for all operating runs. After steady state was achieved, the necessary data were recorded.

The solid particles used in this investigation were glass spheres, broken solids of cement clinker, lead shots, and steel balls ranging from 0.764 to 6.00 mm., as tabulated in Table 1. For the solid particle cut by the Tyler sieves, the geometrical mean particle size was adopted; the square root of the product of the two adjacent sieve openings was taken as the mean particle diameter. The modified Reynolds number based on particle diameter varied from 20 to 800 in this experiment.

Calculations and Results

In a cylindrical packed tube heated from the wall the following partial differential equation for the temperature at steady state may be used:

$$C_p G \frac{\partial t}{\partial l} = k_e \left(\frac{\partial^2 t}{\partial r^2} + \frac{1}{r} \frac{\partial t}{\partial r} \right) \quad (1)$$

TABLE 2. COMPARISON OF EXPERIMENTALLY OBSERVED TEMPERATURES ALONG CENTER AXIS OF BED WITH CALCULATED TEMPERATURES

Run $(F) - 1$
Diameter of bed: $D_T = 36$ mm.
Height of bed: $L = 200$ mm.
Solid particles: glass spheres, $D_p = 6.00$ mm.
Air mass velocity: $G = 2,740$ kg./(sq. m.) (hr.)
Tube wall temperature: $t_w = 100°C$.
Inlet air temperature: $t_0 = 16.5°C$.

Bed height: l, cm.	Temperature at center axis of bed: t_c, °C.	
	Observed values	Calculated values from Equation (2)
0	16.9	
4	21.9	19.9
8	35.3	33.5
12	49.3	47.8
16	61.1	59.4
20	69.8	68.5

Mixed mean temperature of effluent air: $(t_m)_L$,

observed value $= 78.8°C$.
calculated value from Equation (2) $= 77.9°C$.

Table 3. Typical Heat Transfer Results

Run (refer to Table 1)	Air mass velocity G, kg./(sq. m.)(hr.)	Reynolds number D_pG/μ	Inlet air temperature t_0, °C.	Observed values Temperature at center of bed exit $(t_e)_L$, °C.	Mixed mean temperature of effluent air $(t_m)_L$, °C.	* $-\dfrac{k_e\xi_1^2}{C_pG}$ $\dfrac{}{2.303}$, cm.$^{-1}$	Derived results k_e/k_g	h_wD_p/k_g	Calculated temperatures from Equation (2), °C. Temperature at center of bed exit	Mixed mean temperature of effluent air
(F)–1	2,740	234	16.5	69.8	78.8	−0.0277	21.7	15.5	68.5	77.9
2	4,440	382	18.7	63.6	74.8	−0.0232	28.5	21.6	62.1	73.8
3	8,010	691	18.7	56.1	69.2	−0.0189	43.4	30.9	54.1	67.7
(I)–1	5,620	145	16.8	70.5	81.9	−0.0165	19.8	7.61	69.1	81.0
2	7,990	206	16.2	65.1	79.9	−0.0151	22.7	11.8	63.7	79.1
(K)–2	4,220	153	18.6	80.2	88.0	−0.0216	18.6	10.8	79.9	87.8
3	5,710	207	20.7	76.3	85.3	−0.0185	22.5	11.8	75.1	84.5
4	9,660	352	21.2	71.4	82.2	−0.0164	33.9	17.6	70.5	81.7
(O)–1	6,790	105	12.0	69.4	82.2	−0.0172	22.4	6.70	68.2	81.6
2	9,120	141	12.7	58.0	77.7	−0.0137	20.9	9.98	56.5	76.9

*Slope of straight-line portion in plot of $t_w - t_e$ vs. bed height on semilogarithm graph paper.

In the derivation of Equation (1) the following assumptions were made: (1) the temperature difference between solid and fluid is negligible; (2) the mass velocity of fluid is uniform across the tube diameter, and the physical properties of fluid are independent of temperature variation; (3) the effective thermal conductivity is uniform within the bed; and (4) the longitudinal heat conduction is negligible.

A solution of Equation (1), which may be easily obtained, has already been described by Hatta and Maeda (15) and Coberly and Marshall (5) using the following boundary conditions for the uniform inlet temperature and constant wall temperature:

at the inlet:
at $\qquad l = 0, \quad t = t_0$
at the inside surface of the tube wall:
at $\quad r = R, \quad k_e(\partial t/\partial r) = h_w(t_w - t)$

The solution of Equation (1) with these boundary conditions is (5, 15)

$$U = \frac{t_w - t}{t_w - t_0} = 2\sum_{i=1}^{\infty} \frac{(h_wR/k_e) \cdot J_0(r\xi_i) \cdot e^{-k_e\xi_i^2 l/C_pG}}{[(h_wR/k_e)^2 + (R\xi_i)^2] \cdot J_0(R\xi_i)} \quad (2)$$

The term ξ_i is a root of the following transcendental equation:

$$(h_wR/k_e) \cdot J_0(R\xi_i) = (R\xi_i) \cdot J_1(R\xi_i) \quad (3)$$

For regions of sufficiently large values of l it is enough to take only the first term, $i - 1$, of the series in Equation (2). The effective thermal conductivity and the wall heat transfer coefficient are calculated simultaneously from the slope of the straight-line portion in the plot of $t_w = t_e$ against l on a semilogarithmic graph paper, the ratio of the temperature difference at the bed exit, $[t_w - (t_m)_L]/[t_w - (t_e)_L] = 2 \cdot J_1(R\xi_1)/(R\xi_1)$, and with the aid of Equation (3).

Table 2, for a typical run, shows the observed temperatures along the center axis of the tube and those calculated with the help of Equation (2), which uses the
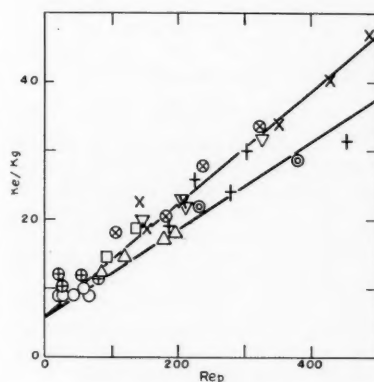

Fig. 2. Correlation of effective thermal conductivities for glass spheres and broken solids of cement clinker. (For symbols see Figure 4.)

derived results of k_e and h_w. It appears that the calculated temperatures are

somewhat lower than the observed ones, owing to the inlet air being heated between the point of temperature measurement and the entrance to the bed, as pointed out by Coberly and Marshall (5).

The typical heat transfer results and the data from which they were derived are shown in Table 3.*

The temperature selected to evaluate the fluid properties is the arithmetical mean of the inlet and outlet temperatures.

The relation of k_e/k_g with $Re_p = D_pG/\mu$ is shown for glass spheres and broken solids of cement clinker in Figure 2 and

*Tabular material has been deposited as document 5828 with the American Documentation Institute, Photoduplication Service, Library of Congress, Washington 25, D. C., and may be obtained for $2.50 for photoprints or $1.75 for 35-mm. microfilm.

for metal spheres in Figure 3. It seems permissible to express the values of the effective thermal conductivity by the following equation (20, 22) if some scattering of points at the relatively low Reynolds number is neglected:

$$k_e/k_g = k_e^0/k_g + (k_e)_{td}/k_g \quad (4)$$
$$= k_e^0/k_g + (\alpha\beta)_H \cdot Pr \cdot Re_p$$

where $(\alpha\beta)_H$ is the parameter for characterizing the fluid mixing in radial direction and is defined as the inverse of the modified Peclet number for heat transfer due to turbulent diffusion of fluid, $(Pe_H)_{td} = D_pC_pG/(k_e)_{td}$. The values of the terms in the right-hand side of Equation (4) may be determined for the experimental range employed in the present work as follows:

for glass spheres and broken solids of cement clinker

$k_e^0/k_g = 6.0$

$(\alpha\beta)_H = 0.11$ for D_p/D_T
$\qquad = 0.021 \sim 0.072$

$(\alpha\beta)_H = 0.09$ for D_p/D_T
$\qquad = 0.12 \sim 0.17$

for metal spheres

$k_e^0/k_g = 13$

$(\alpha\beta)_H = 0.11$ for $D_p/D_T \qquad (5)$
$\qquad = 0.021 \sim 0.086$

The values of $(\alpha\beta)_H$ in the present investigation agree well with the theoretical estimates on the basis of the "random walk" theory of Baron (1) and Ranz (20), and they also agree well with the experimental values of the previous investigators (2, 5, 15, 18, 19, 22). The value of k_e^0/k_g, which is the ratio of the effective thermal conductivity in stagnant
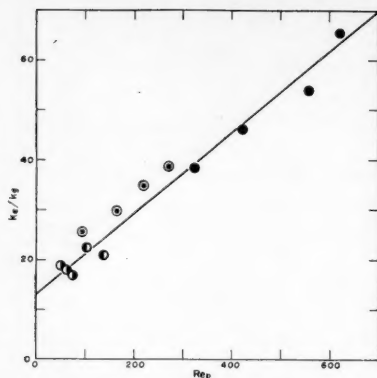
Fig. 3. Correlation of effective thermal conductivities for metal spheres. (For symbols see Figure 4.)

Fig. 4. Plot of wall heat transfer coefficients, for glass spheres, broken solids of cement clinker, and metal spheres of present work with data of Plautz and Johnstone (18), and Felix (9) for glass spheres. Where Felix's data were taken from the literature (11) and $\epsilon = 0.4$ was assumed.

fluid system to the molecular thermal conductivity of the fluid, for metal spheres was obtained as about twofold greater than that for glass spheres and cement clinker particles. The temperature level in the bed was less than 100°C. in all runs; the radiation contribution to $k_e{}^0$ may be neglected. The thermal conductivities of the glass and cement clinkers were less than 1 kcal./(m.)(hr.)(°C.), and those of lead and steel were about 30 and 40 kcal./(m.)(hr.)(°C.), respectively. Therefore it is apparent that the difference between the value of $k_e{}^0$ for glass spheres and cement clinker particles and that for metal spheres is due to the large difference of the thermal conductivities of the solid particles themselves. The values of $k_e{}^0$ agree with the theoretical estimates of Yagi and Kunii (22).

The data of the wall heat transfer coefficient were plotted as $h_w D_p/k_g$ against Re_p in Figure 4, and it was found that the wall coefficient was not so affected by the thermal conductivity of solid particles. The results of Plautz and Johnstone (18) for ½-, and ¾-in. glass spheres in an 8-in. tube, and those of Felix (9) for ⅛-, and ¼-in. glass spheres in a 3-in. tube were added in Figure 4; both of them are for the heating of air flowing in an upward direction through the packed beds. The results of the present investigation were not only for the spheres but also for the broken solids. All data of the present work were obtained by the heating of air flowing downward through the beds. Although the data of Felix, Plautz, et al. seem somewhat larger than those of the present work, the agreement of both sets of results is remarkable in view of the difference in experimental method. The solid line in Figure 4 can be represented by

$$h_w D_p/k_g = 0.18 Re_p{}^{0.80} \qquad (6)$$

The effect of the power of the Prandtl number in the correlation was not determined because the Prandtl number of air had a constant value of 0.70.
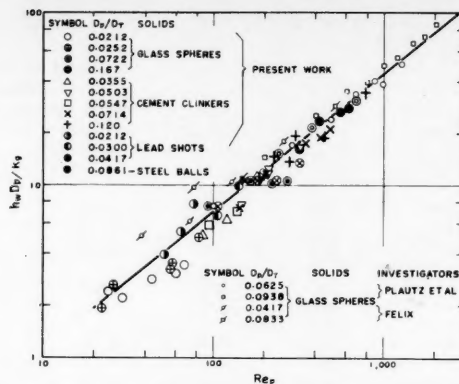
According to the J factor of Chilton and Colburn (3), correlated by $J_H = (h_w/C_p G)(C_p \mu/k_g)^{2/3}$ for heat transfer, Equation (6) may be rewritten as

$$J_H = 0.20 Re_p{}^{-0.20} \qquad (6a)$$

The data for cylinders (5, 9) are notably higher than those for spheres and broken solids owing to the difference in the contact manner of particles adjacent to the wall. Hanratty (11) showed that the wall heat transfer coefficient on cylinders varied with the fluid velocity to the 0.5 power, and he tried to interpret the mechanism of wall heat transfer by applying the *surface renewal* theory of Danckwerts (8).

MASS TRANSFER EXPERIMENTS

Apparatus and Techniques

To explore the relationship between the wall coefficients of heat and mass transfer the rate study of the dissolution of an organic solid coated on the inner wall of the packed tube to the water stream was carried out.

Two-naphthol was chosen for the diffusing solute because of relatively low solubility, known data of the diffusion coefficient, and easy measurement of concentration. The inner wall of the tube was coated by melting 2-naphthol of chemical-pure degree. The coated tube with a circular cross section and smooth inner surface was packed with solid particles.

The city water was introduced to the bed, and the flow was always downward to prevent fluidization of solid particles. When steady state was attained, the effluent water was sampled and analyzed by means of a spectrophotometer at the wave length of 2,850 Å.

Solubility and diffusion coefficient data on the system of 2-naphthol–water had been determined by Moyle and Tyner (17). Solubility of coated material checked experimentally, was found to agree with the values in the literature, used here, within the range of the experimental error.

The 2-naphthol was relatively insoluble in water, and so the tube diameter did not change appreciably during a test. The solid particles used for this work were silver sand and glass spheres. The ranges of the particles and the tube dimensions are shown

TABLE 4. SOLID PARTICLES USED FOR MASS TRANSFER EXPERIMENTS

S.S.—silver sand (granular)
G.S.—glass spheres

Run	Solid material	Particle size* (Tyler mesh range)	Average diameter of particle D_p, mm.	Diameter of bed D_T, mm.	Height of bed L, mm.	D_p/D_T	L/D_T
(A)	S.S.	16–20	0.909	16.0	94	0.0568	5.88
(B)	S.S.	20–24	0.764	11.4	75	0.0670	6.58
(C)	S.S.	20–24	0.764	11.0	108	0.0695	9.82
(D)	S.S.	20–24	0.764	10.8	150	0.0708	13.9
(E)	S.S.	16–20	0.909	11.6	49	0.0784	4.22
(F)	S.S.	16–20	0.909	11.0	108	0.0826	9.82
(G)	S.S.	16–20	0.909	10.8	150	0.0842	13.9
(H)	S.S.	16–20	0.909	10.7	75	0.0850	7.01
(K)	G.S.	20–24	0.764	16.0	100	0.0477	6.25
(L)	G.S.	14–16	1.08	16.0	94	0.0675	5.88
(M)	G.S.	14–16	1.08	11.3	49	0.0956	4.34
(N)	G.S.	14–16	1.08	11.0	108	0.0982	9.82
(O)	G.S.	—	2.50	16.0	100	0.156	6.25

*Geometrical mean size was taken as D_p.

A.I.Ch.E. Journal

TABLE 5. TYPICAL MASS TRANSFER RESULTS

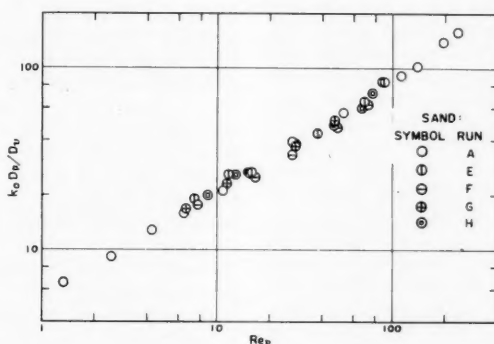| | | | | Concentration of 2-naphthol | | | | Derived results | | |
| Run (refer to Table 4) | Water velocity u_0 m./hr. | Temperature of effluent water, °C. | Reynolds number D_pG/μ | Concentration of effluent water (C_m) L, g.-mole/liter $\times 10^{-4}$ | Saturated concentration C_s, g.-mole/liter $\times 10^{-4}$ | Schmidt number Sc | Over-all mass transfer coefficient k_0D_p/D_v | Wall mass transfer coefficient | | |
								k_wD_p/D_v	$J_D = (k_w/u_0)Sc^{2/3}$	
(A) −1	5.60	18.0	1.34	4.07	40.6	1,100	6.55	7.21	0.523	
3	18.2	17.0	4.23	2.35	39.0	1,150	12.9	13.7	0.309	
5	46.3	17.0	10.8	1.50	39.0	1,150	21.0	21.7	0.191	
8	227	16.7	52.6	0.826	38.5	1,170	56.4	57.3	0.104	
12	824	17.4	194	0.595	39.6	1,130	139	141	0.0700	
(O)− 2	14.9	17.7	9.73	1.61	40.1	1,110	17.7	17.9	0.179	
5	52.0	17.8	34.0	0.992	40.3	1,110	37.5	37.8	0.108	
7	190	16.7	121	0.571	38.5	1,170	84.6	84.9	0.0668	
9	680	17.2	438	0.516	39.2	1,140	262	263	0.0577	
12	1,900	17.0	1,220	0.404	39.0	1,150	580	580	0.0453	

Fig. 5. Over-all mass transfer coefficients for 16 to 20 Tyler mesh of silver sand.
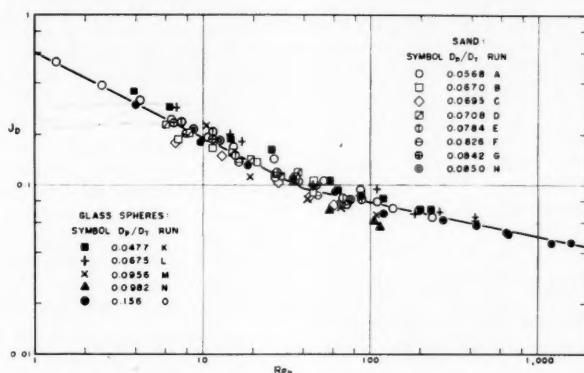
Fig. 6. Plot of J_D, based on wall mass transfer coefficient, vs. Re_p.

in Table 4. In this experiment the modified Reynolds number was from 1 to 1,600, and the Schmidt number ranged from 1,000 to 1,700, depending on the temperature of water.

Calculations and Results

The following assumptions were made on the analysis of the mass transfer rate. The so-called "rodlike" flow occurs in the bed, and the concentration of solute in the fluid adjacent to the inner wall is saturated. Then for the mean concentration over the cross section the following differential equation is set up in the bed:

$$\pi \; D_T k_0(C_s - C_m) \; dl$$
$$= (\pi/4) \; D_T^2 u_0 \; dC_m$$

When one integrates and puts inlet concentration at zero,

$$k_0 = (D_T u_0/4l) \cdot \ln \left[C_s/(C_s - C_m) \right] \quad (7)$$

The derived results and the data from which they were computed are shown in Table 5 for typical runs.

The over-all mass transfer coefficients correlated to k_0D_p/D_v for 16 to 20 Tyler mesh of silver sand are plotted as a function of Re_p in Figure 5. An examination of the figure will show that values of the over-all mass transfer coefficients were not affected by the tube length and that the values of L/D_T were varied from 4.2 to 14. This was similar in experiments for other particles. It was made evident that the bed heights used in this experiment were long enough to obtain the converged values for over-all mass transfer coefficients which would be attained at the infinite bed length.

On the other hand, mass transfer from the wall to the flowing stream in the packed bed is analogous to the heat transfer phenomenon already described. At steady state the following partial differential equation for concentration of the diffusing solute may be written:

$$u_0 \frac{\partial C}{\partial l} = E\left(\frac{\partial^2 C}{\partial r^2} + \frac{1}{r} \frac{\partial C}{\partial r} \right) \quad (8)$$

The boundary conditions for this case are

at

$$l = 0, \quad C = 0$$

at

$$r = R, \quad E(\partial C/\partial r) = k_w(C_s - C)$$

where the effective diffusivity was assumed to be uniform within the bed. The wall mass transfer coefficient was defined in the boundary condition at the inner surface of the wall. The solution of Equation (8) is indicated directly for the mass transfer analogue from Equation (2) for the heat transfer. For the mean concentration the following equation is available:

$$\frac{C_s - C_m}{C_s} = 4 \sum_{i=1}^{\infty} \frac{e^{-E\xi_i^2 l/u_0}}{(R\xi_i)^2 \cdot [1 + (E\xi_i/k_w)^2]} \quad (9)$$

where ξ_i is defined by

$$k_w \cdot J_0(R\xi_i) = (E\xi_i) \cdot J_1(R\xi_i) \quad (10)$$

In a manner similar to the theoretical

development for heat transfer [15] the theoretical relation between k_w, E, and k_0 may be derived. The bed could be regarded as sufficiently long in this experiment. When one substitutes into Equation (7) the equation which is simplified by taking the first term in Equation (9) and putting $l = \infty$,

$$k_0 = E \, D_T \xi_1{}^2/4 \qquad (11)$$

results, where

$$k_w \cdot J_0(R\xi_1) = (E\xi_1) \cdot J_1(R\xi_1) \qquad (10a)$$

The effective diffusivity for mass transfer is the sum of the molecular diffusion and the diffusion process caused by turbulent mixing of fluid through the interstices of the bed. Usually the former contribution may be neglected as compared with the latter. Although there are several additional mechanisms that come into play for heat transfer which are not possible for mass transfer, for example transport of heat through the particles, the modified Peclet number for mass transfer $Pe_D = D_p u_0/E$ was assumed to be equivalent to the value of $(Pe_H)_{td} = D_p C_p G/(k_e)_{td}$ for heat transfer.

$$E/D_v = (\alpha\beta)_D \cdot Sc \cdot Re_p \qquad (12)$$

where $(\alpha\beta)_D$ was assumed to be 0.11. Using Equations (10a), (11), and (12) one can obtain the values of the wall mass transfer coefficient from data of the over-all mass transfer coefficient.

The calculated results of k_w were listed in terms of $k_w D_p/D_v$ and $J_D = (k_w/u_0)(\mu/\rho D_v)^{2/3}$ in Table 5.* It should be noted that values of k_w are larger than those of k_0 by less than 10%, because of a little contribution of the eddy diffusivity on the over-all dissolution rate for the sake of the large values of the Schmidt number in this system. Plautz and Johnstone [18] reported that the value of $(\alpha\beta)_D$ was about 25% below that of $(\alpha\beta)_H$. Even if their result is used for the present calculation, it has little effect on the calculated results of the wall coefficient. The calculated data of the wall mass transfer coefficient are plotted to J_D against Re_p in Figure 6. The data of the glass spheres and those of silver sand agreed well with the solid lines represented by the equations

$$J_D = 0.60 Re_p{}^{-\frac{1}{2}}$$

for laminar flow,

$$Re_p = 1 \sim 40 \qquad (13)$$

$$J_D = 0.20 Re_p{}^{-0.20}$$

for turbulent flow,

$$Re_p = 40 \sim 2,000 \qquad (14)$$

It has been generally recognized that the flow through the packed bed became turbulent at Re_p exceeding about 40, and this appeared in the correlations for the wall mass transfer coefficient as expressed by Equations (13) and (14).

DISCUSSION ON WALL COEFFICIENT

The Prandtl number was omitted in Equation (6) for the wall heat transfer coefficient because it remained constant, 0.70, for air. In the mass transfer experiment the Schmidt number of the 2-napththol–water system was limited in the range of 1,000 to 1,700; therefore the effect of the Schmidt number on the wall mass transfer was not determined. But from comparison of Equation (6a) with Equation (14), it is interesting to note that the same equations of the Reynolds number were obtained for wall coefficients on heat and mass transfer, as far as the data were correlated to the J factor (Figure 7). The present investigation for heat transfer was carried out in the turbulent flow region only, because at the low flow rate it was difficult to obtain exact data owing to the small driving force at the outlet of the bed. On the contrary the experiment of mass transfer could be easily extended to the low Reynolds-number region. The mechanism of heat transfer at the inside of the tube wall is more complicated than that of mass transfer, since heat is transferred through the solid particles adjacent to the wall in addition to being transferred by the fluid flow. Even if the wall heat transfer coefficient is affected by the former contribution, it will be little in comparison with the latter in the turbulent-flow region, because the analogy of the J factor was confirmed to exist between heat and mass transfer.

On the study of the transfer rate from particle to fluid in the packed bed Ranz [20] proposed the model theory that the particle in the bed could be regarded as a single particle obtaining an actual

velocity of jet flowing through a minimum open area formed by particles. For the rhombohedral packing of spheres the ratio of the total cross section to the open area effective for jet formation was calculated as 10.7, and for the data of Gamson, Thodos, and Hougen [10] on the transfer rate from particle to fluid in the packed bed the effective fluid velocity was obtained as 9.1 times the superficial one.

The dependence of the wall mass transfer coefficients on fluid velocity were similar to that for flow over the flat plate in both of the laminar- and turbulent-flow regions. The interpretation of experimental equations for wall coefficients in the turbulent-flow region was attempted by use of the discontinuous boundary-layer model, which means that the boundary layer at the wall is continually replaced with fresh fluid caused by turbulent mixing. In this model theory the wall is assumed to be covered with discontinuous boundary layers having the same length, and the resistance to heat transfer at the inner wall is assumed to be due to the boundary layer existing there. For the interpretation of heat transfer in the fluidized bed a similar model was applied by Levenspiel and Walton [14].

The equation of the wall coefficient in the turbulent flow was obtained by proposing the following simplified models: (1) The effective fluid velocity, nine times the superficial one, makes the discontinuous boundary layers on the wall. (2) The average length of each boundary layer is equal to the diameter of solid particle; the boundary layer develops from the contact point of solid particle adjacent to the wall, is destroyed at the next contact point on the wall, and is replaced with fresh boundary layer. (3) The rate of heat and mass transfer in the boundary layer is similar to that of a flat plate. For the mean heat transfer coefficient in the turbulent flow of a fluid parallel to a flat plate the Colburn relation [7, 16] has been suggested:
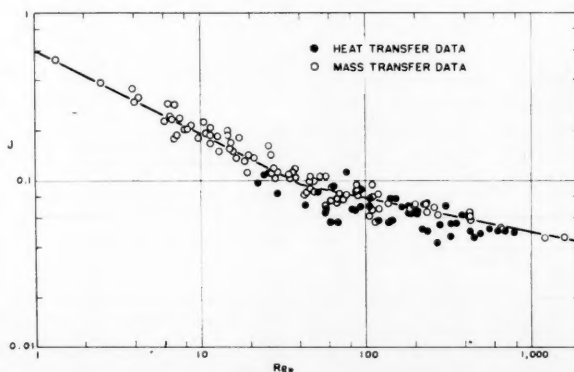
$$h_w x/k_g = 0.036 Pr^{\frac{1}{3}}(xv\rho/\mu)^{0.8}$$

Fig. 7. Comparison of J_H and J_D for wall coefficient of present work.

Substituting $9u_0$ for v and D_p for x, one has

$$J_H = 0.21(D_p u_0 \rho/\mu)^{-0.2} \quad (15)$$

The same equation will be derived for J_D of mass transfer. Equation (15) agrees fairly well with the empirical correlations expressed by Equation (6a) for heat transfer and by Equation (14) for mass transfer.

CONCLUSIONS

Heat and mass transfer from the tube wall to the fluid flowing through the packed beds of various kinds of solid particles were investigated. Air was used as the fluid for heat transfer and water for mass transfer. The results obtained from the investigation were summarized as follows:

1. The effective thermal conductivity of the packed bed was found to be expressed by

$$k_e/k_g = 6.0 + 0.11 Pr Re_p$$

for

$$D_p/D_T = 0.021 \sim 0.072$$

$$k_e/k_g = 6.0 + 0.09 Pr Re_p$$

for

$$D_p/D_T = 0.12 \sim 0.17$$

for glass spheres and broken solids of cement clinker, and by

$$k_e/k_g = 13 + 0.11 Pr Re_p$$

for

$$D_p/D_T = 0.021 \sim 0.086$$

for metal spheres.

2. The following correlation was obtained for the wall heat transfer coefficient:

$$J_H = (h_w/C_p G) Pr^{\frac{1}{3}}$$

$$= 0.20 Re_p^{-0.20}, \quad Re_p > 20$$

3. The following correlations for the wall mass transfer coefficient were obtained for silver sand and glass spheres:

$$J_D = (k_w/u_0) Sc^{\frac{1}{3}}$$

$$= 0.60 Re_p^{-\frac{1}{2}}, \quad Re_p < 40$$

$$J_D = (k_w/u_0) Sc^{\frac{1}{3}}$$

$$= 0.20 Re_p^{-0.20}, \quad Re_p > 40$$

NOTATION

C = concentration of solute in fluid, M/L^3

C_m = mixed mean concentration of solute in fluid over cross section, M/L^3

C_p = specific heat of fluid, Q/MT

C_s = saturated concentration of solute, M/L^3

D_p = diameter of packing particle, L

D_T = tube diameter, L

D_v = molecular diffusion coefficient, L^2/θ

E = effective diffusivity in radial direction, based on void plus nonvoid area, L^2/θ

G = superficial mass velocity of fluid based on empty tube, $M/L^2\theta$

h_w = wall heat transfer coefficient, $Q/L^2\theta T$

J_D = J factor correlating wall mass transfer coefficient = $(k_w/u_0)Sc^{2/3}$, dimensionless

J_H = J factor correlating wall heat transfer coefficient = $(h_w/C_p G)Pr^{2/3}$, dimensionless

$J_0( )$ = Bessel function of first kind of zero order, dimensionless

$J_1( )$ = Bessel function of first kind of first order, dimensionless

k_e = effective thermal conductivity in radial direction, based on void plus nonvoid area, $Q/L\theta T$

k_g = molecular thermal conductivity of fluid, $Q/L\theta T$

k_0 = over-all mass transfer coefficient, L/θ

k_w = wall mass transfer coefficient, L/θ

l = longitudinal distance variable, L

L = length of packed bed, L

Pe_D = modified Peclet number for mass transfer = $D_p u_0/E$, dimensionless

Pe_H = modified Peclet number for heat transfer = $D_p C_p G/k_e$, dimensionless

Pr = Prandtl number = $C_p\mu/k_g$, dimensionless

r = radial distance variable, L

R = radius of tube = $D_T/2$, L

Re_p = modified Reynolds number based on particle diameter = $D_p G/\mu$, dimensionless

Sc = Schmidt number = $\mu/\rho D_v$, dimensionless

t = temperature in packed bed, T

t_c = temperature at center axis of tube, T

t_m = mixed mean temperature of fluid over cross section, T

t_0 = inlet temperature of fluid, T

t_w = temperature of wall, T

u_0 = superficial fluid velocity based on empty tube, L/θ

v = velocity of main stream outside boundary layer, L/θ

x = length of boundary layer, L

Greek Letters

$(\alpha\beta)_D$ = $E/D_p u_0$, dimensionless

$(\alpha\beta)_H$ = $(k_e)_{td}/D_p C_p G$, dimensionless

ϵ = fractional void in bed, dimensionless

μ = viscosity of fluid, $M/L\theta$

ρ = density of fluid, M/L^3

Subscripts

L = bed exit

td = turbulent diffusion

Dimensions

L = length

M = mass

Q = quantity of heat

T = temperature

θ = time

LITERATURE CITED

1. Baron, Thomas, *Chem. Eng. Progr.*, **48**, 118 (1952).
2. Campbell, J. M., and R. L. Huntington, *Petroleum Refiner*, No. 2, **31**, 123 (1952).
3. Chilton, T. H., and A. P. Colburn, *Ind. Eng. Chem.*, **26**, 1183 (1934).
4. Chu, Y. C., and J. A. Storrow, *Chem. Eng. Sci.*, **1**, 230 (1952).
5. Coberly, C. A., and W. R. Marshall, Jr., *Chem. Eng. Progr.*, **47**, 141 (1951).
6. Colburn, A. P., *Ind. Eng. Chem.*, **23**, 910 (1931).
7. Colburn, A. P., *Trans. Am. Inst. Chem. Engrs.*, **29**, 174 (1933).
8. Danckwerts, P. V., *Ind. Eng. Chem.*, **43**, 1460 (1951).
9. Felix, J. R., Ph.D. thesis, Univ. Wisconsin, Madison (June, 1951).
10. Gamson, B. W., George Thodos, and O. A. Hougen, *Trans. Am. Inst. Chem. Engrs.*, **39**, 1 (1943).
11. Hanratty, T. J., *Chem. Eng. Sci.*, **3**, 209 (1954).
12. Kuzuoka, Tsuneo, *Chem. Eng. (Japan)*, **8**, 85 (1944).
13. (a) Leva, Max, *Ind. Eng. Chem.*, **39**, 857 (1947); (b) ——, and Milton Grummer, *ibid.*, **40**, 415 (1948); (c) Leva, Max, Murray Weintraub, Milton Grummer, and E. L. Clark, *ibid.*, p. 747; (d) Leva, Max, *ibid.*, **42**, 2498 (1950).
14. Levenspiel, Octave, and J. S. Walton, *Chem. Eng. Progr. Symposium Ser.* No. 9, **50**, 1 (1954).
15. (a) Hatta, Shiroji, and Shiro Maeda, *Chem. Eng. (Japan)*, **12**, 56 (1948), **13**, 79 (1949); (b) Maeda, Shiro, and Kenjiro Kawazoe, *ibid.*, **17**, 276 (1953), **18**, 279 (1954).
16. McAdams, W. H., "Heat Transmission," 3 ed., McGraw-Hill Book Company, Inc., New York (1954).
17. Moyle, M. P., and Mack Tyner, *Ind. Eng. Chem.*, **45**, 1794 (1953).
18. Plautz, D. A., and H. F. Johnstone, *A.I.Ch.E. Journal*, **1**, 193 (1955).
19. Quinton, J. H., and J. A. Storrow, *Chem. Eng. Sci.*, **5**, 245 (1956).
20. Ranz, W. E., *Chem. Eng. Progr.*, **48**, 247 (1952).
21. (a) Bunnell, D. G., H. B. Irvin, R. W. Olson, and J. M. Smith, *Ind. Eng. Chem.*, **41**, 1977 (1949); (b) Hall, R. E., and J. M. Smith, *Chem. Eng. Progr.*, **45**, 459 (1949); (c) Schuler, R. W., V. P. Stallings, and J. M. Smith, *Chem. Eng. Progr. Symposium Ser.* No. 4, **48**, 19 (1952); (d) Kwong, S. S., and J. M. Smith, *Ind. Eng. Chem.*, **49**, 894 (1957).
22. Yagi, Sakae, and Daizo Kunii, *Chem. Eng. (Japan)*, **18**, 576 (1954); *A.I.Ch.E. Journal*, **3**, 373 (1957).
23. Yagi, Sakae, Daizo Kunii, and Yasuto Shimomura, *Chem. Eng. (Japan)*, **21**, 342 (1957).

Interfacial Resistance in Gas Absorption

PIETRO RAIMONDI and **H. L. TOOR**

Carnegie Institute of Technology, Pittsburgh, Pennsylvania

A laminar jet method for contracting a liquid with a gas for contact times down to 1 msec. has been developed. A jet is formed with a very thin square-edged orifice to minimize boundary-layer effects, and the rate of absorption of carbon dioxide into water is found to depend only upon contact time, an indication that the method is self-consistent.

The rate of absorption of carbon dioxide into pure water is 1 to 4% lower than the theoretical rate for absorption into a jet in rodlike flow the surface of which is instantaneously saturated. This indicates that, at most, interfacial resistance in this system is small and justifies the common assumption of interfacial equilibrium.

Jets with thick boundary layers were formed with other types of orifices, and the absorption rates into these jets were lower than the theoretical value because of the decreased surface velocity. This effect can be easily mistaken for an interfacial resistance.

The presence of a commercial surface-active agent causes an apparent interfacial resistance which is due at least partly to a hydrodynamic effect.

INTERFACIAL RESISTANCE IN GAS ABSORPTION

When two molecular systems which are not in equilibrium with one another are brought into contact, equilibrium between the material on either side of the interface can be attained only when the entire system comes to equilibrium. More specifically, if a gas is contacted with a liquid which is unsaturated with respect to the gas, then, even if there were no transfer of the molecules from the liquid surface to the bulk of the liquid, a finite time would be necessary to saturate the liquid interface because of the finite rate at which the gas molecules strike the interface. In reality gas molecules are continuously transferred from the interface to the bulk liquid until equilibrium is attained, and during this entire time the interface must be unsaturated in order for transfer to take place.

This nonequilibrium at the interface appears as an extra resistance to mass transfer and under certain conditions acts like the usual individual mass transfer coefficient. Because of the lack of knowledge of interfacial phenomena it has been commonly assumed that the interface is always saturated, that is, in gas absorption the gas side of the interface is in equilibrium with the gas molecules dissolved in the liquid surface. This procedure essentially combines any surface resistance with either the liquid or gas side resistance. One reason for separating the surface resistance from the other resistances is that it would be expected to vary in a manner quite different from the other resistances.

The simplest mechanism that will describe the transfer across the interface is a first-order process described by

$$N_A = k_s'(C_i^* - C_i) \qquad (1)$$

Physical significance can be given to k_s by using the kinetic theory of gases to compute the rate at which soluble molecules strike and leave the interface. The net rate is the difference between these rates, and it is found that

$$k_s' = \frac{\alpha H}{\sqrt{2\pi RTM}} \qquad (2)$$

where α, the condensation coefficient, is the fraction of the molecules striking the surface which actually condense. Henry's Law has been assumed.

Another interpretation is that there is a very narrow region in the liquid adjacent to the interface where the diffusivity is very low and Fick's Law holds; so

$$N_A = \frac{D_i}{y_0} (C_i - C_{y0}) \qquad (3)$$
$$= k''(C_i - C_{y0})$$

and from Equations (1) and (3)

$$N_A = k_s(C_i^* - C_{y0}) \qquad (4)$$

where

$$\frac{1}{k_s} = \frac{1}{k_s'} + \frac{1}{k''} \qquad (5)$$

and y_0 is the thickness of the region of resistance.

Thus interfacial resistance may be described by either or both of two first-order processes: one is due to nonequilibrium at the interface, which leads to an apparent resistance at $y = 0$; and the other is due to an extra diffusional type of resistance which leads to nonequilibrium between the interface and y_0, over and above the usual small non-equilibrium which would exist between those two points.

If the over-all process is at a steady state, the rate of transfer from the gas to the interface must be equal to the rate across the interface and in turn to the rate from the interface to the liquid. For the over-all process then,

$$N_A = K_L(C^* - C_L) \qquad (6)$$

$$\frac{1}{K_L} = \frac{1}{Hk_g} + \frac{1}{k_s} + \frac{1}{k_L} \qquad (7)$$

Since k_s can never be infinite, C_i^* and C_i can never be equal when transfer is taking place, and K_L is always less than the value corresponding to zero surface resistance ($k_s = \infty$). However if k_s is much greater than Hk_g or k_L, its effect on K_L is negligible, and, since the transfer rate is then controlled by the other resistance in the system, C_i approaches C_i^* and interfacial equilibrium is essentially attained. For example, if there is no diffusional resistance at the interface, the lack of equilibrium is due only to the finite rate at which gas molecules strike the interface, and if α is one, k_s is enormous and can be completely neglected.

To measure k_s the other resistances in the system must be made as small as possible and should be known. The gas-side resistance can be eliminated by using a pure gas, but owing to the low diffusivities of gases in liquids the liquid side is more difficult to handle. The best method appears to be to use a liquid in laminar flow so that the transfer with and without surface resistance may be directly calculated from diffusion theory and to make the liquid-side resistance as small as possible by reducing the gas-liquid contact time to a minimum.

A number of workers have attempted to measure k_s in gas absorption, and Higbie (9), Emmert and Pigford (6), and Danckwerts and Kennedy (5) have all reported appreciable interfacial resistances in the carbon dioxide–water system; Emmert and Pigford have also reported a large resistance in the O_2–water system. Matsuyama's data, on the contrary, indicated negligible resistance in the carbon dioxide–water system (12).

This work was carried out with unsteady state methods in short and long wetted-wall columns, rotating drums, laminar jets, and gas bubbles moving in tubes. Although the results of the vari-
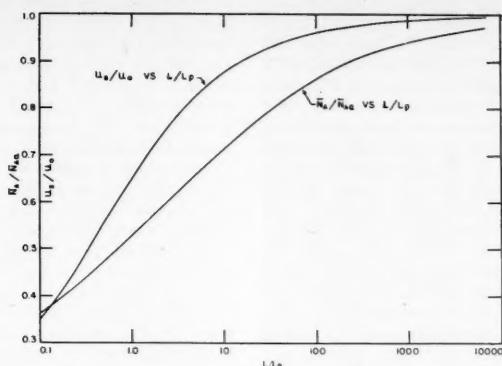
Fig. 1 Effect of boundary layer on the surface velocity and on the average rate of absorption.

Fig. 2 Flow diagram of the apparatus.

1	GAS CYLINDER
2	SATURATORS (3)
3	CONNECTION TO ATM
4	GAS TO BURETTE
5	SOAP BUBBLE MECHANISM
6	BURETTE
7	EXHAUST OPENING
8	ABSORPTION CHAMBER
9	ORIFICE
10	RECEIVER
11	KEROSENE
12	WATER
13	WATER TO ORIFICE
14	CONSTANT LEVEL TANK
15	CONSTANT LEVEL SYPHON
16	MANOMETER
17	JET
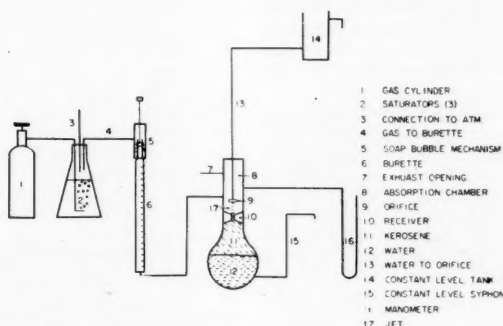
ous methods, except for Matsuyama's, are in rough agreement for carbon dioxide–water, the sensitivity of the conclusions to experimental error makes them inconclusive. More particularly it will be shown that boundary-layer effects, which make the true gas-liquid contact time greater than the apparent contact time, may cause a reduction in the absorption rate which may easily be interpreted as an interfacial resistance. Thus the initial objects of this work were to develop a self-consistent method for measuring gas absorption at short contact times and to determine whether or not the apparent resistances which have been observed for carbon dioxide–water are real.

Since the completion of this work a number of related studies have become available. Cullen and Davidson (3), Nijsing (13), and Scriven (17) have used laminar-jet techniques and concluded that interfacial resistance in the carbon dioxide–water system is negligible. The various techniques differ among themselves and from the work reported here mainly in the method of forming the jet and in treating the effect of the boundary layer.

THEORY

In this work a laminar jet is passed through a pure gas for a short distance and is removed by being directed into a small receiver. The jet method used by Matsuyama was not self-consistent, but it was believed that minimizing end effects would increase the reliability.

To determine the rate of absorption by the jet as a function of k_s the following assumptions are made:

1. Fick's Law for unsteady state diffusion holds.
2. The initial liquid concentration is uniform or zero. There is no gas side resistance.
3. During the exposure period the maximum depth of the liquid at which any appreciable concentration changes have occured is small compared with the diameter of the jet.
4. There is no chemical reaction in the liquid.
5. The rate of transfer across the interface is assumed to be given by Equation (4), and if there is a finite region of interfacial resistance it is thin enough so that the accumulation in the region occurs very rapidly and may be neglected.
6. There is no relative motion within the fluid; that is the jet moves as a rod.
7. Henry's Law holds.

The solution to Fick's Law for these conditions gives the instantaneous rate of absorption, which may be integrated to give the average rate over the jet. When the interfacial resistance is zero,

the point rate is given by the well-known equation (9)

$$N_A = (C^* - C_0) \sqrt{\frac{D_L}{\pi \theta}} \qquad (8)$$

and the mean rate is

$$\bar{N}_A = 2(C^* - C_0) \sqrt{\frac{D_L}{\pi \theta'}} \qquad (9)$$

When there is an interfacial resistance described by Equation (4), the point and mean rates are lower than the values of Equations (8) and (9) (5). The theoretical rates for various values of k_s are shown in Figures 6 and 8. The amount of gas absorbed per unit area of jet surface when there is no interfacial resistance is, from Equation (9),

$$Q = 2(C^* - C_0) \sqrt{\frac{D_L \theta'}{\pi}} \qquad (10)$$

The first assumption is satisfied by use of carbon dioxide–free water and absorbing pure carbon dioxide saturated with water. The water vapor would not be expected to cause a gas-phase resistance, since it is at its saturation point, but this assumption will be checked experimentally. The third assumption may be justified by solving the diffusion equations in cylindrical coordinates; it is found thereby that for the short contact times used in this work the penetration distance is so small that the curvature of the jet has negligible effect (16). The fourth assumption follows from the small amount of dissociation and reaction of carbon dioxide in water, even at equilibrium. The fifth assumption is a working hypothesis, and more complicated surface mechanisms may be dicated by experimental results.

When a liquid leaves an orifice, the surface of the liquid must leave at a velocity approaching zero, since it was in contact with a fixed wall, and a finite distance will be necessary before the surface can be accelerated to its final velocity by the bulk of the jet. Since the sixth assumption assumes instantaneous acceleration, an estimate of the error introduced is necessary. The formation of a boundary layer in a square-edged orifice and its dissipation in the jet are closely related to the boundary layer on a flat plate and the wake behind the plate. The symmetry line in the wake is analogous to the surface of the jet, since the shear stress at the jet surface is negligible. Although the two cases are not identical, the solution for the midpoint of a wake should give an approximate description of the surface velocity of a jet. The surface velocity determined from Goldstein's solution (7, 8) for a wake is shown in Figure 1 as a function of distance along the jet.

If the surface velocity is varying, the the mean absorption rate (18) is

$$\bar{N}_A = \frac{1}{A'} \int_0^{\theta'} 2\pi r u_s N_A \, d\theta$$

$$= \frac{2\pi r}{A'} \int_0^L N_A \, dx \qquad (11)$$

where θ' is the true contact time of any surface element and the jet radius r is taken outside the integral, since it is found to be constant.

If u_s increases from zero to its final value, $\bar{N}_A$ has a lesser value than it would have if the velocity instantaneously attained its final value. However when a boundary layer is present, N_A is not given by the solution to Fick's Law, since the axial velocity varies with axial and radial position, and, in addition, by continuity there must be radial velocity components. These effects tend to increase the point transfer rates so that there are two opposing effects on the mean rate. (The results below indicate that the decrease due to a lowered surface velocity predominates.)

Thus if Equation (8) is used in Equation (11), the result should show the maximum boundary-layer effect. When Equation (11) is integrated by means of the point rate for no interfacial resistance and the surface velocity from Figure 1, the resulting equation is (16)

$$\bar{N}_A = 2(C^* - C_0) \sqrt{\frac{D_L u_0}{\pi L}} \, f\left(\frac{L}{L_p}\right) \quad (12)$$

Since L/u_0 is the apparent contact time, the ratio of the mean rate with a boundary layer to the rate, if the velocity were constant at u_c, is $f(L/L_p)$, and this result is shown in Figure 1. For a plate thickness of about 0.01 cm., as used in this work, the surface velocity reaches 95% of its final value in a distance less than 1 cm., but a jet over 10 cm. long is theoretically needed to bring the mean absorption rate up to the 95% point. These figures cannot be taken too literally, but the general characteristics of the curves would be expected to be correct.

When L/L_p is large, it can be seen that the mean absorption rate depends only upon L/u_0, which is θ' in this limit, and the rate at equal values of L/u_0 should be independent of L and the jet diameter. This result is independent of the transfer mechanism at the surface and gives a general criterion for self-consistency. In the region where the mean absorption rate is greater than about 95% of the constant surface-velocity rate, this technique will not be precise, since Figure 1 shows that the length effect will be small; below the 95% point a significant length effect should appear.

APPARATUS AND EXPERIMENTAL TECHNIQUE

In essence the equipment is designed to contact a laminar jet with a gas for a short period of time under conditions in which the jet area, contact time, and absorption rate can be determined. The length, diameter, and velocity of the jet can all be varied. A flow diagram of the apparatus is shown in Figure 2, with further details in Figure 3.

The gas is taken from a standard cylinder (1), through a pressure regulator, and passed through water saturators. The saturated gas is then led to the soap-bubble mechanism (5), through the measuring burette (6), and to the absorption chamber. An excess of gas is always passed through the saturators. Before a run was made, the connection to the atmosphere was closed off, and all the gas was forced to the absorption chamber and out through the exhaust opening (7). During a run opening (7) was closed, and excess gas was passed to the atmosphere at (3) so that all the gas absorbed by the jet flowed through the connecting tube (4). The pressure in the absorber, therefore, was atmospheric less the small pressure drop across the lines and soap bubble. The gas-flow rate was measured directly by timing the motion of the soap bubble which could be placed on the top of the burette by a wire ring.

Originally the rate of absorption was obtained by measuring the pressure drop across a precision-bore capillary tube insterted in the gas line to the absorption chamber. A two-fluid U-tube manometer which could read a pressure drop of 0.0005 cm. of water was used. This device was calibrated by a liquid-displacement method,
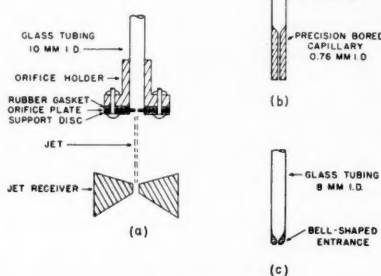
and the calibration checked Poiseuille's Law to within 1%. However it was later found that in use the manometer gave readings between 5 and 8% low owing to the time lag in reaching equilibrium. The equilibrium readings on the manometer checked the soap-bubble readings within 1%.

Four types of orifices were used. Orifice 1, which produced approximate rodlike flow, was a square-edged orifice 0.01 cm. thick. Orifice diameters of 0.0851 and 0.0571 cm. were used and there were no visible surface curves on the jets. Orifice 2, which produced surface waves, was a slightly elliptical orifice of average diameter 0.0851 cm., and these jets had visible standing waves. The orifice plates were mounted on the end of a 1-cm.-I.D., 60-cm.-long glass tube (Figure 3a) in which the flow was always laminar and the length Reynolds numbers in the orifices were always far below the critical value for turbulence. Orifice 3, producing a thick boundary layer, was a bell-mouthed orifice as shown in Figure 3c, and orifice 4, producing an initial parabolic velocity profile, was a precision-bore capillary tube long enough to give a fully developed parabolic velocity profile (Figure 3b). All the jets could be raised and lowered by a screw mechanism.

The absorption chamber is the male part of a ground-glass joint, with the lower part fitted with a Lucite core having a center hole to receive the jet (Figure 3a). Hole
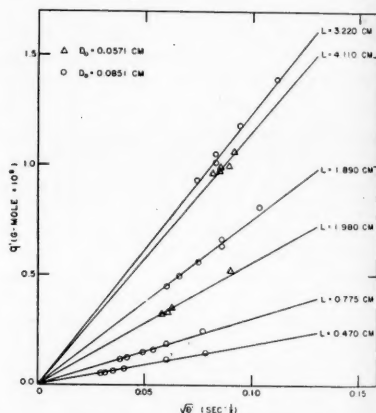
Fig. 3

(a) Sections 7, 8, 9, and 10 of Figure 2 in detail.
(b) Capillary tube entrance.
(c) Tube with bell-shaped entrance.

Fig. 4 Amount of carbon dioxide absorbed for typical jet lengths and diameters vs. square root of contact time.
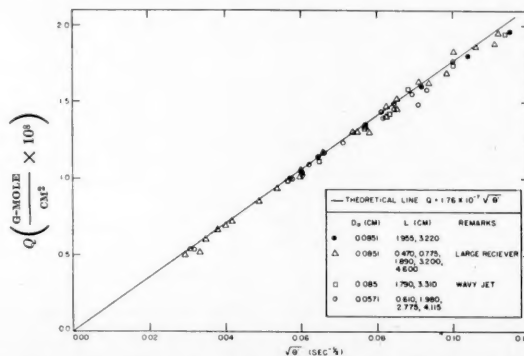
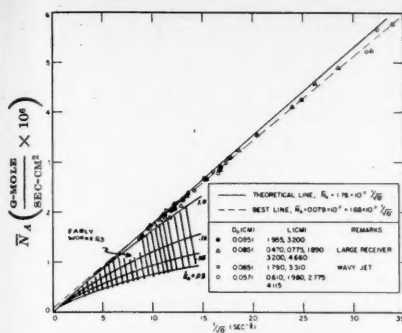**Fig. 5 Absorption of carbon dioxide in water plotted against the square root of the contact time.**

Fig. 6 Rate of carbon dioxide absorption in water, plotted against the inverse of the square root of the contact time.

diameters of 0.30 and 0.10 cm. were used, and the surface of a layer of kerosene was held at the top of the receiving hole by a constant-level siphon (Figure 1). The system was built in a constant-temperature room held at 22.2°C. ± 0.25°C., ordinary distilled water was used, and the carbon dioxide had a purity of 99.8%.

The diffusivity of carbon dioxide in water at 22.2°C. was taken as 1.84×10^{-5} sq. cm./sec. and the solubility as 3.65×10^{-5} g.-mole/cc. (14).

The jet length was measured from the top of the kerosene level to the orifice with a cathetometer which could be read to 0.005 cm. The water flow rate was measured by noting the time to fill a 1,000-ml. flask. The jet diameter was obtained by using a previously prepared calibration chart determined with a microscope.

The jet area and apparent contact time were calculated directly from the measurements of jet length, diameter, and water flow rate. The absorption rate was calculated by subtracting the water vapor from the measured gas flow rate, and it was then corrected to a carbon dioxide partial pressure of 1 atm. as indicated by Equation (9). (Carbon dioxide was always zero.) It was assumed in this calculation that the entering water vapor condensed in the absorber as the carbon dioxide was absorbed.

RESULTS

Contact times from 1 to 20 msec. were obtained by varying the jet length over a tenfold range and the jet velocities over a sevenfold range. Some typical results with a square-edged orifice are shown in Figure 4, where the amount of gas absorbed ($q' = A'Q$) is plotted against $(\theta')^{1/2}$. The data for the various jet lengths and diameters are combined in Figure 5 by plotting the amount of gas absorbed per unit area of jet and are compared to the theoretical line for no interfacial resistance and rodlike flow [Equation (10)]. On this figure are shown the data obtained with the square-edged orifice and the eliptical orifice. Part of the data were obtained with the 0.3-cm.–diameter receiver and part with the 0.1-cm.–diameter receiver.

With the large receiver there was an effect of a jet length on the absorption rate which indicated that measurable

transfer was taking place at the gas-kerosene interface. This extra absorption was made negligible by decreasing the receiver diameter until no length effect could be observed. Replacing the kerosene in the small receiver by water had no effect on the results. The data with the large receiver were corrected for the absorption into the receiver (16).

The data of Figure 5 are also shown in Figure 6, where N_A is plotted against $1/(\theta')^{1/2}$ to spread out the data in the important region of short contact times. The theoretical line for no interfacial resistance and rodlike flow is again shown [Equation (9)]. The standing waves which occur with the elliptical orifice have little effect on the absorption. The range of data of some workers (5, 9) who reported a possible interfacial resistance is also shown here as well as the theoretical lines for various values of k_s.[5] The results with the small receiver and the square-edged orifice, which needed no correction for absorption into the kerosene, are shown separately in Figure 7.

The absorption rates with the capillary orifice are shown in Figure 8, and those with a bell-mouthed orifice are given in Figure 9. Absorption rates in three solutions of Petrowet, a commercial surface-active agent, were obtained and are shown in Figures 10 and 11.
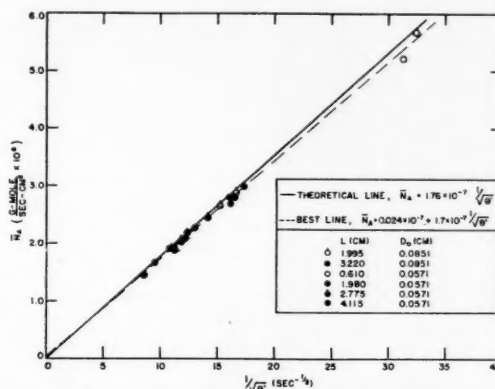
All the original data are given by Raimondi (16).

The following additional results were obtained: (1) using dry instead of saturated gas had no measurable effect on the absorption; (2) the effect of inerts accumulating in the absorber during a run was negligible; (3) dye studies on a large-scale model of the square-edged orifice indicated steady, rectilinear flow in the jet; (4) the jet diameter at a constant flow rate contracted in the first 0.05 cm. or less and then remained constant with length. The diameter decreased slowly as the flow rate was increased and was not changed by the addition of the surface-active agent.

DISCUSSION

The results obtained by using a thin orifice plate follow very closely the theoretical line of no interfacial resistance as shown in Figures 5 to 7. Since the effect of interfacial resistance should increase as the contact time decreases, the fact that the data follow the theoretical line so closely down to a contact time of less than a millisecond indicates a very small interfacial resistance and perhaps none at all for practical purposes. This agrees with the conclusions of other recent workers (3, 17, 13).

Fig. 7 Rate of absorption of carbon dioxide in water. Wave-free jet and small receiver.
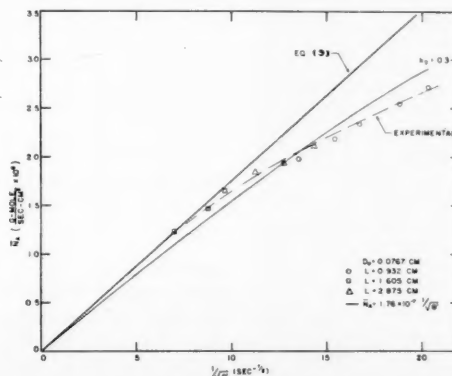
Fig. 8 Rate of absorption of carbon dioxide in water. Jet with parabolic velocity profile.

In an attempt to establish whether or not the results indicate the presence of a small interfacial resistance, a statistical treatment of the data was carried out. The best line obtained by the least-squares method for all the runs with a thin orifice plate is $\bar{N}_A = 0.079 \times 10^{-7} + 1.68 \times 10^{-7} 1/(\theta')^{1/2}$, where the standard deviations of the intercept and of the slope are 0.0434×10^{-7} and $0.0263 \times$
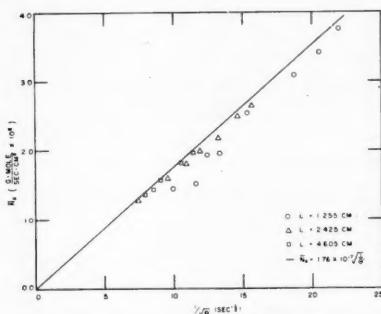

Fig. 9 Rate of absorption of carbon dioxide in water. Jet formed with bell-shaped entrance.

10^{-7}, respectively. Equation (9) requires that if there is no interfacial resistance, in a plot of $\bar{N}_A$ vs $1/\theta'^{1/2}$ the intercept of the straight line through the data should be zero. In this case the intercept is 0.079×10^{-7}, but a t test shows that at the 95% confidence level there is insufficient evidence that the intercept differs from zero by more than can be accounted for by the experimental error. There is stronger support that the data actually give a zero intercept if one considers only those data taken with a waveless jet by use of a small receiver. In this case the equation of the best straight line (Figure 7) is $\bar{N}_A = 0.024 \times 10^{-7} + 1.71 \times 10^{-7} 1/\theta'^{1/2}$, the standard deviation of the intercept and of the slope being 0.0233×10^{-7} and 0.0175×10^{-7}, respectively. This intercept is negligibly different from zero, but the range of slope owing to experimental error is not sufficient to include the theoretical slope of 1.76×10^{-7}. However this is not a conclusive proof that there is, in this range, a small interfacial resistance, since the physical constants D_L and C^* used in the theoretical equation might be in error by a few per cent, and the surface velocity must be somewhat less than the bulk velocity.

If the lower absorption rate is an indication of a true interfacial resistance, then k_s is in the range of 2.6 to 11.8 cm./sec., with corresponding α's of 0.35×10^{-3} to 1.6×10^{-3}. These values are two to three orders of magnitude larger than those reported in early studies (5, 6, 9), and for many purposes this small surface resistance can be neglected in the range of practical contact times,

since most liquid or gas side resistances would be appreciably greater.

Since the absorption rate should be entirely dependent on the contact time, a critical factor in this type of investigation is the velocity at the surface of the jet. The very short orifice used should
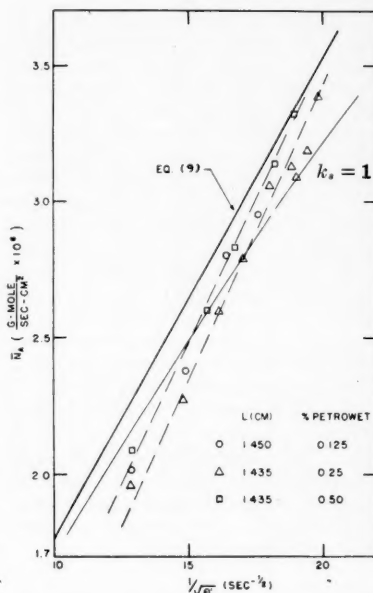

Fig. 10 Effect of Petrowet concentration on the absorption rate at constant jet length.
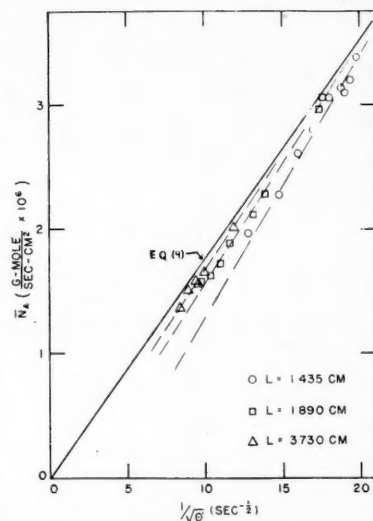

Fig. 11 Rate of carbon dioxide absorption in water containing 0.25% Petrowet.

develop a thin boundary layer which should rapidly accelerate to the bulk jet velocity. With an orifice plate thickness L_p of 0.01 cm., Figure 1 shows that the surface velocity of the jet should be, for example, 95% of the jet bulk velocity at a jet length of 0.5 cm. However the

process of averaging rates of absorption over all the elements of different age shows that the average rate at a jet length of 0.5 cm. is only 82% of the theoretical, that is, of the rate that would be obtained if the surface velocity of the jet had reached the bulk jet velocity instantaneously. If these calculations were correct, then in the range of jet length used here the absorption rate should have varied from 82 to 92% of the theoretical, and a significant length effect should have been detected.

A cross plot of Figure 4 at a constant contact time gives Figure 12, where the amount of carbon dioxide absorbed per unit area is plotted against the jet length at a constant contact time. The horizontal line indicates no effect of jet length over the range studied. The cross plot was made for a contact time in which the various jet lengths overlap, but, since the data in Figure 4 yield straight lines going through the origin, the results should be true over a wide range of contact times. This absence of a length effect indicates that the boundary layer accelerated faster than calculated or that the y components of velocity caused the absorption rate to be higher than calculated. Figure 1 shows that after 96% of the theoretical absorption rate is reached, the rate remains practically constant over a large variation of jet length. Therefore if the boundary layer did accelerate faster than was calculated, and the region of 96 to 99% of the theoretical was reached with a relatively short jet length, then the rate would continue to remain almost constant but about 1 to 4% lower than the theoretical. Thus it is quite possible that the slightly lower than theoretical rates were caused by the boundary layer.

In an attempt to find any errors which would cause the absorption rate to be higher in this work than in others, the possibility that there was some turbulence was considered. That this is not due to unobserved surface waves is shown by the fact that the results obtained with a wavy jet are the same as those obtained on a wave-free jet. The Reynolds number in the tube was always well below the critical, and the Reynolds number based on the length of the orifice was also far below the critical value for a flat plate, and so no turbulence should occur. It would be expected that if a low level of turbulence does exist, it would increase with jet velocity. The data in Figure 12, for example, show no such effect over a variation of velocity of 700%.

It is unlikely that the radial-velocity components which exist when the jet surface is accelerating cause an increase in absorption rate large enough to overcome the decrease in rate brought about by the lowered surface velocity. If this were the case, the rate when a boundary layer is present should be greater than the theoretical value, but work with jets

with thick boundary layers always gave a rate below the theoretical, an indication that the increased surface age caused by a lowered velocity is the predominant factor. Thus boundary-layer effects, when they exist, give an apparent resistance and cannot be used to explain why negligible resistance was found.

Other possible effects which could increase the absorption rate were shown earlier to be negligible.

BOUNDARY-LAYER EFFECTS

Work on jets formed with a capillary tube and with a bell-mouthed orifice was undertaken in an attempt to determine the effect of hydrodynamic conditions on the rate of absorption.

The jet formed with a long capillary tube will leave the tube with a parabolic velocity profile. The velocity of the surface of the jet will start out at zero, but in this case the boundary layer is the radius of the jet, and the distance to accelerate the surface to the bulk velocity will be much greater than in the case of a jet formed with a short orifice.

Figure 8 shows the results obtained on this type of jet. Here the measured rate is plotted against an apparent contact time which was calculated from the jet bulk velocity. The actual contact time was longer, since the surface velocity was lower than that of the bulk of the jet. In this type of plot there is an apparent interfacial resistance because of the lower surface velocity. At the shorter contact times (higher velocity or shorter jet length) the apparent resistance is very high, but at the longer contact times (lower velocity or longer jet length) the rate approaches the theoretical. In the same figure the theoretical line for an interfacial resistance is shown for $k_s = 0.3$ cm./sec. It can be seen that this line and the line through the data are close to each other and have the same characteristic curvature. Thus it appears that the type of surface resistance described by early investigators could very well have been the result of unknown hydrodynamic conditions rather than the result of the physico-chemical behavior at the interface.

Actually these data on a jet with initial parabolic velocity profile do not follow exactly any constant resistance line, since the constant resistance line for a k_s of 0.3 intersects the line through the data. Moreover a close look at the points in Figure 8 shows a discontinuity from one jet length to the other, as would be expected. Unfortunately there is no solution to the equation for the velocity distribution in a free liquid jet with an initial parabolic velocity profile, and so it is not possible to interpret these results quantitatively. However it is clear that the low rate is not due to any constant surface resistance and that the increase in rate due to radial-velocity components is less than the decrease caused by a lowered surface velocity.

The results obtained with the bell-shaped orifice are shown in Figure 9. This orifice is expected to give a boundary layer of thickness intermediate between the orifice plate and the capillary. With the longer jet the rate is as close to the theoretical line as the rate with the short orifice. At the intermediate jet length the effect of the boundary layer begins to appear, as indicated by a slightly lower rate than with the longer jet. With the shortest jet length the rate falls still lower. Thus the rates with the bell-shaped orifice fall between the rates with the short orifice and the capillary, as was expected from boundary-layer considerations. It should be noted that with a carefully designed nozzle Cullen and Davidson were able to go down to lengths of 1.6 in. without detecting any boundary-layer effect (3).

SURFACE-ACTIVE AGENTS

Emmert and Pigford (6), using a long wetted-wall column to measure interfacial resistance, added Petrowet to the water to reduce the ripples on the surface, since the ripples caused the absorption rate to exceed the theoretical; their absorption rates were then found to be well below the theoretical. To determine whether or not the surface-active agent actually hindered the transfer across the interface, they compared rate data in a short wetted-wall column with the surface-active agent present to data obtained without the surface agent. Since there were no ripples present in either case, they found only an 11% decrease owing to the surface active agent and concluded that the lower than theoretical values in the long column were not due to the hindering effect of the surface active agent but indicated a true interfacial resistance for pure water with an α of 1.9×10^{-6} for carbon dioxide. This was close to the value obtained on the short column without surface-active agent, and although it can be argued that the resistance reported in the short column was due to boundary-layer effects, the long-column results cannot be explained in this fashion.

Cullen and Davidson, using a wetted sphere, have recently concluded that Petrowet does cause an interfacial resistance in the carbon dioxide–water system (2). The results with three concentrations of Petrowet are shown in Figure 10 for a fixed jet length. The absorption rate diverges increasingly from the theoretical as the contact time increases, just the reverse of what would be expected if there were a constant interfacial resistance, and the lowest rate occurs at the intermediate concentration. Furthermore there is a marked length effect which is shown in Figure 11 for the 0.25% Petrowet solution. At a constant contact time the rate decreases as the jet length decreases.

The length effect must be at least partly hydrodynamic in nature, since any diffusional or surface-resistance mechanism should depend only upon contact time. Lynn et al. (11) and Cullen and Davidson (3) have observed that in the presence of surface-active agents a stagnant film forms on the surface of a moving liquid when it enters a stagnant liquid. If the absorption rate into this film is relatively small, the effective jet length in this work would be less than the actual value, as found in wetted-wall columns (11), and the absorption rate would vary with jet length and diverge from the theoretical in the observed manner.

By assuming that the lowered rate at the shortest jet length for each Petrowet concentration is due entirely to the stagnant film at the receiver, one might calculate the apparent stagnant film height and use it to correct the results for the longer jets. This correction brings all the jet lengths and Petrowet concentrations into rough agreement with the theoretical line, an indication that the lowered absorption rate might be explained entirely as a receiver effect.

Actually there is stronger evidence that part of the lowered rate may be due to an interfacial resistance, for if only half the apparent stagnant-film height is used to correct the jet lengths, the correlation is greatly improved and the length effect is eliminated with the rate data still below the theoretical.
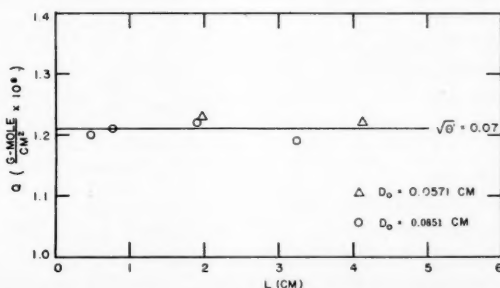
When a fresh surface is formed from

Fig. 12 Comparison of carbon dioxide absorbed per unit area at different jet lengths for the same contact time.

a solution containing a surface active agent, the initial surface concentration is the bulk concentration, and as the surface ages, the interfacial concentration of surface-active agent increases until the surface attains its final large excess of surface-active agent (15). Thus if there is a resistance due to the hindering effect of the surface-active agent, it should increase from a very small value at the orifice to its final value when the interface is saturated.

The surface ages in this work are much less than those studied by Emmert and Pigford (6) or by Cullen and Davidson (2), and so even if negligible resistance were found here, this would not imply that none would exist in a relatively old surface. Thus these results, although inconclusive, are not inconsistent with the conclusions of Cullen and Davidson (2) that the addition of Petrowet causes a true interfacial resistance in the carbon dioxide–water system and that the interfacial resistance reported by Emmert and Pigford is due to the hindering effect of the surface-active agent.

It is interesting to note that at a fixed contact time and jet length (Figure 10) the rate of absorption goes through a minimum as the concentration of surface-active agent increases. This is very similar to the results of Cullen and Davidson (2) and Emmert and Pigford. Since in this work there is a definite hydrodynamic effect present, the question arises as to whether this minimum may not be due at least partly to a hydrodynamic effect rather than entirely to a hindering effect as concluded by Cullen and Davidson (2). Unfortunately, as Emmert and Pigford and Cullen and Davidson (2) worked with a constant length of flow, their data cannot be checked for a length effect.

It does not seem very likely that the minimum is due to a change in the surface waves, since it was shown earlier that even large waves in the jet have little effect on the absorption, and the stagnant film at the receiver is hardly likely to be significant in the long column used by Emmert and Pigford. Since a hydrodynamic effect that could be significant in all the widely different types of apparatus used is not readily apparent (the surface viscosity of water has been reported to be unaffected by Petrowet (2)), the possibility that the minimum in the present work is due entirely to a hindering effect cannot be rejected.

CONCLUSIONS

1. An accurate, self-consistent method of obtaining gas-liquid contact times down to 1 msec., under known hydrodynamic conditions, has been developed.

2. There is at most a very small interfacial resistance at a clean carbon dioxide–water interface. For practical purposes interfacial equilibrium is immediately attained when the gas and liquid are brought into contact.

3. Boundary-layer effects can be easily mistaken for an interfacial resistance, but the two phenomena can be distinguished from each other by varying the jet length and velocity.

4. The presence of a surface-active agent lowers the absorption rate. This is due at least partly to a change of the flow pattern.

NOTATION

A = gas-liquid contact area, sq. cm.

A' = total gas-liquid contact area, sq. cm.

C = solute gas concentration, g.-mole/cc.

C_0 = initial concentration of solute gas, g.-mole/cc.

C_i = concentration of solute gas in liquid at interface, g.-mole/cc.

C_L = concentration of solute gas in bulk of liquid, g.-mole/cc.

C_{y0} = concentration of solute gas at $y = y_0$, g.-mole/cc.

C^* = concentration of solute gas in liquid which would be in equilibrium with gas, g.-mole/cc.

C_i^* = concentration of solute gas in liquid at the interface in equilibrium with gas adjacent to interface, g.-mole/cc.

D_0 = orifice diameter, cm.

D_i = diffusivity of dissolved gas in the hypothetical film of thickness y_0, sq. cm./sec.

D_L = diffusivity of solute gas in liquid, sq. cm./sec.

f = functional symbol

H = Henry's Law constant, atm. cc./g.-mole, or erg./g.-mole in Equation (2)

k_g = gas-side mass transfer coefficient, g.-mole/sec.-sq. cm.-atm.

k_L = liquid-side mass transfer coefficient, cm./sec.

k_s = interfacial mass transfer coefficient, cm./sec.

$k_{s'}$ = restricted interfacial mass transfer coefficient, cm./sec.

$k_{s''} = D_i/y_0$, cm./sec.

K_L = over-all mass transfer coefficient, cm./sec.

L = jet length, cm.

L_p = thickness of orifice plate, cm.

M = molecular weight

N_A = local mass transfer rate per unit area, g.-mole/sec.-sq. cm.

$\bar{N}_A$ = average mass transfer rate per unit area, g.-mole/sec.-sq. cm.

$\bar{N}_{Aa}$ = average mass transfer rate per unit area based on a constant jet surface velocity, in Figure 1, g.-mole/sec.-sq. cm.

q' = total amount of carbon dioxide absorbed by jet. g.-mole

Q = amount of carbon dioxide absorbed per unit area, g.-mole/sq. cm.

r = jet radius, cm.

R = gas constant, erg./(g.-mole)(°K.)

T = temperature, °K.

u_0 = mean jet velocity, cm.

u_s = jet surface velocity, cm./sec.

x = distance along the axis of the jet

y = distance measured from surface of liquid, cm.

y_0 = thickness of hypothetical film at liquid surface, cm.

Greek Letters

α = condensation coefficient

θ = gas-liquid contact time, sec.

θ' = total gas-liquid contact time, sec.

LITERATURE CITED

1. Carslaw, H. S., and J. C. Jaeger, "Conduction of Heat in Solids," Oxford, London (1947).
2. Cullen, E. J., and J. R. Davidson. *Chem. Eng. Sci.*, **6**, 49 (1956).
3. ———, *Trans. Faraday Soc.*, **53**, 113 (1957).
4. Danckwerts, P. V., *Research*, (*London*). **2**, 494 (1949).
5. ———, and A. M. Kennedy, *Trans. Inst. Chem. Engrs.* (*London*), *Supplement 1.*, "Symposium on Gas Absorption," **32**, S53 (1954)
6. Emmert, R. E., and R. L. Pigford, *Chem. Eng. Progr.*, **50**, 87 (1954).
7. Goldstein, S., *Proc. Cambridge Phil. Soc.*, **26**, 1 (1930).
8. ———, *Proc. Roy. Soc.* (*London*), **A142**, 545 (1933).
9. Higbie, R. W., *Trans. Am. Inst. Chem. Engrs.*, **31**, 365 (1935).
10. Hughes, R. R., and E. R. Gilliland, *Chem. Eng. Progr.*, *Symposium Ser.*, 16, **51**, 101 (1955).
11. Lynn, S., J. R. Straatemeier, and H. Kramers, *Chem. Eng. Sci.*, **4**, 58 (1955).
12. Matsuyama, T., *Mem. Fac. Eng. Kyoto Univ.*, Japan, XV, 142 (1953).
13. Nijsing, R. A. T. A., thesis Physische Technologie Der Technische Hogeschoul, Delft, Holland (1957).
14. Perry, J. H., ed., "Chemical Engineer's Handbook," 3 ed., McGraw-Hill New York (1950).
15. Posner, A. M., and A. E. Alexander, *Trans. Faraday Soc.*, **45**, 651 (1949).
16. Raimondi, Pietro, Ph.D. thesis, Carnegie Inst. Technol., Pittsburgh, Pa. (1957).
17. Scriven, E. L., II, Ph.D. thesis, Univ. Delaware, Dover, Del. (1956).
18. Toor, H. L., *A.I.Ch.E. Journal*, **2**, 578 (1956).

Mechanics of Vertical Moving Fluidized Systems

II. Application to Countercurrent Operation

B. G. PRICE, L. LAPIDUS, and J. C. ELGIN

Princeton University, Princeton, New Jersey

Experimental data are presented for two different methods of operating vertical moving fluidized systems of glass spheres and water: free countercurrent fluidization and bottom-restrained nonfed, or batch, fluidization. Data for a lead-shot-and-water system are also reported. A comparison is made of these data with a generalized theoretical analysis of ideal fluidized systems. The validity of a single characteristic holdup vs. slip-velocity relationship is illustrated, and consideration is also given to the prediction of flooding in the free countercurrent systems.

Fluidized systems form an important area of fluid mechanics which is of primary concern to the chemical engineer. They are widely used in bringing two phases continuously into contact in order to permit mass or heat transfer. Subdivision of one phase into particles, bubbles, or droplets to carry out phase contacting is probably more common than the other two available methods: bulk or film contacting.

A fluidized system may be any device in which a mass of particles, whether solid, liquid, or gas, is suspended in a continuously moving fluid because of the motion of the fluid between the particles. When a mixture of particles and fluid is moved through a tower in a continuous stream, the area of contact between the phases available for mass or heat exchange depends upon the feed rate of each to the tower. In addition there is a dependence upon the size of the particles and the physical properties of particles and continuous fluid. The contact area is in turn determined directly by the particle holdup within the tower or its complement, the fractional voidage. The relation between void fraction and feed rates for given particles and fluid is a basic property of the system. The pressure gradient over the contact zone is, for example, fixed by the fractional holdup and the density difference between particles and fluid; it may be calculated if the void fraction is known.

Quantitative knowledge of the relationships between these factors is therefore fundamental to the rational treatment of any rate process within a fluidization zone and for the design of many phase-contacting operations in which one phase appears as a mass of particles. In a previous publication (1) a basic theory of vertical moving fluidized systems was presented which attempted to develop these necessary relationships. The basic premise of this theoretical development was the assumption that

a single, fundamental relationship exists between the void fraction and the slip velocity for the particles and fluid. This relationship was assumed to be valid irrespective of the direction of flow of fluid and of particles in relation to each other and to the walls. It was further

Fig. 1 Schematic diagram of experimental apparatus.

shown that the void fraction for any moving fluidized system could be predicted for all combinations of particle and fluid flow rates if data from a single batch fluidization experiment were available. The present paper reports experimental data for free countercurrent operation of a glass-spheres–water and a lead-shot–water system and for bottom-restrained nonfed, or batch, fluidization of the same system.

The studies were carried out in towers of ¾- to 1.5-in. diameter with glass spheres 0.0183 and 0.0323 in. in diameter and lead shot 0.0500 in. in diameter fluidized by water. Measurements were made of the pressure drop across the fluid bed and of the fluid and particle velocities for various combinations of the physical variables.

The experimental data for countercurrent flow are in excellent agreement with an operating diagram (a plot of holdup vs. fluid velocity with particle velocity as the system parameter) predicted theoretically from experimentally determined batch fluidization data for the same system. Flooding of the experimental systems is also shown to be predictable on the basis of the same batch fluidization data. Thus for the types of operation studied the experimental results support the validity of a single characteristic holdup vs. slip-velocity curve for an ideal moving fluidized system.
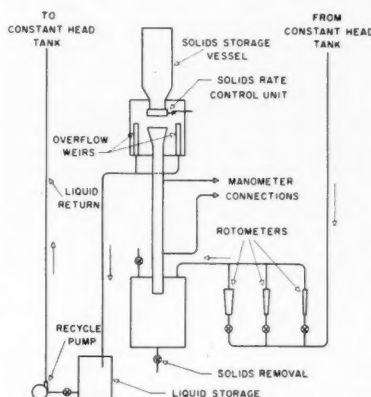
TABLE 1. DESCRIPTION OF TOWERS USED

	I.D., in.	Length, in.	Pressure taps	Conical sections
			Tower 1	
Type A	0.653	58.4	One tap 12 in. from bottom; other tap 36 in. higher	Cone angle of 16 deg.; height of 5.0 in.
Type B	Section 4.56 in. long, 0.653 in. I.D. added to bottom of type A; tapered gradually to an I.D. of 1.00 in.			
Type C	Section 4.56 in. long, 0.653 in. I.D. added to bottom of type A.			
			Tower 2	
Type A	0.970	58.4	One tap 10 in. from bottom; other tap 41.75 in. higher	Cone angle of 17 deg.; height of 4.0 in.
Type B	Section 6.17 in. long added to bottom of type A, tapered gradually to an I.D. of 1.88 in.			
			Tower 3	
Type A	1.50	58.4	Tap 10 in. from each end	Cone angle of 13 deg.; height of 5.0 in.
Type B	Section 6.0 in. long added to bottom of type A; tapered to I.D. of 2.44 in.			

Fig. 2 Solid feed-rate control unit.

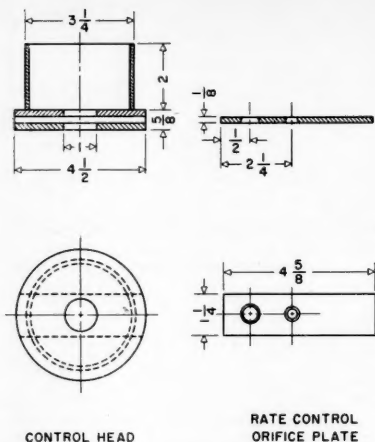Fig. 3 Experimental holdup $(1 - \epsilon)$ vs. slip velocity for 0.0183-in. glass spheres in water

APPARATUS AND PROCEDURE

Countercurrent Flow of Fluid and Solids

The main sections of the apparatus were three interchangeable towers of $\frac{3}{4}$-, 1-, and 1.5-in. nominal diameter borosilicate glass, a constant-head tank for storing the continuous phase, and a storage vessel for holding the amount of solids used during any one experimental run. In addition, provisions were made for equipment to control the rate of solids flow, circulate the fluid through the column, measure the pressure differential across the column, and dry the solids at the conclusion of each run. Figure 1 is a schematic diagram of the over-all equipment. Table 1 presents the dimensions and other pertinent data for the three basic towers and modifications of these.

Solids Properties

Three different spherical solids were used; two were Scotchlite glass beads and the other was lead shot. A random sample of one hundred and fifty of the larger size glass beads had an average diameter of 0.0323 in. and an absolute density of 177.6 lb./cu. ft. Approximately the same number of the smaller glass beads had an average diameter of 0.0183 in. and an absolute density of 180.4 lb./cu. ft. The lead spheres

had an average diameter of 0.0500 in. and an absolute density of 695.6 lb./cu. ft.

Solids Rate-Control Mechanism

Figure 2 shows the construction details of the unit which controlled the rate of solids feed to the tower. The unit was attached to the base of the storage container. By moving the orifice plate back and forth two ranges of solids flow could be obtained. The fabrication of a number of these orifice plates with different-size orifice holes was used to obtain any predetermined solids rate.

During an experimental run the path of solids flow was from the solids control unit, through the air-water interface, down through the tower, and finally into the lower receiving section. The continuous phase, water, was passed upward through the tower countercurrent to the direction of solids flow. Water flowed in a closed circuit through the apparatus.

Procedure for Countercurrent Operation

The principal steps in the procedure were, in sequence, the determination of the weight rate of solids flow; the control and measurement of the fluid flow rate; the recording of manometer interface displacements, which indicated the pressure differential in the tower; the establishment of the flooding point; and the drying of the solids preparatory to the next run.
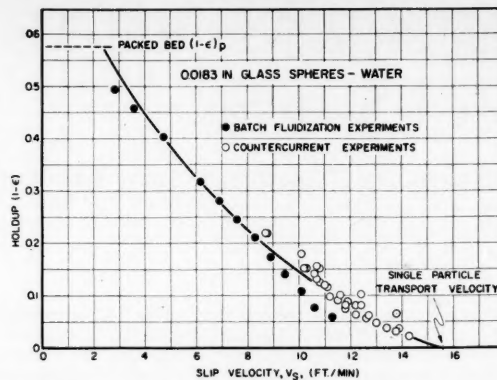
After calibration of the orifice to be used during the run, the solids container was placed in position above the upper receiving section and fully charged with the solids. The tower and both receiving sections were filled with water. The solids flow was then started by sliding the orifice plate into the correct position and initiating and adjusting the fluid flow to the rate desired.

The rotameter float position was recorded along with the associated manometer readings after the latter had remained constant for a minute or more. The process of increasing the fluid flow rate and recording the accompanying manometer readings, after equilibrium conditions had been attained, continued until a small change in rate of fluid flow resulted in the formation of a small ($\frac{1}{2}$- to $\frac{3}{4}$-in.), stable, relatively dense head of solids at the junction of the conical entrance section and the constant-diameter portion of the tower. The tower was then, by definition, flooded. In only a relatively small number of runs was the investigation of pressure drop as a function of fluid flow rate carried beyond the flooding point. After the data at flooding had been recorded, the solids and fluid flow were stopped and the accumulated solids drained and dried.

Unfed Bottom-Supported, or Batch Fluidization

Three columns, $\frac{3}{4}$-, 1.0-, and 1.5-in. nominal diameter by 40 in. long, were used to study the fluid-velocity–fraction-void relationship present during screen-supported fluidization of the same fluid-solids systems used in countercurrent flow. The beds were supported by bronze metal screens with, approximately 0.4-mm. openings, below which there were no calming sections. Some check runs were made with the glass beads in a 2- to 4-in. packed bed of 0.050-in. lead spheres between the screens and the glass beads.

THEORETICAL SUMMARY

In this section a brief résumé will be presented of the salient features of the theory previously presented (1) for ideal fluidized systems and then applied specifically to free countercurrent operation of fluid-particle systems. Certain basic concepts and assumptions are necessary. These may be listed as follows:
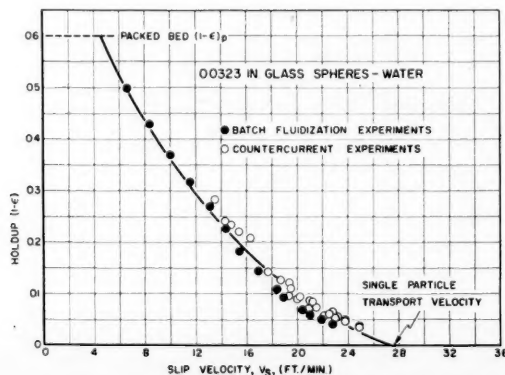

Fig. 4 Experimental holdup $(1 - \epsilon)$ vs. slip velocity for 0.0323-in. glass spheres in water.

1. Any mass of particles, whether solid, liquid, or gaseous, suspended in a continuous fluid because of the motion of the fluid between the particles is a fluidized system governed by the same fundamental laws.

2. The behavior of any vertical fluidized system in the steady state is determined by the slip velocity between fluid and particle, defined as the vector difference between fluid and particle velocities. Mathematically this may be written as

$$V_s = V_f - V_d = \frac{V_f'}{\epsilon} - \frac{V_d'}{1-\epsilon} \quad (1)$$

Velocities are taken as positive in the upward direction and negative in the downward direction.

3. For any mass of particles and any fluid of specified properties the relationship between void fraction and the slip velocity is the same irrespective of their direction of motion relative to each other or to the walls; that is, at the same value of the slip velocity all such systems will have the same holdup. This may be expressed by

$$V_s = \phi(1-\epsilon) \quad (2)$$

4. The basic properties may be generalized in terms of goemetry (size and shape), the physical properties of the system, and the flow rates, regardless of whether the particles are solid, liquid, or gaseous.

Two other quantities and relationships are of interest: the pressure gradient across the fluid bed and the specific contact surface of the particles. These are expressible mathematically by the following two relations for spherical particles:

$$\Delta P/Z = (1-\epsilon)(\rho_d - \rho_f) \quad (3)$$

and

$$\bar{a} = \frac{6(1-\epsilon)}{D_p} \quad (4)$$

It is important to note that the holdup, the pressure drop, and the surface area are directly proportional to each other.

In terms of these quantities it may be shown that all vertical moving fluidized systems can be organized into simple standard classes. One can recognize two general classes: a *free* system in which no obstruction or restraint to net forward particle movement exists in the path of flow, type A, and the *restrained* system, in which the forward particle movement but not the fluid is restrained mechanically as with a screen or membrane nonpermeable to the particles, type B. These two general classes can each be subdivided into a number of standard types depending upon the direction of flow of the two phases. One of these types is countercurrent flow, in which the solids move downward through a rising continuous fluid.

By combining Equations (1) and (2) either graphically or analytically, a generalized operating diagram can be constructed in which the holdup or pressure drop is plotted vs. the fluid velocity with solids velocity as a parameter. The behavior of all the classes and types of fluidized systems can be shown on this diagram. A portion of it will be considered later. In free countercurrent operation with a fixed particle flow rate there exists an upper limit on the fluid velocity or the holdup. At this upper limit, referred to as the flooding point, the system will begin to reject the particle feed. On the generalized operating diagram the locus of all the flooding points is shown and indicates the highest holdup attainable in a free system at a specified solids rate.

At the present time the function of Equation (2) may best be determined experimentally by using the batch expansion of an unfed screen-supported bed. In this case the net particle velocity with respect to the walls is arbitrarily made zero; $V_d = 0$. Thus the slip velocity equals the fluid velocity, and Equation (2) can be determined immediately. It is also possible to predict Equation (2) from empirical correlations in the literature (2, 3, 4, 8). In general these involve plotting the variables included in any one of several possible combinations of dimensionless groups. The present correlations need to be improved and extended over wider ranges of physical properties and Reynolds number before they can be used with complete confidence.

RESULTS AND DISCUSSION

The Invariant-Holdup–Slip-Velocity Relationship

Glass-Spheres–Water System

If the theory and postulates proposed are correct, the holdup–slip-velocity curve should be the same irrespective of the mode of operation of the moving fluidized system. Thus the data for the free countercurrent system and the batch or unfed screen-supported system should coincide. Figures 3 and 4 represent the experimental comparison for the two sizes of glass beads. The slip velocity was calculated by the use of Equation (1)
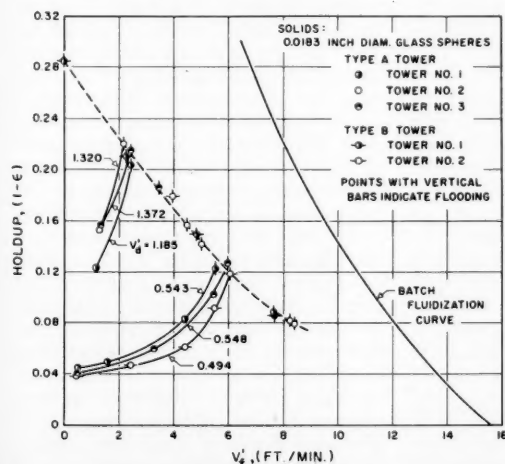

Fig. 5 Experimental holdup $(1 - \epsilon)$ vs. superficial fluid velocity for 0.0183-in. glass spheres in water, superficial solids velocity as parameter.
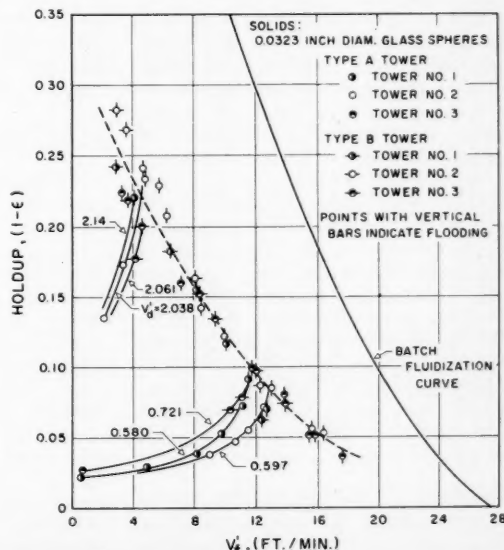

Fig. 6 Experimental holdup $(1 - \epsilon)$ vs. superficial fluid velocity for 0.0323-in. glass spheres in water, superficial solids velocity as parameter.
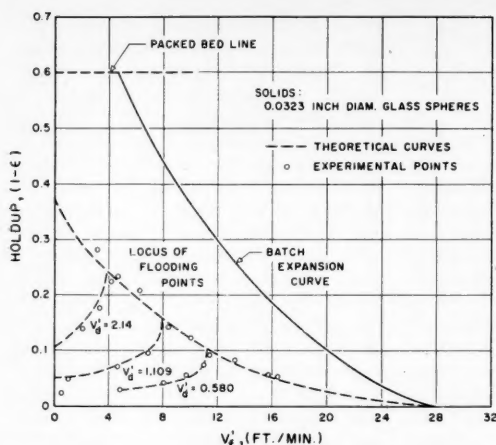
Fig. 7 Experimental vs. theoretically predicted generalized operating diagram for 0.0323-in. glass spheres.
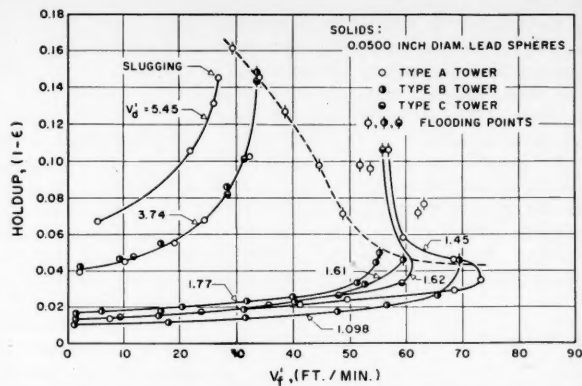

Fig. 8 Experimental holdup $(1 - \epsilon)$ vs. superficial fluid velocity for 0.0500-in. lead shot in water, superficial solids velocity as parameter.

and the holdup by the use of Equation (3) in conjunction with the measured values of the pressure drop. The data represent a very wide range of solids and fluid feed rates. The original data may be found in Price's thesis (7).

The solid line representing the batch fluidization data extends from the left at the packed-bed condition to the right at the single-particle transport velocity. One notes that the agreement between the two types of operation on each graph is excellent. The data illustrated for the countercurrent systems represent only a portion of these collected, but excessive crowding of the points would result if further data were used. The velocity corresponding to zero holdup, that is the single-particle transport velocity, was calculated by the commonly used drag coefficient (6). It is interesting to note that the maximum holdup in free countercurrent operation is limited to approximately 0.22 for the 0.0183-in. glass beads and 0.28 for the 0.0323-in. glass beads, whereas the packed bed corresponds to a void fraction of 0.58 and 0.60 respectively. Thus, as may be predicted theoretically, flooding of the free countercurrent system occurs at moderately low holdups. The data for the 0.0500-in. lead shot fluidized by water exhibit essentially the same behavior. Thus the validity of the single-invariant holdup–slip-velocity curve for any one system, as indicated by Equation (2), would seem to be valid for the types of operations and systems herein considered. The recent work of Mertes and Rhodes (5) in which measurements were made on countercurrent systems has also shown the same dependence of slip velocity on holdup.

Comparison with Predicted Operating Diagram

Figures 5 and 6 are plots of the holdup as a function of V_f' for the free countercurrent flow of water and 0.0183- and 0.0323-in. glass spheres, respectively. The parameter for the curves on both figures is a constant V_d'. Also shown on each figure is the corresponding batch expansion data. Three different tower diameters each with two different end arrangements are represented. The dashed line represents the best line through the flooding points.

The rate of change of holdup as a function of liquid flow rate was similar for both sizes of glass beads. At low liquid rates the holdup changed quite slowly, but, as the flooding point was approached, the holdup was rapidly increased by only small changes in fluid rate.

At low values of holdup the solids-liquid mixture appeared to be homogeneous; however at relatively high holdups small-scale heterogeneity was evident. With a strong source of illumination behind the column the solids appeared to be falling in thin strata. The use of a stroboscope indicated that there was no regular interval of repetition associated with the formation of these layers.

The Flooding Locus Curve

In Figures 5 and 6 any point below the locus of the flooding curve and $V_f' = 0$ represents stable free countercurrent operation. Any point between the batch expansion curve and the locus of the flooding curve represents stable, restrained countercurrent operation. By definition, at flooding the continuous and discontinuous phase rates are such that a slight increase in either will cause the formation of a head of the discontinuous phase in its conical entrance section, in other words the rejection of a portion of the feed of discontinuous particles from the effective zone of the tower. With towers having a constant diameter throughout, flooding at a fixed solids rate occurs at the maximum fluid velocity that will allow the tower to accept all the solids being fed. An increase in the

rate of either phase causes rejection of part of the solids feed at the point of its entrance to the tower.

If a system is operated at any point below the flooding point and the fluid velocity is gradually increased, the holdup will increase along a $V_d' = $ constant curve until flooding of the system occurs. Hence flooding in a free countercurrent system corresponds to the maximum holdup possible in a constant-diameter tower at any constant solids rate. In addition the flooding point may be represented by the equation

$$\left.\frac{\partial V_f'}{\partial (1 - \epsilon)}\right|_{V_d'} = 0 \qquad (5)$$

The rejection of solids increases as V_f' is further increased, and the solids holdup decreases until finally the single-particle terminal velocity is reached.

In general there was no effect of column diameter during either the batch or free countercurrent operation of the glass-spheres fluidized systems. As might further be expected, the locus of the flooding curve was not affected by the column diameter employed.

As has been previously indicated, the use of Equations (1) and (2) combined with data from a single-batch unfed bottom-supported fluidization experiment allows one to illustrate graphically the behavior of all moving fluidized systems. This plot is termed the *generalized operating diagram*. Since there are three parameters involved, a number of different types of plots can be constructed, but the authors find that holdup vs. fluid velocity with solids velocity as the parameter is the most useful and convenient. Figure 7 represents such a diagram for the 0.0323-in. glass beads. The method used in constructing Figure 7 has been described in detail (1) and consists of a graphical procedure. It is possible of course to represent Equation (2) by an empirical least-squares poly-

nomial fitted to the batch fluidization data. Under these conditions the graphical procedure for constructing the operating diagram can be dispensed with and an analytical procedure used. This latter technique will be illustrated in detail in subsequent publications.

The dashed lines on Figure 7 represent the theoretically predicted behavior of the free countercurrent system, and the points represent the corresponding experimentally determined values. Only a few sets of experimental points are shown in order not to crowd the plot. In general the agreement between the predicted and the experimental is quite good. The maximum in the holdup–fluid-rate curve for this free countercurrent flow, measured experimentally, corresponds to the locus of the flooding points as determined visually by rejection of solid particles. This experimentally observed curve also corresponds closely to the one predicted from the theory and batch expansion data by the methods outlined (Figure 7).

Lead-Shot–Water System

Whereas the data for the glass-spheres–water system were found to be independent of the physical dimensions and construction of the towers, this was not true for the lead-shot–water system. In the latter case the construction of the solids outlet section of the tower proved to be important, especially at low solids rates. Figure 8 is a plot of the data for the 0.0500-in. lead shot flowing countercurrently to water in the three different modifications of tower 1. (See Table 1.)

At high and intermediate values of the solids rate the holdup vs. fluid velocity curves were independent of the tower used, and the curves exhibited the type of behavior predicted. At the flooding point for these solid rates a small, very dense, highly turbulent layer of shot was formed in the conical entrance directly above the constant-diameter section of the tower. Another very small increase in liquid rate caused the solids head to continue to build up until, at approximately 4.5 in., bridging of the solids occurred at the junction of the cone and tower proper. The design of the approach angle of the cone proved to be very important in determining when this bridging would occur. During the interval of solids build-up in the cone a fixed volume of the head was fluidized, and the remainder of the particles acted as a slowly moving, fully packed bed. The shot were fed into the tower proper only after falling on top of the solids head in the cone and moved slowly downward through the fully packed region into the fluidized zone.

At low solids and liquid rates extremely low holdups were obtained with a visible solids concentration gradient in the radial direction. All but a few of the particles fell in the region adjacent to the

tower wall, thereby leaving the central core of the tower almost free of solids. At the base of the tower, on the other hand, the solids distribution appeared to be uniform. As the fluid velocity increased in tower type A, there was *channeling* of the solids and liquid at the tower base. Relatively dense groups of particles were observed to by-pass regions of low particle concentration with the resulting formation of swirls and eddies within the solids-liquid mixture with a scale approximately equal to the tower diameter. At some higher fluid velocity there suddenly appeared at the tower base a small region of very high holdup which spread rapidly up the tower. As the average holdup and resulting pressure drop increased, the fluid flow decreased, and a stable condition was attained where the lower half of the tower was filled with a very dense phase and the upper half with a much more dilute one. A small increase in the liquid rate caused the dense phase to move up the tower and into the cone. This lead-shot phenomenon is due to the creation of a partially restrained bed at the solids exit and produces the high holdups. The flooding in this case is not true flooding but rather an expansion of this restrained bed to overflow the top of the tower when the rate of withdrawal at the bottom does not equal the solids feed rate; in other words this is not truly a free countercurrent system.

By the addition of a flaired section to the tower's base (B type of modification) the phenomenon of dense-phase formation was eliminated (Figure 8). There was visual evidence that the tendency to form a dense solids layer at the lower end of the tower porper was still present, but the flaired section reduced the tendency sufficiently so that flooding was reached before any such region of high holdup formed. The removal of the flaired section and the addition of one having a constant diameter equal to that of the tower proper (C type of modification) gave results identical to those obtained in the original tower.

In this system, with a large difference between the density of particles and fluid, one begins to observe deviations from ideal or particulate fluidization. Since the basic theoretical postulates of the present work assume ideal fluidization, it is not surprising that a certain degree of deviation from the theoretical behavior occurs. It is very encouraging however to note that with the proper experimental equipment even these systems behave as predicted.

CONCLUSIONS

The agreement found between the holdup–slip-velocity relations for free countercurrent flow and for batch fluidization supports the basic assumption of the existence of a single fundamental

relationship between holdup and slip velocity for any vertical fluidized system. This indicates that all vertical fluidized systems may be interrelated and generalized in terms of slip velocity and void fraction irrespective of the direction of motion. It also has been shown that the theory developed in a previous publication allows an accurate prediction of the operation of free countercurrent systems. The method of prediction requires data from a single-batch unfed bottom-supported fluidized experiment.

It has been verified experimentally that in free countercurrent flow there exists a maximum in holdup–fluid-rate curves, which corresponds to the flooding point of the system, as indicated by visual observation of the rejection of solid particles, and to the values predicted from batch fluidization data by the theory presented.

NOTATION

V_s = slip velocity, ft./min.
V_f = continuous fluid average velocity, ft./min.
V_d = discontinuous or solids average velocity, ft./min.
V_f' = superficial continuous fluid velocity, ft./min.
V_d' = superficial discontinuous or solids velocity, ft./min.
$1 - \epsilon$ = fraction holdup of solids in tower
ϵ = void fraction of tower
$\Delta P/Z$ = static pressure drop, lb./(sq. ft.) (ft.) of length
ρ_f = density of continuous phase, lb./cu. ft.
ρ_d = density of discontinuous phase, lb./cu. ft.
$\bar{a}$ = specific contact area of solids/ unit volume
D_p = solids diameter
ϕ = slip velocity functionality on $(1 - \epsilon)$

LITERATURE CITED

1. Lapidus, Leon, and J. C. Elgin, *A.I.Ch.E. Journal*, **3**, 63 (1957).
2. Leva, Moe, *J. Chem. Eng., Canada*, **35**, 71 (1957).
3. Lewis, E. W. and E. W. Bowerman. *Chem. Eng. Progr.*, **48**, 603 (1952).
4. Lewis, W. K., E. R. Gilliland, and W. C. Bauer, Ind. Eng. Chem., **41**, 1104 (1949).
5. Mertes, T. S. and H. B. Rhodes, *Chem. Eng. Progr.*, **51**, 429, 517 (1955).
6. Perry, John, ed., "Chemical Engineer's Handbook," McGraw-Hill, New York (1950).
7. Price, B. G., Ph.D. thesis, Princeton University, Princeton, N. J. (1951).
8. Richardson, J. F. and W. N. Zaki, *Trans. Inst. Chem. Engrs. (London)*, **32**. 35 (1954).

Liquid Viscosities of Methane and Propane

G. W. SWIFT, J. A. CHRISTY, and FRED KURATA

University of Kansas, Lawrence, Kansas

The theory and calibration procedure for a cylindrical falling body viscometer is presented.

Experimental viscosity data are given for liquid methane from −150°C. to the critical point and for liquid propane from −185° to +90°C. The maximum experimental error for methane data is ±8% and for propane data ±5%.

A literature survey shows that there are very few data on viscosities of normally gaseous hydrocarbons in the liquid phase above their normal boiling points. Data which are available have been obtained over limited ranges of temperature and pressure. Furthermore there has been no attempt made to consolidate the viscosity data for any hydrocarbon over the complete liquid region.

The data presented here range from from the normal boiling point to the critical point of the hydrocarbon tested. In addition, through calibration procedures, the data are consolidated with those of the American Petroleum Institute (8), which are given from the freezing point to the normal boiling point. The end result is a consistent set of viscosity data for methane and propane which extend over their entire liquid region.

The data which are presented here were obtained on the apparatus described by Swift, et al. (11).

THEORY AND EXPERIMENTAL APPLICATION

The theoretical basis for determining viscosity by the falling-body method comes from the work of Stokes (10), who solved the classical equations of hydrodynamics for the resistive force W, opposing the uniform motion of a sphere through an infinite, viscous medium. Stokes's equation is

$$W = 3\pi \, dv\mu \qquad (1)$$

Rayleigh (7) pointed out that the assumptions leading to Equation (1) were valid only when the Reynolds number was less than unity. Barr (1) proposed that Equation (1) be modified by a shape factor, such that

$$W = 3\pi \, dv\mu/\delta \qquad (2)$$
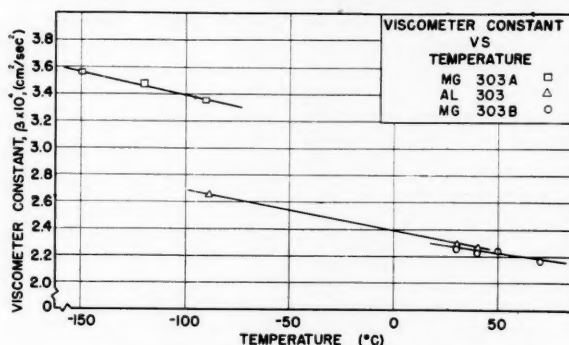
The shape factor, a measure of the

Fig. 1. Viscometer constant vs. temperature.

effect of the geometry of the falling body on the resistive force, is defined for any falling body having three axes of symmetry.

If a cylindrical body with hemispherical ends is used for the falling body, it is possible to derive a formula relating the viscosity to other physical

TABLE 1. DESCRIPTION OF FALLING BODIES

Body number	MM285	MM300	MM308
Description	Hollow cylinder with hemispherical ends; one end of cylinder drilled to equalize pressure on inner and outer surfaces of cylinder.		
Materials of construction	Methyl methacrylate with stainless steel collar		
Nominal diameter, in.	0.285	0.300	0.308
Maximum taper, in.	±0.001	±0.001	±0.001
Length, in.	3 5/16	3 1/16	3 1/16
Density, g./cc.	0.234	0.309	0.237
Total volume, cc.	3.73	3.83	4.07
Void volume, cc.	3.13	2.96	3.34
Body number	MG303A	AL303	MG303B
Description	Solid Cylinder	Hollow cylinder with hemispherical ends	
Materials of construction	Magnesium	Aluminum 5052S alloy	Magnesium
Nominal diameter, in.	0.303	0.303	0.303
Maximum taper, in.	±0.003–0.005 in. on each cylinder.		
Length, in.	2.00	1.70	1.70
Density, g./cc.	1.775	1.051	0.538

properties which can be measured with comparative ease.

The volume of such a body is

$$V = \frac{\pi\,d^2}{2}\,(h/2 + d/3) \qquad (3)$$

When one assumes that the body is moving under the acceleration of gravity, the apparent force on the body in the downward direction is

$$Vg(\sigma - \rho)$$
$$= \frac{\pi\,d^2 g}{2}\,(h/2 + d/3)(\sigma - \rho) \qquad (4)$$

If the body is falling at constant velocity, the apparent downward force may be equated to the resistive force:

$$W = \frac{3\pi\,dv\mu}{\delta}$$
$$= \frac{\pi\,d^2 g}{2}\,(h/2 + d/3)(\sigma - \rho) \qquad (5)$$

When one solves for the viscosity,

$$\mu = \frac{dg\delta}{6v}\,(h/2 + d/3)(\sigma - \rho) \qquad (6)$$

Before Equation (6) is applied in experimental work, it is necessary to consider the assumptions made to complete its derivation:

1. An Infinite Medium

The use of a finite medium introduces two experimental errors, the *end* effect and the *wall* effect. Barr (1) treated the subject of the end effect and found that it could be neglected in finite systems if the velocity of fall was measured at a point removed several body lengths from the end of the containing vessel. He also presented several theoretical derivations in which the correction for wall effect was treated as a function of the diameter of the containing vessel and the diameter of the falling body. If the wall-effect correction is defined as $\psi(D, d)$, the equation for the resistive force is then

$$W = \frac{3\pi\,dv\mu}{\delta\psi(D, d)} \qquad (7)$$

As the ratio of d/D approaches unity, the average velocity of the fluid passing the falling body v is no longer equal to the velocity of the falling body s/θ. These velocities are related, however, by the continuity equation

$$\frac{v}{s/\theta} = \frac{d^2}{D^2 - d^2} \qquad (8)$$

The viscosity in a falling-body viscometer, where $0.5 < d/D < 1$, is

$$\mu = \frac{g\delta\psi(D, d)(h/2 + d/3)(D^2 - d^2)(\sigma - \rho)\theta}{6sd} \qquad (9)$$

Fig. 2. Viscometer constant vs. temperature.

Fig. 3. Temperature correlation factor vs. temperature.

2. $\sigma > \rho$

The derivation implies that the density of the fluid is less than the density of the body. However the equations are equally valid for $\sigma < \rho$, the only difference being the reversal of the motion of the body.

3. Terminal Velocity of Fall

The velocity of the body approaches the limiting (terminal) velocity exponentially. By selecting the point for velocity measurement at a sufficient distance from the initial release point, one can eliminate error from this source.

4. $N_{Re} < 1$

To determine the Reynolds number at which laminar flow is terminated for falling spheres, Barr (1) described Castleman's method, that is, plotting the ratio of resistance per unit cross section to ρv^2 against N_{Re} on logarithmic coordinates. When data are plotted by this method, the points fall on a straight line as required by Stokes's Law for N_{Re} less than 1. Beyond this value of N_{Re} the resistance factor $f = 8W/\pi d^2\rho v^2$ decreases less rapidly with increasing N_{Re} until it
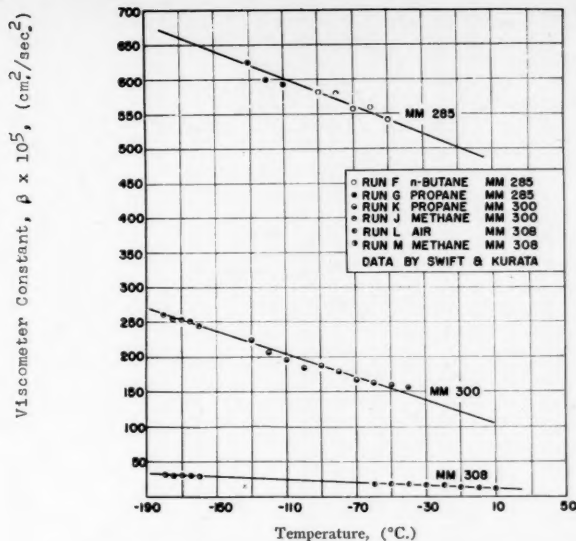
Fig. 4. Temperature corrected resistance function vs. modified Reynolds number.
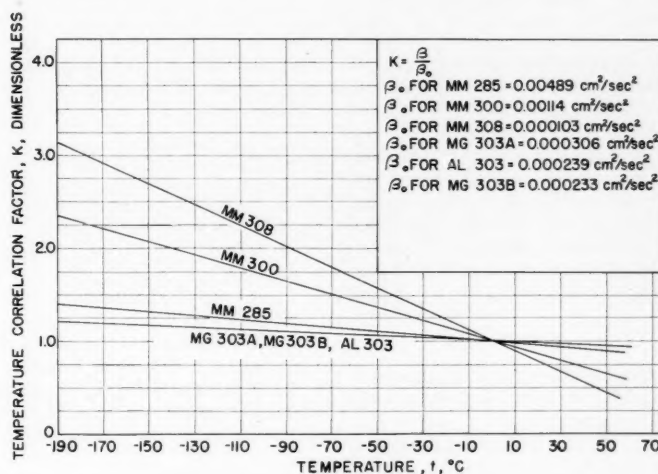

Fig. 5. Resistance function (not corrected for temperature) vs. modified Reynolds number.

becomes independent of viscosity and proportional to ρv^2. The break point at $N_{Re} = 1$ is the critical Reynolds number for viscometry, where $d/D \ll 1$.

Hubbard and Brown (4) plotted data similarly for a rolling-ball viscometry where the ratio of d/D approached unity, and then found that the critical modified Reynolds number was twenty. They used a modified Reynolds number

$$N_{Re'} = \frac{d^2 s \rho}{(D + d) \theta \mu} \qquad (10)$$

to account for the equivalent diameter and the difference between fluid velocity and ball velocity.

Then, for a falling-cylinder viscometer, $0.5 < d/D < 1$

$$f = \frac{4g(D^2 - d^2)^2(h/2 + d/3)(\sigma - \rho)\theta^2}{\rho s^2 d^4} \qquad (11)$$

A plot of the resistance factor [Equation (11)] vs. $N_{Re'}$ on logarithmic coordinates will determine the range of laminar flow for a cylindrical falling-body viscometer.

For precise experimental work Equation (9) is written

$$\mu = \beta(\sigma - \rho)\theta \qquad (12)$$

where the viscometer calibration constant is determined experimentally. This practice is employed for accurate viscometric work because the physical dimensions of the apparatus cannot be measured with the desired accuracy; the wall-effect correction $\psi(D, d)$ is included in the calibration constant; the shape factor is included in the calibration constant; and the effect of temperature and pressure upon the dimensions of the apparatus

can be determined and compensated for by considering $\beta = \phi(t, p)$.

Since

$$\beta = \frac{g\delta(D^2 - d^2)(h/2 + d/3)\psi(D, d)}{6sd} \qquad (13)$$

Equation (11) may be rewritten

$$f = \frac{24\beta(D^2 - d^2)(\sigma - \rho)\theta^2}{\delta\psi(D, d)\rho sd^3} \qquad (14)$$

If β is a function of temperature, the data may be plotted with Equation (14) as the resistance factor. It is possible to use an alternate form by taking the value of β at some arbitrary temperature, say

at 0°C., as was done here and computing the ratio $K = (\beta/\beta_0)$ for various temperatures. Then, substituting $\beta = K\beta_0$ into Equation (14) gives

$$f' = \frac{24\beta_0 K(D^2 - d^2)(\sigma - \rho)\theta^2}{\delta\psi(D, d)\rho sd^3} = \frac{4gK(h/2 + d/3)(D^2 - d^2)^2(\sigma - \rho)\theta^2}{\rho s^2 d^4} \qquad (15)$$

When the logarithm of the temperature-corrected resistance factor is plotted against the logarithm of the modified Reynolds number, the calibration data will be successfully correlated and the limits of laminar flow determined.
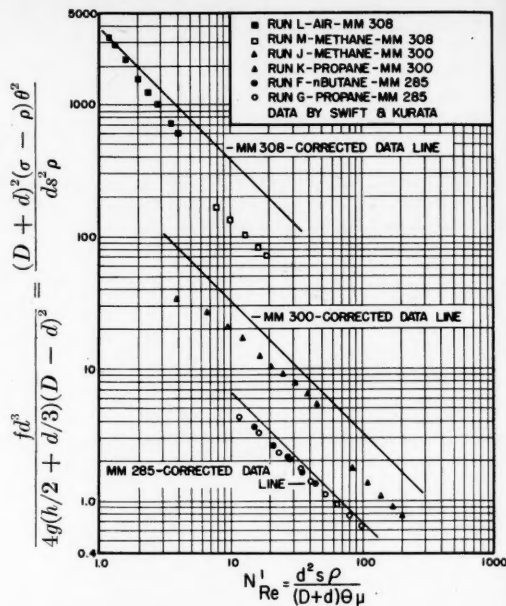
RESULTS

Experimental data were obtained by

means of six falling bodies, the descriptions and dimensions of which appear in Table 1.

Densities of the cylinders MG303A, AL303, and MG303B were assumed to be constant at all temperatures and pressures. Any error in this assumption was compensated for in the experimental calibration constant. The densities of the methyl methacrylate cylinders varied with the densities of the fluids in which they were immersed. The apparent densities of these bodies were computed from a knowledge of the void volumes and total volumes of the bodies.

At least five, and usually ten, readings were obtained for every calibration and experimental fall time. The arithmetic means of these readings were used for computation.

Calibration of the viscometer for the various falling bodies was accomplished by determining experimental fall times in fluids of known viscosities. The accepted values of viscosity and density for the calibration substances, methane,

propane, n-butane, and air, are given in the literature (3, 5, 8). The calibration procedure was carried out at various temperatures and pressures, so that the calibration constant might be expressed as a function of temperature and pressure. For any given temperature the effect of increasing pressure to 800 lb./sq.

TABLE 2. EXPERIMENTAL VISCOSITIES OF METHANE AND PROPANE

Substance	Temperature, °C.	Pressure, lb./sq. in. abs.	Body	$N_{Re'}$	Viscosity, centipoises	Phase
Methane	−150	350	MM308	20	0.0880	l
	−140	550		26	0.0734	
	−130	600		37	0.0599	
	−120	650		47	0.0508	
	−110	710		59	0.0435	
	−100	710		78	0.0357	
	− 95	710		86	0.0327	
	− 90	710		98	0.0294	
	− 85	710		122	0.0251	
	− 83.2	710		88	0.0249	Crit.
	− 83.2	710		100	0.0232	
	− 83.2	710		115	0.0214	
	− 80	695		118	0.0178	g
	− 76	685		209	0.0116	
	−150	365	MM300	234	0.0964	l
	−140	450		283	0.0768	
	−130	500		362	0.0660	
	−120	525		427	0.0578	
	−110	600		392	0.0589	
	−100	650		490	0.0496	
	− 95	700		583	0.0441	
	− 90	700		595	0.0421	
	− 85	700		681	0.0373	
	− 83.2	680		585	0.0346	Crit.
Propane	−185	50	MG303A	0.248	7.36	l
	−180	50		0.484	5.25	
	−170	50		1.58	2.96	
	−160	50		3.53	1.92	
	−150	50		7.13	1.34	
	−140	50		13.3	0.976	
	−130	50		21.5	0.761	
	−120	50		32.6	0.613	
	−110	50		46.4	0.510	
	−100	50		63.8	0.431	
	− 90	50	AL303	24.0	0.375	
	− 80	50		33.3	0.317	
	− 70	50		40.5	0.287	
	− 60	50		50.1	0.258	
	− 50	50		63.5	0.228	
	− 40	50		77.5	0.206	
	− 30	50		94.3	0.186	
	− 20	50		113	0.169	
	− 10	50		138	0.152	
	0	75		170	0.136	
	+ 10	95		196	0.126	
	+ 20	130		239	0.113	
	+ 30	170	MG303B	28.2	0.0987	
	+ 40	225		49.3	0.0845	
	+ 50	275		71.8	0.0766	
	+ 60	330		116	0.0646	
	+ 70	400		170	0.0575	
	+ 80	455		278	0.0478	
	+ 90	560		385	0.0427	

in. abs. had no effect on the fall time, an indication that moderate pressure did not affect either the measured viscosity or the physical dimensions of the viscometer, which is verified by Bridgeman (2). Plots of the viscometer calibration constant vs. temperature are presented in Figures 1 and 2.

A plot of K vs. t is presented in Figure 3. The values of K were computed from the most probable values of β for the various falling bodies.

A logarithmic plot of

$$\frac{[K(D + d)^2(\sigma - \rho)\theta^2]}{ds^2\rho}$$

vs. $N_{Re'}$ (Figure 4) is given using the calibration data. This plot shows that laminar flow existed in the viscometer during all calibration runs. It does not show the break in the curve that would indicate the beginning of turbulent flow. There is, however, other evidence which indicates the value of $N_{Re'}$ where turbulence begins. This evidence will be cited later.

Figure 5, which shows the effect of plotting the experimental calibration data on a modified Castleman plot when the temperature correlation factor is not used, illustrates the necessity of using a temperature-corrected resistance func-
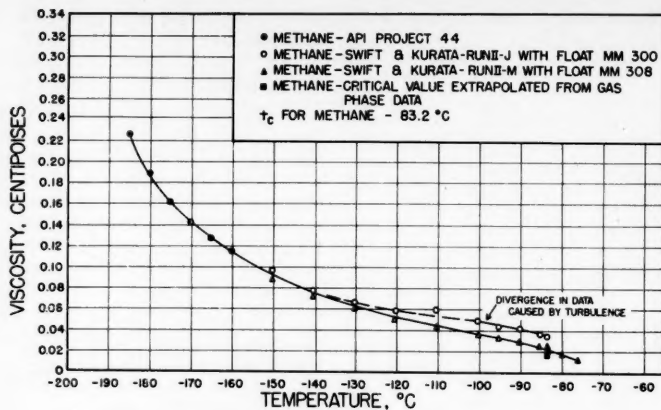
tion to determine accurately the limits of laminar flow.

The experimental viscosities for methane and propane are given in Table 2 and are shown graphically in Figures 6 and 7; they were computed by use of Equation (12). The values of the viscometer calibration constant were determined by the statistical method of least squares, when one assumed that β was a straight-line function of temperature. Densities of liquid methane and propane were obtained from the literature (5, 8).

When turbulence begins in the viscometer, the fall times become greater than would be predicted, thereby giving values for viscosity which are too large. The deviation of the data on methane obtained with MM300 (Figure 6), starting at −140°C. and increasing with temperature, illustrates this. This deviation began at a modified Reynolds number of 285. On this basis the data obtained with MM308 should be reliable, since the highest experimental $N_{Re'}$ attained with this body was 209. Also the viscosity of propane at 80° and 90°C. measured with body MG303B would not be expected to be so reliable as the data obtained at lower $N_{Re'}$ because of the $N_{Re'}$ of 278 and 385 at these two temperatures. However, as can be seen in Figure 7, these two data points are not greatly in error with the data points taken at lower $N_{Re'}$.

The experimental error in determining the viscosity data presented is ±5% maximum for propane and ±8% maximum for methane. These figures are based upon the deviation of calibration data from the most probable values and the deviation of individual fall times from the mean.

CONCLUSIONS

The viscosity data for methane and propane have been obtained over temperature ranges where data were not previously available. Over temperature ranges where data were available the results obtained on the apparatus agree well with those in the literature.

By extensive and repeated calibrations of the viscometer the level of confidence in predicting the most probable value of the viscometer constant will be greatly improved. Since the greatest experimental error lies in the determination of the viscometer constant, the foregoing procedure would greatly reduce the present experimental error (±8% for methane and ±5% for propane).

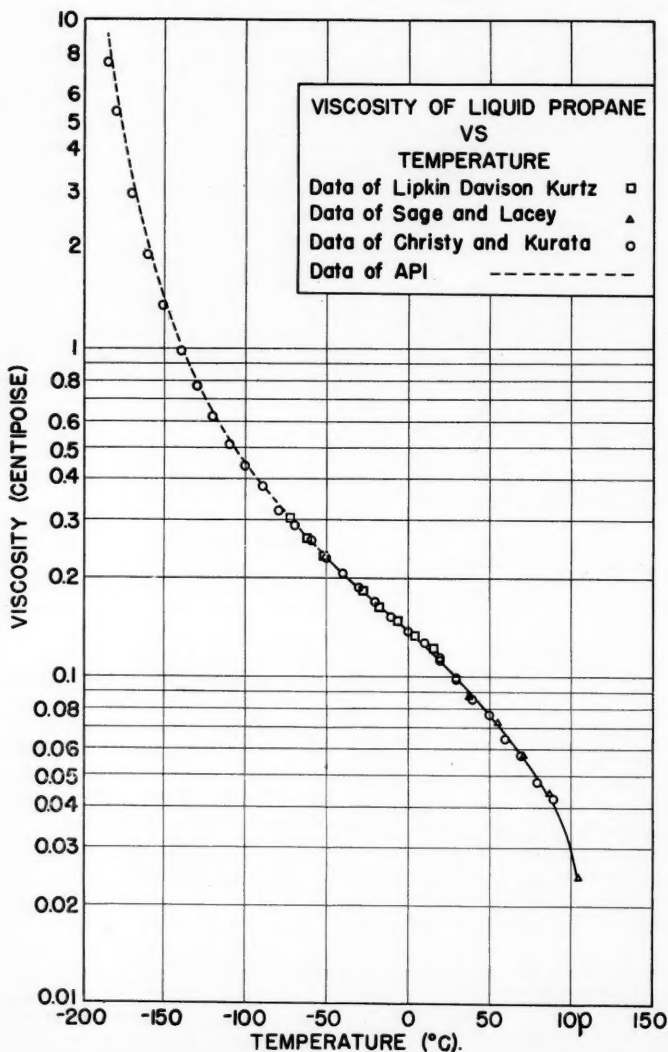Fig. 6. Viscosity of liquid methane vs. temperature.

Fig. 7. Viscosity of liquid propane vs. temperature.

NOTATION

D = diameter of fall tube, cm.

d = diameter of falling body, cm.

f = resistance factor, dimensionless

f' = temperature corrected resistance factor, dimensionless

g = acceleration of gravity, cm./sec.^{2}

h = length of cylindrical portion of falling body, cm.

K = temperature correlation factor, dimensionless

N_{Re} = Reynolds number $dv\rho/\mu$, dimensionless

$N_{Re'}$ = modified Reynolds number $d^2s\rho/(D+d)\theta\mu$, dimensionless

s = timed interval of distance in viscometer cell, cm.

t = temperature, °C.

V = volume, cc.

v = average velocity of fluid, cm./sec.

W = resistance to motion, dynes

Greek Letters

β = viscometer calibration constant, sq. cm./sec.^{2}

β_0 = viscometer calibration constant at 0°C., sq. cm./sec.^{2}

δ = shape factor, dimensionless

θ = time, sec.

μ = viscosity, poise

ρ = density of fluid, g./cc.

σ = density of falling body, g./cc.

ψ = function, dimensionless

ϕ = function, dimensionless

LITERATURE CITED

1. Barr, Guy, "A Monograph of Viscometry," Humphrey Milford, London (1931).
2. Bridgeman, P. W., "The Physics of High Pressure," G. Bell and Sons, Ltd., London (1931).
3. "Handbook of Chemistry and Physics," 30 ed., pp. 1697, 1736, Chemical Rubber Publishing Co., Cleveland, Ohio (1948).
4. Hubbard, R. M., and G. G. Brown, *Ind. Eng. Chem. Anal. Ed.*, **15**, 212 (1943).
5. Matthews, C. S., and C. O. Hurd, *Trans. Am. Inst. Chem. Engrs.*, **42**, 55 (1946).
6. Natural Gasoline Assn. of America, Tech. Committee, *Ind. Eng. Chem.*, **34**, 1240 (1942).
7. Rayleigh, J. W. S., *Phil. Mag.*, **36**, 365 (1893).
8. Rossini, F. D., *Am. Petroleum Inst. Research Project 44*, Carnegie Press, Pittsburgh, Pennsylvania (1953).
9. Sage, B. F., and W. N. Lacey, *Ind. Eng. Chem.*, **30**, 829 (1938).
10. Stokes, G. G., "Mathematical and Physical Papers," Vol. 3, University Press, Cambridge (1901).
11. Swift, G. W., *et al.*, *Chem. Eng. Progr.*, **54**, 6, 47 (June, 1958).

Mechanism of Drying Thick Porous Bodies During the Falling Rate Period

I. The Pseudo-Wet-Bulb Temperature

A. H. NISSAN, W. G. KAYE, and J. R. BELL

The University of Leeds, Leeds, England

The drying of two highly porous thick textiles is studied and compared. Extremes are chosen in that one package is composed of a Terylene (British form of a polyester fiber) net fabric of open structure and the other of a woolen flannel of close structure. The cloths are wound as bobbins and dried by hot air streaming in a wind tunnel, the air flowing parallel to the axis of the cylinder of material. The weight of water as drying progresses is measured by a balance, and thermocouples within the bobbin provide a temperature record.

On investigation of the thermal conductivity of the dry structure, it is found that whereas the coefficient for the wool-air mixture is constant throughout, the coefficient for the Terylene-air mixture applies only in the depths, the apparent thermal conductivity growing larger toward the surface and with increasing air speed, as if the heat transfer through the open structure is assisted by some form of air penetration.

As the thick textiles dry, the rate of evaporation falls off, since heat and water vapor have to pass through an increasing layer of dry material. While this is occurring, a constant temperature, the "pseudo-wet-bulb temperature," is established throughout the wet cloth. This state of equilibrium may be expressed as an equation between the rate of heat conduction inward and that required to produce the vapor diffusion outward. From this equation the pseudo-wet-bulb temperature can be calculated.

The rate of drying of any particular material depends upon the relative magnitudes and modes of variation of two processes, heat and mass transfer. For evaporation to take place heat must be supplied to the evaporating fluid from some heat source. In air drying the heat is contained in the air and must be conveyed through the stagnant surface-air layer to the solid surface and thence must pass to the zone of evaporation. In the later stages of drying this often has to occur through a thick layer of dry material. A knowledge of the thermal conductivity of the dry material is thus important in an investigation of the drying process.

In this paper the heat transfer in the dry material is considered first and then the complete drying sequence. Results are reported for two packages, both of high porosity, one consisting of Terylene (British form of a polyester fiber corresponding to the American Dacron) net fabric of open structure and the other of a woolen flannel of close structure.

THE APPARATUS

The materials were wound as bobbins and supported in hot air streaming through a wind tunnel. Thermocouples throughout the bobbins and in the wind tunnel indicated temperatures. As drying took place, the weight of water leaving the bobbin was determined directly by a continuous weighing with an analytical balance.

A. H. Nissan is with the Rensselaer Polytechnic Institute, Troy, New York, and W. G. Kaye is with the Coal Research Establishment, Stoke Orchard, Cheltenham, Gloucestershire, England.

The Wind Tunnel

The wind tunnel and ancillary components are shown diagrammatically in Figure 1. The main structure was of ⅜-in. asbestos cement sheeting with inside section 8¾ in. square. The upper working section was made hexagonal, and flow straighteners were inserted at the bends ($C_{1,2,3}$) to reduce
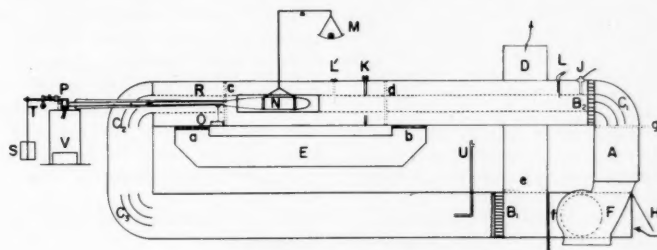

Fig. 1. Sketch of wind tunnel.

transverse flow. Flow mixers (B_1 and B_2) ensured a uniform distribution of air velocity across the tunnel section. The tunnel was usable with continuous recirculation, direct flow through, or proportions of the two by means of the shutters (a to g). The air was blown by a fan (F) through the heating section (A) containing four 1¼-kw. spiral heating elements. Temperature was controlled with a thermostat (J) and vacuum relay to two of the spiral heater elements. The air temperature was measured immediately after this by probe thermocouples at positions L or L'. The air flow was indicated by an inclined alcohol manometer connected to the corner tappings of an orifice plate (K).

The Specimen Bobbins

Figure 2 shows the Terylene bobbin in position in the wind tunnel. The cloth, 6 in. wide, was wound on a spool between Bakelite disks on a Bakelite tube of outer diameter ½ in. and inner diameter ¼ in. The fabric package had an outer diameter of just under 3 in., and there was thus over 1-in. depth of material. Thermocouples were situated between layers of the cloth at various depths, and the wires from the junctions passed to sockets attached behind the rear Bakelite disk. Corresponding plugs were attached to arm R in the tunnel (Figure 1). A streamlined aluminum nose formed the leading edge, and the streamlines were continued in the aluminum cover over the plug-socket connection.

The tube R (Figure 1) passed through the end of the tunnel and was attached to a knife edge (P) from which the counterbalance arm supported weight S and, for fine adjustment, weight T. The thermocouple leads within R being led out at the pivot and clamped to the support (V) exerted no moment on the system. Thus the dry weight of the bobbin could be supported by the lever and the weight of the added water measured by means of the analytical balance (M).
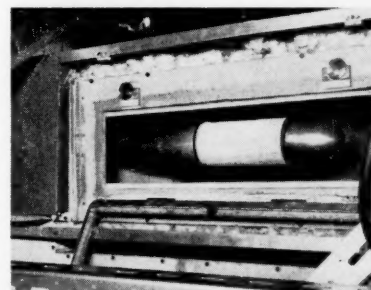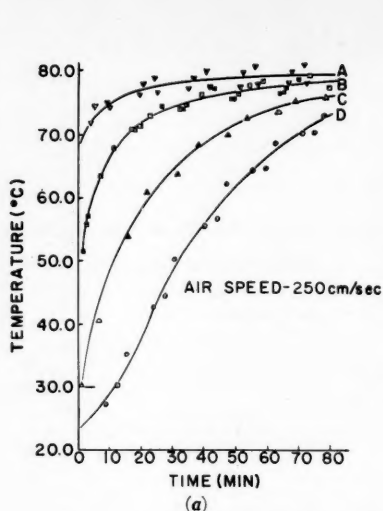

Fig. 2. Bobbin in tunnel.

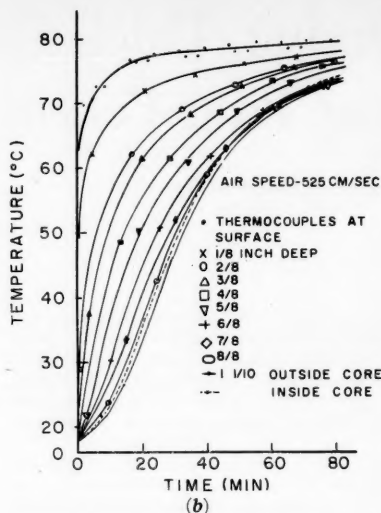Fig. 3a. Temperature vs. time at various depths in the Terylene bobbin (dry).

Fig. 3b. Temperature vs. time at various depths in the wool bobbin (dry).

The Bobbin Materials and Thermocouple Arrangements

From the weight of cloth wound, the density, and the volume the bulk density of the Terylene was 0.366 g./cc. and the porosity (void fraction) 0.735. For the similar wool bobbin the figures were 0.283 g./cc. and 0.762, representing conditions when the wool was in equilibrium with air of tunnel temperature and relative humidity.

Fourteen thermocouples were used in each bobbin. In the Terylene bobbin the couples were placed in the vertical axial plane, a few at each of four levels, for example (a) under the first layer, (b) $\frac{1}{8}$ in. deep, (c) $\frac{3}{8}$ in. deep, and (d) $\frac{7}{8}$ in. deep. They were spread along the length of the bobbin but showed no evidence of any axial flow of heat. Consequently in the wool bobbin the couples were mostly placed in the central plane of the bobbin, a spiral arrangement of placings being used, with one available for each succeeding $\frac{1}{8}$ in. in depth and for the inside and outside of the central core.

The thermocouples were connected in random order to a sixteen-point potentiometer recorder which selected each in turn and printed the temperature on a chart with a number to identify the particular thermocouple.

HEAT CONDUCTION

The apparent thermal conductivity of a dry porous material represents heat transfer by a number of methods. There is conduction in solid and void, and convection and radiation in the voids. For small temperature differences the effect of radiation will be small, and convection will be important only in very open structures. The summation of the conduction in solid and void is complex, being sometimes in series and sometimes in parallel, depending on the particular structure.

The temperature distribution while a dry bobbin is heating gives a means by which a good estimate of the apparent thermal-conductivity coefficient of the dry material may be made, provided sufficient values are calculated to allow of reasonable averaging. A method of dividing the cylinder into small finite elements and using step-by-step calculations was used, as it was suspected that the conductivity might not be constant throughout. Other workers (1, 2, 3, 4) have used similar methods to determine the temperature distributions within a body of a given shape, starting with a knowledge of the conductivity and stated external conditions. The theoretical relationships given graphically by Gurney and Lurie (5) for a long cylinder and their adaptation by Newman (6) for a finite cylinder would not hold for a body of variable conductivity.

Method of Calculating k and h from the Temperature

The bobbin is divided from the surface into annular elements $\frac{1}{8}$ in. thick, and it is assumed that for a short period of time (5 min.) conditions remain sufficiently constant for the steady state Fourier (7) relationship to hold across the annulus considered; that is,

$$q = -kA \frac{d\theta}{dx} \qquad (1)$$

q is given by the rate at which sensible heat is taken up by the layers enclosed by the annulus considered, the increases in temperature in the 5 min. considered being taken from the graphs showing the temperature distribution (Figures 3 and 4). Little error is introduced by using the average annular area in lieu of the logarithmic mean area, and the temperature

gradient is taken from the temperature record. The value of k obtained will be the mean value obtaining for the particular annulus at the particular time.

Outside the cylinder a boundary layer of air occurs before the main air stream, and this is assumed to have an over-all heat transfer coefficient h defined by

$$h = \frac{q}{A(\theta_a - \theta_s)} \qquad (2)$$

q being the rate of supply of sensible heat to the whole bobbin at a particular time, with the heat passing through the perimeter area of the bobbin.

Experimental Results

Procedure

For an investigation of the thermal conductivity of the dry bobbin the balance system was unnecessary, and therefore the experiments were carried out with the suspension wire clamped as it left the tunnel. The bobbin was allowed to stand in uniform air conditions until it attained the same temperature throughout; it was then quickly inserted into the heated tunnel and the recorder switched on.

As a preliminary with the woolen bobbin it was necessary to heat it for some time while the water of absorption was driven off and equilibrium was reached at tunnel temperature and humidity. The bobbin was then inserted in a polythene bag to prevent water from reentering it as it acquired room temperature before being inserted into the tunnel.

Variation of Temperature with Time

The bobbin starts at a uniform temperature, and when it is subjected to the hot air flowing over the surface, heat begins to flow in. The surface layers rapidly reach the air temperature, but layers at greater depths take longer. The curves for this temperature change as the heating proceeds are shown for the various depths in the bobbins in Figure 3.

Variation of Temperature with Depth

The variation of temperature with distance from the center can be found at any particular instant by reading the temperature from the curves given in Figure 3 at that particular instant. From these values of temperature the changes of temperature with distance from the center of the bobbin can be shown for different times. Such curves of temperature against radius for both bobbins are shown in Figure 4.

The curves in Figure 4 show consecutive 5-min. intervals after the start of heating. The lowest curve is at 5 min. and the highest at 60. The temperature at zero time would be represented by a straight line of constant temperature.
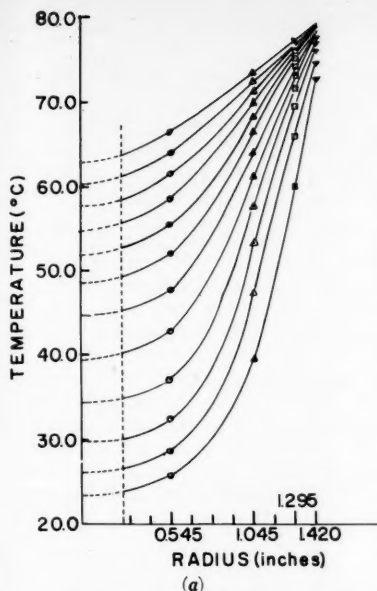
The dotted portion of the Terylene

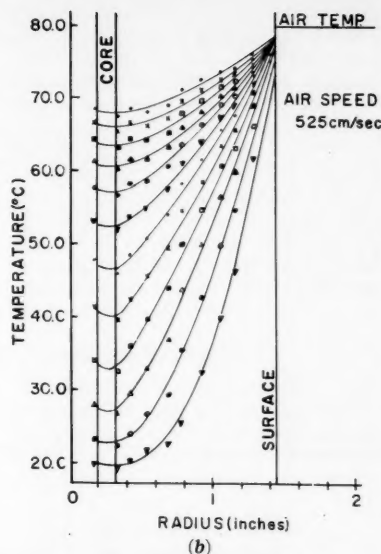Fig. 4a. Temperature vs. radius at various times: Terylene bobbin (dry).

Fig. 4b. Temperature vs. radius at various times: wool bobbin (dry).

curve represents uncertainty as to what is happening in the region of the core. As a result, in the wool bobbin thermocouples were inserted on the inside and outside of the solid core; these indicate that in that bobbin there is a very small flow of heat outward through the core, a heat balance being achieved in the region of the outer surface of the core.

A major difference between the two sets of curves is that the Terylene ones show a small but distinct tendency to flatten out near the surface, whereas within the limits of graphical interpretation there is no such effect in the case of wool. This indicates that the Terylene layers near the surface are reaching the air temperature sooner than theoretical curves which assume constant thermal conductivity would indicate.

Values of Thermal Conductivity Obtained for the Bobbins

The method given above was applied to different annuli of the bobbins. The values of thermal-conductivity coefficients derived during the various experiments are given in Table 1. Each value is the mean of a number of determinations involving the heat passing through an annulus in various 5-min. intervals.

Values beyond the fourth innermost layer in the case of the Terylene were rejected because the dotted portion of Figure 4a was assumed to hold, and a doubtful quantity of heat was thus attributed to the core. If one allows a 50% error in the value of the heat to the core, all results are rejected where the error due to this cause in the final result could be more than 10%. As far as the

wool was concerned, it was assumed that the temperature minima in Figure 4b occurred at the core outer surface and that no heat entered the core via the wool. On this account the values of k for annuli 7 and 8 were lower and have been omitted.

It is clear from Table 1 that in the case of the open structure given by the Terylene there is an increase in the coefficient of thermal conductivity as the surface is approached. In the case of the close structure of the wool the thermal conductivity is constant throughout. The actual value agrees reasonably with that given by Baxter (8) for wool of this bulk density.

Analysis of the Terylene Results

As the temperature of the bobbin increases with increasing radius, the variation in k could be due either to temperature increase or to change of position, the air velocity remaining constant. A statistical analysis showed that the significant variation of k was with increasing radius and not with temperature. The possibility of the temperature effect being thus eliminated, the variation of thermal conductivity with radius can be investigated by the usual graphical methods.

The mean values of the apparent coefficient of thermal conductivity for each $\frac{1}{8}$-in.-thick annulus were plotted as ordinates against the mean radii of the annuli, and the two curves which were obtained, one for each air speed, are shown in Figure 5. These indicated that the thermal conductivity increased in the surface layers but that for the main body of the material a value k_o of $1.0 \times$

10^{-4} cal (cm.$^{-1}$)(sec.$^{-1}$)(°C.$^{-1}$) held. Logarithmic plots then indicated the relationship

$$(k - k_o) \propto V^{0.89} \times e^{(5/3)r} \qquad (3)$$

The graph of $(k - k_o)$ against $V^{0.89} \times e^{(5/3)r}$ is shown in Figure 6, and all the experimental points lie well on this line. The constant of proportionality is 1.94×10^{-9}.

Experimental Values for the Boundary-Layer Heat Transfer Coefficient

This quantity was calculated from Equation (2). Detailed results are given in Table 2 because they illustrate the amount of variation which exists owing to the difficulty in obtaining the small temperature dfference across the boundary layer with any degree of accuracy.

The values obtained for the rough textile cylindrical surfaces might be expected to compare with those quoted for the heat-transfer coefficient in flow in a rough cylindrical pipe. Lander (9) gives the equation

$$h = 0.76 \frac{V_o^{0.56}}{D^{0.44}} \qquad (4)$$

$$\text{B.t.u. (ft.}^{-2})(\text{hr.}^{-1})(°\text{F.}^{-1})$$

Values calculated from this equation are of the same order as those in Table 2.

Discussion on Heat Transfer

Terylene. This material, made with hard twisted yarn and very open weave, gave an open structure with relatively large holes in it. The increase in k values toward the surface has been shown to depend on the external air speed. The power-law index of 0.89 is similar to that quoted for heat transfer to a body by by a fluid flowing over its surface. This suggests that the effect is due to the actual flow of air through the outermost layers of the material. The speed of flow would decrease with increasing depth, and thus the heat transferred by this means would decrease. However it is difficult to visualize the air flowing into the material to a depth of possibly ½ in. and yet revealing no axial flow of heat. It is possible that the slight transverse vibrations of the bobbin in the air stream contribute to the convection effects observed. A different explanation, and one which seems more acceptable, is that the rough surface of the material causes turbulence over the surface which penetrates some way into the material and causes an increase in heat flow.

The still-air value of k in the depths is the mean of the solid and air conductivities, each weighted in proportion to the space it occupies, that is for the Terylene bobbin

$$k = k_o + 1.94 \times 10^{-9} V^{0.89} e^{(5/3)r} \qquad (5)$$

and

$$k_o = [k_s(1 - \epsilon) + k_a\epsilon] \qquad (6)$$

Wool. This material, composed of a bulked yarn in a hairy and felted cloth, has a close structure. There was no evidence of any but uniform still-air conductivity applying throughout, unless there was an effect in the extreme layer of the cloth which is outside the range of experimental measurements. The value of k obtained for this structure is not that given by the simple volume relationship as with the Terylene, expressed in Equation (6).

DRYING

Generally most substances first give a region in which drying occurs at a steady rate, and the laws applying during this constant rate period are well established (10 to 16). At a particular moisture content, the critical moisture content, the rate of evaporation begins to fall as drying continues. The falling-rate period is usually divided into two sections, the rate in the first portion varying linearly with moisture content. The variety of shapes in drying-rate curves have been described by Sherwood (17). McCready and McCabe (29) have discussed the question of drying hygroscopic materials, like the wool in this work.

The accepted chief mechanism, to which water movement in porous solids is attributed, is that of capillarity (18), and in a recent investigation where beds of glass spheres were used Newitt et al. (19) discuss the forces involved and the state of water distribution. With special reference to textiles Coplan (20) visualizes internal evaporation at all depths into the pervading vapor atmosphere in the pores and thence by vapor diffusion across the boundary layer. In this study the temperature distribution in the thick textiles is considered in conjunction with the drying rates, particular reference being made to the second falling-rate period.

Experimental Results

Procedure

Preliminary tests were carried out so that the counterpoise weights on the external end of the bobbin arm supported the weight of the dry bobbin and a suitable weight was ready on the analytical balance to cover the weight of water in the wet bobbin. The bobbin was soaked by immersion in water and, after a suitable drainage time, weighed and inserted into the heated tunnel. The recorder was switched on, the analytical balance was released, and the weights were adjusted to give balance. The weight was reduced 5 g. at a time as the water evaporated. The times at which balance occurred were noted and a further decrement of weight was effected. In the later stages of drying, the amount removed from the pan was reduced as the rate of evaporation decreased. Finally, when the bobbin was dry, the balancing weight representing zero water content was noted. The bobbin was

TABLE 1.

	Terylene								Wool
	Air speed = 250 cm./sec.				Air speed = 525 cm./sec.				Air speed = 525 cm./sec.
Annulus	θ_a 80°C.	65°C.	65°C.	Mean	θ_a 80°C.	65°C.	65°C.	Mean	θ_a 80°C.
				Values of $k \times 10^4$, c.g.s. centigrade units					
1 (outer)	1.75	1.82	1.85	1.81	2.57	2.23	3.01	2.60	0.97
2	1.48	1.56	1.46	1.50	1.88	1.80	2.19	1.96	1.05
3	1.35	1.25	1.27	1.29	1.64	1.66	1.66	1.65	1.10
4	1.17	1.33	1.08	1.22	1.28	1.40	1.47	1.38	1.14
5									1.11
6									1.04

(Wool mean 1.07)

TABLE 2. VALUES OF $h \times 10^3$, c.g.s. CENTIGRADE UNITS

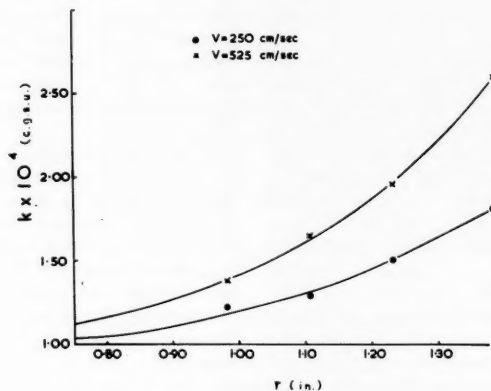| $\bar{l}$	Terylene						Wool
Mean time (min.) in the 5-min. intervals in which heat transfer was considered	525 cm./sec.			250 cm./sec.			525 cm./sec.
	θ_a			θ_a			θ_a
	65°C.	65°C.	80°C.	65°C.	65°C.	80°C.	80°C.
12.5	1.57	1.25	1.08	0.76	0.72	0.63	0.89
22.5	1.54	1.19	1.35	0.97	0.85	1.09	0.82
32.5	1.86	1.14	—	1.04	1.02	0.98	0.64
42.5	1.95	1.13	—	1.12	0.99	0.87	0.53
52.5	2.85	1.05	0.77	1.03	0.88	0.96	0.52
Mean value	1.95	1.15	1.07	0.98	0.89	0.91	0.68
Over-all mean		1.39			0.93		0.68

Fig. 5. k vs. radius for Terylene.
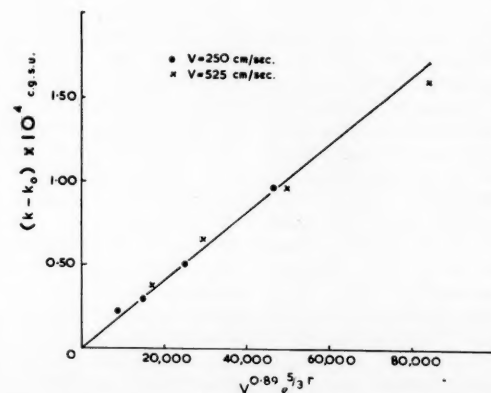
Fig. 6. $k - k_o$ vs. $V^{0.89} \times e^{(5/3)r}$ for Terylene.

removed and weighed to give the dry weight.

The tunnel was run without recirculation of the air and the humidity and temperature of the air were measured by an Assman wet- and dry-bulb hygrometer. Temperatures in the working section were measured both with thermocouples and mercury in glass thermometers.

Variation of Water Content with Time

The initial conditions for the two bobbins differed; water drained more freely from the Terylene, leaving only some 60% of the pore space occupied by water as compared with 90% in the case of wool. The water content vs. time curves were similar for the two materials, differing only insofar as the proportions were concerned. These curves were differentiated graphically to produce drying-rate curves for the two structures which may be compared.

being between 1/4 and 1/5 that of the corresponding Terylene curve. Moreover the second falling-rate period commences much sooner, at a moisture content of 210 g., when some 40% of the pore space is occupied by water, as compared with 45 g., or 10% of pore space occupied, in the case of the Terylene.

In the over-all picture the Terylene curve is similar to that given by Pearce et al. (21) for the drying of beds of glass spheres of radius 6×10^{-3} cm. The proportions of the wool curve are much more like those associated with fine particles of silica flour.

Constant Rates of Evaporation

Values for the Terylene bobbin range from 5.1×10^{-6} to 11.8×10^{-6} g. $(cm.^{-2})(sec.^{-1})(mm. Hg)^{-1}$, and for the case given of the wool bobbin the value is 5.4×10^{-6} g. $(cm.^{-2})(sec.^{-1})(mm. Hg)^{-1}$.

all layers, amply confirming the generalized picture. The lettering in Figure 8a will be used in the following explanation of the temperature record contrasting it with the drying-rate curve, which is also given.

Region AB represents the heating of the wet bobbin from room temperature to the wet-bulb temperature, the temperature distribution being similar to that in Figure 3. The constant-rate period ST agrees with this phase. A period of transition follows. The surface dries, as is indicated by the temperature rise of the surface thermocouples. The water surface recedes, evaporation being no longer directly into the air stream, and gradually evaporation has to depend on diffusion of water vapor outward through

Fig. 8a. The ideal variation of temperature during drying.

Fig. 8b. The actual variation of temperature during drying: wool bobbin.

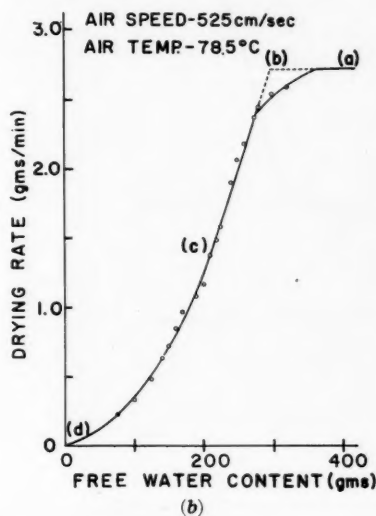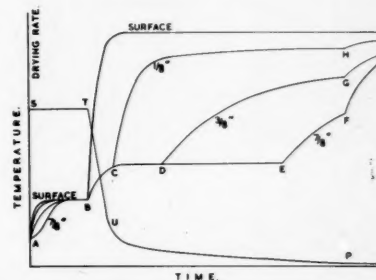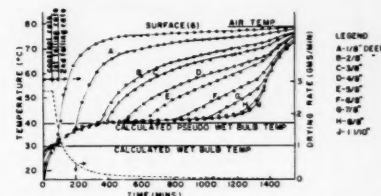Fig. 7a. Drying rate vs. free water content for Terylene bobbin.
Fig. 7b. Drying rate vs. free water content for wool bobbin.

Drying Rates and Critical Points

Figure 7 compares the drying-rate curves. In each case ab is the constant rate, bc the first falling rate, and cd the second falling-rate periods. The zero on the water-content scale for the wool represents the equilibrium moisture content at tunnel temperature and humidity.

In the case of the Terylene the very long constant-rate period ends at a moderate content of 73 g. (a water-to-solid ratio of 0.33), but for the wool a much shorter constant-rate period terminates at a critical moisture content (b) of 296 g. (a water-to-solid ratio of 1.68). A series of experiments does not appear to indicate that the critical moisture content is influenced by the external conditions.

In the linear first falling-rate period the rate falls off much more slowly in the case of the wool, the slope of the line

These values are all higher than those given by other workers, the figures for the Terylene more so than for the wool. The discrepancy may be due to the penetration of the surface layers by the air which produced the increased heat transfer and also to increased turbulence caused by the presence of the orifice plate just before the working section. As the principal aim was the study of the falling-rate period, this latter point was not pursued.

Temperature Changes within the Bobbin

Figure 8 gives a general picture of the variation of the temperature at the various radii as the drying proceeds. Figure 8a is based on the temperature records for the Terylene experiments and shows what happens in the layers considered in those experiments. Figure 8b for the wool fills in the gaps and shows

a layer of dry cloth. Also the temperature of the wet cloth rises to a new level. This new temperature equilibrium is established throughout, somewhere between C and D, and represents the balance between heat passing inward and water vapor diffusing outward as the water surface recedes into the depths of the material. Possibly this whole transitional region would provide a more natural phase of the falling-rate period than that dicated by the linear TU.

Because of the similarity between this second temperature equilibrium between heat and mass transfer and the earlier one, the wet-bulb temperature, the temperature established within the bobbin will be called the *pseudo wet-bulb temperature* (22). The wet portion of the bobbin remains at this temperature as the second falling-rate period continues (CDE), and as the receding water surface

passes each thermocouple in turn, the temperature rises. Finally, when the water surface reaches the core, more heat is made available to heat the dry material, and the final upward surge of temperature occurs from H, G, F, etc., in Figure 8, toward air temperature.

Drying of the Bobbin Surface

The fact that B approximately coincides with T in the Terylene experiments means that the surface of the Terylene bobbin was completely dry at the outset of the linear falling-rate section. In fact the outer $\frac{1}{8}$-in. depth of cloth is almost all dry by the end of it, as C represents

tween (dX/dt) and X as a balance between the increase in the rate of drying due to the rising surface temperature of the water and the decrease in this rate as the surface recedes to the interior. To compare conditions in the wool at this point Figure 9 represents a magnified picture. It must be stressed that all the so-called "surface" thermocouples are beneath one layer of cloth and therefore do not quite mirror true surface conditions. Four such couples are shown here, and it can be observed that whereas two of them rise directly to air temperature, the other two acquire the pseudo-wet-bulb temperature before doing so.

in. Apparently both the drying out of the surface and the establishment of the pseudo-wet-bulb temperature conditions occur during the linear section of the falling-rate period.

Moisture Contents within the Terylene Bobbin

Although the concept of a retreating water surface arose from the temperature records, at a later date a simple experiment was performed to obtain a measure of the various moisture contents. A section 1 in. wide and 1 in. deep was cut transversely in the Terylene bobbin and the unwrapped cloth made up into eight pads 1 in. wide and $\frac{1}{8}$ in. thick which could be replaced as the consecutive $\frac{1}{8}$-in. thick layers to reform the complete bobbin. Experimental conditions were reproduced as nearly as possible to those in the experiment for which the drying-rate curve is given in Figure 7a. When one started with the wet bobbin each time and allowed the necessary drying time, points T, U, C, D, and E (Figure 8a) were reached in turn. At each point the bobbin was taken out of the tunnel and the pads were quickly unwrapped, placed in polythene bags, and weighed. The results are given in Table 3.

Table 3 shows that within the limits of the experiment it is confirmed that there is a retreating water surface as deduced from the temperature record. It is of course extremely difficult to reproduce conditions exactly, and there are the usual errors of any redeployment of water or losses while the cylinders are being unwrapped. Other points of interest are the reduced values in the outermost three layers, possibly due to air penetration; the constant value in the depths; and the fact that the saturation in the depths is slowly reducing as the water surface retreats. This last mentioned point means that there is still some some mechanism by which moisture moves to the water boundary.
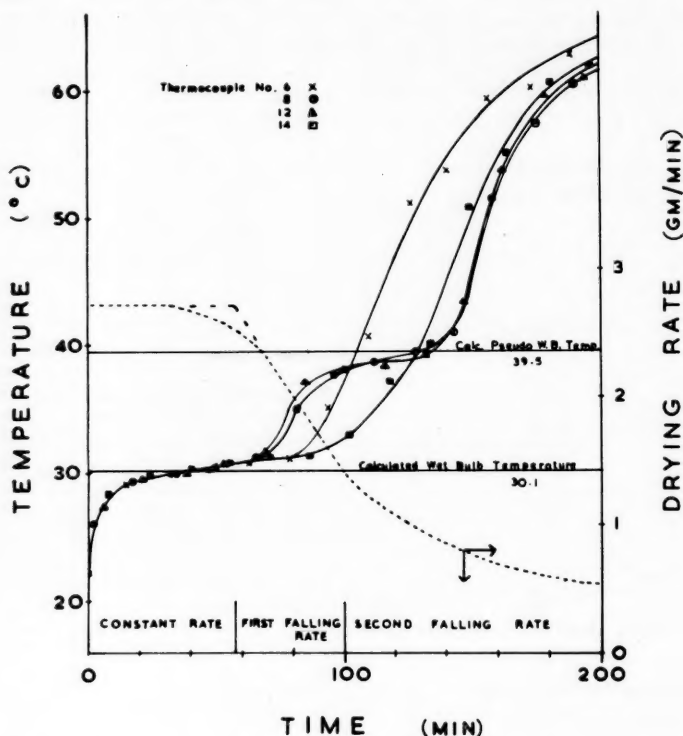

Fig. 9. Surface conditions in the wool at the beginning of the falling rate period.

the time of drying at the $\frac{1}{8}$-in. depth. Thus the theory that the drying of the surface is responsible for the linear first falling-rate period does not fit in the case of the Terylene. A possible alternative is that the transition from wet-bulb to pseudo-wet-bulb temperature conditions fortuitously produces linearity be-

It is suggested that the former are actually nearer the surface and that the water recedes past them before the new equilibrium conditions are established; the latter, being deeper, reflect the changed conditions. This means that the transition occurs through one layer of the woolen cloth, that is in less than 1/16

Pseudo-wet-bulb Temperature

A Theoretical Explanation

The limiting water surface of the wet material is considered to have receded well within the bobbin and, with a cylindrically symmetrical distribution of water assumed, the water surface is at a radius r from the center. The heat transfer through the narrow dry layer, thickness δr, adjoining the water surface must be allowed to cause evaporation and to produce the mass transfer outward through the layer.

Thus

$$q = -\frac{dX}{dt}\,\lambda_w \qquad (7)$$

Therefore if one assumes the rate of evaporation to be governed by diffusion,

TABLE 3. PERCENTAGE OF MOISTURE CONTENTS (DRY BASIS) TO NEAREST 1%, IN CONSECUTIVE $\frac{1}{8}$-IN. LAYERS FROM THE SURFACE

Layer	1	2	3	4	5	6	7	8	
At point T	27	27	29	38	37	38	38	39	
U	8	17	19	23	23	22	22	23	Wet
C	1	13	16	19	18	18	18	18	region
D	0	0	0	5	14	15	15	14	
E	0	0	0	0	0	0	1	8	
				Dry region					

$$kA_m\left(\frac{\delta\theta}{\delta r}\right)_{\text{layer}}$$

$$= -(\epsilon D_v)A_m\left(\frac{\delta c}{\delta r}\right)_{\text{layer}}\lambda_w \qquad (8)$$

For this layer k will be k_o, representing the value applying for the solid-air mixture.

The temperature gradient across the layer and the concentration gradient are unknown, but, because of the analogy in heat, momentum, and mass transfer, it will be assumed that

$$\frac{(\delta\theta)/\delta r)_{\text{layer}}}{(\theta_a - \theta_w)/(R - r)}$$

$$= \frac{(\delta c/\delta r)_{\text{layer}}}{(c_a - c_w)/(R - r)} \qquad (9)$$

The maximum radius of the bobbin should strictly include the outer boundary layer. The concentration boundary layer is not exactly equal to the thermal boundary layer under all conditions, but to a first approximation they will be assumed to be equal. $(R - r)$ cancels, and

$$k(\theta_a - \theta_w) = (\epsilon D_v)\lambda_w(c_w - c_a) \qquad (10)$$

From the ideal gas equation $c = a$ constant $\times p/T$.

Therefore

$$k(\theta_a - \theta_w) = 2.886$$

$$\times 10^{-4}(\epsilon D_v)\lambda_w\left(\frac{p_w}{T_w} - \frac{p_a}{T_a}\right) \qquad (11)$$

where the constant is appropriate for c.g.s. centigrade units.

Thus when heat and mass transfer balance within the bobbin, with vapor diffusion controlling the evaporation, a temperature θ_w will be established at the water surface which has been called the *pseudo-wet-bulb temperature*. As the radius does not come into the equation, the temperature will be the same with the water surface at any level, provided the ratio D_v/k remains constant.

Equation (11) shows a constant differences between θ_a and θ_w. Examination of Figure 8b shows strictly that there is a constant difference between the bobbin

TABLE 4.

Air speed c./sec.	Air tempature, θ_a °C.	Partial vapor pressure in air stream p_a, mm. Hg	θ_w °C. Experimental	Calculated
		Wool		
525	78.5	10.0	39 rising to 41	39.5
		Terylene		
200	96.1	18.5	48.0	44.9
287	81.2	14.9	42.5	40.7
320	78.9	13.6	43.0	39.9
435	50.9	14.5	31.2	31.8
535	49.6	15.4	31.0	31.6

surface temperature and the pseudo-wet-bulb temperature. Indeed this equation could have been as readily, and with fewer assumptions, derived for $(\theta_s - \theta_w)$, where θ_s is the bobbin surface temperature. Unfortunately such a derivation requires knowledge, which is not available, of the vapor concentration at the surface. Accordingly Equation (11) has to be accepted as an approximation.

Sherwood and Pigford (23) report a similar equation given by Maxwell (24)
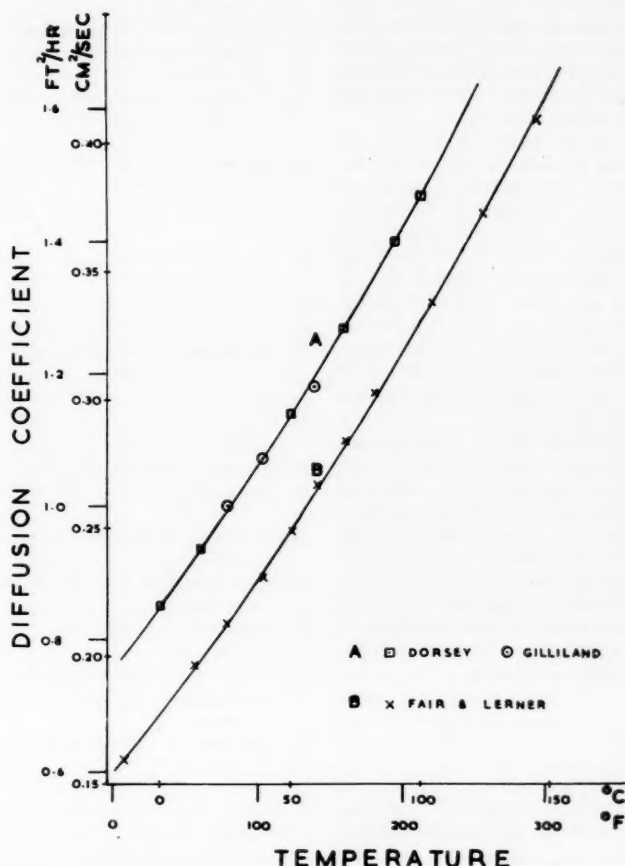

Fig. 10. Diffusion coefficient for water vapor vs. temperature.

to account for the ordinary wet-bulb temperature but point out that it is at fault in making no allowance for eddy diffusion. Here in the depth of the cloth the eddy diffusion is eliminated, and so Maxwell's original concepts apply more particularly in the body of a porous material than in a free air stream.

Calculations of the Pseudo-wet-bulb Temperature by use of the Theoretical Equation

Equation (11) was used to calculate the pseudo-wet-bulb temperature by successive approximations from a first reasonable guess of θ_w. Values are given in Table 4 for a set of experiments with the Terylene bobbin along with a value for

the wool bobbin. The latter value is marked in Figure 8b.

The values of D_v used in the calculations were taken from Figure 10. In Figure 10 curve A represents earlier experimental values given by Dorsey (25) and Gilliland (26), and curve B represents values based on a recent correlation of Fair and Lerner (27) depending on the Hirschfelder, Bird, and Spotz (28) equation. Values from curve B, being considered the best available, were used.

Discussion on Drying

The establishment of a pseudo-wet-bulb temperature during the falling-rate period within the thick textiles considered appears to be accounted for by the simple heat-transfer–mass-transfer balance, and Equation (11) provides a means of calculating this temperature and the rate of evaporation. It must be remembered however that the sensible heat required for the dry material and for raising the temperature of the vapor formed to that of the air stream was omitted. Moreover it is impossible to insulate the depths of the bobbin perfectly, and in the case of the Terylene instances occurred when the recorded temperatures at a lower level

crossed and came above the line representing the temperature further out. This would be due to a little heat flow from the core outward. In the case of the later wool bobbin this effect seemed to be almost eliminated by keeping the return thermocouple leads between layers of the cloth at the level of the couple; previously some of these wires had returned to the rear end of the bobbin packed fairly tightly in the center of the solid core and had apparently carried heat from the ends of the bobbin to the core. There will be some radiation from the surroundings, mainly absorbed by the surface layers. This is evidenced by the fact that the experimental wet-bulb temperature is a little higher than the calculated value (Figure 8b).

As far as the wool is concerned, no account has been taken of the heat required by the evaporation of the bound water held by the fibers in the air-dry region. As the vapor pressure in the various layers slowly decreases, this adsorbed water will be released, heat of adsorption and latent heat of vaporisation being necessary in the process. It would appear that for this particular highly porous structure such heat is of secondary importance in the general equilibrium established.

The transition period, including the first falling-rate section, requires further study. The drying out of the surface, as some factor limits the water supply, is accompanied by the change from one equilibrium condition of heat and mass transfer across the boundary layer to another through a layer of cloth. The exact relationships of these processes, to produce the rates obtaining and the linearity, need elucidation.

SUMMARY

Highly porous thick textiles have at depth a thermal-conductivity coefficient which depends on the relative volumes and distribution of solid and air. Near the surface, if the structure be sufficiently open, a higher apparent thermal-conductivity coefficient can apply, being affected by the air speed at the surface and apparently due to some form of air penetration.

When such structures are drying, the rate of evaporation falls off as heat and water vapor have to pass through an increasing layer of dry material left by a receding water surface. While this is occurring, a temperature equilibrium is maintained within the wet portion, and this temperature has been called the *pseudo-wet-bulb temperature*. The formula giving the simple heat balance is

$$k(\theta_a - \theta_w) = 2.886$$
$$\times 10^{-4}(\epsilon D_v)\lambda_w\left(\frac{p_w}{T_w} - \frac{p_a}{T_a}\right)$$

NOTATION

A = area, sq. cm.

A_m = mean area of annular section, sq. cm.

c = vapor concentration, g. cm.$^{-3}$

c_a = vapor concentration in air stream, g. cm.$^{-3}$

c_w = vapor concentration at water surface, g. cm.$^{-3}$

D = pipe diameter, ft.

D_v = coefficient of vapor diffusion, sq. cm. sec.$^{-1}$

h = surface heat-transfer coefficient, cal. (cm.$^{-2}$)(sec.$^{-1}$)(°C.)$^{-1}$

k = thermal-conductivity coefficient, cal. (cm.$^{-1}$)(sec.$^{-1}$)(°C.)$^{-1}$

k_a = thermal-conductivity coefficient of air, cal. (cm.$^{-1}$)(sec.$^{-1}$)(°C.)$^{-1}$

k_o = thermal-conductivity coefficient within depths of material, cal. cm.$^{-1}$ sec.$^{-1}$ (°C.)$^{-1}$

k_s = thermal-conductivity coefficient of solid, cal. (cm.$^{-1}$)(sec.$^{-1}$)(°C.)$^{-1}$

p = vapor pressure, mm. Hg

p_a = partial pressure in air stream, mm. Hg

p_w = vapor pressure at water surface, mm. Hg

q = rate of flow of heat, cal. sec.$^{-1}$

r = radius, cm.

R = radius of bobbin, cm.

t = time, sec.

T = absolute temperature, °$_{absolute}$

T_a = absolute temperature of air stream, °$_{absolute}$

T_w = absolute temperature of water surface, °$_{absolute}$

V = air speed, cm. sec.$^{-1}$

V_o = air speed at normal temperature and pressure, ft. sec.$^{-1}$

X = free water content of bobbin, g.

Greek Letters

ϵ = void fraction or porosity

ϵD_v = diffusion coefficient for layer next to water corrected for presence of solids (assumed to be of zero diffusion) and occupying $(1 - \epsilon)$ of total area

θ = temperature, °C.

$\left(\dfrac{\delta\theta}{\delta r}\right)_{layer}$ = temperature gradient across layer

θ_a = temperature of air stream, °C.

$\left(\dfrac{\delta c}{\delta r}\right)_{layer}$ = concentration gradient

θ_s = temperature of bobbin surface

θ_w = temperature of water surface, °C., pseudo-wet-bulb temperature, °C.

λ_w = latent heat of evaporation at temperature of water surface, cal. g.$^{-1}$

LITERATURE CITED

1. Binder, L., Dissertation, Univ. Munich, Munich, Germany (1911).
2. Schmidt, E. *Forsch. Gebiete Ingenieurw.*, 13, 177 (1942).
3. Dusinberre, G. M. "Numerical Analysis of Heat Flow," McGraw-Hill, New York (1949).
4. Dusinberre, G. M., *Trans. Am. Soc. Mech. Engrs.*, 65, 703 (1945).
5. Gurney, H. P., and J. Lurie, *Ind. Eng. Chem.*, 15, 1170 (1923).
6. Newman, A. B., *Trans. Am. Inst. Chem. Engrs.*, 24, 44 (1930).
7. Fourier, J. B., "Theorie analytique de la chaleur," Gauthier-Villars, Paris (1882).
8. Baxter, S., *Proc. Phys. Soc. London*, 58, 105 (1946).
9. Lander, C. H., *J. Inst. Mech. Engrs.*, 95, (April, 1943).
10. Sherwood, T. K., *Ind. Eng. Chem.*, 21, 12, 976 (1929); 22, 132 (1930).
11. Gilliland, E. R., *Ind. Eng. Chem.*, 30, 506 (1938).
12. ———, and T. K. Sherwood, *ibid.*, 26, 516 (1934).
13. Hinchley, J. W., and G. W. Himus, *Trans. Inst. Chem. Engrs. (London)*, 2, 57 (1924).
14. Hine, T. B., *Phys. Rev.*, 24, 79 (1924).
15. Powell, R. W., and E. Griffiths, *Trans. Inst. Chem. Engrs. (London)*, 175 (1936).
16. Powell, R. W., *ibid.*, 18, 36 (1940).
17. Sherwood, T. K., *Trans. Am. Inst. Chem. Engrs.*, 32, 150 (1936).
18. Ceaglske, N. H., and O. A. Hougen, *Ind. Eng. Chem.*, 29, 805 (1937); *Trans. Am. Inst. Chem. Engrs.*, 33, 283 (1937).
19. Newitt, D. M., and M. Coleman, *Trans. Inst. Chem. Engrs. (London)*, 30, 28 (1952).
   Oliver, T. R., and D. M. Newitt, *ibid.*, 27, 9 (1949).
   Corben, R. W., and D. M. Newitt, *ibid.*, 33, 52 (1953).
   King, A. R., and D. M. Newitt, *ibid.*, 33, 64 (1955).
20. Coplan, M. J., *Textile Research J.*, 23 897 (1953).
21. Pearce, J. F., T. R. Oliver, and D. M. Newitt, *Trans. Inst. Chem. Engrs. (London)*, 27, 1(1949).
22. Nissan, A. H., and W. G. Kaye, *Nature*, 180, 142 (1957).
23. Sherwood, T. K., and R. L. Pigford, "Absorption and Extraction," 2nd ed., McGraw-Hill, New York (1952).
24. Maxwell, J. C., "Diffusion," *Encyclopedia Britannica*, 9th ed. (1877).
25. Dorsey, N. E., "Properties of Ordinary Water Substances," Reinhold, New York (1940).
26. Gilliland, E. R., *Ind. Eng. Chem.*, 26, 681 (1934).
27. Fair, J. R., and B. J. Lerner, *A.I.Ch.E. Journal*, 2, 13 (1956).
28. Hirschfelder, J. O., R. B. Bird, and E. L. Spotz, *Trans. Am. Soc. Mech. Engrs.*, 71, 921 (1949).
29. McCready, D. W., and W. L. McCabe, *Trans. Am. Inst. Chem. Engrs.*, 29, 131 (1933).

Engineering Applications of Relaxation Procedures by Digital Computation

M. E. RADD and **M. R. TEK**

Phillips Petroleum Company, Idaho Falls, Idaho

A generalized computing method is developed to perform mathematical "relaxation" on a Datatron digital computer. The application of the developed relaxation or iteration procedures results in obtaining numerical solutions to several engineering boundary-value problems expressed by elliptic differential equations. The developed digital relaxation routine is found to be effective, fast, and practical in solving numerous steady-state heat and mass transfer problems with arbitrary and quite often complex boundary conditions. While the specific speed and accuracy of the developed digital method is found to depend upon the type of differential equation, the grid size, and computational tolerance requirements, a typical problem indicates that 250 iterations/min. speed and 1% accuracy may be achieved in an average case.

The examples presented in this paper are chosen from the more classical heat transfer and temperature and pressure distribution problems in order to indicate some other areas where similar engineering problems can be solved however complex the boundary conditions may be.

Certain types of boundary-value problems can be solved by replacing the differential equation by a finite-difference equation which is next solved by a process of iteration (1, 2). This method of solving partial differential equations was developed and first used by L. F. Richardson in 1910. Improvements on Richardson's original work were later introduced by Liebmann (4), Thom (5), and Shortley and Weller (6). A somewhat similar method is credited to Southwell (7, 8) and called *relaxation*. This method, quite analogous to the previous finite-difference method called *iteration*, was developed for application to problems of structural engineering (8, 9). An excellent comparison between iteration and relaxation methods is given in some detail by Scarborough (2). The application of relaxation methods to oil field research has been published by Dykstra and Parsons (10).

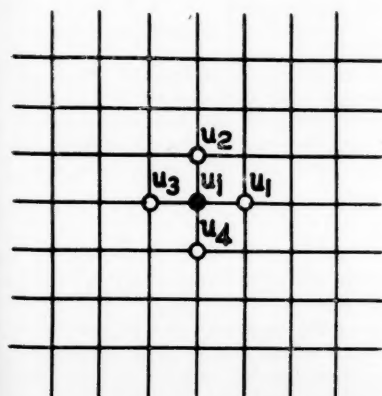It is well known that while relaxation is rapid and liable to errors, iteration is slow, sure, but frequently long. Computa-

tional errors in the method of iteration are self-correcting; the ones likely to occur in the method of relaxation usually remain hidden. Although the choice of an appropriate method often depends on the problem to be solved, it becomes quite evident that relaxation is best suited to long-hand or desk-calculator types of computations and that iteration can readily and efficiently be performed on digital computers.

The primary objectives of this work have been to develop a generalized routine to perform this iteration on electronic digital computers and to apply this method to solve several engineering problems in areas such as heat and mass transfer, steady state fluid flow, and temperature or pressure distributions.

ANALYSIS

Basic Differential Equations

The partial-differential equations commonly encountered in engineering problems are of second order in at least one of the dependent variables and also linear with respect to second-order derivatives. These equations are usually classified in three groups: elliptic, parabolic, and hyperbolic equations.

Elliptic Equations

$$\frac{\partial^2 u}{\partial x^2} + \frac{\partial^2 u}{\partial y^2} = a(x, y) \qquad (1)$$

Equation (1), denoting one of the most frequently used partial differential equa-

tions, is called *Poisson's equation*. A special case is obtained when $a(x, y) = 0$, and the equation is then called *Laplace's equation*:

$$\frac{\partial^2 u}{\partial x^2} + \frac{\partial^2 u}{\partial y^2} = 0 \qquad (2)$$

When the Navier-Stokes equations are written and simplified for the case of steady state, streamline, viscous pipe flow, an equation quite similar to Equation (1) is obtained:

$$\frac{\partial^2 w}{\partial x^2} + \frac{\partial^2 w}{\partial y^2} = \frac{1}{\mu}\frac{dP}{dZ} = a \qquad (3)$$

Calculations of steady state temperature distributions in heat-conduction and boundary-value problems resulting from theories of elasticity, plasticity, stress analysis, and electrostatic or electromagnetic field potentials are typical of applications of elliptic partial-differential equations.

When elliptic equations are considered, it becomes necessary to specify boundary conditions at every point of a well-defined closed boundary. Parabolic and hyperbolic equations are usually associated with a domain which is at least open in the direction of one variable, usually the time variable. The techniques and methods for the numerical solutions of parabolic and hyperbolic equations have been much less explored than those for the elliptic equations.

In this study computer solutions are developed for the elliptic equations of types 1, 2, and 3. In particular a digital solution for the case.

$$\frac{\partial^2 u}{\partial x^2} + \frac{\partial^2 u}{\partial y^2} = -fu - g \qquad (4)$$

has also been developed.

The Finite-Difference Equations

As indicated in Figure 1, when a network (x = constant, y = constant) is laid
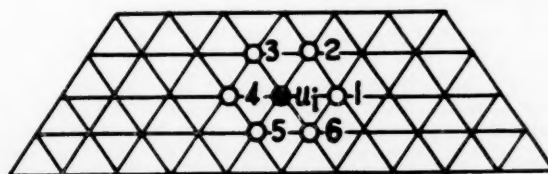

Fig. 1. Two-dimensional square grid.

Fig. 2. Two-dimensional triangular grid.

upon a given continuum of points in two-dimensional space, the finite-difference equation corresponding to Poisson's Equation (1) is given by

$$u_i = \tfrac{1}{4}[u_1 + u_2 + u_3 \\ \qquad + u_4 - h^2 g(x_i, y_i)] \tag{1a}$$

which can also be written as

$$u_i = \tfrac{1}{4} \sum_{i=1}^{4} u_i - \frac{h^2}{4} g(x_i, y_i) \tag{1b}$$

where h represents Δx and Δy in a square grid.

The finite-difference equation corresponding to Laplace's equation can be simply given as
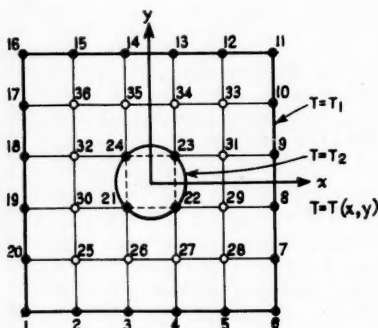
Fig. 3. Approximate network representation of a boundary-value problem.

Fig. 6. Cross sectional area for pipe flow.

$$u_i = \tfrac{1}{4} \sum_{i=1}^{4} u_i \tag{2a}$$

A similar derivation for Equation (4) gives

$$u_i = \left(\frac{1}{4 - h^2 f} \right) \sum_{i=1}^{4} u_i + \frac{h^2 g}{4 - h^2 f} \tag{4a}$$

It will be noticed that most of the examples given in this study are based on a square grid network. However this generally is not necessary. Although the square network is the simplest, a network of equilateral triangles sometimes becomes more suitable to a particular problem. In the case of an equilateral-

triangular network (Figure 2) the finite difference equation corresponding to Laplace's equation is given as

$$u_i = \tfrac{1}{6} \sum_{i=1}^{6} u_i \tag{5}$$

The computer solutions developed in this report are, however, prepared for applications on square grids only.

Development of Digital Techniques
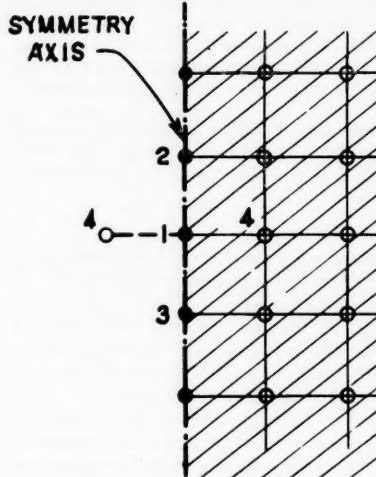
To illustrate the iterative procedure, a

Fig. 4. Iteration at symmetry axis.

Fig. 7. The velocity profile.

typical problem is presented. Figure 3 indicates the boundaries and the interior grid points of a two-dimensional model, where the distribution of a $T = T(x, y)$ function is desired. The points 1 through 20 represent the outside boundaries, and the points 21 through 24 represent the inside boundaries. The points 25 through 36 are the interior grid points at which the values of $T = T(x, y)$ are desired. T may represent the temperature function in a homogeneous solid (Figure 3), where constant temperatures are maintained at the inside and outside boundaries.

The differential equation to be satisfied

is $(\partial^2 T)/(\partial x^2) + (\partial^2 T)/(\partial y^2) = 0$. The boundary conditions are $T_i = T_1(i = 1, 2, 3, \cdots 20)$ and $T_i = T_2(j = 21, 22, 23, 24)$. The finite-difference equation corresponding to this is

$$T_i = \tfrac{1}{4} \sum_{j=1}^{4} T_j \tag{6}$$

To start the process, rough approximations are first made on all unknown internal grid-point temperatures.
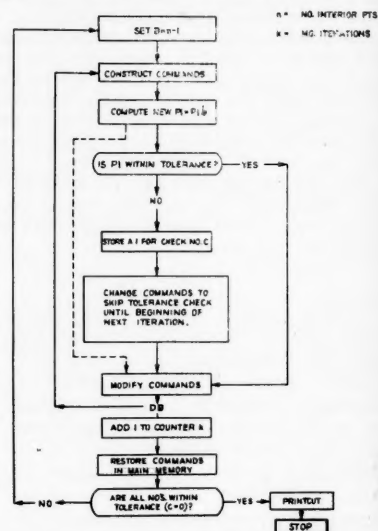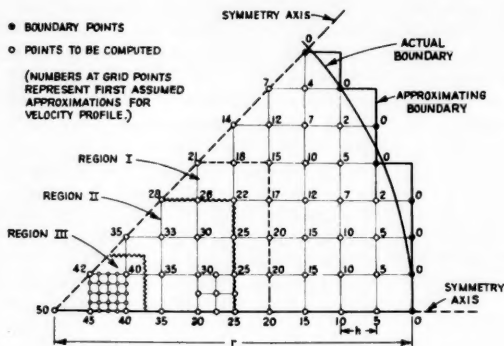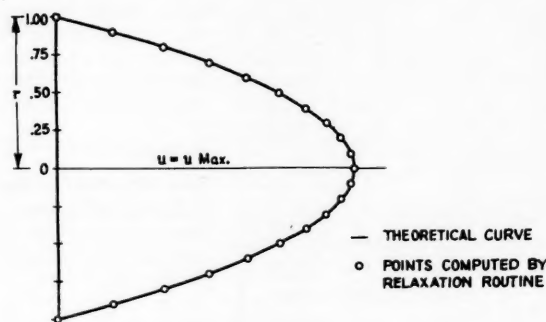

Fig. 5. Block diagram digital relaxation.

An example is point 25. If the superscripts refer to the order of successive approximations, the first approximation being the orginal assumed temperature, the second approximation is given by

$$T_{25}{}^{(2)} = \tfrac{1}{4}[T_2 + T_{26}{}^{(1)} \\ \qquad + T_{30}{}^{(1)} + T_{20}] \tag{7}$$

Next the second approximation for T_{26} is calculated in a similar manner by using the improved values of its adjacent points as soon as they are available.

Equations (6) and (7) are thus successively used at each point until such time as the modifications become in-
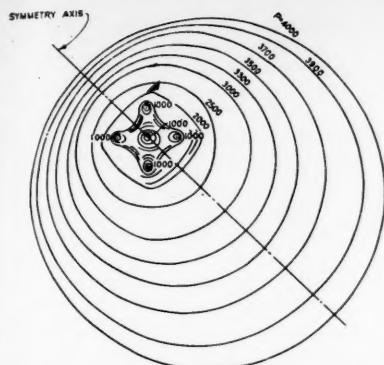
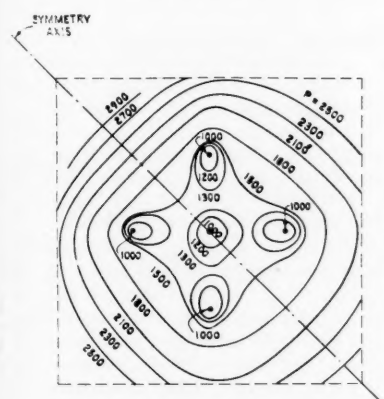Fig. 8. Steady state pressure distribution in a reservoir.

Fig. 9. Steady state pressure distribution (enlarged subregion of reservoir).

appreciable. Every step thus relieves some particular constraint due to forcing the original assumed or subsequent approximated value of the unknown function. The successive iterations are stopped only when the dependent variable becomes relaxed, that is, can no longer be further improved by repeating earlier steps.

As shown in Figure 4, whenever a certain symmetry becomes evident, the problem needs only to be solved for regions bounded by the symmetry axes. This saves a considerable amount of duplicated effort.

In the event that a point to be iterated falls on one of the symmetry axes (note Figure 4) in performing its iteration, the point off the axis of symmetry must be counted twice to include the effect of its image with respect to the axis of symmetry; that is

$$T_1 = \tfrac{1}{4}[T_2 + T_3 + 2T_4] \qquad (7a)$$

It usually is advisable to start with a coarse grid, then to repeat with a finer grid, especially in some interesting subregion of the problem.

Digital Relaxation on the Datatron

The systematic and mechanical nature of the iteration technique described sug-

gested its programmability on a digital computer. A Datatron routine was developed and is now available to perform *relaxation by digital computation.* This routine handles as many as 1,000 interior and 800 boundary grid points. Two main memory cells are allocated to each interior grid point. The data in these cells identify the serial numbers of each considered point and the adjacent grid points. The input data as well as the program are on paper tape. The output is on the line printer.

The routine is coded, fixed-point arithmetic; therefore the true decimal-point location could be anywhere as long as all points are consistent. When the value at every computed point shows no change from the previous iteration, the line printer records the number of iterations and the answers with the corresponding index numbers. The iterations continue as long as there is at least one point that is not within a given tolerance.

Figure 5 represents the *block diagram* of the digital relaxation routine, indicating the programming logic used. The *B*-register is set at the beginning to $(n - 1)$. Next commands to perform the relaxation calculations are constructed and stored.

For a given point i the unknown function P_i is computed and checked. If the calculated value is within the required tolerance, the next point P_{i+1} is computed and checked; if one point is not within the tolerance, then for the remaining points during that particular iteration the tolerance checks are omitted. The number of iterations is tallied in a counter k and, when all the computed points meet the tolerance check, the answers are printed and the computer stops.

APPLICATIONS

The digital relaxation method developed during this study has been successfully applied to several engineering problems. Some of these applications were purposely chosen from heat transfer, pressure, and flow distribution problems for which theoretical solutions were readily available. These applications were quite useful as checkout tools; they also provided valuable information regarding the over-all computing time, accuracy, and reliability of the answers.

The following typical problems are given as examples of direct engineering applications to emphasize the practical
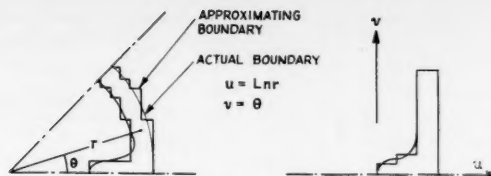

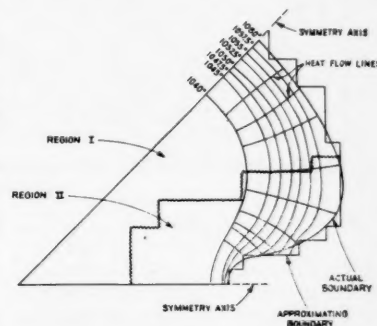Fig. 10. Sector of internally finned tubular reactor and its conformal mapping.

Fig. 11. Butane dehydrogenation isotherms and heat flow lines in an internally finned catalyst tube.

significance of this method in solving a large number of steady state problems. It is hoped that through these examples the reader will see some areas of application where his problems may be solved no matter how complicated the boundary conditions may be.

Pipe-Flow Velocity Distribution

The classical case of steady state (streamline) pipe flow is given as a prominent example of an elliptic boundary-value problem and as an illustration of some techniques developed for proper choice of space increments and tolerance specifications. When the Navier-Stokes equations are written for the general case and then simplifications are introduced owing to steady state, unidirectional, and incompressible flow conditions, the following equations are developed:

$$\rho \frac{Dw}{Dt} = -\frac{\partial P}{\partial Z} + \rho F_z$$
$$+ \mu \nabla^2 w + \tfrac{1}{3}\mu \frac{\partial \theta}{\partial Z} \qquad (8)$$

where

$Dw/Dt = 0$ steady-state condition
$\partial P/\partial Z = $ constant $= dP/dZ$, (unidirectional flow, constant-rate pressure drop)
$F_z \quad = 0$ assumed
$\theta \quad = 0$ incompressible flow

Then

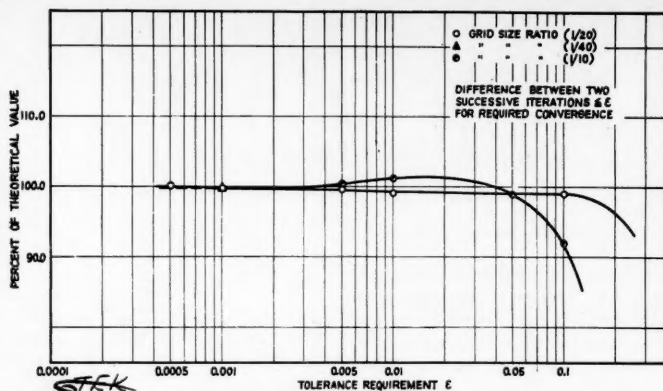$$\nabla^2 w = \frac{1}{\mu} \frac{dP}{dZ} \qquad (9)$$

Fig. 12. The effect of grid size and tolerance requirement on the ratio of computed and theoretical values.

Figure 6 represents the cross-sectional area of pipe and its geometric boundaries as approximated by the indicated grid points. The black dots represent the boundary points where the fluid velocity w must equal zero. The interior points are denoted by white circles. The velocity field is computed on the Datatron by this relaxation routine, the results being given in Figure 7, where the circular points represent calculated velocities plotted against the background of theoretical parabolic velocity profile.

A large amount of practical information is obtained by starting the calculations on coarse grids and then repeating these calculations on smaller and smaller grids on specific cross-sectional areas of interest. The regions denoted as I, II, and III in Figure 6 indicate the subregions computed on smaller grid sizes.

Steady State Pressure Distribution in an Oil Reservoir

In an undersaturated reservoir the flow of oil in the steady state is usually governed by an elliptic partial differential equation

$$\nabla^2 P = 0 \qquad (10)$$

$$\frac{\partial^2 P}{\partial x^2} + \frac{\partial^2 P}{\partial y^2} = 0 \qquad (11)$$

The assumed boundary conditions are $P = 4,000$ at boundaries, $P_i = 1,000$ at $i = 1, 2, 3, 4, 5$ (producing wells). A circular reservoir as indicated in Figure 8 is considered with a five-spot group of wells producing at a constant bottom hole pressure. For this particular reservoir it is further assumed that the pressure is constant at the reservoir boundaries.

The steady state pressure distribution over the entire reservoir (approximated by the network as indicated) is calculated on the Datatron in approximately 12 min. The geometric location of wells, reservoir boundaries, and several computed isobars are given in Figures 8 and 9.

Heat Transfer in a Tubular Reactor

Steady state heat transfer calculations have been performed by using the developed relaxation routine to determine temperature distributions through the walls and within the packed interior of an internally finned vertical tubular reactor. Figure 10 represents the boundary geometry and the approximating network used on this problem and its conformal analogue. Only one half of the first quadrant is used owing to considerations of the inherent polar symmetry. For the first part of the problem, steady state, two-dimensional temperature distribution across the pipe walls, the differential equation is

$$\nabla^2 T = 0 \qquad (12)$$

To calculate the temperature distribution through the packed catalyst bed owing to heat dissipation throughout the inside volume the following equation is used:

$$\frac{\partial^2 T}{\partial x^2} + \frac{\partial^2 T}{\partial y^2} = -fT - g \qquad (13)$$

A square grid is used for this computation. The finite-difference equation used in this solution is given earlier as Equation

4a. Figure 11 represents the isotherms and heat-flow lines plotted after the results of relaxation calculations are performed on the computer.

Conformal Mapping

In solving the temperature-distribution problem through the pipe walls it became quite apparent that appreciably better representation of the geometric boundaries could be effected by performing the rectangular relaxation calculations on the conformal transform of the polar model. As indicated in Figure 10 the conformal transformation of the polar model by equations

$$\left.\begin{array}{l} u = \ln r \\ v = \theta \end{array}\right\} \qquad (14)$$

results in a rectangular transform in the u, v, coordinate system. The model on the u, v plane is computed by the developed digitized relaxation routine, and the final temperature-distribution results are plotted on the actual model by using the transformation Equations (14).

Discussion of the Results and Conclusions

The digital relaxation routine developed for the Datatron is found to be effective fast, and practical in solving several steady state heat and mass transfer problems with arbitrary boundary conditions. In several cited examples the over-all computing speed is found to be about 250 iterations/min.

The computational accuracy achieved in these applications is studied in calculating several cases for which theoretically correct answers are available. This study indicates that the accuracy achieved during these computations is a function of both the grid size and tolerance specification incorporated in the routine. The effect of these two variables on the ratio of computed to theoretically known quantities is indicated in Figure 12. The tolerance requirement in this chart is a predetermined small number compared with the difference between two successive computed values at a given point. If the difference is equal to,

TABLE 1. SUMMARY ON TIME, GRID SIZE, AND TOLERANCES USED ON DIFFERENT PROBLEMS

Type of problem	Pressure distribution		Pipe flow		Heat transfer across reactor tube		Heat transfer across catalyst bed	
Elliptic equation solved	Laplace		Poisson		Laplace		Equation (7)	
Number of grid points	97	97	45	45	96	96	56	56
Tolerance requirement $u_n - u_{n-1}$	10 lb./ sq. in.	0.5 lb./ sq. in.	.1 ft./sec.	0.005 ft./sec.	0.1 °F.	0.01 °F.	0.1 °F.	0.01 °F.
Maximum value of dependent variable	4,000 lb./ sq. in.	4,000 lb./ sq. in.	50 ft./sec.	50 ft./sec.	1,172 °F.	1,172 °F.	1,135 °F.	1,135 °F.
Number of iterations	20	47	47	156	9	33	24	91
Total time, min.	6.5	15.2	7.5	26	2.3	8.9	3.7	14.1
Time/point, min.	0.07	0.16	0.16	0.57	0.02	0.09	0.07	0.25

or smaller than, (ϵ), the convergence at that point is considered satisfactory.

The data obtained from theoretically known laminar pipe-flow velocity-distribution calculations indicate that for a given grid size the computational accuracy increases with decreasing magnitude of tolerance requirement. As the tolerance becomes equal to, or smaller than, 0.05, the computation predicts the theoretical value approximately within 1%.

For tolerances less than 0.05 the computational accuracy also appears to be less affected by the grid size. In cases relating to extremely small grid sizes (that is, 40 or more increments per major geometric dimension), however, there are not enough data available to permit evaluating the effect of tolerance requirements.

The availability of as many as 1,000 interior and 800 boundary points, the average computational speed and accuracy proved in several case studies, indicate that this method is practical and useful in a large number of one- or two-dimensional steady state problems satisfying general Laplace-type differential equations. In addition, problems satisfying equations of the type of Equation (4) can also be solved by this digital technique.

The apparent rate of convergence is much faster in Laplace's equation than in Poisson's, or Equation (4). This is consistently observed in all calculated cases. Decreasing the tolerance scarcely affects the approximate results of the Laplace equations, but the approximate results of the Poisson-type equations are affected more drastically. Therefore one should be very careful in solving boundary-value problems satisfying Poisson's equation, since the fact that two consecutive iterations at each point differ by a very small quantity (ϵ) does not

necessarily mean that the unknown function is as close as (ϵ) to its true value. The proved case studies in pipe-flow calculation however should give a fair indication of the nature of accuracy expected in solving the Poisson type of equation by this routine.

Table 1 summarizes the number of grid points used, tolerance requirements, the number of iterations, and time requirements on several types of problems solved.

NOTATION

a	=	function of x and y
D/D_t	=	substantial time derivative
F_z	=	extraneous body force per unit mass
f	=	constant
g	=	constant
$g(x, y)$	=	function of x and y variables
h	=	increment on a square grid
i	=	subscript
j	=	superscript or a subscript
n	=	interger representing the number of grid points considered
P	=	pressure, a dependent variable
r	=	radius, a polar coordinate
T	=	temperature, a dependent variable
u	=	dependent variable, function of x and y
w	=	velocity function in pipe flow
x	=	independent space variable
y	=	independent space variable
z	=	independent space variable
$\partial/\partial x$	=	partial differentiation
∇^2	=	Laplacian in Cartesian coordinates $\nabla^2 \equiv \partial^2/\partial x^2 + \partial^2/\partial y^2 + \partial^2/\partial z^2$
Δ	=	finite difference, or increment
ρ	=	mass density
μ	=	viscosity
Σ	=	summation
θ	=	divergence of the velocity vector
ϵ	=	tolerance requirement on dependent variable

LITERATURE CITED

1. Hartree, D. R., "Numerical Analysis," Oxford University Press (1955).
2. Scarborough, J. B., "Numerical Mathematical Analysis," 3 ed., The Johns Hopkins Press, Baltimore (1955).
3. Richardson, L. F., *Trans. Roy. Soc.*, **A, 210**, p. 307 (1910).
4. Liebmann, H., *Sitzber. math. physik, Kl. bayer. Akad. Wiss. Munchen*, 385 (1918).
5. Thom, A., *Aero Res. Comm. Rep. and Mem.*, No. 1194, 1928.
6. Shortley, G. H., and R. Weller, *J. Appl. Phys.*, **9** (May, 1938).
7. Southwell, R. V., "Relaxation Methods in Engineering Science," 1 ed., Oxford at the Clarendon Press (1946).
8. Southwell, R. V., "Relaxation Methods in Theoretical Physics," Oxford at the Clarendon Press (1949).
9. Shaw, F. S., "An Introduction to Relaxation Methods," Dover Publications, New York (1953).
10. Dykstra, H., and R. L. Parsons, *Trans. Am. Inst. Metall. Engrs.*, **192**, 227 (1951).

Kinetics of the Thermal Decomposition of Calcium Carbonate

CHARLES N. SATTERFIELD and FRANK FEAKES

Massachusetts Institute of Technology, Cambridge, Massachusetts

There is considerable indication that the decomposition of calcium carbonate in the shape of, say, a sphere takes place essentially in the following manner. The reaction starts at the outside surface and proceeds towards the center in a relatively thin spherical reaction zone (Figure 1). At a given instant the center core is undecomposed calcium carbonate and the outer shell calcium oxide. The observed reaction rate is presumably determined by the interrelationships between three major rate processes:

1. *Heat Transfer*. Heat must first be

transferred to the surface of the mass and then through the outer layer of calcium oxide to the reaction zone.

2. *Mass Transfer*. The carbon dioxide released at the reaction zone must escape through the outer shell of calcium oxide. Consequently, at finite rates of decomposition the pressure at the reaction zone must be greater than that at the surface of the sphere. The increase in pressure requires an increase in the temperature of the reaction zone to maintain decomposition. This in turn decreases the temperature difference causing heat transfer

and consequently decreases the rate of reaction.

3. *Chemical Reaction*. The question here is whether any process associated with the decomposition reaction itself can be an over-all rate-limiting factor, for example whether the rate of nucleation or the nature of the interfacial surface at the reaction zone can affect the over-all rate of decomposition.

A considerable number of studies of calcination of calcium carbonate have been reported (*3, 5, 21, 22*), but the experimental results have usually been

treated as though chemical kinetics were the only rate-limiting step. Conversely, in one case the decomposition has been treated as a problem of heat transfer alone with mass transfer and chemical kinetics neglected (8).

The purpose of the present study was to elucidate the nature of the calcination process with careful consideration of the various possible rate-limiting factors and their interrelationships. Gas-solid reactions in general characteristically involve these three possible rate-limiting steps. Therefore the method of analysis and kind of results obtained may be of interest as typical of this class of chemical reaction. Rate measurements were made on cylinders and spheres formed by agglomeration of powdered calcium carbonate under high pressure. Use of such agglomerates made it possible to employ high-purity material, to form suitable shapes and sizes that would permit heat and mass transfer characteristics to be calculated, and to measure internal temperatures by compressing the powder around a thermocouple.

SAMPLE PREPARATION

Unless otherwise specified Mallinckrodt reagent grade calcium carbonate was used in all studies. A microscopic examination indicated that the crystal type was calcite, and the average particle diameter was 10 to 15 μ. The B.E.T. (Brunauer, Emmett, Teller) nitrogen surface area was found to be 0.7 sq. meter/g. In several runs calcium carbonate with an average particle diameter of 0.2 μ was used. This was prepared by the rapid mixing of equimolar quantities of calcium chloride (as a solution containing 55.5 g. calcium chloride/100 g. water) and sodium carbonate (as a solution containing 18 g. sodium carbonate/100 g. water) at temperatures below 30°C. The crystals were washed with water before drying and had a sodium chloride content of 0.25% by weight.

The dry calcium carbonate was compressed around a platinum–10%-rhodium-in-platinum thermocouple in the axial position. The technique involved packing the calcium carbonate into a metal cylinder pierced with 1/16-in. holes, lined with Gooch rubber tubing, and fitted at one end with a sintered glass filter stick through which air was removed by vacuum during the packing operation. Final degassing was achieved through a hypodermic needle inserted into the mass, and the assembly was then sealed and subjected to 27,000 lb./sq. in. in a press containing glycerine. This method provided dense and reproducible packing and masses that were hard and mechanically strong. Light turning was sufficient to produce a cylinder with diameter variations of less than 0.002 in. If required, spheres could be shaped from the cylinder obtained.

CALCINATION APPARATUS

Figure 2 shows a schematic representation of the calcination apparatus. In its final form the furnace was of double porcelain tube construction, the inner tube being 36 in.

long, 2 in. I.D., and 2-1/4 in. O.D. The outer tube was 2-1/2 in. I.D., 2-3/4 O.D., and 33 in. long. This double-tube arrangement reduced diffusion of gas through the porcelain to a negligible figure. Both porcelain tubes were wound for 30 in. of their center lengths with 3/32- by 1/32-in. Kanthal A ribbon set in alundum cement. The outer winding was used as a constant heater to supply the major fraction of the heat requirements of the furnace. The inner winding was used as an on-off control heater and was controlled by the potential from a platinum–10%-rhodium thermocouple placed near the center of the winding of the inner heater. Heating was by direct instead of alternating current to avoid induced currents from being picked up by the control thermocouple. The outer porcelain tube was sealed against the inner tube with neoprene O rings. The outer section of the furnace was insulated for a length of 30 in. with a 6-in. thickness of insulating brick. Two insulating plugs 12 in. long and 1-15/16 in. in diameter were used to insulate the inner section of the center tube. The plugs also served to reduce the gas volume of the furnace. The exit plug, on the left hand side in Figure 2, was an alundum-clay mixture baked at a high temperature. It had a 3/8-in.-diameter hole down the center axis to carry a thermocouple to the main furnace zone. The entrance plug, on the right hand side of Figure 2, was firebrick 12 in. long and 1-7/8 in. in diameter. It was grooved along the upper edge to allow space for an alundum rod used to support the calcium carbonate sample and to carry the sample thermocouple leads out of the furnace. Both ends of the furnace were sealed with rubber stoppers kept cool by water coils on the adjacent area of the porcelain tube.

Carbon dioxide generated during the reaction passed out of the furnace, through a water-cooled condenser, through a capillary flow meter, and into a flexible rubber balloon immersed in water saturated with carbon dioxide. The flow of water from the sealed jar which contained the balloon was regulated to maintain constant pressure in the system, as indicated by the manometer. By measuring the weight of water removed with time, one could accurately determine the amount and rate of carbon dioxide evolution. Instantaneous gas-flow rates were also available from the capillary flowmeter, and the total gas evolved could be checked against the total loss in weight of the calcium carbonate sample. Gas-volume measurements were accurate to ±1 cc., and temperatures measured were reproducible and considered accurate to ±2°F.

For each run the furnace was maintained at the desired temperature for about 1 hr. to achieve normal temperature distribution throughout the apparatus. The system was then purged with a stream of dry carbon dioxide added in such a manner that, after the carbon dioxide volume-measuring equipment had been purged, carbon dioxide could be blown through the furnace during the sample-loading operation. After thorough purging, the insulating plug at the entrance end of the furnace was rapidly pulled out of the furnace onto an external support. The calcium carbonate sample, which had previously been weighed, measured, and loaded onto the thermocouple insulating rod, was quickly placed in the

insulating-plug groove and the assembly returned to the furnace. The flow of carbon dioxide was then stopped and the rubber stopper at the entrance pushed into the porcelain tube to seal the furnace. The loading operation required less than 1/2 min. Some slight cooling of the furnace necessarily took place during this time, but it was not sufficient to affect the results.

After reaction was complete and generation of carbon dioxide had ceased, the seal on the furnace was broken and the carbon dioxide removed with a helium purge. This prevented readsorption of carbon dioxide during removal of the calcined product. On some occasions the sample was allowed to cool in the helium atmosphere overnight before removal. Otherwise it was removed at the completion of gas generation while still at furnace temperature. When this latter procedure was used, the sample was allowed to cool in a desiccator before it was weighed and the length and diameter were measured.

RESULTS

Nature of the Reaction Pattern

Furnas (5) and others have suggested the *shell* model (Figure 1) for the decomposition of calcium carbonate. In the decomposition of crystals of calcite this model is certainly applicable. Visual observation of a section through a partially decomposed crystal shows the outer edges of the crystal to be white, amorphous, and opaque; the inner section remains crystalline, transparent, and completely undecomposed. The interface between the oxide layer and undecomposed calcite is sharply defined.

However with the more porous agglomerates the decomposition should tend to be shell-like and more uniform in nature. It seems reasonable to assume that completely uniform decomposition rates would be obtained throughout a highly porous powder of calcium carbonate heated slowly to a temperature just above the decomposition temperature. Under these conditions temperature and carbon dioxide pressure gradients would be negligible, and decomposition should proceed at substantially equal rates in all sections of the mass. On the basis of this reasoning the conditions which favor *shell-like* decomposition should be (1) a high ratio of carbon dioxide permeability in the calcium oxide to that in the undecomposed carbonate and (2) a rapid increase in the rate of decomposition with temperature. Since heat must be transferred to the carbonate for decomposition, higher temperatures in general exist in the outer sections of a sample than in the inner sections. The greater the temperature coefficient of the reaction, the more the decomposition pattern would become shell-like.

As a test of the foregoing reasoning, masses of calcium carbonate of different porosities were partially calcined, and samples taken at various radial distances from the center were ana-

Distance of sample from center, cm.	Calcination, % Theoretically expected for shell-like reaction	By analysis
Run 13: sphere; minus 200 mesh Iceland spar, unpressed; furnace temperature 1,748°F.; 79.5% over-all conversion		
0.00 to 0.40	0.0	16.8
0.40 to 0.60	0.0	18.7
0.60 to 0.75	100.0	40.3
0.75 to 1.05	100.0	89.4
1.05 to 1.25	100.0	92.8
Run 40: Cylinder; 10-μ Mallinckrodt calcium carbonate: pressed at 27,000 lb./sq. in.; furnace temperature 1,901°F.; 50.1% over-all conversion.		
0.00 to 0.30	0.0	3.9
0.30 to 0.50	0.0	2.1
0.90 to 1.00	100.0	77.8

lyzed to determine the oxide-carbonate ratio.

Table 1 summarizes the results obtained with two typical masses. In agreement with the preceding discussion, the more tightly packed calcium carbonate mass (run 40) shows a much closer approach to the shell-type model. Indeed, it is very likely that the actual decomposition in both cases was closer to the shell-like model than shown by the analyses because, although the mass was withdrawn from the furnace rapidly and cooled in air, it is possible that some carbon dioxide could have transferred from the hotter inner core to the cooler outer shell during the cooling.

Attempts were also made to test this reaction model by sealing a small cylinder of radioactive CaC^{14}O$_3$ concentrically inside a larger cylinder of calcium carbonate and measuring the radioactivity of the gas evolved as reaction proceeded. However the results are inconclusive since considerable exchange of radioactive carbon dioxide was found to take place at temperatures slightly below the decomposition temperature. Haul (9) and coworkers have also observed considerable interchange between radioactive C^{13}O$_2$ and solid calcium carbonate at temperatures below the decomposition temperature.

The agglomerates used in this study were pressed under conditions similar to run 40 of Table 1, and it is probable that decomposition followed the shell-like model quite closely. For calcite crystals and dense limestones it is probably a good engineering assumption to consider the decomposition shell-like.

When a cylinder or sphere of calcium carbonate was calcined, considerable shrinkage took place, the amount of which increased with higher decomposition temperatures. For example, a series of nine runs was made with calcium carbonate with a particle size of about 10 μ, pressed to 27,000 lb./sq. in., shaped into spheres of 0.5- to 1.4-in. diameter, and completely calcined at atmospheric pressure. The calcium carbonate densities varied from 1.90 to 1.95 g./cc. The final oxide densities increased almost linearly with furnace temperature, from about 1.26 for a furnace temperature of 1,673°F. to about 1.47 at 1,897°F.

In view of the shell-like decomposition pattern the shrinkage which occurs on decomposition must set up strains within the sample. Consider, for example, the decomposition of a sphere of calcium carbonate. Initially the reaction is most rapid at the outer surface of the sphere. But the calcium oxide which is formed contracts, and cracks form in the outer layer. Fresh carbonate is then exposed, and the decomposition is facilitated. However the oxide layer, once formed, has radial dimensions determined by the radius of the underlying calcium carbonate. Consequently as the reaction proceeds and shrinkage continues to take place at the reaction zone, the cracks in the outer layer will close. The completely reacted sphere will then have a smaller radius than the original carbonate sphere, and the outer surface will appear smooth and uncracked. But if the shrinkage has been considerable, as occurs at high temperatures, the inside of the sphere will be partially hollowed out and irregularly cracked. This characteristic has also been noticed in the decomposition of crystals of calcite. The oxide tends to retain the hexagonal form of the original crystal, but the center of the oxide mass is often hollow and extensively cracked.

Effect of Mass Transfer on the Rate of Reaction

The aim of this part of the investigation was to determine the extent to which the outer layer of calcium oxide hinders the escape of carbon dioxide from the reaction zone, thereby increasing the gas pressure and consequently decreasing the rate of decomposition. Direct measurements were made of the permeability of calcium oxide prepared under conditions identical with those used for the over-all rate determinations. These measurements permitted an estimation to be made of the increase in pressure at the reaction zone for each measured rate of carbon dioxide evolution. By assuming that the decomposition followed the shell model and that the effect of pressure on the decomposition temperature followed that at equilibrium conditions (11), one could estimate the increase in temperature at the reaction zone for various rates and degrees of decomposition.

Permeability measurements of the calcium oxide were made in three different ways:

1. The pressure-drop–flow-rate relationship was determined for the flow of carbon dioxide through a plug of calcium oxide held at the furnace temperature used for the preparation of the oxide sample. Attempts were made to use gold and silver foil to seal the plug in the pressure-drop apparatus, but deformation of the oxide occured at the high temperatures. The permeability values obtained by this method were so high that presumably leakage around the seals occurred.

2. The pressure-drop–flow-rate relationships for carbon dioxide at the reaction temperatures were calculated from pressure-drop–flow-rate measurements made with argon, helium, and hydrogen at room temperatures. An apparatus similar to that used by Russell (19) was used in these tests. With these three gases it was possible to calculate both the Poiseuille and Knudsen contributions to flow and hence the effect of temperature, viscosity, and molecular weight.

3. The procedure outlined by Kraus, Ross, and Girifalco (14) was used to calculate the permeability from measured values of the surface area of the calcium oxide (B. E. T. krypton adsorption).

Method 2 gave values for the permeability to carbon dioxide at 1,800°F. of 0.0076 to 0.0096 moles/(hr.)(ft.)(mm. Hg); two measurements by method 3 gave values of 0.0023 and 0.00066. These results indicate that the value of the permeability of the calcium oxide is probably of the order of 0.01 mole/(hr.)(ft.)(mm. Hg) and almost certainly not less than 0.001 mole/(hr.)(ft.)(mm. Hg). However, even for the latter value, the average reaction temperature was calculated to increase by only 0.4°F. for decomposition at a furnace temperature of 1,782°F. and an equilibrium decomposition temperature of 1,652°F. Under these circumstances the resistance offered by the calcium oxide layer has a negligible effect on the reaction rate.

With the use of the B. E. T. surface-area measurements of Murray, Fischer, and Sabean (17), the pressure drop effect was also calculated for the decomposition of a single crystal of pure calcite, which represents the form of calcium carbonate for which a mass transfer effect would presumably be of greatest importance. When one takes representative values such as

Surface area	16 sq. meters/g.
Specific gravity, CaO	1.74
Specific gravity, CaCO$_3$	2.73
Porosity, CaO	48%

the permeability is calculated to be 0.00008 mole/(hr.)(ft.)(mm. Hg). The resulting effect on the reaction temperature is such that the average difference between the furnace and reaction temperatures throughout decomposition would have been decreased by about 3.4% from that expected for complete decomposition at the equilibrium pressure. Consequently the resistance offered to the passage of carbon dioxide through
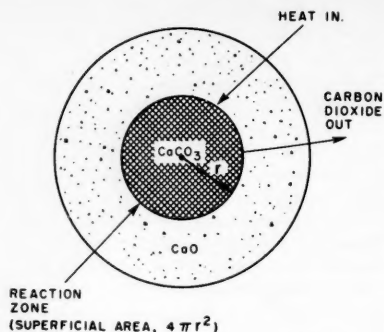
Fig. 1. Decomposition of a sphere of calcium carbonate (shell or layer model).

HEAT IN.

CARBON DIOXIDE OUT

CaCO₃

r

CaO

REACTION ZONE
(SUPERFICIAL AREA, 4 π r²)

Fig. 2. Schematic arrangement of furnace and ancillary equipment.

the calcium oxide has only a minor effect on the over-all rate of decomposition of any form of calcium carbonate.

Effect of Heat Transfer and Chemical Kinetics

To make a quantitative analysis of these rate-determining factors, a group of tests, summarized in Table 2, was made in which the temperature at the center of the sample (mostly cylinders) was measured. Usually bare platinum–platinum-10%-rhodium thermocouples with a diameter of 0.010 in. were used. However identical results were obtained with thermocouples of a diameter of only 0.001 in., an indication that heat conduction along the thermocouples did not affect the measured temperatures.

Figure 3 illustrates a typical time-center temperature history for the studies made with agglomerates formed from 10 to 15-μ calcium carbonate. There are two striking observations which were common to this entire series of runs. (1) After the sample had been placed in the furnace, the temperature at the center of the sample rose rapidly, passed through a sharp maximum, and then, after a small temperature drop, through a minimum. The temperature then remained practically constant for the major part of the reaction time. (2) This center temperature remained substantially in

excess of the equilibrium decomposition temperature throughout the run.

The plot indicates that the time required to heat the calcium carbonate from room temperature to the equilibrium decomposition temperature (1,652°F. at 769 mm. Hg pressure carbon dioxide) was about 11 min., or less than 10% of that required for complete decomposition. The major fraction of the reaction occurred during the time interval between the initial maximum in the center temperature and the final rise to the furnace temperature.

Also included in Figure 3 are two plots of the calculated value of the reaction temperature that would be predicted during shell-like decomposition, for a permeability of the calcium oxide outer layer to carbon dioxide of 0.001 or 0.0001 mole/(hr.)(ft.)(mm. Hg), respectively. The plots show that even for a permeability as low as 0.0001 mole/(hr.)(ft.)(mm. Hg) the theoretical reaction temperature is only slightly above the equilibrium decomposition temperature of 1,652°F. for the ambient pressure of 769 mm. Hg of carbon dioxide. Since the calcium oxide formed in these studies had a permeability not less than 0.001 mole/(hr.)(ft.)(mm. Hg), the resistance

offered by the calcium oxide to the escape of carbon dioxide is clearly *not* the cause of the increase of the center temperature above that of equilibrium (1,652°F.).

The reaction temperature is determined by a balance between two rate processes, the rate of heat transfer to the reaction zone and the rate of heat consumption by the endothermic reaction. The existence of a *maximum* in the center temperature at an early stage of the decomposition reflects the effect of one or both of the following factors:

1. The rate of heat transfer to the reaction zone is highest at the beginning of a run. Thereafter the rate of heat transfer is reduced by the development of a layer of calcium oxide through which heat must be transferred by conduction.

2. The rate of reaction increases with an increase in temperature and possibly also with the extent to which the reaction zone has penetrated into the mass (because of an increase in available reaction area, to be discussed later).

For all the 10 to 15-μ agglomerates studied (runs 39 to 45) the temperature at the center of the mass was consistently
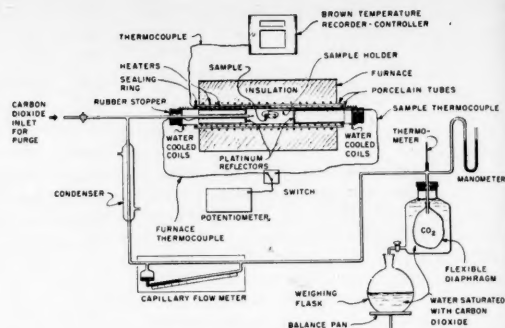
TABLE 2. CALCIUM CARBONATE DECOMPOSITION STUDIES, SUMMARIZED DATA

Run	Shape	Radius, cm.	Length, cm.	Thermo-couple diam., in.	Density CaCO₃ g./cc.	Density CaO g./cc.	Furnace temp., °F.	CO₂ Pressure mm. Hg.	% reacted	Reaction[1] time, hr.	Temperatures inside reaction mass, °F.		
											Max.	Min.	Equil. temp.
Series A (agglomerates of 10- to 15-μ diameter)													
39	Cylinder	1.06	6.79	0.010	1.86	1.31	1,782 ± 2	769	100	1.84	1,683	1,672	1,652
40	Cylinder	1.04	6.14	0.010	1.90	—[5]	1,901 ± 2	765	50.1	0.28	1,690	1,677[6]	1,651
41	Cylinder	1.07	6.69	0.010	1.85	1.28	1,705 ± 4	762	100	4.34	1,673	1,657	1,650
42	Sphere	1.08	—	0.010[2]	1.84	1.34	1,835 ± 5	770	100	0.75	1,688	1,674	1,652
43	Cylinder	1.09	6.62	—[3]	1.87	—[5]	1,751 ± 3	765	100	2.02	1,679	1,660[7]	1,651
45	Cylinder	1.04	6.84	0.001[4]	1.80	1.43	1,814 ± 3	772	100	1.36	1,685	1,673	1,652
Series B (agglomerates of approx. 0.2-μ diameter)													
48	Cylinder	1.09	6.52	0.010	1.64	—[5]	1,844 ± 4	760	100	0.70			
49	Cylinder	1.105	7.59	0.010	1.68	—[5]	1,905 ± 5	774	100	0.63			

[1]Reaction time, the time during which gas evolution occurred.
[2]In run 42 the sphere was made by turning down a cylinder, and it was later found that the thermocouple junction was at 0.37 of the diameter instead of 0.50.
[3]In run 43 0.010-in.–diameter wire was used, but two 1-in. sections on each side of the junction were flattened to a cross section of 0.003 in. × 0.026 in.
[4]In run 45 four strands of 0.001-in.–diam. wire were used for mechanical strength.
[5]In runs 40, 43, 48, and 49 the calcium oxide was so extensively cracked that density figures were not determined. The cracking in runs 39 and 45 was negligible.
[6]Reaction carried only to 50% completion mark, and minimum center temperature was not reached. Minimum was estimated at 1,677°F.
[7]Later in this run a second minimum of 1,655°F. was obtained. The results of this run were probably affected by extensive cracking.
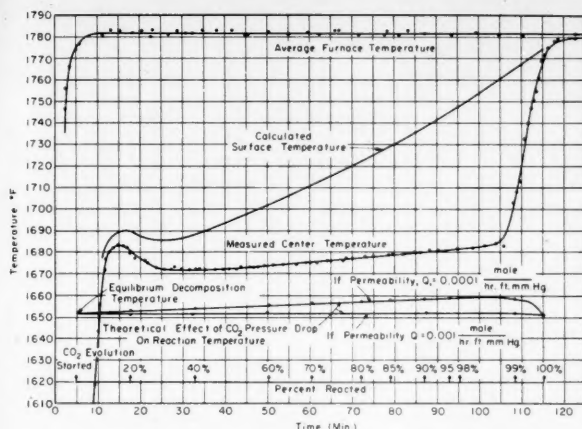
Fig. 3. Time-temperature variations in decomposition of cylinder of agglomerated 10- to 15-μ calcium carbonate; run 39.
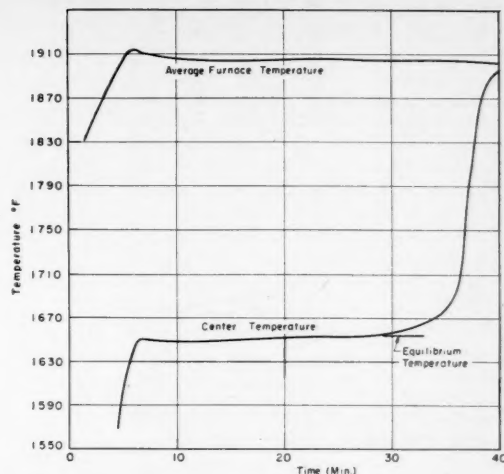

Fig. 4. Time-temperature variation in decomposition of cylinder of agglomerated 0.2-μ calcium carbonate; run 49.

greater than the equilibrium decomposition temperature throughout the reaction. This excess in temperature over the equilibrium value increased with higher furnace temperatures. On the other hand when agglomerated calcium carbonate of a smaller particle size (approximately 0.2 μ) was studied, the center temperature-time curve was considerably different (Figure 4) from that for the coarser material. The temperature maximum in the early part of the run is almost nonexistent, and in addition the center temperature remained practically constant for the major part of the reaction time at a temperature substantially equal to that of the equilibrium decomposition temperature. This occurred even when the furnace temperature was as high as 1,905°F. It therefore appears that the size of the crystal present in the agglomerate has a pronounced effect on the temperature at the center of the reaction mass. For the major part of the decomposition time the sensible heat requirements of the undecomposed carbonate are negligible. Consequently it is evident that the decomposition is dependent upon the size of the crystals in the agglomerate. Calcium carbonate with a small particle size (0.2 μ) decomposes, even at the high rates, at reaction temperatures and carbon dioxide pressures approximating those of equilibrium. Consequently this is a case in which reaction rate is determined by the rate of heat transfer alone.

However calcium carbonate agglomerates of 10 to 15-μ particles require temperatures considerably in excess of equilibrium. It is apparent that here some nucleation or chemical activation process plays a part in the over-all rate of the reaction. One method of obtaining a measure of the relative importance of heat transfer and the chemical activation effect on the over-all rate of reaction is to compare the temperature drop actually available for heat transfer with that

which would have resulted if there had been no chemical resistance, that is, if the reaction had proceeded at the equilibrium temperature. Several such comparisons are summarized in Table 3.

These results indicate that the increase in the temperature at the reaction zone decreased the over-all temperature difference theoretically available for heat transfer ($T_F - T_E$) by about 10 to 20%. Hence although heat transfer still remains the major rate-controlling factor, a chemical reaction effect does become important for larger crystal sizes of calcium carbonate; this is discussed in more detail later.

It has been assumed here that the temperature measured at the center of the sample equals the reaction temperature. This seems reasonable considering that for the major fraction of the decomposition time the center temperature changed relatively slowly. Moreover the thermal diffusivity of the calcium carbonate is relatively high, and so the center temperature does not greatly lag behind even during the transient heating periods at the beginning and end of the run. For instance, if the surface temperature of a 1-in.-diameter calcium carbonate sphere were instantaneously raised 5°F., thermal diffusivity calculations indicate that the center temperature would be raised 4°F. within 0.8 min.

Thermal Properties of the Solid Phases

When one assumes shell-like decomposition, it is possible to calculate both the thermal absorptivity of the surface of the sample and the thermal conductivity of the outer layer of calcium oxide. From the rate of evolution of carbon dioxide the rate of heat intake by the sample can be calculated. A value is assumed for the thermal conductivity of the calcium oxide, and from the temperature at the reaction zone (equal to the center temperature) and the heat flux it is

possible to calculate the surface temperature. Consequently, with a knowledge of the surface area and the furnace temperature it is then possible to calculate the thermal absorptivity of the surface. These calculations are made for conditions at some instant during the early part of the run. At this time the outer layer of calcium oxide is thin, the temperature drop through it is small, and the value obtained for the thermal absorptivity is insensitive to the value assumed for the thermal conductivity of the calcium oxide. In practice it was possible to extend this type of calculation (1) to estimate the change in thermal absorptivity of the surface with time and (2) to check the assumed value of the thermal conductivity of the calcium oxide by reversing the calculational procedure for a time late in the decomposition run, when the surface temperature is less sensitive to the thermal absorptivity value and more strongly dependent on the conductivity value. In the latter case a value could be assumed for the absorptivity, and the thermal conductivity could be calculated. This trial-and-error procedure was repeated until consistent values were obtained for the thermal absorptivity of the surface and the thermal conductivity of the calcium oxide layer.

The variation of calculated absorptivity of the surface with the extent of reaction is shown in Figure 5. Variations with time and temperature in the extent of sintering of the oxide surface and of surface cracking will affect the absorptivity. However it seems reasonable to assume that the decrease shown in Figure 5 was caused primarily by a change in the thermal absorptivity as the surface changed from calcium carbonate to calcium oxide. The only reliable value for the emissivity of calcium carbonate appears to be the value of 0.93 quoted by McAdams (16)
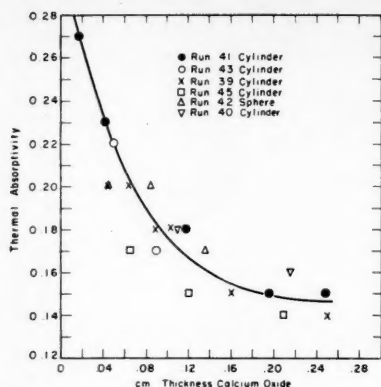
Fig. 5. Variation of thermal absorptivity with thickness of calcium oxide layer.

Fig. 6. Variation of rate of decomposition of agglomerated 10- to 15-μ calcium carbonate with reaction temperature.

for marble at 72°F. The absorptivity of the calcium carbonate used in this investigation is probably not too different from that of marble. According to the literature few determinations of the absorptivity of calcium oxide have been made in the past. The most reliable is probably that of Hild (10), who found the emissivity of a calcium oxide powder with a particle size of 3 to 5 μ to be 0.27 in the range of 900° to 1300°C. In any case the absorptivity of the surface is low enough to require a very substantial temperature difference between the furnace wall and the oxide surface at the rates of heat transfer called for by the reaction rates observed here. The calculated variation in oxide surface temperature with time, for a typical run, is shown on Figure 3.

The values calculated for the thermal conductivity of the outer layer of calcium oxide were within the range 0.36 ± 0.06 B.t.u./(hr.)(ft./°F.) for calcium oxide with a bulk density of 1.30 g./cc. The shrinkage which occurred during calcination very probably caused fine cracks to form in this calcium oxide, which would lower the thermal conductivity below that expected for a homogeneous mass.

To test this hypothesis, a sample of calcium carbonate was calcined at 1,417°F. at a total pressure of 60 mm. Hg pressure of carbon dioxide. The resulting oxide had a density of 1.14 g./cc. and had

undergone less than 8% shrinkage during calcination. A sample of this oxide was found to have a thermal conductivity of 0.46 B.t.u./(hr.)(ft./°F.) at 690°C. when compared to a zirconia standard in an apparatus similar to that described by Francl and Kingery (4).

These values generally agree with the value of 0.4 B.t.u./(hr.)(ft./°F.) quoted by Tadokaro (23) for lime.

Chemical Kinetics

It has been shown that with the calcium carbonate of small particle size (0.2 μ) the chemical reaction rate (or nucleation rate) was sufficiently high to offer no resistance to the over-all rate of decomposition. Under these conditions the reaction rate was completely heat transfer controlled. However for the calcium
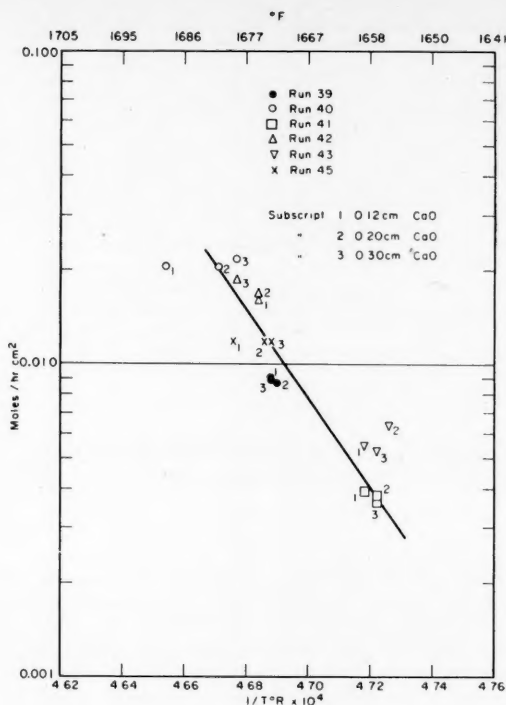
TABLE 4. VARIATION OF REACTION RATE DURING DECOMPOSITION

Run 39		Run 45	
CaO thickness, cm.	M moles (hr.)(sq. cm.)	CaO thickness, cm.	M moles (hr.)(sq. cm.)
0.047	0.00996	0.064	0.0126
0.052	0.00975	0.119	0.0118
0.074	0.00938	0.209	0.0124
0.082	0.00933	0.298	0.0121
0.130	0.00883	0.454	0.0136
0.208	0.00997		
0.372	0.00970		
0.534	0.01080		

carbonate with a larger size (10 to 15 μ) the average temperature difference available for heat transfer was decreased some 10 to 20% by a rise in the reaction temperature over the equilibrium temperature of decomposition corresponding to the pressure of carbon dioxide present at the reaction zone.

A considerable number of previous workers have used an equation developed by Polanyi and Wigner (18) to correlate the rate of decomposition of carbonates. For the purposes of this discussion the equation may be simplified to

$$M = ke^{(-E/RT)}$$

where

M = reaction rate, expressed as mole/ (hr.)(sq. cm.) of reaction area

TABLE 3. RELATIVE EFFECT OF HEAT TRANSFER AND CHEMICAL REACTION ON OVER-ALL REACTION RATE

Agglomerated Calcium Carbonate, Particle Size of 10 to 15 μ

Run	Furnace temperature* T_F, °F.	Reaction temperature* T_R, °F.	Equilibrium decomposition temperature T_E, °F.	Ratio $\dfrac{T_F - T_R}{T_F - T_E}$
39	1,782	1,677	1,652	0.81
41	1,705	1,658	1,650	0.80
42	1,835	1,679	1,652	0.85
43	1,751	1,661	1,651	0.90
45	1,814	1,682	1,652	0.82

*The furnace and reaction temperatures quoted are time-average values for the period 10 to 98% of total decomposition. These limits were taken to exclude transient temperature effects.

k = reaction rate constant
E = activation energy, cal./g.-mole
R = gas constant
T = absolute temperature, °K.

To test the applicability of an equation of this type, values were calculated for the reaction rate M (expressed as moles of carbon dioxide evolved per hour per square centimeter of superficial reaction area $4\pi r^2$ as indicated for the sphere in Figure 1) at three different thicknesses of penetration of the reaction zone for each of the runs. The depths taken for the calculation of M were 0.12, 0.20, and 0.30 cm., respectively. The values thus calculated are plotted in Figure 6 against the reciprocal of the respective absolute temperature (°R) existing at the center of the sample. In general for any one run the variation of M with the degree of penetration of the reaction zone was small, as shown by the data in Table 4 for two typical runs. This supports the Polanyi-Wigner analysis. However the rate of change of the reaction rate M with temperature was large. The "activation energy" corresponding to the straight line drawn in Figure 6 is 360 kcal./g.-mole. (Rather lower weight was given to the results of run 43, because it is possible that here surface cracking increased the value of M.) Such an activation energy is exceedingly high, and being an order of magnitude greater than the enthalpy change for the reaction, 39.4 kcal./g.-mole, it is rather unbelievable. On the other hand the determinations of the activation energy by several previous workers have approximated the enthalpy change for the reaction. A summary of their results follows:

Ref.	Activation energy reported kcal./g.-mole
3	35.5 to 41.6
21	40.8 to 44.3
13	48.7 to 50.1
22	37.0

However these workers assumed that the reaction temperature equaled the furnace temperature and indeed, if this assumption is used with the results of the present investigation, an activation energy of 48.2 kcal./g.-mole is obtained. But it has been conclusively shown in this work that the reaction temperature is not equal to the furnace temperature. It appears merely fortuitous that the activation energies reported by previous workers on the basis of furnace temperatures should approximate the enthalpy change.

On the other hand the abnormally high activation energy obtained here, when one uses a reaction area equal to the superficial area (or a constant ratio of the actual reaction area to the superficial area), does not seem at all reasonable. Rather the value of 360 kcal./g.-mole is a reflection of the inadequacy of the simplified model, which assumes that
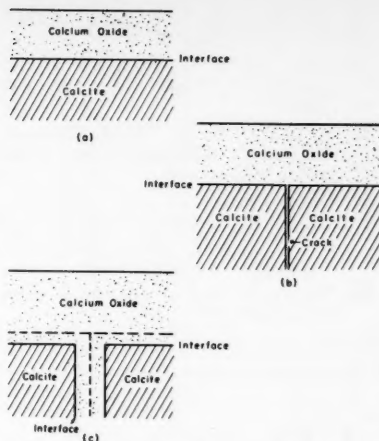

Fig. 7. Mechanism of increase in reaction area by formation of cracks.

all the reaction occurs on a spherical surface of vanishingly small thickness. Consider, for instance, a small part of the decomposition zone of a calcite crystal. After partial decomposition the model assumed in the analysis up to this point has been that depicted in Figure 7a; that is, the reaction has been pictured as proceeding at an interface which gradually penetrates into the calcite. However microscopic examination of the decomposition of crystals of calcite has indicated that the decomposition region is, in fact, a complex zone. Cracks very frequently are formed in the calcite (Figure 7b), and the reaction then proceeds also at the new surface formed (Figure 7c). In many cases it appears that whole blocks of calcite are broken out of the parent crystal. As a result the total area on which the reaction is proceeding at any given instant is strongly dependent on the degree to which cracking and block formation is occurring.

Within any one run at a constant furnace temperature (and substantially constant reaction temperature) the calculated value of the reaction rate M remained practically constant (Figure 6 and Table 4). This indicates that the ratio of the true reaction area (along all the surfaces of cracks and blocks) to the superficial area of the model remained virtually constant within a run. However the tremendous increase in the value of M with the reaction temperature suggests that the increase largely results from an increase in the degree of cracking and block formation rather than from an increase in the rate of penetration of an interface into the parent crystal. This in turn suggests that the rate of new surface generation by cracking, etc., is strongly dependent on temperature.

The splitting-out mechanism for the progress of the reaction zone in a decomposing solid was predicted by Garner and Hailes (6) in 1933, and its importance

has been emphasized recently in the theoretical work of Schultz and Dekker (20). Bowden and Singh (2) have recently published data on the decomposition of lead azide, for which they obtained electron micrographs indicating that the crystal breaks up into small blocks, about 10^{-5} cm. across, at the decomposition interface. Decomposition appeared to take place at the surface of these blocks. Without some knowledge of the degree to which surface development takes place, experimental verification of theoretical rate equations is impossible.

In conjunction with the present investigation Jones (12) studied the decomposition of calcite and obtained a number of photomicrographs of well-developed calcium oxide nuclei. Each developed nucleus was square in section, and the appearance of many suggested that they were inverted pyramids hollowed out of the calcite, possibly by successive block removals. The similarity to the nuclei found on the 001 face of alum by Garner (7) is remarkable.

The present investigation did not yield any quantitative information on the kinetics of the nucleation process. However the qualitative results suggest that nucleation does play an important role, particularly with the larger crystal sizes; it is also important during the initial stages of decomposition and for high rates of decomposition. A resistance to nucleation appears to be the most reasonable explanation for the early maximum in the time-reaction temperature curve (Figure 3). Apparently a considerable amount of superheat is required to increase the rate of nucleation to the degree that the rate of decomposition is commensurate with the heat input. Once this condition is reached, nuclei continue to form, since the temperature decreases despite the high reaction rate now in effect. During the latter part of a calcination run it is difficult to determine whether or not nucleation plays an important role. However it is well known (1) that larger crystals of pure calcite require higher temperatures and longer times for decomposition than the more amorphous limestone. This again appears to represent a case of nucleation acting as a rate-limiting process.

LITERATURE CITED

1. Azbe, V. J., *Rock Products*, **47**, No. 9, 68 (1944).
2. Bowden, F. P., and K. Singh, *Proc. Roy. Soc. (London)*, **A227**, 22 (1954).
3. Britton, H. T. S., S. J. Gregg, and G. W. Winsor, *Trans. Faraday Soc.*, **48**, 63 (1952).
4. Francl, J., and W. D. Kingery, *J. Am. Ceram. Soc.*, **37**, No. 2, 80 (1954).
5. Furnas, C. C., *Ind. Eng. Chem.*, **23**, 534 (1931).
6. Garner, W. E., and H. R. Hailes, *Proc. Roy. Soc. (London)*, **A139**, 576 (1933).

7. Garner, W. E., "Chemistry of the Solid State," p. 217, Academic Press, New York, (1955).

8. Haslam, R. T., and V. C. Smith, *Ind. Eng. Chem.*, **20**, 170 (1928).

9. Haul, R. A. W., L. H. Stein, and J. W. L. de Villiers, Nature **171**, 619 (1953).

10. Hild, K., *Mitt. Kaiser-Wilhelm-Inst. Eisenforsch.*, **14**, 59 (1932).

11. Johnston, J., *J. Am. Chem. Soc.*, **32**, 938 (1910).

12. Jones, R. E., S. M. thesis, Mass. Inst. Technol., Cambridge (1955).

13. Kappel, H., and G. F. Huttig, *Kolloid. Zs.*, **91**, 117 (1940).

14. Kraus, G., J. W. Ross, and L. W. Girifalco, *J. Phys. Chem.*, **57**, 330 (1953).

15. McAdams, W. H., "Heat Transmission," p. 59, McGraw-Hill, New York, (1942).

16. *Ibid.*, p. 395.

17. Murray, J. A., H. C. Fischer, and D. W. Sabean, *Proc. Amer. Soc. Testing Mat.*, **50**, 1263 (1950).

18. Polanyi, M., and E. Wigner, *Z. phys. Chem.*, **A139**, 439 (1928).

19. Russell, J. L., Sc.D. thesis, Mass. Inst. Technol., Cambridge (1955).

20. Schultz, R. D., and A. O. Dekker, Rept. 961, OSE-TR-55-12, Aerojet-General Corp., Azusa, Calif. (April, 1955).

21. Slonim, C., *Z. Elektrochem.*, **36**, 439 (1930).

22. Splichal, J., St. Skramovoky, and J. Goll, *Coll. Czech. Chem. Comm.*, **9**, 302 (1937).

23. Tadokaro, Y., *Sc. Rep. Tohuku Imp. Univ. Japan*, **10**, 339 (1921–22).

Rates of Thermal Decomposition of Barium Carbonate–Carbon Mixtures

CHARLES N. SATTERFIELD and FRANK FEAKES

Massachusetts Institute of Technology, Cambridge, Massachusetts

The thermal decomposition of pure barium carbonate to form barium oxide and carbon dioxide requires relatively high temperatures; for example, at 1,030°C. the equilibrium partial pressure of carbon dioxide is only 2 mm. Hg (3). Unfortunately temperatures in excess of 1,030°C. tend to produce a dense, nonporous form of barium oxide. According to Lander (3), a barium carbonate–barium oxide eutectic exists at 1,030°C., and apparently above this temperature barium carbonate–barium oxide solutions form which continue to exist as solid solutions below the melting point. Therefore the thermal decomposition of barium carbonate is usually facilitated by the addition of carbon (1, 2). The carbon dioxide partial pressure becomes greatly reduced, since the following reaction proceeds far to the right:

$$C + CO_2 \rightarrow 2CO \qquad (1)$$
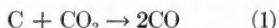
The observed rate of the over-all reaction may therefore be affected by heat or mass transfer rates or by the kinetics of two separate reactions.

EXPERIMENTAL

Barium carbonate was mixed with one of several forms of carbon, and the mixture was pressed (at 27,000 lb./sq. in.) into a cylinder around a platinum, rhodium–in-platinum thermocouple. The cylinder was calcined in a constant-temperature furnace of special design, and the rate of reaction was determined by the rate of the evolution of gas. The apparatus and methods employed were substantially the same as those used previously for studying the decomposition of calcium carbonate (6). This earlier paper also discusses the accuracy of the experimental data.

Lieberson and Oster (5) found that the rate of reaction of barium carbonate and carbon mixtures was not greatly influenced by the amount of carbon used in excess of that stoichiometrically required for the over-all reaction:

$$BaCO_3 + C \rightarrow BaO + 2CO \qquad (2)$$

(The stoichiometric ratio is 6.085 g. carbon/100 g. barium carbonate.) However to decrease the possibility of the carbon content being a rate-controlling factor, and also to decrease the effect of imperfect mixing, a 50% excess of carbon over the stoichiometric quantity was used in each run beyond the first.

Since it was also desirable to carry out the reaction at temperatures below that of the barium carbonate–barium oxide eutectic (1,030°C. or 1,886°F.), vacuum conditions were required. A mechanical vacuum pump was used to exhaust the furnace, and a Cartesian Diver manostat reduced pressure fluctuations. The rate of the evolution of gas (which was almost 100% carbon monoxide) was measured with a capillary flow meter. The over-all degree of decomposition of the barium carbonate was determined by measuring the weight of the sample before and after reaction.

Mallinckrodt reagent-grade barium carbonate was used in all runs. The average particle diameter was found to be about 0.13 μ; the B.E.T. surface area (by nitrogen adsorption) was about 10 sq. m./g. The properties of the different types of carbon studied are outlined in Table 1. The components were mixed dry, then wet (with water), and then again dry after removing the water by evaporation. The most efficient mixing probably took place when the mass was a thick paste. However despite the considerable care devoted to obtaining good mixing the degree of mixing was not so high as desired. Small "islands" of white barium carbonate, up to approximately 0.15 mm. in diameter, were visible in the pressed samples. Nevertheless, the degree of mixing was apparently sufficient to give complete decomposition of the barium carbonate, if reaction conditions were favorable.

In all cases a 0.010-in.-diameter platinum, 10% rhodium-in-platinum thermo-

TABLE 1. PROPERTIES OF CARBON BLACKS AND GRAPHITES STUDIED

Carbon Blacks

Code name	Type	Surface area, sq. m./g., by B.E.T.-Nitrogen Method	Mean particle diameter, (μ)	Ash content, wt. %
Elftex 5	Furnace black	77	0.03	0.5
Elf 8	Channel black	100	0.03	0.1
Sterling FT	Thermal black	15.7	0.20	0.1
Same-after partial graphitization		12.7	0.20	0.1

Graphites

Code name	Minimum graphitic carbon content, wt. %	Maximum ash, wt. %	Particle size
Dixon 2	94	5	30% + 100 mesh 30% − 200 mesh
Microfyne	94	5	97% − 325 mesh

TABLE 2. EXPERIMENTAL RESULTS

Run	Type of carbon	Excess carbon %	Cylinder radius, cm.	Length, cm.	Density, Before Reaction g./cc.	Furnace temperature, °F.	Furnace pressure, mm. Hg.	Reaction time, hr.	Conversion, %	Internal temperature range*, °F.
1	Elftex 5	5	1.13	7.06	1.42	1,834 ± 4	192 ± 5	5.75	90.3	1,726 to 1,743
2	Elf 8	50	1.045	6.49	1.25	1,767 ± 6	74 ± 2	3.5	103.1	1,626 to 1,633
3	Elf 8	50	1.11	6.02	1.16	1,720 ± 10	51 ± 4	4.17	102.1	1,605 to 1,611
4	Elf 8	50	1.12	7.11	1.21	1,817 ± 10	115 ± 10	3.27	102.3	1,682 to 1,690
5	Graphite Dixon 2	50	1.05	6.34	1.33	1,823 ± 8	53 ± 9	2.0	65.4	1,760 to 1,815
6	Graphite Microfyne	50	1.02	6.33	1.29	1,826 ± 2	26.5 ± 4	2.0	87.6	1,720 to 1,821
7	Graphitized Sterling FT	50	1.11	5.66	1.35	1,821 ± 8	54 ± 4	3.60	99.4	1,721 to 1,821
8	Sterling FT	50	1.12	5.72	1.34	1,815 ± 4	101 ± 8	2.07	100.8	1,677 to 1,685

*Temperature range quoted excludes transient conditions at beginning and end of run. The time-temperature curves for runs 2, 3, 4, and 8 were similar in shape to those shown on Figure 1. Those for runs 5 and 6 resembled Figure 2. Run 7 was intermediate between the two types.
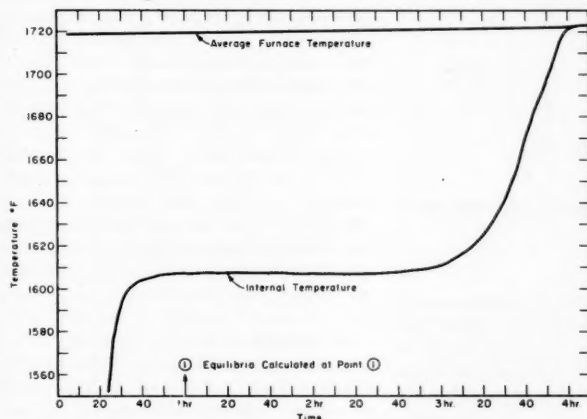
Fig. 1. Calcination of barium carbonate-carbon black mixture (run no. 3).

Fig. 2. Calcination of barium carbonategraphite mixture (run no. 5). Equilibria calculated at points 1 and 2.
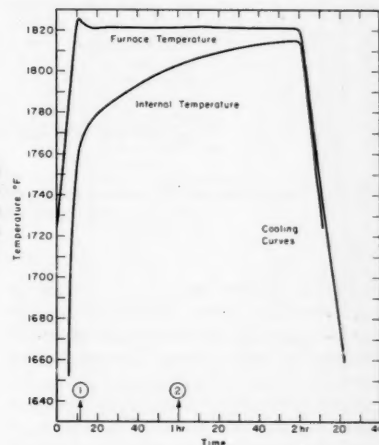
couple was embedded axially within the cylinder. Since carbon is a conductor, in all runs after run 2 the thermocouple was insulated with alundum cement baked on by resistance heating of the thermocouple. After coating, the resistance from the thermocouple to the carbon mixture exceeded 50 mohm. However judging from the data one concludes that this precaution was unnecessary here.

RESULTS

The experimental results are summarized in Table 2. Following are some general observations and explanatory notes.

Cracking

In all runs severe cracking of the cylinders occurred during the reaction. On occasion small pieces of the product flaked away from the main agglomerate.

Percentage Conversion

The results quoted in Table 2 for the percentage conversions were calculated from the sample weights before and after the reaction, when one assumes that the gaseous reaction product is solely carbon monoxide. In several of the runs conversions slightly greater than 100% were thus calculated. These high values were probably caused by loss of weight arising from slight spalling of the

sample during reaction. In runs 2, 3, 4, 7, and 8 no carbon dioxide was evolved on treating the slaked product with hydrochloric acid. The amount of carbonate present was therefore negligible, and complete conversion was confirmed. In the other runs carbonate was present in the final product according to the hydrochloric acid test.

Reaction Time

The reaction time was taken as the total time during which gas evolution occurred, as indicated by a capillary flow meter. Even though the rate of gas evolution was low at the final stages of reaction, it was possible to determine the cessation of flow to within ±0.1 hr. In runs 5 and 6, in which incomplete decomposition was obtained, the reaction rate had decreased to a very low value at the time the run was terminated.

The product obtained from the runs in which graphite was used was harder and less porous than that obtained from the studies with carbon black.

DISCUSSION

When a carbon black was admixed with the barium carbonate, time-temperature curves similar to those in Figure 1 were obtained. The internal temperature, which is equal to the reaction temperature

(see reference 6), remained practically constant for almost the entire reaction.

However when a natural graphite such as Dixon Microfyne was mixed with the barium carbonate, time-temperature curves similar to Figure 2 were obtained. The center temperature rose continuously, and the temperature difference available for heat transfer from the furnace to the reaction zone decreased steadily with time. Relatively low rates of reaction were obtained, and the internal reaction temperatures measured were higher than those observed with the runs with carbon black. The reduced rate of decomposition resulting from the use of graphite was presumably caused by either one or a combination of the following factors: (1) larger particle size of the natural graphite, and (2) the difference between the reactivity of the more crystalline graphite vs. that of the more amorphous carbon black.

To determine the relative importance of each of these factors rate determinations were made with each of two samples of carbon black which had similar particle sizes but different physical structures. The first run of this pair (run 7) used a sample of Sterling FT which previously had been heated in a nitrogen atmosphere for 2 hr. at 2,700°C. The resulting black was found to have
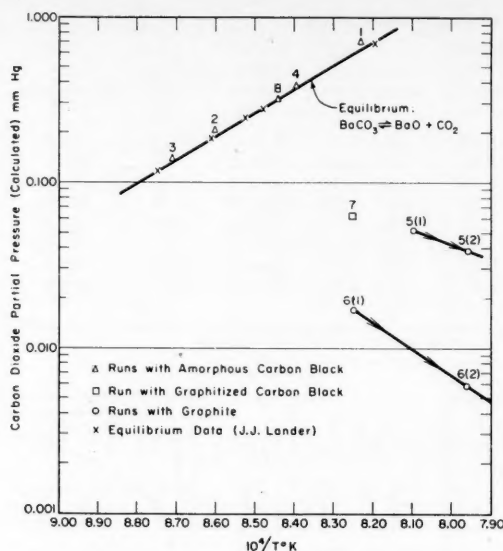
Fig. 3. Comparison of CO_2 partial pressures calculated from experimental data with those for equilibrium conditions.

a B.E.T. surface area of 12.7 sq. m./g. and gave an X-ray diffraction pattern which indicated that substantial graphitization had taken place. The second run (run 8) contained untreated Sterling FT carbon black which had a B.E.T. surface area of 15.7 sq. m./g. The results of the two runs are compared in Table 2.

The data show that, even though a higher pressure was maintained in run 8, the reaction temperature was lower and the time for complete reaction was much less than in run 7. It is apparent that use of a more amorphous carbon considerably accelerates the over-all reaction rate over that obtainable with graphitized carbon.

It is reasonable to assume that reaction 2 is the result of reactions 1 and 3 in series.

$$BaCO_3 \rightarrow BaO + CO_2 \qquad (3)$$
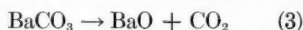
Consequently for finite reaction rates the measured pressure and reaction temperature may approximate those of equilibrium for both reactions 1 and 3, for either one of the reactions, or for neither. To compare the experimental conditions with equilibrium values the partial pressure of carbon dioxide that would be present if reaction 1 were occurring at equilibrium was calculated from the equilibrium constant for reaction 1 (4) and the experimental value for the total pressure. (Solid carbon is present at all times, and only carbon dioxide and carbon monoxide are present in the gas phase, carbon monoxide being overwhelmingly predominant.)

If reactions 1 and 3 both took place at equilibrium, the value of the carbon dioxide partial pressure thus calculated would equal that reported for equilibrium for reaction 3. If one or both of the reactions occurred under nonequilibrium conditions, the calculated pressure would be less than the equilibrium value. The comparison is made in Figure 3. It is seen that all the runs with carbon black occurred under equilibrium conditions; indeed the agreement with Lander's data is remarkably good. This means that the rate at which decomposition occurred was controlled completely by the rate of heat transfer to the reaction zone and was unaffected by mass transfer or chemical reaction kinetics. The time-temperature curves for all these runs were of the type shown in Figure 1, which is the same type as that obtained in an earlier study of the decomposition of cylinders of compacted calcium carbonate agglomerates of small particle size, a process which previously has been shown to occur under conditions approximating those of equilibrium (6).

For the runs with natural graphite the reaction temperature rose steadily, and the calculated carbon dioxide partial pressures are given in Figure 3 for two temperatures, when decomposition commenced and after 1 hr. (These are indicated by points 1 and 2 on Figures 2 and 3.) With partially graphitized carbon black a substantial fraction of the reaction occurred at a temperature of about 1,720° to 1,730°F., indicated by a square on Figure 3. It is evident that with graphite the rate of reaction 1 becomes much slower than with carbon black, and a comparison of runs 7 and 8 shows that this is not caused by gross particle size or total surface area of the particles but must rather reflect a much greater reactivity of carbon black surfaces over that of graphite.

Smith and Polley (7) recently have studied the rate of oxidation in air of Sterling FT carbon black before and after graphitization. After graphitizing at 2,700°C. they found it necessary to increase the reaction temperature to 800° to 900°C. to achieve the same rate of oxidation as that obtained with the original carbon black at 600°C. This change in chemical reactivity was related to the nature of the surface as revealed by physical adsorption and other methods; for example the carbon black particles were found to develop considerable porosity as indicated by a substantially increased area after reaction, while there was little change in area of the graphiticized carbon. On the other hand this moderate increase in area is insufficient to explain the enormous difference between the reactivities of the two carbons. Smith and Polley concluded that oxygen attack occurred preferentially at specific high-energy sites on the surface that may be edge-carbon atoms in the layer lattice, the number of these sites being greatly reduced by the heat treatment. The reactivity of the various forms of carbon to carbon dioxide in the present work exactly parallels the results they reported on comparative reactivity to oxygen and can be interpreted in the same way.

The extent to which this or any other decomposition reaction is controlled by heat transfer vs. some kinetic process is, of course, determined by many factors, the most important of which are the size of the mass being studied, the rate of heat transfer to the mass, the sizes of the individual particles, their compactness, and their reactivities. These studies show, for a few combinations, the relative importance of some of these variables in their effect on the over-all observed rate of reaction.

LITERATURE CITED

1. Askenasy, P., and R. Rose, *Z. anorg. u. allgem. Chem.*, **189**, 1, 10 (1930).
2. Bornemann, K., *U. S. Patent* 1,041,583 (1912).
3. Lander, J. J., *J. Amer. Chem. Soc.*, **73**, 5893 (1951).
4. Lewis, Bernard, and Guenther von Elbe, "Combustion, Flames and Explosions of Gases," p. 742, Academic Press, New York (1951).
5. Lieberson, N. G., and E. A. Oster, S.B. thesis, Mass. Inst. Technol., Cambridge (1951).
6. Satterfield, C. N., and Frank Feakes, *A.I.Ch.E. Journal*, **5**, 115 (1958).
7. Smith, W. R., and Polley, M. H., *J. Phys. Chem.*, **60**, 689 (1956).

Physical and Thermodynamic Properties of Trifluoromethane

Y. C. HOU and J. J. MARTIN

The University of Michigan, Ann Arbor, Michigan

Trifluoromethane is commonly called fluoroform after the corresponding chloro-compound, chloroform. It is also known in the trade as Freon-23 refrigerant, and has various low-temperature applications. For the design of refrigeration units using trifluoromethane it is essential that the physical and thermodynamic properties of the compound be available over the desired ranges. The reported data on trifluoromethane are far from complete and are in some discrepancy among different investigators (1, 2).

The present investigation included determinations of the vapor pressure, saturated liquid density, critical constants, pressure-volume-temperature behavior, and heat capacity at zero pressure over the desirable ranges.

The sample of trifluoromethane, supplied by E. I. du Pont de Nemours and Company, was obtained from middle cuts in repeated fractionation processes and was therefore of very high purity. According to du Pont's analysis (3) the liquid phase had a moisture content of 0.0005 wt. %, and the vapor of the cylinder contained 0.021 vol. % noncondensables in liquid nitrogen.

EXPERIMENTAL WORK

Vapor Pressure

The measurements were made by a static method over the range of 254° to 537°R., which is equivalent to a pressure range of 0.25 to 690 lb./sq. in. abs. Two sets of equipment were designed for different pressure ranges. The low-pressure equipment, shown in Figure 1, was used for pressures up to 1.5 atm. abs. and was mostly made of glass. The high-pressure equipment, made of steel, as shown in Figure 2, was used for pressure determinations from 1.5 atm. to the critical point (about 700 lb./sq. in.).

Trifluoromethane was condensed in the isoteniscope at low temperature after the system had been evacuated down to a pressure of a few microns of mercury with a combination of Hyvac and mercury diffusion pumps. Then the isoteniscope was kept at constant temperature by submerging it in a constant-temperature bath. The temperature of the bath was measured by a platinum-resistance thermometer which had been calibrated by the National Bureau of Standards. The pressure was measured when the equilibrium between the vapor and liquid trifluoromethane was reached. The low-

Fig. 1. Low–vapor-pressure equipment.

boiling impurities such as air were removed by letting a part of the liquid boil off. The equilibrium pressure was again measured, and the boil off and pressure measurement were repeated until a constant equilibrium pressure was obtained. This constant pressure was taken to be the vapor pressure of trifluoromethane at the temperature of the surrounding bath. The pressure in the low-pressure equipment was measured by a mercury manometer, and that in the high-pressure equipment was measured by pressure gauges. The gauges were calibrated against a Mansfield and Green dead-weight tester before and after each charge of trifluoromethane was made to the isoteniscope.

Saturated Liquid Density and Critical Temperature

The saturated liquid density of trifluoromethane was determined from 370° to 538°R. by the method described by Benning and McHarness (4). The technique employed in the measurement was to find the temperature at which the density of the saturated liquid matched that of a precalibrated density float.

The critical temperature was determined as the average temperature at which the liquid meniscus would appear and disappear; it was found to be 538.33°R. for trifluoromethane.

Pressure-Volume-Temperature Behavior

The pressure-volume-temperature studies were carried out as a series of approximately constant density measurements. The ranges of variables were from

400° to 710°R. in temperature, 1 to 60 lb./cu. ft. in density, and 50 to 2,000 lb./sq. in. abs. pressure. The equipment is sketched in Figure 3. Trifluoromethane was charged into the steel bomb after it had been evacuated to a pressure of a few microns of mercury. The vapor in the connecting line was recovered into the recovery tube by cooling the latter with liquid nitrogen. The weight of trifluoromethane charged was calculated from the weights of the storage bulb and recovery tube before and after the charging. The whole system was kept submerged in a large constant-tempera-
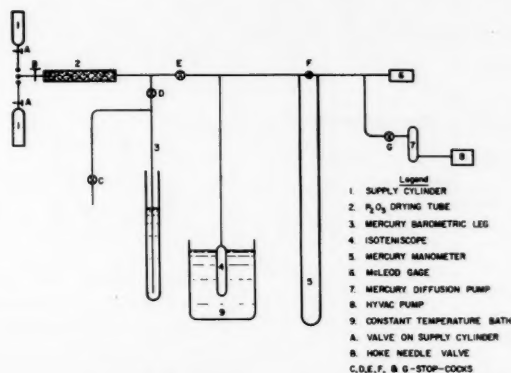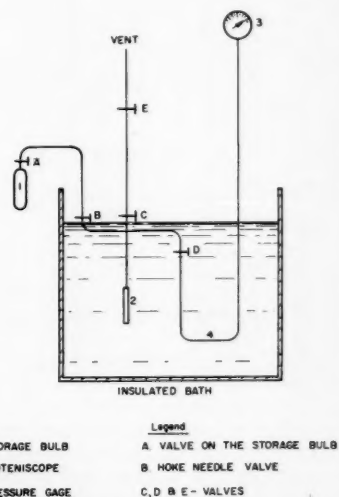

Fig. 2. High–vapor-pressure equipment.

Fig. 3. Pressure–volume-temperature equipment.
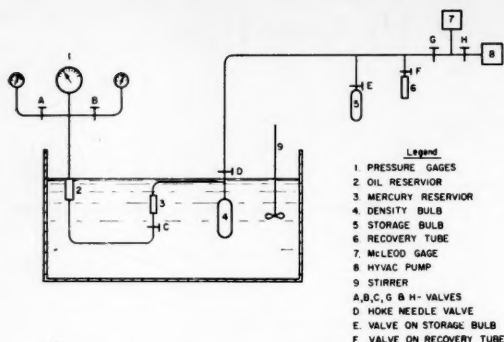

Fig. 4. Vapor-pressure data.

TABLE 1. EXPERIMENTAL VAPOR-PRESSURE DATA

Temperature, °R.	Pressure, lb./sq. in.
253.91	0.2370
263.36	0.4306
278.25	0.9863
285.17	1.4068
287.68	1.5904
287.71	1.5964
300.37	2.8620
304.96	3.4713
309.60	4.2195
309.84	4.2454
309.87	4.2591
317.88	5.8852
327.91	8.5437
337.24	11.7875
337.27	11.788
341.24	13.437
348.98	17.187
352.31	19.029
357.02	21.957
361.84	25.275
368.19	30.213
375.15	36.60
382.61	44.40
391.11	54.60
398.22	64.55
403.92	73.40
404.97	74.97
411.91	87.52
417.86	98.92
424.64	113.92
425.48	115.57
433.98	136.92
443.22	162.52
450.81	186.42
457.97	211.72
465.30	239.19
473.53	273.70
481.61	310.78
491.69	363.3
501.52	418.2
509.60	472.3
518.22	533.3
526.30	595.4
527.35	604.3
527.36	604.3
533.52	656.3
536.74	687.3

ture bath. The reading on the pressure gauge was taken when the system reached thermal equilibrium with the bath. The corresponding temperature of the bath was measured by the platinum-resist-

ance thermometer. A series of pressure and temperature measurements for one charging of trifluoromethane gives an approximate isometric. (If the bomb were perfectly rigid for all temperatures and pressures, a true isometric would be obtained.)

After the isometric had been completed, the trifluoromethane in the system was recovered and replaced in the storage bulb and recovery tube. From the weights of the bulb and the tube before and after the recovery the weight of trifluoromethane recovered from the system is known. The weight of trifluoromethane charged and recovered had to agree within a few hundredths of a per cent or the run was rejected because of apparent leakage. Two steel isometric bombs were used in this work. One, with a volume of about 600 cc., was used for higher density isometrics, and the other, with a volume of about 4,100 cc., was used for lower density runs when the pressure did not exceed 300 lb./sq. in. The volume of each bomb was calibrated carefully by weighing when evacuated and when filled with distilled water. Pressure gauges with suitable ranges were used for measuring all pressures. Each gauge was calibrated against the Mansfield and Green dead-weight gauge tester before and after each isometric run.

RESULTS AND CORRELATIONS

Vapor Pressure

The data are plotted as $\ln P$ vs. $1/T$ in Figure 4 and tabulated in Table 1. The curve shows a definite S shape as emphasized by Thodos (5). For this reason the simple Clausius-Clapeyron equation, the Antoine equation (6), or even the Kirchoff-Rankine-Dupré equation (7, 8) would not give satisfactory representations of the data, since the inflection of the curve is not predicted by these algebraic forms. It was concluded that at least one more term must be added to modify the Kirchoff-Rankine-
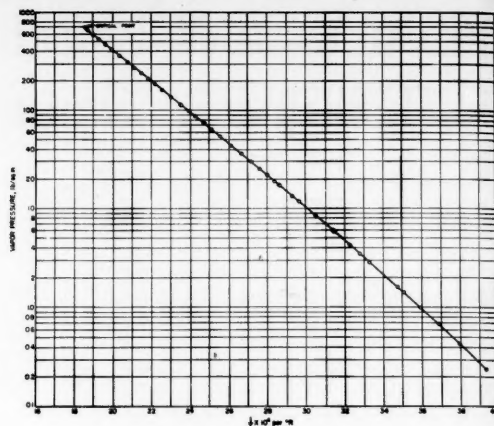
TABLE 2. EXPERIMENTAL SATURATED LIQUID-DENSITY DATA

Temperature, °R.	d_1, lb./cu. ft.
370.79	86.587
454.14	73.037
466.70	70.317
480.73	67.195
*498.1	62.285
512.77	57.429
529.76	49.322
*529.8	49.233
*533.1	46.459
*534.9	44.172
536.69	41.827
537.60	39.763

*Obtained from the extrapolation of isometric curves to saturation temperatures.

Dupré equation to take care of the reversal of the curvature. The following equation:

$$\ln P = 757.3398770 - \frac{18311.92765}{T}$$
$$- 144.5142304 \ln T$$
$$+ 0.5574904317\, T \qquad (1)$$
$$- 4.900054254 \times 10^{-4} T^2$$
$$+ 2.17247877 \times 10^{-7} T^3$$

with P in pounds per square inch absolute and T in degrees Rankine satisfactorily represents both the data and the general characteristics of the vapor-pressure behavior over this wide range. The average deviation between the equation and the data is 0.19%, and the maximum deviation is 0.58% and occurs at the lowest pressure.

Saturated Liquid Density and Critical Constants

The data on saturated liquid densities were corrected for thermal expansion of the density float. The data are presented in Table 2 and plotted in Figure 5 as
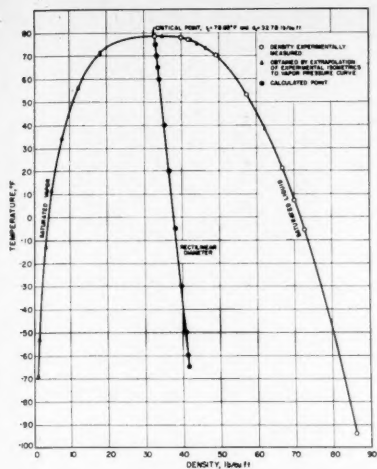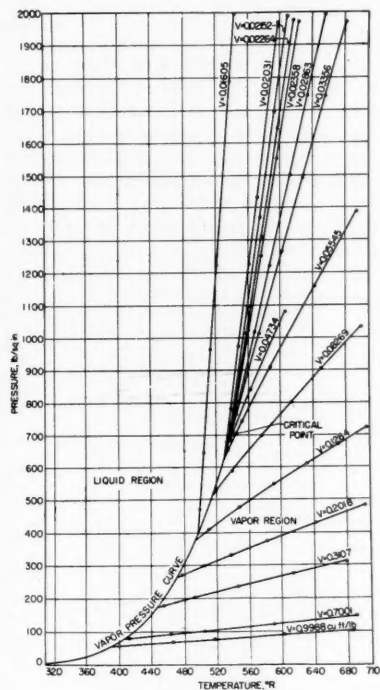
Fig. 5. Saturated liquid and vapor density plot.

Fig. 6. Pressure–volume–temperature data for trifluoromethane.

Fig. 7. Compressibility factor for trifluoromethane.

liquid density d_l vs. temperature T. Different types of equations were studied for representing the data. The possibility of equations with density expressed as functions containing only integer powers of temperature was ruled out because such forms cannot give zero slope at the critical point $(dT/dd_l = 0)$, as do the experimental data.

A combination of the equations

$$\frac{d_l + d_v}{2\,d_c} = 1 + \frac{3}{4}\left(1 - \frac{T}{T_c}\right) \qquad (2)$$

and

$$\frac{d_l - d_v}{d_c} = \frac{7}{2}\left(1 - \frac{T}{T_c}\right)^{\frac{1}{3}} \qquad (3)$$

given by Guggenheim (9) yields an equation for the saturated liquid density of the form

$$d_l = d_c + a\left(1 - \frac{T}{T_c}\right)^{\frac{1}{3}} \qquad (4)$$
$$+ b\left(1 - \frac{T}{T_c}\right)$$

With a parametric power of n replacing $\frac{1}{3}$ in the second term, the correlation was not significantly improved. One way of generalizing Equation (4) is to consider d_l as a function of $[1 - (T/T_c)]^{n/3}$,

$$d_l = \phi\left(1 - \frac{T}{T_c}\right)^{n/3} \qquad (5)$$

or in a power series form,

$$d_l = \sum_n a_n\left(1 - \frac{T}{T_c}\right)^{n/3} \qquad (6)$$

It is readily seen that a_0 must be identical with the critical density. Equation (4) may be considered as a sort of special case of Equation (6) obtained by setting all the coefficients, except a_0, a_1, and a_3, equal to zero. Testing the data showed that equations with a_0, a_1, a_3, and any

other two a's (all the rest of the a's were put equal to zero) gave correlations with almost equally high degrees of precision. It was decided that only a_0, a_1, a_2, a_3, and a_4 would be used. Therefore the saturated liquid density data were finally fitted by the equation

$$d_l = 32.7758$$
$$+ 63.37784\left(1 - \frac{T}{T_c}\right)^{1/3}$$
$$- 25.30533\left(1 - \frac{T}{T_c}\right)^{2/3}$$
$$+ 144.16182\left(1 - \frac{T}{T_c}\right) \qquad (7)$$
$$- 106.13280\left(1 - \frac{T}{T_c}\right)^{4/3}$$

lb. mass/cu. ft.

Equation (7) represents the data with an average deviation of 0.24% and a maximum deviation of 0.67%. The use of more terms after a_4 in Equation (6) may be justified for more precise work.

The critical temperature of trifluoromethane was found to be 538.33°R. Inserting this value into the vapor-pressure equation (1), one calculates the critical pressure as 701.4 lb./sq. in. abs. The critical density was determined

Table 3. Experimental PVT Data

Volume, cu. ft./lb.	Temperature, °R.	Pressure, lb./sq. in.
0.99879	400.10	55.61
	466.40	67.20
	517.66	76.30
	602.60	90.25
	687.91	104.17
0.70008	412.49	79.45
	463.35	92.46
	504.59	103.13
	590.22	123.92
	691.63	148.08
0.31066	455.44	179.78
	493.07	203.82
	546.04	236.26
	614.02	276.15
	679.54	313.09
0.20158	479.89	270.8
	505.55	298.0
	536.95	330.7
	538.33	332.2
	582.52	375.2
	642.47	430.3
	703.64	484.3
0.12836	510.78	409.0
	548.42	476.9
	591.05	548.0
	632.09	612.2
	670.58	672.5
	705.91	725.5
0.082677	519.08	525.8
	539.42	589.9
	576.68	699.2
	613.11	802.0
	650.58	906.1
	700.06	1036.5
0.055465	534.86	654.3
	552.38	742.7
	587.93	910.0
	643.00	1162.6
	694.80	1392.5
0.047352*	537.68	684.3
	563.06	834.1
	606.44	1082.2
0.033604	545.67	764.1
	574.22	1014.7
	602.73	1268.9
	628.97	1496.4
	657.22	1748.6
	583.05	1973.1
0.028644	545.69	775.0
	568.67	1019.0
	587.21	1224.4
	613.06	1504.1
	634.82	1749.9
	656.98	1995.4
0.023589	538.33	705.8
	561.00	1024.3
	576.86	1254.5
	596.89	1555.7
	624.23	1974.3
0.022646	536.71	693.2
	538.33	715.7
	558.08	1014.3
	577.12	1313.6
	597.56	1649.1
	617.85	1978.2
0.021531	536.54	706.6
	538.33	736.6
	559.85	1097.5
	575.60	1374.6
	593.64	1698.1
	610.16	1991.0
0.020316	532.91	680.8
	538.33	781.5
	548.51	974.8
	561.74	1229.1

Table 3. (Continued)

Volume, cu. ft./lb.	Temperature, °R.	Pressure, lb./sq. in.
	572.13	1435.8
	598.68	1971.5
0.016045	500.02	467.8
	505.25	645.3
	514.58	965.4
	522.15	1226.6
	538.33	1793.4
	544.27	1997.9

*There was a leakage of trifluoromethane during the run.

from the rectilinear diagram described in the following section.

Pressure-Volume-Temperature Behavior

The data were corrected for the expansion of the density bombs, the mercury, and the oil in the whole equipment and then adjusted to true isometrics graphically with the aid of an approximate pressure-volume plot. The adjusted data were tabulated (Table 3) and then plotted as isometric curves in the pressure-temperature plane in Figure 6 and as compressibility curves in Figure 7. The isometric curves were extrapolated to intersect the vapor-pressure curve on the pressure-temperature diagram. The points of intersection gave the saturation temperatures for various vapor densities. These saturated vapor densities together with the saturated liquid density were plotted as temperature vs. density in Figure 5. The rectilinear diameter (average of saturated liquid and vapor densities) was constructed and appeared to be straight within the precision of the data. The critical density was determined from this diagram as 32.776 lb./cu. ft., with no greater precision than 0.05 lb./cu. ft.

The adjusted PVT data were then correlated with the generalized equation of state developed by Martin and Hou (10). A slight modification was made to the original equation by adding one more condition to improve it in the high-density liquid region. This was done by including a C_5 term and recognizing the fact that the isometric curve of trifluoromethane is practically straight at about twice the critical density (Figure 6). It was found for trifluoromethane that the condition of $(d^2P/dT^2)_V = 0$ at $V = V_c/2.1$ gave the best representation of the data. The equation of state has the form

$$P = \frac{RT}{V - b}$$

$$+ \frac{A_2 + B_2T + C_2e^{-(kT/T_c)}}{(V - b)^2}$$

$$+ \frac{A_3 + B_3T + C_3e^{-(kT/T_c)}}{(V - b)^3} \qquad (8)$$

$$+ \frac{A_4}{(V - b)^4}$$

Table 4. Zero Pressure Heat Capacity

Temperature, °R.	C_p^0
250	8.636
300	9.171
400	10.424
500	11.778
600	13.144
700	14.447
800	15.641

Table 5. Comparison of Critical Constants

	Critical temperature, °R.	Critical Pressure, lb./sq. in.	Critical density, lb./cu. ft.
This investigation	538.33	701.42	32.78
Ruff et al.	550.8	691	32.2
Seger	518.7	—	32.21

$$+ \frac{B_5T + C_5e^{-(kT/T_c)}}{(V - b)^5}$$

Since sufficient data were taken in this investigation, the values estimated from the generalized correlations of certain parameters, β, T', and $m = -MP_c/T_c$, were slightly adjusted, as described in Part III of the original paper (10), to give a better representation. The final value of the constants in the equation of state are as follows:

R = gas law constant

$\quad = 0.153266$ (lb.-force)(cu. ft.)

$\qquad$ /(lb.-mass)(°R.)(sq. in.)

$A_2 = -5.016053028$

$B_2 = 0.00310516248$

$C_2 = -130.8703305$

$A_3 = 0.09781899057$

$B_3 = -0.380613864 \times 10^{-4}$

$C_3 = 3.53359637$

$A_4 = -0.1094517281 \times 10^{-2}$

$B_5 = 1.112366387 \times 10^{-8}$

$C_5 = -0.000182469146$

$b = 0.00579112510$

These constants result from using values of the parameters as follows: $\beta = 3.15$, $T' = 0.815\ T_c$, $M = 7.65$, and $T_B = 1,256$°R., with P in pounds per square inch absolute and V in cubic feet per pound mass.

The equation was developed for densities up to about 1.5 times the critical density. Up to this density the average deviation between the equation and the data is only 0.45%, but right at this density the deviation is as great as 4.14%.

Heat Capacity at Zero Pressure

The heat capacities of trifluoromethane at zero pressure were calculated for the

range of 250° to 800°R. from the spectroscopic data reported in the literature. Among the various sets of assignments of fundamental vibrational frequencies given by different investigators (11, to 17), the infrared frequencies reported by Plyler and Benedict (15) with W_2 given by Edgell and May (17) were adopted. The final assignment of fundamental frequencies is as follows:

$$W_1 = 3,031$$
$$W_2 = 1,137$$
$$W_3 = 700$$
$$W_4 = W_7 = 1,372$$
$$W_5 = W_8 = 1,152$$
$$W_6 = W_9 = 507$$

The method of evaluating the harmonic vibrational contribution by the use of statistical mechanics is outlined by Wenner (18). The anharmonic contribution for this compound was arbitrarily estimated to be 0.75% of the harmonic contribution at 800°R. and 0.3% at 250°R. and was assumed to vary linearly with temperature in this range. The zero-pressure heat capacity at any temperature is the sum of the contributions due to harmonic and anharmonic vibrations and to translation and rotation. The results of adding the various contributions were represented by the equation

$$C_p^0 = 7.327 - 529.47 \times 10^{-6}T$$
$$+ 27.35341 \times 10^{-6}T^2 \qquad (9)$$
$$- 0.017189 \times 10^{-6}T^3 \text{ B.t.u.}$$
$$/(\text{lb.-mole})(°R.)$$

where T is in °R.

The cubic form of the equation was found desirable because the temperature range included the region where the heat-capacity curve shows a reversal of curvature. Table 4 gives a summary of the calculated heat capacities, which are represented by Equation (9) within a maximum deviation of 0.3%.

DISCUSSION

The data obtained in this investigation do not agree too well with those reported by different investigators (1, 2, 19); however the disagreement between the earlier workers themselves is even greater. The purity of the trifluoromethane sample could be the factor that accounts for most of the discrepancies between all investigators.

The vapor pressures in the low-temperature region showed the slope of the curve of ln P vs. $1/T$ to be numerically smaller than that given by Ruff et al. (1). As a result the normal boiling point given by Ruff et al. is −84.4°C. instead of −81.8°C. from this investigation. Seger (2) estimated the normal boiling point to be −90°C.

The critical constants are compared with those of the other investigators in Table 5. It is apparent that the most significant discrepancy is in the critical temperature.

The internal consistency of the PVT data taken in this investigation is shown clearly by the smoothness of the curves in Figures 6 and 7. Unfortunately there are no published data with which to compare the PVT data taken in this work.

The statistical mechanical method of calculation of the heat capacity at zero pressure from the infrared and Raman frequencies is generally very satisfactory, if the fundamentals can be identified and the anharmonic effect is negligible. The assumptions made in this investigation on anharmonic contributions can be tested only when accurate calorimetric data are taken on the heat capacity. On the basis of other compounds it is believed that the final values of the heat capacity are probably not more than ½% in error.

The properties needed for evaluation of thermodynamic functions such as enthalpy and entropy have been determined in this investigation and represented in analytical form. The heat of vaporization can be calculated by using the Clapeyron equation with the vapor pressure and saturated liquid and vapor densities. The changes of enthalpy and entropy between any two gas states can be evaluated from the following formulas, derived for these thermodynamic properties:

$$\Delta H = \int_{T_1}^{T_2} C_V^0 \, dT + \left[PV + \frac{A_2 + (1 + kT_r)C_2 e^{-kT_r}}{V - b} \right.$$
$$\left. + \frac{A_3 + (1 + kT_r)C_3 e^{-kT_r}}{2(V - b)^2} + \frac{A_4}{3(V - b)^3} + \frac{(1 + kT_r)C_5 e^{-kT_r}}{4(V - b)^4} \right]_{V_1, T_1}^{V_2, T_2} \qquad (10)$$

$$\Delta S = \int_{T_1}^{T_2} \frac{C_V^0}{T} \, dT + \left[R \ln (V - b) - \frac{B_2}{V - b} - \frac{B_3}{2(V - b)^2} \right.$$
$$\left. - \frac{B_5}{4(V - b)^4} + \left\{ \frac{C_2}{V - b} + \frac{C_2}{2(V - b)^2} + \frac{C_5}{4(V - b)^4} \right\} \frac{k}{T_c} e^{-kT_r} \right]_{V_1, T_1}^{V_2, T_2} \qquad (11)$$

These equations require only the PVT relation and the heat capacity equation. With a modern automatic calculating machine a table of enthalpy and entropy values can therefore be easily evaluated from the information presented here.

NOTATION

d_v = density of saturated vapor
d_c = critical density
k = 5.475
A, B, C, a_n, b = empirical constants
T_r = T/T_c
C_p^0 = $C_V^0 + R$ = constant-pressure heat capacity of ideal gas
C_V^0 = constant-volume heat capacity of ideal gas

LITERATURE CITED

1. Ruff, O., O. Bretschneider, W. Luchsinger, and G. Miltschitsky, *Ber. deut. chem. Ges.*, 69, 299 (1936).
2. Seger, G., *Die Chemie*, 55, 58 (1942).
3. McHarness, R. C., private communication.
4. Benning, A. F., and R. C. McHarness, *Ind. Eng. Chem.*, 32, 814 (1940).
5. Thodos, George, *Ind. Eng. Chem.*, 42, 1514 (August, 1950).
6. Antoine, C., *Compt. rend.*, 107, 681, 836, 1143 (1888).
7. Kirchhoff, G., *Ann. Physik*, 104, 612 (1858).
8. Rankine, W. J. M., *Edinburgh New Phil. J.*, 94, 235 (1849).
9. Guggenheim, E. A., "Thermodynamics," 2 ed., Interscience Publishers, New York (1950).
10. Martin, J. J., and Y. C. Hou, *A.I.Ch.E. Journal*, 1, No. 2, 142 (June, 1955).
11. Glockler, G., and W. F. Edgell, *J. Chem. Phys.*, 9, No. 3, 224 (March, 1941).
12. Rank, D. H., E. R. Schull, and E. L. Pace, *J. Chem. Phys.*, 18, No. 6, 885 (June, 1950).
13. Claassen, H. H., and J. R. Nielsen, *J. Opt. Soc. Amer.*, 43, No. 5, 352 (May, 1953).
14. Bernstein, H. J., and G. Herzberg, *J. Chem. Phys.*, 16, No. 1, 30 (January, 1948).
15. Plyler, E. K., and W. S. Benedict, *J. Research Natl. Bur. Standards*, 47, No. 3, 202 (September, 1951).
16. Rix, H. D., *J. Chem. Phys.*, 21, No. 6, 1077 (June, 1953).
17. Edgell, W. F., and C. May, *J. Chem. Phys.*, 21, No. 10, 1901 (October, 1953).
18. Wenner, R. R., "Thermochemical Calculations," 1 ed., McGraw-Hill, New York (1941).

Theoretical Explanation of Heat Transfer in Laminar Region of Bingham Fluid

E. HIRAI

Kanazawa University, Ishikawa Pref., Japan

The purpose of this study is to derive theoretically the average temperature difference in a Bingham fluid. Bingham flow is quite different from viscous flow and consists of two patterns, plug and nonplug flow. Figure 1 shows a schematic diagram.

The theoretical solution of the nonplug flow was computed by employing Graetz's *(2)*, Nusselt's *(7)* and the author's *(5)* solutions. Since temperature in plug flow varies along the y axis, Stokes's findings *(6 and 11)* were employed. Calculations were made at relative plug radius = 0.5.

THEORETICAL SOLUTION OF HEAT TRANSFER OF BINGHAM FLOW

Theoretical Solution

In the case of laminar flow in the pipes the basic differential equation for heat transfer is expressed by

$$u_y \frac{\partial t}{\partial y} = k\left(\frac{\partial^2 t}{\partial r^2} + \frac{1}{r}\frac{\partial t}{\partial r}\right) \quad (1.1)$$

where

$$k \equiv \lambda/C_p\rho \quad (1.2)$$

It is assumed that physical constants, such as specific heat and thermal conductivity, are constant and that wall temperature t_w is constant regardless of position along the y axis.

In well-developed Bingham flow the velocity distribution is expressed by Oyama and Ito *(8)* as follows: In nonplug flow

$$u_y = \frac{(1 - a)^2}{2a\alpha}\bar{u}\left\{1 - \left(\frac{r - r_p}{R - r_p}\right)^2\right\} \quad (1.3)$$

In plug part

$$u_{ap} = (1 - a)^2\bar{u}/2a\alpha \quad (1.4)$$

Velocity distribution and plug radius are assumed to be constant with temperature changes.

In nonplug flow θ is assumed to be

$$\theta = (t - t_w)/(t_1 - t_w) \quad (1.5)$$

From Equations (1.1), (1.3), and (1.5)

$$\frac{(1 - a)^2}{2a\alpha}\bar{u}\left\{1 - \left(\frac{r - r_p}{R - r_p}\right)^2\right\}\frac{\partial\theta}{\partial y} = k\left(\frac{\partial^2\theta}{\partial r^2} + \frac{1}{r}\frac{\partial\theta}{\partial r}\right) \quad (1.6)$$

Boundary conditions are

$$\theta = 1,\ (t = t_1) \quad \text{at} \quad y = 0$$
$$\theta = 0,\ (t = t_w) \quad \text{at} \quad r = R \quad (1.7)$$

In Equation (1.6)

$$S = 2a\alpha k/(1 - a)^2\bar{u} \quad (1.8)$$

The particular solution of Equation (1.6) is obtained by the separation of variables method:

$$\theta = A\,\exp\left[-Sy/b^2\right]\cdot P \quad (1.9)$$

Accordingly Equation (1.6) becomes:

$$\frac{d^2P}{d\mu^2} + \frac{1}{\mu}\frac{dP}{d\mu} + \left[1 - \left(\frac{\mu - \xi}{\beta - \xi}\right)^2\right]P = 0 \quad (1.10)$$

where

$$\left.\begin{array}{c} r/b = \mu \\ R/b = \beta \\ r_P/b = \xi \end{array}\right\} \quad (1.11)$$

For the particular solution of Equation (1.10)

$$P = \sum_{m=0}^{\infty} B_m\mu^m \quad (1.12)$$

By substituting Equation (1.12) in Equation (1.10) one can determine B_m as

$$B_0 = 1$$
$$B_1 = 0$$
$$B_2 = \frac{-1}{4}\left\{\frac{(1 - a)^2 - a^2}{(1 - a)^2}\right\} \quad (1.13)$$
$$B_m = \frac{-1}{m^2}\left[\left\{\frac{(1 - a)^2 - a^2}{(1 - a)^2}\right\}\cdot B_{m-2} + \frac{2a}{(1 - a)^2\beta}B_{m-3} - \frac{1}{(1 - a)^2\beta^2}B_{m-4}\right]$$

From Equation (1.11)

$$r_p/R = \xi/\beta = a \quad (1.14)$$

At the pipe wall $r = R$, from Equation (1.1) $\mu = \beta$; from Equation (1.7) the boundary condition is $\theta = 0$. Thus Equation (1.12) must be

$$P(\beta) = \sum_{m=0}^{\infty} B_m\beta^m = 0 \quad (1.15)$$

The values of $\beta_0, \beta_1 \cdots$ are the roots of Equation $P(\beta) = 0$. Since $\beta_{01}, \beta_1 \cdots$ are changed with relative plug radius a, the following calculation was based on $a = 0.5$. The solution of Equation (1.6) would be

$$\theta = \sum_{m=0}^{\infty} A_m\,\exp\left[-\frac{S\beta_m^2 y}{R^2}\right]\cdot P_m(r/R) \quad (1.16)$$

P_m can be obtained from the following equation, since one knows that $\mu = \zeta\beta$ from Equation (1.11).

$$P_m = \sum_{m=0}^{\infty} B_m(\beta_m) \times (\zeta\beta_m)^m \quad (1.17)$$

From Equation (1.7) $y = 0$, and $\theta = 1$

$$1 = \sum_{m=0}^{\infty} A_mP_m \quad (1.18)$$

From Equation (1.10)

$$\int_a^1 P_m\zeta\left[1 - \left(\frac{\zeta - a}{1 - a}\right)^2\right]d\zeta = -\frac{1}{\beta_m^2}\left[\zeta\frac{dP_m}{d\zeta}\right]_{\zeta=a}^{\zeta=1} \quad (1.19)$$

Therefore from Equations (1.18) and (1.19)

$$A_m = \frac{-\dfrac{1}{\beta_m^2}\left[\zeta \dfrac{dP_m}{d\zeta}\right]_{\zeta=a}^{\zeta=1}}{\displaystyle\int_a^1 P_m^2 \zeta\left[1 - \left(\frac{\zeta - a}{1 - a}\right)^2\right] d\zeta} \qquad (1.20)$$

A_m can be defined from the preceding equation. If temperature t_{rp} at r_p is expressed as θ_{rp}

$$\theta_{rp} = \sum_{m=0}^{\infty} A_m e^{-(s\beta_m^2/R^2)y} P_m(a) \qquad (1.21)$$

In the case of plug flow, from Equations (1.1) and (1.4),

$$\frac{(1-a)^2}{2a\alpha}\bar{u}\frac{\partial t_p}{\partial y}$$
$$= k\left(\frac{\partial^2 t_p}{\partial y^2} + \frac{1}{r}\frac{\partial t_p}{\partial r}\right) \qquad (1.22)$$

Since velocity distribution is independent of radius, the solution of Equation (1.22) is expressed as a Bessel function. The temperature at $r = r_p$ is not constant but varies along the y axis as shown in Equation (1.21). Equation (1.21) can be solved by Stokes's method (6 and 11). If θ_p is expressed as

$$\theta_p = (t_p - t_w)/(t_1 - t_w) \qquad (1.23)$$

Equation (1.22) is expressed as

$$\frac{\partial \theta_p}{\partial y} = S\left(\frac{\partial^2 \theta_p}{\partial y^2} + \frac{1}{r}\frac{\partial \theta_p}{\partial r}\right) \qquad (1.24)$$

Boundary conditions are

$\theta_p = 1, (t_p = t_1)$ at $y = 0$

$\theta_p = F(y)$

$$= \sum_{m=0}^{\infty} A_m e^{-(s\beta_m^2/R^2)y} P_m(a) \qquad (1.25)$$

at $r = r_p$

$(\partial\theta/\partial r)_{r=r_p}$

$= (\partial\theta_p/\partial r)_{r=r_p}$

at $r = r_p$

if

$$\theta_p = \frac{2}{r_p^2}\sum_{s=1}^{\infty}\frac{Y_s J_0(\psi_s \cdot r/r_p)}{[J_1(\psi_s)]^2} \qquad (1.26)$$

where

$$Y_s = \int_0^{r_p}\theta_p(r, y)J_0$$
$$\cdot\left(\psi_s\frac{r}{r_p}\right)r\,dr \qquad (1.27)$$

ψ_s is the sth root of the Bessel function $J_0(\psi) = 0$. From Equations (1.24) and (1.25)

$$\frac{\partial^2\theta_p}{\partial r^2} + \frac{1}{r}\frac{\partial\theta_p}{\partial r}$$

$$= \frac{2}{r_p^2}\sum_{s=1}^{\infty}\frac{J_0(\psi_s \cdot r/r_p)}{[J_1(\psi_s)]^2}$$
$$\cdot\int_0^{r_p}J_0\left(\psi_s\frac{r}{r_p}\right)\frac{\partial}{\partial r} \qquad (1.28)$$
$$\cdot\left\{r\frac{\partial\theta_p(r, y)}{\partial r}\right\}dr$$

$$= \frac{2}{r_p^2}\sum_{s=1}^{\infty}\frac{J_0(\psi_s \cdot r/r_p)}{[J_1(\psi_s)]^2}$$
$$\cdot\left[\psi_s F(y)J_1(\psi_s) - \frac{\psi_s^2}{r_p^2}Y_s\right]$$

Also

$$\frac{\partial\theta_p}{\partial y} = \frac{2}{r_p^2}\sum_{s=1}^{\infty}\frac{J_0(\psi_s \cdot r/r_p)}{[J_1(\psi_s)]^2}\frac{dY_s}{dy} \qquad (1.29)$$

From Equations (1.24), (1.28), and (1.29),

$$\frac{dY_s}{dy} + \frac{\psi_s^2}{r_p^2}SY_s$$
$$= S\psi_s F(y)J_1(\psi_s) \qquad (1.30)$$

This equation can be solved easily. The result is

$$Y_s = S\psi_s J_1(\psi_s)$$
$$\cdot\int_0^y F(v)e^{-(s\psi_s^2/r_p^2)(y-v)} \qquad (1.31)$$
$$\cdot dv + Ce^{-(s\psi_s^2/r_p^2)y}$$

where C in Equation (1.31) is a constant

of integration and can be defined when Y_s is fixed at $y = 0$. From boundary conditions $y = 0$ and $\theta_p = 1$ Equation (1.26) must be

$$(Y_s)_{y=0} = \frac{r_p^2}{\psi_s}J_1(\psi_s) \qquad (1.32)$$

Therefore Equation (1.31) is

$$Y_s = S\psi_s J_1(\psi_s)$$
$$\cdot\int_0^y F(v)e^{-(s\psi_s^2/r_p^2)(y-v)}\,dv \qquad (1.33)$$
$$+ \frac{r_p^2}{\psi_s}J_1(\psi_s)e^{-(s\psi_s^2/r_p^2)y}$$

From these equations Equation (1.26) becomes

$$\theta_p = 2\sum_{s=1}^{\infty}\frac{J_0(\psi_s \cdot r/r_p)}{\psi_s J_1(\psi_s)}e^{-(S\psi_s^2/r_p^2)y}$$
$$+ \frac{2S}{r_p^2}\sum_{s=1}^{\infty}\frac{\psi_s J_0(\psi_s \cdot r/r_p)}{J_1(\psi_s)} \qquad (1.34)$$
$$\times \int_0^y F(v)e^{-(s\psi_s^2/r_p^2)(y-v)}\,dv$$

From boundary conditions (1.25)

$$F(v) = \sum_{m=0}^{\infty}A_m e^{-(s\beta_m^2/R^2)v}P_m(a) \qquad (1.35)$$

Substituting Equation (1.35) in Equation (1.34) one can obtain

$$\theta_p = 2\sum_{s=1}^{\infty}\frac{J_0(\psi_s \cdot r/r_p)}{\psi_s J_1(\psi_s)}e^{-(s\psi_s^2/r_p^2)y} + \sum_{m=0}^{\infty}A_m e^{-(s\beta_m^2/R^2)y}P_m(a)$$
$$+ 2\sum_{m=0}^{\infty}\sum_{s=1}^{\infty}\frac{A_m P_m(a)a^2\beta_m^2 J_0(\psi_s \cdot r/r_p)}{(\psi_s^2 - a^2\beta_m^2)\psi_s J_1(\psi_s)}e^{-(s\beta_m^2/R^2)y} \qquad (1.36)$$
$$- 2\sum_{m=0}^{\infty}\sum_{s=1}^{\infty}\frac{A_m P_m(a)\psi_s J_0(\psi_s \cdot r/r_p)}{(\psi_s^2 - a^2\beta_m^2)J_1(\psi_s)}e^{-(s\psi_s^2/r_p^2)y}$$

The temperature at any radius in the plug flow can be obtained from this equation.

From the last condition in Equation (1.25)

$$\sum_{m=0}^{\infty}A_m e^{-(s\beta_m^2/R^2)y}\left(\zeta\frac{\partial P_m}{\partial\zeta}\right)_{\zeta=a} = -2\sum_{s=1}^{\infty}e^{-(s\psi_s^2/r_p^2)y}$$
$$- 2\sum_{m=0}^{\infty}\sum_{s=1}^{\infty}\frac{A_m P_m(a)a^2\beta_m^2}{\psi_s^2 - a^2\beta_m^2}e^{-(s\beta_m^2/R^2)y} \qquad (1.37)$$
$$+ 2\sum_{m=0}^{\infty}\sum_{s=1}^{\infty}\frac{A_m P_m(a)\psi_s^2}{\psi_s^2 - a^2\beta_m^2}e^{-(s\psi_s^2/r_p^2)y}$$

To obtain the heat transfer coefficient the average temperature should be known. If the average temperature t_M at $y = y$ is expressed as θ_M,

$$\theta_M = (t_M - t_w)/(t_1 - t_w) \qquad (1.38)$$

The small average temperature is

$$\theta_M = \frac{\int_0^{r_p} 2\pi r u_{vp}\theta_p\, dr + \int_{r_p}^{R} 2\pi r u_v \theta\, dr}{\pi R^2 \bar{u}}$$

$$= -2\frac{(1-a)^2}{2a\alpha}\sum_{m=0}^{\infty} A_m e^{-(s\beta_m^2/R^2)y}\frac{1}{\beta_m^2}\left[\zeta\frac{dP_m}{d\zeta}\right]_{\zeta=a}^{\zeta=1}$$

$$+ 4a^2\frac{(1-a)^2}{2a\alpha}\left[\sum_{s=1}^{\infty}\frac{e^{-(s\psi_s^2/r_p^2)y}}{\psi_s^2}\right. \tag{1.39}$$

$$+ \sum_{m=0}^{\infty}\sum_{s=1}^{\infty}\frac{A_m P_m(a)}{\psi_s^2 - a^2\beta_m^2}e^{-(s\beta_m^2/R^2)y}$$

$$\left. - \sum_{m=0}^{\infty}\sum_{s=1}^{\infty}\frac{A_m P_m(a)}{\psi_s^2 - a^2\beta_m^2}e^{-(s\psi_s^2/r_p^2)y}\right]$$

The relationship between the local heat transfer rate Q_y at $y = y$ and the local coefficient of heat transfer h_y is expressed as

$$Q_y = -\lambda(t_1 - t_w)\left(\frac{\partial\theta}{\partial\gamma}\right)_{r=R} \tag{1.40}$$

$$= (t_1 - t_w)h y\theta_M$$

Therefore h_y is expressed as

$$h_y = \frac{-\dfrac{\lambda}{R}\sum_{m=0}^{\infty} A_m e^{-(s\beta_m^2/R^2)y}\left(\zeta\dfrac{\partial P_m}{\partial\zeta}\right)_{\zeta=1}}{\theta_M} \tag{1.41}$$

If the same solution as in laminar flow of pseudoplastic fluid (5) is applied, the average coefficient of heat transfer h_M is expressed as

$$h_M = -\frac{2\lambda}{Dl}\int_0^l \frac{\sum_{m=0}^{\infty} A_m e^{-(s\beta_m^2/R^2)y}\left(\zeta\dfrac{\partial P_m}{\partial\zeta}\right)_{\zeta=1}}{\theta_M}\, dy \tag{1.42}$$

In Equation (1.39) θ_M is a function of y, and P_m is a function of ζ independent of y; that is $(\partial P_m/\partial\zeta = dP_m/d\zeta)$. From Equation (1.37) the following equation can be obtained:

$$\frac{d\theta_M}{dy} = 2\frac{k}{\bar{u}R^2}\sum_{m=0}^{\infty} A_m e^{-(s\beta_m^2/R^2)y}$$
$$\cdot\left(\zeta\frac{dP_m}{d\zeta}\right)_{\zeta=1}$$

Therefore Equation (1.42) becomes

$$\frac{h_M D}{\lambda} = \frac{1}{4}\left(\frac{\bar{u}D}{kl}\right)\ln\left(\frac{1}{\theta_{Ml}}\right)$$
$$= \frac{1}{\pi}\left(\frac{WC_p}{\lambda l}\right)\ln\left(\frac{1}{\theta_{Ml}}\right) \tag{1.43}$$

If at $y = 1$, the average temperatures t_M and θ_M in Equation (1.38) are expressed as t_{Ml} and θ_{Ml}, respectively,

$$\theta_{Ml} = \frac{-(1-a)^2}{2a\alpha}$$

$$\cdot\sum_{m=0}^{\infty} A_m e^{-(s\beta_m^2/R^2)l}$$

$$\cdot\frac{1}{\beta_m^2}\left[\zeta\frac{dP_m}{d\zeta}\right]_{\zeta=a}^{\zeta=1}$$

$$+ 4a^2\frac{(1-a)^2}{2a\alpha} \tag{1.44}$$

$$\left[\sum_{s=1}^{\infty}\frac{e - (s\psi_s^2/r_p^2)l}{\psi_s^2}\right.$$

$$+ \sum_{m=0}^{\infty}\sum_{s=1}^{\infty}\frac{A_m P_m(a)}{\psi_s^2 - a^2\beta_m^2}$$
$$\cdot e^{-(s\beta_m^2/R^2)l}$$

$$\left. - \sum_{m=0}^{\infty}\sum_{s=1}^{\infty}\frac{A_m P_m(a)}{\psi_s^2 - a^2\beta_m^2}\right.$$
$$\left. \cdot e^{-(s\psi_s^2/r_p^2)l}\right]$$

The average-temperature difference is expressed as a logarithmic average by heat balance around the pipe.

In these theoretical calculations more calculations of β_m would result in greater application of the theoretical solution. To compute β_m to such an extent however requires much labor. It is convenient to use the following approximate solutions when the Graetz number is large.

Approximate Solution

The basic equation for heat transfer is presented as

$$u_y\frac{\partial t}{\partial y} = k\frac{\partial^2 t}{\partial x^2} \tag{2.1}$$

Velocity u_y is the same as that in Equation (1.3) and is near the pipe wall. If $r = R - x$ and $x \ll R$, the following equation is derived:

$$u_y = \frac{4(1-a)}{4a\alpha}\frac{\bar{u}x}{R} \tag{2.2}$$

Equation (2.1) becomes

$$\frac{4(1-a)\bar{u}}{4a\alpha kR}x\frac{\partial t}{\partial y} = \frac{\partial^2 t}{\partial x^2} \tag{2.3}$$

If the following equation is defined as

$$\frac{4(1-a)\bar{u}}{4a\alpha kR} = U \tag{2.4}$$

Equation (2.3) can be solved:

$$\left.\begin{aligned}\frac{h_M D}{\lambda} &= 1.62\left\{\left(\frac{\bar{u}D^2}{kl}\right)\left(\frac{1-a}{4a\alpha}\right)\right\}^{\frac{1}{3}}\\ &= 1.75\left\{\left(\frac{WC_p}{\lambda l}\right)\left(\frac{1-a}{4a\alpha}\right)\right\}^{\frac{1}{3}}\end{aligned}\right\} \tag{2.5}$$

$$\theta_{Ml} = 1 - 5.50\left(\frac{WC_p}{\lambda l}\right)^{-\frac{1}{3}}$$
$$\cdot\left(\frac{1-a}{4a\alpha}\right)^{\frac{1}{3}} \tag{2.6}$$

and Equation (2.5) is applicable in the following range:

$$\left(\frac{WC_p}{\lambda l}\right)\left(\frac{1-a}{4a\alpha}\right) > 1,000 \tag{2.7}$$

In other words when the left term in the equation is greater than 1,000, an approximate solution can be used. $\{(1-a)/4a\alpha\}$ is the only function of a. Calculated results are shown in Figure 2 and Table 1.

Theoretical Solution When Flow Is Rodlike and Wall Temperature Is Not Constant

These calculations were based on constant wall temperature. In many practical cases however wall temperature is not constant is a function of y position. Moreover the velocity distribution generally is a function of ζ; therefore computation requires much labor. The following calculations are based on rod-like flow $a = 1$, where wall temperature is not constant.

When $a = 1$, Equation (1.8) becomes

$$S = k/\bar{u} \tag{3.1}$$

If $S = k/\bar{u}$ and $r_p = R$ are substituted in Equation (1.34), the wall temperature is the solution of $F(y)$.

$$\theta_p = 2\sum_{s=1}^{\infty}\frac{J_0\left(\psi_s\dfrac{r}{R}\right)}{\psi_s J_1(\psi_s)}$$

$\cdot e^{-\pi \psi_s{}^2 (\lambda y/WC_p)}$

$$+ 2\pi \frac{\lambda}{WC_p} \sum_{s=1}^{\infty} \frac{\psi_s J_0\left(\psi_s \frac{r}{R}\right)}{J_1(\psi_s)} \quad (3.2)$$

$$\cdot \int_0^y F(v) e^{-\pi \psi_s{}^2 (\lambda/WC_p)(y-v)} \, dv$$

where θ_p is the same as that in Equation (1.23). Since wall temperature varies along the y axis, t_w is defined as the wall temperature at $y = 0$, and t_{wy} as the wall temperature at $y = y$.

$$t_{wy} = (1 + C_y)t_w \quad (3.3)$$

Wall temperature is assumed to change linearly. The boundary condition in this case is

$$\theta_p = 1, \ (t = t_1) \quad \text{at} \quad y = 0$$

$$\theta_p = F(y) = Ct_w y/(t_1 - t_w) \quad (3.4)$$

$$\text{at} \quad r = R$$

From Equations (3.2) and (3.4)

$$\theta_p = 2 \sum_{s=1}^{\infty} \frac{J_0\left(\psi_s \frac{r}{R}\right)}{\psi_s J_1(\psi_s)}$$

$$\cdot e^{-\pi \psi_s{}^2 (\lambda y/WC_p)}$$

$$+ \frac{Ct_w}{t_1 - t_w} \frac{y}{\pi(\lambda y/WC_p)} \quad (3.5)$$

$$\left[\pi\left(\frac{\lambda y}{WC_p}\right) - \frac{1}{4}\left\{1 - \left(\frac{r}{R}\right)^2\right\}\right]$$

$$+ 2 \sum_{s=1}^{\infty} \frac{J_0(\psi_s \cdot r/R)}{\psi_s{}^3 J_1(\psi_s)}$$

$$\cdot e^{-\pi \psi_s{}^2 (\lambda y/WC_p)}\Bigg]$$

This equation is the same as that derived from integration (1). When Equation (3.5) was derived, the Fourier-Bessel series (3) was used.

$$\sum_{s=1}^{\infty} \frac{J_0(\psi_s \cdot r/R)}{\psi_s{}^3 J(\psi_s)} = \frac{1}{8}\left\{1 - \left(\frac{r}{R}\right)^2\right\}$$

Average temperature is expressed as;

$$\theta_M = 4 \sum_{s=1}^{\infty} \frac{1}{\psi_s{}^2} e^{-\pi \psi_s{}^2 (\lambda y/WC_p)}$$

$$+ \frac{ct_w}{t_1 - t_w} \frac{y}{\pi(\lambda y/WC_p)}$$

$$\left[\pi\left(\frac{\lambda y}{WC_p}\right) - \frac{1}{8} + 4\right] \quad (3.6)$$

$$\cdot \sum_{s=1}^{\infty} \frac{1}{\psi_s{}^4} e^{-\pi \psi_s{}^2 (\lambda y/WC_p)}\Bigg]$$

The local coefficient of heat transfer and the average coefficient of heat transfer are considered to be the same as

when the theoretical solution was obtained.

$$\frac{h_M D}{\lambda} = \frac{1}{\pi}\left(\frac{WC_p}{\lambda l}\right) \ln\left(\frac{1}{\theta_{Ml}}\right) \quad (3.7)$$

The average-temperature difference is expressed as a logarithmic mean. If the average temperature θ_M in Equation (3.6) is expressed as θ_{Ml} at $y = 1$,

$$\theta_{Ml} = 4 \sum_{s=1}^{\infty} \frac{1}{\psi_s{}^2} e^{-\pi \psi_s{}^2 (\lambda l/WC_p)}$$

$$+ \frac{Ct_w}{t_1 - t_w} \frac{l}{\pi(\lambda l/WC_p)}$$

$$\left[\pi\left(\frac{\lambda l}{WC_p}\right) - \frac{1}{8}\right] \quad (3.8)$$

$$+ 4 \sum_{s=1}^{\infty} \frac{1}{\psi_s{}^4} e^{-\pi \psi_s{}^2 (\lambda l/WC_p)}\Bigg]$$

When wall temperature is constant, $C = 0$ in Equation (3.3), and average temperature θ_{Ml} is expressed by only the first term in Equation (3.8). The average Nusselt number can be calculated by giving the values $(WC_p/\lambda l)$, t_w, t_1, and C in Equation (3.8).

CALCULATIONS AND CONSIDERATIONS

In the calculation of $a = 0.5$, since B_m is a function of β, β_m' is obtained by calculating $\sum_{m=0}^{\infty} B_m \beta_m$ and is shown in Table 2, where odd numbers of B_m' are all zero. From Equation (1.15),

$$P(\beta) = \sum_{m=0}^{\infty} B_m \beta^m$$

$$= \sum_{m=0}^{\infty} B_m' \beta_m = 0 \quad (4.1)$$

When one calculates the roots β_m in Equation (4.1)

$$\beta_0 = 2.64150$$

$$\beta_1 = 6.6544 \quad (4.2)$$

$$\beta_2 = 10.654$$

P_m was calculated from Equation (1.17), and the results are shown in Figure 3 and Table 3. The value $1/\beta_m{}^2 \cdot [\zeta dP_m/d\zeta]_{\zeta=a}{}^{\zeta-1}$ is given as

$$\frac{1}{\beta_0{}^2}\left[\zeta \frac{dP_0}{d\zeta}\right]_{\zeta=a}^{\zeta=1}$$

$$= -9.8878 \times 10^{-2}$$

$$\frac{1}{\beta_1{}^2}\left[\zeta \frac{dP_1}{d\zeta}\right]_{\zeta=a}^{\zeta=1} \quad (4.3)$$

$$= 7.6542 \times 10^{-2}$$

$$\frac{1}{\beta_2{}^2}\left[\zeta \frac{dP_2}{d\zeta}\right]_{\zeta=a}^{\zeta=1}$$

$$= -2.265 \times 10^{-2}$$

A_m was obtained by graphical integration from Equation (1.20)

$$A_0 = 1.5219$$

$$A_1 = -2.660 \quad (4.4)$$

$$A_2 = 1.504$$

The value of θ_{Ml} was obtained from Equation (1.14):

$$\theta_{Ml} = 0.9192 e^{-15.562(\lambda l/WC_p)}$$

$$- 0.0892 e^{-51.746(\lambda l/WC_p)} \quad (4.5)$$

$$+ 0.502 e^{-98.54(\lambda l/WC_p)}$$

$$- 0.303 e^{-252.58(\lambda l/WC_p)} + \cdots$$

The relationship between $(1 - \theta_{Ml})$ and the Graetz number must be related to the relative plug radius. Two extreme cases, that is $a = 1$ and $a = 0$, were considered. When $a = 1$, $(1 - \theta_{Ml})$ is obtained by using $C = 0$ (see Section on theoretical solution when flow is rodlike and wall temperature is not constant).

$$1 - \theta_{Ml} = 1 - 4$$

$$\cdot \sum_{m=0}^{\infty} e^{-\pi \psi_s{}^2 (\lambda l/WC_p)}/\psi_s{}^2 \quad (4.6)$$

When the Graetz number in Equation (4.6) is increased, the approximate solution at $n = \infty$ is obtained:

$$1 - \theta_{Ml} = 4(WC_p/\lambda l)^{-1/2} \quad (4.7)$$

When $a = 0$, the fluid corresponds to viscous fluid; that is, $n = 1$. When the Graetz number is above 1,000, the relationship between $(1 - \theta_{Ml})$ and the Graetz number can be obtained by using $a = 0$ in Equation (2.6).

$$1 - \theta_{Ml} = 5.50(WC_p/\lambda l)^{-2/3} \quad (4.8)$$

When $a = 0.5$, Equation (4.5) can be used. When the Graetz number is large, the following equation obtained from Equation (2.6) may be used:

$$1 - \theta_{Ml} = 6.17(WC_p/\lambda l)^{-2/3} \quad (4.9)$$

The relation between $(1 - \theta_{Ml})$ and the Graetz number at three a values is shown in Figure 4.

The average Nusselt number vs. Graetz number calculated from Equation (1.43) is shown in Figure 5; the relation is linear when the Graetz number is greater than 100. By comparing Equation (1.43) with (2.5) the following equation holds when $\{(WC_p/\lambda l)(1 - a)/4a\alpha\} > 100$.

$$\frac{h_M D}{\lambda} = 1.75\left\{\left(\frac{WC_p}{\lambda l}\right)\left(\frac{1 - a}{4a\alpha}\right)\right\}^{\frac{1}{3}} \quad (4.10)$$

COMMUNICATIONS
TO THE EDITOR

Flow Measurements with Ball Meters

P. V. DANCKWERTS

Imperial College of Science and Technology, South Kensington, London, England

The communication from Shulman and van Wormer (1) on this subject appeared while a similar investigation was in progress in this department. Although the correlation equation (4) proposed by these authors is sound, the arguments leading to it are oversimplified. In its equilibrium position the ball comes to rest in contact with the outermost part of the wall of the tube; generally there will be a tangential frictional force acting on the ball at the point of contact.

When the ball is at equilibrium, the moments about its point of contact with the tube wall balance. The tangential component of gravitational force on the ball is ($W \sin \theta$) and acts through the center of the ball. The hydrodynamic force on the ball is f; its resultant will almost certainly be off-center, and so instead of acting through the center of the ball it acts through a point distant X from the wall (Figure 1). Assuming that the radius of curvature of the tube is irrelevant (this is justified by experiment), one finds that the quantities $(f/A_b \rho_f u^2)$ and (X/D_b) are functions of

(D_b/D_t) and the Reynolds number only When one equates moments,

$$\frac{wD_b}{2} \cdot \sin \theta = fX \qquad (1)$$
$$= A_b D_b \rho_f u^2 \cdot F(Re, D_b/D_t)$$

This can be reduced to a form identical with Equation (4) of Shulman and van Wormer, but their empirically determined coefficient C has a significance different from that which they assign to it, unless f acts through the center of the ball.

If f is off-center ($X \neq D_b/2$), the ball will spin at high values of θ because the frictional force required to stop it from spinning exceeds the limit imposed by the coefficient of friction, μ. This will occur when

$$\tan \theta \gtrless \left| \frac{\mu}{1 - D_b/2X} \right|, \qquad \left(\theta < \frac{\pi}{2}\right) \qquad (2)$$

Thereafter a different analysis must be
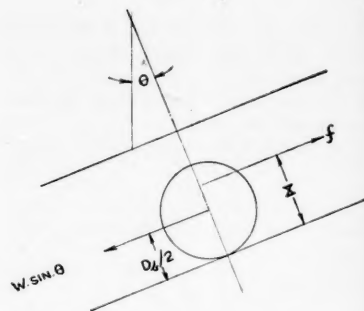
Fig. 1.

applied. There is thus a limit to the value of θ to which the correlation equation (4) can be applied, and the limit depends on the coefficient of friction between the ball and the tube, which may in part be determined by the physical properties of the fluid.

The direction of spin will be clockwise (Figure 1) if $X > D_b/2$ and counterclockwise if $X < D_b/2$. If the force f acts through the center of the ball ($X = D_b/2$), the ball will not spin at any value of θ. Observation shows that the ball actually spins clockwise.

LITERATURE CITED

1. Shulman, H. L., and K. A. van Wormer, A.I.Ch.E. Journal, 4, 380 (1958).

Reply

H. L. SHULMAN

Clarkson College of Technology, Potsdam, New York

Professor Danckwerts's rigorous treatment of the ball flow meter leads to an equation which is identical with our Equation (4), but it has the advantage of predicting the onset of spinning at high values of θ. We observed this phenomenon and found that at still higher values of θ the ball not only spins but tends to move to and away from the outer wall. When this occurred, the the meter reading θ did not remain constant for a constant flow rate. For this reason, we pointed out, readings were not taken above 60°, and we recommend

that the meters be designed conservatively for a midscale reading of 25° to 30°.

The correlation presented applies only when the ball is at rest, that is when it is not spinning. Unfortunately Professor Danckwerts's Equation (2) cannot be used to predict the onset of spinning unless the coefficient of friction is known and a method developed to predict X. Until this information is available, the conservative design method is recommended, and the calculated calibration curve should not be used at values of θ above the observed onset of spinning.

ERRATUM

The caption for Figure 7 in "Heat Transfer to a Liquid Fluidized Bed" by Robert Lemlich and Isidoro Caldas, Jr., appearing on page 377 of the September, 1958, issue, should read: *Effect of flow rate and particle diameter on heat transfer, with methanol as the heating medium.* (*Symbols are identified in Figure 5.*)

It is unfortunate that in a number of studies on the evaporation of solids and liquids at low pressures the influence of heat transfer has not been properly taken into account. The result is that the true temperature of the evaporating surface was not used in the analysis of the data and so the reported evaporation coefficients are in error.

A case in point is the very low value for the evaporation coefficient of naphthalene recently reported by Sherwood and Cooke (5). This value appears to be low by at least an order of magnitude, owing to a temperature depression of the surface of the evaporating naphthalene sphere which was not considered. The authors indicate that, since the evaporation rate was very small, the evaporative cooling of the surface was negligible. At first glance this seems to be quite reasonable, since only 0.178 g. was evaporated in 1 hr. at the highest rate, and the heat requirement for sublimation amounts to a mere 24 cal. Indeed the very low heat duty of 24 cal./hr. would suggest no problem. However at a pressure of 0.1 μ Hg substantially all heat reaching the sphere must be supplied by radiation from the enclosure walls, and a rather sizable temperature difference is required. With the enclosure maintained at 0°C. the equivalent radiant heat transfer coefficient is about 0.36 cal./(hr.) (sq. cm./°C.). (This is the maximum coefficient when all emissivities are assumed to be 1.0.) Hence the sphere, 1.0 cm. in diameter, evaporating at a pressure of 0.1 μ, would tend to attain a steady-state surface temperature of about −21°C. It is to be noted that the vapor pressure of naphthlene at −21°C. is about 0.38 μ Hg compared with 5.74 μ Hg at 0°C.

With the true vapor pressure of the surface introduced into Equation (1) of their paper and the evaporation coefficient assumed to be unity, the maximum evaporation rate at a pressure of 0.1 μ Hg would be about 0.177 g./hr. This agrees almost exactly with the observed result. Thus it appears that the evaporation coefficient of naphthalene is in reality close to unity, and the low apparent value reported (about 0.056) merely reflected the temperature depression of the naphthalene surface. The same argument also suggests that the true evaporation coefficient of diethyl adipate is close to unity, rather than 0.177 as reported.

While the largest temperature depression of the surface was encountered in the experiments at the lowest pressure, 0.1 μ, where heat transfer to the sphere was most unfavorable, some temperature depression also was involved at the higher pressures studied. This temperature depression tended to decrease with increasing pressure for two reasons: (1) increased diffusional resistance in the gas reduced the evaporation rate and

hence the required heat duty, and (2) heat transfer to the sphere was improved at the higher pressures because of increased heat conduction through the gas.

As the evaporation of spheres (or drops) has been studied in a number of cases, a general equation has been developed for predicting the temperature depression of the surface accompanying evaporation into a quiescent gas at low pressures. The equation is shown to reduce to simplified forms for the limiting cases of very low pressures and relatively high pressures. The term *relatively* high pressures is used, as the pressure must be low enough to assure the absence of convection. As a rough guide, the upper pressure limit would be of the order of 1 mm. Hg.

EVAPORATION OF SPHERES AT LOW PRESSURES

The evaporation rate for a sphere in a gas at low pressures has been considered in detail by Bradley, Evans, and Whytlaw-Gray (1). Considering the enclosure to be very large and the concentration of the evaporating substance to be zero at the walls of the enclosure, one can develop the following equation for the rate of evaporation:

$$-\frac{dm}{dt} = \frac{4\pi a\, D_v C_s}{\dfrac{D_v}{\alpha_M \Upsilon a} + \dfrac{a}{a + \Delta}}$$

$$= \frac{4\pi a^2 C_s}{\dfrac{1}{\alpha_M \Upsilon} + \dfrac{a^2}{(a + \Delta)\, D_v}} \quad (1)$$

This equation was developed on the basis of an evaporation model proposed by Fuchs (2). In his treatment evaporation from the sphere occurs through a surrounding vacuous shell of thickness Δ at the theoretical vacuum rate. In the steady state, molecules arriving at the shell surface at a distance $a + \Delta$ from the sphere center leave by diffusion through the gas.

Under high vacuum conditions, where $\Delta \gg a$, and $a/(a + \Delta) \to 0$, this equation reduces to the familiar form for the evaporation rate in an absolute vacuum:

$$-\frac{dm}{dt} = 4\pi a^2 \alpha_M \Upsilon C_s \quad (2)$$

HEAT TRANSFER TO A SPHERE AT LOW PRESSURES

When one follows the evaporation model of Fuchs, heat conduction to the sphere may be assumed to take place in the following manner. Conduction occurs

through the gas up to the outer surface of the vacuous shell and then by free molecule conduction across the vacuous shell to the sphere surface. A similar argument was used previously by Kyte, Madden, and Piret (4).

The heat flow to the sphere by conduction through the gas will then be given by an equation analogous to Equation (1),

$$\frac{dQ_c}{dt} = \frac{4\pi a^2 (T_\infty - T_s)}{\dfrac{1}{\alpha_H\,\Lambda_0 P \sqrt{\dfrac{T_s}{273}}} + \dfrac{a^2}{(a + \Delta)k}} \quad (3)$$

At low pressures, where $\Delta \gg a$, Equation (3) reduces to

$$\frac{dQ_c}{dt} = 4\pi a^2 \alpha_H\,\Lambda_0 P$$
$$\cdot \sqrt{\frac{273}{T_s}}\,(T_\infty - T_s). \quad (4)$$

This will be recognized as the equation for heat transport by free molecule conduction. At the other extreme, where the gas pressure is relatively high, $\Delta \ll a$, Equation (3) reduces to

$$\frac{dQ_c}{dt} = 4\pi a k (T_\infty - T_s) \quad (5)$$

the usual equation for heat conduction to a sphere through a surrounding infinite medium.

The total heat transfer to a sphere will include simultaneous radiant heat transfer. Hence the total heat transfer may be represented by

$$\frac{dQ}{dt} = \left[h_r \right.$$
$$\left. + \frac{1}{\dfrac{1}{\alpha_H\,\Lambda_0 P \sqrt{\dfrac{T_s}{273}}} + \dfrac{a^2}{(a + \Delta)k}} \right] \quad (6)$$
$$\cdot 4\pi a^2 (T_\infty - T_s)$$

HEAT BALANCE

In the steady state the heat transfer to the sphere will satisfy the latent heat requirement for evaporation (or sublimation). Hence

$$-\frac{dm}{dt} = \frac{1}{L_v}\frac{dQ}{dt} \quad (7)$$

thus

$$\frac{4\pi a^2 C_s}{\dfrac{1}{\alpha_M \Upsilon} + \dfrac{a^2}{(a + \Delta)\, D_v}}$$

$$= \left[h_r \right.$$

$$+ \frac{1}{\dfrac{1}{\alpha_H \, \Lambda_0 P \sqrt{\dfrac{T_s}{273}}} + \dfrac{a^2}{(a + \Delta)k}} \right] \tag{8}$$

$$\cdot \frac{4\pi a^2 (T_\infty - T_s)}{L_v}$$

Equation (8) may be rearranged to give

$$C_s = \left[\frac{1}{\alpha_M \Upsilon} + \frac{a^2}{(a + \Delta) \, D_v} \right] \left[h_r \right.$$

$$+ \frac{1}{\dfrac{a^2}{(a + \Delta)k} + \dfrac{1}{\alpha_H \, \Lambda_0 P \sqrt{\dfrac{T_s}{273}}}} \right] \tag{9}$$

$$\cdot \frac{(T_\infty - T_s)}{L_v}$$

The heat balance, Equation (9), gives one relationship for C_s and hence p_s as a function of the surface temperature. Simultaneous solution of this with the vapor-pressure–temperature relationship for the substance enables one to determine the surface temperature.

LIMITING CASES

At very low pressures conduction through gas becomes negligible, and all heat transfer is by radiation. Also since D_v varies inversely with gas pressure, the term $a^2/[(a + \Delta)D_v]$ becomes very small. For this case Equation (9) reduces to

$$C_s = \frac{h_r (T_\infty - T_s)}{\alpha_M \Upsilon L_s} \tag{10}$$

At higher pressures, $\Delta \ll a$, $1/(\alpha_M \Upsilon) \ll a/D_v$, and $[1/(\alpha_H \Lambda_0 p \sqrt{T_s/273})] \ll a/k$, Equation (9) becomes

$$C_s = \frac{a}{D_v} \left[h_r + \frac{k}{a} \right] \left(\frac{T_\infty - T_s}{L_v} \right) \tag{11}$$

If in addition the sphere diameter is small, radiant heat transfer will be small compared with that by conduction, and Equation (11) simplifies further to

$$C_s = \frac{k}{D_v} \left(\frac{T_\infty - T_s}{L_s} \right) \tag{12}$$

Equation (12) with a slight modification was used by Johnson (3) in analyzing measurements of the surface temperature of evaporating water drops. (In Johnson's case the left-hand side of the equation was given as $C_s - C_\infty$, where C_∞ is the concentration of water vapor in the ambient gas. In the present case C_∞ was assumed to be zero by use of a suitable absorbent.)

A few measurements have been made of the temperature depression of a hollow sphere, coated with naphthalene, evaporating in air inside an 18-in.–diameter bell jar. In the pressure range 500 to 800 μ Hg the results agree rather well with the prediction of Equation (11). Further experimental work is in progress to cover a wider pressure range. The assistance of the National Science Foundation under grant G1617 is gratefully acknowledged.

NOTATION

a = sphere radius
C_s = concentration of evaporating substance in gas in equilibrium with sphere surface
D_v = diffusivity of evaporating substance in gas
e = emissivity
h_r = coefficient for radiant heat transfer

$$\equiv \frac{e\sigma(T_\infty{}^4 - T_s{}^4)}{T_\infty - T_s}$$

k = gas thermal conductivity
L_v = latent heat of evaporation (or sublimation) per unit mass of evaporating substance
M = molecular weight of evaporating substance
P = gas pressure
T_∞ = temperature of enclosure walls
T_s = temperature of evaporating surface, sphere surface temperature

Greek Letters

α_H = evaporation coefficient
α_H = thermal accomodation coefficient
Δ = distance of order of one mean free-path length
Λ_0 = free molecule heat conductivity at $0°C.$
σ = Boltzmann's constant

$$\Upsilon = \sqrt{\frac{RT_s}{2\pi M}}$$

LITERATURE CITED

1. Bradley, R. S., M. G. Evans, and R. W. Whytlaw-Gray, *Proc. Roy. Soc.* (*London*), **186A**, 368 (1946).
2. Fuchs, N., *Phys. Z. Sowjet*, **6**, 225 (1934); trans.: *Natl. Advisory Comm. Aeronaut. Tech. Memo.* 1160, (Aug., 1947).
3. Johnson, J. C., *J. Appl. Phys.*, **21**, 22 (1950).
4. Kyte, J. R., A. J. Madden, and E. L. Piret, *Chem. Eng. Progr.*, **49**, 653 (1953).
5. Sherwood, T. K., and N. E. Cooke, *A.I.Ch.E. Journal*, **3**, 37 (1957).

Reply

T. K. SHERWOOD and N. E. COOKE, Massachusetts Institute of Technology, Cambridge, Massachusetts

Professor Madden's suggestion that the surface temperature of the naphthalene sphere employed in our study must have fallen considerably below 0°C. seems to be correct. We had reached the same conclusion shortly after our article appeared in print, when we noted the paper by Littlewood and Rideal (1). In effect these authors questioned practically all the values of accommodation coefficients reported in the literature, suggesting that few, if any, had been based on reliable measurements of surface temperature. This led us to repeat an earlier calculation of the temperature depression owing to evaporation, and we found that we had indeed made an error in the calculation of some two years previous which had indicated the effect to be trivial. To rectify the situation work was undertaken along two lines.

First, following a suggestion of H. C. Hottel, Conrad Johannes initiated an experimental study to employ a radiometer for the accurate measurement of the surface temperature of a solid subliming at low pressure. The necessary equipment is complex, and it will be some time yet before the results can be reported.

Second, the data which we had obtained were analyzed carefully to see whether the accommodation coefficient might not be calculated by allowing for the cooling of the surface of the naphthalene spheres.

In a series of eleven tests below 3μ the rate of sublimation decreased during the first hour but remained quite constant at 0.0344 cm. (radius)/hr. during the subsequent 1-hr. period. When one assumes the surroundings to be at 0°C., the following values of the equilibrium surface temperature and accommodation coefficient are calculated for various assumed values of the emissivity of the surface:

Emissivity	0.927	0.878	0.833	0.794
Temperature, °C.	−16	−17	−18	−19
Accommodation coefficient	0.336	0.381	0.434	0.494

If the emissivity is taken to be 0.85 (2), the calculated accommodation coefficient is about 0.41—considerably greater than the value which we reported but much smaller than the value unity, suggested by Professor Madden.

This discussion would appear to emphasize the point of Littlewood and Rideal's paper: that reliable values of accommodation coefficients require accurate measurements of the surface temperature of the evaporating substance.

LITERATURE CITED

1. Littlewood, R., and Eric Rideal, *Trans. Faraday Soc.*, **52**, 1598 (1956).
2. Mathers, W. G., A. J. Madden, and E. L. Piret, *Ind. Eng. Chem.*, **49**, 961 (1957).

Fluidized-bed Heat Transfer Correlation

MAX LEVA and C. Y. WEN

In the March, 1958, issue of the *A. I. Ch. E. Journal* Wender and Cooper published a fluidized-bed heat transfer correlation which is open to question on a number of counts. It is the purpose of this discussion to elaborate on a few of these aspects.

It must be regretted that the authors did not include the data of van Heerden and coworkers in their analysis. Some of the exterior-wall–fluidized-bed heat transfer studies more frequently referred to are indicated in the accompanying tabulation, and it is readily seen that the van Heerden study is the most comprehensive. The experiments were carefully designed to disclose the complicated effects of the system variables, and the quality of the work and its accuracy are high. Hence much would have been gained had the authors chosen to use these data.

As the reason for omitting the van Heerden data from their analysis the authors cited the fact that van Heerden and co-workers did not accompany their data with bed-voidage values. This reason is however difficult to accept, especially as the final correlation of the authors contains a bed-voidage term, which must somehow be predictable in advance if their correlation is to have any application at all. There are several methods which permit estimation of the bed voidage with quite good results, and it is hard to conceive that the authors were not aware of some of these. One of the methods was published as early as 1951 (1). Over the years it has been thoroughly tested and found to apply to many sets of data quite satisfactorily. It has therefore been applied to the van Heerden data in order to examine what agreement there is between these and the exterior-wall–bed correlation of the

Max Leva is a consultant engineer in Pittsburgh, Pennsylvania, and C. Y. Wen is at West Virginia University, Morgantown, West Virginia.

authors. The comparison is given in the accompanying graph. Merely three sets of data have been selected for this demonstration. The solids chosen are all nonvesicular; hence there is little likelihood that the calculated voidages are in substantial error. But even if these voidages were in error by, say, 1 to 5 percentage points, as they conceivably could in the limit be, the magnitude of the calculated heat transfer coefficients and their path would not be greatly different. In addition to the data shown in Figure 1 other runs pertaining to a number of other solids and gases were examined similarly, and the comparisons with the proposed correlation were of the same order as is shown by these selected data.

Considering first comparison 1, one sees a fine agreement at $Re = 0.1$; however at $Re = 2.0$ van Heerden reported an experimental coefficient of about 75 B.t.u./(hr.)(sq. ft.)(°F.), whereas the correlation predicts a value of nearly 200 B.t.u./(hr.)(sq. ft.)(°F.) This is a very severe deviation in a wrong and unsafe direction, as far as application to design is concerned. The reason for the deviation is of course that the correlation does not incorporate properly the functional relationship between fluid mass velocity and bed expansion.

In comparison 2 a solid of essentially similar physical properties and virtually the same particle diameter has been fluidized, but with a gas of much greater thermal conductivity and lesser density. First one observes that the course of the calculated data is still the same as in comparison 1, and hence at variance with the experimental values. It appears in addition that now the calculated data are for the greater part much lower than the experimental data. This severe deviation leads to the conclusion that the correlation apparently does not properly

account for the thermal and any other physical properties of the fluidizing fluid.

A third comparison is shown which pertains to a larger solid, fluidized at a higher range of Reynolds numbers. Here again the calculated data are unduly high, though the course of the calculated data is now in agreement with the path of the experimental values. As a matter of general interest the data predicted by our generalized correlation are shown (2).

In closing this discussion, we appreciate the immense amount of tedious calculation procedure, plotting, and cross plotting which is associated with this working method. However, though the numbers of runs covered and cited in support of a correlation may be quite impressive, it is doubtless of more value to point out the reasons why some particular data points may fail to agree, simply because such lack of agreement may hold the key to a basic understanding of the phenomenon. Unfortunately this has not been achieved in this work to the extent which would have been desirable and constructive. It must be borne in mind that apparatus details, such as gas-inlet devices, hence entrance effects, exposed bed sections, temperature-measuring devices, and other internals in the bed must affect fluidization performance and therefore the heat transfer coefficients.

Little if anything at all will be said about the internal surface-bed correlation. It is of an entirely different form and type from the exterior-wall–bed correlation. Nevertheless both expressions refer to one and the same phenomenon, namely fluidization, occuring though under somewhat different conditions. The question may rightly be asked whether in the light of two such different formulations as have been proposed, a unified correlation for both external as well as internal surface data is possible.

LITERATURE CITED

1. Leva, Max, *et al.*, *U. S. Bur. Mines, Bull. No. 504* (1951).
2. Wen, C. Y., and Max Leva, *A. I. Ch. E. Journal*, **2**, 482 (1956).

EXPERIMENTAL VARIABLES, DENSE PHASE DATA

Investigator	Materials	D_p - feet	Solids Density lbs/ft³	Fluids
van Heerden et al	Carborundum, Iron Oxide, Coke, Lead, Fly Ash, Dev Alloy	0.000262 to 0.00213	112 — 694	Air, Argon, CH₄ CO₂, Town Gas H₂+N₂ mixtures
Dow - Jakob	Aerocat, Coke, Iron Powder	0.000252 - 0.000560	121 — 466	Air
Leva et al	Sand, Fe-Catalyst Silica Gel	0.000129 - 0.00149	80 — 500	Air, CO₂, Helium
Toomey - Johnstone	Glass Beads	0.000179 to 0.00278	167 — 179	Air
Bartholomew - Katz	Sand, Aluminum Powder, Ca CO₃	0.000277 - 0.000822	160 — 167	Air

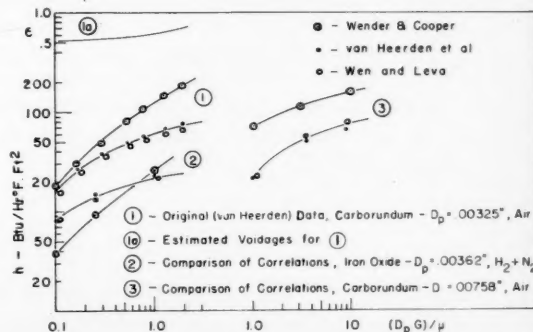**Fig. 1. Some typical data of van Heerden, and how they are predicted by the correlation of Wender and Cooper.**

This means that the approximate solution can be used in a wider range. When the Graetz number becomes smaller, the average Nusselt number becomes

$$\left(\frac{h_M D}{\lambda}\right)_{(WC_p/\lambda l)\to 0} \quad (4.11)$$

$$= \frac{2a\alpha}{(1-a)^2}\beta_0{}^2 = 4.94$$

When $a = 0.5$, the average Nusselt number is not theoretically existent below 4.94.

Example

Average bulk temperature and average temperature at the exit of the pipe, when synthetic resin powder at 20°C. is extruded by the piston at the rates of 2.0 and 0.2 cm./sec., are computed. The resin has the following characteristics: heat conductivity = 0.14 kcal./meter-hr. (°C.), specific heat = 0.4 kcal./(kg.)(°C.) and density = 1,400 kg./cu. meter. The dimensions of the pipe are 1 meter in length and 3 cm. in diam. The pipe is heated externally and the wall temperature changed linearly with the axis, if it is assumed that 150°C. at the inlet and 200°C. at the exit are maintained.

Solution

This example is a practical case when synthetic resin is molded. In this case the information in the section on theoretical solution when flow is rodlike and

wall temperature is not constant can be applied; thus $t_1 = 20$°C., $t_w = 150$°C., and $t_{w1} = 200$°C. From Equation (3.3) $C = \frac{1}{3}$. Graetz numbers are

$$WC_p/\lambda l = 203.55$$

$$\text{at } \bar{u} = 2.0 \text{ cm./sec.}$$

$$WC_p/\lambda l = 20.35$$

$$\text{at } \bar{u} = 0.2 \text{ cm./sec.}$$

The bulk temperature at the exit is obtained from Equation (3.5)

$$\theta_{pl0} = 2\sum_{s=1}^{\infty} e^{-\pi\psi_s{}^2(\lambda l/WC_p)}/\psi_s J_1(\psi_s)$$

$$+ \frac{ct_w}{t_1 - t_w}\frac{l}{\pi(\lambda l/WC_p)}\left[\pi\left(\frac{\lambda l}{WC_p}\right) - \frac{1}{4}\right]$$

$$+ 2\sum_{s=1}^{\infty} e^{-\pi\psi_s{}^2(\lambda l/WC_p)}/\psi_s{}^3 J_1(\psi_s)\Bigg]$$

In the case of $\bar{u} = 0.2$ cm./sec. from the table of Bessel function

$$\psi_1 = 2.40483 \quad J_1(\psi_1) = 0.51915$$

$$\psi_2 = 5.52008 \quad J_1(\psi_2) = -0.34026$$

$$\psi_3 = 8.65374 \quad J_1(\psi_3) = 0.27145$$

$$\psi_4 = 1.17915 \quad J_1(\psi_4) = -0.23246$$

$$\vdots \qquad \vdots \qquad \vdots$$

By substituting these values in this equation

$$\theta_{pl0} = (t_{pl0} - t_w)/(t_1 - t_w)$$

$$= 2\{3.2825 \times 10^{-1}$$

$$- 4.832 \times 10^{-3}$$

$$+ 7.109 \times 10^{-6} - \cdots\}$$

$$- 2.4924[-9.569 \times 10^{-2}$$

$$+ 2\{5.676 \times 10^{-2}$$

$$- 1.588 \times 10^{-4}$$

$$+ 9.49 \times 10^{-8} - \cdots\}]$$

$$= 0.6318$$

Therefore

$$t_{pl0} = 71.59°C.$$

The average temperature at the exit can be calculated from Equation (3.8), and the result is shown in Table 4. The bulk temperature is not different from the inlet temperature, even at Graetz number = 203, as shown in Table 4.

When the wall temperature is constant, θ_{Ml} can be obtained either from Figures 4 and 5 or from the equations in the section on theoretical solution when flow is rodlike and wall temperature is not constant by substituting $C = 0$. The calculated result is also given in Table 4. This shows that the average Nusselt number and the average coefficient of heat transfer at the constant wall temperature are considerably smaller than that in the case of increasing wall temperature along the y axis.

CONCLUSION

The results of this study show that the logarithmic mean of the difference between average bulk temperature and wall temperature can be used in the calculations of average Nusselt number or average heat transfer coefficient. The average bulk temperature at the exit is given in Equation (1.44). When $a = 0.5$, the average bulk temperature can be calculated by Equation (4.5).

Figure 5 shows the relationship between the Nusselt number and Graetz number. From both theoretical and approximate solutions the following equation was derived:

$$\frac{h_M D}{\lambda} = 1.75 \left\{ \left(\frac{WC_p}{\lambda l} \right) \left(\frac{1-a}{4a\alpha} \right) \right\}$$

when

$$\{(WC_p/\lambda l) \cdot (1-a)/(4a\alpha)\} > 100$$

When wall temperature changes linearly along the y axis and velocity distribution is rodlike flow, the logarithmic mean can be used as the average-temperature difference. It is assumed that the logarithmic mean can be used even in the case of laminar flow, where the velocity distribution is not the same as it is in rodlike flow.

BOOKS

Viscous Flow Theory I, Laminar Flow, Shih-I Pai, D. Van Nostrand Company, Inc. 384 pages.

The development of aircraft and missiles which travel at velocities in excess of the velocity of sound has necessitated much new research in the hydrodynamics of compressible fluids. For though it is possible to neglect the compressibility of air at low speeds (circa 200 miles per hour), this is not possible at higher speeds. The book under review is concerned with the laminar flow of viscous, compressible fluids with special attention to aerodynamics. Three major topics are discussed: (a) the classical hydrodynamic theory of fluids, including some elementary kinetic theory of gases; (b) generalizations derivable from the theory without explicit solution of the differential equations, such as similarity and dimensional analysis and general properties of the Navier-Stokes equation; and (c) boundary layer theory. The latter is by far the largest section, occupying some 216 pages. Considerable detail is given, and numerous tables of useful data are included in the text. Turbulent flow is treated in part II of this work.

This reviewer feels that the major omission from the text is a discussion of the properties of gases at extremely low pressures. Under circumstances prevailing in the upper atmosphere the mean free path of a molecule may easily be of the order of magnitude of the dimensions of the flying object. Under these conditions the relative
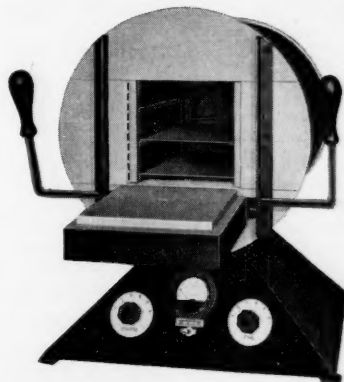
variation of macroscopic quantities over a mean free path is not negligible. For the limiting case of the Knudsen gas there are striking differences with phenomena under moderate pressures. For instance in Couette flow the force does not depend upon the velocity gradient but rather on the velocity difference; the force depends linearly on the pressure, etc. The transition region between ordinary gas pressures and those for which Knudsen behaviour subsists has been the subject of several studies recently. As anticipated the results differ from those of classical hydrodynamics.

Despite this omission *Viscous Flow Theory* by Shih-I Pai is to be recommended to engineers and advanced students interested in the hydrodynamics of viscous compressible flow.

STUART A. RICE

Ion Exchange Resins, by Robert Kunin, John Wiley & Sons, Inc. 466 pages.

One of the first books on ion exchange, *Ion Exchange Resins* by Kunin and Myers, has been revised and doubled in length by Dr. Kunin. In the years since the first edition appeared, other books have been published which cover some portions of its subject more intensively. Still this volume is unique in its comprehensiveness.

The title of this book is not indicative of the range of its contents. A few chapters are devoted to the characteristics of anion and cation exchange resins and the synthesis of resins. A greater portion of the work deals with the technological aspects of specific applications of ion exchange.

Because the book is so broad in its coverage one cannot expect to find depth in all areas. Engineers interested in ion exchange rate theory or the principles of fixed bed will be disappointed by the treatment of these topics. On the other hand those concerned with the operation of commercial ion-exchange equipment will find one of the new chapters, "Stability of ion exchange resins," especially valuable because it brings together much information which hitherto was available only piece-meal in service literature from the manufacturers of resins.

Some of the topics treated are highly specialized, so it is unlikely that any one reader will be interested in the entire book. This applies particularly to some of the new chapters on the treatment of sugar and glycerine, hydrometallurgic applications, water softening, and catalysis with ion exchange resins. There is also a chapter covering the subject of permselective membranes from electrochemical theory to the economics of the treatment of waste pickle liquor which uses membrane cells.

There are unfortunately a number of incorrectly listed references, and in one case there is discussion of a figure which does not appear. When one considers that over a thousand references are listed, these few mistakes do not seriously impair its usefulness.

This book will be a well-used reference in the library of any company in the process industries. It provides an excellent starting point for any reading on ion exchange.
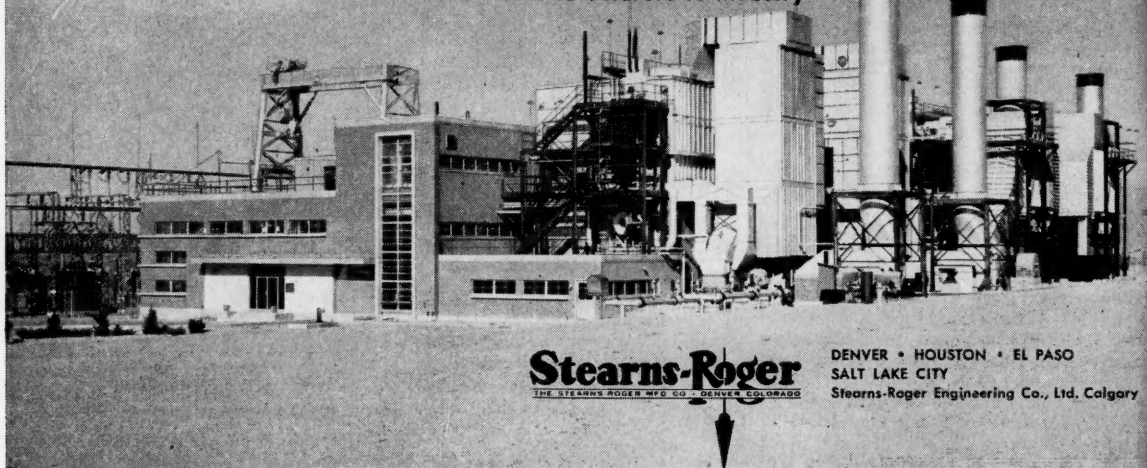
W. A. SELKE

Advertising Offices

New York 36—Lansing T. Dupree, Adv. Mgr.; Carl G. Lassen, Asst. Adv. Mgr.; Paul A. Jolcuvar, Dist. Mgr.; Donald J. Stroop, Dist. Mgr.; 25 W. 45th St., Columbus 5-7330.

Chicago 4—Martin J. Crowley, Jr., Dist. Mgr.; Robert Kliesch, Dist. Mgr.; 53 W. Jackson Blvd. Harrison 7-0382.

Cleveland 15—Harry L. Gebauer, Dist. Mgr., 434 Bulkley Bldg., Superior 1-3315.

Pasadena 1—Richard P. McKey, Dist. Mgr., 465 East Union St., Ryan 1-8779.

Dallas 18—Richard E. Hoierman, Dist. Mgr., 9006 Capri Drive, Diamond 8-1229.

Birmingham 9, Ala.—Fred W. Smith, Dist. Mgr., 1201 Forest View Lane—Vesthaven, Tremont 1-5762.

Mgr.;
ul A.
Dist.

Mgr.;
ackson

Mgr.,

., 465

Mgr.,

Mgr.,
emont

lgary